MOBILE COMMUNICATIONS SERIES

Radio Propagation in Cellular Networks

Nathan Blaunstein

Artech House Publishers

Radio Propagation in Cellular Networks

For a recent listing of titles in the *Artech House Mobile Communications Library*, turn to the back of this book.

Radio Propagation in Cellular Networks

Nathan Blaunstein

Artech House
Boston • London

Library of Congress Cataloging-in-Publication Data
Blaunstein, Nathan.
Radio propagation in cellular networks / Nathan Blaunstein.
p. cm. — (Artech House mobile communications library)
Includes bibliographical references and index.
ISBN 1-58053-067-2 (alk. paper)
1. Cellular telephone systems. 2. Radio wave propagation. 3. Radio—
Interference. I. Title. II. Series.
TK6570.M6 B53 1999 99-045836
621.3845—dc21 CIP

British Library Cataloguing in Publication Data
Blaunstein, Nathan
Radio propagation in cellular networks. — (Artech House
mobile communications library)
1.Wireless communication systems 2. Radio wave propagation
I. Title
621.3'8456

ISBN 1-58053-067-2

Cover design by Lynda Fishbourne

685 Canton Street
Norwood, MA 02062

International Standard Book Number: 1-58053-067-2
Cataloging-In-Publication: 99-045836

10 9 8 7 6 5 4 3 2 1

Contents

Preface

This book is intended to appeal to any practicing engineer and/or student who is concerned with the operation and service of cellular radio, including personal, local, fixed, and mobile wireless communication systems. It examines the different situations of wireless communication in an urban scene and various propagation phenomena that influence the transmission of radio signals through urban communication channels, both in line-of-sight (LOS) and obstructive (no line-of-sight (NLOS)) propagation conditions for the transmitter and receiver antennas. The phenomena treated include free-space propagation above regular and irregular terrain, reflection and diffraction by various obstacles (e.g., hills, buildings, trees) regularly or randomly distributed on the terrain (smooth or rough), effects of scattering from such obstacles and from the ground surface. In view of wireless-communications practice, behavior of waves in the UHF/L-frequency band is emphasized throughout.

In recent decades, the personal communication network was developed to satisfy continually increasing demands for personal, local, and mobile communications. The wireless local-loop system is now used in local networks, serving as an alternative to conventional loop-distribution networks. To design such systems successfully, it is important to predict the propagation characteristics of urban radio channels, to define optimal locations simultaneously for the base station (radio port) and for each local stationary and/or moving receiver, and to make performance prediction for the individual subscribers (stationary or moving).

This book presents the reader with the full picture of propagation mechanisms in cellular propagation channels, aspects that do not yet have a complete and finished form. Propagation phenomena are presented in many excellent books separately from other subjects, such as cellular map construction, signal

processing, and so forth. The main goal of this book is to show the reader how to use specific propagation models for each situation in an urban scene, how to obtain from such models the propagation channel characteristics, how to obtain from these characteristics the coverage effects, and, finally, how to construct the radio maps and the cellular maps of investigated terrain areas using the propagation characteristics for different cellular urban environments (macrocell and microcell).

The book does not consider practical recommendations for wireless communication systems design; it principally addresses the radio propagation aspects of personal and mobile communication, and supposes that the reader is already familiar with the basic aspects of higher mathematics, electrodynamics, and wave propagation. Nevertheless, it briefly summarizes some applied aspects of electromagnetism to describe land and urban radio wave propagation problems.

The material and chapter sequence in the book's text follow the courses mentioned below. It is composed of four parts. Part I consists of two chapters. Chapter 1 introduces the subject of the book, that is, it describes how I differentiate between various urban environments by using different kinds of terrain surfaces and antenna positions, both for the transmitter and the receiver, relative to the obstructions surrounding them. I discuss how I see the concept of "propagation channel" and its main characteristics, and explain my view by introducing different kinds of cellular environments. Chapter 2 discusses the applied aspects of electromagnetism and wave propagation using the unified approach of the time harmonic form of the wave equation to describe wave propagation in free space.

Part II consists of two chapters that describe the propagation phenomena in *open* and *rural* areas. Chapter 3 deals with the radio wave propagation over flat and curved smooth terrain. Here the "two-ray" model which is well-known from the related literature is briefly described for LOS conditions between antennas. Chapter 4 describes the propagation effects from rough and hilly terrain for LOS and obstructive NLOS conditions, respectively. The criterion of roughness of the ground surface is introduced. For LOS conditions, the scattered field characteristics are obtained by using the perturbation theory and the Kirchhoff's approximation. For NLOS conditions between antennas, the deterministic and empirical models are used.

Part III consists of four chapters which describe the propagation phenomena in *built-up areas.* In Chapter 5, the evaluation by means of my "multislit street waveguide" model is introduced to describe the propagation characteristics along straight rectangular streets in cases where both antennas, receiver and transmitter, are placed in direct visibility (LOS conditions) at lower than rooftop level. In Chapter 6, the conditions of regular terrain are considered further, but here the obstructive conditions (NLOS) for antennas are described

in the case of urban environments with a rectangular crossing-street plan for different positions of both antennas relative to the rooftops. In this case, the "crossing-waveguides" model I constructed and the "two-dimensional multidiffraction" model Bertoni and his co-authors constructed (references are given in Chapter 6) are presented for describing the propagation characteristics and the coverage effects.

In Chapter 7, I consider irregular built-up terrain, and present existing empirical and semi-empirical models for describing propagation characteristics above rough terrain with many obstacles randomly distributed around the transmitter and receiver antennas. Chapter 8 continues this subject by introducing the "multiparametric" model, which is based on the combination of a deterministic and a probabilistic approach first introduced by Ponomarev and his colleagues (references are given in Chapter 8). This model describes the field characteristics above irregular terrain with randomly distributed obstacles. I added some modifications in the model by introducing a more realistic description of the diffraction phenomena and a more general description of the built-up terrain. The method of obtaining the coverage effects by using propagation characteristics is described for the more general case of built-up terrain.

Part IV considers the special aspects of cellular maps' construction. In Chapter 9, I introduce the main characteristics of cellular areas and give the reader a useful technique for predicting the dimensions and the geometry of contours of cellular maps by using the propagation characteristics for each cellular propagation channel. Here, the concept of cellular map construction using the loss characteristic prediction based on previously developed propagation models is discussed. The special algorithm for constructing radio and cellular maps is fully described in the final section of this book and is recommended to the reader for practical use.

This page intentionally left blank

Acknowledgments

This book is a continuation of the research activity in cellular radio communication that I carried out many years ago with Professor G. A. Ponomarev, who introduced me to the field of radio wave propagation in random media when I joined the Radiophysical Faculty of Tomsk University (Soviet Union). He stimulated my interest in urban propagation during my B.S. (1968–1972) and M.S. (1972–1975) research under his guidance. Together we started to investigate the propagation phenomena in the urban scene both for the case of regular (using the street-guided wave deterministic approach) and of irregular (based on the probabilistic approach) terrain.

I suspended these investigations during a long period after leaving Tomsk, but when I joined Tadiran Telecom (in Israel) in 1992, I was encouraged by Dr. Moshe Levin's inspiring advice and support to continue my research on this subject based on numerous experiments carried out by their communication group. Together with Dr. Ran Giladi from Ben-Gurion University (Beer Sheva), he helped me to understand the useful applications of my theoretical investigations. Professor Dan Censor, Professor Reuven Mazar, and Professor Ehud Heyman stimulated me to create the special courses "Characterization of Cellular Communication Channels" and "Radiowave Propagation for Cellular Systems" for undergraduate and postgraduate students at Beer Sheva University and Tel Aviv University, respectively. This manuscript is based on the material of these courses.

The theoretical models presented in Chapters 5, 6, and 8 were proven through the numerous propagation experiments carried out together with Ilan Mattitiahu and Amit Gil and theoretical discussions with Dr. Avi Freedman and Dr. Michael Shalukhin, my colleagues from the communication group of

Innowave-ECI Telecom. Dr. Avi Freedman helped me prepare this book and I wish to acknowledge his contributions.

Many additions that I introduced during the preparation of this book were inspired by discussions with Professor Henry Bertoni from New York Polytechnic University and Professor Jorgen Bach Andersen from Aalborg University (Denmark). Furthermore, Professor Andersen gave me useful recommendations on how to write this book in a logically sound form. I wish to acknowledge my discussions with all of them.

All figures and schemes were drawn by my colleague from the Department of Electrical and Computer Engineering, Luba Feldman, and by my graduate student Dima Katz, who prepared some numerical examples for me. My thanks are offered to Peter Lambert, who also helped me prepare this book.

In developing this book, I realized that it is impossible for me to include all my ideas in one book's pages. Subjects such as characteristic distribution of signals in the angle and time and frequency domains for the multipath urban channel had to be omitted. I hope that this part of multipath propagation phenomena, which is important for the performance of future mobile and stationary cellular systems, will be included in a second book, as a continuation of this one.

Finally, I must state that it would have been impossible for me to do any important work as a researcher without the warm support of my family, Osnat and Alexander. They surrounded me with a very kind atmosphere and plenty of understanding. This allowed me the time to write I should have enjoyed with them both instead.

Objective

This page intentionally left blank

1

Introduction to the Wireless Propagation Environment

1.1 Background

Wireless communication links include several channels having different physical principles and processes, with their own independent or correlated working characteristics and operating elements. A simple scheme of such a link consists of the transmitter (T), the receiver (R), and the propagation channel, the main output characteristics of which depend on the conditions of radio propagation in different kinds of environments (see Figure 1.1).

As follows from the simple scheme, depicted in Figure 1.1, there are three main independent electronic and electromagnetic design tasks related to these communication channels. The first task is the specification of the electronic equipment that controls all operations within the transmitter, including the transmitter antenna operation. The third task concerns the same operations and signals, but for the receiver, with its own peculiarities. For both of these channels an important problem is the influence of different kinds of obstacles placed around the antennas, and of the environmental conditions. Another important question for a personal receiver (hand-held) antenna is also the influence of the human body on the operating characteristics of the working antenna. The radio propagation channel, denoted as a second channel in the scheme presented in Figure 1.1, plays a separate independent role. Its main output characteristics depend on the conditions of radiowave propagation in the various operational environments of such wireless communication links.

In the literature dedicated to wireless communication, fixed and/or mobile, most of the attention is given to descriptions of the electronic equipment

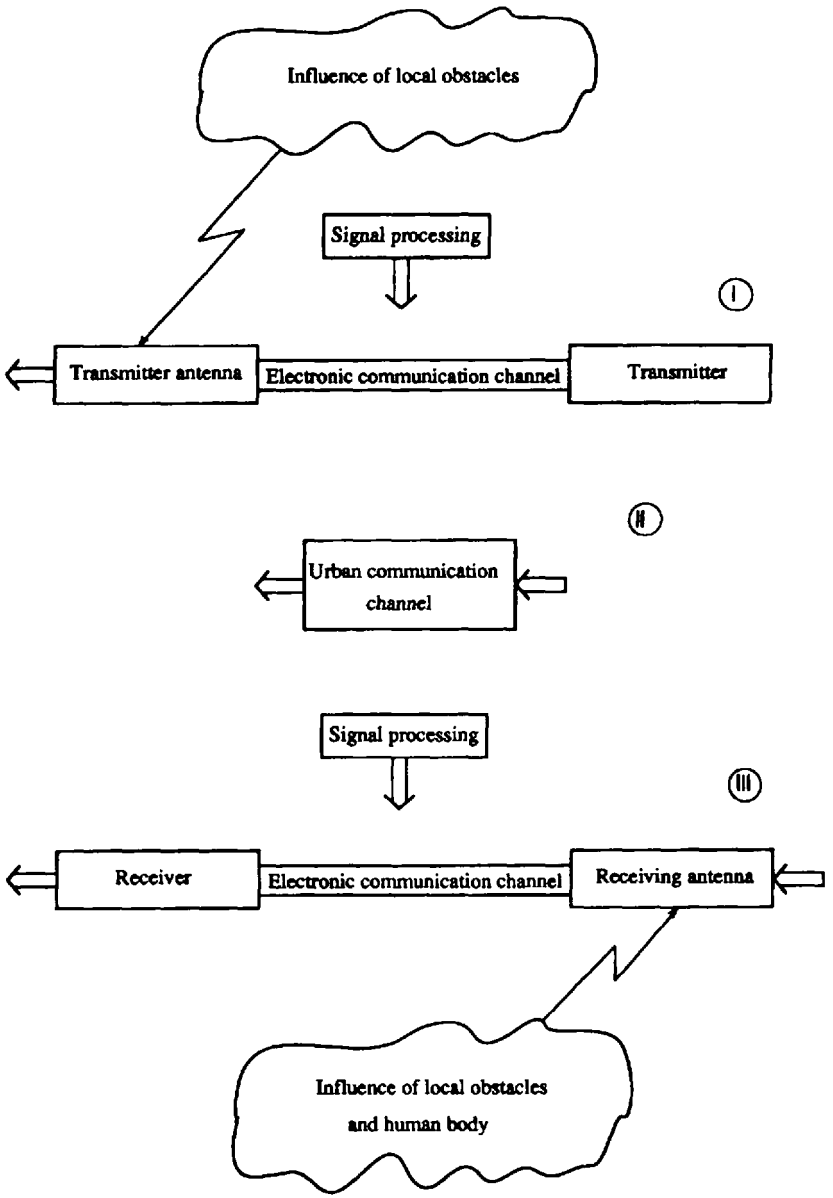

Figure 1.1 The simple scheme of three main independent electronic and electromagnetic design tasks related to the communication channels.

and the signal processing within it; less attention is given to propagation aspects [1–8]. We think that only the wave propagation phenomena and its explanation as presented, for example, in [4], satisfy the increasing interest of designers of wireless communication systems in this subject.

In this book we have also pointed out some aspects of propagation phenomena presented in [4]. But in our opinion, there is a deep "gap" in all the reference books in the description of propagation phenomena in urban communication environments. There is no clear explanation of questions such as how to obtain the output propagation characteristics for predicting the efficiency of wireless links (as a completed communication system), how to correlate the output propagation characteristics with those used for the constructions of radio maps for operating and servicing areas, and so on. Moreover, in numerous practical cases of operation with the "cell" splitting concept for built-up areas, and the design of wireless communication systems, the questions of how to obtain the real output propagation characteristics for predicting the cell characteristics, how to develop the algorithms for constructing cellular maps and, finally, how to plan for an effective quality of service for each subscriber within each cell in various cellular propagation environments are very important.

This is why we examine all the propagation phenomena that can be observed in urban propagation channels in detail for the effective prediction of their output parameters in order to increase the efficiency of control of the operation characteristics of wireless communication systems.

On the other hand, the conditions of EM-wave propagation in a built-up urban environment are the most problematic of all the types found in ground-radio communication. In city areas with regularly and/or irregularly planned buildings, rays reflected, scattered, and diffracted from buildings and other obstructions lead to significant amplitude and phase variations of the received signals [1–30].

Many experimental and theoretical investigations carried out in city areas show that most of the buildings in built-up regions are practically nontransparent. The total field for ground objects at heights lower than roof level is formed mainly by radio waves reflected from walls and diffracted from corners [9–14, 20–22, 27–30]. In this case, wide shadow regions with sharp transitions to illuminated zones with laminated interference pictures are observed [20–22, 27–30]. In general, the main influence on field formation in city areas with dense building arises from the local building plan [9–12, 16–19].

This is why the processes of radio wave propagation in city areas cannot be described by general statistical [9, 20–21, 30] or empirical (see bibliography in [2]) models. Acceptable results can be obtained only for specific circumstances and for particular features of the city regional planning [1–4, 9–12, 16–19]. These effects are more apparent in the case of the connection between the

base station (radio port) and a stationary or moving object. Either both are located on the flat- or rough-ground surface at the street level below the rooftops of buildings, or one of them is above the roof level.

In other words, the use of each model must relate to a specific situation in an urban propagation channel. Therefore, in Section 1.5, we classify the situations into various special cases which exist in practice in wireless communication systems' construction and servicing. We will then describe the respective propagation conditions for any communication link that has some practical interest.

1.2 Historical Perspective of Wireless Communication Developments

First we present some important aspects of the development of radio communication channels.

In 1873, Clerk James Maxwell united all the well-known laws of electrostatics and magnetostatics, and electrodynamics and magnetodynamics, as a result of the work of Poisson (in electrostatics), Gauss (in magnetostatics), Ampere (in electrodynamics), and Faraday (in magnetodynamics), in a unified theory of electromagnetism. He described these laws in the completed form of four coupling equations (see Section 2.1).

Fifteen years later, in 1888, Heinrich Rudolf Hertz demonstrated practically the phenomena which Maxwell had obtained mathematically. In 1901, Gugliemo Marconi showed the possibility of constructing radio communication links between two stations at a range of 3,000 km. As an example of information transmission, he used the Morse signal "S."

During the mid-1930s, two-way radio communication links were designed at frequencies of 30–40 MHz. A decade later, broadcasting systems using mobile communication channels were operated at frequencies of 100–200 MHz. At the beginning of the 1960s, in developing land wireless communication links, designers of communication systems started to employ the frequency band up to 450 MHz.

Today one can observe the fast growth of various types of wireless communication systems, such as personal fixed and mobile, land and satellite, that use a wide frequency band from 500 MHz up to 3–10 GHz (see Section 1.3 for explanations of how to use each frequency band in practical wireless systems).

1.3 Frequency Band for Wireless Communication Systems

The *frequency band* is a main characteristic for predicting the effectiveness of wireless communication systems that we consider separately. The optimal

frequency band for each propagation channel is determined and limited by the technical requirements of each communication system and by the conditions of radio propagation through each channel.

First of all, we consider the spectrum of radio frequencies and their practical use in various communication channels.

Extremely low (ELF) and very low frequencies (VLF) are frequencies below 3 kHz and from 3 to 30 kHz, respectively. The VLF-band corresponds to waves which propagate through the waveguide formed by the earth's surface and ionosphere at long distances with a low degree of attenuation [0.1–0.5 decibel (dB) per 1000 km]. Frequencies lower than 3 kHz (ELF-band) are effective for underwater communication channels and for mines and subterranean communication.

Low frequencies (LF) are frequencies from 30 kHz up to 3 MHz. In the 1950s and 1960s, they were used for radio communication with ships and aircraft, but since the 1960s they are used by broadcasting stations. Such radio waves propagate along the ground surface, and in the literature are called "surface" waves.

High frequencies (HF) are those which are located in the band from 3 to 30 MHz. Signals in this spectrum propagate by means of reflections caused by the ionospheric layers and are used for communications with aircrafts and satellites, and for long-distance land communications by use of broadcasting stations.

Very high frequencies (VHF) are located in the band from 30 to 300 MHz. They are usually used for television communications, in long-range radar systems, and in radio-navigation systems.

Ultra high frequencies (UHF) are those that are located in the band from 300 MHz up to 3 GHz (in some literature its upper part from 0.5 GHz to 3 GHz is also divided into P, L, S bands). This frequency band is very effective for wireless microwave links for cellular systems (fixed and mobile) constructions, for mobile-satellite communication channels, and medium-range radars.

In recent decades radio waves with frequencies higher than 3 GHz (C, X, and K bands up to several hundred GHz, which are called *micro*waves in the literature) have begun to be used for constructing new kinds of wireless communication channels. However, waves in this frequency band propagating through the atmosphere suffer great attenuation caused by absorption by different air components, such as (Figure 1.2):

- Water (H_2O), at frequencies of about 22 GHz;
- Oxygen molecules (O_2), at frequencies of about 60 GHz.

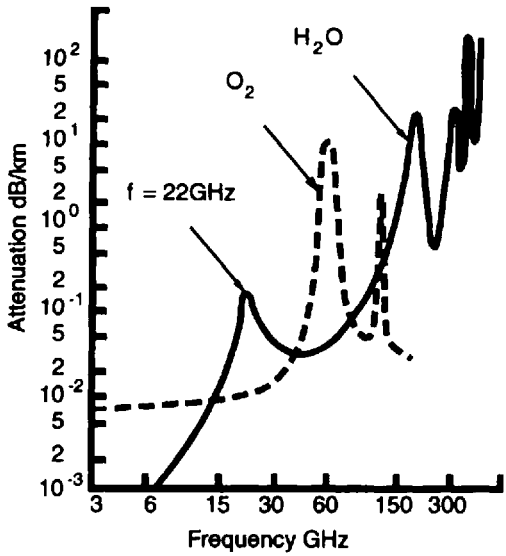

Figure 1.2 The wave propagation through the atmosphere with absorption by H_2O at frequencies of about 22 MHz and by molecules of O_2 at frequencies of about 60 MHz.

We now consider the question of how to determine the most effective operating frequencies in various communication systems. The effectiveness of each complete communication system depends on such parameters, as:

- Losses in the transmitter and in the receiver antennas;
- Noise within the electronic equipment that communicate with both antennas;
- Background and ambient noise (e.g., galactic, atmospheric, artificial man-made).

Now let us consider each type of noise which exists in a complete communication system. The simple explanation of noise is that noise is generated within each element of electronic communication channel due to random motion of the electrons within the various components of the equipment. According to the theory of thermodynamics, the energy generated is determined by the average background temperature, T_0, as:

$$E_N = k_B T_0 \tag{1.1}$$

where $k_B = 1.38 \cdot 10^{-23}$ W · s · K^{-1} is Boltzman's constant, $T_0 = 290°K = 17°C$. This energy is uniformly distributed in the frequency band and, hence, it is called "white noise." If so, the power of a signal inside the transmitter-receiver electronic channel at a given system bandwidth B_w shall be given by:

$$N_F = k_B T_0 B_w \tag{1.2}$$

At the same time, there are other sources of noise which we can describe as uniform over the system bandwidth. We can present their energy by their own effective temperature. The basic ambient noise is the galactic noise which is described by its temperature, denoted as T_b, and is equal to 4K. This is the effective temperature of the galaxy that characterizes the spreading process of the universe after the "Big Bang." In fact, the discovery of this noise was one of the evidences supporting the Big Bang theory.

Another noise source is manmade noise of which the temperature is measured to be $\sim 7.0 \cdot 10^{26}/f^3$ [4, 8], and atmospheric pollution (smoke, ice, water, clouds, air streams, and so forth) of which the noise temperature is $\sim f^3/3 \cdot 10^{26}$. The total effective noise temperature at the receiver input is:

$$T_e = k_B T_0 - \frac{7.0 \cdot 10^{26}}{f^3} + T_b + \frac{f^3}{3 \cdot 10^{26}} \tag{1.3}$$

Then the total effective noise power at the receiver input is given by the following expression:

$$N_T = k_B T_0 B_w F \tag{1.4}$$

where F is the noise figure of the receiver representing the additional noise (Chapter 9 in [4] gives a detailed description of man-made noise). In [8], the other form of the total effective noise presentation in decibels (dB) is done by:

$$N_T = -10 \log\left\{\frac{T_e}{T_0} + 10^{-0.1 G_T}[10^{0.1 N_F} - 1]\right\} \tag{1.5}$$

Here, G_T is the average gain of the transmitter/receiver antenna (in decibels), N_F is the noise within the electronic equipment according to (1.2), T_e is the full noise temperature for the sources in the propagation medium with its own temperature T_0 in Kelvin (according to (1.3)).

All noise characteristics, including artificial man-made noise, are shown in Figure 1.3(a,b) as a function of operating frequencies. As seen from the

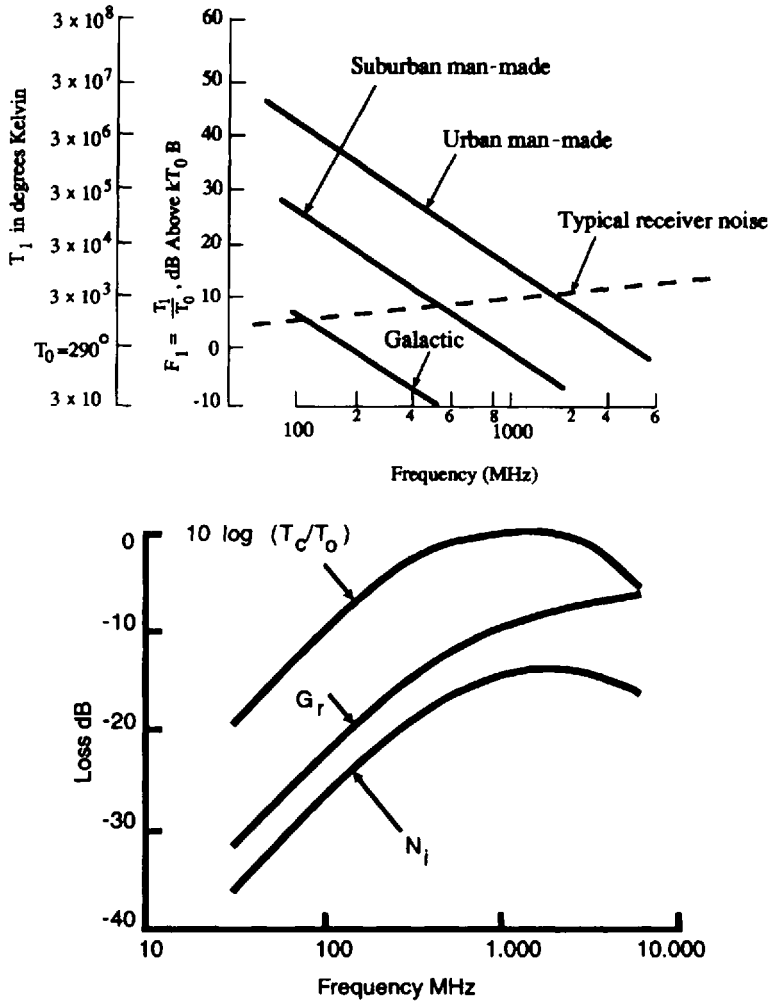

Figure 1.3 The noise characteristics, including artificial man-made noise, as a function of operating frequencies.

curves in Figure 1.3, with the growth of operating frequencies in communication channels all artificial man-made noises, as well as the Galactic noise, have a decreased effect. At the same time, typical noises in the transmitter-receiver communication channel are slightly increased as frequencies increase from 300 MHz up to 3 GHz.

1.4 Main Propagation Characteristics

Let us now consider the main propagation characteristics of a wireless communication channel. The principal characteristic that determines the effectiveness

of the propagation channel in various kinds of environment is the *path loss*. It defines variations of the signal amplitude or field intensity along the propagation trajectory (*path*) from point to point within the communication channel.

For its quantitative evaluation we will assume that the signal/wave amplitude in the point $\mathbf{r}_1$ along the propagation path is $A_1(\mathbf{r}_1)$, or the signal/wave intensity is $J(\mathbf{r}_1) = A_1^2(\mathbf{r}_1)$. In the process of propagation along the path at any next point $\mathbf{r}_2$ the signal/wave amplitude is $A_2(\mathbf{r}_2)$ or intensity $J(\mathbf{r}_2) = A_2^2(\mathbf{r}_2)$. In the literature the path loss is defined as a logarithmic difference between the amplitude or the intensity (sometimes called *power*) at any two different points $\mathbf{r}_1$ and $\mathbf{r}_2$ along the propagation path in the medium. Actually, these points describe the position of both terminals at the ends of the propagation channel, the transmitter and the receiver.

In other words, path loss, which is denoted by L and is measured in decibels (dB), can be evaluated for signal/wave amplitude $A(\mathbf{r}_j)$ at two points $\mathbf{r}_1$ and $\mathbf{r}_2$ along the propagation path as:

$$\begin{aligned} L &= 10 \cdot \log\frac{A^2(\mathbf{r}_2)}{A^2(\mathbf{r}_1)} = 10 \cdot \log A^2(\mathbf{r}_2) - 10 \cdot \log A^2(\mathbf{r}_1) \\ &= 20 \cdot \log A(\mathbf{r}_2) - 20 \cdot \log A(\mathbf{r}_1) \text{ [dB]} \end{aligned} \tag{1.6}$$

for signal/wave intensity $J(\mathbf{r}_j)$ at two points $\mathbf{r}_1$ and $\mathbf{r}_2$ along the propagation path

$$L = 10 \cdot \log\frac{J(\mathbf{r}_2)}{J(\mathbf{r}_1)} = 10 \cdot \log J(\mathbf{r}_2) - 10 \cdot \log J(\mathbf{r}_1) \text{ [dB]} \tag{1.7}$$

If we take point $\mathbf{r}_1$ as the origin of the radiopath (the transmitter location) and assume $A(\mathbf{r}_1) = 1$, then

$$L = 20 \cdot \log A(\mathbf{r}) \text{ [dB]} \tag{1.8a}$$

and

$$L = 10 \cdot \log J(\mathbf{r}) \text{ [dB]} \tag{1.8b}$$

So, according to the above-presented definitions, if one refers to signal/wave amplitude, the value of path loss is determined by formulas (1.6), (1.8a) with "20" before the sign "log," if one speaks about signal/wave intensity or power, the value of path loss is determined by (1.7), (1.8b) with "10" before the sign "log."

The next question is: What are the units by which the *losses* are measured at the receiver? Let us assume that the signal/wave amplitude is measured in millivolts (mV) per meter and the signal/wave power in milliwatt (mW). In this case, the resulting output value must be presented in decibels above 1mV/m for measured amplitude and in decibels above 1mW for measured power,

$$[L]_A = \text{dB/(mV)} \qquad (1.9)$$
$$[L]_J = \text{dB/(mW)} = \text{dBm}$$

Finally, the resulting output value is denoted in dB/(V/m), dB(mV/m), and dB(μV/m), if the signal/wave amplitude was measured in decibels regarding V/m, mV/m, and μV/m, respectively. In the same way, the resulting output value is denoted in dB, dBm, and dBμ, if the signal/wave power was measured in decibels regarding W (watt), mW, and μW, respectively.

Example: In some measurements the signal power of $P_R = -6.0$ dBm was obtained.

The question is: What is the *real power* (in power units) that we have measured at the input of the receiver?

Solution: Using the definition (1.8b), one can write:

$$-6.0 = 10 \cdot \log P_R \text{ [dBm]}$$

or

$$P_R = 10^{-0.6} = 0.251 \text{ mW} = 251 \ \mu\text{W}$$

Hence, one can see that the power $P_R = -6.0$ dBm corresponds to the real measured power $P_R = 251$ μW.

Since any signal passing through the propagation channel first passes through the transmitter electronic channel and antenna, and, secondly, has to reach the receiving antenna before coming to the receiver input (see Figure 1.1), both electronic channels together with the environment introduce some noise into the wireless communication system. Therefore, the second main characteristic of communication channels is the signal-to-noise ratio (SNR or S/N). In decibels this characteristic can be presented as follows: For the receiver (output) channel where noise (artificial and natural) is significant

$$SNR = P_R - N_R \text{ [dB]} \qquad (1.10)$$

For special cases of urban wireless communication in clutter conditions other propagation characteristics are usually used. We consider these characteristics in Chapter 9.

1.5 Characterization of Terrain Configurations

The process of classification of terrain configurations is an important stage in the construction of propagation models above the ground surface and, finally, in predicting the signal/wave attenuation (or path loss) within each specific propagation channel. The simple classification of *terrain configuration* follows from practical research and experience of designers of such communication systems. It can be presented as:

- Open area;
- Flat-ground surface;
- Curved, but smooth terrain;
- Hilly terrain;
- Mountains.

The *built-up areas* can also be simply classified as:

- Rural areas;
- Suburban areas;
- Urban areas.

Many experiments carried out in different built-up areas have shown that there are many specific factors which must be taken into account to describe specific propagation phenomena in built-up areas, such as:

- Buildings' density or terrain coverage by buildings (in percents);
- Buildings' contours or their individual dimensions;
- Buildings' average height;
- Positions of buildings with respect to the base station and fixed or mobile receivers;
- Positions of both antennas, receiver and transmitter, with respect to the rooftop level;

- Density of vegetation, presence of gardens, parks, lakes, and so on;
- Degree of "roughness" or "hilliness" of a terrain surface.

Based on these factors and parameters of terrain, British Telecom (BT) has constructed ten categories of terrain configuration [4], that are presented in Table 1.1.

According to Table 1.1, one can classify the terrain surface using specific notations:

Sign 0 denotes the category that describes the water surface; signs 2 to 4 are the categories that describe open rural areas, with some specifications of ground-surface configurations. Signs 5 to 6 denote the categories that describe suburban areas; signs 7 to 9 describe the urban areas with growth of buildings' density and urban area dimensions. A compromise variant (the use of seven categories of the terrain) has been introduced after comparison with the standards of some other countries, such as Germany, Denmark, and Japan, which are presented in Table 1.2.

Moreover, a new standard of terrain classification has been introduced for the analysis of urban topographic maps. This standard was based on the following characteristics of terrain:

1. Position and distribution of buildings regarding the observer;
2. Dimensions of buildings or useful built-up area;
3. Number of buildings at the tested area;

Table 1.1
Terrain Configuration

Category	Description of the Terrain
0	Rivers, lakes, and seas
1	Open rural areas (e.g., fields and heathland with few trees)
2	Rural areas, similar to the above, but with some wooded areas
3	Wooded or forested rural areas
4	Hilly or mountainous rural areas
5	Suburban areas, low-density dwellings, and modern industrial estates
6	Suburban areas, higher density dwellings (e.g., council estates)
7	Urban areas with buildings of up to four stories with gaps in-between
8	Higher density urban areas in which some buildings have more than four stories
9	Dense urban areas in which most of the buildings have more than four stories and some can be classed as "skyscrapers"

Table 1.2
Compromise Variant

BT (U.K.)	Germany	BBC (U.K.)	Denmark	Okumura (Japan)
0	4	—	—	Land/sea
1	2	1	0–2	—
2	3	1	1–2	—
3	2	1	4	—
4	2–3	1	—	Undulating
5	1	2	3	Suburban
6	1	2	6	Suburban
7	1	3	7	Urban
8	1	3	8	Urban
9	1	4	9	Urban

4. Height of ground surface and its degree of "roughness";
5. Presence of vegetation.

Using these five characteristics as basic ones, the following parameters have been introduced to describe the terrain configuration [4]:

1. Buildings' dimensions (sizes) distribution (BSD);
2. Built-up area index (BAI) due to buildings' coverage effects;
3. Buildings' height distribution (BHD);
4. Buildings' position distribution (BPD) regarding receiver and transmitter;
5. Vegetation index (VI) due to vegetation coverage effects;
6. Degree of roughness of the ground surface (Δh).

To simplify the problem of terrain surface modeling, the modern classification of terrain was introduced recently by splitting all characteristics of terrain configurations into three classes with their subclasses.

Class 1: For rural areas

Subclasses: *A* is a flat terrain; *B* is a hilly terrain; *C* is a mountainous terrain.

Class 2: For suburban areas

Subclasses: *A* is a homogeneous and uniform terrain; *B* is a uniform terrain with closed zones; *C* is a uniform terrain with strong "shadow zones."

Class 3: For urban/city areas

Subclasses: A is a trading part of city; B is a commercial part of city; C is an industrial part of city.

Classes 2 and 3 with all specific parameters are presented in Table 1.3.

Here, μ is the mean value of parameters BSD and BHD; σ is their standard deviations around the mean values of BSD and BHD, that is, the deviations from μ.

Using these classes, their specific characteristics, and parameters, one can easily classify various kinds of terrain by examinating topographic maps for each deployment of a wireless communication system.

1.6 Various Propagation Situations in Urban Areas

As remarked earlier, an important characteristic of the propagation channel is the location and position of both antennas with respect to the obstacles placed around them. Usually there are three possible situations:

1. Both antennas, receiver and transmitter, are placed above the tops of obstacles (in a built-up area this means that they are above the rooftop level. See Figure 1.4(a)).
2. One of the antennas is higher than the tops of the obstacles (namely, the roofs), but the second one is lower (Figure 1.4(b)).
3. Both antennas are below the tops of the obstacles (Figure 1.4(c)).

In the first situation they are in *direct visibility* or LOS conditions. In the last two situations, one or both antennas are in *clutter* or obstructive conditions. In all these cases the profile of terrain surface is important and may vary from flat and smooth, with curvature, up to rough and hilly terrain.

Table 1.3
Classification Parameters

Class	BAI (%)	BSD (m)		BHD		VI (%)
		μ_s	σ_s	μ_H	σ_H	
2A	12–20	95–115	55–70	2	1	>2.5
2B	20–30	100–120	70–90	2–3	1	<5
2C	≥12	≥500	>90	≥4	1	≤2
3A	≥45	200–250	≥180	≥4	1	0
3B	30–40	150–200	≥160	3	1	0
3C	35–45	≥250	≥200	2–3	1	≤1

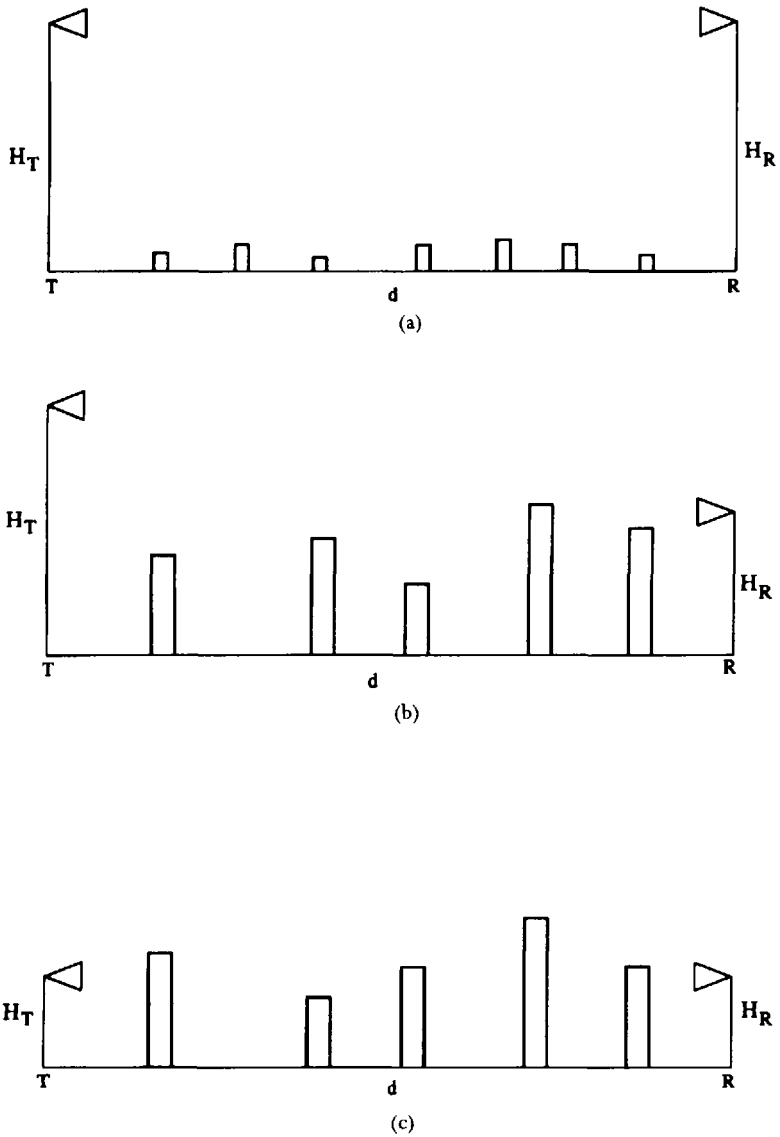

Figure 1.4 Three possible situations with receiving and transmitting antennas.

In Figure 1.5 a full classification of terrain surface for all three variants of antenna locations is presented. Using the simple scheme presented in Figure 1.5, one can describe the specific propagation phenomena for various ambient conditions of the radio propagation over the terrain and, finally, obtain the appropriate propagation model for each specific communication channel.

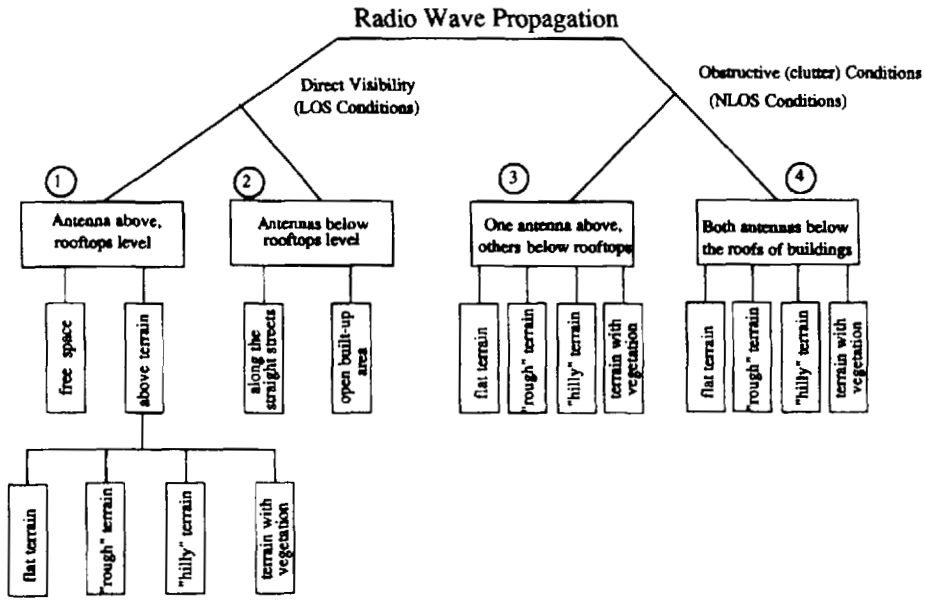

Figure 1.5 The classification of terrain surface.

1.7 Cellular Environments Concept

The terms *macrocell, microcell,* and *picocell* have been introduced in the literature [1–8] to differentiate among various kinds of cell areas. The term *macrocell* is usually used in land communication channels for describing radio-propagation phenomena at ranges more than 10–20 km (i.e., it is mostly related to radio propagation over open or rural areas). The term *microcell* is usually used for describing radio-propagation phenomena in built-up environments at ranges from 200m up to 3–5 km. The term *picocell* is usually used for describing radio propagation channels within buildings at ranges less than 200m. As the subject of the book is urban communication channels, indoor propagation, or picocells, will not be described here.

References

[1] Jakes, W. C., *Microwave Mobile Communications*, New York: John Wiley and Sons, 1974.

[2] Lee, W. Y. C., *Mobile Communication Engineering*, New York: McGraw Hill Publications, 1985.

[3] Feuerstein, M. L., and T. S. Rappaport, *Wireless Personal Communication*, Norwood, MA: Artech House, 1992.

[4] Parsons, L. D., *The Mobile Radio Propagation Channels*, New York: Pentech Press, 1992.

[5] Rappaport, T. S., *Wireless Communications*, New York: Prentice Hall PTR, 1996.

[6] Lee, W. Y. C., *Mobile Cellular Telecommunications Systems*, New York: McGraw Hill Publications, 1989.

[7] Linnartz, J. P., *Narrowband Land-Mobile Radio Networks*, Norwood, MA: Artech House, 1993.

[8] Mehrotra, A., *Cellular Radio Performance Engineering*, Norwood, MA: Artech House, 1994.

[9] Maciel, L. R., H. L. Bertoni, and H. H. Xia, "Unified approach to prediction of propagation over buildings for all ranges of base station antenna height," *IEEE Trans. Vehic. Technol.*, Vol. 42, No. 1, 1993, pp. 41–45.

[10] Walfisch, J., and H. L. Bertoni, "A theoretical model of UHF propagation in urban environments," *IEEE Trans. Anten. Prop.*, Vol. 36, No. 12, 1988, pp. 1788–1796.

[11] Xia, H. H., and H. L. Bertoni, "Diffraction of cylindrical and plane waves by an array of absorbing half-screens," *IEEE Trans. Anten. and Prop.*, Vol. 40, No. 2, 1992, pp. 170–177.

[12] Milstein, L. B., et al., "On the feasibility of a CDMA overlay for personal communications networks," *IEEE Select. Areas in Commun.*, Vol. 10, No. 4, 1992, pp. 665–668.

[13] Xia, H., et al., "Radio propagation characteristics for line-of-sight microcellular and personal communications," *IEEE Trans. Anten. and Prop.*, Vol. 41, No. 10, 1993, pp. 1439–1447.

[14] Bertoni, H. L., et al., "UHF propagation prediction for wireless personal communications," *Proc. IEEE*, Vol. 82, No. 9, 1994, pp. 1333–1359.

[15] Fumio, J., and J. Susumi, "Analysis of multipath propagation structure in urban mobile radio environments," *IEEE Trans. Anten. and Propag.*, Vol. 28, No. 4, 1980, pp. 531–538.

[16] Hata, M., "Empirical formula for propagation loss in land mobile radio services," *IEEE Trans. Veh. Technol.*, Vol. 29, No. 3, 1980, pp. 317–325.

[17] Ikegami, F., S. Yoshida, and M. Takahar, "Analysis of multipath propagation structure in urban mobile radio environments," *IEEE Trans. Anten and Propag.*, Vol. 20, No. 4, 1980, pp. 531–537.

[18] Ikegami, F., T. Takeuch, and S. Yoshida, "Theoretical prediction of mean field strength for urban mobile radio," *IEEE Trans. Anten. and Propag.*, Vol. 39, No. 3, 1991, pp. 299–302.

[19] Rustako, A. J., Jr., et al., "Radio propagation at microwave frequencies for line-of-sight microcellular mobile and personal communications," *IEEE Trans. Veh. Technol.*, Vol. 40, No. 2, 1991, pp. 203–210.

[20] Blaunstein, N., R. Giladi, and M. Levin, "LOS characteristics' prediction in urban and suburban environments," *IEEE Trans. on Vehic. Technol.*, Vol. 47, No. 1, 1998, pp. 11–21.

[21] Blaunstein, N., "Average field attenuation in the nonregular impedance street waveguide," *IEEE Trans. on Antennas Propagat.*, Vol. 46, No. 12, 1998, pp. 1782–1789.

[22] Hughes, K. A., "Mobile propagation in London at 936 MHz," *Electron. Letters*, Vol. 18, No. 3, 1982, pp. 141–143.

[23] Ponomarev, G. A., A. N. Kulikov, and E. D. Telpukhovsky, *Propagation of Ultra-Short Waves in Urban Environments*, Tomsk, USSR: Rasko, 1991.

[24] Whitteker, J. H., "Measurements of path loss at 910 MHz for proposed microcell urban mobile systems," *IEEE Trans. Veh. Technol.*, Vol. 37, No. 3, 1988, pp. 376–381.

[25] Harley, P., "Short distance attenuation measurements at 900 MHz and 1.86 MHz using low antenna heights for microcells," *IEEE Sel. Areas Comm.*, Vol. 10, No.1, 1989, pp. 7–16.

[26] Turin, G. L, et al., "A statistic model of urban multipath propagation," *IEEE Trans. Veh. Technol.*, Vol. 26, No. 4, 1977, pp. 358–362.

[27] Levy, A. J., "Fine structure of the urban mobile propagation channel," *Proc. Commsphere 91*, Herzlia, Israel, Dec. 14–17, 1991, pp. 5.1.1–5.1.6.

[28] Tan, S. Y., and H. S. Tan, "A theory of propagation path loss characteristics in a city street-grid scene," *IEEE Trans. Electromagn. Compat.*, Vol. 37, No. 2, 1995, pp. 333–342.

[29] Blaunstein, N., and M. Levin, "VHF/UHF wave attenuation in a city with regularly spaced buildings," *Radio Sci.*, Vol. 31, No. 2, 1996, pp. 313–323.

[30] Blaunstein, N., and M. Levin, "Propagation loss prediction in the urban environment with rectangular grid-plan streets," *Radio Sci.*, Vol. 32, No. 2, 1997, pp. 453–467.

2

Radio Wave Propagation in Free Space

2.1 Electromagnetic Aspects of EM-Wave Propagation

Maxwell's unified theory (see Section 1.2) postulates that an electromagnetic field could be represented as a wave. The coupled wave components, the electric and magnetic fields, are depicted in Figure 2.1, from which it follows that the electromagnetic (EM) wave travels in a direction perpendicular to both EM field components. In Figure 2.1, this direction is denoted as the z-axis in the Cartesian coordinate system. In their orthogonal space-planes, the magnetic and electric oscillatory components repeat their waveform after a distance of

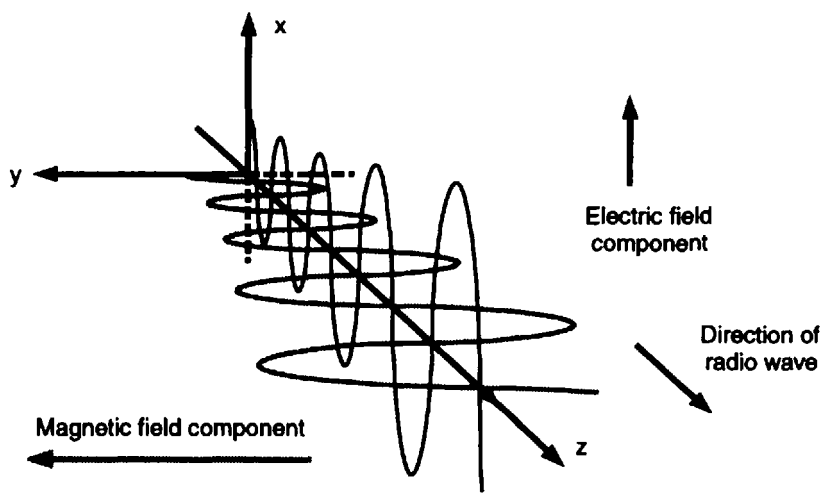

Figure 2.1 Presentation of an electromagnetic wave moving through free space.

one wavelength along the y-axis and x-axis, respectively (see Figure 2.1). Both components of the EM wave are in phase in the time domain, but not in the space domain. Moreover, the magnetic component value of the EM field is closely related to the electric component value, from which one can obtain the radiated power of the EM wave propagating along the z-axis. Let us now assess these phenomena theoretically using Maxwell's unified theory.

2.1.1 Differential Representation of Maxwell's Equations

The theoretical analysis of EM wave propagation is based on Maxwell's equations. In vector notation and in SI-units system, their representations in the uniform macroscopic form are:

$$\nabla \times \mathbf{E}(\mathbf{r}, t) = -\frac{\partial}{\partial t}\mathbf{B}(\mathbf{r}, t) \tag{2.1a}$$

$$\nabla \times \mathbf{H}(\mathbf{r}, t) = \frac{\partial}{\partial t}\mathbf{D}(\mathbf{r}, t) + \mathbf{j}(\mathbf{r}, t) \tag{2.1b}$$

$$\nabla \cdot \mathbf{B}(\mathbf{r}, t) = 0 \tag{2.1c}$$

$$\nabla \cdot \mathbf{D}(\mathbf{r}, t) = \rho(\mathbf{r}, t) \tag{2.1d}$$

Here, $\mathbf{E}(\mathbf{r}, t)$ is the electric field strength vector, in volts per meter (V/m); $\mathbf{H}(\mathbf{r}, t)$ is the magnetic field strength vector, in amperes per meter (A/m); $\mathbf{D}(\mathbf{r}, t)$ is the electric flux induced in the medium by the electric field, in coulombs/m^3 (this is why, in the literature, it is sometimes called an "induction" of an electric field); $\mathbf{B}(\mathbf{r}, t)$ is the magnetic flux induced by the magnetic field, in webers/m^2 (it is also called an "induction" of a magnetic field); $\mathbf{j}(\mathbf{r}, t)$ is the vector of electric current density, in amperes/m^2; $\rho(\mathbf{r}, t)$ is the charge density in coulombs/m^2. The curl operator, $\nabla \times$, is a measure of field rotation, and the divergence operator, $\nabla \cdot$, is a measure of the total flux radiated from a point.

It should be noted that for a time-varying EM-wave field, (2.1c–d) can be derived from (2.1a) and (2.1b), respectively. In fact, taking the divergence of (2.1a) (by use of the divergence operator $\nabla \cdot$) one can immediately obtain (2.1c). Similarly, taking the divergence of (2.1b) and using the well-known continuity equation [1–3]

$$\nabla \cdot \mathbf{j}(\mathbf{r}, t) + \frac{\partial \rho(\mathbf{r}, t)}{\partial t} = 0 \tag{2.2}$$

one can arrive at (2.1d). Hence, only two equations, (2.1a–b) are independent.

In electrostatics and magnetostatics, where $\frac{\partial}{\partial t} = 0$, the electric and magnetic fields are decoupled. For static problems (2.1d) limits to the Coulomb law [1, 2], which implies that the electric flux $\mathbf{D}$ is produced by a charge density ρ in the medium. The same result is obtained with (2.1c), which assumes the absence of free magnetic charges in the medium. This magnetostatic law is the consequence of Gauss's law [1, 2], which is a statement of the conservation of magnetic flux in the medium. Equation (2.1a) is the Faraday law and indicates that a time-varying magnetic flux generates an electric field with rotation; (2.1b) without the term $\frac{\partial \mathbf{D}}{\partial t}$ (displacement current term [1, 2]) limits to the Ampere law and indicates that a current or a time-varying electric flux (displacement current [1, 2]) generates a magnetic field with rotation.

Because one now has only two independent equations, (2.1a–b), which describe the four unknown vectors: $\mathbf{E}$, $\mathbf{D}$, $\mathbf{H}$, $\mathbf{B}$, two more equations relating these vectors are needed. To do this, we introduce relations between $\mathbf{E}$ and $\mathbf{D}$, $\mathbf{H}$ and $\mathbf{B}$, $\mathbf{j}$, and $\mathbf{E}$ which are well-known in electrodynamics. In fact, for isotropic media, which are usually considered in problems of land-radio propagation, the electric and magnetic fluxes are related to the electric and magnetic fields, and the electric current is related to the electric field, via the constitutive relations [1–3]:

$$\mathbf{D} = \epsilon(\mathbf{r})\mathbf{E} \tag{2.3a}$$

$$\mathbf{B} = \mu(\mathbf{r})\mathbf{H} \tag{2.3b}$$

$$\mathbf{j} = \sigma(\mathbf{r})\mathbf{E} \tag{2.3c}$$

It is important to note that relations (2.3a–c) are valid only for propagation processes in linear isotropic media, which are characterized by the three scalar functions of any point $\mathbf{r}$ in the medium: permittivity $\epsilon(\mathbf{r})$, permeability $\mu(\mathbf{r})$, and conductivity $\sigma(\mathbf{r})$. In *anisotropic media* such functions transform into tensors (matrixes), but this case is not important for terrestrial radio propagation, and we will not deal with this case here. In relations (2.3a–c), we have assumed that the medium is inhomogeneous. In a homogeneous medium the functions $\epsilon(\mathbf{r})$, $\mu(\mathbf{r})$, and $\sigma(\mathbf{r})$ transform to simple scalar values ϵ, μ and σ. If, in this case, they are also functions of frequency, ω:

$$\epsilon = \epsilon(\omega), \quad \mu = \mu(\omega), \quad \sigma = \sigma(\omega) \tag{2.4}$$

the medium is *frequency dispersive*. Below we will talk about a nondispersive, isotropic, linear, and inhomogeneous medium. In free space, these functions are simple constants (i.e., $\epsilon = \epsilon_0 = 8.854 \cdot 10^{-12}$ Farad/meter, while $\mu = \mu_0 = 4\pi \cdot 10^{-7}$ Henry/meter). The constant $c = \dfrac{1}{\sqrt{\epsilon_0 \mu_0}}$ is the velocity of light, which has been measured very accurately and is close to $3 \cdot 10^8$ m/s. In many practical cases of wireless communication environments, the value μ is close to unity, and we can assume $\mathbf{B} = \mathbf{H}$ in (2.3b) with great accuracy.

The system (2.1) can be further simplified if we assume that the fields are time harmonic. If the fields time-dependence is not harmonic, then, using the fact that (2.1) are linear, we may treat these fields as sums of harmonic components and consider each component separately. In this case, the time harmonic field is a complex vector and can be expressed via its real part as

$$\mathbf{A}(\mathbf{r}, t) = \mathrm{Re}[\mathbf{A}(\mathbf{r}) e^{-i\omega t}] \tag{2.5}$$

where $i = \sqrt{-1}$, ω is the angular frequency in radians per second, $\omega = 2\pi f$, f is the radiated frequency in Hz = s^{-1}, and $\mathbf{A}(\mathbf{r}, t)$ is the complex vector ($\mathbf{E}$, $\mathbf{D}$, $\mathbf{H}$, $\mathbf{B}$, or $\mathbf{j}$). The time dependence $\sim e^{-i\omega t}$ is commonly used in the literature of electrodynamics and wave propagation. If $\sim e^{i\omega t}$ is used, then one must substitute $-i$ for i and i for $-i$, in all equivalent formulations of Maxwell's equations.

In (2.5), $e^{-i\omega t}$ presents the harmonic time dependence of any complex vector $\mathbf{A}(\mathbf{r}, t)$ which satisfies the relationship:

$$\frac{\partial}{\partial t}\mathbf{A}(\mathbf{r}, t) = \mathrm{Re}[-i\omega \mathbf{A}(\mathbf{r}) e^{-i\omega t}] \tag{2.6}$$

Using this transformation, one can easily obtain from the system (2.1)

$$\nabla \times \mathbf{E}(\mathbf{r}) = i\omega \mathbf{B}(\mathbf{r}) \tag{2.7a}$$

$$\nabla \times \mathbf{H}(\mathbf{r}) = -i\omega \mathbf{D}(\mathbf{r}) + \mathbf{j}(\mathbf{r}) \tag{2.7b}$$

$$\nabla \cdot \mathbf{B}(\mathbf{r}) = 0 \tag{2.7c}$$

$$\nabla \cdot \mathbf{D}(\mathbf{r}) = \rho(\mathbf{r}) \tag{2.7d}$$

It can be observed that system (2.7) was obtained from system (2.1) by replacing $\partial/\partial t$ with $-i\omega$. Alternatively, the same transformation can be obtained by the use of the Fourier transform of (2.1) with respect to time [4]. In (2.7a–d) all vectors and functions are actually the Fourier transforms with respect to the *time domain*, and the fields **E**, **D**, **H**, and **B** are functions of frequency as well. Hence, they are also known as the *frequency domain solutions* of the EM field according to system (2.7). Conversely, the solutions of system (2.1) are the *time domain solutions* of the EM field. It is more convenient to work with system (2.7) instead of system (2.1) because of the absence of the time dependence and time derivatives in it. This is why, in this chapter and the next we use Maxwell's equations in the form (2.7a–d) and their *frequency domain* solutions to describe various electromagnetic phenomena related to land-radio propagation.

2.1.2 Integral Presentation of Maxwell's Equations

We now present Maxwell's equations in their integral representations. To derive the integral forms of (2.1a) and (2.1b), we integrate them over a cross-sectional area S and use Stokes's theorem [1–3, 5],

$$\int_S d\mathbf{s} \cdot \nabla \times \mathbf{E}(\mathbf{r}, t) = \oint_C \mathbf{dl} \cdot \mathbf{E}(\mathbf{r}, t) \tag{2.8}$$

In (2.8), C is the contour that forms the perimeter of the area S (see Figure 2.2). This expression states that the sum of all the rotations due to field **E** over the area S is equal to the "torque" produced by these rotations on the perimeter of S with C. Here the left-hand side is the summation over all the rotations, while the right-hand side of (2.8) is the evaluation of the net "torque" on the perimeter C. The neighboring rotations within the area S cancel each other, leaving a net rotation on the perimeter.

Using Stokes's theorem [1–3, 5], one can convert (2.1a) and (2.1b) to:

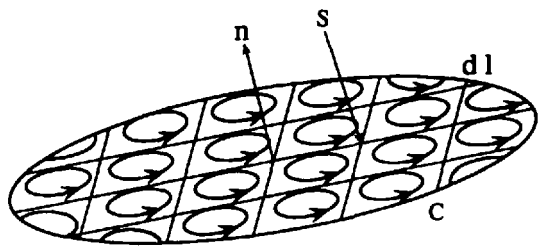

Figure 2.2 The geometry for the derivation of Stokes's theorem.

$$\oint_C d\mathbf{l} \cdot \mathbf{E}(\mathbf{r}, t) = -\frac{\partial}{\partial t}\int_S d\mathbf{s} \cdot \mathbf{B}(\mathbf{r}, t) \tag{2.9}$$

$$\oint_C d\mathbf{l} \cdot \mathbf{H}(\mathbf{r}, t) = \frac{\partial}{\partial t}\int_S d\mathbf{s} \cdot \mathbf{D}(\mathbf{r}, t) + \int_S d\mathbf{s} \cdot \mathbf{j}(\mathbf{r}, t) \tag{2.10}$$

To convert (2.1c) and (2.1d) into integral form, one can integrate them over a volume V and use Gauss's theorem [1–3, 5], which states that

$$\int_V dv\nabla \cdot \mathbf{B}(\mathbf{r}, t) = \int_S d\mathbf{s} \cdot \mathbf{B}(\mathbf{r}, t) \tag{2.11}$$

This states that the sum of all divergences of a flux **B** in a volume V is equal to the net flux which is leaving the volume V through the surface S. In other words, neighboring divergences tend to cancel each other within the volume V (see Figure 2.3). Consequently, (2.1c) and (2.1d) become

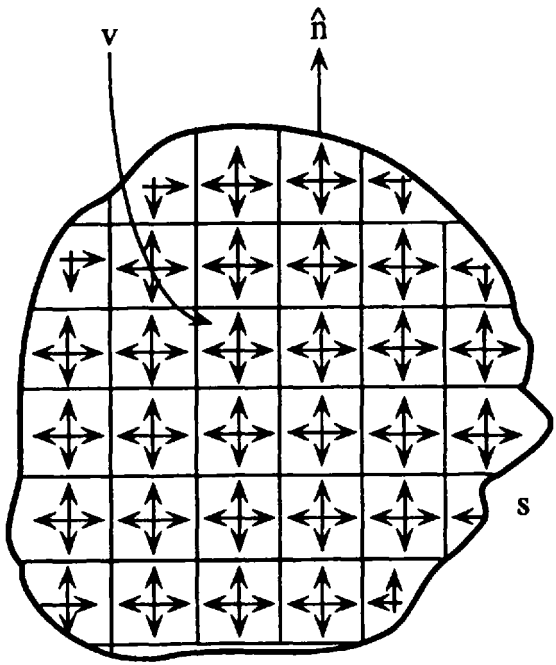

Figure 2.3 The geometry for the derivation of Gauss's theorem.

$$\int_S d\mathbf{s} \cdot \mathbf{B}(\mathbf{r}, t) = 0 \tag{2.12}$$

$$\int_S d\mathbf{s} \cdot \mathbf{D}(\mathbf{r}, t) = \int_V dv \cdot \rho(\mathbf{r}, t) = Q \tag{2.13}$$

where Q is the total charge in volume V.

Equation (2.9) implies that a time-varying magnetic flux through an area S generates an electromotive force (the left-hand side in (2.9)) around a loop C. In the same way, (2.10) implies that a time-varying electric flux (displacement current) or a conductivity current will generate a magnetomotive force (the left-hand side in (2.10)) that loops around the currents.

Equations (2.12) and (2.13) are statements of the conservation of fluxes. In fact, (2.13) implies that the net flux through a surface S equals the total charge Q inside S (see Figure 2.3).

2.1.3 Vector and Scalar Potentials

Maxwell's equations can be directly solved only for simple configurations [1–3], but in common cases it is convenient to introduce so-called potentials, with the purpose of decreasing the number of equations. In this case, some of Maxwell's equations are satisfied automatically. In electrostatics and magnetism, two potentials, the scalar, Φ, and the vector, $\mathbf{A}$, have been introduced [1–3]. In fact, because $\nabla \cdot \mathbf{B}(\mathbf{r}, t) = 0$, one can express through vector potential as:

$$\mathbf{B} = \nabla \times \mathbf{A} \tag{2.14}$$

Introducing this relation in (2.1a), we finally obtain

$$\nabla \times \left(\mathbf{E} + \frac{\partial \mathbf{A}}{\partial t} \right) = 0 \tag{2.15}$$

From vector algebra [5, 6] it is well known that any value for which the *curl* is equal to zero can be presented as a gradient of any scalar function. Therefore we can present the value in brackets as a gradient of scalar potential Φ,

$$\mathbf{E} + \frac{\partial \mathbf{A}}{\partial t} = -\nabla\Phi \tag{2.16}$$

$$\mathbf{E} = -\frac{\partial \mathbf{A}}{\partial t} - \nabla\Phi$$

Hence, the fields **E** and **H** that can be determined through the potentials **A** and Φ according to (2.14) and (2.16) satisfy the inhomogeneous Maxwell's equations (2.1b) and (2.1d). Using relations (2.14) to (2.16), one can rewrite these equations as:

$$\nabla^2\Phi + \frac{\partial}{\partial t}\nabla \cdot \mathbf{A} = -\rho \tag{2.17}$$

$$\nabla^2\mathbf{A} - \frac{\partial^2\mathbf{A}}{\partial t^2} - \nabla\left(\nabla \cdot \mathbf{A} + \frac{\partial\Phi}{\partial t}\right) = -\mathbf{j} \tag{2.18}$$

Thus we reduced the total number of equations to two. Moreover, these potentials are not independent [1–3]; the relation between them can be presented as follows:

$$\nabla \cdot \mathbf{A} + \frac{\partial\Phi}{\partial t} = 0 \tag{2.19}$$

Equations (2.17) and (2.18) can be converted into two separate inhomogeneous equations for Φ and **A**, respectively:

$$\nabla^2\Phi - \frac{\partial^2\Phi}{\partial t^2} = -\rho \tag{2.20a}$$

$$\nabla^2\mathbf{A} - \frac{\partial^2\mathbf{A}}{\partial t^2} = -\mathbf{j} \tag{2.20b}$$

Equations (2.20a–b) together with relation (2.19) create a system which is fully equivalent to Maxwell's system (2.1). The form of such equations is called a *wave equation*, a term which will be obvious later in this chapter. Often, the so-called Hertzian electric (Π_E) and magnetic (Π_H) vectors are introduced instead of the above-mentioned electrodynamic potentials. The electric and magnetic fields in free space can be presented by use of these vectors as:

$$\begin{aligned} \mathbf{E} &= \nabla \times \nabla \times \Pi_E + \nabla^2\Pi_E + k^2\Pi_E = \nabla(\nabla \cdot \Pi_E) + k^2\Pi_E \\ \mathbf{H} &= -ik\nabla \times \Pi_E \end{aligned} \tag{2.21a}$$

and

$$\mathbf{E} = -ik\nabla \times \Pi_H$$
$$\mathbf{E} = \nabla \times \nabla \times \Pi_H + \nabla^2\Pi_H + k^2\Pi_H = \nabla(\nabla \cdot \Pi_H) + k^2\Pi_H \tag{2.21b}$$

Hence, the Maxwell equations reduce to two wave equations for Hertzian electric and magnetic vectors, which we present here for free space, respectively:

$$\nabla^2\Pi_E - k^2\Pi_E = \mathbf{j}$$
$$\nabla^2\Pi_H - k^2\Pi_H = \mathbf{M} \tag{2.22}$$

Here, $\mathbf{M}$ is the vector of the magnetic current density [1–3, 5]; $k = \omega\sqrt{\epsilon\mu}$ is a wavenumber.

2.1.4 Poynting Theorem

This theorem is the simple law of EM-wave energy conservation. It is known from electrostatics and magnetostatics that the work of the electric field to move a single charge q is equal to $q \cdot \mathbf{v} \cdot \mathbf{E}$, where $\mathbf{v}$ is the vector of the charge velocity. The same work of the magnetic field for this charge is equal to zero, because the magnetic field direction is perpendicular to the velocity vector [1–3]. For a continuous distribution of charges and currents in a medium, the total work of the EM field in the volume V in unit time is equal [1–3]:

$$\int_V \mathbf{j} \cdot \mathbf{E} dv \tag{2.23a}$$

This expression determines the velocity of the decrease in the field energy within the volume V.

Let us now obtain the law of energy conservation, using Maxwell's equations (2.1). We shall substitute the current density $\mathbf{j}$ in (2.23a) using (2.10) and (2.11)

$$\int_V \mathbf{j} \cdot \mathbf{E} dv = \int_V \left[\mathbf{E} \cdot \nabla \times \mathbf{H} - \mathbf{E} \cdot \frac{\partial \mathbf{D}}{\partial t}\right] dv \tag{2.23b}$$

Taking into account the vector equality [5]

$$\nabla \cdot (\mathbf{E} \times \mathbf{H}) = \mathbf{H} \cdot \nabla \times \mathbf{E} - \mathbf{E} \cdot \nabla \times \mathbf{H}$$

and (2.1), one can easily rewrite (2.23) as:

$$\int_V \mathbf{j} \cdot \mathbf{E} dv = -\int_V \left[\nabla \cdot (\mathbf{E} \times \mathbf{H}) + \mathbf{E} \cdot \frac{\partial \mathbf{D}}{\partial t} + \mathbf{H} \cdot \frac{\partial \mathbf{B}}{\partial t} \right] dv \qquad (2.24)$$

If we now present the density of total field energy according to [1–3] as

$$W = (\mathbf{E} \cdot \mathbf{D} + \mathbf{B} \cdot \mathbf{H}), \qquad (2.25)$$

then (2.24) will be rewritten in the following form:

$$-\int_V \mathbf{j} \cdot \mathbf{E} dv = \int_V \left[\frac{\partial W}{\partial t} + \nabla \cdot (\mathbf{E} \times \mathbf{H}) \right] dv \qquad (2.26)$$

Because (2.26) is written for any volume V, it can be presented in differential form:

$$\frac{\partial W}{\partial t} + \nabla \cdot \mathbf{S} = -\mathbf{j} \cdot \mathbf{E} \qquad (2.27)$$

Equation (2.27) is the equation of EM-field energy conservation, or the equation of continuity. It can be shown that the vector $\mathbf{S} = \mathbf{E} \times \mathbf{H}$ in the brackets on the right-hand side of (2.26) has the dimension of watt/m^2, which is that of power density. From (2.27) is clear that it may be associated with the direction of power flow.

The vector that determines the power flow of EM field is called the *Poynting vector.* Equation (2.26) is the *integral Poynting theorem* and (2.27) is its *vector presentation.*

Using the time harmonic presentation of Maxwell's equations, one can convert (2.26) to the time-harmonic form. If we now introduce, instead of the derivation $\frac{\partial}{\partial t}$, the term $i\omega$, and present the operation of averaging $<\mathbf{E} \times \mathbf{H}>$, as $\frac{1}{2}\mathrm{Re}\{\mathbf{E} \times \mathbf{H}^*\}$, taking into account Gauss's theorem for the term $\nabla \cdot (\mathbf{E} \times \mathbf{H}^*)$, we finally obtain from (2.26) the Poynting theorem presented in *time harmonic form*:

$$\int_S d\mathbf{s} \cdot (\mathbf{E} \times \mathbf{H}^*) = \int_V dv(\mathbf{H}^* \cdot \mathbf{B} - \mathbf{E} \cdot \mathbf{D}^*) - \int_V dv\mathbf{E} \cdot \mathbf{j} \qquad (2.28)$$

2.1.5 Wave Equations

Physically, EM-wave propagation phenomena can be described by use of both the scalar and vector wave equation presentations. In the case of an isotropic inhomogeneous medium, one can present Maxwell's equations in the following form, using their time-harmonic presentations (2.7):

$$\begin{aligned} \nabla \times \mu^{-1}(\mathbf{r})\nabla \times \mathbf{E}(\mathbf{r}) - \omega^2\epsilon(\mathbf{r})\mathbf{E}(\mathbf{r}) &= i\omega\mathbf{j}(\mathbf{r}) - \nabla \times \mu^{-1}(\mathbf{r})\mathbf{M}(\mathbf{r}) \\ \nabla \times \epsilon^{-1}(\mathbf{r})\nabla \times \mathbf{H}(\mathbf{r}) - \omega^2\mu(\mathbf{r})\mathbf{H}(\mathbf{r}) &= i\omega\mathbf{M}(\mathbf{r}) - \nabla \times \epsilon^{-1}(\mathbf{r})\mathbf{j}(\mathbf{r}) \end{aligned} \tag{2.29}$$

Because most problems of wave propagation above the terrain, including built-up environments, reduce to propagation in a homogeneous, source-free isotropic medium, this system can be easily simplified from system (2.7) by taking into account the relations (2.3a–c) with $\epsilon(\mathbf{r}) \equiv \epsilon$, $\mu(\mathbf{r}) \equiv \mu$, $\sigma(\mathbf{r}) \equiv \sigma$, that is,

$$\begin{aligned} \nabla \times \nabla \times \mathbf{E}(\mathbf{r}) - \omega^2\epsilon\mu\mathbf{E}(\mathbf{r}) &= 0 \\ \nabla \times \nabla \times \mathbf{H}(\mathbf{r}) - \omega^2\epsilon\mu\mathbf{H}(\mathbf{r}) &= 0 \end{aligned} \tag{2.30}$$

Because both equations are symmetric, one can use one of them, namely that for $\mathbf{E}$, and by introducing the vector relation $\nabla \times \nabla \times \mathbf{E} = \nabla(\nabla \cdot \mathbf{E}) - \nabla^2\mathbf{E}$ and taking into account that $\nabla \cdot \mathbf{E} = 0$, finally obtain

$$\nabla^2\mathbf{E}(\mathbf{r}) + k^2\mathbf{E}(\mathbf{r}) = 0, \tag{2.31}$$

where $k^2 = \omega^2\epsilon\mu$. It can be shown that all other electromagnetic vectors satisfy as well the same *wave equation* as (2.31) (see, particularly, (2.22) for Hertzian vectors in a source-free medium).

In special cases of a homogeneous, source-free, isotropic medium, the three-dimensional wave equation reduces to a set of scalar wave equation. This is because in Cartesian coordinates, $\mathbf{E}(\mathbf{r}) = E_x\mathbf{x}_0 + E_y\mathbf{y}_0 + E_z\mathbf{z}_0$, where $\mathbf{x}_0$, $\mathbf{y}_0$, $\mathbf{z}_0$ are unit vectors in the directions of the x, y, z coordinates, respectively. Hence, (2.31) consists of three scalar equations such as

$$\nabla^2\Psi(\mathbf{r}) + k^2\Psi(\mathbf{r}) = 0, \tag{2.32}$$

where $\Psi(\mathbf{r})$ can be either E_x, E_y, or E_z. This statement is not true in cylindrical or spherical coordinate systems. The problems of independent solution of each scalar wave equation, such as (2.32), are the subject of Section 2.2.

2.1.6 Boundary Conditions

Equation (2.29) describes all the propagation phenomena within an infinite inhomogeneous isotropic medium. But if we consider two inhomogeneous finite or semifinite regions, we need to introduce *boundary conditions* at the interface between these two regions in order to solve one of the two equations in (2.29). In this case, the procedure to solve the vector wave equation is as follows.

As a first step, this equation is solved separately for each region. Then, in the second step, by patching the solution together via boundary conditions, we obtain the solution for two neighboring regions. It can be shown that the boundary conditions follow from one of the two vector wave equations in (2.29). To do so, we integrate the first equation of (2.29) within a small region in the interface of the two inhomogeneous semifinite or finite regions, as presented in Figure 2.4. Then using Stokes's theorem for the surface integral of a curl, and using the same integration over surface S for both equations in (2.29), we finally obtain after straightforward derivations and taking the limit $\delta \to 0$ (see Figure 2.4) respectively for the magnetic-field component

$$\mathbf{n} \times \mathbf{H}_1 - \mathbf{n} \times \mathbf{H}_2 = \mathbf{j}_S \tag{2.33}$$

and for electric-field component

$$\mathbf{n} \times \mathbf{E}_1 - \mathbf{n} \times \mathbf{E}_2 = -\mathbf{M}_S \tag{2.34}$$

where $\mathbf{M}_S$ and $\mathbf{j}_S$ is a magnetic and electric current sheet at the interface, respectively. Equation (2.33) states that the discontinuity in the tangential component of the magnetic field is proportional to the electric current sheet $\mathbf{j}_S$. This is the *first boundary condition* for solving any one vector electromagnetic

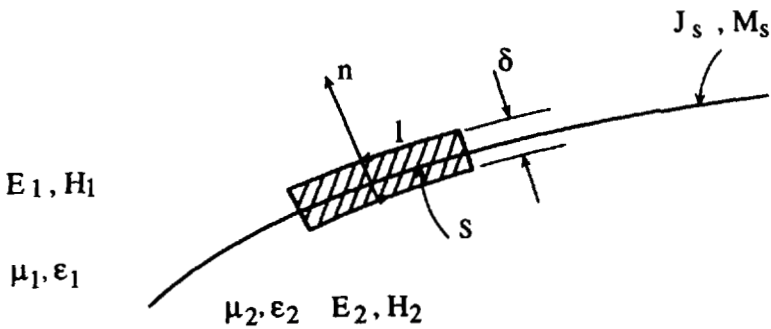

Figure 2.4 The geometry for the derivation of the boundary conditions.

equation from (2.29). Equation (2.34) states that the discontinuity in the tangential component of the electric field is proportional to the magnetic current sheet $\mathbf{M}_S$. This is the *second boundary condition* for (2.29).

Both boundary conditions (2.33) and (2.34) can be simplified for the case of radio wave propagation above a flat terrain. In this case, there are two semi-infinite neighboring regions (air-ground) separated by the boundary, as shown in Figure 2.5.

In the case considered, the first boundary condition (2.33) for an isotropic nonmagnetized ($\mu = 1$) source-free ($\mathbf{M}_S = 0$, $\mathbf{j}_S = 0$) subsoil medium reduces to

$$\begin{aligned} H_{1n} &= H_{2n} \\ H_{1\tau} &= H_{2\tau} \end{aligned} \tag{2.35}$$

Both conditions are valid in the case of finite conductivity of each medium, which is satisfied within the air-ground surface. The first condition in (2.35) states that the normal components of the magnetic field of an EM wave is continuous at the interface of air-ground surface. The second condition in (2.35) states that the tangential component of magnetic field is also continuous at the interface of the air-ground surface.

As for the second boundary condition (2.34), it also can be simplified for the interface of the air-ground surface as

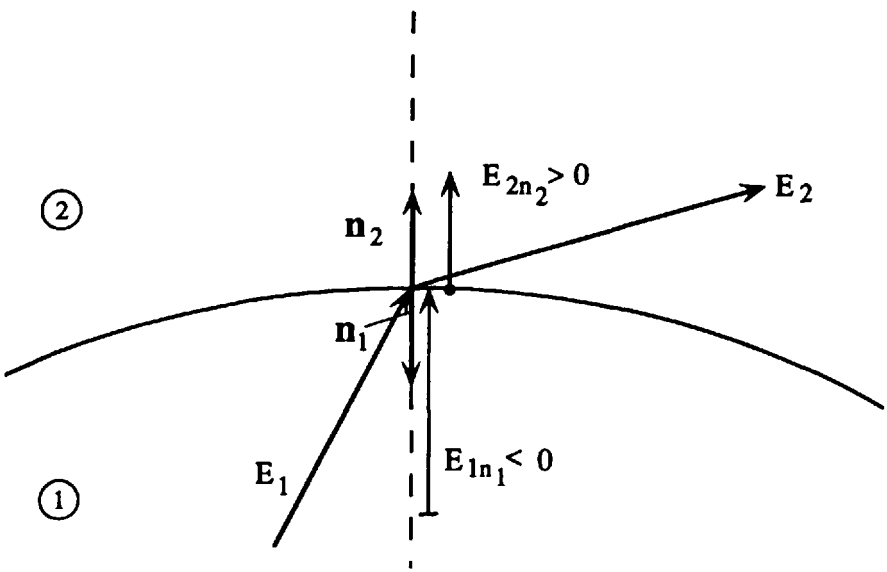

Figure 2.5 Presentation of air-ground surface boundary conditions.

$$\begin{aligned} \mathbf{n} \times \mathbf{E}_1 &= \mathbf{n} \times \mathbf{E}_2 \\ E_{1\tau} &= E_{2\tau} \end{aligned} \tag{2.36}$$

Condition (2.36) states that the tangential components of the electric field of an EM wave are continuous at the interface of the air-ground surface.

One may notice that conditions (2.33) and (2.34) are more general than those described by (2.35) and (2.36), and satisfy various kinds of isotropic inhomogeneous media that consist of both electric and magnetic sources.

2.2 Propagation in Free Space

In free space, an infinite isotropic homogeneous source-free medium, the vector-wave equation can be presented in a simple form (2.30) to (2.31) for one of the components of the EM field, or by use of the Hertzian vector $\Pi(\mathbf{r})$:

$$\nabla^2\Pi(\mathbf{r}) + k^2\Pi(\mathbf{r}) = 0 \tag{2.37}$$

where, once more, the wavenumber $k = \omega\sqrt{\mu\epsilon}$ (in many practical cases of terrain propagation $\mu = 1$ with great accuracy, and one can rewrite it as $k = \omega\sqrt{\epsilon}$).

2.2.1 Plane Waves in Free Space

For plane waves in a Cartesian coordinate system each of (2.31) or (2.37) can be rewritten in scalar form (2.32) for any Cartesian component of vectors $\mathbf{E}(\mathbf{r})$, $\mathbf{H}(\mathbf{r})$, or $\Pi(\mathbf{r})$. Usually, the literature presents another form of (2.32) by introducing wave number k instead, the phase velocity $v_{\text{ph}} \equiv v = \dfrac{\omega}{k} = \dfrac{c}{\sqrt{\mu\epsilon}}$. In this case (2.32) can be rewrittten as:

$$\nabla^2\Psi(\mathbf{r}) + \frac{\omega^2}{v^2}\Psi(\mathbf{r}) = 0 \tag{2.38}$$

Wave equations (2.32) or (2.38) have the well-known solution [1–3]

$$\Psi(\mathbf{r}) = \exp(i\mathbf{k} \cdot \mathbf{r}) \tag{2.39}$$

The waves that satisfy scalar (2.38) and are determined by (2.39) are called *plane waves*. Wave vector $\mathbf{k}$ denotes the direction of propagation of the

plane wave in free space (see Figure 2.1). If one considers the plane wave that propagates in any direction, say along the x-axis, then the fundamental solution of (2.38) is

$$\Psi(x) = A\exp(ikx) + B\exp(-ikx) \tag{2.40}$$

This solution describes the waves, propagating in the positive direction (with the sign "+" in the exponent) and in the negative direction (with the sign "−" in the exponent), respectively, along the x-axis with phase velocity $v_{ph} = \dfrac{c}{\sqrt{\mu\epsilon}}$ which equals c in an ideal free space.

But one can note that EM fields have a vector character and satisfy Maxwell's equations in (2.7) or wave equations such as (2.31) and (2.37). Thus one can find the field vectors in the following form:

$$\begin{aligned} \mathbf{E}(\mathbf{r}) &= \mathbf{e}_E E_0 \exp(i\mathbf{k}\cdot\mathbf{r}) \\ \mathbf{H}(\mathbf{r}) &= \mathbf{e}_H H_0 \exp(i\mathbf{k}\cdot\mathbf{r}) \end{aligned} \tag{2.41}$$

where $\mathbf{e}_E$ and $\mathbf{e}_H$ are the constant unit vectors (i.e., $|\mathbf{e}_E| = |\mathbf{e}_H| = 1$; E_0 and H_0 are the complex amplitudes), which are constant in space and time. From conditions in free space without sources

$$\nabla\cdot\mathbf{E} = 0 \quad \text{and} \quad \nabla\cdot\mathbf{H} = 0$$

it follows that

$$\mathbf{e}_E\cdot\mathbf{k} = 0 \quad \text{and} \quad \mathbf{e}_H\cdot\mathbf{k} = 0 \tag{2.42}$$

which denote that $\mathbf{E}$ and $\mathbf{H}$ are perpendicular to direction of wave propagation $\mathbf{k}$. Moreover, because in free space the first Maxwell equation (2.1a) or (2.7a) reduces to

$$\nabla\times\mathbf{E} - i\omega\mathbf{B} = 0, \quad \mathbf{B} = \mu\mathbf{H} \equiv \mathbf{H} \tag{2.43}$$

we can finally obtain from (2.43) for a plane wave (2.41) in free space (with $\mu = 1$):

$$i[(\mathbf{k}\times\mathbf{e}_E)E_0 - k\mathbf{e}_H B_0]\exp(i\mathbf{k}\cdot\mathbf{r}) = 0 \tag{2.44}$$

Equation (2.44) has solutions:

$$\mathbf{e}_H = \frac{\mathbf{k} \times \mathbf{e}_E}{k}, \quad B_0 = \sqrt{\epsilon} E_0 \tag{2.45}$$

Hence, vectors $\mathbf{e}_E$, $\mathbf{e}_H$, and $\mathbf{k}$ form the system of orthogonal vectors, where vectors **E** and **B** oscillate in phase and their ratio is constant (see Figure 2.6). The wave which is described by relations (2.41) and (2.45) is a *transverse wave* propagating in the **k**-direction.

2.2.2 Wave Polarization

The vector of electric field in the plane wave as described by formula (2.41) is directed along unit vector $\mathbf{e}_E$. To obtain the more general case of wave polarization we need an additional linear-polarized wave independent of the first one. It can be easily shown that two linear-independent solutions which satisfy wave (2.30) or (2.31) can be presented in the following form:

$$\begin{aligned} \mathbf{E}_1 &= \mathbf{e}_1 E_1 \exp(i\mathbf{k} \cdot \mathbf{r}) \\ \mathbf{E}_2 &= \mathbf{e}_2 E_2 \exp(i\mathbf{k} \cdot \mathbf{r}) \end{aligned} \tag{2.46}$$

The magnetic field components of the EM wave satisfy, according to (2.41) in free space ($\mu = 1$), the following relations:

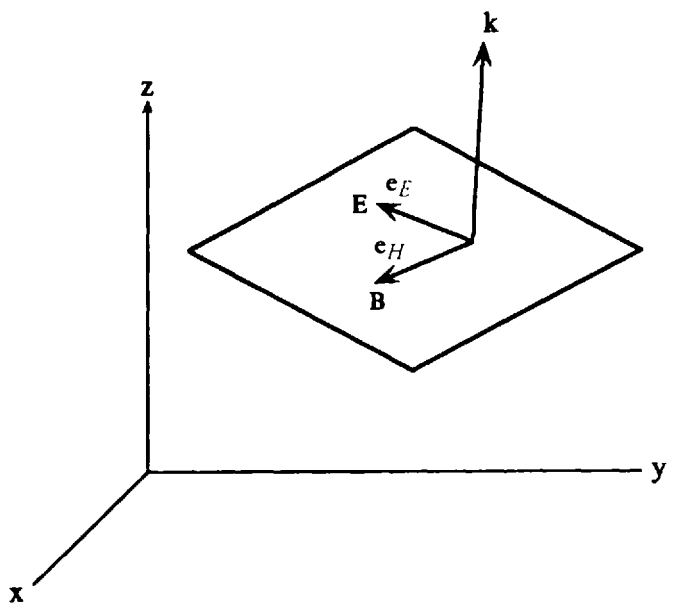

Figure 2.6 The transverse wave components presentation in free space.

$$\mathbf{B}_j = \sqrt{\epsilon}\frac{\mathbf{k} \times \mathbf{E}_j}{k}, \quad \mathbf{B}_j = \mathbf{H}_j, \quad j = 1, 2 \tag{2.47}$$

Here, amplitudes $E_1(H_1)$ and $E_2(H_2)$ are the complex values, which enable us to introduce the phase difference between the two components of the EM wave. Thus the common solution for the plane EM wave propagated along vector $\mathbf{k}$ can be presented as a linear combination of $\mathbf{E}_1$ and $\mathbf{E}_2$:

$$\mathbf{E}(\mathbf{r}) = \{\mathbf{e}_1 E_1 + \mathbf{e}_2 E_2\} \exp(i\mathbf{k} \cdot \mathbf{r}) \tag{2.48}$$

If $\mathbf{E}_1$ and $\mathbf{E}_2$ have the *same phase*, then solution (2.48) describes the *linear polarized wave* with polarization vector directed to the $\mathbf{e}_1$ axis at angle

$$\theta = \tan^{-1}\left(\frac{E_2}{E_1}\right) \tag{2.49a}$$

and with amplitude

$$E = (E_1^2 + E_2^2)^{1/2} \tag{2.49b}$$

as presented in Figure 2.7.

If $\mathbf{E}_1$ and $\mathbf{E}_2$ have different phases, then the EM wave (2.48) is *elliptically polarized.* If $\mathbf{E}_1 = \mathbf{E}_2$ and phase difference equal $\pi/2$, then the elliptically polarized wave becomes a *circularly polarized wave.* In this case solution (2.48) can be rewritten as

$$\mathbf{E}(\mathbf{r}) = E_0\{\mathbf{e}_1 \pm \mathbf{e}_2\} \exp(i\mathbf{k} \cdot \mathbf{r}) \tag{2.50}$$

The sign "+" corresponds to anticlockwise rotation (sometimes called the wave with *left-hand* circular polarization). The sign "−" corresponds to the

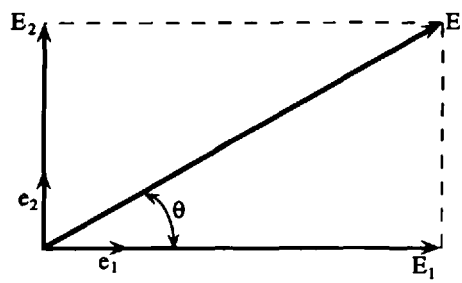

Figure 2.7 The linear polarized wave geometrical presentation.

wave with *right-hand* circular polarization (see Figure 2.8). Then two waves with *circular polarization* can be considered as a basic system for describing the common case of polarized waves. Let us introduce in the common case the orthogonal complex unit vectors

$$\mathbf{e}_{\pm} = \frac{1}{\sqrt{2}}(\mathbf{e}_1 \pm i\mathbf{e}_2) \tag{2.51}$$

Then, the common presentation of a polarized wave (2.48) by the use of linearly polarized waves, and two circularly polarized waves (2.50) and (2.51), can be rewritten as

$$\mathbf{E}(\mathbf{r}) = \{\mathbf{e}_+ E_+ + \mathbf{e}_- E_-\}\exp(i\mathbf{k} \cdot \mathbf{r}) \tag{2.52}$$

where E_+ and E_- are the complex amplitudes of two circularly polarized waves with opposite directions of rotation. If their modulii are different, but their phases are equal, then (2.52) describes, as above, an elliptically polarized wave with main elliptical axes directed along $\mathbf{e}_1$ and $\mathbf{e}_2$. The ratio of these semi-axes equals $(1 - q)/(1 + q)$, where $q = \dfrac{E_-}{E_+}$. If the complex amplitudes have different phases, so that

$$\frac{E_-}{E_+} = q \cdot \exp(i\alpha) \tag{2.53}$$

then the ellipses' axes for **E**-vector are rotated by angle $\alpha/2$. In Figure 2.9 the common case of an elliptical polarized EM wave is presented. At each spatial point the vector (the same applies to the vectors **H** or **B**) describes ellipses, as

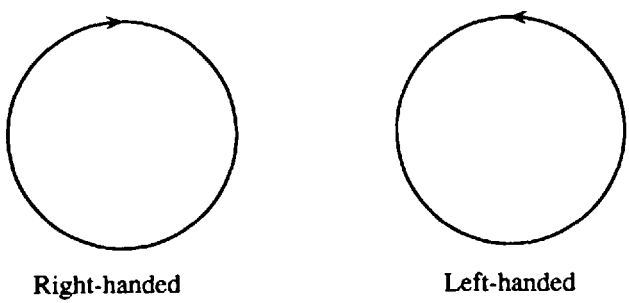

Figure 2.8 Schematical presentation of two kinds of waves with circular polarization.

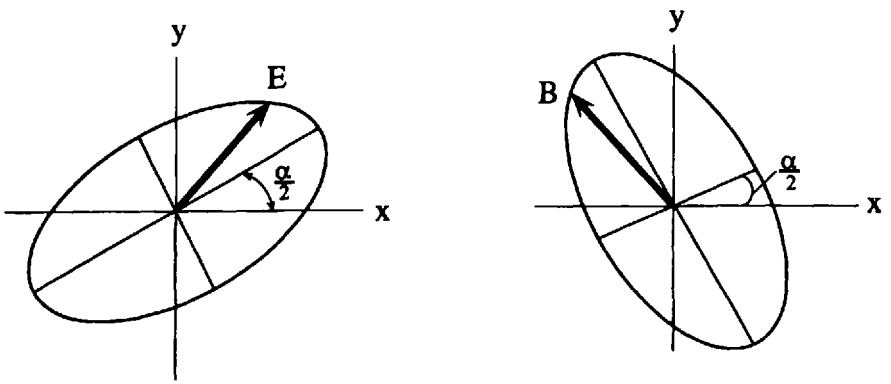

Figure 2.9 Presentation of two ellipses for the E-component and the H-component of EM-field.

shown in Figure 2.9. For the case $q = \pm 1$, we once more return to the case of linearly polarized wave.

2.2.3 Cylindrical and Spherical Waves in Free Space

As mentioned in the literature [1–4, 7–8], to obtain the common vector presentation of cylindrical and spherical waves is a very complicated problem, which can be reduced for the case of an isotropic homogeneous source-free medium (with properties which limit to those in free space, but with $\mu \neq 1$) to the simple scalar form, as was done above for the plane wave in the Cartesian coordinate system.

The scalar wave equation in the cylindrical coordinate system $\{\rho, \varphi, z\}$ can be written as:

$$\left(\frac{1}{\rho}\frac{\partial}{\partial\rho}\rho\frac{\partial}{\partial\rho} + \frac{1}{\rho^2}\frac{\partial}{\partial\varphi^2} + \frac{\partial^2}{\partial z^2} + k^2\right)\Psi(\mathbf{r}) = 0 \tag{2.54}$$

The above partial differential equation can be solved by separation of variables, and its one-dimensional (along the z-axis) solution can be presented in the following form [5]

$$\Psi(\mathbf{r}) = \Psi_n(\rho)\exp\{in\varphi + ik_z z\} \tag{2.55}$$

where n is an integer since the wave field has to be 2π periodic in φ. Then, by substituting (2.55) in (2.54), we reduce it to an ordinary differential equation with the full derivative (d/dx, x is variable) presentation [5]:

$$\left(\frac{1}{\rho}\frac{d}{d\rho}\rho\frac{d}{d\rho} - \frac{n^2}{\rho^2} + k_r^2\right)\Psi_n(\rho) = 0 \tag{2.56}$$

where $k_r = (k^2 - k_z^2)^{1/2}$. One may notice that (2.56) is the Bessel equation [6] with two linear independent solutions. Its general solution is a linear superposition of any two of the following four spectral functions [5]: Bessel function, $J_n(k_r\rho)$, Neumann function, $N_n(k_r\rho)$, Hankel functions of first order, $H_n^{(1)}(k_r\rho)$, and second order, $H_n^{(2)}(k_r\rho)$, respectively. Full information about the properties of these special functions can be obtained from reference books [5, 6] which describe all mathematical functions. For our purposes the exponential approximation of those functions is very important. For example, the general representation of a cylindrical wave (2.55) can be approximated by a simple exponential form:

$$\Psi(\mathbf{r}) \sim \sqrt{\frac{2}{\pi k_r \rho}}\exp\left\{-i\frac{n\pi}{2} - i\frac{\pi}{4}\right\}\exp\left\{i\left(\frac{n}{\rho}(\rho\varphi) + ik_z z + ik_r\rho\right)\right\} \tag{2.57}$$

Here, $\rho\varphi$ is the arc length in the φ direction, and n/ρ can be thought of as the component of vector $\mathbf{k}$, if one compares the *cylindrical wave* presentation (2.57) with that for a *plane wave* (2.39). Consequently, (2.57) looks like a plane wave propagating mainly in the direction $\mathbf{k} = \mathbf{k}_z z + \mathbf{k}_r\rho$, when $\rho \to \infty$.

We now consider a *spherical wave* presentation in free space. In the spherical coordinate system $\{r, \theta, \varphi\}$, the scalar wave equation is [5]:

$$\left(\frac{1}{r^2}\frac{\partial}{\partial r}r^2\frac{\partial}{\partial r} + \frac{1}{r^2\sin\theta}\frac{\partial}{\partial\theta}\sin\theta\frac{\partial}{\partial\theta} + \frac{1}{r^2\sin^2\theta}\frac{\partial^2}{\partial\varphi^2} + k^2\right)\Psi(\mathbf{r}) = 0 \tag{2.58}$$

Following [3], we present the solution of this equation in the form:

$$\Psi(\mathbf{r}) = \Psi(r, \theta)\exp\{im\varphi\} \tag{2.59}$$

The general (2.58) can be further simplified by the separation of variables by letting

$$\Psi(r, \theta) = b_n(kr)\,P_n^m(\cos\theta) \tag{2.60}$$

where $P_n^m(\cos\theta)$ is the associate Legendre polynomial satisfying the equation

$$\left\{\frac{1}{\sin\theta}\frac{d}{d\theta}\sin\theta\frac{d}{d\theta} + \left[n(n+1) - \frac{m^2}{\sin^2\theta}\right]\right\} P_n^m(\cos\theta) = 0 \qquad (2.61)$$

Analogously, $b_n(kr)$ satisfies the equation

$$\left(\frac{1}{r^2}\frac{d}{dr}r^2\frac{d}{dr} + k^2 - \frac{n(n+1)}{r^2}\right) b_n(kr) = 0 \qquad (2.62)$$

Equation (2.62) is just the spherical Bessel equation, and $b_n(kr)$ is either the spherical Bessel function, $j_n(kr)$, spherical Neumann function, $n_n(kr)$, or the spherical Hankel functions, $h_n^{(1)}(kr)$ and $h_n^{(2)}(kr)$ [5, 6].

As shown in [5, 6], the spherical special functions can be approximated by the spherical functions proportional to $\sim\dfrac{\exp\{ikr\}}{r}$. If so, one can represent the *spherical* wave as a *plane* one when $\rho \to \infty$.

In fact, we can easily obtain relations between spherical and plane waves. Following [8–10], we will consider the plane wave propagating in an infinite homogeneous source-free space, and will present it in the same form as in (2.31), but by using the Hertzian vector instead of the field component presentation,

$$\nabla^2\Pi(\mathbf{r}) + k^2\Pi(\mathbf{r}) = 0 \qquad (2.63)$$

The solution of (2.63) is the same as with (2.39), but for the Hertzian vector:

$$\Pi(\mathbf{r}) = \Pi_0\exp\{i(k_x x + k_y y + k_z z)\} \qquad (2.64)$$

where the complex wavenumbers of the plane wave, k_x, k_y, and k_z, satisfy the condition $k^2 = k_x^2 + k_y^2 + k_z^2$. Let us split all wavenumbers at the real and imaginary parts, that is:

$$k = k_1 + ik_2; \qquad (2.65a)$$
$$k_x = k_{1x} + ik_{2x},\ k_y = k_{1y} + ik_{2y},\ k_z = k_{1z} + ik_{2z}$$

and present the components (k_{1x}, k_{1y}, k_{1z}) by introducing real vector $\mathbf{q}$, and those of (k_{2x}, k_{2y}, k_{2z}) by introducing real vector $\mathbf{p}$, such that

$$k_{1x} = q\sin\theta\cos\varphi, \quad k_{2x} = p\sin\alpha\cos\beta$$
$$k_{1y} = q\sin\theta\sin\varphi, \quad k_{2y} = p\sin\alpha\sin\beta \tag{2.65b}$$
$$k_{1z} = q\cos\theta, \quad k_{2z} = p\cos\beta$$

If so, any spherical function of three variables $\frac{\exp\{ikR\}}{R}$, $R = |\mathbf{r}|$, can be presented by introducing the three-dimensional Fourier integral

$$\frac{\exp\{ikR\}}{R} = \int_{-\infty}^{+\infty} A(\mathbf{q}')\exp\{i\mathbf{q}' \cdot \mathbf{R}\}d\mathbf{q}' \tag{2.66}$$

in which each of the plane waves from superposition (2.66) is a solution of the homogeneous equation

$$(\nabla^2 - q'^2)\exp\{i\mathbf{q}' \cdot \mathbf{R}\} = 0, \; q'^2 = q_x'^2 + q_y'^2 + q_z'^2 \tag{2.67}$$

The amplitude $A(\mathbf{q}')$ can be easily obtained by multiplying both sides of (2.66) by $\exp\{i\mathbf{q}' \cdot \mathbf{R}\}$ and integrating both sides over the whole infinite space. After some straightforward derivations one can obtain the expression for wave amplitude

$$A(\mathbf{q}) = \frac{1}{2\pi^2}\frac{1}{q^2 - k^2} \tag{2.68}$$

Hence, the representation of a spherical wave by plane waves can be given, finally, as

$$\frac{\exp\{ikR\}}{R} = \frac{1}{2\pi}\int_{-\infty}^{+\infty}\frac{\exp\{i(q_x x + q_y y + q_z z)\}}{q_x^2 + q_y^2 + q_z^2 - k^2}\,dq_x dq_y dq_z \tag{2.69}$$

The expression in the right-hand side of (2.69) describes plane waves with *different* wavenumbers $q = (q_x^2 + q_y^2 + q_z^2)^{1/2}$. This is an important result, because if this is not so, that is, if all plane waves propagate with the same wavelength $\lambda = \frac{2\pi}{k}$, then all of them satisfy the *homogeneous* (2.63). But, at the same time, the spherical wave in the left-hand side of (2.69), having a singularity for $R = 0$, is the solution of a particular *inhomogeneous* equation

with the point source in the right-hand side of (2.63). Hence, the spherical wave with the wavelength $\lambda = \frac{2\pi}{k}$ can be represented as a superposition (2.69) of simple plane waves (with real wavenumber q), but with various wavelengths, each different from $\frac{2\pi}{k}$. At the same time, as was shown in [8], the spherical wave can be presented as a superposition of complex plane waves (with complex vector of propagation $\mathbf{q}$), but where each wave corresponds to a definite wavelength ($q^2 = q_x^2 + q_y^2 + q_z^2 \equiv k^2$). In this case we have the expansion of spherical waves into plane waves with complex wave vector $\mathbf{q}$. In fact, if we integrate the spherical wave representation (2.69) with complex wavenumber q along the z-direction as the direction of wave propagation, we have

$$\frac{\exp\{ikR\}}{R} = \frac{1}{2\pi i}\int_{-\infty}^{+\infty} \frac{\exp\{i(q_x x + q_y y) + z\sqrt{k^2 - q_x^2 - q_y^2}\}}{\sqrt{k^2 - q_x^2 - q_y^2}}\, dq_x dq_y \tag{2.70}$$

It follows from additional examination of (2.70), according to [8], that the above integral consists of two parts. The first summand has the image expression before the root in the exponential function for the z-coordinate $z\sqrt{k^2 - q_x^2 - q_y^2}$, because $k^2 > (q_x^2 + q_y^2)$ and the term $iz\sqrt{k^2 - q_x^2 - q_y^2}$ in the exponent is imaginary and describes a superposition of simple plane waves which propagate with complex vector $\mathbf{q}$ and with the same wavelength $\lambda = \frac{2\pi}{k}$, as that for the spherical wave. The second summand, inversely, has the real term of $iz\sqrt{k^2 - q_x^2 - q_y^2}$ in the exponent of the integrand in (2.70), because here $k^2 < (q_x^2 + q_y^2)$. Thus this summand describes real plane waves that lie in the (x, y) plane (their wavelengths in this plane are different from the wavelength of the spherical wave $\sim\frac{2\pi}{k}$) and propagate along the z-axis with exponential attenuation for $z \to \pm\infty$.

Of course, one could integrate (2.70) not only along the z-axis, each direction can be used for integration of (2.70). In any case we obtain an exponential attenuation of plane waves along the selected axis. Thus we have two general possibilities for expanding a spherical wave as the superposition of plane waves: with different, but real, wavenumbers $q \neq k$, and with a complex, but the same wavenumber $q = k$, with respect to the spherical wave.

The above results allow us to present in the future all propagation phenomena through the prism of spherical and plane waves' propagation and by use of the spherical-wave expansion into the superposition of plane waves.

2.2.4 Green's Function Presentation

In an unbounded homogeneous medium using any kind of source, it is a difficult problem to obtain a strict solution of the wave equation, which describes EM-wave propagation in such a medium. Usually, to obtain a particular solution of a wave equation one can assume that the source is a *point* with respect to volume metric dimensions around this source. In the literature [1–3, 7–10] to determine the criterion of a point source requires that the linear dimensions of the source, 1, must be smaller than the wavelength in the considered medium, that is, $1 << \frac{\lambda}{\pi}$. In this case Green's function, as a solution of the wave equation for a point source, can be introduced. Moreover, if any real antenna can be represented as a general real source by a linear superposition of point sources, one can obtain a general solution for the wave equation with such a source by using the solution of the wave equation for a point source, in other words, by use of Green's function as a point-source function. This result is also connected with the topic of linearity of the wave equation in the considered medium. Below, we will examine the boundary-value problems both for scalar and vector waves by employing Green's function presentation.

Green's function presentation in electrodynamics. First of all, we examine the Green's function presentation for the scalar wave equation. In this case let us construct the solution of a scalar wave equation in any volume V of free space having an arbitrary source $s(\mathbf{r})$ (see Figure 2.10). Such a solution can be written in the same form, as (2.32), but with a source in its right-hand side:

$$\nabla^2\Psi(\mathbf{r}) + k^2\Psi(\mathbf{r}) = s(\mathbf{r}) \tag{2.71}$$

First, we will introduce the same equation for Green's function, but with a point source in its right-hand side:

$$\nabla^2 G(\mathbf{r},\mathbf{r}') + k^2 G(\mathbf{r},\mathbf{r}') = -\delta(\mathbf{r}-\mathbf{r}') \tag{2.72}$$

The given functions $G(\mathbf{r},\mathbf{r}')$ and $\Psi(\mathbf{r})$ can be easily found from the principle of linear superposition, since $G(\mathbf{r},\mathbf{r}')$, as was mentioned above, is the solution of (2.71) with a point source in the right-hand side. In fact, one can notice that an arbitrary source $s(\mathbf{r})$ is just

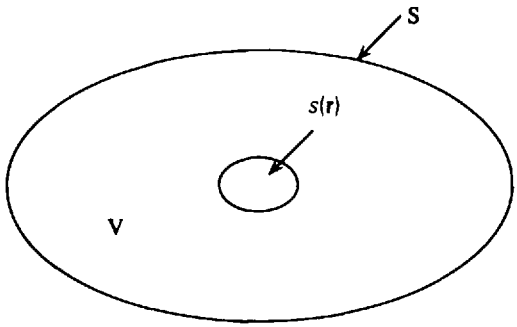

The radiation of a source S(r) in a volume V

Figure 2.10 The geometry of a source $s(\mathbf{r})$ in a volume V.

$$s(\mathbf{r}) = \int d\mathbf{r}'\, s(\mathbf{r}')\, \delta(\mathbf{r} - \mathbf{r}') \tag{2.73}$$

which is actually a linear superposition of point sources in mathematical terms. Consequently, the solution of (2.71) is

$$\Psi(\mathbf{r}) = -\int_V d\mathbf{r}'\, G(\mathbf{r}, \mathbf{r}')\, s(\mathbf{r}') \tag{2.74}$$

which is the linear superposition of the solution of (2.72).

To find the solution of (2.72) for free space, or more correctly, for an unbounded, homogeneous medium, one can solve it in spherical coordinates with the origin at vector $\mathbf{r}'$. In this case (2.72) reduces to

$$\nabla^2 G(\mathbf{r}) + k^2 G(\mathbf{r}) = -\delta(\mathbf{r}) \tag{2.75}$$

But due to the spherical symmetry of a point source, $G(\mathbf{r})$ must also be spherically symmetric. Then, for $\mathbf{r} \neq 0$, the homogeneous, spherically symmetric solution of (2.75) is given by

$$G(\mathbf{r}) = A\frac{\exp\{ikr\}}{r} + B\frac{\exp\{-ikr\}}{r} \tag{2.76a}$$

Since sources are absent at infinity, a physically correct solution of (2.76) can be presented as

$$G(\mathbf{r}) = A\frac{\exp\{ikr\}}{r} \tag{2.76b}$$

To determine the unknown constant A, we substitute (2.76b) into (2.75) and integrate it over a small volume about the origin to yield

$$\int_{\Delta V} dv \cdot \nabla \cdot \nabla \frac{A\exp\{ikr\}}{r} + \int_{\Delta V} dv \cdot k^2 \frac{A\exp\{ikr\}}{r} = -1 \tag{2.77}$$

Note that the second integral in (2.77) vanishes when $\Delta V \to 0$, because $dv = 4\pi r^2 \cdot dr$.

The first integral in (2.77) can be converted into a surface integral using Gauss's theorem to obtain

$$\left[4\pi r^2 \frac{d}{dr} A\frac{\exp\{ikr\}}{r}\right]_{r\to 0} = -1 \tag{2.78}$$

or

$$A = \frac{1}{4\pi}$$

As was mentioned above, the solution of (2.72) must depend only on $|\mathbf{r} - \mathbf{r}'|$.

Therefore, Green's function must be presented, as a solution of (2.72), in the following form:

$$G(\mathbf{r},\mathbf{r}') = G(\mathbf{r} - \mathbf{r}') = \frac{\exp\{ik|\mathbf{r} - \mathbf{r}'|\}}{|\mathbf{r} - \mathbf{r}'|} \tag{2.79}$$

Moreover, it can be seen that $G(\mathbf{r}, \mathbf{r}') = G(\mathbf{r}', \mathbf{r})$ from reciprocity, irrespective of the shape of volume V[3]. This fact and formula (2.79) imply that Green's function is translationally invariant for unbounded, homogeneous media. Consequently, a general solution of inhomogeneous (2.71) by using (2.74) can be finally presented as

$$\Psi(\mathbf{r}) = -\int_V d\mathbf{r}' \frac{\exp\{ik|\mathbf{r} - \mathbf{r}'|\}}{|\mathbf{r} - \mathbf{r}'|} s(\mathbf{r}') \tag{2.80}$$

Green's function for the scalar wave (2.79) could be used to find the *dyadic* Green's function for the *vector wave equation* in a unbounded homoge-

neous isotropic medium. For this case we return to (2.30), taking into account the electric source in such a medium:

$$\nabla \times \nabla \times \mathbf{E}(\mathbf{r}) - k^2\mathbf{E}(\mathbf{r}) = i\omega\mu\mathbf{j}(\mathbf{r}) \tag{2.81}$$

Using the fact that $\nabla \times \nabla \times \mathbf{E} = -\nabla^2\mathbf{E} + \nabla(\nabla \cdot \mathbf{E})$, and that $\nabla \cdot \mathbf{E} = \frac{\rho}{\epsilon} = \frac{\nabla \cdot \mathbf{j}}{i\omega\epsilon}$, which follows from the continuity (2.2) in the time-harmonic presentation, we can rewrite (2.81) as

$$\nabla \times \nabla \times \mathbf{E}(\mathbf{r}) + k^2\mathbf{E}(\mathbf{r}) = -i\omega\mu\left[\mathbf{I} + \frac{\nabla\nabla}{k^2}\right] \cdot \mathbf{j}(\mathbf{r}) \tag{2.82}$$

where $\mathbf{I}$ is an identity operator.

In the Cartesian coordinate system, as was shown earlier, there are three scalar-wave equations embedded in the above vector (2.82), each of which can be easily solved in the manner of (2.74). Consequently,

$$E(\mathbf{r}) = i\omega\mu \int_V d\mathbf{r}' G(\mathbf{r} - \mathbf{r}')\left[\mathbf{I} + \frac{\nabla\nabla}{k^2}\right] \cdot \mathbf{j}(\mathbf{r}) \tag{2.83}$$

where $G(\mathbf{r} - \mathbf{r}')$ is the scalar Green's function in an unbounded homogeneous isotropic medium.

Then, by using the vector identities $\nabla fg = g\nabla f + f\nabla g$, $\nabla \cdot g\mathbf{F} = g\nabla \cdot \mathbf{F} + (\nabla g) \cdot \mathbf{F}$, after some straightforward derivations, one can rewrite (2.83) as

$$E(\mathbf{r}) = i\omega\mu \int_V d\mathbf{r}'\mathbf{j}(\mathbf{r}) \cdot \bar{G}_e(\mathbf{r}, \mathbf{r}') \tag{2.84}$$

where

$$\bar{G}_e(\mathbf{r}, \mathbf{r}') = G(\mathbf{r} - \mathbf{r}')\left[\mathbf{I} + \frac{\nabla\nabla}{k^2}\right] \tag{2.85}$$

is a dyad known as the *dyadic Green's function* for the electric component of the EM field in an unbounded homogeneous medium. This function for an unbounded homogeneous medium can also be rewritten as [3]:

$$\bar{G}_e(\mathbf{r},\mathbf{r}') = \frac{1}{k^2}[\nabla \times \nabla \times \mathbf{I}G(\mathbf{r}-\mathbf{r}') - \mathbf{I}\delta(\mathbf{r}-\mathbf{r}')] \tag{2.86}$$

By substituting (2.84) in the initial (2.81) and writing

$$\mathbf{j}(\mathbf{r}) = \int d\mathbf{r}'\mathbf{I}\delta(\mathbf{r}-\mathbf{r}') \cdot \mathbf{j}(\mathbf{r}') \tag{2.87}$$

we can show quite easily that the equation for the dyadic Green's function for a vector wave equation can be presented in the following form:

$$\nabla \times \nabla \times \bar{G}_e(\mathbf{r},\mathbf{r}') - k^2\bar{G}_e(\mathbf{r},\mathbf{r}') = \mathbf{I}\delta(\mathbf{r}-\mathbf{r}') \tag{2.88}$$

We can note that if the simple Green's function obtained for a scalar wave equation and the source $J(r)$ distribution are known for the case of unbounded homogeneous media, one can, using relation (2.85), obtain the dyadic Green's function which satisfies (2.88). In any case, for wave propagation above the terrain, including built-up areas, propagation phenomena in an isotropic medium for different kinds of the EM-field source can be examined using the scalar presentation of Green's function (2.79) and the EM-field presentation (2.80), taking into account the principle of linear superposition (2.73) for any real source of radiation.

2.2.5 Huygens's Principle

Huygens's principle, which comes from the Danish researcher Christian Huygens, shows how a wave field on the surface S determines the wave field off the surface S (Figure 2.11(a)) or, inversely, inside the area bounded by the surface S (Figure 2.11(b)). In other words, each point on the surface S can be interpreted as a source of a spherical wave, which can be observed at any point A, either in the outside space with volume V, if a source O is inside it (Figure 2.11(a)), or inside the bounded area S, if a source O is outside the surface S (Figure 2.11(b)).

This concept can be examined for both scalar and vector waves. Because both concepts are the same physically, and the vector representation needs to present completed mathematical expressions, we shall discuss the scalar case only. The reader who is also interested in examining the electromagnetic case should refer to [1–3].

We indicated above that any scalar wave in an unbounded source-free homogeneous isotropic medium can be described by the homogeneous (2.32)

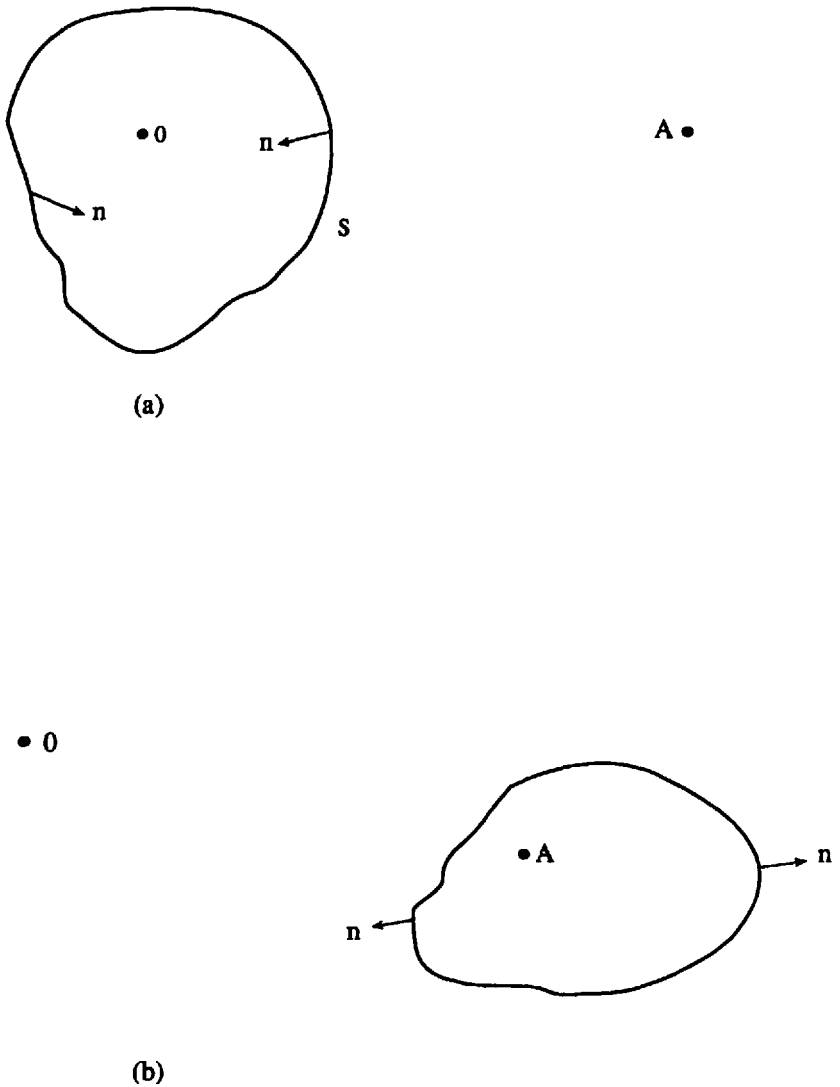

Figure 2.11 The geometry of Huygens's principle in bounded space in two cases of observed point *A*: (a) presentation outside, and (b) inside the surface *S*.

(or (2.71) without the right-hand side). If one wishes to take into account the radiated source in such a medium, then one must introduce and derive (2.72) for *a point source* Green's function.

If we now multiply (2.32) by $G(\mathbf{r}, \mathbf{r}')$ and (2.72) by $\Psi(\mathbf{r})$, subtracting the resulting equations and integrating over a volume V containing vector $\mathbf{r}'$ (see Figure 2.12), we have

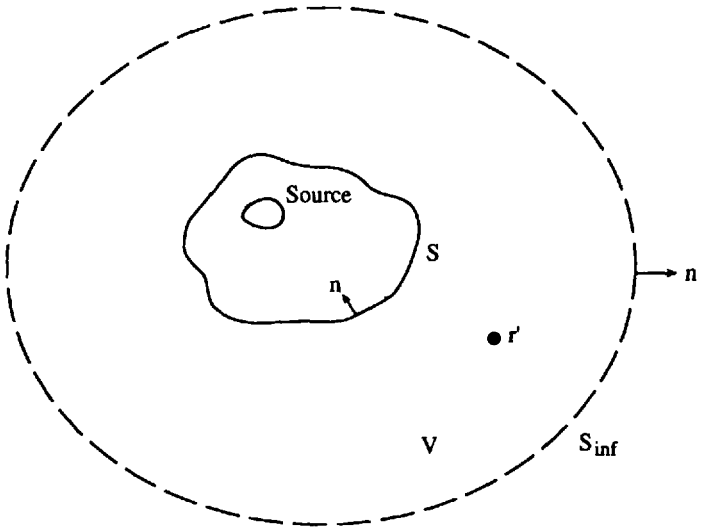

Figure 2.12 The geometry for the derivation of Huygens's principle.

$$\int_V d\mathbf{r}[G(\mathbf{r},\mathbf{r}')\nabla^2\Psi(\mathbf{r}) - \Psi(\mathbf{r})\nabla^2 G(\mathbf{r},\mathbf{r}')] = \Psi(\mathbf{r}') \tag{2.89}$$

Taking into account the following relations [5]

$$G\nabla^2\Psi - \Psi\nabla^2 G = \nabla \cdot [G\nabla\Psi - \Psi\nabla G]$$

we can rewrite (2.73) by use of Green's theorem.

Green's theorem or, as it is sometimes called, the *second Green formula* [2] states the equivalence of *volume* integral (2.89) with the *surface* one, that is,

$$\int_V d\mathbf{r}[G(\mathbf{r},\mathbf{r}')\nabla^2\Psi(\mathbf{r}) - \Psi(\mathbf{r})\nabla^2 G(\mathbf{r},\mathbf{r}')] = \oint_S ds\left[G(\mathbf{r},\mathbf{r}')\frac{\partial\Psi}{\partial\mathbf{n}} - \Psi(\mathbf{r})\frac{\partial G(\mathbf{r},\mathbf{r}')}{\partial\mathbf{n}}\right] \tag{2.90}$$

Here S is the surface bounding volume V, $\dfrac{\partial}{\partial\mathbf{n}}$ is the normal derivative at the surface S, $\mathbf{n}$ is the unit vector directed outside to V normally to the surface S bounding the volume V, as is shown in Figure 2.12. It is well known [5] that for any two scalar functions f and g, there is some relation between

them: $f g \cdot \mathbf{n} = f\dfrac{\partial g}{\partial \mathbf{n}}$. Taking into account this relation and Green's theorem, based on Gauss's divergence law, one can rewrite the left-hand side of (2.89) as:

$$\Psi(\mathbf{r}') = \oint_S ds\mathbf{n} \cdot [G(\mathbf{r},\mathbf{r}')\nabla\Psi(\mathbf{r}) - \Psi(\mathbf{r})\nabla G(\mathbf{r},\mathbf{r}')] \tag{2.91a}$$

Equation (2.91a) is the mathematical expression of the statement that once $\Psi(\mathbf{r})$ and $\mathbf{n} \cdot \nabla\Psi(\mathbf{r})$ are known on surface S, then $\Psi(\mathbf{r}')$ away from S can be found. If the volume V is bounded by S and S_{inf} (surface on infinity S_{inf} together with S, are shown in Figure 2.12), then the surface integral in (2.91a) should include an integral over S_{inf}. But when $S_{\text{inf}} \to \infty$, all fields look like plane wave, and $\nabla \to \mathbf{r}ik$ on surface S_{inf}. Moreover, in this case $G(\mathbf{r},\mathbf{r}')$ is of the order of magnitude of $\sim\dfrac{1}{r}$, when $r \to \infty$; $\Psi(\mathbf{r})$ is of the order of magnitude of $\sim\dfrac{1}{r}$, when $r \to \infty$, if $\Psi(\mathbf{r})$ is due to a source of finite extent (less than a wavelength). Then, the integral in (2.91) over surface S_{inf} vanishes, and (2.91a) is valid for the case shown in Figure 2.12 as well. Hence, the field outside S at $\mathbf{r}'$ is expressed in terms of the field on S.

From (2.91a) one can obtain two different situations at the bounded surface S. In fact, if $G(\mathbf{r}, \mathbf{r}')$ satisfies (2.32) or (2.71) (without its right-hand side) with the boundary conditions $\mathbf{n} \cdot \nabla G(\mathbf{r}, \mathbf{r}') = 0$ for $\mathbf{r} \in S$, then (2.91a) becomes

$$\Psi(\mathbf{r}') = \oint_S dsG(\mathbf{r}, \mathbf{r}')\mathbf{n} \cdot \nabla\Psi(\mathbf{r}) \tag{2.91b}$$

On the other hand, if now $G(\mathbf{r}, \mathbf{r}')$ has only to satisfy (2.32) or (2.71) (without its right-hand side) for both $\mathbf{r}$ and $\mathbf{r}'$ in volume V, and no boundary condition has yet been imposed on $G(\mathbf{r}, \mathbf{r}')$, then, in the case of $G(\mathbf{r}, \mathbf{r}') = 0$ for $\mathbf{r} \in S$, (2.91a) becomes

$$\Psi(\mathbf{r}') = -\oint_S ds\Psi(\mathbf{r})\mathbf{n} \cdot \nabla G(\mathbf{r}, \mathbf{r}') \tag{2.91c}$$

Equations (2.91a), (2.91b), and (2.91c) are various forms of Huygens's principle depending on the definition of Green's function, $G(\mathbf{r}, \mathbf{r}')$, on the bounded surface S. For example, (2.91b) and (2.91c) state that only

$\mathbf{n} \cdot \nabla\Psi(\mathbf{r})$ or $\Psi(\mathbf{r})$ need be known, respectively, on the surface S in order to determine wave function $\Psi(\mathbf{r}')$.

Let us now formulate Huygens's principle for free space without obstacles or discontinuities (i.e., for an unbounded homogeneous medium). This case was an early description of what actually happens with wave energy when it travels in free space in a straight manner. Here, in simple terms, the principle suggests that the energy from each point propagates in all forward directions to form many elementary spherical wavefronts, which Huygens called wavelets. The envelope of these wavelets forms the new wavefront. In other words, each point on a wavefront acts as the source of secondary elementary spherical waves described by Green's function, $G(\mathbf{r}, \mathbf{r}')$. These waves combine to produce a new wavefront in the direction of wave propagation. With great accuracy each wavefront can be represented by the plane which is normal to wave vector $\mathbf{k}$ (see Figure 2.13, line AA', as a starting wave position). Spherical elementary waves originate from every point on AA' to form a new wavefront BB' which is drawn tangential to all elementary waves with equal radii. As can be seen from the illustration of Huygens's principle in Figure 2.13, the secondary waves originating from points along AA' do not have a uniform amplitude in all directions. If α represents the angle between the direction to any point C on the elementary sphere (see Figure 2.13) and the normal to the wavefront (or parallel to $\mathbf{k}$), then the amplitude of the secondary wave in a given direction is proportional to $(1 + \cos\alpha)$. If so, the amplitude in the $\mathbf{k}$-direction is proportional to $\sim(1 + \cos 0) = 2$. In any other direction the amplitude is less than two. In particular, the amplitude of any elementary wave in the backward direction is $\sim(1 + \cos\pi) = 0$, that is, the waves do not propagate backward. The waves propagate forward along straight lines normal to their wavefronts. Moreover, the consideration of elementary waves originating from all points on AA' leads to the expressions for the field at any point on BB' in the same integral form as (2.11a–b), but presented for unbounded space, the solution of which shows that the field at any point on BB' is exactly the same as that at the nearest point on AA'. The phase difference between the oscillations at these neighboring points of lines AA' and BB' depends on the distance between them, d, and is therefore proportional to $\sim kd = 2\pi d/\lambda$. If $d = \lambda$, all points at AA' and BB' oscillate in phase; if $d = \lambda/2$, all points oscillate in antiphase, and so on. Hence, from Huygens's principle in the particular case of unbounded free space follows the phenomenon of straight-line wave propagation, as light rays in optics. As we will see later, this principle also states some limits and violations for the straight-line propagation of light, related to diffraction phenomena.

2.2.6 Fresnel-Zone Concept for Free Space

The existence of Fresnel zones also follows from Huygens's principle not only in obstructive conditions for both terminals, transmitter and receiver, when

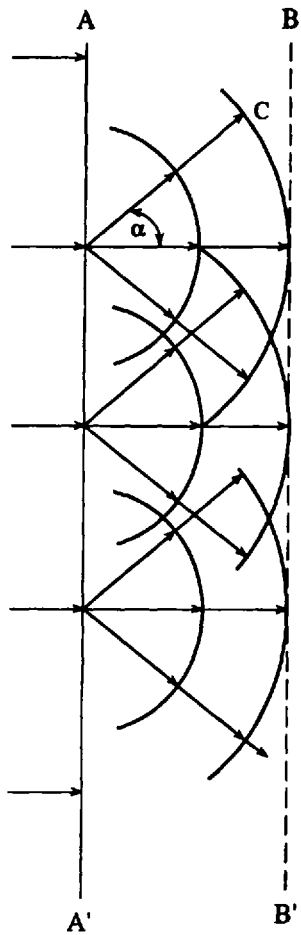

Figure 2.13 The geometry of Huygens's principle presentation in unbounded free space.

any obstacles are placed around them and diffraction phenomenon is predominant. As will be seen in Chapter 4, based on the Fresnel-zone concept, diffraction phenomenon can be understood by means of its qualitative presentation through the prism of Fresnel-zone space distribution. Nevertheless, because Huygens's principle successfully describes propagation phenomena for both unbounded free space and bounded finite areas, as well as with sharp boundaries, it is useful to show mathematically and physically the meaning of the Fresnel-zone concept for describing any radio link for which a clear line-of-sight over terrain exists.

In the case of free unbounded space, let us once more return to the integral form (2.91) of EM-field presentation at any point **r** between the observer and the source of radiation, using Green's function source presentation.

In the case of free space, instead of the *virtual* sources at any boundary limit of the space volume V, within which the real source exists, we will introduce *virtual* sources to describe the EM field in each point of the wavefront in space along the wave propagation path (see, for example, wavefront BB' in Figure 2.13). A main result which follows from Huygens's principle is that at any point of a source-free unbounded medium, the total field is a superposition of elementary spherical waves, which are radiated by virtual sources in space and reach to the observation point along straight paths.

Thus, let us consider that the radiation source is placed in free space at point A and the receiver is at point B, as shown in Figure 2.14. We also consider an imaginary plane with area S normal to the line-of-sight path at any point between A and B, which passes across the point O at the line AB (see Figure 2.14). Now, if we "work" with infinite volume V, Green's theorem (2.90) can be represented for any vector of the EM wave, namely, the Hertzian vector, as

$$\Pi(\mathbf{R}) = \int \frac{\partial \Pi(\mathbf{R}')}{\partial \mathbf{n}} \frac{\exp\{ik|\mathbf{R} - \mathbf{R}'|\}}{|\mathbf{R} - \mathbf{R}'|} ds \tag{2.92}$$

where $|\mathbf{R} - \mathbf{R}'| = r$ is the distance from any point in the imaginary plane S and observer at point B. If the initial radiation source can be assumed to be a point source with Green's function $G \sim \frac{e^{ikr_1}}{r_1}$, then for any point in the plane S, because $\frac{\partial r_1}{\partial n} = -\frac{r_0}{r_1}$, we finally obtain:

$$\Pi(\mathbf{R}) \sim \frac{1}{2\pi} \int \left(\frac{1}{r_1} - -ik \right) \frac{r_0}{r_1} \frac{\exp\{ik(r_1 + r_1')\}}{r_1 r_1'} ds \tag{2.93}$$

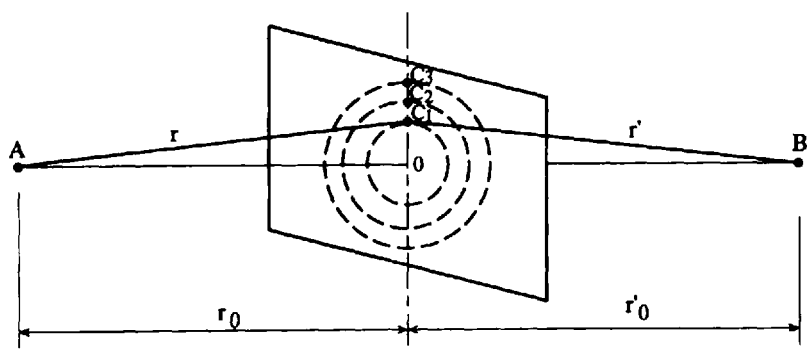

Figure 2.14 Presentation of Fresnel-zone concept in line-of-sight conditions.

All the mentioned distances are presented schematically in Figure 2.14.

We will talk about the *wave zone* or far zone between the plane S and two terminals A and B, that is, when

$$kr_1 >> 1, \qquad kr_1' >> 1 \tag{2.94}$$

In this case, the first term in brackets within integral (2.93) is less than the second one, and can be neglected. Moreover, in the process of integration the variables r_2' and r_1 are changed. Therefore, because the inequality (2.94) is valid for line-of-sight propagation links in free space, relatively small changes of variable r cause fast oscillations of the product $\sim\exp\{ik(r_1 + r_1')\}$. On the other hand, this fact leads to fast changes of sign both for real and imaginary parts of integrand in (2.93). At the same time, other products in the integrand of (2.93) have a weak change with relatively small deviations of r_1' and r_1. In this case, the well known method of *stationary phase* is usually used to derive such an integral, containing both slow and fast terms inside the integrand [5, 6, 8]. We will not present here all the complicated analyses and derivations of the integral in (2.93), only its final form for the observed point B, as

$$\Pi(B) \sim -\frac{ik}{2\pi r_0 r_0'}\exp\{ik(r_0 + r_0')\}\int\int dxdy\exp\left\{i\frac{k}{2}\left(\frac{1}{r_0} + \frac{1}{r_0'}\right)x^2\right\} \times \exp\left\{i\frac{k}{2}\left(\frac{1}{r_0} + \frac{1}{r_0'}\right)y^2\right\} \tag{2.95}$$

For each integral in the two-dimensional integral of (2.95) one can use the integral presentation [4, 6]

$$\int_{-\infty}^{+\infty}\exp(i\alpha\xi^2)d\xi = \sqrt{i\frac{\pi}{\alpha}} \tag{2.96}$$

Therefore,

$$\Pi(B) \sim -\frac{ik}{2\pi r_0 r_0'}\exp\{ik(r_0 + r_0')\}\frac{i\pi}{\frac{k}{2}\left(\frac{1}{r_0} + \frac{1}{r_0'}\right)} = \frac{\exp\{ikd\}}{d} \tag{2.97}$$

where $d = r_0 + r_0'$ is the distance between the source (point A) and the observer (point B). Hence, as is shown from (2.97), if at the plane S the source A

creates a field $\sim \frac{e^{ikr_1}}{r_1}$, then at the observed point B, the virtual dipoles, uniformly distributed at S, will create a field $\sim \frac{e^{ikd}}{d}$, the same as for the direct wave from A to B. This is the main content of Huygens's principle.

Additional analysis of integral (2.93), extended above S for the farthest wave zones

$$\Pi(B) \sim -\frac{ik}{2\pi} \int \frac{r_0}{r_1} \frac{\exp\{ik(r_1 + r_1')\}}{r_1 r_1'} ds \tag{2.98}$$

shows that the plane S can be split into the concentric circles (*hoops*) of arbitrary radius. It is apparent that any wave which has propagated from A to B via point C_i, $i = 1, 2, \ldots$ on any of these hoops has traversed a longer path than AOB (namely, $AC_iB > AOB$ at Figure 2.14). While passing from one hoop to another, the real and imaginary part of the integrand in (2.98) changes its sign. The boundaries of these hoops are determined by the condition:

$$k\{(r_1 + r_1') - (r_0 + r_0')\} = n\frac{\pi}{2}, \quad n = 1, 2, \ldots \tag{2.99}$$

The physical meaning of these hoops for wave propagation is that if the virtual sources of the elementary waves lie within the first hoop, they send observer radiation with the same phase for each elementary wave. Sources from two neighboring hoops send respective radiation which extinguish each other. Some elementary, not strict, analysis of integral (2.98) shows that a no-vanishing result exists only from the first, central hoop. The hoops are usually called the *Fresnel zones* [1–4, 8–10]. Let us derive the width of these zones Δb. For the first Fresnel zone, assuming $x^2 + y^2 = b^2$, and using (2.95) and (2.99) for $n = 1$, we have:

$$\frac{k}{2}\left(\frac{1}{r_0} + \frac{1}{r_0'}\right)(x^2 + y^2) = \frac{\pi}{2} \tag{2.100}$$

and

$$b_1 = \sqrt{(x^2 + y^2)} = \sqrt{\frac{\pi}{k}\left(\frac{1}{r_0} + \frac{1}{r_0'}\right)} = \sqrt{\frac{\lambda r_0 r_0'}{(r_0 + r_0')}} \sim \sqrt{\lambda R} \tag{2.101}$$

where R is the minimal range from each r_0 and r_0'.

Hence, the width of the first Fresnel zone is larger than wavelength (i.e., $b_1 \sim \sqrt{\lambda R} >> \lambda$). For greater zones (with number $n > 1$), in which the width Δb is smaller than the distance to each zone center (simply, the radius of each circle $b \equiv b_n$), one can easily obtain after differentiation of (2.101) the following equation:

$$kb\Delta b\left(\frac{1}{r_0} + \frac{1}{r_0'}\right) = \frac{\pi}{2} \tag{2.102}$$

and

$$\Delta b \sim \frac{\pi}{2k}\frac{R}{b} \sim \frac{b_1^2}{b} << b_1 \tag{2.103}$$

Here R is, once more, the minimal range from each r_0 and r_0'.

Thus, the width of the hoops with $n > 1$ decreases with an increase of radius in each zone b_n. At the same time it can be shown that the radius of each Fresnel zone of any specific number of the family of zones can be expressed in terms of zone numbers n and the distance between both points A and B and the imaginary plane S as [1–3, 8–10]

$$b \equiv b_n = \sqrt{\frac{n\lambda r_0 r_0'}{(r_0 + r_0')}} \tag{2.104}$$

from which, introducing in (2.104) $n = 1$, one can immediately obtain (2.101) for the radius of the first Fresnel zone. As follows from (2.103) and (2.104), the width of the Fresnel zones Δb decreases with increasing zone number n. At the same time, the area of these zones is not dependent on zone number n, that is,

$$2\pi b\Delta b \sim \frac{\pi}{2}\lambda R \tag{2.105}$$

It is clear that the radii of the individual hoops depend on the location of the imaginary plane with respect to points A and B. The radii are largest midway between points A and B and become smaller as the points are approached. Moreover, as follows from (2.99), the family of hoops have a specific property: the path length from A and B via each circle is $n\frac{\lambda}{2}$ longer than the direct path AOB (i.e., for $n = 1$ (first zone) $ACB - AOB = \frac{\lambda}{2}$), so the

excess path length for the innermost circle is $\frac{\lambda}{2}$. Other zones will have an excess proportional to $\frac{\lambda}{2}$ with a parameter of proportionality $n = 2, 3, 4, \ldots$. The loci of the points for which the excess $AC_iB - AOB = n\frac{\lambda}{2}$ define a family of ellipsoids, the radii of which are described by (2.104). But in free space without any obstacles, as we showed mathematically, only the first ellipsoid is valid and presents the first Fresnel zone which passes through both points, transmitter (T) and receiver (R), as illustrated in Figure 2.15. This is why, despite the fact that in free space the diffraction phenomenon is not observed, and no effect of interference between neighboring zones exists (see Chapter 4), to describe the loss-less phenomenon of wave propagation, the concept of Fresnel zones is also used. This approach allows us to obtain the first hoop's width in line-of-sight propagation conditions and then to estimate through formula (2.101), by use of the "working" frequency for the respective radio link, the range R of wave propagation in conditions of direct visibility between any receiver and transmitter.

2.3 Free-Space Transmission Loss

Let us consider a nonisotropic source placed in free unbounded space as a transmitter antenna of P_T watts and with a directivity gain G_T. At an arbitrary large distance r ($r >> \lambda$) from the source, the radiated power is uniformly distributed over the surface area of a sphere of that radius. If so, the power density at distance r can be represented by the modulus of Poynting vector $S \equiv |\mathbf{S}|$ as

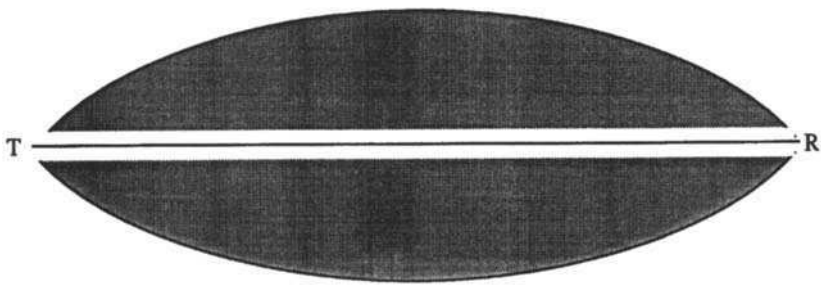

Figure 2.15 The geometry of first Fresnel zone which passes through receiver R and transmitter T in free space.

$$S = \frac{P_T G_T}{4\pi r^2} \text{ [W/m}^2\text{]} \tag{2.106}$$

On the other hand, as was presented in Section 2.1.4, the Poynting vector relates to the field components of the EM wave E and H as

$$S = H \cdot E \text{ [W/m}^2\text{]} \tag{2.107}$$

where the H-component relates to the E-component of the EM field though the impedance of free space $Z_0 = 120 \cdot \pi$, as

$$H = \frac{E}{120\pi} \text{ [A/m]} \tag{2.108}$$

From (2.106) to (2.108) one can easily obtain the expression of the maximum $E' = \sqrt{2} \cdot E$ of the E-field component:

$$E' = \sqrt{60 G_T P_T}/r \text{ [V/m]} \tag{2.109}$$

But this is the maximum value of the electric component of the total EM field. Generally, the amplitude of the electric field is a function of time and of distance r.

$$E(t) = \frac{\sqrt{60 G_T P_T}}{d} \cos(\omega t - kd) \text{ [V/m]} \tag{2.110}$$

In free space the path loss can be obtained by use of the following procedure. If P is the power at the observed point, as a receiving antenna, which is located at distance r from the transmitter antenna, then

$$P_R = \frac{E^2}{120\pi} A_R \text{ [W]} \tag{2.111}$$

where $A_R = \dfrac{G_R \lambda^2}{4\pi}$ is the effective aperture of the receiving antenna according to [4, 7–10]; G_R is its antenna gain. By substitution one obtains

$$P_R = \frac{\left(\dfrac{E \cdot \lambda}{2\pi}\right)^2 G_R}{120} \text{ [W]} \tag{2.112}$$

At the same time, from (2.109), we obtain

$$P_T = \frac{E_T^2 r^2}{60 G_T} \text{ [W]} \tag{2.113}$$

As was defined in Chapter 1, the path loss in decibels is the logarithm of the ratio between the transmitted and the received power,

$$L = 10 \log \frac{P_T}{P_R} = 10 \log \left[\frac{\left(\frac{4\pi r}{\lambda}\right)^2}{G_T G_R} \right] = L_0 + 10 \log \left(\frac{1}{G_T G_R} \right) \tag{2.114}$$

Here L_0 is the path loss for an isotropic point source (with $G_T = G_R = 1$) in free space, which in decibels, using the simple relation $\lambda = cT = c/f$, can be presented as:

$$L_0 = 10 \log \left(\frac{4\pi f r}{c} \right)^2 = 20 \log \left(\frac{4\pi f r}{c} \right) = 34.44 + 20 \log r + 20 \log f \tag{2.115}$$

where the value 34.44 is obtained by the use of simple calculations, taking into account that the speed of light $c = 3 \cdot 10^8$ (m/s):

$$32.44 = 20 \log \left(\frac{4\pi \cdot 10^3 \ (m) \cdot 10^6 \ (1/s)}{3 \cdot 10^8 \ (m/s)} \right) = 20 \log \left(\frac{40\pi}{3} \right)$$

In (2.115) the distance r is in kilometers (km), and frequency f is in megahertz (MHz).

As the result, the path loss of both directive antennas, receiver and transmitter, finally can be given as:

$$L_F = 34.44 + 20 \log d_{[km]} + 20 \log f_{[MHz]} - 10 \log G_T - 10 \log G_R \tag{2.116}$$

This is a general formulation of path loss for two directive antennas, receiver and transmitter, in free unbounded space.

References

[1] Stratton, J. A., *Electromagnetic Theory*, New York: McGraw-Hill, 1941.

[2] Jackson, J. D., *Classical Electrodynamics*, New York: John Wiley & Sons, 1962.

[3] Chew, W. C., *Waves and Fields in Inhomogeneous Media*, New York: IEEE Press, 1995.

[4] Elliott, R. S., *Electromagnetics: History, Theory, and Applications*, New York: IEEE Press, 1993.

[5] Abramowitz, M., and I. A. Stegun, *Handbook of Mathematical Functions*, New York: Dover Publications, 1965.

[6] Dudley, D. G., *Mathematical Foundations for Electromagnetic Theory*, New York: IEEE Press, 1994.

[7] Felsen, L. B., and N. Marcuvitz, *Radiation and Scattering of Waves*, New York: IEEE Press, 1994.

[8] Al'pert, Ia. L., V. L. Ginzburg, and E. L. Feinberg, *Radio Wave Propagation*, Moscow: State Printing House for Technical-Theoretical Literature, 1953.

[9] Kong, J. A., *Electromagnetic Wave Theory*, New York: John Wiley & Sons, 1986.

[10] Parsons, J. D., *The Mobile Radio Propagation Channel*, New York: John Wiley & Sons, 1992.

This page intentionally left blank

II

Propagation in Open and Rural Areas

This page intentionally left blank

3

EM-Wave Propagation Over Smooth Terrain

In this chapter we consider wave propagation over smooth terrain, based on phenomena described earlier in Chapter 2.

3.1 Reflection From Flat Terrain

The simplest case of radio wave propagation over terrain is that where the ground surface is assumed to be a flat and perfectly conductive medium. The first assumption of "flat terrain" is valid for radio links between subscribers 10–20 km apart [1–7]. The second condition of a "perfectly conductive" soil medium can be satisfied only for some special cases, because the combination of conductivity σ and frequency ω, such as $4\pi\sigma/\omega$, that appears in the total formula of permittivity $\epsilon = \epsilon_{r0} - i4\pi\sigma/\omega$ plays an important role for high frequencies (VHF/L-band, usually used for terrain communication channel design) and finite subsoil conductivity, as well as for small grazing angles of incident waves [1–7]. We will later discuss almost all of these features, considering the reflection coefficients from flat terrain. However, to introduce the subject of the main problem of reflection from the terrain, we start with the simplest case of perfectly conductive flat-ground surface.

For a perfectly conductive ground surface the total electric field vector is equal to zero (i.e., $\mathbf{E} = 0$), as shown in Section 2.1.6, the tangential component of the electric field vanishes at the perfectly conductive flat-ground surface, that is,

$$E_T = 0 \tag{3.1}$$

Consequently, as follows from Maxwell's equation $\nabla \times \mathbf{E}(\mathbf{r}) = i\omega\mathbf{H}(\mathbf{r})$ (see formulas (2.7a–d) in Section 2.1.1 for the case of $\mu = 1$ and $\mathbf{B} \equiv \mathbf{H}$), at such a flat perfectly conductive ground surface the normal component of the magnetic field also vanishes,

$$H_n = 0 \tag{3.2}$$

As also follows from Maxwell's equations (2.7a–d), the tangential component of the magnetic field does not vanish because of its compensation by the surface electric current. At the same time, the normal component of the electric field is also compensated by pulsing electrical charge at the ground surface. Hence, by introducing the Cartesian coordinate system (see Figure 3.1), one can present the boundary conditions (3.1) to (3.2) at the flat perfectly conductive ground surface as follows:

$$E_x(x, y, z = 0) = E_y(x, y, z = 0) = H_z(x, y, z = 0) = 0 \tag{3.3}$$

3.1.1 The Strict Reflection Theorem

To obtain a solution of the wave equation which describes radio wave propagation over flat perfectly conductive terrain, let us, first of all, describe the problem by introducing the physically simply explained qualitative picture presented in Figure 3.2. Because each antenna, as a source of electromagnetic waves, can be presented as a superposition of point sources—dipoles [1–4], we can replace such an antenna by two elementary dipoles, the vertical (z) and the horizontal

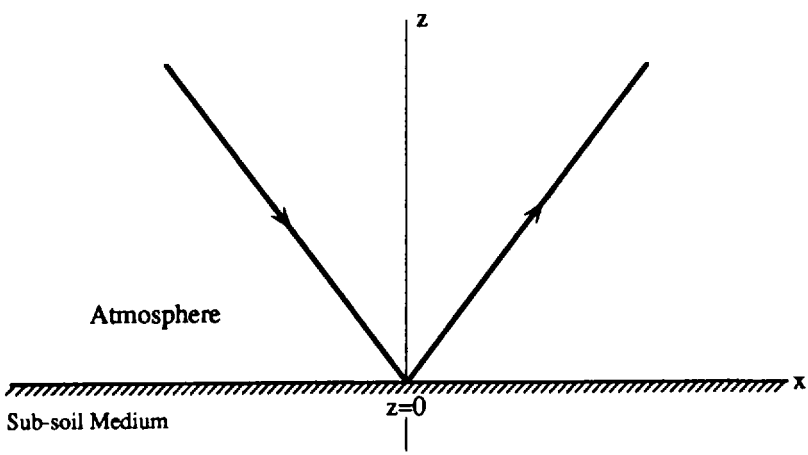

Figure 3.1 Ray reflection from the flat terrain.

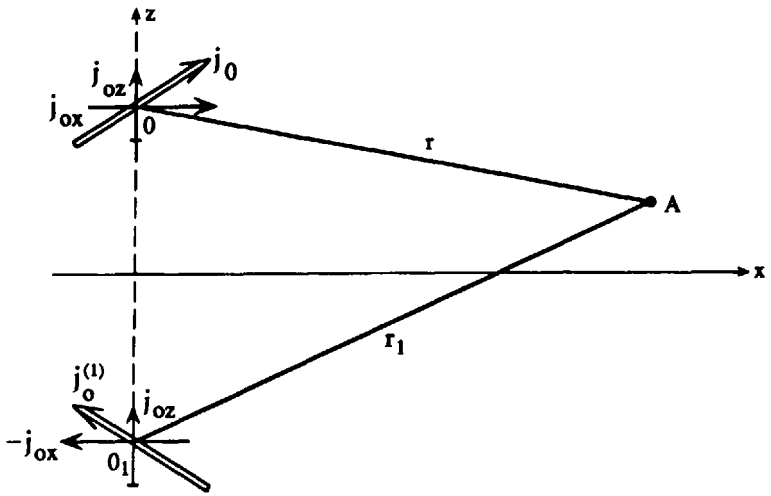

Figure 3.2 The source presentation as a superposition of the vertical and horizontal elementary dipoles.

(x), with their own current densities, $\mathbf{j}_z$ and $\mathbf{j}_x$, respectively, as shown in Figure 3.2. If we now add to a vertical current element its image vector $\mathbf{j}_z^{(1)}$ relative to the plane $z = 0$ with the same current direction (as presented in Figure 3.2), then each vertical dipole $\mathbf{j}_z$ and $\mathbf{j}_z^{(1)}$ gives at the plane $z = 0$ only the horizontal component of the magnetic field, that is, satisfies the boundary condition (3.3).

In the same way, the horizontal dipole with current density $\mathbf{j}_x$ can also be added to its image source having the opposite sign of current density, (i.e., $\mathbf{j}_x^{(1)} = -\mathbf{j}_x$). Then the vertical component of the magnetic field will be completely compensated by the field of the additional dipole $\mathbf{j}_x^{(1)}$. Hence, by introducing the real and imaginary sources $\mathbf{j}$ and $\mathbf{j}^{(1)}$, one can describe the total field above the flat perfectly conductive plane $z = 0$ which at this plane satisfies the boundary conditions for the magnetic field described by (3.2). Moreover, such a combination of sources, real and imaginary, satisfies the boundary conditions for electric field (3.1). In fact, at any point of the plane $z = 0$, the tangential components of electric field of both sources, $\mathbf{j}_x$ and $\mathbf{j}_x^{(1)}$, as well as the normal components of both sources, $\mathbf{j}_z$ and $\mathbf{j}_z^{(1)}$, are compensated by each other, as seen from the simple qualitative picture presented in Figure 3.2. If one will continue the same construction for each element of a real antenna, one can obtain the total field solution above the flat-ground surface, because the total field of such a combination of antenna elements satisfies the wave equation and respective boundary conditions (3.1) to (3.3).

The result presented in Figure 3.2 can be obtained by strictly using the following mathematical formalism and the results described in Section 2.1.6.

In this section we have introduced common wave equations (2.29) for electric and magnetic components of a wave field. Now we will rewrite them for the case of two semi-infinite homogeneous planes without taking into account the virtual magnetic source $\mathbf{M}(\mathbf{r})$:

$$\begin{aligned} \nabla^2\mathbf{E}(\mathbf{r}) - k^2\mathbf{E}(\mathbf{r}) &= i\omega\mathbf{j}(\mathbf{r}) \\ \nabla^2\mathbf{H}(\mathbf{r}) - k^2\mathbf{H}(\mathbf{r}) &= \nabla \times \mathbf{j}(\mathbf{r}) \end{aligned} \tag{3.4}$$

where, as was introduced earlier, $k^2 = \omega^2\epsilon\mu$. Because both fields, **E** and **H**, can be obtained by the simple operation of divergence from each other, for us it is enough to determine one of them, say the **H**-field, assuming that the current density distribution $\mathbf{j}(\mathbf{r})$ of the electric source is known. According to (2.7b), which we will rewrite in the following form

$$\nabla \times \mathbf{H}(\mathbf{r}) = -i \cdot k \cdot \mathbf{E}(\mathbf{r}) \tag{3.5}$$

the boundary conditions (2.33) can be rewritten as

$$[\nabla \times \mathbf{H}]_x = \frac{\partial H_z}{\partial y} - \frac{\partial H_y}{\partial z} = -ik_x E_x = 0 \quad \text{for } z = 0 \tag{3.6}$$

$$[\nabla \times \mathbf{H}]_y = \frac{\partial H_x}{\partial z} - \frac{\partial H_z}{\partial x} = -ik_y E_y = 0 \quad \text{for } z = 0$$

But, because $H_z(x, y, 0) = 0$, we obtain two additional boundary conditions:

$$\frac{\partial H_y}{\partial z} = \frac{\partial H_x}{\partial z} = 0 \quad \text{for } z = 0 \tag{3.7}$$

If we now use the integral presentation of Green's theorem [1–4] and the scalar Green's function according to (2.79), we may present the **H**-field components in the following integral form:

$$H_x(\mathbf{r}) = \int_V [\nabla \times \mathbf{H}]_x \cdot G_+ d^3r' \tag{3.8a}$$

$$H_y(\mathbf{r}) = \int_V [\nabla \times \mathbf{H}]_y \cdot G_+ d^3r' \tag{3.8b}$$

$$H_z(\mathbf{r}) = \int_V [\nabla \times \mathbf{H}]_z \cdot G_- d^3r' \tag{3.8c}$$

where Green's functions can be presented as [5]:

$$G_{\pm} = \frac{\exp\{i \cdot k \cdot |\mathbf{R} - \mathbf{R}'|\}}{|\mathbf{R} - \mathbf{R}'|} \pm \frac{\exp\{i \cdot k \cdot |\mathbf{R}_1 - \mathbf{R}'|\}}{|\mathbf{R}_1 - \mathbf{R}'|} \tag{3.9}$$

Here, $r = |\mathbf{R} - \mathbf{R}'|$ is the distance between the source point O and observed point A, $r_1 = |\mathbf{R}_1 - \mathbf{R}'|$ is the distance between the source point O and the image source (because of reflection from the plane $z = 0$, see Figure 3.3(a)). The distance $r_1 = |\mathbf{R}_1 - \mathbf{R}'|$ equals the distance $|\mathbf{R}_1 - \mathbf{R}_1'|$ between the observer at point A and the reflection at point $O_1(\mathbf{R}_1')$ for the real source $O(\mathbf{R}')$(see Figure 3.3(b)). Therefore, each integral in (3.8) can be written, for example, for component H_x as

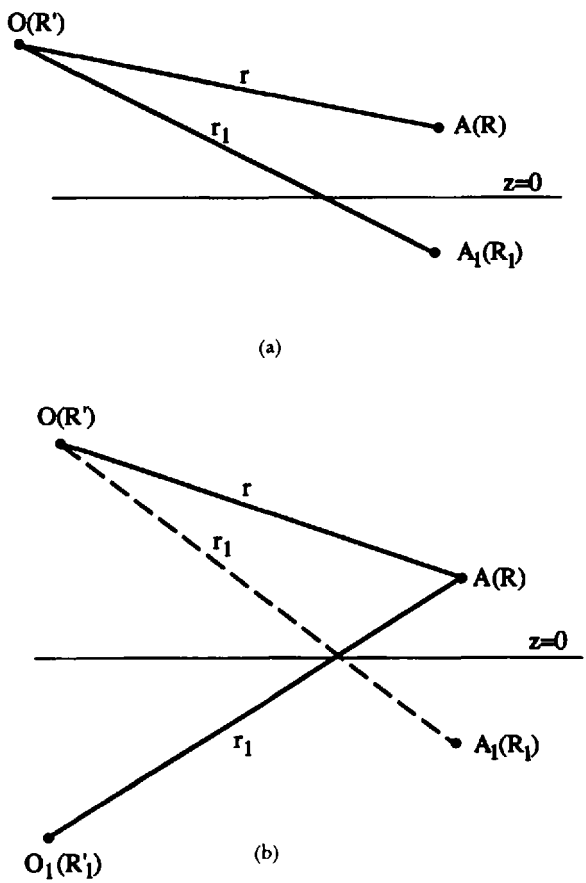

Figure 3.3 Geometrical presentation of the imaginary source effect due to reflection from the flat terrain.

$$H_x(\mathbf{r}) = \int_V [\nabla \times \mathbf{j}]_x \cdot \frac{e^{ikr}}{r} d^3r' + \int_V [\nabla \times \mathbf{j}]_x \cdot \frac{e^{ikr_1}}{r_1} d^3r' \qquad (3.10)$$

This equation describes the physical result, that is, the first term gives the field which satisfies the solution of wave equation for an infinite homogeneous atmosphere without the earth-surface bound. The second term describes the effect of the earth surface's influence. It gives the same effect if, in the nondisturbed field for an infinite atmosphere, the effect of an additional *reflected source* is introduced. This result follows from the sketch in Figure 3.3(b), where, except for the real source placed at the point $O(x', y', z')$, the image source $O(x', y', -z')$ is due to reflection from plane $z = 0$, the field of which together with the field of the real source, as we will show later, creates a complicated interference picture.

The same results, as above, can be obtained for the components of the total **H**-field, $H_y(\mathbf{r})$ and $H_z(\mathbf{r})$, but for $H_z(\mathbf{r})$ one must put in the integrals (3.10) the function G_- instead of the function G_+ from (3.9), with the inverse sign for the "reflected" source (second term in (3.9)). Hence, if at any point (x', y', z') above the earth's surface there exists some source with the current density $\mathbf{j}(\mathbf{r})$, then due to the reflection from plane $z = 0$ the current density $\mathbf{j}^{(1)}(\mathbf{r})$ must be introduced at the image point $(x', y', -z')$, and thus

$$\begin{aligned} [\nabla \times \mathbf{j}]_x &= [\nabla \times \mathbf{j}^{(1)}]_x \\ [\nabla \times \mathbf{j}]_y &= [\nabla \times \mathbf{j}^{(1)}]_y \\ [\nabla \times \mathbf{j}]_z &= -[\nabla \times \mathbf{j}^{(1)}]_z \end{aligned} \qquad (3.11)$$

Using mathematical formalism [4], one can obtain that for relations (3.11) it is enough to put:

$$\begin{aligned} j_x^{(1)} &= -j_x \\ j_y^{(1)} &= -j_y \\ j_z^{(1)} &= j_z \end{aligned} \qquad (3.12)$$

Therefore, the effect of a flat-earth surface leads to existence of, in addition to the direct field, the field reflected from the ground. This reflected field can be thus constructed: to each source at the point (x', y', z') with current density $\mathbf{j}(x', y', z')$ there corresponds an image source at the point $(x', y', -z')$ with the current density $\mathbf{j}^{(1)}(x', y', -z')$. The field of this source is derived in the

same manner as if it is located in free space. If one now replaces the element of current $\mathbf{j}(\mathbf{r})$ by its components, the reflection sketched in Figure 3.2 appears. This principal result is usually called the *strict theorem of reflection.*

3.1.2 Areas Significant for Reflection

We will now explain the zones which are significant for reflection from the flat terrain for three typical positions of transmitter and receiver according to the variants presented in Section 1.4. Let us consider the total field at the observed point $A(x_A, y_A, z_A)$ above the perfectly conductive flat and homogeneous earth surface. We will discuss the influence of inhomogeneities and roughness of the ground in Chapter 7.

In the first case, the source is also placed above the ground surface at the point $O(x_0, y_0, z_0)$. Without any limitation for the general situation within the above-terrain propagation channel, we can assume and choose the coordinate system so that $x_0 = 0$ $y_0 = y_A = 0$ (see Figure 3.4). Using the main integral presentation of total field (2.90) to (2.91) from Section 2.2.5, rewritten for the atmosphere-earth boundary surface and for the vector Hertz presentation of total field [3–5] (i.e., for $\tilde{\Psi}(\mathbf{r}) \equiv \Pi(\mathbf{r})$), one obtains the following result. According to this formula and the discussion presented above in Section 3.1.1, in the situation over the flat terrain, the total field $\Pi(\mathbf{r}) = |\Pi(\mathbf{r})|$ at the observed point A is the superposition of the nondisturbed field $\Pi_0(A)$, which describes the wave field in the unbounded homogeneous atmosphere, and the disturbed field $\Pi_1(A)$, which describes the reflection phenomenon caused by the virtual sources placed at the ground surface S (the area of integration in (2.91)). The integral on the surface S in (2.90) to (2.91) will always consist of products of the order of $\sim \frac{e^{ikr}}{r}\Pi(\mathbf{r})$ for any selected Green's function in the form of (3.9). Consequently, the field $\Pi(\mathbf{r})$ at the ground surface can also be considered as a product of the nondisturbed field $\Pi_0(\rho) = |\mathbf{p}| \cdot \frac{e^{ik\rho}}{\rho}$ and some slowly changing attenuation function $W(\rho)$. In this case we can once more return, as in Section 2.2.5, to the integral (2.93) from the product of a quickly oscillating function and a slowly changing function. We use the method of stationary phase for the description of zones at the surface S which give minor contributions in reflection phenomena from the flat-ground surface. We consider the integral (2.93), for which the argument of oscillations for exponential function inside this integral is $i \cdot \phi = i \cdot k \cdot (r + \rho)$, on the surface of integration $S\{x, y, z = 0\}$ and will find the point (x_0, y_0) at which this integral has some

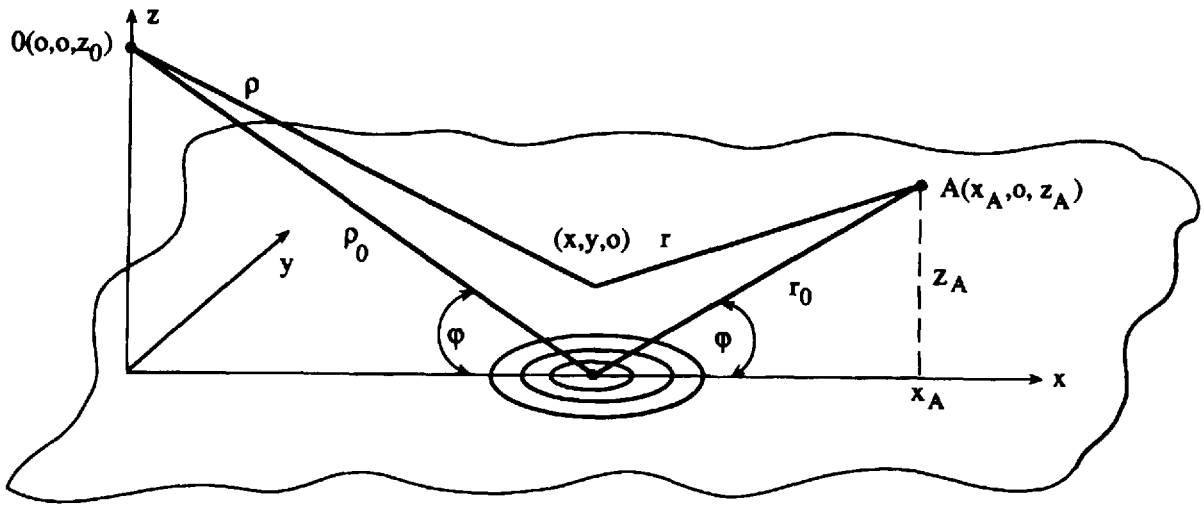

Figure 3.4 The area significant for reflection when both antennas are above the ground surface.

extremum. From Figure 3.4 it follows that $r = \sqrt{(x_A - x)^2 + y^2 + z^2}$ and $\rho = \sqrt{x^2 + y^2 + z_0^2}$. Then the conditions of extremum can be written as:

$$\left[\frac{\partial \phi}{\partial x}\right]_{x=x_0, y=y_0} = k \cdot \left(\frac{x}{\rho_0} - \frac{x_A - x}{r_0}\right) = 0$$
$$\left[\frac{\partial \phi}{\partial y}\right]_{x=x_0, y=y_0} = k \cdot \left(\frac{y}{\rho_0} - \frac{y}{r_0}\right) = 0 \tag{3.13}$$

Hence, the point of extremum is placed on the x-axis ($y_0 = 0$), and Snell's law is valid at this point: the incident angle θ_0 equals the reflected angle θ_1 (see Figure 3.8), that is,

$$\frac{x_0}{\rho_0} = \frac{x_A - x_0}{r_0} = \cos\varphi \tag{3.14}$$

where $\varphi = \frac{\pi}{2} - \theta_0$ is the grazing angle. We will talk later about Snell's law.

Results obtained from (3.14) show that the essential effect for reflection phenomenon arises from the area that lies near the point of specular reflection (x_0, y_0, 0). Let us examine the behavior of the exponential function within integral (2.95); $\phi = k \cdot (r + \rho)$ near this point. For this purpose let us also introduce new variables:

$$\varsigma = x - x_0, \ \eta = y - y_0 \tag{3.15}$$

assuming ς, $\eta << r$, ρ, and expand r and ρ into series, taking into account only the second order summands in such series (other terms are vanishingly small),

$$r \approx r_0 + \varsigma \cdot \cos\varphi + \frac{\varsigma^2 \sin^2\varphi + \eta^2}{2 \cdot r_0}$$
$$\rho \approx \rho_0 + \varsigma \cdot \cos\varphi + \frac{\varsigma^2 \sin^2\varphi + \eta^2}{2 \cdot r_0} \tag{3.16}$$

Thus the phase function $\phi = k \cdot (r + \rho)$ in the exponent of integrand within (2.95) is

$$\phi = k \cdot (r + \rho) \approx k \cdot \left\{ (r_0 + \rho_0) + \frac{\varsigma^2 \sin^2\varphi + \eta^2}{2} \left(\frac{1}{r_0} + \frac{1}{\rho_0} \right) \right\} \tag{3.17}$$

where we denoted r_0' from integrand within (2.95) as ρ_0 according to the geometry presented in Figure 3.4. The lines of equal phase $\phi(\varsigma, \eta) = const$ have the form of ellipses placed around the point of specular reflection (Figure 3.4). The factor of oscillations changes the sign of the real and imaginary part of the exponent while passing through the ellipses. In fact, the equation

$$\frac{k}{2} \cdot \left(\frac{1}{r_0} + \frac{1}{\rho_0} \right) (\varsigma^2 \sin^2\varphi + \eta^2) = m \frac{\pi}{2}, \quad m = 0, 1, 2, \ldots \tag{3.18a}$$

or its strict mathematical presentation

$$\frac{\varsigma^2}{\dfrac{\pi \cdot m}{k \cdot \left(\dfrac{1}{r_0} + \dfrac{1}{\rho_0} \right) \cdot \sin^2\varphi}} + \frac{\eta^2}{\dfrac{\pi \cdot m}{k \cdot \left(\dfrac{1}{r_0} + \dfrac{1}{\rho_0} \right) \cdot \sin^2\varphi}} = 1 \tag{3.18b}$$

is an equation of ellipses with semi-axes, respectively,

along the x-axis:

$$a_m = \frac{1}{\sin\varphi} \sqrt{\frac{\pi \cdot m}{k} \frac{r_0 \cdot \rho_0}{(r_0 + \rho_0)}} \tag{3.19a}$$

along the y-axis:

$$b_m = \sqrt{\frac{\pi \cdot m}{k} \frac{r_0 \cdot \rho_0}{(r_0 + \rho_0)}} \tag{3.19b}$$

These ellipses are the real boundaries of zones of specular reflection from the flat-ground surface. For small grazing angles where $\varphi \to 0°$, that is, $a_m >> b_m$, all ellipses are elongated along the x-axis (i.e., along the direction of wave propagation). As in Section 2.2.6, these ellipses describe the Fresnel zones, but for the case of the existence of the ground surface along the propagation path and the reflection phenomenon from such a surface. As will be shown later in the explanation of diffraction phenomenon from various obstacles placed on the flat terrain, the total field after the *reflection phenomenon*, as also

in free space (Section 2.2.6), can be obtained as an integral effect from the area which embraces several first Fresnel zones by use of the Fresnel integral presentation:

$$F(v) = \int_0^v \exp\left\{-i\frac{\pi}{2}v^2\right\}dv = -F(-v) \tag{3.20}$$

We will use this integral for describing diffraction phenomena in propagation over terrain with various obstacles. We only note that if we first consider $m = 8$ Fresnel zones around the specular reflected point as significant zones for reflection phenomenon, we obtain the error from the strict solution by use of integral (3.20) with infinite limits, which equals $\approx 15\%$. In this case, the approximate scales of the reflecting area can be estimated by using simple formulas, such as,

along the x-axis:

$$2a_R = \frac{4}{\sin\varphi}\sqrt{\lambda R} \tag{3.21a}$$

along the y-axis:

$$2b_R = 4\sqrt{\lambda R} \tag{3.21b}$$

where R is the lesser of the two distances, r_0 and ρ_0.

We previously talk about the situation when both points, transmitter and receiver, are above the earth's surface. What will happen if one of the points, for example point A, lies close to the ground plane $z = 0$?

In the second case, $z_A \approx 0$, as shown in Figure 3.5, and the term $(r + \rho)$ in the exponent of $\exp\{i \cdot \phi\} = \exp\{i \cdot k \cdot (r + \rho)\}$ in integral (2.95) has a minimum at the point A (i.e., when $x = x_A$, $y = y_A$).

Let us, as above, also assume that $y_A \approx 0$ and introduce the polar coordinate system (r, α) with the center at point A (see Figure 3.5). Then

$$x = x_A + r \cdot \cos\alpha, \quad y = r \cdot \sin\alpha \tag{3.22}$$

If we now repeat the same expansion of r and ρ into the series and take into account only terms that are linear with respect to r and ρ, we obtain:

$$\begin{aligned} \rho &\approx \rho_0 + r \cdot \cos\alpha \cdot \cos\varphi \\ i\phi &\approx ik\rho_0 = i \cdot k \cdot r \cdot (1 + \cos\alpha \cdot \cos\varphi) \end{aligned} \tag{3.23}$$

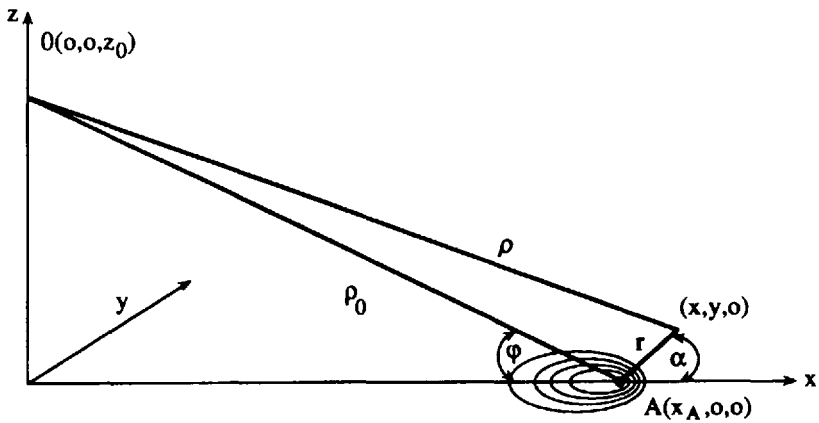

Figure 3.5 The area significant for reflection when one of the antenna is near the ground surface.

Using these expressions, one can again obtain for the fast-oscillating term in integral (2.93) the significant area, the boundaries of which are described by the following equation:

$$k \cdot r \cdot (1 + \cos\alpha \cdot \cos\varphi) = m\frac{\pi}{2}, \quad m = 0, 1, 2, \ldots \tag{3.24a}$$

or

$$r = \frac{\dfrac{m \cdot \pi}{2 \cdot k}}{(1 + \cos\alpha \cdot \cos\varphi)} \tag{3.24b}$$

Equation (3.24b) is the equation of ellipses with their focus at the point $r = 0$ (point A). Their big semi-axis is elongated along the x-axis and is described by

$$a_m = \frac{m \cdot \pi}{2 \cdot k \cdot \sin^2\varphi} \tag{3.25a}$$

and their small semi-axis is elongated along the y-axis and equals

$$b_m = \frac{m \cdot \pi}{2 \cdot k \cdot \sin\varphi} \tag{3.25b}$$

These ellipses are strongly elongated in the direction of the source, as shown in Figure 3.5. In this case, the distance from point A to each successive ellipse is

$$(d)_{\alpha=\pi} = \frac{m \cdot \pi}{2 \cdot k \cdot (1 - \cos\varphi)} \tag{3.26}$$

The same value, but in the direction opposite to the source is

$$(d)_{\alpha=0} = \frac{m \cdot \pi}{2 \cdot k \cdot (1 + \cos\varphi)} \tag{3.27}$$

In the case of a wave incident with a small grazing angle φ ($\varphi \approx 0$), the several initial Fresnel zones will embrace most of the radio path between points O and A (the source and observer, respectively).

If, as above, we consider that the significant reflected area embraces the initial $m = 8$ Fresnel zones, we will obtain for $\varphi = 15°$ the scale of this reflected area $(d)_{\alpha=\pi} \approx 64 \cdot \lambda$ in the direction of source O, and $(d)_{\alpha=0} \approx \lambda$ in the direction of the observed point A. For $\varphi = 30°$ we obtain $(d)_{\alpha=\pi} \approx 16 \cdot \lambda$ and $(d)_{\alpha=0} \approx \lambda$, respectively. These estimations show that the area in front of an observer placed at point A with its location near the earth's surface, is very important for propagation. At the same time, the area behind the observer is not significant. The conditions of propagation and, hence, of communication between points O and A become more effective with an increase of grazing angle φ, or, of course, with a decrease of radio range between the source and the observed point.

The third possible variant of source and observer location is when both of them are placed near the earth's surface (let us say, in the plane $z = 0$, as is shown in Figure 3.6). In this case the position and the configuration of the Fresnel zones are determined by the condition of equality of the phase of field oscillations, introduced earlier, that is, $k \cdot (r + \rho) = const.$

From this condition we once more obtain the equation of ellipses with their focus at points O (source) and A (observer). Because the minimum value of such a constant can be achieved for $(r + \rho) = x_A$, then the boundaries of the Fresnel zones are determined by the following conditions:

$$k \cdot (r + \rho) = k \cdot x_A + m\frac{\pi}{2}, \quad m = 0, 1, 2, \ldots \tag{3.28}$$

The large semi-axis of each ellipse is

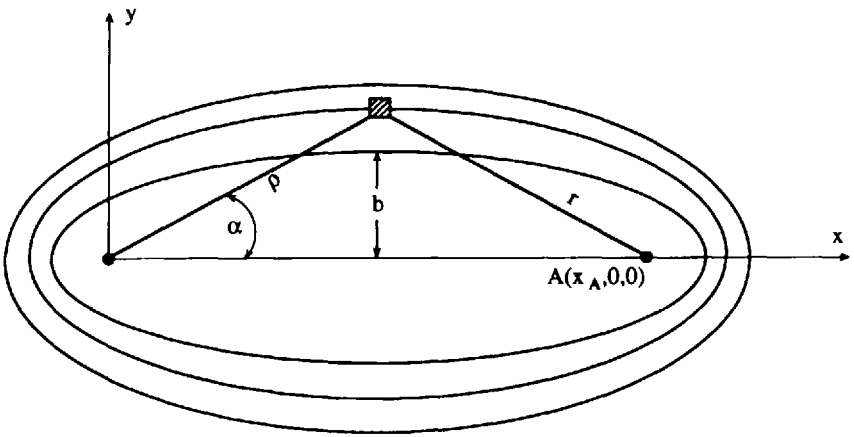

Figure 3.6 The area significant for reflection when both antennas are near the ground surface $z = 0$.

$$a_m = \frac{r + \rho}{2} = \frac{x_A}{2} + \frac{m \cdot \pi}{4 \cdot k} \tag{3.29}$$

Behind points O and A these ellipses are close to each other, and they are very elongated along the x-axis, because the small semi-axis is

$$b_m = \frac{r + \rho}{2}\sin\alpha = \sqrt{\frac{m \cdot \pi}{k}\left(x_A + \frac{m \cdot \pi}{4 \cdot k}\right)} \approx \sqrt{\frac{m}{8}\lambda \cdot x_A} \tag{3.30}$$

for moderate values of m.

Therefore we conclude that the ellipses depicted in Figure 3.6 are not real, because $b_m << a_m$. If we now assume that $x_A >> \lambda$ (for real radio paths above a flat terrain), then $x_A >> b_m$, that is, the specular reflection area is narrow enough. As above, only a few ellipses (for example, for $m < 9$), which embrace the source (O) and observer (A), determine the significant area of specular reflection. The distances between neighboring ellipses behind points O and A are very small. They can be determined by the following condition: $\frac{1}{2}(r + \rho - x_A) = m\frac{\lambda}{8}$, that is, these distances are equal to one eighth of a wavelength. Thus, we have found the significant area of specular reflection from a flat terrain for various combinations of transmitter and receiver location above the earth's surface. One can combine all these cases by use of a more general situation for various positions of points O and A, introducing a system

of rotating ellipsoids in space, which have focuses at these points. These ellipsoids can be described by the following equation:

$$k \cdot (r + \rho) = k \cdot d + n\frac{\pi}{2}, \quad n = 0, 1, 2, \ldots \tag{3.31}$$

where d is the range between points O and A, while r and ρ are the distances from A and O to the current spatial point, respectively. Beginning from any number $n = n_1$ these ellipsoids are crossed by the earth's surface. The first point, where the first contact with the ground's surface takes place, is the point of specular reflection:

$$k \cdot (r_0 + \rho_0) = k \cdot d + n_1\frac{\pi}{2} \tag{3.32}$$

The following values of $n = n_1 + m$, $m = 0, 1, 2, \ldots$, will give at the ground plane the contours of the Fresnel reflection zones. If the heights of points O and A are large (the first case described above), we obtain for small m ($m < 9$) a family of ellipses (Figure 3.7a). If one of these points, or both of them, are located near the earth's surface, then the cross-sections at the plane $z = 0$ have the form of ellipses with one focus (Figure 3.7b) or with two common focuses (Figure 3.7c), respectively.

3.1.3 Main Reflection and Refraction Formulas

As was shown above, the influence of a flat terrain on wave propagation leads to phenomena such as reflection. Because all kinds of waves can be represented by the concept of the plane waves (see Section 2.3), let us obtain the main reflection and refraction formulas for a plane wave incident on a plane surface between two media, the atmosphere and the earth, as shown in Figure 3.8. The media have different dielectric properties which are described above and below the boundary plane $z = 0$ by the permittivities and permeabilities ϵ_1, μ_1 and ϵ_2, μ_2, respectively. Then the indexes of refraction for both media can be defined as: $n_1 = \sqrt{\epsilon_1 \cdot \mu_1}$ and $n_2 = \sqrt{\epsilon_2 \cdot \mu_2}$.

Without reducing the general problem, let us consider a plane wave with wave vector $\mathbf{k}$ and frequency $\omega = 2\pi f$ incident from a medium described by parameters ϵ_1 and μ_1. The reflected and refracted waves are described by wave vectors $\mathbf{k}_1$ and $\mathbf{k}_2$, respectively. Vector $\mathbf{n}$ is a unit normal vector directed from medium (ϵ_2, μ_2) into medium (ϵ_1, μ_1). According to (2.41), and (2.43) to (2.45) the incident wave can be represented as follows:

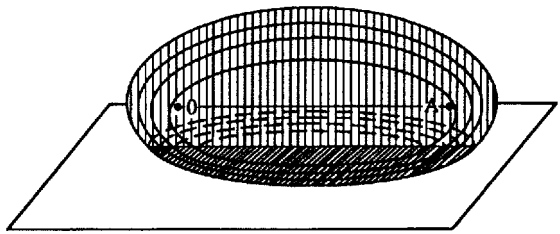

(a)

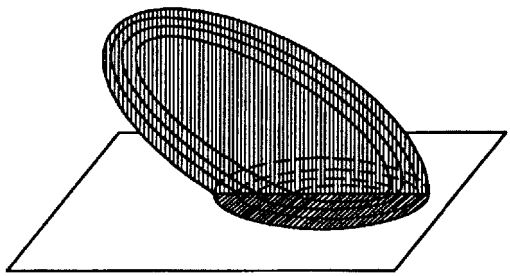

(b)

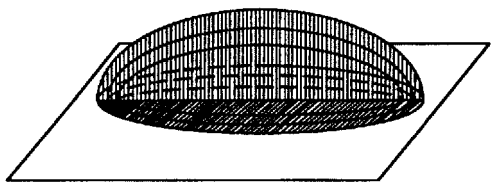

(c)

Figure 3.7 Three-dimensional presentation of areas significant for reflection: the case (a) corresponds to Figure 3.4; the case (b) to Figure 3.5; the case (c) to Figure 3.6.

$$\mathbf{E} = \mathbf{E}_0 \exp\{i(\mathbf{k} \cdot \mathbf{x} - \omega \cdot t)\}, \quad \mathbf{H} = \sqrt{\frac{\epsilon_1}{\mu_1}} \cdot \frac{\mathbf{k} \times \mathbf{E}}{|\mathbf{k}|} \tag{3.33}$$

The same can be done for the reflected wave

$$\mathbf{E}_1 = \mathbf{E}_{01} \exp\{i(\mathbf{k}_1 \cdot \mathbf{x} - \omega \cdot t)\}, \quad \mathbf{H} = \sqrt{\frac{\epsilon_1}{\mu_1}} \cdot \frac{\mathbf{k}_1 \times \mathbf{E}_1}{|\mathbf{k}_1|} \tag{3.34}$$

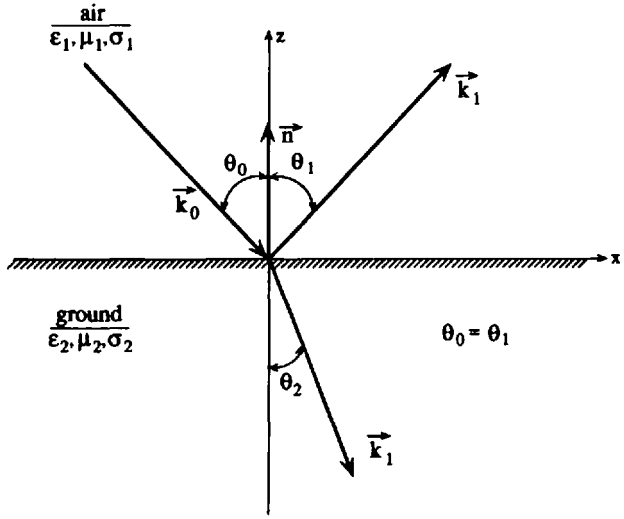

Figure 3.8 Schematical presentation of Snell's law.

and for the refracted wave

$$\mathbf{E}_2 = \mathbf{E}_{02}\exp\{i(\mathbf{k}_2 \cdot \mathbf{x} - \omega \cdot t)\}, \quad \mathbf{H} = \sqrt{\frac{\epsilon_2}{\mu_2}} \cdot \frac{\mathbf{k}_2 \times \mathbf{E}_2}{|\mathbf{k}_2|} \tag{3.35}$$

The values of the wave vectors are related by the following expressions:

$$|\mathbf{k}| = |\mathbf{k}_1| \equiv k = \frac{\omega}{c}\sqrt{\epsilon_1\mu_1}, \quad |\mathbf{k}_2| \equiv k_2 = \frac{\omega}{c}\sqrt{\epsilon_2\mu_2} \tag{3.36}$$

From the boundary conditions that were described earlier in Section 3.1.1, one can obtain the condition of the equality of phase for each wave at the plane $z = 0$:

$$(\mathbf{k} \cdot \mathbf{x})_{z=0} = (\mathbf{k}_1 \cdot \mathbf{x})_{z=0} = (\mathbf{k}_2 \cdot \mathbf{x})_{z=0} \tag{3.37}$$

which is independent of the nature of the boundary condition. Equation (3.37) describes the condition that all three wave vectors must lie in a same plane. From this equation it also follows that

$$k \sin\theta_0 = k_1 \sin\theta_1 = k_2 \sin\theta_2 \tag{3.38}$$

which is the analogue of Snell's law:

$$n_1 \sin\theta_0 = n_2 \sin\theta_2 \tag{3.39}$$

Moreover, because $|\mathbf{k}_0| = |\mathbf{k}_1|$, we find $\theta_0 = \theta_1$; the angle of incidence equals the angle of reflection.

It also follows from the boundary conditions that the normal components of vectors **D** and **B** are continuous. In terms of the field presentation (3.33) to (3.35), these boundary conditions at the plane $z = 0$ can be written as

$$\begin{aligned}
&[\epsilon_1(\mathbf{E}_0 + \mathbf{E}_1) - \epsilon_2\mathbf{E}_2] \cdot \mathbf{n} = 0 \\
&[\mathbf{k} \times \mathbf{E}_0 + \mathbf{k}_1 \times \mathbf{E}_1 - \mathbf{k}_2 \times \mathbf{E}_2] \cdot \mathbf{n} = 0 \\
&[\mathbf{E}_0 + \mathbf{E}_1 - \mathbf{E}_2] \times \mathbf{n} = 0 \\
&\left[\frac{1}{\mu_1}(\mathbf{k} \times \mathbf{E}_0 + \mathbf{k}_1 \times \mathbf{E}_1) - \frac{1}{\mu_2}(\mathbf{k}_2 \times \mathbf{E}_2)\right] \times \mathbf{n} = 0
\end{aligned} \tag{3.40}$$

Usually, in applying these boundary conditions for estimating the influence of the flat-ground surface on wave propagation over terrain, it is convenient to consider two separate situations. The first one is when the vector of the wave's electric field **E** component is perpendicular to the plane of incidence (the plane defined by vectors **k** and **n**), but the vector of the wave's magnetic field component **H** lies in this plane. The other one is when the vector of the wave's electric field component **E** is parallel to the plane of incidence, but the vector of the wave's magnetic field component **H** is perpendicular to this plane. In the literature which describes wave propagation aspects, they are usually called the *TE* wave (transverse electric) and the *TM* wave (transverse magnetic), or waves with *vertical* and *horizontal* polarization, respectively. We will derive the reflection and refraction coefficients for the case of an incident plane wave with linear polarization; the general case of arbitrary elliptic polarization can be obtained by use of the appropriate linear combinations of the two results, following the approach presented in Section 2.2.2.

First of all, we consider the incident plane linearly polarized wave with its electric field perpendicular to the plane of incidence (*TE* wave), as shown in Figure 3.9. The orientations of the magnetic field components of the incident, reflected, and refracted waves, $\mathbf{H}_i$, $i = 0, 1, 2$, are chosen to give a positive flow of energy in the direction of wave vectors **k**, $\mathbf{k}_1$, and $\mathbf{k}_2$, respectively. Since the electric fields are all parallel to the boundary surface, the first boundary condition in (3.40) yields nothing. The third and fourth conditions in (3.40) give

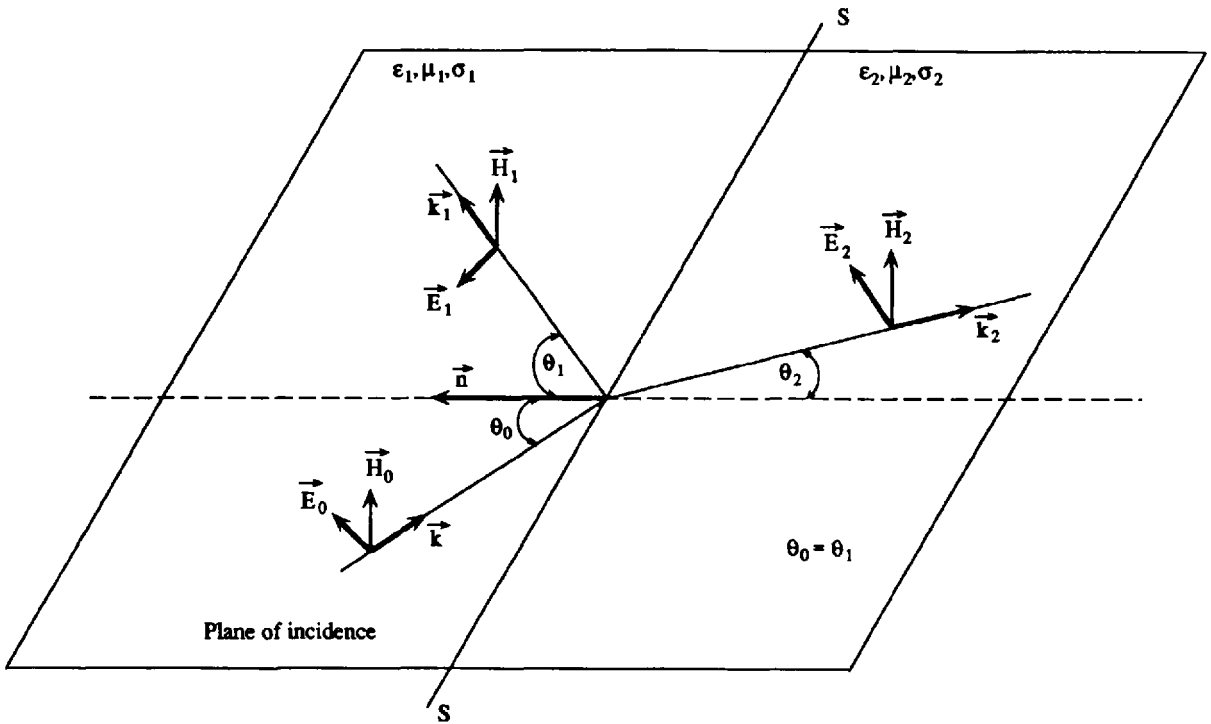

Figure 3.9 TE-plane wave reflection and refraction from the boundary of two media.

$$E_0 + E_1 - E_2 = 0 \tag{3.41}$$
$$\sqrt{\frac{\epsilon_1}{\mu_1}}(E_0 - E_1)\cos\theta_0 - \sqrt{\frac{\epsilon_2}{\mu_2}}E_2\cos\theta_2 = 0$$

while the second condition in (3.40), using Snell's law (3.39), duplicates the third condition. Now, from (3.41), we can obtain the amplitudes of the reflected and refracted waves respectively:

$$|\mathbf{E}_1| = |\mathbf{E}_0|\frac{n_1\cos\theta_0 - \frac{\mu_1}{\mu_2}\sqrt{n_2^2 - n_1^2\sin^2\theta_0}}{n_1\cos\theta_0 + \frac{\mu_1}{\mu_2}\sqrt{n_2^2 - n_1^2\sin^2\theta_0}} \tag{3.42a}$$

$$|\mathbf{E}_2| = |\mathbf{E}_0|\frac{2n_1\cos\theta_0}{n_1\cos\theta_0 + \frac{\mu_1}{\mu_2}\sqrt{n_2^2 - n_1^2\sin^2\theta_0}} \tag{3.42b}$$

The same results can be obtained from (3.40) for the case of the TM wave, when the electric field vectors are parallel to the plane of incidence, as is shown in Figure 3.10. The boundary conditions for the normal component of vector **D** and for the tangential components of vectors **E** and **H** lead to the first, third and fourth equations in (3.40), from which follow:

$$(E_0 - E_1)\cos\theta_0 - E_2\cos\theta_2 = 0 \tag{3.43}$$
$$\sqrt{\frac{\epsilon_1}{\mu_1}}(E_0 + E_1) - \sqrt{\frac{\epsilon_2}{\mu_2}}E_2 = 0$$

The continuity of the normal components of the vector **D**, plus Snell's law (3.39), merely duplicates the second of equations (3.40). Therefore the amplitudes of the reflected and refracted waves can be written as:

$$|\mathbf{E}_1| = |\mathbf{E}_0|\frac{\frac{\mu_1}{\mu_2}n_2^2\cos\theta_0 - n_1\sqrt{n_2^2 - n_1^2\sin^2\theta_0}}{\frac{\mu_1}{\mu_2}n_2^2\cos\theta_0 - n_1\sqrt{n_2^2 - n_1^2\sin^2\theta_0}} \tag{3.44a}$$

$$|\mathbf{E}_2| = |\mathbf{E}_0|\frac{2n_1n_2\cos\theta_0}{\frac{\mu_1}{\mu_2}n_2^2\cos\theta_0 - n_1\sqrt{n_2^2 - n_1^2\sin^2\theta_0}} \tag{3.44b}$$

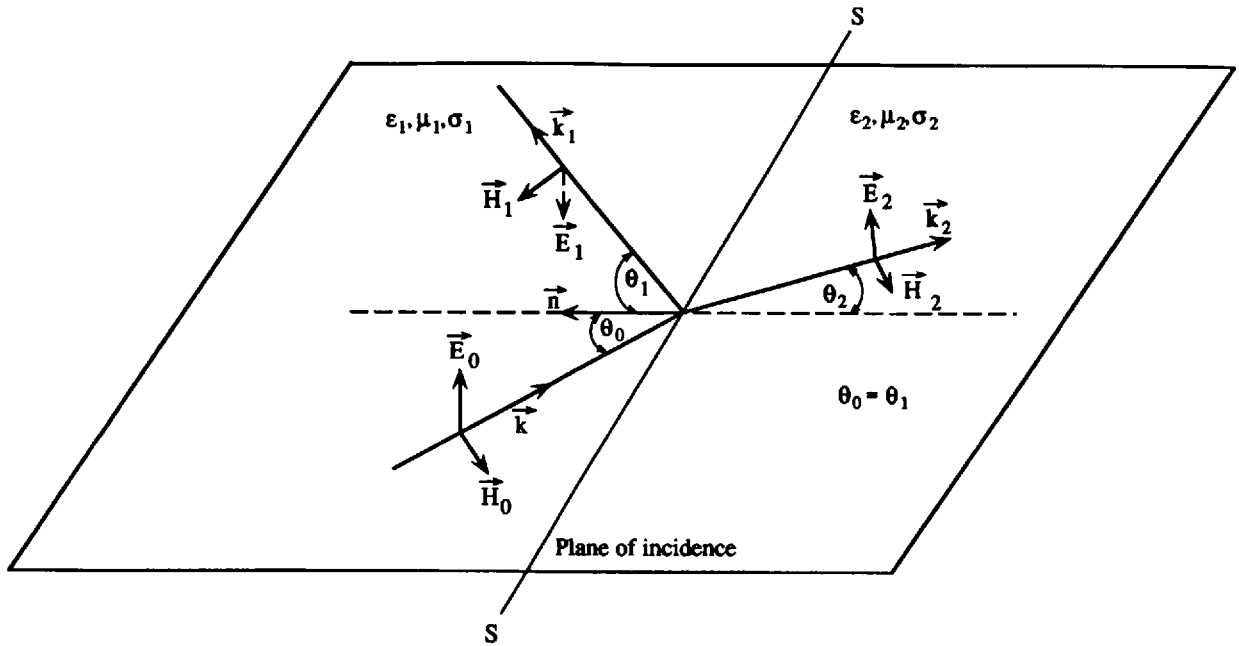

Figure 3.10 The same, as in Figure 3.9, but for TM-plane wave.

For the real situation of radio wave propagation over terrain, it is usually permitted to put $\frac{\mu_1}{\mu_2} = 1$. Also taking into account the relations between the refractive index and the permittivity of the medium, that is, $n_1^2 = \mu_1\epsilon_1$ and $n_2^2 = \mu_2\epsilon_2$, and introducing the relative permittivity (with respect to the air), $\epsilon_r = \epsilon_2/\epsilon_1$, we obtain, by use of (3.42) and (3.44), the expressions for the complex coefficients of reflection (Γ) and refraction (T) for waves with vertical (denoted by index V) and horizontal (denoted by index H) polarization, respectively.

For *vertical* polarization:

$$\Gamma_V = |\Gamma_V| e^{j\varphi_V} = \frac{\epsilon_r \cos\theta_0 - \sqrt{\epsilon_r - \sin^2\theta_0}}{\epsilon_r \cos\theta_0 + \sqrt{\epsilon_r - \sin^2\theta_0}}$$

$$T_V = |T_V| e^{j\varphi_V'} = \frac{2\sqrt{\epsilon_r}\cos\theta_0}{\epsilon_r \cos\theta_0 + \sqrt{\epsilon_r - \sin^2\theta_0}} \tag{3.45}$$

For *horizontal* polarization:

$$\Gamma_H = |\Gamma_H| e^{j\varphi_H} = \frac{\cos\theta_0 - \sqrt{\epsilon_r - \sin^2\theta_0}}{\cos\theta_0 + \sqrt{\epsilon_r - \sin^2\theta_0}}$$

$$T_H = |T_H| e^{j\varphi_H'} = \frac{2\cos\theta_0}{\cos\theta_0 + \sqrt{\epsilon_r - \sin^2\theta_0}} \tag{3.46}$$

Here, $|\Gamma_V|$, $|\Gamma_H|$, $|T_V|$, $|T_H|$ and φ_V, φ_H, φ_V', φ_H' are the modulus and phase of the coefficients of reflection and refraction for vertical and horizontal polarization, respectively. It is important to note that for normal incidences of a radio wave on a flat-ground surface there is no difference between vertical and horizontal wave polarization. In fact, for $\theta_0 = 0$, $\cos\theta_0 = 1$, $\sin\theta_0 = 0$, all the formulas above reduce to:

$$|\mathbf{E}_1| = |\mathbf{E}_0| \frac{\sqrt{\epsilon_r} - 1}{\sqrt{\epsilon_r} + 1}$$

$$|\mathbf{E}_2| = |\mathbf{E}_0| \frac{2}{\sqrt{\epsilon_r} + 1} \tag{3.47}$$

$$\Gamma_V = \Gamma_H = \frac{\sqrt{\epsilon_r} - 1}{\sqrt{\epsilon_r} + 1}$$
$$T_V = T_H = \frac{2}{\sqrt{\epsilon_r} + 1} \tag{3.48}$$

It should be noted that the results presented by (3.47) are correct only for $\mu_1 = \mu_2$ [6]. Moreover, for the reflected wave $\mathbf{E}_1$ the sign convention is that for vertical polarization (3.45). This means that if $\epsilon_2 > \epsilon_1$ there is a phase reversal of the reflected wave. In the case of vertical polarization there is a special angle of incidence, called the *Brewster angle*, for which there is no reflected wave. For simplicity we will assume that the condition $\mu_1 = \mu_2$ is valid. Then from (3.45) it follows that the reflected wave $\mathbf{E}_1$ limits to zero when the angle of incidence is equal to Brewster's angle

$$\theta_0 \equiv \theta_{Br} = \tan^{-1}\left(\frac{\epsilon_2}{\epsilon_1}\right) \tag{3.49}$$

Another interesting phenomenon that follows from the presented formulas is called *total reflection.* It takes place when the condition of $\epsilon_2 >> \epsilon_1$ (or $n_2 >> n_1$) is valid. In this case, from Snell's law (3.39) it follows that, if $n_2 >> n_1$, then $\theta_1 >> \theta_0$. Consequently, when $\theta_0 >> \theta_{0kr}$ the reflection angle $\theta_1 = \frac{\pi}{2}$, where

$$\theta_{0kr} = \sin^{-1}\left(\frac{\epsilon_2}{\epsilon_1}\right) \tag{3.50}$$

For waves incident at the surface (this case is realistic for the wall surfaces of ferro-concrete buildings) under the critical angle $\theta_0 = \theta_{0kr}$ there is no refracted wave within the second medium; the refracted wave is propagated along the boundary between the first and second media and there is no energy flow across the boundary of these two media.

3.1.4 Analysis of Reflection Coefficient for Various Propagation Conditions

The knowledge of reflection coefficient amplitude and phase variations is an important factor in the prediction of propagation characteristics for different situations in the over–terrain propagation channels. As follows from expressions

(3.45) to (3.46), the amplitude and phase variations of the reflected wave from a flat-ground surface depend on the reflection coefficient's amplitude and phase changes at the point of reflection (i.e., on the ground's properties) and on the initial polarization of the incident wave. In practice, for wave propagation over terrain, the ground properties are determined by the conductivity and the absolute dielectric permittivity (dielectric constant) of the subsoil medium, $\epsilon = \epsilon_0 \epsilon_r$, where ϵ_0 is the dielectric constant of vacuum, ϵ_r is the relative permittivity of the ground surface, $\epsilon_r = \epsilon_{\text{Re}} - i\epsilon_{\text{Im}} = \epsilon_{\text{Re}} - j60\sigma$. Here ϵ_{Re} and ϵ_{Im} are the real and imaginary parts of the relative permittivity of the subsoil medium, respectively. In practice, instead of the incident angle θ_0, the grazing angle $\psi = \frac{\pi}{2} - \theta_0$ is used. Then introducing ψ in formulas (3.45) to (3.46) instead of θ_0 yields:

for horizontal polarization:

$$\Gamma_H = |\Gamma_H| e^{-j\varphi_H} = \frac{\sin\psi - (\epsilon_r - \cos^2\psi)^{1/2}}{\sin\psi + (\epsilon_r - \cos^2\psi)^{1/2}} \tag{3.51}$$

for vertical polarization:

$$\Gamma_V = |\Gamma_V| e^{-j\varphi_V} = \frac{\epsilon_r \sin\psi - (\epsilon_r - \cos^2\psi)^{1/2}}{\epsilon_r \sin\psi + (\epsilon_r - \cos^2\psi)^{1/2}} \tag{3.52}$$

Because both the coefficients presented by (3.51) to (3.52) are the complex values, the reflected wave will therefore differ both in magnitude and phase from the incident wave. Moreover, both coefficients in (3.51)–(3.52) differ from each other. In fact, for horizontal polarization, for $\epsilon_r \to \infty$ and $\sigma \to \infty$ (i.e., for very conductive ground surface), the relative phase of the incident and reflected waves is nearly 180 degrees for all angles of incidence. On the other hand, for very small grazing angles, as follows from (3.51), the reflected and incident waves are equal in magnitude, but differ by 180 degrees in phase for all ground permittivities and conductivities. In other words, $\Gamma_H = -1$, and $\varphi_H = 180°$ $(0 < \psi < 180°)$. Moreover, with an increase of angle ψ the magnitude and phase of the reflected wave change, but only by a relatively small amount. With a decrease in conductivity of the ground surface and with an increase of frequency $f = \frac{c}{\lambda}$ of wave radiation, the changes of Γ_H and φ_H become greater. In the case of a real conductive ground surface ($\epsilon_r > 1$ and $\sigma > 0$) for small grazing angles ($\psi \approx 0°$), the reflection coefficient for a wave with vertical polarization does not change its properties with respect to

that for horizontal polarization, as follows from (3.52), that is, for $\psi \approx 0 << \frac{\pi}{2}$ $\Gamma_V = -1$, and $\varphi_V = 180°$. At the same time, for $\epsilon_r \to \infty$ and for $0 < \psi < 180°$, $\Gamma_V = 1$. However, with increase of angle ψ, substantial differences appear, that is, both a rapid decrease of magnitude and phase of the reflected wave takes place. For $\psi \to 90°$ ($\theta_0 \to 0°$, θ_0 is the Brewster angle) the magnitude $|\Gamma_V|$ becomes a minimum and the phase φ_V reaches −90 degrees. At values of ψ greater than the Brewster angle, $|\Gamma_V|$ increases again and the phase φ_V tends towards zero, that is, $\Gamma_V \to 1$. These sharp changes of $|\Gamma_V|$ and φ_V are shown in Figure 3.11 (according to our estimations) versus grazing angle ψ for various frequencies from 1 to 1,000 MHz. Here the

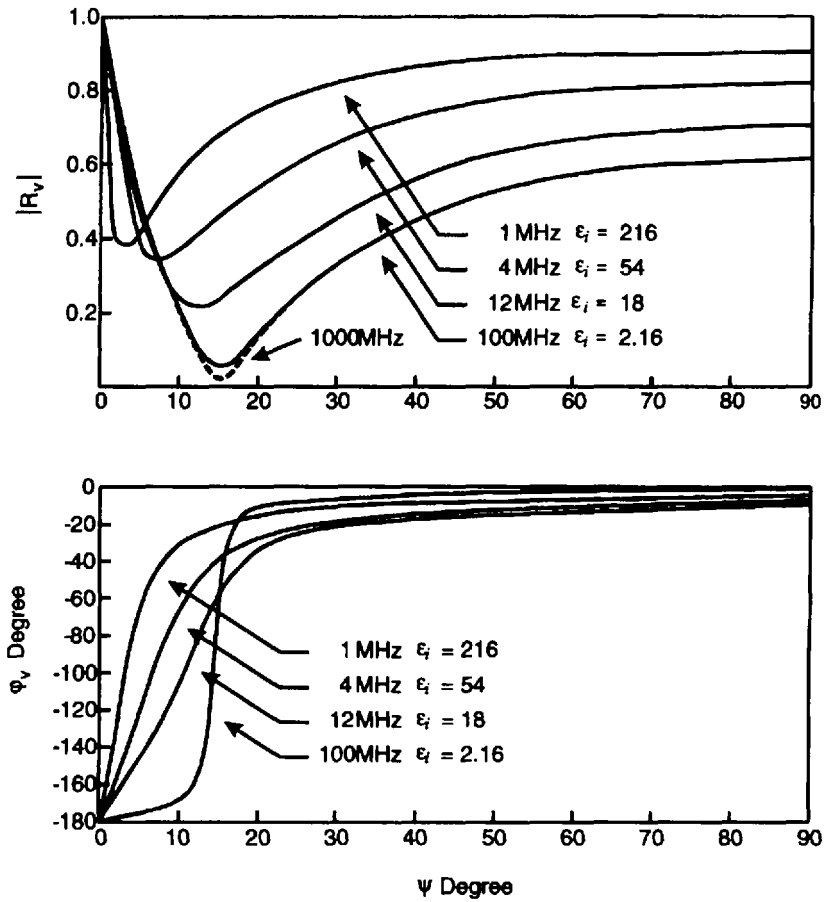

Figure 3.11 The value and phase of reflection coefficient presentation versus to the angle above horizon.

parameter ϵ_i denotes the imaginary part of the relative permittivity, ϵ_{Im}, and varies from 216 (f = 1 MHz) to 0.216 (f = 1000 MHz), ϵ_r = 15, and $\sigma = 12 \cdot 10^{-3}$ (Sm/m). The Brewster angle is about 15 degrees at higher frequencies (when $\epsilon_{\text{Re}} >> X \equiv \epsilon_{\text{Im}}$), (i.e., in cases which are very important for wireless over-terrain communication). At lower frequencies and higher conductivities (X increases and $\epsilon_{\text{Re}} << X \equiv \epsilon_{\text{Im}}$), the Brewster angle becomes smaller, approaching zero.

Because the reflection phenomenon depends on the parameters of ground surface, let us now present typical values of ground permittivity and conductivity. Table 3.1 shows how these parameters affect the value of the reflection coefficient.

The conductivity of flat perfectly conductive ground is higher than that of higher impedance ground, namely, that found in hilly terrain, whilst the relative permittivity can differ from 4 to 30 with a typical average value of 15.

3.2 Two-Ray Model

The two-ray model was first proposed for describing the process of radiowave propagation over flat terrain. Using this model in [6, 7] the basic formulas for field intensity attenuation and path loss were evaluated. Let us consider the two-ray model using the approach proposed in [6, 7], which is based on the superposition of a direct ray from the source, and a ray reflected from the flat-ground surface, as shown in Figure 3.12. Earlier, in Section 2.3, the field intensity of the direct wave (from the transmitter) in free space was presented. We will rewrite it in the following form:

$$E = \sqrt{30 G_T G_R P_T}/r_1 \tag{3.53}$$

Table 3.1
Parameters Affecting the Value of the Reflection Coefficient

Surface	Conductivity, σ (Siemens)	Relative Permittivity, ϵ_r
Dry ground	10^{-3}	4–7
Average ground	$5 \cdot 10^{-3}$	15
Wet ground	$2 \cdot 10^{-2}$	25–30
Sea water	5	81
Fresh water	10^{-2}	81

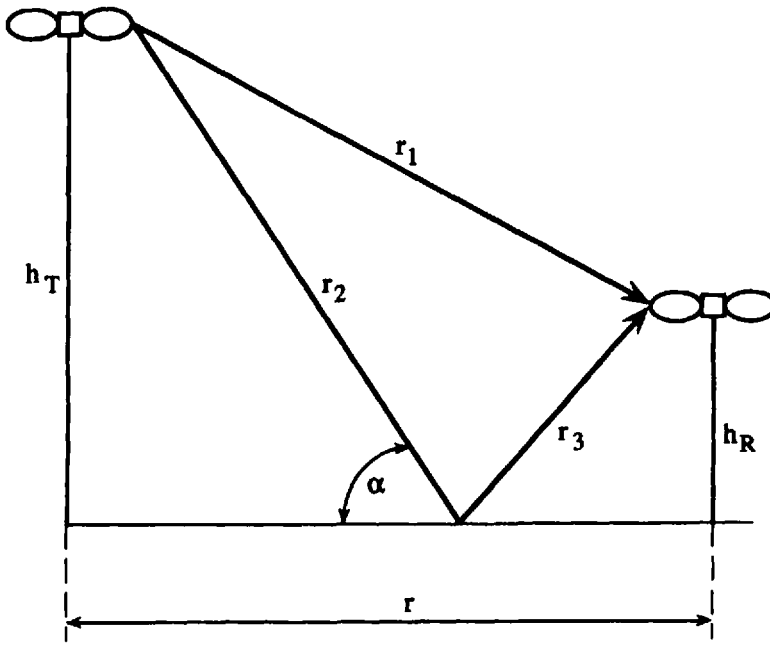

Figure 3.12 The geometry of the two-ray model.

where r_1 is the radiopath of direct wave as presented in Figure 3.12, G_R and G_T are the antenna gains for receiver and transmitter, respectively and P_T is the transmitted power.

As was shown above, the total field at the receiver is the sum of direct and received waves, that is,

$$E_R = E_T\left(1 + \frac{r_1}{r_2 + r_3}\Gamma(\psi)e^{-jk\Delta r}\right) \tag{3.54}$$

Here, $\Gamma(\psi)$ is the reflection coefficient described by formulas (3.51)–(3.52) for horizontal and vertical polarization, respectively; $\Delta r = (r_2 + r_3) - r_1$ (see Figure 3.12) is the difference in the radio paths of the two waves, $\Delta\varphi = k \cdot \Delta r$ is the phase difference between the reflected and direct waves which can be presented as

$$\Delta\varphi = k \cdot \Delta r = \frac{2\pi}{\lambda} \cdot r \cdot \left[\left(1 + \left(\frac{h_R + h_T}{r}\right)^2\right)^{1/2} - \left(1 + \left(\frac{h_R - h_T}{r}\right)^2\right)^{1/2}\right] \tag{3.55}$$

where h_R and h_T are the receiver and transmitter antenna heights, respectively and r is the distance between them. For $r_1 >> (h_T \pm h_R)$ and $r >> (h_T \pm h_R)$, as was shown in [6, 7], using the assumption that $r_1 \approx r_2 + r_3 \approx r$, (3.55) can be rewritten as:

$$\Delta\varphi = \frac{4\pi h_R h_T}{\lambda \cdot r} \tag{3.56}$$

Furthermore, if we now assume that $G_R \approx G_T = 1$ (omnidirectional antennas) and that $\Gamma(\psi) \approx -1$ for the farthest ranges from transmitter (when the grazing angle is small), we will finally obtain the power at the receiver as:

$$P_R = P_T\left(\frac{\lambda}{4\pi r}\right)^2 |1 - e^{-jk\Delta r}|^2 = P_T\left(\frac{\lambda}{4\pi r}\right)^2 \times |1 + \cos k\Delta r + j\sin k\Delta r|^2 \tag{3.57a}$$

or in absolute values:

$$|P_R| = |P_T|\left(\frac{\lambda}{4\pi r}\right)^2 |1 + \cos^2 k\Delta r - 2\cos k\Delta r + \sin^2 k\Delta r| \tag{3.57b}$$

$$= |P_T|\left(\frac{\lambda}{4\pi r}\right)^2 \sin^2 \frac{k\Delta r}{2}$$

As follows from (3.57b), the largest distance from transmitter, for which there is some maximum of received power, occurs when

$$\frac{k\Delta r}{2} \approx \frac{\pi}{2}, \quad \sin\frac{k\Delta r}{2} \approx 1 \tag{3.58}$$

This distance is called the *critical range*, denoted by r_b and approximately determined according to (3.58) by the following formula [6, 7]:

$$r_b \approx \frac{4h_R h_T}{\lambda} \tag{3.59}$$

Then, according to the definition of the parameter path loss introduced in Chapter 1, and using the following formula (instead of formula (3.54))

$$L = 20 \log|E_T| + 20 \log\left|1 + \frac{r_1}{r_2 + r_3}\Gamma(\psi)e^{-jk\Delta r}\right|$$

and taking into account all the assumptions presented above, one can easily obtain the path loss over flat terrain by use of the *critical range* presentation [6]:

$$L = L_b + 20 \log\left(\frac{r}{r_b}\right), \quad r \le r_b \tag{3.60}$$

$$L = L_b + 40 \log\left(\frac{r}{r_b}\right), \quad r > r_b$$

where L_b is the path loss in free space at the distance that equals the critical range, (i.e., $r = r_b$), which can be calculated from the following formula:

$$L_b = 32.44 + 20 \log r_{b[km]} + 20 \log f_{[MHz]} \tag{3.61}$$

As follows from formulas (3.60), there are two modes of field intensity decay at distances r less than the *break point* $r = r_b$, and beyond this point, that is, $\sim r^{-q}$, $q = 2$ for $r \le r_b$, and $\sim r^{-q}$, $q = 4$ for $r > r_b$. Such decay of signal above flat terrain can be seen from the results of path loss calculations according to the two-ray model [6, 7], which are shown in Figure 3.13. As follows from the two-ray model, there is a break point at the range r_b = 150m–300m from the source at which the transformation of field intensity attenuation from the mode $\sim r^{-2}$ with essential intensity oscillations to the smooth mode $\sim r^{-4}$ is observed up to 1–2 km from the source; the effect depends, according to (3.59), on both antennas' heights and the wavelength.

3.3 Effects of the Earth's Curvature

Let us now consider the case when terrain is smooth, but curved. In this case the degree of curvature must be taken into account for field characteristics' evaluation.

3.3.1 Based Parameters

As follows from the illustration (Figure 3.14), the real heights of two antennas, transmitting, h_T, and receiving, h_R, must be turned into "image" heights h_T' and h_R', respectively, taking into account the radius of the earth, R_e. If so,

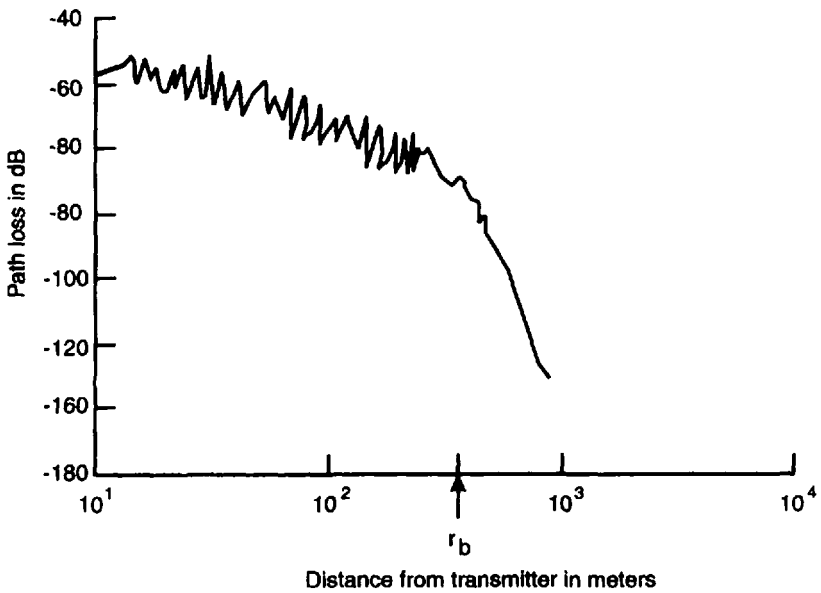

Figure 3.13 A field intensity decay (in decibels) versus the distance r from the transmitter (in meters) obtained by Milshtein et al. according to the two-ray model [6].

now h_T' and h_R' are the heights of two antennas placed on the flat earth's surface, but h_T and h_R are those for the curved earth's surface. From simple geometrical constructions that follow from Figure 3.14, one can obtain the distances d_1 and d_2 from both antennas to the center of the radio path:

$$\begin{aligned} d_1^2 &= [R_e + (h_T - h_T')]^2 - R_e^2 = (h_T - h_T')^2 + 2R_e(h_T - h_T') \\ d_2^2 &= [R_e + (h_R - h_R')]^2 - R_e^2 = (h_R - h_R')^2 + 2R_e(h_R - h_R') \end{aligned} \tag{3.62}$$

Because $R_e \approx 6480$ km and, therefore, $R_e >> d_1$, d_2, h_R, h_T, (3.62) reduces to the simple relations:

$$\begin{aligned} d_1^2 &\approx 2R_e(h_T - h_T') \\ d_2^2 &\approx 2R_e(h_R - h_R') \end{aligned} \tag{3.63}$$

and one can immediately obtain from the real antenna heights their "image" values:

$$h_T' = h_T - \frac{d_1^2}{2R_e}, \quad h_R' = h_R - \frac{d_2^2}{2R_e} \tag{3.64}$$

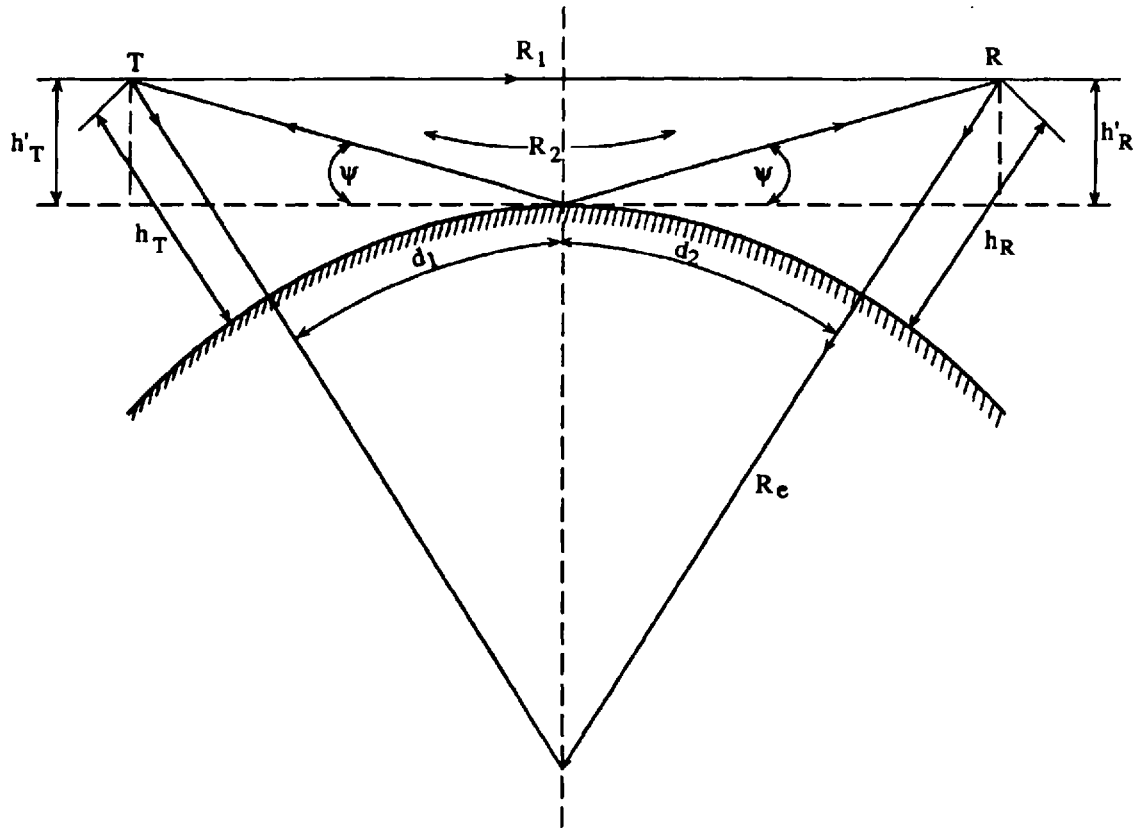

Figure 3.14 The geometry of reflection from the curved smooth ground surface.

Because at the points of the wave's specular reflection from a curved surface Snell's law is also valid, that is $\psi_1 = \psi_2$, where $\psi_1 = \frac{h_T'}{d_1}$, and $\psi_2 = \frac{h_R'}{d_2}$ (see Figure 3.14), then we obtain

$$\frac{h_T'}{h_R'} = \frac{d_1}{d_2} \tag{3.65}$$

Moreover, because $d = d_1 + d_2$, one can exclude one of the variables, for example, $d_2 = d - d_1$, and obtain the equation for only one variable, d_1, that is:

$$2d_1^3 - 3dd_1^2 + [d^2 - 2R_e(h_T + h_R)]d_1 + 2R_e h_T d = 0 \tag{3.66}$$

Using the standard mathematical approach to solve the cubic (3.66), one can obtain its solution in the following form:

$$d_1 \approx \frac{d}{1 + h_T/h_R} \tag{3.67a}$$

from which, and from equality $d_2 = d - d_1$, it follows that the second variable equals

$$d_2 = d\frac{h_T/h_R}{1 + h_T/h_R} \tag{3.67b}$$

Now let us derive the radio path for the direct wave from transmitter (T) to receiver (R) denoted as R_1 in Figure 3.14. From geometry it follows that

$$R_1 = d\left[1 + \frac{(h_T' - h_R')^2}{d^2}\right]^{1/2} \tag{3.68a}$$

The same radio path, but for the reflected wave denoted R_2 in Figure 3.14, it follows from simple geometry, from the picture presented there, that:

$$R_2 = d\left[1 + \frac{(h_T' + h_R')^2}{d^2}\right]^{1/2} \tag{3.68b}$$

Then the difference between radio paths for the direct and reflected waves equals

$$\Delta R = R_2 - R_1 = d\left\{\left[1 + \frac{(h_T' + h_R')^2}{d^2}\right]^{1/2} - \left[1 + \frac{(h_T' - h_R')^2}{d^2}\right]^{1/2}\right\} \tag{3.69}$$

Because in practical wave propagation over the terrain $d >> h_T'$, h_R', (3.69) reduces to:

$$\Delta R \approx \frac{2h_T'h_R'}{d} \tag{3.70}$$

Hence, the phase difference between the reflected and direct waves equals:

$$\Delta\phi = \frac{2\pi}{\lambda}\Delta R = \frac{4\pi h_T'h_R'}{\lambda d} \tag{3.71}$$

These parameters describe the total wave variations at the observed point.

3.3.2 Spread Factor

Increase of degree of curvature of terrain leads to diffusion and spreading of reflected rays, as is sketched in Figure 3.15. The area denoted by S_0 is the illuminated area if the wave is reflected from the *flat* earth's surface. This area spreads and diffuses when the reflection is from *curved* terrain. Usually, to take into account the degree of curvature of the terrain, the parameter SF is introduced in the main equation that describes propagation phenomena over flat terrain, that is:

$$SF \approx \left[1 + \frac{2d_1d_2}{R_e(h_T' + h_R')}\right]^{-1/2} \tag{3.72}$$

If so, the main equation for path loss prediction above the curved terrain is obtained from that for flat terrain (3.54a) by introducing the spread factor SF into it:

$$L = 20\log|E_T| + 20\log[1 + SF \cdot |\Gamma(\psi)|e^{-j(\Delta\phi - \varphi)}] \tag{3.73}$$

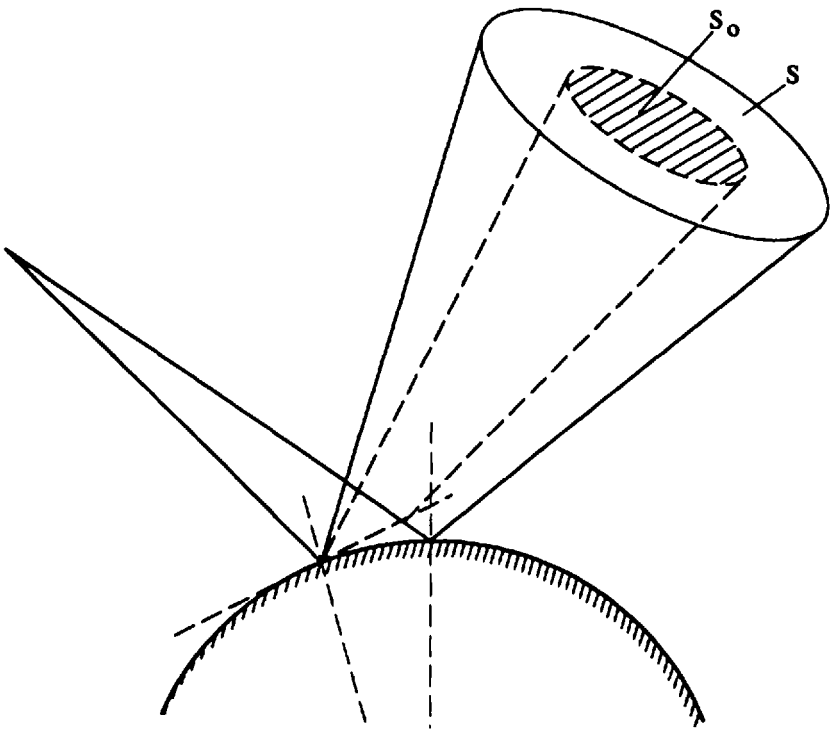

Figure 3.15 Spreading effect due to reflection from the curved smooth ground surface.

Here, $\Delta\phi$ is the phase difference defined by (3.71); $\Gamma(\psi) = |\Gamma(\psi)|e^{j\varphi}$ is the complex coefficient of reflection from flat terrain presented above in Section 3.1.4 for both vertical and horizontal polarization; $|\Gamma(\psi)|$ and φ is its magnitude and phase.

The maximum value SF, as it follows from (3.72), is $SF_{\max} \approx 1$. When $0.5 < SF < 1$, there is no influence of curvature of the terrain on wave propagation; the reflection is specular and the surface can be considered to be smooth. When $0 < SF < 0.5$, the terrain surface is regarded as curved. For the first case of $0.5 < SF < 1$ from (3.72) it follows that

$$0 < \frac{2d_1d_2}{R_e(h_T' + h_R')} < 1 \tag{3.74}$$

From the second case of $0 < SF < 0.5$ it follows that

$$\frac{2d_1d_2}{R_e(h_T' + h_R')} > 1 \tag{3.75}$$

For the practice of land communication it is important to note that it is only for radio paths longer than 20–30 km that the influence of the curvature of the earth's surface must be taken into account.

References

[1] Jakes, W. C., *Microwave Mobile Communications*, New York: John Wiley and Son, 1974.

[2] Parsons, L. D., *The Mobile Radio Propagation Channels*, New York: Pentech Press, 1992.

[3] Lee, W. Y. C., *Mobile Cellular Telecommunications Systems*, New York: McGraw-Hill Publications, 1989.

[4] Al'pert, Ia. L., V. L. Ginzburg, and E. L. Feinberg, *Radio Wave Propagation*, Moscow: State Printing House for Technical-Theoretical Literature, 1953.

[5] Jackson, J. D., *Classical Electrodynamics*, New York: John Wiley & Sons, 1962.

[6] Milstein, L. B., et al., "On the feasibility of a CDMA overlay for personal communications networks," *IEEE Select. Areas in Commun.*, Vol. 10, No. 4, 1992, pp. 665–668.

[7] Xia, H. H., et al., "Radio propagation characteristics for line-of-sight microcellular and personal communications," *IEEE Trans. Anten. Propagat.*, Vol. 41, No. 10, 1993, pp. 1439–1447.

This page intentionally left blank

4

Radio Wave Propagation Over Irregular Terrain

In this chapter we consider EM-wave propagation above rough terrain where both antennas are placed above the rough ground surface in LOS and NLOS conditions. In the first case there is no obstruction between the two antennas and they are placed at the rough earth surface in conditions of direct visibility. In the second case one or many obstacles lie between the two antennas, receiver and transmitter, and there is no line-of-sight between them.

4.1 Propagation Over Rough Terrain in LOS Conditions Between Antennas

In conditions of direct visibility between transmitter and receiver (case one presented in Section 1.6), which are placed on the rough-ground surface above all obstacles surrounding them, the total field is the superposition of the direct wave, the wave specularly reflected from the surface (which was presented for flat terrain in Section 3.1), and the waves scattered in all directions from the irregularities of the terrain (as shown in Figure 4.1(a)). In order to predict the propagation loss characteristics over the irregular terrain, and to estimate the role of each kind of wave in the total field, one needs to obtain some criterion about the surface roughness and, then, to find the influence of each wave in the total field at the receiver.

4.1.1 Criterion of Surface Roughness

Rayleigh proposed a rough-surface criterion and introduced the degree of roughness of terrain. Moreover, using this criterion, one can estimate the

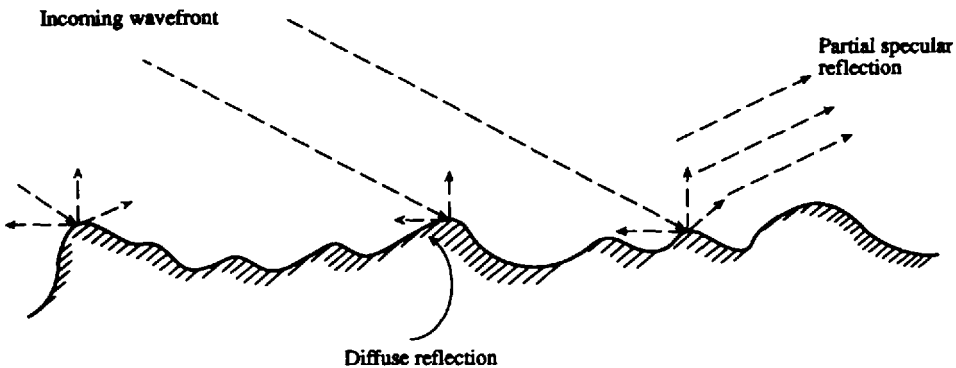

Figure 4.1 Reflection from a rough-ground surface: (a) realistic terrain situation, (b) idealized terrain model.

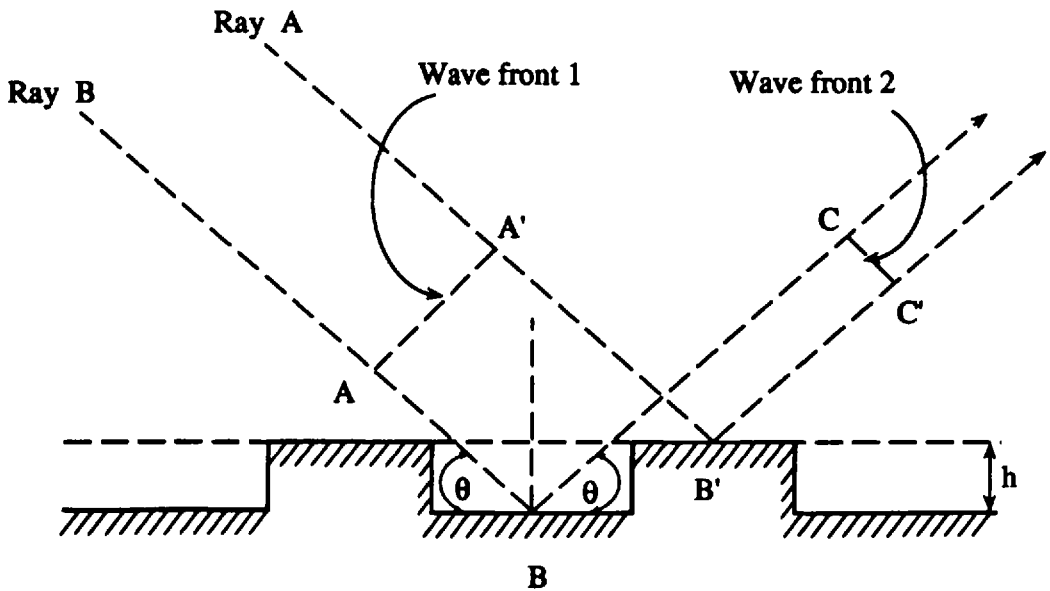

Figure 4.1 (continued).

influence of scattering effects with respect to the effect of specular reflection which takes place for the case of flat terrain (see Chapter 3). To obtain this criterion, Rayleigh introduced the ideal model of quasi-periodical surface relief, as shown in Figure 4.1(b), instead of the real rough terrain, presented in Figure 4.1(a). Let us follow his analysis and consider two rays, "A" and "B," which are specularly reflected from the top side and the bottom side of the ideal rough surface, respectively, as is shown in Figure 4.1(b). From the geometry presented, one can obtain the path difference between these two rays when they reach the points C and C' at the wavefront CC' after their reflection from points B and B', respectively:

$$\Delta l = (AB + BC) - (A'B' - B'C') = \frac{h}{\sin\theta}(1 - \cos 2\theta) = 2h\sin\theta \tag{4.1}$$

Then, the phase difference between these two rays in points C and C' is:

$$\Delta\Phi = k\Delta l = \frac{2\pi}{\lambda}\Delta l = \frac{4\pi\sin\theta}{\lambda} \tag{4.2}$$

As follows from (4.2), the phase difference $\Delta\Phi$ is small if the height h_i of irregularities placed at the rough surface is small with respect to wavelength λ (i.e., $h_i < \lambda$). In this case, the ground surface is defined as a smooth flat surface. For the real terrain the phase difference runs from 0 up to π over the whole angle range. But, for $\Delta\Phi = \pi$, the total field from two reflected rays equals zero. If the reflection coefficients from two points B and B' are the same (i.e., $\Gamma_B = \Gamma_{B'} \equiv \Gamma$), then the total field, as a superposition of two reflected fields, equals:

$$\begin{aligned}\Gamma_B\exp(j\Phi) + \Gamma_{B'}\exp(j(\Phi + \Delta\Phi)) &= \Gamma_B\exp(j\Phi) + \Gamma_{B'}\exp(j\Phi)\exp(j\pi)\\ &= \Gamma\exp(j\Phi) - \Gamma\exp(j\Phi) = 0,\\ &\quad \text{because } \exp(j\pi) = -1.\end{aligned}$$

This case is not realistic in over-the-terrain propagation. A more practical case is when $\frac{\pi}{2} \le \Delta\Phi < \pi$. Substituting into (4.2) the bottom limit of the phase difference $\Delta\Phi = \frac{\pi}{2}$, yields the expression of *critical height*, h_R, of the irregularities:

$$\frac{4\pi h_R \sin\theta}{\lambda} = \frac{\pi}{2}$$

or

$$h_R = \frac{\lambda}{8\sin\theta} \tag{4.3}$$

This height determines the degree of any earth surface roughness. The rough-surface Rayleigh criterion can then be presented as

$$h_i \geq h_R \equiv \frac{\lambda}{8\sin\theta} \tag{4.4}$$

In other words, the ground surface is rough if the height of an arbitrary irregularity placed on this surface is greater than the critical height described by (4.3). At the same time, the critical height is determined by the wavelength and the grazing angle θ with respect to the rough surface (see Figure 4.1(b)).

In practice of over-the-terrain communications, the grazing angle is sufficiently small (i.e., $0.5° \leq \theta \leq 3° - 5°$). In this case, taking into account that $\sin\theta \approx \theta$ for $\theta \to 0°$, the Rayleigh criterion (4.4) reduces to

$$h_i \geq \frac{\lambda}{8 \cdot \theta} \tag{4.5}$$

where the grazing angle θ is measured in radians from the horizontal plane. For instance, for grazing angle $\theta = 1°$ at frequency $f = 900$ MHz ($\lambda = 0.333$m), the computed value for critical height according to (4.4) to (4.5) is $h_R = 2.38$m; so the Rayleigh criterion is $h_i \geq 2.4$m. Thus, if the irregularity in heights exceeds, in our case, $h_R = 2.38$m, the surface is regarded as rough. We must note, however, that the above criterion of surface roughness was obtained for the ideal quasi-periodic model of terrain. In the real case, as shown in Figure 4.1(a), to obtain the rough-surface criterion the probabilistic approach is usually used [1–3]. Following this approach, one can consider the array of irregularities placed on a real rough surface and randomly distributed according to Gauss's law [1–3]. The terrain in this case can be described by a "relief function" $z = S(x)$, as shown in Figure 4.2. If the irregularities, with the arbitrary height z, are normally distributed according to Gauss's law with a mean value $\bar{z}$ and a variance of σ_z^2, then the probability density of surface irregularity distribution is given by the following formula:

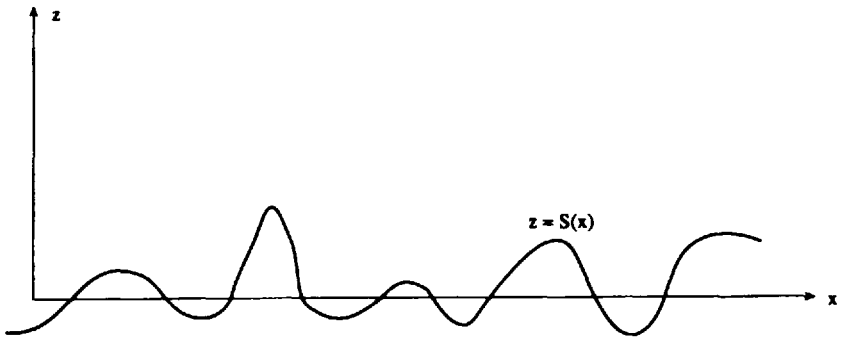

Figure 4.2 The rough surface presentation by the relief function $z = S(x)$.

$$P_z = \frac{1}{(2\pi)^{1/2}\sigma_z^{1/2}} \exp\left(-\frac{(z-\bar{z})^2}{2\sigma_z^2}\right) \tag{4.6}$$

where the standard deviation of surface is $\sigma_z = \sqrt{<(z-\bar{z})^2>}$.

In Figure 4.3, the criterion of roughness of terrain is presented schematically for various values of σ_z for understanding, at the qualitative level, the role of reflected and scattered rays in the total field pattern. Thus, the case $\sigma_z = 0$ or $\sigma_z << \lambda$ describes the pure reflection from flat terrain where the reflected wave is predominant in creating the total field pattern resulting from the terrain. In the cases $\sigma_z > \lambda$ and $\sigma_z >> \lambda$, one can consider the surface as rough and irregular with an increased role of the scattered wave in the total field pattern. In the last case, the scattered component of the total field is predominant and forms the isotropic field distribution above the terrain around arbitrary irregularities, as is shown in the last illustration in Figure 4.3.

Using the probabilistic approach, we will rewrite the Rayleigh rough-surface criterion by introducing, according to [1–3], the parameter of roughness:

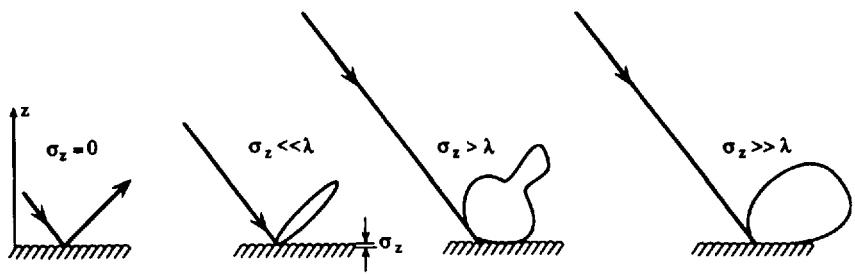

Figure 4.3 The schematical presentation of the criterion of rough terrain.

$$C \approx 4\pi\sigma_z \theta/\lambda \tag{4.7}$$

For the case $0.1 < C < 10$, the ground surface is slightly rough. For $C > 10$, the surface is regarded as rough. In the last case the scattered component is once more predominant. We must note here that the criterion (4.7) is stronger than that obtained above and described by formulas (4.4) to (4.5). For the same conditions as presented above in the example, that is, for grazing angle $\theta = 1°$ and at frequency $f = 900$ MHz ($\lambda = 0.333$m), the computed value for critical height according to (4.7) is $\sigma_z \geq 15$m. Moreover, this approach requires us to introduce a statistical description of the height distribution above the terrain.

4.1.2 Field Characteristics in LOS Conditions Above the Rough Surface

As follows from the illustrations in Figure 4.3, the roughness affects the wave propagation characteristics and, as a result of its influence, these characteristics differ from those for a smooth surface. For the case of smooth terrain, only the *specular reflected* component, together with the line-of-sight component, forms the total field at the observed point. If the surface is slightly rough, as follows from the middle sketch in Figure 4.3, the specular reflected ray gets attenuated slightly due to the scattering phenomenon. In other words, the total field also contains the *scattered* component (which is also called the *diffuse* component) together with direct and specular reflected fields. The diffuse component in this case is weaker than the latter components. The specular field component corresponds to the *coherent* part of total field intensity and is equal to the square of the average field which is the result of the direct and reflected fields. The diffuse component corresponds to the *incoherent* part of the total field intensity which is caused by the rough surface (i.e., by the scattering phenomenon). If the surface becomes very rough (third case sketched in Figure 4.3), the specular (coherent) component of total field almost disappears and the diffuse (incoherent) component of total field dominates.

At present, there are two general approaches to solving the wave-scattering problems which arise from rough terrain:

1. The *perturbation technique*, that applies to a surface which is slightly rough and whose surface slope is smaller than unity [4–15];
2. The *Kirchhoff approximation*, which is applicable to a surface whose radius of curvature is much greater than a wavelength [16–25].

We will not go into a detailed mathematical analysis of these two techniques which are described further in [4–6]. We will present the main propaga-

tion characteristics, such as the components of total field intensity, which successfully describe the scattering phenomenon for radio wave propagation over rough terrain in LOS conditions of transmitter and receiver.

The first-order perturbation solution. In this section we present a derivation of the scattered field components for a vertically and horizontally polarized incident wave using the perturbation method. This method is applicable to a slightly rough surface that can be described as follows. Let us consider the height of a rough surface to be given by some function (see Figure 4.4)

$$z = \varsigma(x, y) \tag{4.8}$$

We choose $z = 0$ so that (4.8) represents the deviation from the average height: $\langle \varsigma(x, y) \rangle = 0$. Moreover, the perturbation method is valid when the phase difference due to the height variation is small, that is, when [4]

$$\begin{aligned} &|k \cdot \varsigma(x, y) \cdot \cos\theta_i| << 1 \\ &\left|\frac{\partial \varsigma}{\partial x}\right| << 1, \left|\frac{\partial \varsigma}{\partial y}\right| << 1 \end{aligned} \tag{4.9}$$

The boundary condition for the electric field at this surface (according to (2.42) from Section 2.1.6), requires that the tangential components of **E** vanish at the surface $z = \varsigma(x, y)$, that is,

$$\mathbf{E} \times \mathbf{n} = 0 \tag{4.10}$$

where **n** is the vector normal to the surface $z = \varsigma$ at the considered point (x, y). The normal vector **n** has the components:

$$\begin{aligned} n_x &= \frac{-\dfrac{\partial \varsigma}{\partial x}}{\sqrt{1 - \left(\dfrac{\partial \varsigma}{\partial x}\right)^2 - \left(\dfrac{\partial \varsigma}{\partial y}\right)^2}} \\ n_y &= \frac{-\dfrac{\partial \varsigma}{\partial y}}{\sqrt{1 - \left(\dfrac{\partial \varsigma}{\partial x}\right)^2 - \left(\dfrac{\partial \varsigma}{\partial y}\right)^2}} \\ n_z &= \frac{-\dfrac{\partial \varsigma}{\partial z}}{\sqrt{1 - \left(\dfrac{\partial \varsigma}{\partial x}\right)^2 - \left(\dfrac{\partial \varsigma}{\partial y}\right)^2}} \end{aligned} \tag{4.11}$$

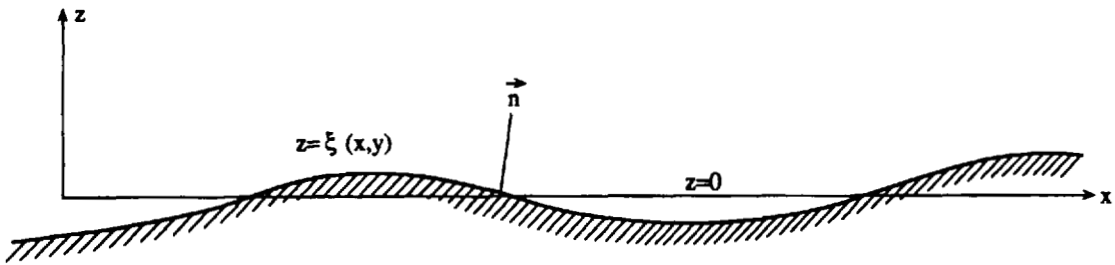

Figure 4.4 The simple presentation of rough terrain.

Ignoring all values with a second order of the derivatives $\frac{\partial \varsigma}{\partial x}$, $\frac{\partial \varsigma}{\partial y}$, and $\frac{\partial \varsigma}{\partial z}$, we obtain, according to (4.10), at the surface $z = \varsigma$,

$$E_y + E_z \frac{\partial \varsigma}{\partial y} = 0, \; E_x + E_z \frac{\partial \varsigma}{\partial x} = 0 \tag{4.12}$$

The third condition according to (4.10) follows from those two presented above by (4.12). Such conditions are for the surface $z = \varsigma(x, y)$. As to boundary conditions for the flat surface $z = 0$, using (4.12), let us rewrite them by splitting the field components E_x, E_y, and E_z on small orders of height deviation ς and its gradient, $\nabla\varsigma$:

$$\begin{aligned} E_x(x, y, z = 0) &= -E_z(x, y, z = 0) \cdot \frac{\partial \varsigma}{\partial x} - \frac{\partial E_x(x, y, z = 0)}{\partial z} \cdot \varsigma \\ E_y(x, y, z = 0) &= -E_z(x, y, z = 0) \cdot \frac{\partial \varsigma}{\partial y} - \frac{\partial Ey(x, y, z = 0)}{\partial z} \cdot \varsigma \end{aligned} \tag{4.13}$$

Thus, if the surface profile (4.8) and the position of sources are known, the problem is to determine the field in semispace $z > 0$, when their boundary conditions (4.13) are known. Let us consider the influence of roughness as a small perturbation, such that the total field is

$$\mathbf{E} = \mathbf{E}^{(0)} + \mathbf{E}^{(1)} \tag{4.14}$$

where $\mathbf{E}^{(0)}$ is the field that could be derived for the condition $\varsigma = 0$, which is well known from the strict theorem of reflections discussed in Section 3.1. The second term $\mathbf{E}^{(1)}$, that describes the field perturbations, can be obtained from wave equations by use of the boundary conditions, which lead from (4.13) by substituting (4.14) into it,

$$\begin{aligned} E_x^{(1)} &= -E_z^{(0)} \cdot \frac{\partial \varsigma}{\partial x} - \frac{\partial E_x^{(0)}}{\partial z} \cdot \varsigma \\ E_y^{(1)} &= -E_z^{(0)} \cdot \frac{\partial \varsigma}{\partial x} - \frac{\partial E_y^{(0)}}{\partial z} \cdot \varsigma \end{aligned} \tag{4.15}$$

To present this perturbation term, let us consider two special cases which are practical with regard to over-the-terrain propagation channels.

The *vertical dipole* is located at point O as shown in Figure 4.5. Its reflection from flat surface $z = 0$ at the point O_1 according to the strict reflection theorem must also be directed vertically. By introducing the spherical coordinate systems $\{R, \vartheta, \varphi\}$ and $\{R_1, \vartheta_1, \varphi_1 \equiv \varphi\}$ for each dipole and taking into account the relations between the field components, and the Hertz vector introduced in Section 2.1.3, we can present the components of nonperturbed field $\mathbf{E}^{(0)}$ as:

$$E_x^{(0)} = \left\{-k_0^2 p \sin\vartheta\cos\vartheta\frac{e^{i(\omega t-k_0R)}}{R} - k_0^2 p\sin\vartheta_1\cos\vartheta_1\frac{e^{i(\omega t-k_0R_1)}}{R_1}\right\}\cos\varphi$$

$$E_y^{(0)} = \left\{-k_0^2 p \sin\vartheta\cos\vartheta\frac{e^{i(\omega t-k_0R)}}{R} - k_0^2 p\sin\vartheta_1\cos\vartheta_1\frac{e^{i(\omega t-k_0R_1)}}{R_1}\right\}\sin\varphi \quad (4.16a)$$

$$E_z^{(0)} = \left\{k_0^2 p\sin^2\vartheta\frac{e^{i(\omega t-k_0R)}}{R} + k_0^2 p\sin^2\vartheta_1\frac{e^{i(\omega t-k_0R_1)}}{R_1}\right\}$$

Then, in the plane $z = 0$ ($R = R_1$, $\vartheta = \pi - \vartheta_1$):

$$E_x^{(0)} = E_y^{(0)} = 0, \quad E_z^{(0)} = 2k_0^2 p\sin^2\vartheta\frac{e^{i(\omega t-k_0R)}}{R}. \quad (4.16b)$$

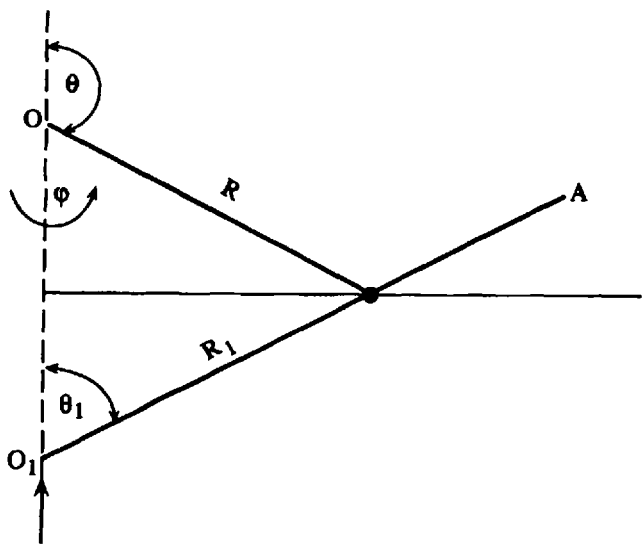

Figure 4.5 The geometry of vertical dipole field reflection from the ground.

Here p is the modulus of the momentum of the point vertical dipole, which is well known from the literature (see, for example, [4–6]).

Because in practical terrain propagation the source and the observed point are far from the surface $z = 0$, we can, following to [5], present simple formulas for the perturbed part of the total field due to roughness of the terrain in the case when the incident wave lies in the xy-plane (i.e., when $\varphi = 0$, $p\dfrac{e^{-ik_0R}}{R} = qe^{-ik_0x'\sin\vartheta}$, where q is constant):

$$
\begin{aligned}
E_x^{(1)} &= \frac{k_0^2}{2\pi}(2q)\int\left\{ik_0\cos^2\vartheta + \sin\vartheta\frac{\partial\varsigma}{\partial x'}\right\}\frac{\partial}{\partial z}\frac{e^{-ik_0(\rho+x'\sin\vartheta)}}{\rho}dx'dy' \\
E_y^{(1)} &= \frac{k_0^2}{2\pi}(2q)\int\left\{\sin^2\vartheta\frac{\partial\varsigma}{\partial y'}\right\}\frac{\partial}{\partial z}\frac{e^{-ik_0(\rho+x'\sin\vartheta)}}{\rho}dx'dy' \qquad (4.17)\\
E_z^{(1)} &= \frac{k_0^2}{2\pi}(2q)\int\left\{ik_0\frac{\partial\varsigma}{\partial x'}\left(\cos^2\vartheta - \sin^2\vartheta\right) + \left(\frac{\partial^2\varsigma}{\partial x'^2} + \frac{\partial^2\varsigma}{\partial y'^2}\right)\sin\vartheta\right. \\
&\quad \left. + k_0^2\cos^2\vartheta\sin\vartheta\right\}\frac{e^{-ik_0(\rho+x'\sin\vartheta)}}{\rho}dx'dy'
\end{aligned}
$$

Here $\rho = \sqrt{(x-x')^2 + (y-y')^2 + (z-z')^2}$, where x, y, z are the coordinates of the observed point.

For small grazing angles $\left(\vartheta \to \dfrac{\pi}{2}\right)$, (i.e., in the case of *slipped* incident waves), which is very realistic for mobile and personal communication, these formulas can be significantly simplified,

$$
\begin{aligned}
E_x^{(1)} &\approx -2k_0^2qe^{-ik_0x\sin\vartheta}\frac{\partial\varsigma}{\partial x} \\
E_y^{(1)} &\approx -2k_0^2qe^{-ik_0x\sin\vartheta}\frac{\partial\varsigma}{\partial y} \qquad (4.18)\\
E_z^{(1)} &\approx \frac{k_0^2}{2\pi}(2q)\int\left(\frac{\partial^2\varsigma}{\partial x'^2} + \frac{\partial^2\varsigma}{\partial x'^2} - ik_0\frac{\partial\varsigma}{\partial x'}\right)\frac{e^{-ik_0(\rho+x'\sin\vartheta)}}{\rho}dx'dy'
\end{aligned}
$$

The *horizontal dipole* is located at the point O and oriented along the y-axis. Its reflection from flat surface $z = 0$ at the point O_1 according to the strict reflection theorem is oriented in the opposite direction. In this case, at the plane $z = 0$, we have

$$
\begin{aligned}
E_x^{(0)} &= E_y^{(0)} = 0 \\
\left(\frac{\partial E_x^{(0)}}{\partial z}\right)_{z=0} &= 2ik_0^3 p \frac{e^{i(\omega t - k_0 R)}}{R} \sin^2\vartheta \cos\vartheta \cos\varphi \sin\varphi \\
\left(\frac{\partial E_y^{(0)}}{\partial z}\right)_{z=0} &= 2ik_0^3 p \frac{e^{i(\omega t - k_0 R)}}{R} \cos\vartheta (\sin^2\vartheta \sin^2\varphi - 1)
\end{aligned}
\tag{4.19}
$$

The same approach, as above, allows us to present, according to [5], the perturbation part of the total field due to the roughness of terrain for a horizontal dipole oriented along the y-axis:

$$
\begin{aligned}
E_x^{(1)} &= 0 \\
E_y^{(1)} &= -\frac{k_0^2}{2\pi}(2q) \int \{ik_0 \varsigma \cos\vartheta\} \frac{\partial}{\partial z} \frac{e^{-ik_0(\rho + x' \sin\vartheta)}}{\rho} dx'dy' \\
E_z^{(1)} &= \frac{k_0^2}{2\pi}(2q) \int \left\{ ik_0 \frac{\partial \varsigma}{\partial y'} \cos\vartheta \right\} \frac{e^{-ik_0(\rho + x' \sin\vartheta)}}{\rho} dx'dy'
\end{aligned}
\tag{4.20}
$$

Then, in the same case of *slipped* waves (i.e., for small grazing angles ($\vartheta \to \pi/2$)) one can obtain from (4.20) simple formulas for the perturbed part of the total field:

$$
\begin{aligned}
E_x^{(1)} &= 0 \\
E_y^{(1)} &= -2ik_0^3 \varsigma q \cos\vartheta e^{-ik_0 x \sin\vartheta} \approx 0 \\
E_z^{(1)} &= \frac{k_0^3}{2\pi}(2iq) \int \frac{\partial \varsigma}{\partial y'} \cos\vartheta \frac{e^{-ik_0(\rho + x' \sin\vartheta)}}{\rho} dx'dy'
\end{aligned}
\tag{4.21}
$$

Comparison between formulas (4.18) to (4.19) and (4.20) to (4.21), for both kinds of wave field polarizations, shows that the field of the horizontal dipole is weaker and affected by the roughness of terrain than that of the vertical dipole.

The formulas presented above can predict the propagation characteristics over rough terrain in conditions of direct visibility between the source and the observer, if the profile $\varsigma(x, y)$ of the ground surface is known for each concrete situation.

Moreover, these formulas allow us to obtain the coherent and noncoherent parts of the total field energy. The coherent power predominates for the case of a smooth surface and is determined by the use of the nonperturbed field

$\mathbf{E}^{(0)}$, the components of which are described by (4.16). The incoherent power is determined by use of the perturbed field $\mathbf{E}^{(1)}$ described by (4.17) to (4.18) and (4.20) to (4.21) for both kinds of field polarization.

The limitation of the perturbation method is connected with the requirement of smallness not only for $\nabla\varsigma$, but also for the earth's surface deviations $\varsigma(x, y)$. The last condition can be ignored, however, because, if we derive the second *perturbation* term $\mathbf{E}^{(2)}$ in (4.14), we obtain for the case of vertical dipole the following condition:

$$(|k_0 \cdot \varsigma \cdot \nabla\varsigma|)^{1/2} << 1 \tag{4.22}$$

from which, assuming that $|\nabla\varsigma| \approx \varsigma/l$, where l is the characteristic length of roughness, we obtain that

$$\varsigma << \sqrt{\lambda \cdot l} \tag{4.23}$$

Therefore, for sufficiently small slope angles, the described perturbation technique is valid even for deviations ς, similar or larger than the wavelength λ.

The Kirchhoff approximation solution. Now we consider the other limiting case, when the characteristic scales of roughness of the earth's surface significantly exceed a wavelength of the radiated field from the source. In this case, the Kirchhoff approximation may be used to obtain a simple solution. What is important to note is that this method requires the absence of shadow zones between all roughnesses and/or multireflection and multiscattering between each roughness placed on the flat surface $z = 0$. In the other words, we suppose that the surface S is slowly varying so that the radius of curvature is much greater than a wavelength (Figure 4.6). If so, we assume, following [5–9], that at each point $\mathbf{r}$ on the quasi-smooth surface S the wave field is a superposition of the incident field $\mathbf{E}_0$ (i.e., the field resulting from sources placed at an infinite distance) and the field $\mathbf{E}$ reflected from the plane G_r according to the geometric optics' law. This plane is tangential to the surface S at the point $\mathbf{r}$, as is shown in Figure 4.6.

The scattered electromagnetic wave at the observed point R can be represented by means of the values of $\mathbf{E}$ and $\mathbf{H}$ on the surface S by use of Green's theorem (see Section 2.2.5), the simple presentation of the source fields

$$\mathbf{E}_i(\mathbf{r} \in S) = \mathbf{E}_0 \frac{\exp\{ikR_1\}}{R_1}, \quad \mathbf{H}_i(\mathbf{r} \in S) = \mathbf{H}_0 \frac{\exp\{ikR_1\}}{R_1} \tag{4.24}$$

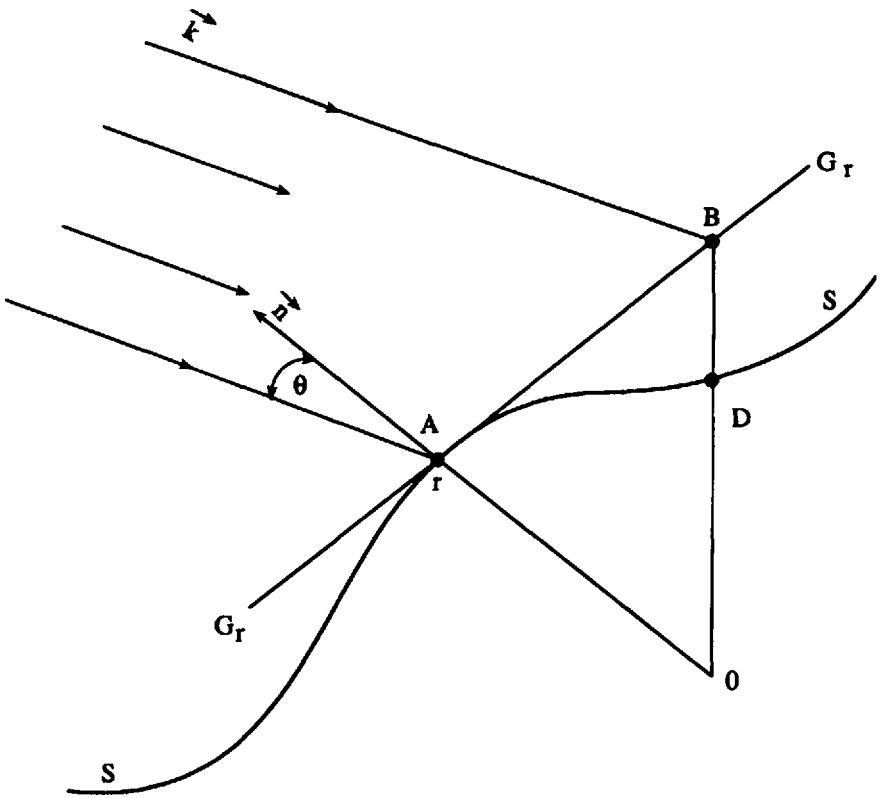

Figure 4.6 The presentation of smooth terrain described by the Kirchhoff approximation.

and the Green's function representation of the point source according to Section 2.2.4 $G = \dfrac{\exp\{ikR\}}{R}$:

$$\mathbf{E}(\mathbf{R}) = \frac{ik}{4\pi}\int_S \frac{e^{ik(\tilde{R}_1+\tilde{R}_2)}}{\tilde{R}_1\tilde{R}_2}\{[\mathbf{n}\times(\mathbf{H}-\mathbf{H}_0)] + [\mathbf{n}\cdot(\mathbf{E}-\mathbf{E}_0)\cdot\nabla_r\tilde{R}_2] - [\nabla_r\tilde{R}_2\times\mathbf{n}\times(\mathbf{E}-\mathbf{E}_0)]\}ds \qquad (4.25)$$

Here, as follows from Figure 4.7, R_1 and R_2 are the distances from the current point $\mathbf{r}(x, y, z = 0)$ at the flat surface $z = 0$ to the source point O and the observed point R; $\tilde{R}_1$ and $\tilde{R}_2$ are the distances from the current point $\mathbf{r}(x, y, z)$ at the surface S over which the integration in (4.25) takes place; $\varsigma(\mathbf{r})$ is the height of the surface S at the arbitrary point $\mathbf{r}(x, y, z)$. If the source and the observed point are located in the far wave zone relative to surface S,

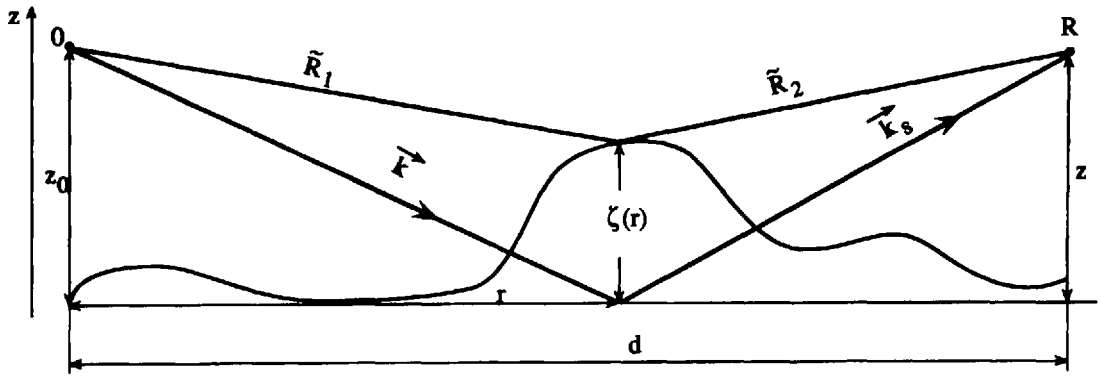

Figure 4.7 The geometry of reflection from the quasi-smooth surface $S(r)$.

that is, $k\bar{R}_1 >> 1$ and $k\bar{R}_2 >> 1$, the integral in (4.25) for the scattered field in direction $\mathbf{k}_s$ can be rewritten as

$$\mathbf{E}(\mathbf{k}, \mathbf{k}_s) = \frac{ik}{4\pi} \frac{e^{ik(R_{10}+R_{20})}}{R_{10}R_{20}} \int_{S_0} \{[\mathbf{n} \times (\mathbf{H} - \mathbf{H}_0)] + [\mathbf{n} \cdot (\mathbf{E} - \mathbf{E}_0) \cdot \nabla_r R_2] - [\nabla_r R_2 \times \mathbf{n} \times (\mathbf{E} - \mathbf{E}_0)]\} \exp\{i[(\mathbf{k} - \mathbf{k}_s)\mathbf{r} + (k_z - k_{sz})\varsigma(\mathbf{r})]\} \frac{d\mathbf{r}}{q_z} \tag{4.26}$$

Here R_{10} and R_{20} are the distances between the arbitrary point $\mathbf{r}(x, y, z = 0)$ on the surface S_0, which is the projection of the rough surface S at the plane $z = 0$, and the source O and observed point R, respectively.

For future analysis of the integral in (4.26), it is convenient to present the distances $\bar{R}_1$ and $\bar{R}_2$ through the vector $\mathbf{r}(x, y, z = 0)$ that lies on the flat surface $z = 0$ and the value of surface height $\varsigma(\mathbf{r})$ at this current point (see Figure 4.7)

$$\begin{aligned} \bar{R}_1 &= \sqrt{r^2 + (z_0 - \varsigma)^2} \approx R_1 + \alpha_z \varsigma \\ \bar{R}_2 &= \sqrt{(d - r)^2 + (z - \varsigma)^2} \approx R_2 + \beta_z \varsigma \end{aligned} \tag{4.27}$$

where $R_1 = \sqrt{r^2 + z^2}$, $R_2 = \sqrt{(d - r)^2 + z^2}$; $\alpha_z = -\frac{z_0}{R_1}$ and $\beta_z = \frac{z}{R_2}$ are the z-components of vectors $\mathbf{a} = \nabla_r R_1$ and $\mathbf{b} = -\nabla_r R_2$ (i.e., the projections of these vectors at the z-axis).

We analyze (4.26) that describes the scattered field for two cases that are useful in practice for over-the-terrain propagation by introducing some new variables according to [6–8]: $\mathbf{q} = \mathbf{k}_s - \mathbf{k}$, $\mathbf{k} = k\mathbf{a} = k\nabla_r R_1$, and $\mathbf{k}_s = k\mathbf{b} = -k\nabla_r R_2$.

In the case of a *perfectly conductive* earth surface, when according to results presented in Chapter 3, $\mathbf{n} \cdot \mathbf{E} = 2 \cdot (\mathbf{n} \cdot \mathbf{E}_0)$ and $\mathbf{n} \times \mathbf{H} = 2 \cdot (\mathbf{n} \times \mathbf{H}_0)$, for the scattered component of total field, (4.26) can be simplified taking into account that electric and magnetic components of the electromagnetic field are mutually perpendicular, $\mathbf{H}_0 = \mathbf{k} \times \mathbf{E}_0/k$, that is,

$$\mathbf{E}(\mathbf{k}, \mathbf{k}_s) = \frac{ik}{4\pi} \frac{e^{ik(R_{10}+R_{20})}}{R_{10}R_{20}} \int_{S_0} \{[\mathbf{n} \times (\mathbf{a} \times \mathbf{E}_0)] - [\mathbf{n} \cdot \mathbf{E}_0 \cdot \mathbf{b}] + [\mathbf{b} \times \mathbf{n} \times \mathbf{E}_0]\} \exp\{-i[\mathbf{q} \cdot \mathbf{r} + q_z \varsigma(\mathbf{r})]\} \frac{d\mathbf{r}}{q_z} \tag{4.28}$$

Because we investigate here only the case of short-wavelength propagation (high-frequency band), the short-wave approximation ($q_z\varsigma >> 1$) of integral in (4.28) is [6–8]:

$$\mathbf{E}(\mathbf{k}, \mathbf{k}_s) \approx \frac{ik}{2\pi} \frac{e^{ik(R_{10}+R_{20})}}{R_{10}R_{20}} \frac{[\mathbf{b} \times (\mathbf{E}_0 \times \mathbf{q})]}{q_z} \int_{S_0} \exp\{-i[\mathbf{q} \cdot \mathbf{r} + q_z\varsigma(\mathbf{r})]\} d\mathbf{r} \tag{4.29}$$

Hence, we have finally obtained that the vector multiplyer $[\mathbf{b} \times (\mathbf{E}_0 \times \mathbf{q})]$ is outside the integral and determines the polarization characteristics of the scattered field. We will investigate the polarization phenomenon later. Now we must note that all statistical characteristics of the scattered field caused by the rough surface are determined by the following integral:

$$\int_{S_0} \exp\{-i[\mathbf{q} \cdot \mathbf{r} + q_z\varsigma(\mathbf{r})]\} d\mathbf{r} \tag{4.30}$$

Additional investigations of integral (4.30) after its statistical averaging have shown that the average value of exponent $\langle \exp\{-iq_z\varsigma(\mathbf{r})\}\rangle$ in (4.30) is the one-dimensional characteristic function that describes the effect of rough terrain and does not depend on coordinate $\mathbf{r}$. Moreover, the reflection coefficient of the average (coherent) field coincides with this one-dimensional characteristic function. In fact, because the average scattered field can be presented through this function as

$$<\mathbf{E}(\mathbf{k}, \mathbf{k}_s)> = \mathbf{E}^{(0)}(\mathbf{k}, \mathbf{k}_s)\chi(q_z) \tag{4.31}$$

where the field

$$\mathbf{E}^{(0)}(\mathbf{k}, \mathbf{k}_s) = \frac{ik}{2\pi} \frac{e^{ik(R_{10}+R_{20})}}{R_{10}R_{20}} \frac{[\mathbf{b} \times (\mathbf{E}_0 \times \mathbf{q})]}{q_z} \int_{S_0} \exp\{-i\mathbf{q} \cdot \mathbf{r}\} d\mathbf{r} \tag{4.32}$$

is the field reflected from the area S_0 of plane $z = 0$; the effective reflection coefficient from rough terrain, as follows from relationship (4.31) and the strict reflection theorem, according which $\langle \mathbf{E}(\mathbf{k}, \mathbf{k}_s)\rangle = \mathbf{E}^{(0)}(\mathbf{k}, \mathbf{k}_s)R_f(\psi)$ (Section 3.2), is described by this characteristic function, that is, $R_f(\psi) \equiv \chi(q_z)$. Here ψ is the slip angle (for the geometry of the problem presented in Figure 4.7

$k_s = k \cdot \cos\psi$, $k_y = 0$ and $k_s = -k \cdot \sin\psi$). As an example, for the surface S with Gaussian-coordinate distribution, we find that the effective coefficient of reflection

$$R_f(\psi) \approx \exp\{-2k^2\varsigma^2\sin^2\psi\} \tag{4.33}$$

exponentially decreases with increase of characteristic height of roughness $\varsigma(\mathbf{r})$.

As follows also from (4.29), the polarization characteristic of the reflected wave $\mathbf{E}$ is different from that for incident wave $\mathbf{E}_i$. The unit normal vector $\mathbf{n}_0$ to the surface S is related to vectors $\mathbf{q}$, $\mathbf{a}$ and $\mathbf{b}$ through the simple formulas:

$$\mathbf{b} = \mathbf{a} - 2\mathbf{n}_0 \cdot (\mathbf{n}_0 \cdot \mathbf{a}),\ \mathbf{q} = k(\mathbf{b} - \mathbf{a}) = 2k\mathbf{n}_0 \cdot (\mathbf{n}_0 \cdot \mathbf{b}), \tag{4.34a}$$

substitution of which in the polarized multiplyer in (4.29) gives:

$$[\mathbf{b} \times (\mathbf{E}_0 \times \mathbf{q})] = 2k(\mathbf{n}_0 \cdot \mathbf{a})^2\{\mathbf{E}_0 - 2\mathbf{n}_0 \cdot (\mathbf{n}_0 \cdot \mathbf{E}_0)\},\quad \mathbf{n}_0 = \frac{\mathbf{q}}{q} \tag{4.34b}$$

Hence, the depolarization of scattered field from rough terrain is the same as that for the specular reflection from a perfectly conductive flat surface with unit normal vector equal $\mathbf{n}_0$. This result can be easily understood if one takes into account that for $k \to \infty$ (short-wave approximation) the contribution in the scattered field gives only specular reflected points with $\mathbf{n} = \mathbf{n}_0 = \mathbf{q}/q$, and reflection from each of them at the surface S takes place in the same way as from the tangential plate G_r (see Figure 4.6).

Substituting (4.34a) in (4.29) and introducing the tensor coefficient of reflections $R^E_{je} = -\delta_{je} + 2n_j n_e$, where the double repeated index e indicates the summation from 1 to 3, and δ_{fe} is the unit tensor, which equal 1, if $j = e$, and 0, if $j \neq e$, one can finally obtain from (4.29) the solution for the $\mathbf{E}_j$-component of the scattered field:

$$\mathbf{E}_{je}(\mathbf{k}, \mathbf{k}_s) \approx \frac{e^{ik(R_{10}+R_{20})}}{4\pi i R_{10}R_{20}}\frac{q^2}{q_z} R^E_{je} \cdot \mathbf{E}_{0e}\int_{S_0} \exp\{-i[\mathbf{q} \cdot \mathbf{r} + q_z\varsigma(\mathbf{r})]\}d\mathbf{r} \tag{4.35}$$

The same result can be obtained for the $\mathbf{H}_j$-component of the scattered field by introducing in (4.35) the following terms: $\mathbf{H}_{je}$, $\mathbf{H}_{0e}$, and $R^H_{je} = -R^E_{je}$, respectively.

Let us now generalize the above obtained results for the case of scattering from the *impedance* rough surface with arbitrary conductivity and dielectric

permittivity. Here we also use the short-wave approximation ($k \to \infty$), which is usually used in the practice of over-the-terrain propagation. This approximation allows us to carry from integral (4.26) the vector multiplyers for $\mathbf{n} = \mathbf{n}_0$, which describe the polarization phenomena. Let us also introduce the vector amplitudes of the reflected wave $\mathbf{E}_r = \mathbf{E} - \mathbf{E}_0$ and $\mathbf{H}_r = \mathbf{H} - \mathbf{H}_0 = \mathbf{b} \times \mathbf{E}_r$ on the plane G_r tangential to the surface S at the points of specular reflection. Then the vector multiplyers that are carried out from the integral can be presented as:

$$\begin{aligned}
&[\mathbf{n}_0 \times (\mathbf{H} - \mathbf{H}_0)] - [\mathbf{n}_0 \cdot (\mathbf{E} - \mathbf{E}_0)] \cdot \mathbf{b} + [\mathbf{b} \times [\mathbf{n}_0 \times (\mathbf{E} - \mathbf{E}_0)]] \\
&\quad = [[\mathbf{n}_0 \times (\mathbf{b} \times \mathbf{E}_r)] - [(\mathbf{n}_0 \cdot \mathbf{E}_r)] \cdot \mathbf{b} + \mathbf{b} \times [(\mathbf{n}_0 \times \mathbf{E}_r)] \\
&\quad = -2[(\mathbf{n}_0 \cdot \mathbf{b}) \cdot \mathbf{E}_r]
\end{aligned} \tag{4.36}$$

On the other hand, from (4.34) it follows that

$$2\frac{\mathbf{n}_0 \cdot \mathbf{b}}{n_z} = \frac{q^2}{kq_z} \tag{4.37}$$

Substituting these expressions into (4.26), we have for $k \to \infty$:

$$\mathbf{E}(\mathbf{k}, \mathbf{k}_s) \approx \frac{e^{ik(R_{10}+R_{20})}}{4\pi i R_{10} R_{20}} \frac{q^2}{q_z} \mathbf{E}_r \int_{S_0} \exp\{-i[\mathbf{q} \cdot \mathbf{r} + q_z \varsigma(\mathbf{r})]\} d\mathbf{r} \tag{4.38}$$

where the reflected field $\mathbf{E}_r$ can be expressed through the incident field $\mathbf{E}_0$ by help of tensor reflection coefficients from the surface with $\mathbf{n} = \mathbf{n}_0$: $\mathbf{E}_{je} = R^E_{je}(\mathbf{n}_0)\mathbf{E}_{0e}$.

Hence, we come to the same formula, as expressed by (4.35) for the *perfectly conductive* ground surface, but with more complicated formula for the components of the reflection tensor:

$$\begin{aligned}
R^E_{je} &= R_V \delta_{je} - \frac{1}{\sin\vartheta}\{(R_H + R_V \cos\vartheta) n_j n_e + \cos\vartheta (R_H + R_V) \alpha_j n_e\} \\
R^H_{je} &= R_V \delta_{je} - \frac{1}{\sin\vartheta}\{(R_V + R_H \cos\vartheta) n_j n_e + \cos\vartheta (R_H + R_V) \alpha_j n_e\}
\end{aligned} \tag{4.39a}$$

which are significantly simplified for the case of the perfectly conductive surface and can be presented in the invariant form:

$$R_{je}^{H} = -R_{je}^{E} = \delta_{je} - 2n_j n_e \tag{4.39b}$$

Let us note that the invariant form of record presented in (4.35) and (4.38) allows us to use these formulas for scattering phenomena from the surface with arbitrary dielectric permittivity not only for a linearly polarized wave, but also for an elliptically polarized wave. Moreover, because this permittivity has a nonzero imaginary part, the components of reflection tensors are also complex values that lead to conversion of the wave's polarization. For example, the linearly polarized wave, after scattering from the impedance rough surface, becomes elliptically polarized. But what is more interesting, the depolarization phenomenon is not connected with the statistical properties of rough terrain; it is completely determined by the inclination of tangential plane G_r to the surface S at the points of specular reflection. The direction of normal vector $\mathbf{n}_0$ to this plane (and, hence, the polarization of reflected field) connects with the direction of wave vector $\mathbf{k}$ of the incident wave and with the direction to the observed point $\mathbf{k}_s$ through the relation: $\mathbf{n}_0 = \dfrac{\mathbf{k}_s - \mathbf{k}}{|\mathbf{k}_s - \mathbf{k}|}$. Therefore, to determine the type of polarization of the scattered wave, one can directly use the tensor presentation of the Fresnel reflection coefficients with $\mathbf{n} = \mathbf{n}_0$ and $\vartheta = \vartheta_0 = \cos^{-1}(\mathbf{n} \cdot \mathbf{b})$.

4.2 Propagation Over Rough Terrain in NLOS Conditions Between Antennas

In the case where both antennas, receiver and transmitter, are in obstructive conditions (i.e., there is no line-of-sight, denoted in the literature as NLOS, see also cases 2 and 3 in Section 1.6) between the source and the observer, a new effect of diffraction phenomena arises from various kinds of obstacles, such as trees and hills, placed in the rural environment around both antennas. The diffraction phenomenon is also based on the Huygens's principle, introduced in Sections 2.2.5 and 2.2.6, and used for the description of reflection phenomenon from flat terrain in Section 3.1.2. Let us briefly describe the diffraction from obstacles which form a *hilly terrain* (i.e., from different kinds of hills), using the Huygens's principle and the deterministic approach in a qualitative manner, replacing each hill by a *knife edge.*

4.2.1 Propagation Over a Single Knife Edge

The analysis described in Section 2.2.5 for propagation in free space applies if the wavefront AA' (Figure 4.8) of an arbitrary electromagnetic wave is infinite

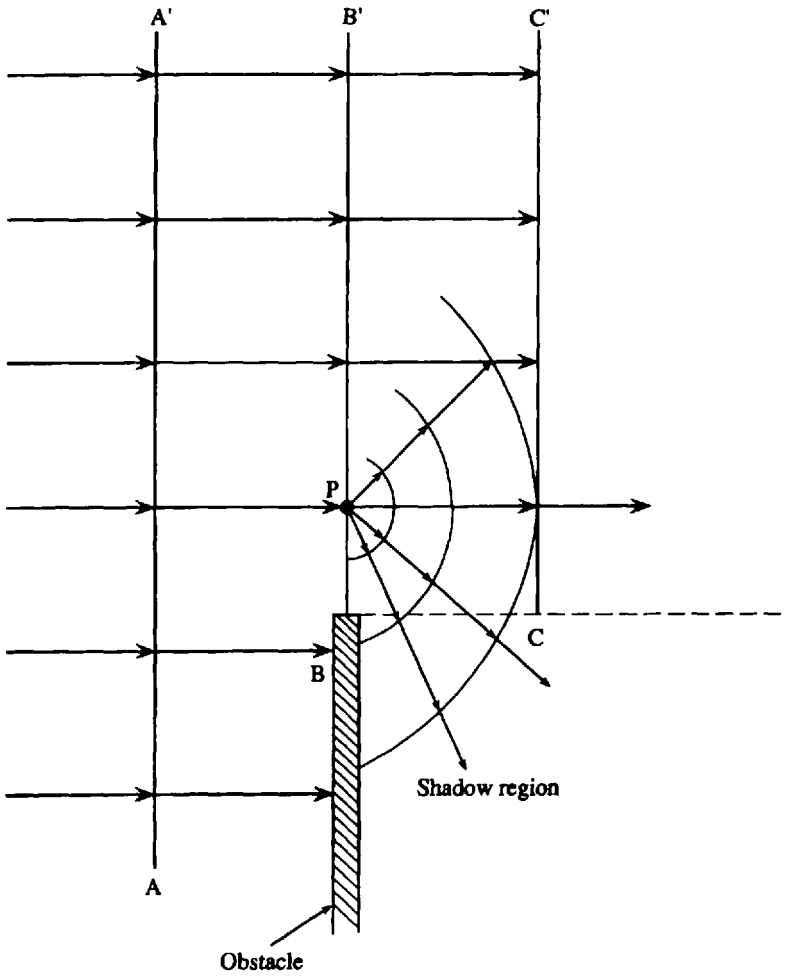

Figure 4.8 Diffraction at the edge of an obstruction.

(more strictly, much greater than the wavelength). If there is now some obstacle that we may model as the simple knife edge which lies between the receiver and the transmitter, only a semi-infinite wavefront CC' exists (Figure 4.8). The classical optical ray theory states that no field exists in the shadow region below the dotted line BC. However, according to Huygens's principle, the wavelets originating from all points on line BB', (e.g., point P), propagate into a shadow region. This will tend to fill in the shadow behind an obstruction, as shown in Figure 4.8. When the wavefront encounters an obstruction and penetrates from the illuminated (light) zone to nonilluminated (shadow) zone due to the existence of a second source of wavelets at the edges, tips, wedges,

and so on of arbitrary obstructions, the effect is known as the *diffraction phenomenon.*

Fresnel-Kirchhoff parameter and Fresnel-zone concept. With the help of this concept, which also appeared in Chapters 2 and 3 to explain the free-space propagation and the reflection phenomena, one can determine and describe the meaning of the main parameter of diffraction, which in the literature is called the Fresnel-Kirchhoff diffraction parameter. As follows from the illustration in Figure 4.9, the phase difference $\Delta\Phi$ between the direct ray from the source (at point O) denoted TOR, and that diffracted from the point O', denoted $TO'R$, can be obtained in the standard manner by use of the path difference Δd between these rays, assuming that the height of the obstacle is much smaller than the characteristic ranges between the antennas and the obstacle ($h << d_1, d_2$):

$$\Delta d \approx \frac{h^2}{2}\frac{(d_1 + d_2)}{d_1 d_2}$$
$$\Delta\Phi = \frac{2\pi}{\lambda}\Delta d = \frac{2\pi}{\lambda}\frac{h^2}{2}\frac{(d_1 + d_2)}{d_1 d_2} \tag{4.40}$$

If we now introduce the Fresnel-Kirchhoff diffraction parameter, v, according to [1–3], as a simple function of the path difference, Δd, expressed in wavelengths

$$v = \pm h\sqrt{\frac{2(d_1 + d_2)}{\lambda d_1 d_2}} = \pm 2\sqrt{\frac{\Delta d}{\lambda}} \tag{4.41}$$

the phase difference may be rewritten in terms of this parameter,

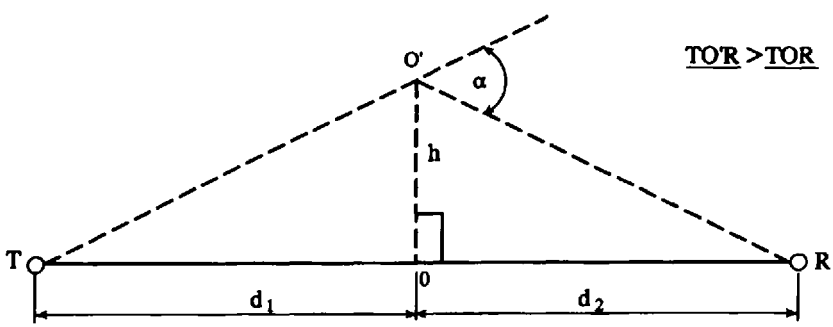

Figure 4.9 The geometry of knife-edge diffraction.

$$\Delta\Phi = \frac{\pi}{2}v^2 \tag{4.42}$$

Usually, the additional parameter, α, is introduced together with the Fresnel-Kirchhoff parameter v:

$$\alpha^2 = v^2\frac{\lambda(d_1 + d_2)}{2d_1d_2} \tag{4.43}$$

If so, the phase difference between the diffracted and the direct rays can be rewritten as:

$$\Delta\Phi = \frac{\pi}{\lambda}\frac{d_1d_2}{(d_1 + d_2)}\alpha^2 \tag{4.44}$$

Before going into the details of the problem we must note that the Fresnel-Kirchhoff parameter is presented in (4.41) with the two signs, "−" and "+," before the square root, as are usually used for estimating it in the literature. Below, following in [1], we will use the diffraction parameter presentation (4.41) with the "+" sign before the square root. The results of estimating this parameter by using the "−" sign in (4.41) may be found in [3] (we will only present some results relative to this case).

Now, as was mentioned in Section 2.2.6, it is necessary to keep the region known as the *first Fresnel zone* substantially free of obstructions in order to obtain wave transmission under free-space conditions. To now estimate the effect of diffraction around obstructions we need a quantitative measure of the required clearance over any terrain obstruction. As was shown in Section 2.2.6, this may be obtained analytically in terms of Fresnel-zone ellipsoids drawn around both ends of the radio link, receiver and transmitter (Figure 4.10).

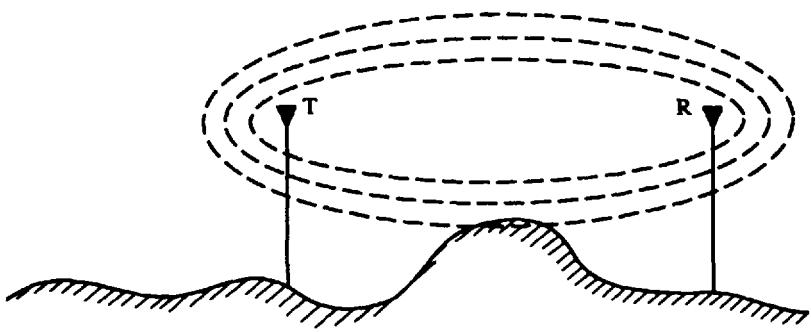

Figure 4.10 The Fresnel-zone ellipsoids around the transmitter and the receiver.

The reader can find Fresnel ellipsoids discussed in detail in Chapters 2 and 3. Here we will only repeat that the radius of any ellipsoid with number n from the family of ellipsoids can be presented as a function of parameter n and the distances between both antennas and the obstruction, d_1 and d_2, respectively:

$$r_n \equiv h_n = \left[\frac{n\lambda d_1 d_2}{(d_1 + d_2)}\right]^{1/2} \tag{4.45}$$

Then from (4.41) one can obtain the physical meaning of the Fresnel-Kirchhoff diffraction parameter:

$$v_n = h_n \cdot \left[\frac{2(d_1 + d_2)}{\lambda d_1 d_2}\right]^{1/2} = \left[\frac{2(d_1 + d_2)}{\lambda d_1 d_2} \frac{n\lambda d_1 d_2}{(d_1 + d_2)}\right]^{1/2} = (2n)^{1/2} \tag{4.46}$$

Thus the diffraction parameter v increases with the number n of ellipsoids. All the above formulas are corrected for $h_n << d_1, d_2$, (i.e., far from both antennas). The volume enclosed by the ellipsoid defined by $n = 1$ is known as a *first Fresnel zone.* The volume between this ellipsoid and that defined by $n = 2$ is the *second Fresnel zone.* As a result, the contributions to the total field at the receiving point from successive Fresnel zones tend to be in phase opposition and therefore interfere destructively rather than constructively. If an obstruction OO' is placed at the middle of radio path $TO'R$ (i.e., $TO' = O'R$) then if the height of obstruction h increases from $h = r_1$ (corresponding to the *first* Fresnel zone) to $h = r_2$ (defining the limit of the *second* Fresnel zone), then to $h = r_3$ (to the *third* Fresnel zone) and so on, then the field at the receiver R would oscillate. The amplitude of oscillations would essentially decrease since a smaller amount of wave energy penetrates into the outer zone.

Fresnel clearance. As follows from the material discussed in detail in Chapters 2 and 3 and mentioned above, any radio path in obstructive conditions (as illustrated in Figure 4.10) requires a certain amount of clearance around the central ray if the signal expected from free-space propagation is to be received. This phenomenon can be understood by use of the principle of Fresnel clearance, which is important in design of point-to-point radio links, where communication is required along a single radio path. Fresnel clearance is quoted in terms of Fresnel zones. In fact, the first Fresnel zone (for $n = 1$) encloses all radio paths for which the additional path length Δd, according to (4.40), does not exceed $\lambda/2$, that is, a phase change of $\Delta\Phi_1 = \pi$. The second Fresnel zone (for $n = 2$) encloses all paths for which

the additional path length Δd does not exceed $2 \cdot \frac{\lambda}{2} \equiv \lambda$ ($\Delta\Phi_2 = 2\pi$), and so on.

The radius of a Fresnel zone at any point along the radio path can be obtained by replacing Δd, in (4.40), by the required number n of wavelengths, changing the obstruction height h_n to the Fresnel radius r_n according to (4.45). Thus the radius of the first Fresnel zone r_1 is given by setting $\Delta d = \lambda/2$ in (4.45). As a result, $r_1 = (\lambda d_1 \cdot d_2/(d_1 + d_2))^{1/2} = (300 \cdot d_1 \cdot d_2)/(f \cdot d)^{1/2}$, where f is measured in GHz and $d = d_1 + d_2$ in km. The shape of the first Fresnel zone (a Fresnel ellipsoid) is shown in Figure 4.10. For a given Fresnel clearance no obstructions should exist inside the volume of this ellipsoid, that is, the volume produced by rotating the ellipse around the direct ray TR. As seen below from calculations of diffraction losses from any obstruction (presented in Figure 4.14), in practice a clearance of 60% of the first Fresnel zone is normally considered adequate for the land point-to-point radio links, corresponding to the diffraction parameter $\nu = -1.1$. We must also note that the approximate formula (4.45) and, hence, the principle of Fresnel clearance was obtained for the case of $d_1, d_2 >> r_n$, which is correct for most practical cases of land-radio links construction.

Diffraction losses. If between the transmitter and receiver there is any single obstacle which can be modeled by a single "knife edge," losses of the wave energy take place. Such losses in the literature are called *diffraction losses.* These losses can be strictly obtained analytically by use of the Fresnel-complex integrals presented earlier in Chapter 2 in the use of Huygens's principle. In fact, from the classical theory of plane-wave propagation [1–3], the total wave field E_{total} after diffraction at the tip or edge of some arbitrary obstruction (such a hill, tree, etc.) can be presented in the following form:

$$E_{total} = E_i \cdot D \cdot \exp\{j\Delta\Phi\}, \tag{4.47}$$

where E_i is the incident wave from the transmitter located in free space; D is the diffraction coefficient (see Chapter 5); $\Delta\Phi$ is the phase difference between the diffracted and direct waves mentioned above. Then the path loss (the reader can find the definition of such a wave characteristic in Chapter 1) due to diffraction can be determined in the standard manner:

$$L_D = 20 \cdot \log D \tag{4.48}$$

The main goal of strict diffraction theory by the use of the analytical deterministic approach is to obtain parameters D and $\Delta\Phi$ by use of Fresnel integrals. Let us obtain the relationships between these parameters and the

Fresnel integral. As is well known, the total diffracted field at the observed point can be presented in the following integral form by using the Fresnel integral:

$$E = E_0 \frac{(1+j)}{2} \int_v^{\infty} \exp\left\{-j\frac{\pi}{2}t^2\right\} dt \tag{4.49}$$

The integral in the right side of (4.49) is the complex integral with parameter of integration v defined by (4.41) for the height of the obstruction under consideration. We note that if the path TR, between the transmitter and receiver (line-of-sight path), is actually obstructed by some obstacle modeled by a knife edge, as is shown in Figure 4.11(a), then the height h and the diffraction parameter v are positive (it follows from (4.41) with the "+" sign). If the knife edge lies below the line-of-sight path (line TR in Figure 4.11(b)), so that there is no interruption between T and R, then h, and hence v, are negative (because we "work" by use of (4.41) with the "+" sign).

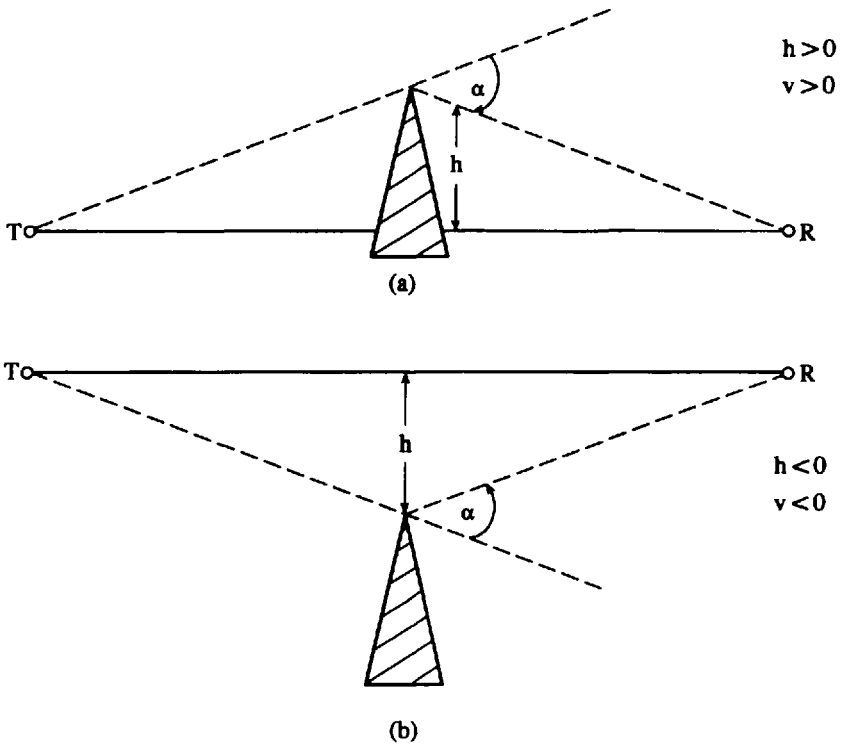

Figure 4.11 Knife-edge diffraction: (a) $h > 0$ and $v > 0$; (b) $h < 0$ and $v < 0$.

The field at point R will then be the free-space value E_i. It will begin to oscillate as the height of the knife edge is increased. The oscillations are stronger when more of the Fresnel zones below the TR-line are blocked by this knife edge. The amplitude of oscillations increases until the tip of the knife edge is just at the TR-line, at which point the field strength is exactly half the incident field (i.e., $E_i/2$). The same two situations along the radio link are shown, but for the Fresnel-Kirchhoff parameter description by (4.41) with the "−" sign. These two situations are shown in Figure 4.12, where the top figure presents the nonobstructive condition between T and R with knife-edge height negative, $h < 0$ and $v > 0$. The bottom figure presents the inverse situation with $h > 0$ and $v < 0$. Because both variants of the formula (4.41), with "+" and "−" signs are usually used in the literature, we will briefly summarize results of the calculation for the last case and present all useful formulas for both of the cases mentioned above. In all the graphs below, however, we will present the results of calculation by use of (4.41) with a "+" sign according to [1]. In both cases, when the knife-edge height is higher than the TR-line, we must obtain the essential decay of field strength (i.e., increase of path loss relative to free-space value E_i) without oscillations of wave amplitude. Let us show this by using the analytical approach. The Fresnel integral in (4.49) can be presented in the standard manner as

$$\int_v^\infty \exp\left\{-j\frac{\pi}{2}t^2\right\}dt = \int_v^\infty \cos\left\{-\frac{\pi}{2}t^2\right\}dt - j\int_v^\infty \sin\left\{-\frac{\pi}{2}t^2\right\}dt \qquad (4.50)$$

But

$$\int_v^\infty \cos\left\{-\frac{\pi}{2}t^2\right\}dt = \frac{1}{2} \pm \int_0^v \cos\left\{-\frac{\pi}{2}t^2\right\}dt = \frac{1}{2} \pm C(v) \qquad (4.51a)$$

Similarly

$$\int_v^\infty \sin\left\{-\frac{\pi}{2}t^2\right\}dt = \frac{1}{2} \pm \int_0^v \sin\left\{-\frac{\pi}{2}t^2\right\}dt = \frac{1}{2} \pm S(v) \qquad (4.51b)$$

Here the "−" sign in all the formulas above corresponds to the case presented by Figure 4.11, and the "+" sign corresponds to the case presented by Figure 4.12. Then the total field according to (4.49) can be rewritten as:

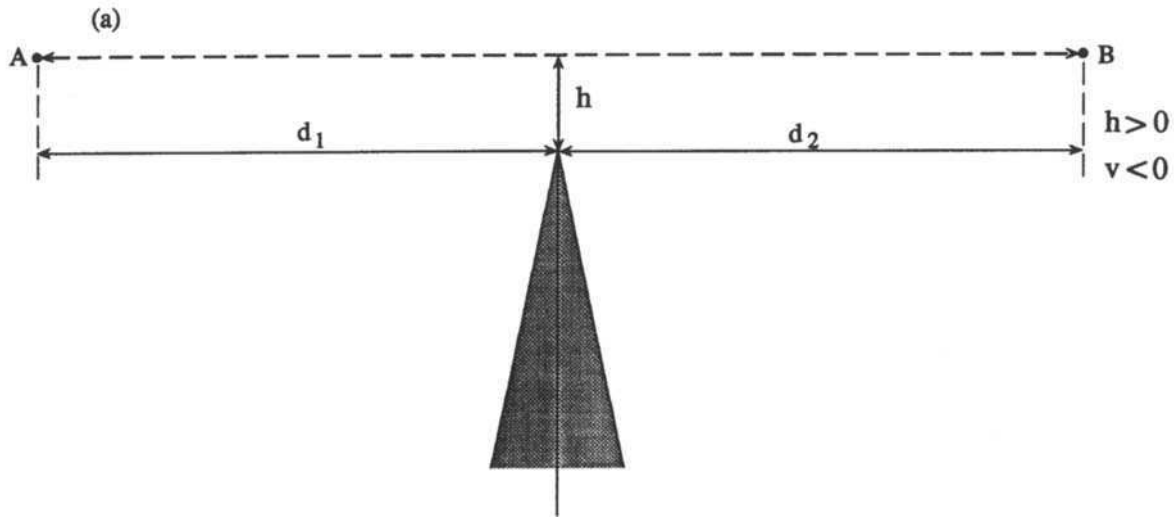

Figure 4.12 Knife-edge diffraction: (a) $h > 0$ and $v < 0$; (b) $h < 0$ and $v > 0$.

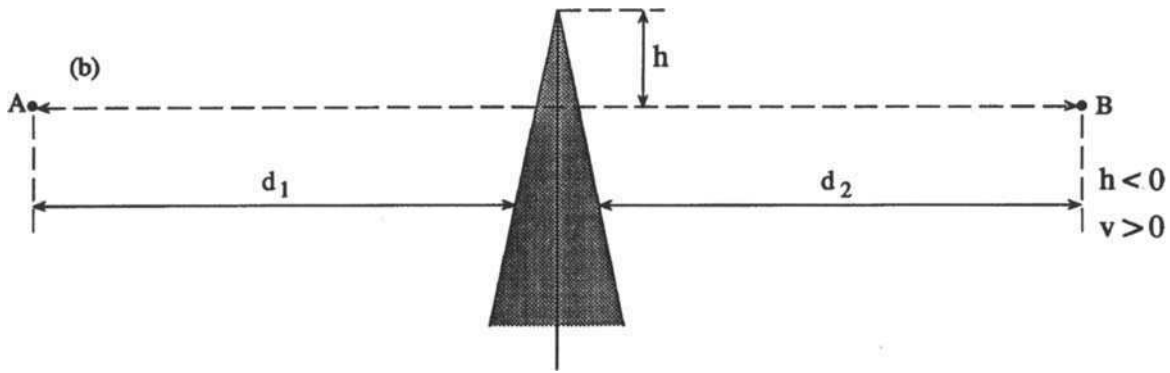

Figure 4.12 (continued).

$$E = E_0 \frac{(1+j)}{2}\left\{\left(\frac{1}{2} \pm C(v)\right) - j\left(\frac{1}{2} \pm S(v)\right)\right\} \tag{4.52}$$

By introducing the sin-integral $S(v)$ and the cosin-integral $C(v)$ in (4.51) we finally can construct such an integral:

$$C(v) - jS(v) = \int_0^v \exp\left\{-j\frac{\pi}{2}t^2\right\}dt \tag{4.53}$$

Plotting this integral in the complex plane with $C(v)$ as the abscissa and $S(v)$ as the ordinate results in the curve shown in Figure 4.13 which is known as Cornu's Spiral [1–3]. Positive values of v appear in the first quadrant and negative values in the third quadrant. Let us briefly describe the main properties of this spiral.

Equation (4.52) shows that v equals the length of the arc along the Cornu's spiral, measured from the origin at $v = 0$ (at the top of the knife edge P in Figure 4.8, determined as the optical cutoff point), with the curve turning around the point $\left(\frac{1}{2}, \frac{1}{2}\right)$ or $\left(-\frac{1}{2}, -\frac{1}{2}\right)$ an infinite number of times. If one draws a vector from the origin to any point on the curve, this vector will represent the magnitude A and phase Φ of (4.53), that is, $A = \sqrt{S^2 + C^2}$, $\Phi = \tan^{-1}\frac{S}{C}$. Moreover, the measures $\left(\frac{1}{2} \pm S(v)\right)$ and $\left(\frac{1}{2} \pm C(v)\right)$ represent the real and imaginary parts of a vector drawn from the point $\left(\frac{1}{2}, \frac{1}{2}\right)$ or $\left(-\frac{1}{2}, -\frac{1}{2}\right)$ to a point on the spiral. Therefore the magnitude of total field $|E|$ for any considered value $v = v_0$ is proportional to the length of the vector joining point $\left(\frac{1}{2}, \frac{1}{2}\right)$ or $\left(-\frac{1}{2}, -\frac{1}{2}\right)$ to the point on the spiral corresponding to v_0. Thus Cornu's spiral gives a visual indication of the amplitude and phase variations of total diffracted field E versus the Fresnel parameter v.

Diffraction losses calculated for the case when in (4.52) both summands are written with the "–" sign before the Fresnel-integral functions (the case which corresponds to Figure 4.11) relative to the free-space loss versus parameter v are shown in Figure 4.14. Above the line-of-sight line TR the loss oscillates about its free-space value (here relative path loss is equal to 0 dB), the amplitude

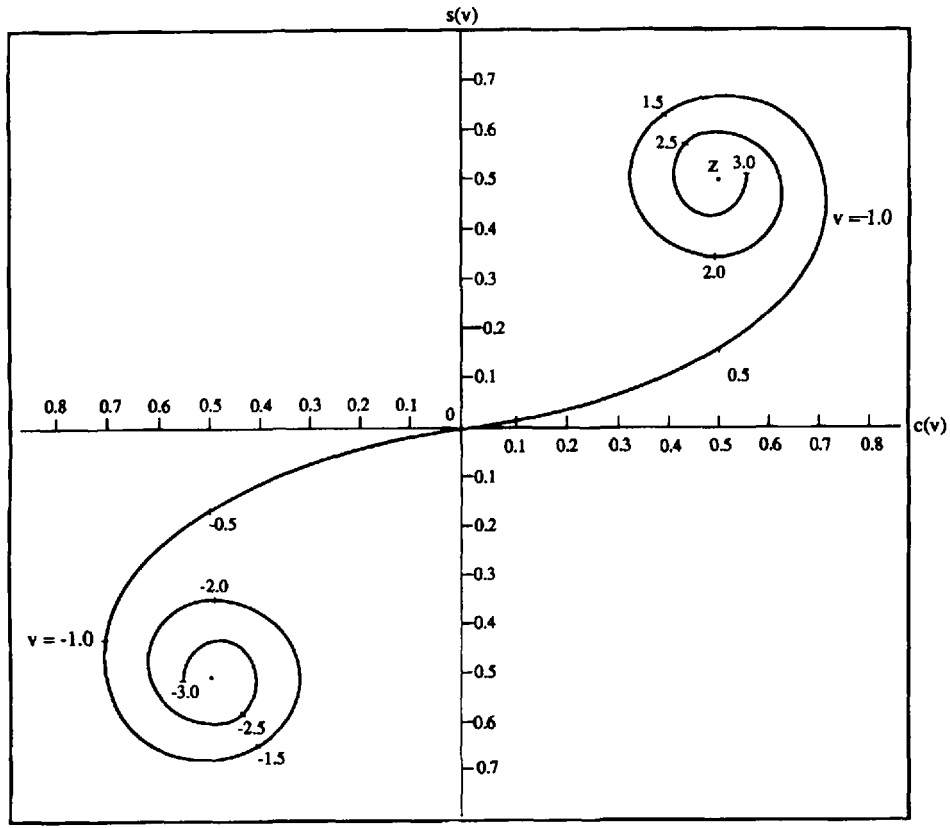

Figure 4.13 Fresnel integral versus the diffraction parameter v (Cornu's spiral).

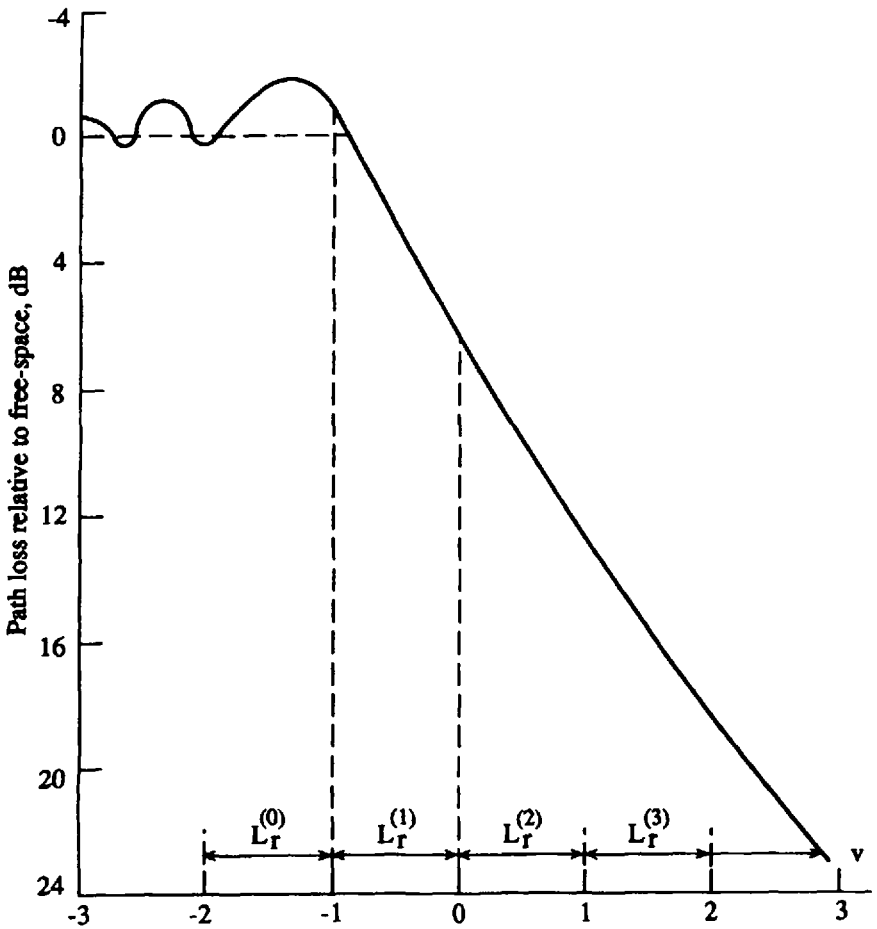

Figure 4.14 Diffraction loss over a single knife edge versus the parameter v.

of oscillations decreasing as knife-edge height h and, hence v, becomes more negative (according to (4.41) and Figure 4.11(b)). When wave is incident below the grazing angle at the optical cutoff point (when $v \approx 0$), there is a 6 dB loss (i.e., the field strength is half E_0). At the same time, as follows from Figure 4.14, if $v \approx 0.8$, which corresponds to about 56% of the first Fresnel zone being clear of obstructions, this loss is avoided. Therefore, in the practice of radio link construction, designers try to make the heights of antenna masts such that the majority of the first Fresnel zone is not obstructed. To obtain a strict solution by use of an integral equation such as (4.49) or (4.52), which connected with the complex Fresnel integral is a very complicated problem to obtain a strict analytical presentation of, diffraction losses from any obstruction

are considered. In this case, *empirical* and *semi-empirical* models that are based on, and lead from, numerous experimental data are used. As an example of a more effective empirical model to obtain the knife-edge diffraction losses, we will employ Lee's approximate model [2], from which it follows that:

1. For the case of parameter v given by formula (4.41) with the "+" sign (presented in Figure 4.14) the diffraction losses are:

$$L(v) = L_{\Gamma}^{(0)} = 0 \ (dB), \quad v \leq -1 \tag{4.54a}$$

$$L(v) = L_{\Gamma}^{(1)} = 20 \log(0.5 - 0.62 \cdot v) \ (dB), \quad -0.8 < v < 0 \tag{4.54b}$$

$$L(v) = L_{\Gamma}^{(2)} = 20 \log\{0.5 \cdot \exp(-0.95 \cdot v)\} \ (dB), \quad 0 < v < 1 \tag{4.54c}$$

$$L(v) = L_{\Gamma}^{(3)} = 20 \log[0.4 - (0.1184 - (0.38 - 0.1 \cdot v)^2)^{1/2}] \ (dB), \quad 1 < v < 2.4 \tag{4.54d}$$

$$L(v) = L_{\Gamma}^{(4)} = 20 \log\left(\frac{0.225}{v}\right) \ (dB), \quad v > 2.4 \tag{4.54e}$$

2. For the case of parameter v given by formula (4.41) with the "−" sign, one must introduce in formulas (4.54) $-v$ instead of v, which finally gives for diffraction losses:

$$L(v) = L_{\Gamma}^{(0)} = 0 \ (dB), \quad v \geq 1 \tag{4.55a}$$

$$L(v) = L_{\Gamma}^{(1)} = 20 \log(0.5 + 0.62 \cdot v) \ (dB), \quad 1 \geq v > 0 \tag{4.55b}$$

$$L(v) = L_{\Gamma}^{(2)} = 20 \log\{0.5 \cdot \exp(0.95 \cdot v)\} \ (dB), \quad 0 \geq v \geq -1 \tag{4.55c}$$

$$L(v) = L_{\Gamma}^{(3)} = 20 \log[0.4 - (0.1184 - (0.1 \cdot v + 0.38)^2)^{1/2}] \ (dB), \quad -1 \geq v > -2.4 \tag{4.55d}$$

$$L(v) = L_{\Gamma}^{(4)} = 20 \log\left(-\frac{0.225}{v}\right) \ (dB), \quad v < -2.4 \tag{4.55e}$$

All $L_{\Gamma}^{(i)}$ that correspond to (4.54) are presented in Figure 4.14. As shown in [1], the approximation (4.54e) used for $v > 2.4$ arises from the fact that as v becomes larger and positive then (4.49) limits to:

$$\left|\frac{E}{E_0}\right| \rightarrow \frac{2^{1/2}}{2\pi v} \tag{4.56}$$

This asymptotic result holds with an accuracy better than 1 dB for $v > 1$, but breaks down rapidly as $v \rightarrow 0$. Lee's approximate model can be

modified to take into account the ground reflections, as shown in Figure 4.15. Here, the four rays are depicted with their own paths; the first is after pure diffraction from the top of the knife edge, the second and third are after a single diffraction and a single reflection from the ground surface, and the fourth is after single diffraction and double reflection. Because all the rays have traveled different paths, they have different phases at the receiver R. For each ray the Fresnel-Kirchhoff parameter v is different and the total field at the receiver must be computed according to the following formula:

$$E = E_0 \sum_{k=1}^{4} L(v_k) \cdot \exp[j\Delta\Phi_k] \tag{4.57}$$

In any particular situation a ground reflection may exist only on the transmitter or the receiver side of the obstruction (the case when one of the antennas is high enough). In this situation only three rays must be taken into account.

In a real situation in hilly terrain, hills cannot be physically represented by knife edges, because their tips have dimensions which are bigger than the wavelength of the transmitted wave. This problem was investigated by Hacking [24] who showed that the loss due to rounded obstacles exceeds the knife-edge losses. In his derivations he replaced a rounded hilltop by a cylinder of radius r equal to that of the crest (Figure 4.16). Then the cylinder supports reflections on either side of the hypothetical knife edge that coincides with the top, and the Huygens wavefront above that point is therefore modified. The excess loss which can be added to the knife-edge diffraction can be given, according to [24], by

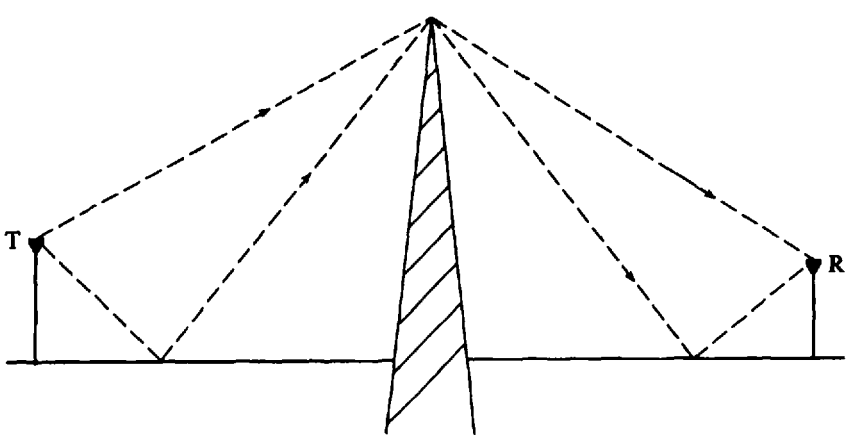

Figure 4.15 Knife-edge diffraction with ground reflection ("four-ray" model).

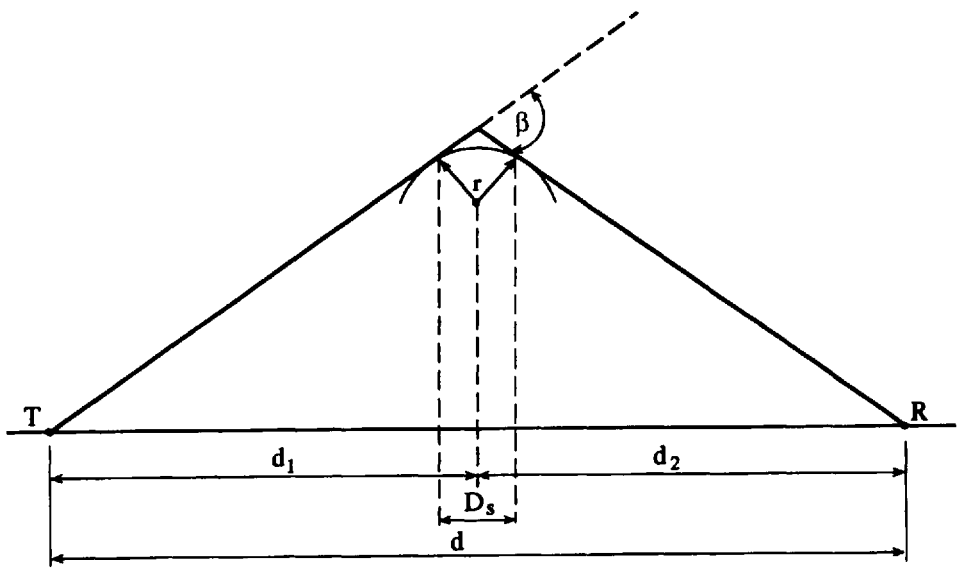

Figure 4.16 Diffraction over a rounded obstacle.

$$L_{ex} = 11.7 \cdot \left(\frac{\pi \cdot r}{\lambda}\right)^{1/2} \cdot \alpha, \quad \alpha = v \cdot \left[\frac{\lambda(d_1 + d_2)}{2 \cdot d_1 \cdot d_2}\right]^{1/2} \tag{4.58}$$

Then the radius of a hill crest may be estimated as

$$r = \frac{2 \cdot D_s \cdot d_1 \cdot d_2}{\alpha \cdot (d_1^2 + d_2^2)} \tag{4.59}$$

All parameters presented in formulas (4.58) to (4.59) are shown in Figure 4.16.

An alternative solution is available through a dimensionless parameter defined as [25]:

$$\rho = \left(\frac{\lambda}{\pi}\right)^{1/6} r^{1/3} \left(\frac{d_1 + d_2}{d_1 \cdot d_2}\right)^{1/2} \tag{4.60}$$

In [1] the special function $A(v, \rho)$, expressed in decibels, was introduced to describe the diffraction loss from a rounded obstruction. Its relation with the ideal knife-edge loss $A(v, 0)$ is as follows:

$$A(v, \rho) = A(v, 0) + A(0, \rho) + U(v\rho) \tag{4.61}$$

Here, $U(v, \rho)$ is the correction factor given at the top of Figure 4.17, and $A(0, \rho)$ is shown at the bottom of Figure 4.17. The losses of an ideal knife edge $A(v, 0)$ are given in Figure 4.14. In [26], there are approximations for $A(0, \rho)$ and $U(v, \rho)$, which were derived as follows:

$$A(0, \rho) = 6.0 + 7.19 \cdot \rho - 2.02 \cdot \rho^2 + 3.63 \cdot \rho^3 - 0.75 \cdot \rho^4, \quad \rho < 1.4, \tag{4.62a}$$

$$U(v \cdot \rho) = (43.6 + 23.5 \cdot v \cdot \rho) \cdot \log(1 + v \cdot \rho) - 6.0 - 6.7 \cdot v \cdot \rho, \quad v \cdot \rho < 2, \tag{4.62b}$$

$$U(v \cdot \rho) = 22 \cdot v \cdot \rho - 20 \log(v \cdot \rho) - 14.13, \quad v \cdot \rho < 2, \tag{4.62c}$$

As follows from some measurements [24] for UHF-band radiowave propagation, both methods, described in [25] and [26], are valid for both types of field polarization.

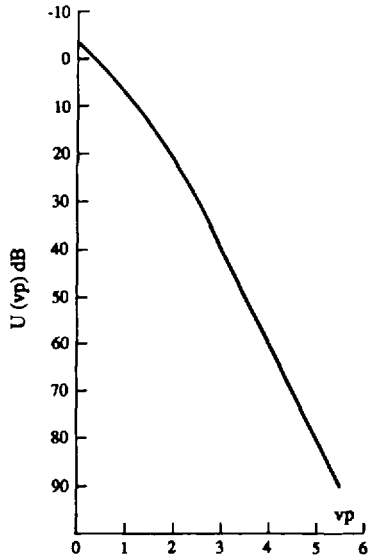

(a)

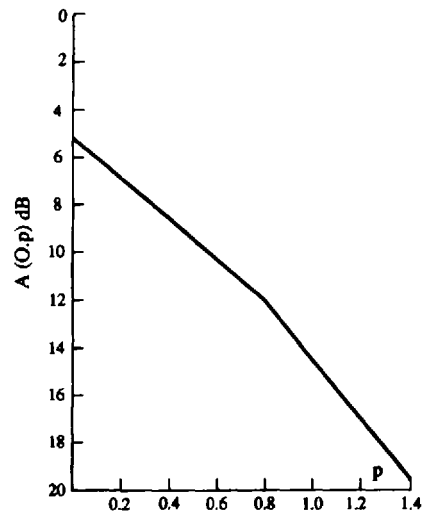

(b)

Figure 4.17 (a) the correction factor $U(\nu\rho)$; (b) the rounded-obstacle loss $A(0, \rho)$.

4.2.2 Propagation Over Multiple Obstructions Placed on Rough Terrain

The extension of the single knife-edge diffraction theory to two or more obstructions (see Figure 4.18) is not an easy matter. The problem is complicated both mathematically and physically, but it can be reduced to multiple Fresnel's

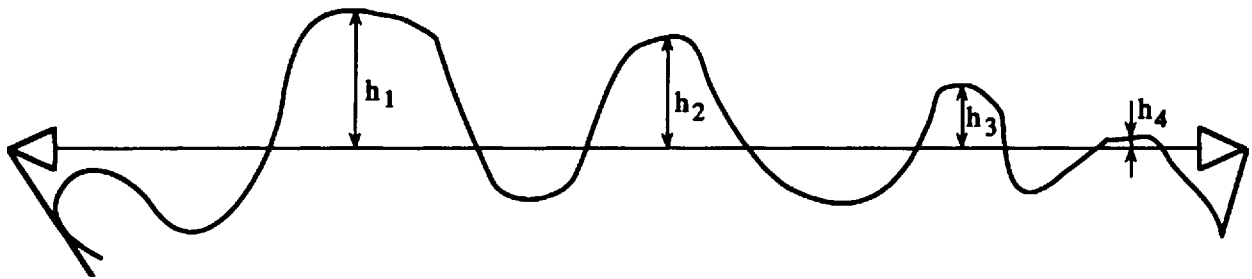

Figure 4.18 The hilly terrain schematical presentation.

form integrals over a plane above each obstruction that is modeled by a single knife edge.

Deterministic Models

Expressions for an n-times diffracted field were obtained in [27–30] by use of strict analytical approaches. Below we briefly describe the main steps and results of these analytical investigations.

Vogler's multiple knife-edge diffraction. To compute the diffraction effects by arbitrary obstacles, such as hills, they were replaced by several knife edges or wedges [28, 29]. This knife-edge approximation was derived by replacing each obstruction either by an absorbing screen, in which case the absorbing-screen diffraction coefficient was used to compute the diffraction over obstructions [28, 29]. The effect of knife-edge diffraction on wave propagation over the hilly terrain was examined in [28, 29] by introducing a diffraction attenuation function. This function was presented in a multiple integral form which was then transformed into a series representation.

Figure 4.19 presents the geometry associated with the multiple knife-edge diffraction problem. Here each obstructive is replaced by a perfectly absorbing knife edge. The geometrical quantities needed to calculate the parameters used in the solution for N knife edges are:

the $N + 1$ separation distances between obstructions: $r_1, \ldots, r_{N+1}$;
the heights of the knife edges above the ground surface: $h_1, \ldots, h_N$; (4.63)
the heights of the transmitter and receiver: $h_T \equiv h_{N+1}$ and $h_R \equiv h_0$.

As for the diffraction angles, $\theta_1, \ldots, \theta_N$, they can be successfully obtained from the knife-edge heights and separation distances (see Figure 4.19). The above geometrical quantities together with radio frequency $f = c/\lambda$, introduced through the wave number $k = 2\pi/\lambda$, are used to define two sets of parameters, α and β:

$$\alpha_m = \left[\frac{r_m \cdot r_{m+2}}{(r_m + r_{m+1})(r_{m+1} + r_{m+2})}\right]^{1/2}, \quad m = 1, 2, \ldots, N-1 \tag{4.64a}$$

$$\beta_m = \theta_m \cdot \left[\frac{j \cdot k \cdot r_m \cdot r_{m+1}}{2 \cdot (r_m + r_{m+1})}\right]^{1/2}, \quad m = 1, 2, \ldots, N \tag{4.64b}$$

Using these relations, one can present the total field strength attenuation relative to free space, A, over a path of total distance, r_{tot}, and consisting of N knife edges

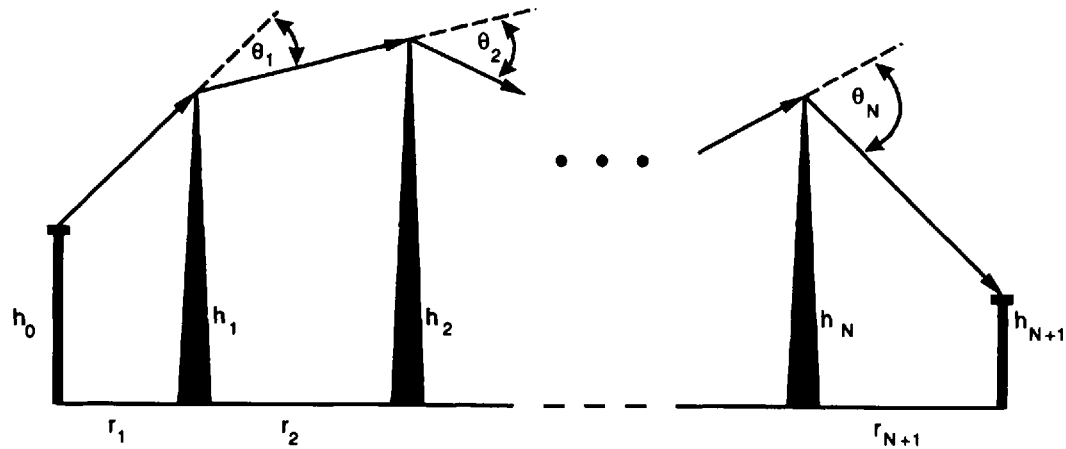

Figure 4.19 Geometry of multiple knife-edge diffraction.

$$A = \left(\frac{1}{2}\right)^N C_N \exp(\sigma_N)\left(\frac{2}{\pi^{1/2}}\right)^N \int_{\beta_1}^{\infty} \cdots \int_{\beta_N}^{\infty} \exp(2 \cdot F) \times \{\exp[-(x_1^2 + x_2^2 + \ldots + x_N^2)]\} dx_1 \cdot dx_2 \ldots dx_N \tag{4.65}$$

where

$$F = 0 \text{ for } N = 1 \tag{4.66a}$$

$$F = \sum_{m=1}^{N-1} \alpha_m (x_m - \beta_m)(x_{m+1} - \beta_{m+1}) \text{ for } N \geq 2 \tag{4.66b}$$

$$\sigma_N = \beta_1^2 + \beta_2^2 + \ldots + \beta_N^2 \tag{4.67}$$

$$C_N = 1 \text{ for } N = 1 \tag{4.68a}$$

$$C_N = \left[\frac{r_1 \cdot r_2 \ldots r_N \cdot r_{tot}}{(r_1 + r_2)(r_2 + r_3) \ldots (r_N + r_{N+1})}\right]^{1/2} \text{ for } N \geq 2 \tag{4.68b}$$

$$r_{tot} = r_1 + r_2 + r_3 + \ldots + r_{N+1} \tag{4.69}$$

As an example, we obtain the attenuation for diffraction from two knife edges:

$$A(N = 2) = \frac{1}{2\pi}\left[\frac{\pi}{2} + \tan^{-1}\left(\frac{\alpha_1}{C_2}\right)\right], (\theta_1, \theta_2 = 0) \tag{4.70}$$

where α_1 and C_2 can be obtained from (4.64) and (4.68b), respectively, for $N = 1, 2$.

The attenuation over a triple knife-edge path for all $\theta_m = 0$ (small grazing angles) can be presented as:

$$A(N = 3) = \frac{1}{4\pi}\left[\frac{\pi}{2} + \tan^{-1}\left(\frac{\alpha_1}{C_3}\right) + \tan^{-1}\left(\frac{\alpha_2}{C_3}\right) + \tan^{-1}\left(\frac{\alpha_1 \alpha_2}{C_3}\right)\right] \tag{4.71}$$

All the above parameters can be obtained from (4.64) and (4.68b) for $N = 1, 2, 3$. Obtaining the strict analytical solution of (4.65) is a very complicated computational problem. In [28, 29] regression analysis was used to obtain

some series of integrals of error functions $I(n, \beta)$ to present the N-time diffracted field:

$$I(n, \beta) = \frac{1}{n!} \cdot \left(\frac{1}{\pi^{1/2}}\right) \cdot \int_{\beta}^{\infty} (x - \beta)^n e^{-x^2} dx \tag{4.72}$$

In terms of the function $I(n, \beta)$, for which a number of computational algorithms are available, the attenuation function after N-time diffraction from N edges becomes

$$A = \left(\frac{1}{2}\right)^N C_N \exp(\sigma_N) \left(\frac{2}{\pi^{1/2}}\right) \sum_{m=1}^{\infty} I_m \tag{4.73}$$

where I_m can be presented in the following form:

$$I_m = 2^m \sum \alpha_1^{m_0 - m_1} \cdot I(m_0 - m_1, \beta_1) \cdot C(2, m_1, m_0) \tag{4.74}$$

by introducing the recursive relationship

$$C(N - L, j, k) = \sum_{i=0}^{j} \left\{\frac{(k - i)!}{(j - i)!}\right\} \cdot \alpha_{N-L}^{j-i} \cdot I(k - i, \beta_{N-L}) \cdot C(N - L + 1, i, j) \tag{4.75}$$

and using the notations

$$\begin{aligned} &i = m_{N-L}, \; j = m_{N-L-1}, \; k = m_{N-L-2} \\ &2 \le L \le N - 2, \; N \ge 4 \\ &\alpha_N \equiv 1, \; m_0 \equiv m, \; m_k \equiv 0, \; k \ge N - 1 \end{aligned} \tag{4.76}$$

Equations (4.73), (4.75), and (4.76) can be implemented in a computer program which evaluates the attenuation A for propagation paths consisting of N obstructions, as N knife edges, where $0 < N < 50$-100. In other words, this method cannot represent a full multidiffraction solution from knife-edge tops in any convenient analytical form. Only some complicated numerical computation of (4.72) with (4.74) and (4.75) might give such a result.

Slope-diffraction approach. The heuristic extension of the UTD has been used to compute the diffraction by the wedges forming the profile of an

obstruction [30], taking into account the profile that results from the intersection of the obstruction with the vertical plane. The theoretical approach proposed by Andersen [30] includes the analytical application of slope diffraction, which is a first-order effect in the transition zone. This approach is based on a strict ray-tracing tool that allows an approximate yet accurate and fast determination of the field diffracted around a multiplicity of obstacles, such as hills and columns. The key point of the heuristic theory presented in [30] is to include slope diffraction, which is usually neglected as a higher order term in UTD using an asymptotic expansion. However, in transition-zone diffraction this term is of the same order of magnitude as the ordinary amplitude diffraction terms. Because the distances between obstacles are not large, slope diffraction becomes important for the diffraction process in the transition zones between them. Schematically, a scenario of three obstructions as screens distinguishing between ordinary amplitude diffraction and slope diffraction, is shown in Figure 4.20. Two different ray tracings must be performed for such a scenario: the upper one with screen "1" absent leading to a slope wave after the third screen and a lower one via screen "1" with slope diffraction after the second screen, as shown in Figure 4.20. The slope diffraction describes the field attenuation in the transition zones between obstacles. The basic UTD theory gives the following equation for the total diffracted field for a simple absorbing half-screen:

$$E_d = \left[E_i(0) \cdot D + \frac{\partial E_i(0)}{\partial n} D_s \right] \cdot A(s) \cdot \exp\{-jks\} \tag{4.77}$$

or

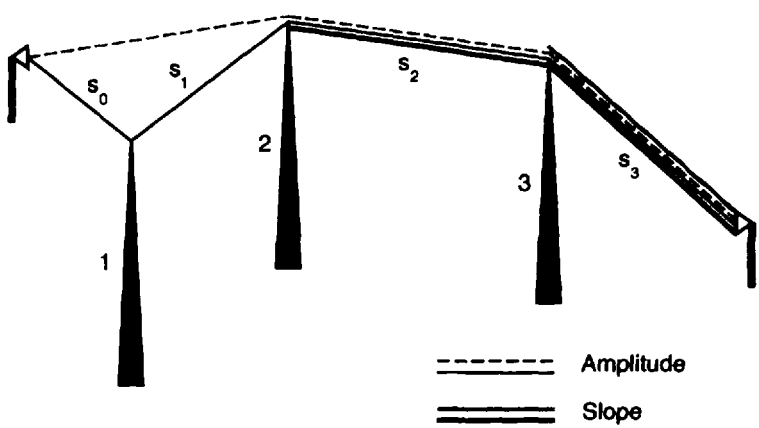

Figure 4.20 Slope-diffraction over three-obstacle radio path.

$$E_d = [E_{da} + E_{ds}] \cdot A(s) \cdot \exp\{-jks\} \tag{4.78}$$

where

$$D(\alpha) = \frac{\exp(-j\pi/4)}{2\sqrt{2\pi k} \cdot \sin(\alpha/2)} \cdot F\left(2kL \sin^2\frac{\alpha}{2}\right) \tag{4.79}$$

A distance factor L will be determined later; α is the angle above the shadow boundary (see Figure 4.20) and $A(s)$ is the so-called spreading factor

$$A(s) = \left[\frac{s_0}{s(s + s_0)}\right]^{1/2} \tag{4.80}$$

where s_0 is the distance to the first obstacle as shown in Figure 4.20. The slope diffraction coefficient D_s is related to the diffraction coefficient D of (4.79) as

$$D_s = \frac{1}{j \cdot k}\frac{\partial D}{\partial \alpha} \tag{4.81}$$

The transition function $F(X)$ is, as usual, given by the Fresnel integral:

$$F(X) = \sqrt{X}e^{jX}\int_{\sqrt{X}}^{\infty} e^{-ju^2}\,du \tag{4.82}$$

Because we need derivatives of the function F in the following expressions, we will use the relation (given here without proof)

$$F'(X) = j \cdot [F(X) - 1] + \frac{F(X)}{2 \cdot X} \tag{4.83}$$

The slope diffraction coefficient may now be determined from (4.81) as

$$D_s = \frac{e^{-j(\pi/4)}}{\sqrt{2\pi k}}\, L \cdot \cos\left(\frac{\alpha}{2}\right) \cdot [1 - F(X)] \tag{4.84}$$

As examples, let us examine the diffraction over two and three obstructions, modeled as absorbing screens.

Diffraction over two screens. For simplicity, assume the antennas and the obstacle edges have the same height. The slope of the incident field is zero. The incident wave on the *second edge* consists now of two components: an ordinary amplitude wave and a slope wave, where the amplitude wave is the combined incident and amplitude diffracted waves. With this assumption the total incident field on the second edge is:

$$E_2 = E_i + E_1 \cdot D_1 \cdot A_1(s_1) \tag{4.85}$$

where the suffix "1" refers to the *first edge*; E_i is the incident field at edge "2" without the first screen present if line-of-sight; E_1 is the incident wave from the source evaluated at edge "1;" D_1 is given by (4.79) for edge "1." The parameter L must be found from continuity of field across the shadow line. Along the shadow line the coefficient of amplitude diffraction D simplifies to

$$D \approx -0.5\sqrt{L} \cdot sign(\alpha) \tag{4.86}$$

To have continuity, the discontinuity of the diffracted field should cancel the discontinuity of the incident field (i.e., the diffracted field E_d should be one-half of the incident field for all values of distance s from the edge),

$$E_d = -\frac{e^{-jks_0}}{s_0}\frac{\sqrt{L}}{2}\sqrt{\frac{s_0}{s \cdot (s + s_0)}}e^{-jks} = -0.5\frac{e^{-jk(s+s_0)}}{(s + s_0)} \tag{4.87}$$

from which the value L may be found as

$$L = \frac{s_0 \cdot s}{(s + s_0)} \tag{4.88}$$

Finally, the total incident field on the edge "2" can be written as

$$E_2 = \frac{0.5}{s_0}\sqrt{\frac{s_0 \cdot s_1}{(s_1 + s_0)}}\sqrt{\frac{s_0}{s_1 \cdot (s_1 + s_0)}} = -\frac{0.5}{(s_1 + s_0)} \tag{4.89}$$

We obtained the trivial result, that the *first edge* halves the incident field. In the last formulas, the phase terms have been suppressed since they are trivial. The phase progresses uniformly with distance. To find the slope wave it is necessary to find the slope of the incident field as a function of distance from the first edge:

$$\frac{\partial E_2}{\partial n} = E_1 \frac{1}{s} \frac{\partial D_1}{\partial \alpha} A_1(s) = E_1 \frac{1}{s} j \cdot k \cdot D_s(L_s) \cdot A_1(s) \tag{4.90}$$
$$= \frac{\sqrt{k} \cdot e^{j(\pi/4)}}{\sqrt{2\pi} \cdot (s + s_0)^{3/2}} \sqrt{\frac{s_0}{s}}$$

The value at the second edge is found by setting $s = s_1$. For the value of L_s, the L for the slope wave is found by forcing L_s in the slope wave after the second edge to have a value that exactly balances the discontinuity of the slope of the E_2 wave:

$$\frac{1}{2} \frac{\partial E_2(s_1 + s_2)}{\partial n} = -0.5 \frac{\partial E_2(s_1)}{\partial n} \frac{\partial D_s}{\partial \alpha} A_2(s_2) \frac{e^{j(\pi/4)}}{\sqrt{2\pi}} \sqrt{\frac{k \cdot s_0}{(s_1 + s_2)}} \frac{1}{(s_0 + s_1 + s_2)^{3/2}}$$
$$= \frac{e^{j(\pi/4)}}{\sqrt{2\pi} \cdot (s + s_0)^{3/2}} \sqrt{\frac{k \cdot s_0}{s_1}} \frac{(-1)}{2s_2} L_s^{3/2} \sqrt{\frac{(s_0 + s_1)}{s_2(s_0 + s_1 + s_2)}} \tag{4.91}$$

which leads to

$$L_s = \left[\frac{(s_0 + s_1)}{(s_0 + s_1 + s_2)}\right]^{2/3} \left[\frac{s_1}{(s_1 + s_2)}\right]^{1/3} \cdot s_2 \tag{4.92}$$

It is now a simple matter to find the field after the second edge:

$$E_3 = E_i + E_2 \cdot D_2 \cdot A_2 + \frac{\partial E_2}{\partial n} D_{s2} \cdot A_2$$
$$= \frac{0.25}{(s_0 + s_1 + s_2)} + \frac{e^{j(\pi/4)}}{\sqrt{2\pi} \cdot (s_1 + s_0)^{3/2}} \sqrt{\frac{k \cdot s_0}{s_1}} \frac{e^{-j(\pi/4)} \cdot L_s}{\sqrt{2\pi k}} A_2(s_2) \tag{4.93}$$

where

$$A_2(s_2) = \left[\frac{(s_0 + s_1)}{s_2 \cdot (s_0 + s_1 + s_2)}\right]^{1/2} \tag{4.94}$$

By normalizing the field with the free-space field the result can be expressed as a combined diffraction coefficient D_c:

$$D_c = 0.25 + \frac{(s_0 + s_1 + s_2)}{(s_0 + s_1)^{3/2}} \sqrt{\frac{s_0}{s_1}} \frac{L_s}{2\pi} A_2(s_2) \tag{4.95}$$

This expression in all its simplicity is remarkably accurate. For the case where all the distances are equal, $s_0 = s_1 = s_2$, the result is 0.3335, while the exact result that follows from the path integrals approach [31], is 1/3.

Diffraction over several screens. The previous result can be generalized to the case of N screens by applying the following procedure. The diffracted field after each screen has an ordinary amplitude and slope component, each determined by its own length parameter L and L_s, which are found by enforcing amplitude and slope continuity over the shadow boundary. This process becomes complicated analytically, but it is easily treated by use of a numerical recursive algorithm. It may best be understood by following an example for *three screens,* as presented by Figure 4.20. The incident wave on edge "2" has contributions from the source and from edge "1." Thus, there are two shadow lines and, after edge "2," *two ordinary amplitude waves* and *one slope wave.* After edge "3," there are then *two amplitude waves* and *two slope waves* for this particular configuration of edges. At each point the values L must be found along the shadow lines all the way back to the original source. Then, in the case of three screens, the value of the total field at the receiver after triple diffractions can be found by use of the basic UTD formula:

$$E_4(s) = E_{i4} + \left[E_3(0) \cdot D_3(s) + \frac{\partial E_3(0)}{\partial n} D_{s3}(s)\right] \cdot A_3(s) \tag{4.96}$$

for each set of waves coming from edge "2," where E_{i4} is the incident wave at the receiver point with screen "3" absent. To find this value, we need the incident field E_{i3} when screen "2" is absent, and to find the last value, we finally need the incident field E_{i2} when screen "1" is absent, which is presented in formula (4.85). Thus we follow all the way back to the original source. The field at the given point after N screens needs information from all previous screens for that point. Transition zone diffraction has "memory" in contrast to the usual geometrical theory of diffraction (GTD) multiplication of independent factors. In Figure 4.21 the diffraction over $N = 10$ screens of equal heights and equal spacing is presented by the points according to the UTD solution using slope diffraction presentation and by the continuous curve according to the exact solution [31–33]. The slope diffraction gives an error of about 1 dB after ten screens.

As shown in [30] both analytically and numerically the agreement between strict multidiffraction solution [31–33] and approximate slope diffraction solu-

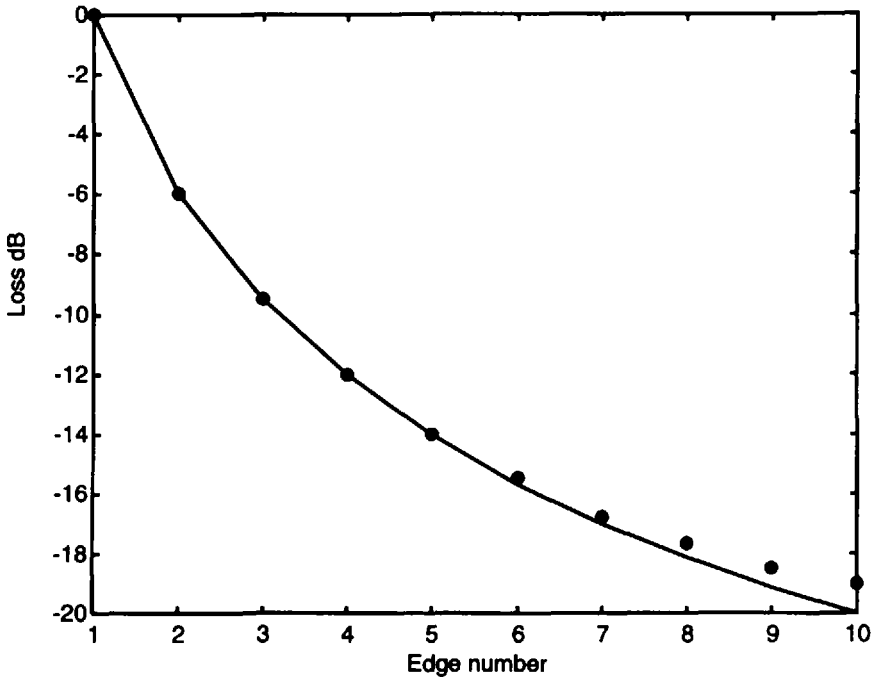

Figure 4.21 Diffraction over ten-obstacle radio path.

tion [30] is very good, except for short distances between two neighboring screens.

Approximate Models of Multiple Knife-Edge Diffraction

Together with the strict analytical models, there are some approximate models which were constructed to model the problem of multiple knife-edge diffraction. And, as mentioned above, because of the length and computation problems of the exact solutions, the use of approximate models has become widespread. Below we will briefly describe some of the more effective ones.

Bullington's equivalent knife edge [34]. In this approach, the real hilly terrain is replaced by a single "equivalent" knife edge at the point of intersection of the horizonal ray from each of the antennas, transmitting and receiving, that passes through the peaks A and B, respectively, as shown in Figure 4.22. The diffraction loss is determined by using formulas (4.54) or (4.55) presented in Section 4.2.1, and describing the diffraction losses $L = f(d_1, d_2, h)$ for two cases of diffraction parameter v. Bullington's method has a primary limitation related to the fact that important obstacles along the radio path can be ignored which can cause large errors. In fact, as shown in Figure 4.23, the obstruction

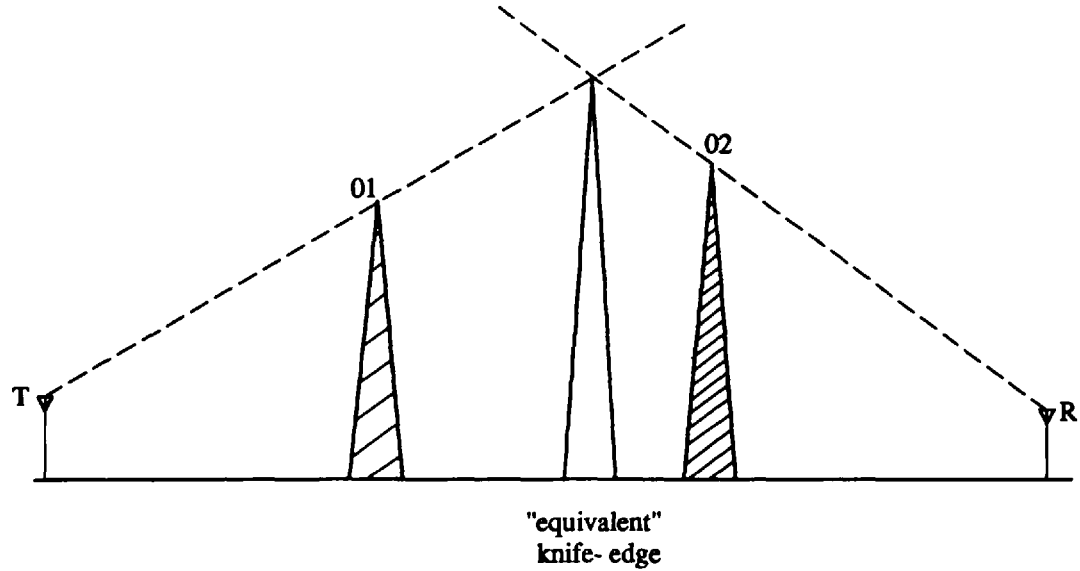

Figure 4.22 The Bullington "equivalent" knife-edge construction.

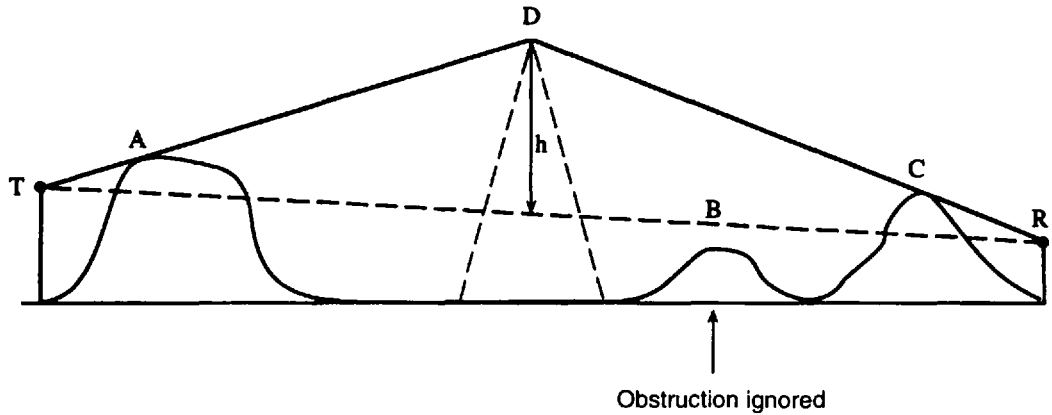

Figure 4.23 Accuracy of the Bullington predicting model.

B is completely ignored, as the intersecting line from T to R is above the peak of the obstruction B.

The Epstein-Peterson method [35]. In their approximate model, the overall loss was presented as a superposition of attenuation due to each knife edge. The two losses were calculated in decibels. A two-obstruction path is presented in Figure 4.24(a) and the method used is as follows. The loss due to knife edge A is first calculated by considering the height of the obstruction h_A above the line TB joining point T with the top of second obstruction B. Then the diffraction loss due to the second knife edge B is computed by considering the height h_B above line AR, as shown in Figure 4.24(a). The total diffraction loss is the sum of these two losses.

Comparison of these results with those obtained in [35] have shown that the Epstein-Peterson method produces large errors when obstructions are close to each other, as shown in Figure 4.24(b). This solution was corrected in [35] for the case when the diffraction parameter v is much greater than unity and for a three-obstacle path (see Figure 4.25). This correction is added to the loss obtained by the Epstein-Peterson technique and is expressed through a spacing parameter γ_i as

$$L_{ex} = 20 \log(\cos ec\gamma_i) \tag{4.97}$$

where, for edges 01 and 02,

$$\cos ec\gamma_i = \frac{(d_1 + d_2)(d_2 + d_3)}{d_2(d_1 + d_2 + d_3)} \tag{4.98}$$

The Japanese method. In this technique, proposed by Japanese Atlas [36], the diffraction loss for obstruction A is computed by the same technique as in the Epstein-Peterson method, that is, the path TAB is considered according to the illustration in Figure 4.25, and the height of the obstruction h_A is taken into account to calculate the diffraction loss by use of the above formulas (4.54) or (4.55) (depending on the sign before the square root in (4.41)). The loss due to obstruction B is calculated by extending the ray AB to the left until it intersects the transmitter T axis at point T'. The diffraction loss due to this obstacle is now calculated by finding the height of the obstruction h_B above line $T'R$. Once again, the sum of these two losses gives the total loss. For the three-path case illustrated in Figure 4.26, the total path loss is computed as the sum of the losses over paths *T-01-02, T'-02-03* and *T''-03-R*. Then the correction (4.97), according to [35], must be added, as an excess loss. Thus, the use of this technique is exactly equivalent to the Epstein-Peterson method.

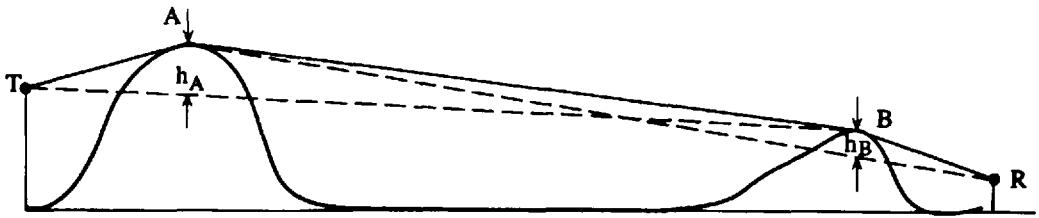

(a)

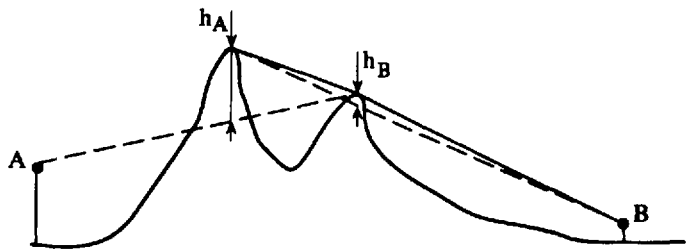

(b)

Figure 4.24 (a) The Epstein-Peterson diffraction over two knife-edge construction. (b) Accuracy of the Epstein-Peterson predicting model.

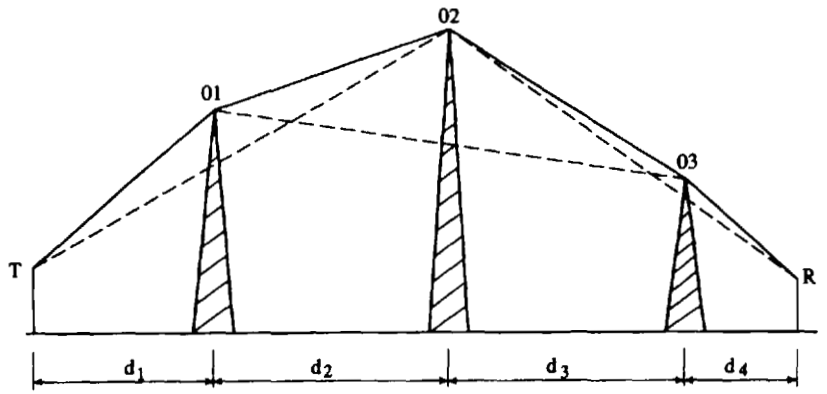

Figure 4.25 The Epstein-Peterson diffraction over three knife-edge construction.

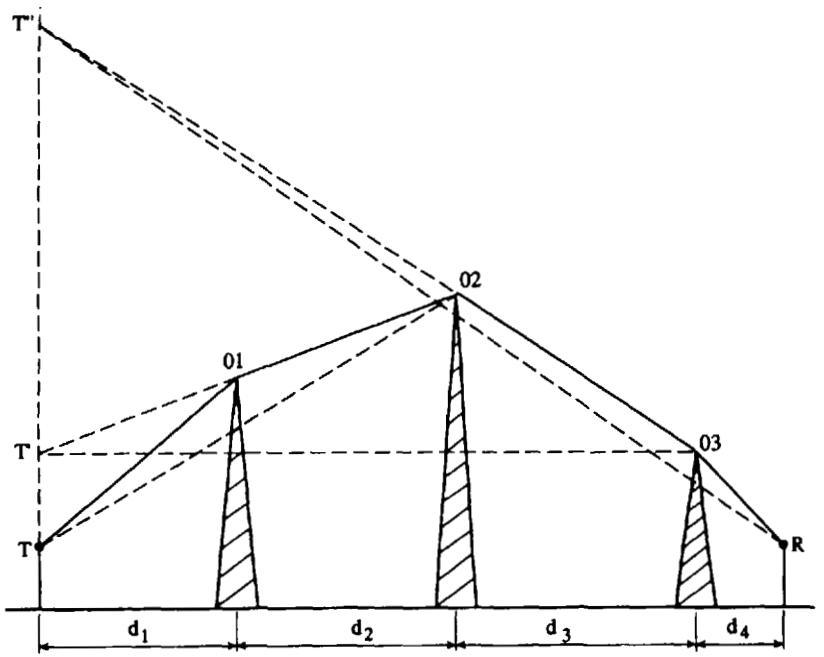

Figure 4.26 The "Japanese Atlas" diffraction over three knife-edge construction.

The Deygout method [37]. This method is closer to the rigorous approach than those mentioned above. As illustrated in Figure 4.27 for the three-paths case, the diffraction parameter v is calculated according to (4.41) for each knife edge alone, as if all other edges were absent, for paths *T-01-R*, *T-02-R*, and *T-03-R*. The edge having the biggest value of the v-parameter is termed the

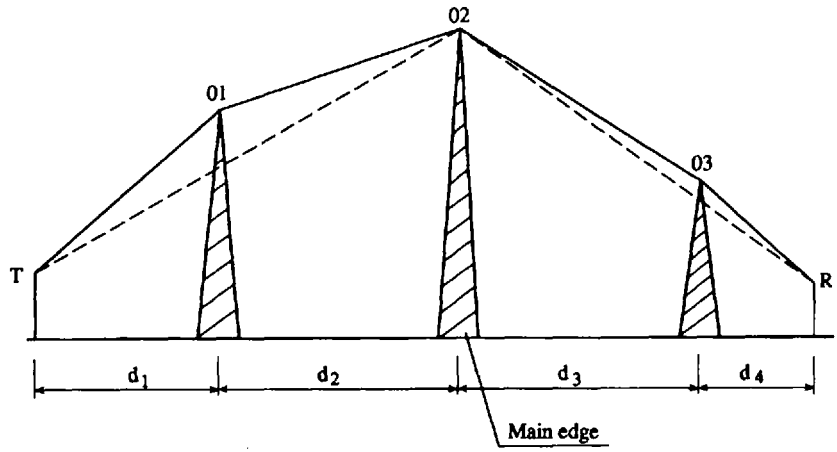

Figure 4.27 The Deygout diffraction over three knife-edge construction.

main edge and its loss is calculated in the standard manner by use of (4.54) or (4.55). If, as shown in Figure 4.27, edge 02 is the main edge, then the diffraction losses for edges 01 and 03 are found with respect to a line joining the main edge to points T and R and then added to the main edge loss to obtain a total diffraction loss. This result can be extended for the case of several obstacles, taking into account the contribution of each individual loss in the total loss. This method produces good results only when the obstructions are not too close to each other. Therefore, according to [37], for the case of more than two obstacles ($N > 2$) the additional corrections must be taken into account using the spacing parameter γ_i described above by (4.98). In fact, when, for example, $v_1 \geq v_2$ and v_1, v_2, $(v_2 \operatorname{cosec}\gamma_i - v_1 \cot\gamma_i) > 1$, the required correction is

$$L' = 20 \log\left(\operatorname{cosec}^2\gamma_i - \frac{v_2}{v_1}\operatorname{cosec}\gamma_i \cdot \cot\gamma_i\right) \tag{4.99}$$

where angles γ_i are described by (4.98) according to geometry shown in Figure 4.27.

Comparison between all methods presented above shows that Bullington's technique is simpler than others, but gives a greater error than the strict solutions obtained by Vogler [28, 29]. The Epstein-Peterson model as well as the Japanese scheme are better but can also provide diffraction loss predictions that are too low. At the same time, the Deygout technique shows good agreement with the rigorous diffraction theory [28–31] for two edges. However, it has an increasing error with increase of the number of obstructions. This is

why calculations by use of this method are often terminated after consideration of three edges.

Empirical and Semi-Empirical Models

As was mentioned in Chapter 1, the initial step of each wireless communication system planning is to predict the loss characteristics. To do this for over-the-terrain communication channels, one must first determine the correlation between parameters of terrain and those of the radio systems, which then allow designers of such systems to find the influence of all factors, those dependent on environment and those intrinsic to the communication system, on signal strength variation, and on the effects of shadowing and scattering from arbitrary land obstructions that finally decrease signal-to-noise ratio inside the propagation channel. In other words, the accuracy of prediction models plays an important role in the provision of efficient and reliable coverage of areas of service for the specific purposes of each subscriber.

Existing prediction models of radio wave propagation over irregular terrain in open and rural environments are based mostly on experimentally obtained data and, therefore, are usually called empirical and semi-empirical models in the literature [1–4]. These models differ in their applicability for different over-the-terrain propagation channels and for different ambient conditions. As mentioned in Chapter 1, until now there is no general model that predicts all specific propagation phenomena in such wireless channels and can be ideally adjusted to suit all environments. Each model describes some specific situation in the over-the-terrain scene. Most empirical models predict the average loss L_{50}, that is, the path loss not exceeded at 50% of locations and for 50% of the time, and then by use of signal statistics, allow estimation of deviation of the signal so that the percentage of the investigated area with adequate signal-strength variations can be determined.

We will now consider models that are based on experimental data obtained in numerous measurements of loss characteristics in conditions of open and rural environments for rough and hilly terrain. Below we present a brief survey of some of the better-known empirical models adapted to the description of wave propagation over rough and hilly terrain in obstructive (clutter) conditions. For more details the reader can refer to the reference section in this chapter.

The Egli model. This model is based on the flat-terrain propagation model presented in Chapter 3 which gives an inverse fourth-power law of signal decay with range r from the source. This tendency of signal-strength attenuation is also found for rough terrain and follows from a series of measurements carried out over irregular terrain at frequencies of 90 MHz–1,0 GHz in a micro-cellular environment ($r < 2$ km) [38].

It was therefore natural for Egli to use a well-known model by introducing into it some excess loss that depends upon the frequency and the terrain profile:

$$L_{50} = G_T G_R \left(\frac{h_T h_R}{r^2}\right)^2 \cdot \beta \tag{4.100}$$

We must note that here and in the following text we put notations h_T and h_R for the transmitting and receiving antenna heights, respectively. But actually these notations are relative, because in wireless communication systems each vehicle can simultaneously operate as the transmitter and the receiver. In (4.100) β is the factor which takes into account the excess loss and was presented by Egli as a function of frequency in the following form:

$$\beta = \left(\frac{40}{f}\right)^2, \quad f \text{ in MHz} \tag{4.101}$$

from which it follows that 40 MHz is the reference frequency at which the average path loss reduces to those obtained for the flat-terrain model, regardless of any undulations of the terrain. However, Egli found from numerous experimental data that parameter β described by (4.101) is an average value. He obtained the standard deviation of β as a function of terrain undulations by assuming that terrain height is log-normal distributed about its average value. If so, a family of curves can be obtained (see Figure 4.28) that shows how parameter β varies from its average value at 40 MHz, as a function of terrain undulation factor (in dB), and the radiated frequency. Egli suggested that in rural areas the standard deviation of received signal level is related to the radiated frequency by

$$\sigma = 5 \log f_0 + 2dB \tag{4.102}$$

where f_0 is the frequency in MHz.

As follows from this empirical model, one can use it to take into account the r^{-4} law of signal decay and the log-normal variations of signal strength inside one microcell.

The JRC method. This method was proposed in the United Kingdom by the Joint Radio Committee (JRC) and is based on the technique developed in [39, 40]. The main principle of this method is to use a computer-based topographic map data to reconstruct the terrain profile between two terminals, transmitter and receiver (the location of the latter is chosen), by introducing some special interpolations of obtained data. Using information about the

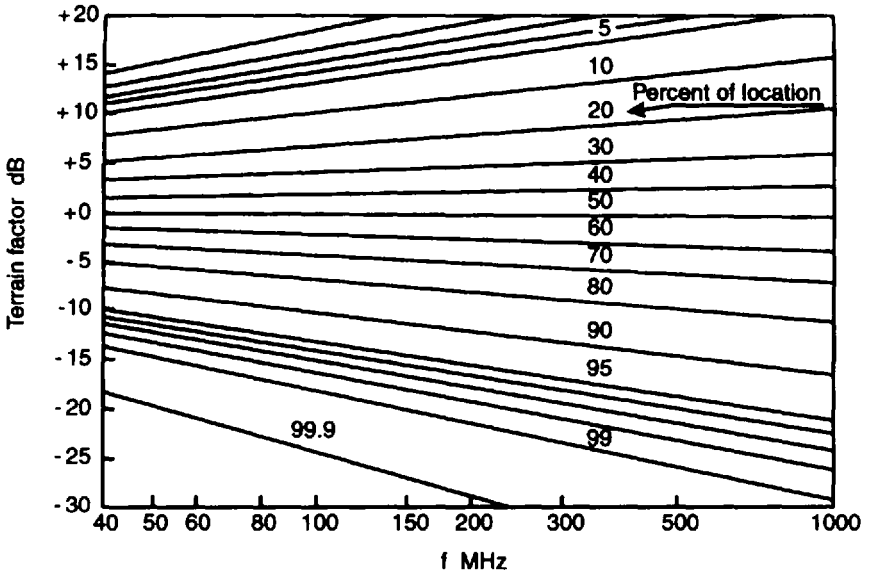

Figure 4.28 Variations of the terrain factor β versus the terrain undulation and the radiated frequency.

heights and position of each obstruction placed on the rough terrain, the program tests for the existence of line-of-sight paths and whether adequate Fresnel-zone clearance exists over searching paths. Then the bigger path loss from free-space (L_{FS}, obtained in Section 2.3) and flat-terrain (L_{FT}, obtained in Section 3.2) is declared as a real path loss:

$$L = \max(L_{FS}, L_{FT}) \tag{4.103}$$

If there are no line-of-sight conditions or if there is inadequate Fresnel-zone clearance, the program estimates the diffraction loss L_D along the radio path by using the Epstein-Peterson model for up to three knife edges (see Section 4.2.2), and computes the total path loss as

$$L = \max(L_{FS}, L_{FT}) + L_D \tag{4.104}$$

If more than three obstructions exist along the radio path, an equivalent knife-edge model is taken into account to obtain the diffraction losses by use of the Bullington technique (see Section 4.2.2).

The Blomquist-Ladell model. This method considers the same type of losses as obtained in [41, 42], but combines them in a different way to obtain

a smooth transition between points where the prediction is based on L_{FS} and those where L_{FT} is used [43]. The basic formula for path loss is:

$$L = L_{FS} + [(L'_{PT} - L_{FS})^2 + L_D^2]^{1/2} \tag{4.105}$$

Here L'_{PT} is a modified flat-terrain path loss which takes into account factors such as the effects of the troposphere and the earth's curvature, when one considers a long path between antennas. An approximate expression for $(L'_{PT} - L_{FS})$ is given by Delisle [44]. Diffraction losses can be obtained following the Epstein-Peterson technique. As follows from (4.105), for the highly obstructed radio path, for which $(L'_{PT} - L_{FS}) << L_D$, the total field can be approximated by

$$L = L_{FS} + L_D \tag{4.106}$$

Conversely, for unobstructed paths, when $L_D \rightarrow 0$, the total losses become

$$L = L'_{PT} \tag{4.107}$$

As follows from (4.105) to (4.107), the total loss will never be less than L_{FS}.

Longley-Rice models. These methods were introduced for computation of the average path loss over irregular terrain by the use of point-to-point transitions in the frequency range 40 MHz to 100 GHz over all type of terrain (see classification of terrain in Chapter 1). The technique [45] is based on experimental data obtained for a wide range between terminals of 1 to 2,000 km, for wide variations of antenna heights of 0.5m to 3000m, and for both types of field polarization. They also account for the ground curvature, the subsoil media properties, and the climate. Some specific parameters that are important for path loss prediction were also introduced, such as the horizon distances of both antennas, d_{LT} and d_{LR}, the horizon elevation angles, θ_{eT} and θ_{eR}, the angular distance for a horizon path θ_e, and the terrain irregularity parameter Δh. The definition of some parameters are illustrated in Figure 4.29.

If a terrain topographic map is available, then for any particular path these parameters can be determined, and the prediction technique operates in a *point-to-point model.* However, if the terrain profile is not available, this technique gives other methods to estimate the above parameters. In fact, to estimate the roughness indicator, another parameter $\Delta h(d)$, instead of parameter Δh, is evaluated at fixed distances along the path:

$$\Delta h(d) = \Delta h[1 - 0.8 \cdot \exp(-0.002 \cdot d)] \tag{4.108}$$

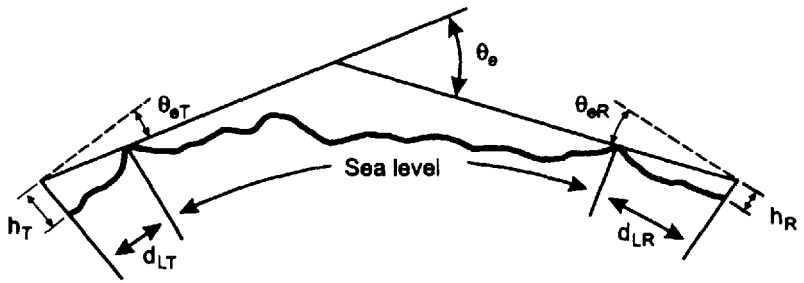

Figure 4.29 Geometry of a trans-horizon radio path.

Estimations of Δh for different types of terrain are presented in Table 4.1.

We will not present here the algorithm to estimate the other parameters mentioned above. However, we will show the reader how to obtain diffraction loss by use of this empirical approach. For this purpose let us express the distance d_1 and d_2 to two knife edges that model real obstructions in terms of the total horizon distance $d_L = d_{LT} + d_{LR}$ (see Figure 4.29). The expression used for the first obstruction (knife edge) is

$$\begin{aligned} d_1 &= d_L,\ d_1' \le d_L \\ d_1 &= d_1',\ d_1' > d_L \end{aligned} \tag{4.109}$$

where

$$d_1' = d_L + \frac{1}{2} \cdot \left(\frac{72.16 \cdot 10^6}{f_0} \right)^{1/3}, \text{ [km]} \tag{4.110}$$

and the same for the second knife edge:

Table 4.1
Estimations for Different Types of Terrain

Type of Terrain	$\Delta h(m)$
Very smooth plains	0–5
Plains	~30
Hills	80–150
Mountains	150–300
Rugged mountains	300–700

$$d_2 = d_1 + \frac{1}{2} \cdot \left(\frac{72.16 \cdot 10^6}{f_0} \right)^{1/3}, \text{ [km]} \tag{4.111}$$

Here the radiation frequency f_0 is in Hz.

Then the Fresnel-Kirchhoff diffraction parameter v to obstructions at distances d_1 and d_2 can be obtained from following expressions:

$$\begin{aligned} v_{Ti} &= 1.2915 \cdot \theta_{eTi} \left[\frac{f_0 d_{LT}(d_i - d_L)}{(d_i - d_{LR})} \right]^{1/2} \\ v_{Ti} &= 1.2915 \cdot \theta_{eRi} \left[\frac{f_0 d_{LR}(d_i - d_L)}{(d_i - d_{LT})} \right]^{1/2} \end{aligned} \tag{4.112}$$

with $i = 1, 2$. Here angles θ_{eTi} and θ_{eRi} are given by

$$\begin{aligned} \theta_{eTi} &= \frac{5 \cdot 10^{-4}}{d_{LSTi}} \left[1.3 \cdot \left(\frac{d_{LSTi}}{d_{LTi}} - 1 \right) \Delta h - \Delta h_{eTi} \right] \\ \theta_{eRi} &= \frac{5 \cdot 10^{-4}}{d_{LSRii}} \left[1.3 \cdot \left(\frac{d_{LRTi}}{d_{LRi}} - 1 \right) \Delta h - \Delta h_{eRi} \right] \end{aligned} \tag{4.113}$$

where d_{LSTi} and d_{LSRi} are the horizon distances for flat terrain; d_{LTi} and d_{LRi} are the horizon distances for rough terrain, that are related with each other thus:

$$\begin{aligned} d_{LTi} &= d_{LSTi} \cdot \exp\left\{ -0.07 \sqrt{\frac{\Delta h}{h_{eTi}}} \right\}, \\ d_{LRi} &= d_{LSRi} \cdot \exp\left\{ -0.07 \sqrt{\frac{\Delta h}{h_{eRi}}} \right\}, \end{aligned} \tag{4.114}$$

Here once more, $i = 1, 2$, corresponding to the first and second obstructions, respectively. The angle depicted in Figure 4.29 is given by:

$$\theta_e = \max\left[\theta_{eT}, \theta_{eR} - \frac{(d_{LT} - d_{LR})}{8.495 \cdot 10^3} \right] + \frac{d_i}{8.495 \cdot 10^3} \tag{4.115}$$

where transmission path d_i is in kilometers.

Finally, the diffraction losses for two knife edges A_1 and A_2 can be estimated using the approximation for $A(v)$ given by (4.61) to (4.63):

$$A_1 = A(v_{T1}) + A(v_{R1})$$
$$A_2 = A(v_{T2}) + A(v_{R2}) \tag{4.116}$$

The total diffraction loss L_D in dB for the vehicle (moving or stationary) located at the distance "d" from the base station is

$$L_D = \frac{A_1 - A_2}{d_2 - d_1} \cdot d - A_0 \text{ (dB)} \tag{4.117}$$

where

$$A_0 = A_{f_0} + A_2 - \frac{A_1 - A_2}{d_2 - d_1} \cdot d \text{ (dB)} \tag{4.118}$$

Equation (4.118) includes an empirical clutter factor A_{f_0}, estimated as

$$A_{f_0} = \min[A'_{f_0}, 15] \tag{4.119}$$

where

$$A'_{f_0} = 5 \cdot \log[1 + h_T \cdot h_R \cdot f_0 \cdot \sigma(d_{LS}) \cdot 10^{-5}] \text{ (dB)} \tag{4.120}$$

and the standard deviation from the mean terrain profile at the horizon distance d_{LS} between the receiver and transmitter is

$$\sigma(d_{LS}) = 0.78 \cdot \Delta h(d) \cdot \exp\{-0.5 \cdot [\Delta h(d)]^{1/4}\} \text{ (dB)} \tag{4.121}$$

Delisle et al. [44] state that the Longley-Rice model gives reasonably accurate prediction and is not restricted to short radio paths. To now predict the total transmission loss we must add to (4.117) the free-space loss at each distance considered according to Section 2.3. Longley has shown [45, 46] that the standard deviation of the receiving signal is related to the radiated frequency by

$$\sigma = 3 \cdot \log f_0 + 3.6 \text{ (dB)} \tag{4.122}$$

and to the terrain irregularity factor by

$$\sigma_1 = 6 + 5.5 \cdot 10^{-1} \cdot \left(\frac{\Delta h}{\lambda}\right)^{1/2} - 4 \cdot 10^{-3} \cdot \left(\frac{\Delta h}{\lambda}\right) \text{ dB}, \frac{\Delta h}{\lambda} < 4.7 \cdot 10^3$$

$$\sigma_2 = 24.9 \text{ dB}, \frac{\Delta h}{\lambda} > 4.7 \cdot 10^3 \tag{4.123}$$

So, in the context of terrain irregularity, Longley has combined the irregularity factor Δh with wavelength λ to obtain the dimensionless parameter $\frac{\Delta h}{\lambda}$, which increases if Δh and/or $f_0 = \frac{c}{\lambda}$ increase.

CCIR methods [47]. Using a statistical analysis of a considerable amount of experimental data collected in many countries, the CCIR committee proposed constructing a family of signal-strength prediction curves (see Figure 4.30). These curves are applicable over hilly and mountain terrain found in many parts of Europe and America for which the terrain irregularity factor Δh was typically $\Delta h \geq 50$m. Values are given for 50% of the locations and 50% of the time. The reference curves are given for a moving vehicle with antenna height of $h_T = 1.5$m and for base station antenna height h_R variations from 30m to 1,000m. As follows from illustrations presented in Figure 4.30, the value of field strength measured in a small area are log-normally distributed around the predicted average value, that is, the field strength in dB follows a Gaussian (normal) distribution. However, despite the recommendation of the CCIR committee to use it, this technique gives a prediction error of about 10 dB [47].

Therefore, as an improvement of CCIR recommendations, a new method called the *clearance-angle method* was proposed by the European Broadcasting Union (EBU) which has now been adopted by the CCIR committee. The principle of the new technique was to retain the CCIR reference field-strength curves, and hence, the simplicity of application. Also, to improve the prediction accuracy by taking into account the terrain variations in a small area surrounding the receiver (base station), and, instead of the global parameter of terrain undulation Δh, to account for the local effects of terrain by introducing a terrain *clearance angle* as a correction to the CCIR method [48]. This angle is meant to be representative of those angles in the receiving area which are measured between the horizontal through the receiver and a line that clears all obstructions within the path in a direction towards the transmitter. The geometry of the problem and the sign of the corresponding clearance angle for the path of 16 km is shown in Figure 4.31(a). The two curves in Figure 4.31(b) give values for the required correction factor in dB in terms of clearance angle. This factor must added to the field strength obtained from the CCIR reference curves (Figure 4.30). As follows from Figure 4.31(b), the difference

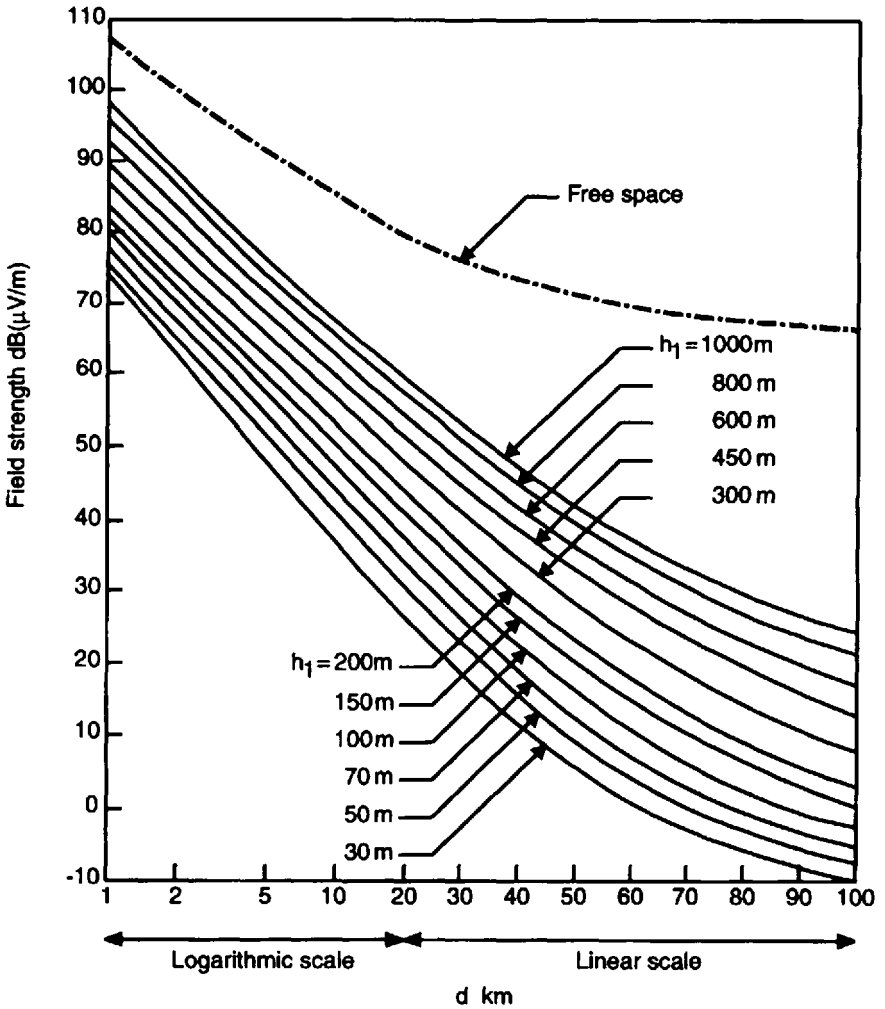

Figure 4.30 CCIR field-strength prediction curves for urban areas at 900 MHz (50% of the time, 50% of locations) for 1kW ERP and h_T = 1.5m.

between VHF- and UHF-band propagation is not essential. Depending on the clearance angles, this correction factor can improve the CCIR results by adding measures from −30 to 30 dB to the field strength obtained from the CCIR prediction curves.

Carey model. This model was derived from the CCIR curves giving field strength E, as a function of distance d and base station antenna height h_R variations for propagation under average terrain conditions [49]. In his model Carey proposed to derive $E(50, 50)$ and $E(50, 10)$, that is the field strength

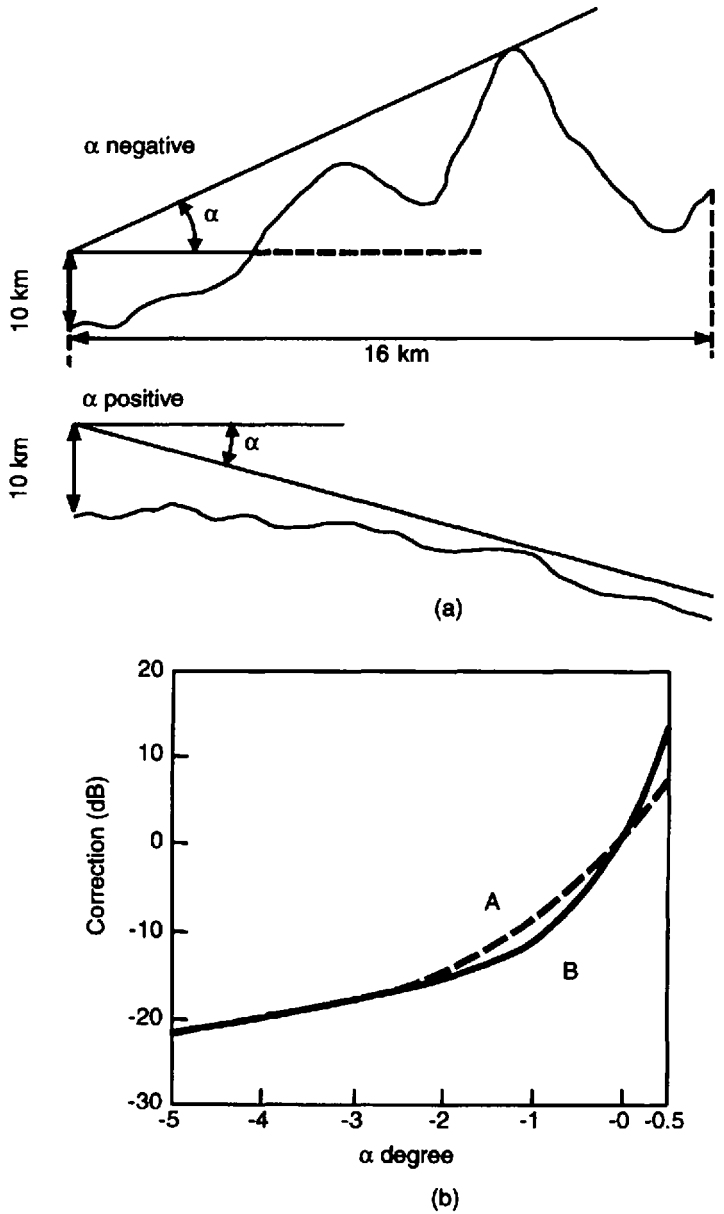

Figure 4.31 The clearance angle method: (a) sign convention; (b) correction factors; the curve *A* corresponds to VHF, the curve *B* to UHF.

for 50% of the locations and 50% or 10% of the time. In his derivations he took the height of the moving vehicle as 1.8m, the base station antenna heights varying from 30m to 1500m above the terrain, and for radio paths up to 130 km (for $E(50, 50)$) and up to 240 km (for $E(50, 10)$). The frequency band investigated was 450–1,000 MHz. According to the predicting curves, Carey gives the average transmission loss in dB at 900 MHz as

$$\begin{aligned} L &= 110.7 - 19.1 \cdot \log h_R + 55 \cdot \log d,\ 8 \le d \le 48 \text{ km} \\ L &= 91.8 - 18 \cdot \log h_R + 66 \cdot \log d,\ 48 \le d \le 96 \text{ km} \end{aligned} \tag{4.124}$$

where h_R is in meters.

4.3 Propagation Over Vegetation

Vegetation is a significant feature which affects radio wave propagation in suburban and rural areas, but usually it can be neglected in most built-up areas. In rural areas, shadowing, scattering, and absorption by trees and other vegetation can cause substantial path losses, mostly at the UHF/X-band. Predictions of signal decay in the case of irregular terrain at frequencies less than 500 MHz have been made by a number of authors [50–53] during the initial period (end of the 1950s to the beginning of the 1960s). Usually their estimations are fairly involved and aimed at calculating the loss of point-to-point paths. Later, during the 1970s, vegetation and foliage losses have been reported [54–56] at frequencies up to 3 GHz but for relatively few paths.

As follows from the literature, trees have both absorbing and scattering effects, mainly for propagation over the trees [50–70]. We summarize below the most important published works [59–70], treating the effects of vegetation, namely trees, foliage, and leaves.

4.3.1 Deterministic Model of Lateral Wave Propagation

In the 1960s and the beginning of the 1970s the deterministic model of wave propagation over forest areas was introduced and discussed to describe the absorption and diffraction effects of vegetation [59–61]. Here the trees were modeled as a homogeneous dielectric slab-layer. As was shown, this model is a good approximation for a forest up to frequencies of 200–500 MHz. Nevertheless, as was shown experimentally by [54–58], the model of homogeneous dielectric layer might be a good approximation for higher frequencies, up to 900 MHz, for calculating the reflections of rays incident with a grazing angle over the tree layer. In fact, the grazing incidence makes the cross-section of

the irregularities of the trees "look" smaller and therefore the tree layer "appears" to be smooth. Let us briefly describe the dielectric layer model.

"Forest" model. A forest is modeled as a dielectric layer dividing two layers—air and ground. The geometry of the "forest" model is shown in Figure 4.32. The forest layer having an effective tree height h is shown to the left of the $x = b$ plane, with the space to the right of that plane being a bare-ground region. Within the frequency band of 20–200 MHz, the tree layer can be assumed to be a homogeneous refractive medium with a relative permittivity $\epsilon_1 = n^2$, where n is the complex refractive index of the forest layer. Similarly, the relative permittivity of the ground surface is denoted by $\epsilon_2 = N^2$, where N is the complex refractive index of the ground surface.

To arrive at simple field considerations, it has been assumed in [59–61] that a dipole antenna is placed at the point $T(0, 0, z_0)$, where its height z_0 can be considered either inside or outside the forest layer (these two situations are described below by formulas (4.125) and (4.128), respectively). Both vertical and horizontal polarization have been examined in [59–61] but, for simplicity, only the field detected at the receiving point $R(x, 0, z)$ by a dipole oriented for maximum reception of the transmitting signal was considered. Thus, for vertical polarization, both dipoles at T and R were oriented parallel to the z-axis; for horizontal polarization, both dipoles were oriented parallel to the y-axis (see Figure 4.32). The electromagnetic field along any direction at any point $y \neq 0$ can be deduced if the electric field detected by the dipole at R is known. As shown in [59–61], the foliage fills only a small portion of the volume occupied by the forest slab, the remainder is filled by air. In this case, it was verified by measurements in [59–61] that the magnitude of the complex equivalent refractive index of the forest slab, $n = n_r + j \cdot n_i$, is close to unity, such that $n_r \approx 1$ and $n_i = 60\sigma\lambda << 1$, where σ is the conductivity of the

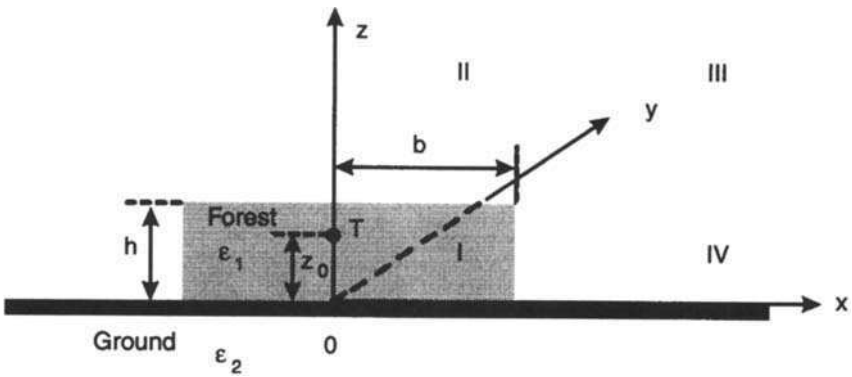

Figure 4.32 Geometry of the Tamir forest model.

forest slab and λ is the wavelength of radiated wave field. Hence the forest dielectric slab represents a weak discontinuity relative to the air because a wave impinging on the forest-air boundary undergoes only a negligible reflection, most of its energy being transmitted across that boundary. In other words, the dominant wave is the surface or *lateral* wave that propagates along the forest-air boundary. This property will be discussed below for different mixed paths.

Another important feature of the forest-layer geometry is that, depending on the particular location of the transmitting (T) and observation (R) points, four different actual situations of wave propagation exist, each of which is characterized by a different type of wave mechanism and therefore by a different expression of the wave field. As indicated in Figure 4.32 by the Roman numerals, these various regimes correspond to the receiving point R being located as follows: I—inside the vegetation; II—in the air region above the forest layer; III—at the relatively high altitude in the air above the bare ground region; IV—at the relatively low height above the bare ground region.

Loss characteristics prediction. We present below formulas describing propagation phenomena within the forest layer (i.e., in region I). The reader can successfully find results of calculations for other regions in [59–61]. In region I, there are two variants of transmitting point T. Location exists in this case: outside the forest layer, as presented by Figure 4.33(a), and inside the forest layer, as is shown in Figure 4.33(b).

In the first case, the field strength at point B is evaluated from the path loss of the lateral wave (depicted by the line AB in Figure 4.33(a)) within the forest dielectric layer, based on the incident wave at point A. The surface (lateral) wave AB represents a whole class of rays. The path loss downward due to the foliage along the BR path must also be added. In this case, using a time dependence $\sim\exp(-j\omega t)$, one can obtain according to [59–61] for region I the following expression for relative signal strenght $\bar{E}_I$ (relative to the dipole momentum $\sim Ia$, where a is the effective length of the receiving dipole, I is its current):

$$\bar{E}_I = \frac{60}{(n^2-1)} \frac{\exp\{j\cdot[k\cdot b + k_L\cdot(h-h_R)]\}}{d^2} F(90°, h_R)\cdot F(90°, h) \tag{4.125}$$

where $k = \dfrac{2\pi}{\lambda} = 2\pi f(\mu_0\epsilon_0)^{1/2}$ is the plane-wave propagation factor in air, f is the radiated frequency, μ_0 is the constant permeability of air, and ϵ_0 is the constant permittivity of air; $k_L = k\cdot(n^2-1)^{1/2}$, all geometrical parameters of the problem are depicted in Figure 4.33(a). Other functions in (4.125) are as follows:

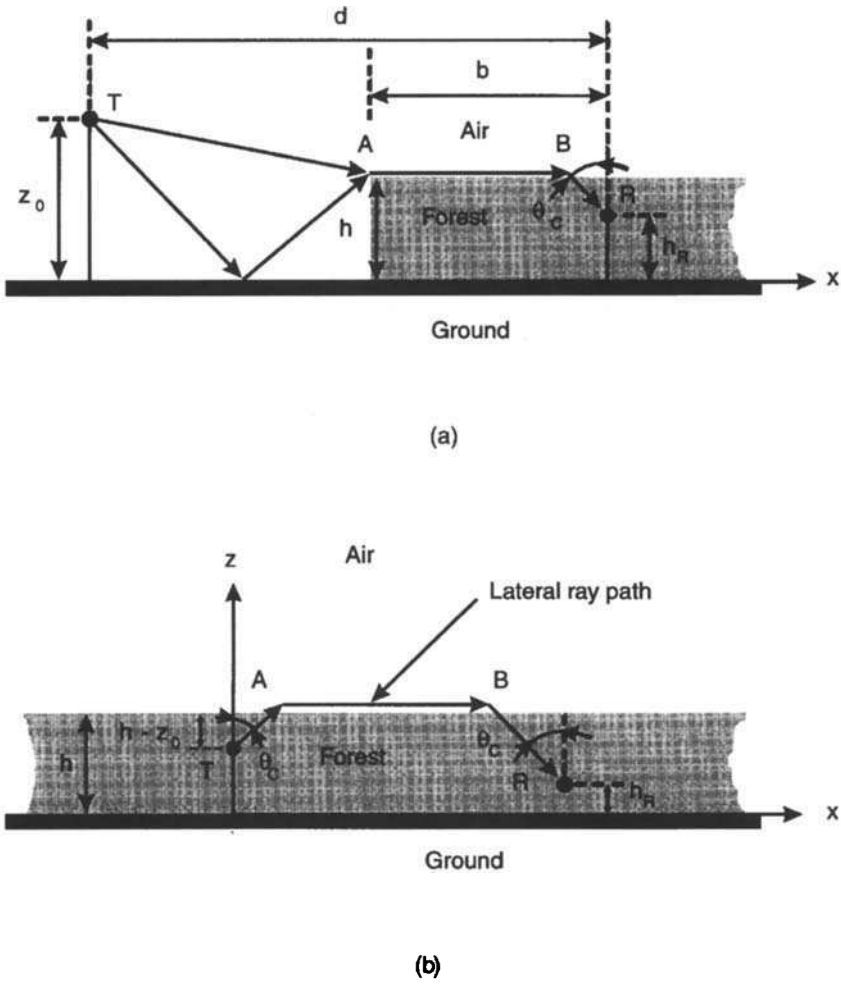

Figure 4.33 The forest model: (a) the transmitter T is outside the forest layer; (b) the transmitter T is inside the forest layer.

$$F(\theta, z) = \frac{1 + B(\theta, z)}{1 - B(\theta, h)}, \quad F(\theta, h_R) = \frac{1 + B(\theta, h_R)}{1 - B(\theta, h)} \tag{4.126}$$

The factors as $F(90°, z)$ from (4.126) describe the effects of reflections from the ground plane, which affects the surface-wave amplitude by reflecting some energy back towards the forest-air boundary [59]. This ground proximity effect becomes negligible for large values of z_0, h_R, and h, in which case $F(90°, z)$ approaches unity. Here,

$$B(\theta, z) = \Gamma_{V/H}(\theta) \cdot e^{j2k_L z},$$
$$B(\theta, h_R) = \Gamma_{V/H}(\theta) \cdot e^{j2k_L h_R}, \tag{4.127}$$
$$B(\theta, h) = \Gamma_{V/H}(\theta) \cdot e^{j2k_L h},$$

where $\Gamma_V(\theta)$ and $\Gamma_H(\theta)$ are the reflection coefficients for reflection at the forest-layer-soil interface for vertical and horizontal polarization, respectively, θ is the angle of incidence (Figure 4.33(a)), which was introduced in Chapter 3.

The same results can be obtained for the second case presented in Figure 4.33(b) for region I, when the transmitting point T is also located within the forest layer (using Tamir's approach [59, 61]). In this case, because the wave reflections are negligible at the forest-air interface, the effects of the forest boundary $x = b$ may be neglected for the receiving point R located inside the vegetation layer. In this case, the forest may be assumed to extend over the entire region $x > b$, as shown in Figure 4.33(b), where $0 < z < h$. For large distances $|x| = d$ between T and R, one can obtain from [59–61] that the relative field strength in region I is

$$\tilde{E}_I' = \frac{60}{(n^2 - 1)} \frac{\exp\{j \cdot [k \cdot |x| + k_L \cdot (2h - z - z_0)]\}}{x^2} F(90°, z) \cdot F(90°, z_0) \tag{4.128}$$

where all the terms in (4.128) were described earlier by (4.126) to (4.127).

Fields given by $\tilde{E}_I$ and $\tilde{E}_I'$ are those of *lateral* waves, which follow the paths *TABR* depicted both in Figure 4.33(a) and 4.33(b). For example, as can be verified from Figure 4.33(b), an electrical length can be written as

$$k \cdot n \cdot (|TA| + |BR|) + k \cdot |AB| = k(n \cdot s \cdot \sec\theta_c + x - s \cdot \tan\theta_c)$$
$$= k(|x| - \sqrt{n^2 - 1} \cdot s)$$

where $s = (h - z) + (h - z_0) = 2h - z - z_0$, θ_c is shown in Figure 4.33(b), as the critical angle of total reflection: $\theta_c = \sin^{-1}(1/n)$. Of couse, θ_c is generally complex because n is a complex quantity. However, for small losses $n_i << n_r$, the real part of θ_c is predominant and it then yields the physical interpretation of the ray-paths *TA* and *BR* in Figure 4.33(b).

From (4.125) or (4.128) one can obtain the initial loss L_0 in the case of absence of the ground plane and the additional losses L_s, taking into account the situation when both antennas are located within the forest layer. The total loss for this case can be presented as a sum of such path losses (i.e.,

$L_{Total} = L_0 + L_s$). The first term can be obtained by use of a half-space propagation model, taking into account the radiation resistance of a small dipole in unbounded free space $R_0 = 80 \cdot \left(\frac{\pi \cdot a}{\lambda}\right)^2$, where a is a dipole size, and that $s_0 = 2h - z - z_0 = 0$ [59–61]:

$$L_0 = 20 \log\left[\left(\frac{8}{3}\right) \cdot \pi^2 \cdot |n^2 - 1| \cdot \left(\frac{x}{\lambda}\right)^2\right] \text{ [dB]} \qquad (4.129a)$$

Expression (4.129a) shows that the loss L_0 is strongly dependent on the wavelength and dielectric properties of the forest which are characterized by the refractive index n.

The additional losses follow from (4.128) when two antennas, T and R, are located below the forest-air interface (Figures 4.33(a) and 4.33(b)) by use of the exponent $\sim\exp\{-jk_L s\}$, $k_L = k\sqrt{n^2 - 1}$. Hence, it follows that the loss incurred due to lowering the antennas to a combined depth s below the treetops can be described according to [59, 60] by

$$L_s \approx 8.7 \cdot \left(\frac{2\pi}{\lambda}\right) \cdot \mathrm{Im}[\sqrt{n^2 - 1}] \cdot s \text{ [dB]} \qquad (4.129b)$$

It should be noted that the surface (lateral) wave is a diffracted-nature field component, which varies with distance according to (4.125) and (4.128) as $\sim x^{-2}$, decreasing more rapidly than spherical waves, which vary as $\sim x^{-1}$. In the present case, spherical waves also occur and they correspond to direct wave or to waves that would arrive at point R by reflectors at the ground plane and/or at the forest-air boundary [59–61]. These spherical waves have to travel a long distance inside a lossy forest layer, so that their amplitudes decay to exponentially small values. In contrast, the surface (lateral) wave decays only over the relatively smaller distances TA and BR, the large path AB being through the lossless air region. Hence, this wave remains as the only significant contribution to the field E_I in the region (I).

Comparison with experimental data. As was obtained experimentally by [62, 63], there exists a good agreement between a decrease in the measured field $\tilde{E}_I$ with the distance squared, and the theoretical predictions according to (4.125) and (4.128) that give us the same law of total field attenuation $\sim x^{-2}$. Also, the field was found to generally increase with the height z_R of the observation point R. This gain as a function of height is also predicted correctly by formulas (4.125) and (4.128).

An experimental study in Texas at frequencies in the range of 500–3,000 MHz have shown that there is a good correlation with the theoretically predicted field decay based on diffraction effects of lateral wave from the forest tops according to formula (4.129) for the observer point position both above and below the treetop level [64].

They also have obtained that the path loss increases as the fourth power of the frequency for distances ~1 km and for both transmitter and receiver at the treetop level. Moreover, the signal loss for vertical polarization was higher than that for horizontal polarization. But the phenomenon that cannot be explained by the theoretical prediction based on the works of Tamir and others [59–61], is that vegetation produces a constant loss independent of distance as long as the T and R distance exceeds 1 km for radio paths within the forest.

4.3.2 Empirical Model Approach

Weissberger model. Based on numerous published works covering the results of measurement data and empirical and theoretical predictions carried out at frequencies from 230 MHz to 95 GHz, Weissberger summarized their results and also considered several specific exponential models based on different attenuation phenomena in terms of dB per meter of path length [65]. His modified exponential decay which applies in areas with vegetation, where a ray path is obstructed by dense, dry, and leafy trees, can be presented as additional loss (excess) to free space attenuation

$$\begin{aligned} L &= 1.33 f_0^{0.284} \cdot d_t^{0.588}, \quad 14 \le d_t \le 400\text{m} \\ L &= 0.45 f_0^{0.284} \cdot d_t^{1.0}, \quad 0 \le d_t \le 14\text{m} \end{aligned} \tag{4.130}$$

where L is the loss in dB, f_0 is the radiated frequency in GHz, and d_t is the distance between the antennas within the vegetation. The difference in path loss for trees with and without leaves is 3–5 dB.

4.3.3 Stochastic Model of Scattering From the Canopy

A theoretical approach based on random media scattering theory was proposed by Lang et al. [69, 70], based upon the earlier developed stochastic models of scattering from discrete scatters [71–74] in order to calculate the absorption effects of trees. Expressions have been derived by modeling of the crown (top) of the tree as an ellipsoidal region containing branches and leaves all having prescribed location and orientation statistics. The leaves were modeled as flat, circular, lossy-dielectric discs and the branches as finitely long, circular, lossy-

dielectric cylinders. The bistatic scattering of the tree for different incident and scattering angles were calculated using the Born approximation, as a single scattering approximation, where the scatters are assumed to be embedded in the equivalent medium of the canopy of the tree to account for the attenuation of the incident and the scattered fields in the scattering region.

The studies in [69, 70] have justified the exponential decay of the signal intensity of scattered rays crossing a short distance of trees. To apply this approach, the physical parameters of a tree, such as permittivity, conductivity, and geometrical distribution of the branches and leaves, must be taken into account. The electrical parameters of the leaves, such as permittivity and conductivity, can be obtained from [75]. As was shown in [75], the permittivity of leaves strongly differs from unity (i.e., $|\epsilon_L| >> 1$). But the Born approximation is valid if the permittivity of the scatterers is close to unity, that is, when $|\epsilon_L| \approx 1$. Therefore, we will not consider this sophisticated approach because of the complexity of the computations and because of the existing limitations of this method based on the assumption that the fractional volume of the scatterers should be small with respect to the wavelength, and that the permittivity of leaves differs from unity. These features are in contradiction with real geometrical structure of trees and their own dielectrical parameters. Moreover, due to uncertainty on the dielectrical parameters of the trees, it is expected that the accuracy of this approach is within the same range of accuracy as the simple empirical models available. Furthermore no validation with measurements is available using this approach.

Summary

A number of propagation models of radio wave propagation above the rough terrain that consists of different obstructions, such as hills and canopy, have been described in this chapter to predict loss characteristics in quasi-open and rural environments. They all aim to predict path loss at the receiver or in an immediate vicinity around it. All methods, as follows from discussions above, differ widely in approach, mathematical complexity and accuracy. Nevertheless, what is quite clear is that there is no one method that covers all the various conditions of propagation over terrain.

In general, most models described are a mixture of empirical and deterministic approaches that follow from strict propagation theory. The empirical methods are based on fitting curves or analytical expressions, such as the free-space model, the plane-earth model, and the two-ray model (see Sections 2.3 and 3.2), to sets of measured data.

The use of diffraction calculation for obstructive conditions over the terrain, based on knife-edge theory by use of Fresnel's integral (4.49) and on corresponding empirical formulas (4.54) to (4.55) to account for the diffraction losses caused by real obstruction, as well as of diffraction loss estimation over radio paths with multiple obstructions by use of Andersen's deterministic approach [30], provides reasonably accurate, simple and efficient solutions. In this context, in all presented diffraction models the diffraction losses are added either to the free-space path loss L_{FS}, or to the flat-terrain (plane-earth model) path loss, L_{FT}, if $L_{FT} > L_{FS}$.

Moreover, comparison between all empirical methods presented above has shown that Bullington's technique is simpler than others, but gives a greater error relative to the strict numerical solutions obtained by Vogler [28, 29] than do other methods. The Epstein-Peterson technique as well as a Japanese scheme are better but can also provide diffraction loss predictions that are too low. At the same time, the Deygout technique shows good agreement with the rigorous diffraction theory [28–30] for two-three obstructions but has an increasing error and becomes pessimistic with increase of their number. This is why estimations by use of this method are often terminated after consideration of three edges.

As for propagation models over vegetation, the *deterministic approach* of lateral waves propagation is presented in [59–61]. To summarize the discussion above, in order to model a real forest as a homogeneous dielectric slab, one must postulate that the wavelength should be larger than the separation of the trees. Based on such consideration and on average gaps between trees in the range of 1m to 5m, Tamir and others [59–61] have derived the frequency range of validity from 2 to 200 MHz. This postulate is in conflict with many experiments (see, for example, [53–55, 62–64]), which have shown that even for frequencies up to 1 GHz , there is a good agreement with the lateral wave approach [59–61]. Other limits also exist, particularly, the minimum distance between points T and R (the length of the communication channel) for the lateral-wave propagation must be at least 300m long. All these facts limit the application of the slab-forest model to predict various situations in rural and suburban areas with vegetation, for operating frequencies higher than 1 GHz and for distances less than 300m and longer than 1 km. In any other case one can use the dielectric-slab "forest" model with a great accuracy, including for VHF/UHF-band propagation.

As for the empirical approach, based on numerous experiments, one can summarize that the Weissberger model is sufficiently good and predicts the exponential excess decay of signal strength at frequencies from 230 MHz to 95 GHz in areas with vegetation, where a ray path is obstructed by dense, dry, and leafy trees. Moreover, because this model gives the same exponential signal

decay within the forest as the stochastic model presented in [69, 70] by use of more complicated computation formulas, and because of some principal limitation of later model, which deals with scatters smaller than wavelength and with permittivity of the leaves close to unity, it is simpler to use the empirical model of Weissberger [65] to describe the real situation in areas with vegetation.

References

[1] Parsons, L. D., *The Mobile Radio Propagation Channels*, New York: Pentech Press, 1992.

[2] Mehrotra, A., *Cellular Radio Performance Engineering*, Norwood, MA: Artech House, 1994.

[3] Lee, W. C. Y., *Mobile Communication Engineering*, New York: McGraw-Hill Book Co., 1982.

[4] Ishimaru, A., *Electromagnetic Wave Propagation, Radiation, and Scattering*, Englewood Cliffs, NJ: Prentice-Hall, 1991.

[5] Al'pert, Ya. L., V. L. Ginsburg, and E. L. Feinberg, *Radiowave Propagation*, Moscow: State Printing House for Technical-Theoretical Literature, 1953.

[6] Bass, F. G., and I. M. Fuks, *Wave Scattering from Statistically Rough Surfaces*, Oxford: Pergamon Press, 1979.

[7] Voronovich, A. G., *Wave Scattering from Rough Surfaces*, New York: Springer-Verlag, 1994.

[8] Rice, S. O., "Reflection of electromagnetic waves from slightly rough surfaces," *Comm. Pure Appl. Math.*, Vol. 4, No. 3, 1951, pp. 351–378.

[9] Barrick, D. E., and W. H. Peake, "A review of scattering from surfaces with different roughness scales," *Radio Sci.*, Vol. 3, No. 7, 1968, pp. 865–868.

[10] Barrick, D. E., "Theory of HF and VHF propagation across the rough sea—Parts I and II," *Radio Sci.*, Vol. 6, No. 3, 1971, pp. 517–533.

[11] Barrick, D. E., "First order theory and analysis of MF/HF/VHF scatter from the sea," *IEEE Trans. Anten. Propagat.*, Vol. 20, No. 1, 1972, pp. 2–10.

[12] Wait, J. R., "Perturbation analysis for reflection from two-dimensional periodic sea waves," *Radio Sci.*, Vol. 6, No. 3, 1971, pp. 387–391.

[13] Valenzuela, G. R., "Scattering of electromagnetic waves from a slightly rough surface moving with uniform velocity," *Radio Sci.*, Vol. 3, No. 1, 1968, pp. 12–21.

[14] Valenzuela, G. R., "Scattering of electromagnetic waves from a tilted slightly rough surface," *Radio Sci.*, Vol. 3, No. 6, 1968, pp. 1057–1066.

[15] Valenzuela, G. R., "The effective reflection coefficients in forward scatter from a dielectric slightly rough surface," *Proc. IEEE*, Vol. 58, No. 12, 1970, pp. 1279–1285.

[16] Ruffine, R., "Note of the scattering of waves by rough surface," *IEEE Trans. Anten. Propagat.*, Vol. 12, No. 6, 1964, pp. 802–803.

[17] Krishen, K., "Scattering of electromagnetic waves from a layer with rough front and plane back (small perturbation method by Rice)," *IEEE Trans. Anten. Propagat.*, Vol. 19, No. 4, 1970, pp. 573–576.

[18] Davies, H., "The reflection of electromagnetic waves from a rough surface," *Proc. IEEE*, Vol. 101, No. 2, 1954, pp. 209–214.

[19] Bullington, K., "Reflection coefficient of irregular terrain," *Proc. IRE*, Vol. 42, No. 11, 1954, pp. 1258–1262.

[20] Beckmann, P., and A. Spizzichino, *The Scattering of Electromagnetic Waves from Rough Surfaces*, Oxford: Pergamon, 1963.

[21] Ament, W. S., "Toward a theory of reflection by a rough surface," *Proc. IRE*, Vol. 41, No. 2, 1953, pp. 142–146.

[22] Twersky, V., "On multiple scattering and reflection of waves by rough surfaces," *IRE Trans. Anten. Propagat.*, Vol. 5, No. 1, 1957, pp. 81–86.

[23] Twersky, V., "On propagation in random media of discrete scatterers," *Proc. Am. Math. Soc. Symp. Stochas. Proc. Math. Phys. Eng.*, Vol. 16, 1964, pp. 84–116.

[24] Hacking, K., "Propagation over rounded hills," *BBC Research Report*, RA-21, 1968.

[25] Dougherty, H. T., and L. J. Maloney, "Applications of diffraction by convex surfaces to irregular terrain situation," *Radio Sci.*, Vol. 68-D, No. 2, 1964, pp. 284–305.

[26] Causebrook, J. K., and B. Davies, "Tropospheric radio wave propagation over irregular terrain: the computation of field strength for UHF broadcasting," *BBC Research Report*, 43, 1971.

[27] Sheng, P., *Scattering and Localization of Classical Waves in Random Media*, Singapore: World Scientific, 1990.

[28] Vogler, L. E., "The attenuation of electromagnetic waves by multiple knife-edge diffraction," *NTIA Report*, 1981, pp. 81–86.

[29] Vogler, L.E., "An attenuation function for multiple knife-edge diffraction," *Radio Sci.*, Vol. 17, No. 9, 1982, pp. 1541–1546.

[30] Andersen, J. B., "UTD multiple-edge transition zone diffraction," *IEEE Trans. Anten. Propagat.*, Vol. 45, No. 7, 1997, pp. 1093–1097.

[31] Lee, S. W., "Path integrals for solving some electromagnetic edge diffraction problems," *J. Math. Phys.*, Vol. 19, No. 10, 1978, pp. 1414–1422.

[32] Honl, H., A. W. Maue, and K. Westpfahl, *Theory of Diffraction*, Berlin: Springer-Verlag, 1961.

[33] Bertoni, H. L., and J. Walfisch, "A theoretical model of UHF propagation in urban environment," *IEEE Trans. Anten. Propagat.*, Vol. 36, No. 12, pp. 1788–1796, 1988.

[34] Bullington, K., "Radio propagation at frequencies about 30 Mc," *Proc. IRE*, Vol. 35, No. 10, 1947, pp. 1122–1136.

[35] Epstein, J., and D. W. Peterson, "An experimental study of wave propagation at 850 Mc," *Proc. IRE*, Vol. 41, No. 5, 1953, pp. 595–611.

[36] *Atlas of Radio Wave Propagation Curves for Frequencies Between 30 and 10,000 Mcls*, Radio Research Lab., Ministry of Postal Services, Tokyo, Japan, 1957, pp. 172–179.

[37] Deygout, J., "Multiple knife-edge diffraction of microwaves," *IEEE Trans. Anten. Propagat.*, Vol. 14, No. 4, 1966, pp. 480–489.

[38] Egli, J. J., "Radio propagation above 40 MC over irregular terrain," *Proc. IRE*, Vol. 45, No. 10, 1957, pp. 1383–1391.

[39] Frazer, E. L., and D. J. Targett, "A comparison of models for prediction of service area of cellular telephone sites," *4th Int. Conf. on Anten. and Propagat. (ICAP'85)*, Conference Publication No. 248, 1985, pp. 390–394.

[40] Dadson, C. E., "Radio network and radio link surveys derived by computer from a terrain data base," *NATO-AGARD*, Conference Publication CPP-269, 1979.

[41] Edwards, R., and J. Durkin, "Computer prediction of service area for VHF mobile radio network," *Proc. IEE*, Vol. 116, No. 12, 1969, pp. 1493–1500.

[42] Ibrahim, M. F., J. D. Parsons, and C. E. Dadson, "Signal strength prediction in urban areas using a topographical and environmental data base," *Proc. ICC'83*, Conference Record, 1983, pp. A.2.5.1–A.2.5.4.

[43] Blomquist, A., and L. Ladell, "Prediction and calculation of transmission loss in different types of terrain," *NATO-AGARD*, Conference Publication CPP-144, 1974.

[44] Delisle, G. Y., J. P. Lefevre, M. Lecours, and J. Y. Chouin, "Propagation loss prediction: A comparative study with application to the mobile radio channel," *IEEE Trans. Vehic. Technol.*, Vol. 34, No. 1, 1985, pp. 85–95.

[45] Longley, A. G., and P. L. Rice, "Prediction of tropospheric radio transmission over irregular terrain: A computer method," *ESSA Tech. Report*, ERL 79-ITS 67, 1968.

[46] Longley, A. G., "Location variability of transmission loss for land mobile and broadcast systems," *OT Report 76-87* (NTIS Accession No. PB-254472), 1967.

[47] *Method and Statistics for Estimating Field Strength Values in the Land Mobile Services Using the Frequency Range 30 MHz to 1 GHz*, CCIR XV Plenary Assembly, Geneva, Report 567, Vol. 5, 1982.

[48] Allsebrook, K., and J. D. Parsons, "Mobile radio propagation in British cities at frequencies in the VHF and UHF bands," *IEEE Proc.*, Vol. 124, No. 1, 1977, pp. 95–102.

[49] Carey, R., "Technical factors affecting the assignment of frequencies on the domestic public land mobile radio service," *FCC*, Washington DC, Report R-6406, 1964.

[50] Bullington, K., "Radio propagation fundamentals," *Bell Syst. Tech. J.*, Vol. 36, No. 5, 1957, pp. 593–597.

[51] Anderson, L. J., and L. G. Trolese, "Simplified method for computing knife edge diffraction in the shadow region," *IRE Trans. Anten. Propagat.*, Vol. AP-6, No. 2, 1958, pp. 281–286.

[52] Dougherty, H. T., and L. J. Maloney, "Application of diffraction by convex surfaces to irregular terrain situations," *Radio Phone*, Vol. 68B, 1964, p. 239.

[53] Matzler, C., "Microwave (1–100 GHz) dielectric model of leaves," *IEEE Trans. Geosci. and Remote Sens.*, Vol. 32, No. 8, 1994, pp. 947–949.

[54] Longley, A. G., and R. K. Reasoner, "Comparison of propagation measurements with predicted values in the 20 to 10,000 MHz range," Environmental Science Services Admin., *Tech. Rep. ERL 148-ITS 97*, Jan. 1970.

[55] Reudink, D. O., and M. F. Wazowicz, "Some propagation experiments relating foliage loss and diffraction loss at X-band and UHF frequencies," *IEEE Trans. Commun.*, Vol. 21, No. 11, 1973, pp. 1198–1206.

[56] Swarup, S., and R. K. Tewari, "Depolarization of radio waves in jungle environment," *IEEE Trans. Anten. Propagat.*, Vol. 27, No. 1, 1979, pp. 113–116.

[57] Wait, J. R., "Asymptotic theory for dipole radiation in the presence of a lossy slab lying on a conducting half-plane," *IEEE Trans. Anten. Propagat.*, Vol. 15, No. 6, 1967, pp. 645–648.

[58] Sachs, D. L., and P. J. Wyatt, "A conducting-slab model for electromagnetic propagation of lateral waves in an inhomogeneous jungle," *Radio Sci.*, Vol. 3, No. 2, 1968, pp. 125–134.

[59] Tamir, T, "On radio-wave propagation in forest environment," *IEEE Trans. Anten. Propagat.*, Vol. 15, No. 7, 1967, pp. 806–817.

[60] Dence, D., and T. Tamir, "Radio loss of lateral waves in forest environments," *Radio Sci.*, Vol. 4, No. 2, 1969, pp. 307–318.

[61] Tamir, T., "Radio wave propagation along mixed paths in forest environments," *IEEE Trans. Anten. Propagat.*, Vol. 25, No. 4, 1977, pp. 471–477.

[62] Tewari, R. K., S. Swarup, and M. N. Roy, "Radio wave propagation through rain forests in India," *IEEE Trans. Anten. Propagat.*, Vol. 38, No. 4, 1990, pp. 433–449.

[63] Tewari, R. K., and S. Swarup, "An empirical result for the height gain in forest medium," *IEEE Trans. Anten. Propagat.*, Vol. 32, No. 11, 1984, pp. 1265–1268.

[64] Sturgill, and Staff, L. G., "Tropical propagation research," Jansky and Bailey Research and Enging. Dept., *Final Report*, Atlantic Research Corp., Alexandria, VA, Vol. I, June 1966.

[65] Weissberger, M. A., "An initial critical summary of models for predicting the attenuation of radio waves by trees," *ESD-TR-81-101*, EMC Analysis Center, Annapolis, MD, USA, 1982.

[66] Hicks, J. J., et al., "Tropical propagation research," Jansky and Bailey Research and Enging. Dept., *Final Report*, Atlantic Research Corp., Alexandria, VA, Vol. II, Nov. 1969.

[67] Barker, G. E., J. Taylor, and G. H. Hagn, "Summary of measurements and modeling of the radiation patterns of simple HF field antennas in open (level) terrain, mountains and forests," *Special Tech. Rept.*, Stanford Research Inst., Menlo Park, CA, 45, Dec. 1971.

[68] Hagn, G. H., and G. E. Barker, "Research engineering and support for tropical communications," *Final Report*, Stanford Research Inst., Menlo Park, CA, Feb. 1970.

[69] S. A. Torrico and R. H. Lang, "Bistatic scattering effects from a tree in a vegetated residential environment," *Proc. of National URSI Meeting*, Boulder, CO, 1998, pp. 24–25.

[70] Torrico, S. A., H. L. Bertoni, and R. H. Lang, "Modeling tree effect on path loss in a residential environment," *IEEE Trans. Anten. Propagat.*, Vol. 46, No. 6, 1998, pp. 872–880.

[71] Foldy, L. L., "The multiple scattering of waves," *Phys. Rev.*, Vol. 67, No. 3, 1957, pp. 107–119.

[72] Lax, M. X., "Multiple scattering of waves," *Rev. Mod. Phys.*, Vol. 23, No. 4, 1951, pp. 287–310.

[73] Twersky, V., "Multiple scattering of electromagnetic waves by arbitrary configurations," *J. Math. Phys.*, Vol. 8, No. 3, 1967, pp. 569–610.

[74] Lang, R. H., "Electromagnetic backscattering from a sparse distribution of lossy dielectric scatterers," *Radio Sci.*, Vol. 16, No. 1, 1981, pp. 15–30.

[75] Vogel, W. J., and J. Goldhirsch, "Tree attenuation at 869 MHz derived from remotely piloted aircraft measurements," *IEEE Trans. Anten. Propagat.*, Vol. 34, No. 12, 1986, pp. 1460–1464.

This page intentionally left blank

III

Propagation in Built-Up Areas

This page intentionally left blank

5

Propagation in LOS Conditions Along Straight Streets

In this chapter we consider several urban propagation environments. We will start with the simplest case of EM-wave propagation in the urban scene, when both antennas are placed above the flat-ground surface with conditions of direct visibility between them, below the rooftop level. Such conditions of direct visibility are usually called line-of-sight conditions (see Chapter 1) and all propagation characteristics, namely, path loss, signal decay, and coverage parameters, are determined by using the *two-ray model* (see Chapter 3). As mentioned in [1–15], the conditions of LOS propagation along a straight street, on which the base station is located, will be of great importance in defining the coverage area for low antennas because of the low path loss as compared to propagation over the rooftops.

On the other hand, a new model, the *multislit waveguide model*, was recently introduced for describing the propagation of EM-waves in a city scene with regularly planned streets (i.e., a model of a straight streets with buildings lining their sides) [16–19].

The street is considered a planar multislit waveguide with a Poisson distribution of screens (building walls) and slits (intervals between buildings). The electrical properties of the buildings' walls are taken into account by introducing the electrical impedance, a function of their surface permittivity and conductivity. As was shown in [16–19], this model can be used for predicting wave propagation in street-planned urban and suburban microcells having a radius less than 2–3 km in LOS conditions.

In Section 3.2 we presented the two-ray model for the case of radio propagation over the flat-ground surface. Below, we will focus on the multislit

waveguide model, which was found to be in agreement with experimental data of wave propagation in urban areas with a regular crossing-street plan. Section 5.1 presents the initial conditions of a nonregular multislit waveguide model. In Section 5.3, the total field construction in a continuous impedance waveguide is described. Section 5.3 presents the method of construction wave fields which are reflected and diffracted n-times from the broken waveguide screens, taking into account their nonideal electrical impedance properties.

In Section 5.4, the procedure of averaging the total field in a multislit impedance waveguide, using the direct and inverse Fourier transforms for the average total field are examined. The discrete and continuous spectra of the total field are investigated. In Section 5.5, we will evaluate the total field intensity decay and path loss distribution along the street multislit waveguide. Comparison of theoretical predictions based on the multislit waveguide model with numerous experimental data obtained in LOS conditions in various urban environments is presented in Section 5.6.

5.1 The Street Multislit Waveguide Model

In Figure 5.1, a three-dimensional waveguide model of a city region with regular planned building, and with receiver and transmitter at street level below the rooftops, is presented. The reflection from the ground surface is also considered using an imaginary source (Figure 5.1). The projection of such waveguide on the zy-plane presents the impedance parallel multislit waveguide with randomly distributed screens and can be considered as a two-dimensional model of a city street (see Figure 5.2). One waveguide plane is placed at the waveguide (street) side $z = 0$, and the second one at $z = a$ (Figure 5.2). The screen L_n and slit l_n lengths are distributed according to the Poisson law with the average values of $\langle L \rangle = L$ and $\langle l \rangle = l$, respectively:

$$f(L_n) = L^{-1} \exp\left\{-\frac{L_n}{L}\right\}, f(l_n) = l^{-1} \exp\left\{-\frac{l_n}{l}\right\} \tag{5.1}$$

Let us assume that a horizontal electric dipole as a source of EM-waves is placed at the point (H, 0, h), where $0 < h < a$, $0 < H < h_b$, h_b is the average height of buildings lining the street. Its projection on the zy-plane is presented in Figure 5.2, the top view of Figure 5.1. The resulting reflected field is considered a sum of mirror reflecting imaginary sources.

The propagation of EM-waves is observed at a point inside the waveguide at the image surface (dotted line in Figure 5.2). The real electrical properties of screens (walls) are determined by the surface impedance:

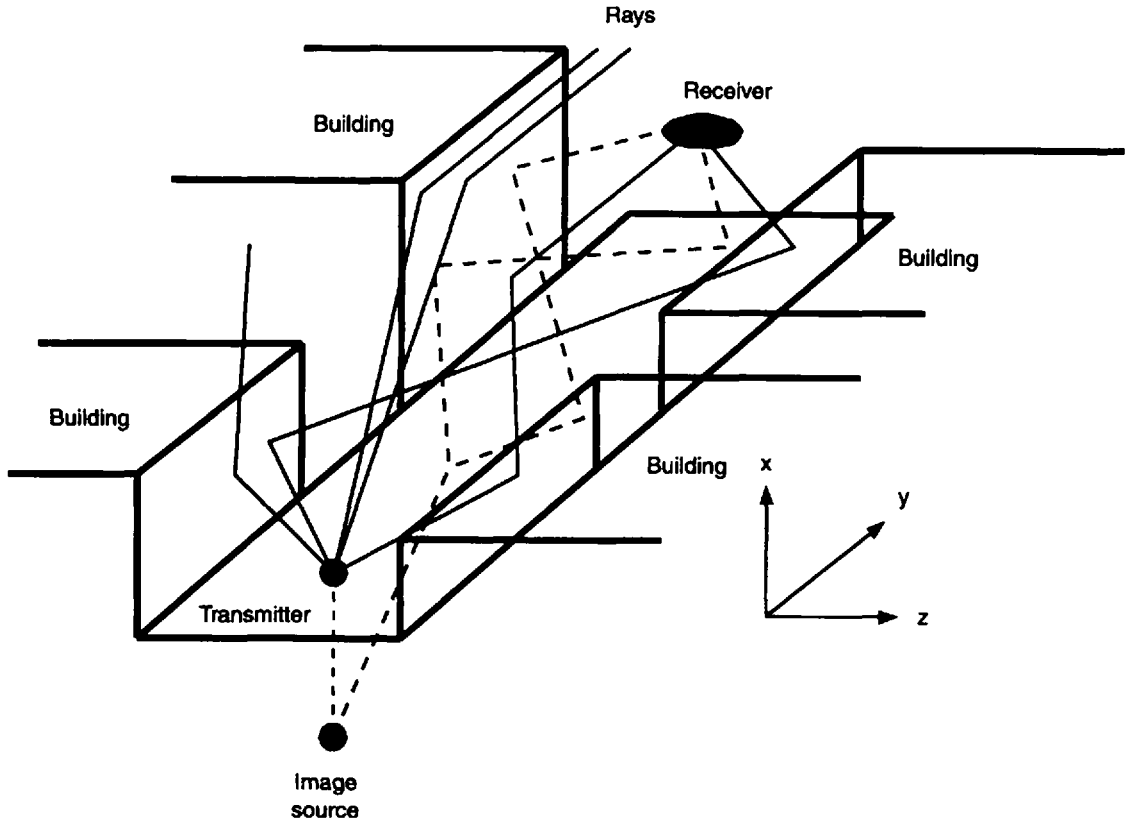

Figure 5.1 A three-dimensional model of the street waveguide.

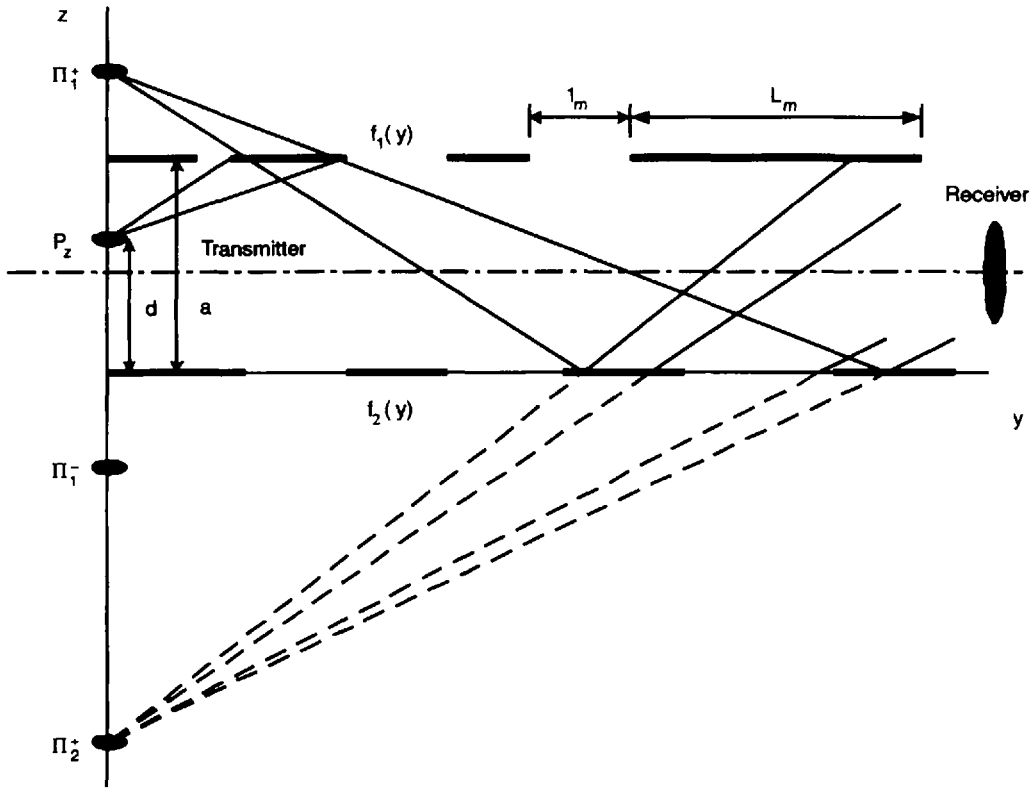

Figure 5.2 A two-dimensional diagram of the street waveguide in the *zy*-plane. The coordinates of source are $y = 0$ and $z = d$, a is the street width.

$$Z_{EM} \sim \epsilon^{-1/2}, \ \epsilon = \epsilon_0 - i\frac{4\pi\sigma}{\omega} \tag{5.2}$$

where ϵ is the relative dielectric permittivity of the wall's surface, ϵ_0 is the dielectric constant of vacuum, σ is the electric conductivity, ω is the angular frequency of the radiated wave. Using the harmonic time-dependence $\sim\exp(-i\omega t)$ and the definition of the dipole field using the Hertzian potential vector $\Pi_z(x, y, z)$, we obtain the well-known equation (see also Section 2.4):

$$\nabla^2\Pi_z^i - k^2\Pi_z^i = -\frac{4\pi i}{\omega}\mathbf{p}_z\delta(x)\delta(y)\delta(z-h) \tag{5.3}$$

the solution of which can be presented using Green's function (as also follows from Section 2.2.5):

$$\Pi_z^i(x, y, z) = \frac{i\mathbf{p}_z}{\omega}\frac{e^{ikR}}{R} \tag{5.4}$$

Here $\mathbf{p}_z$ is the electric momentum of a point horizontal electric dipole, $R = |\mathbf{r}|$, where $\mathbf{r}$ is the distance from the source. In real city built-up conditions, the screen and slit lengths are much greater than the radiation wavelength λ (i.e., $L_n >> \lambda$, $l_n >> \lambda$). In this case, we can use the approximations of the GTD first introduced by Keller for the problems of diffraction at the half-plane and wedge [20]. According to the GTD, the reflected and diffracted waves have the same nature, and the total field can be presented as a superposition of direct (incident) wave fields from the source and reflected and diffracted fields from the screens.

Moreover, following the previously constructed model [16–19], we consider the resulting reflected and diffracted fields as a sum of the fields reaching the observer from the virtual image sources Π_n^+ (for the reflections from plate $z = a$) and Π_n^- (for the reflections from plate $z = 0$) (see Figure 5.2).

5.2 Total Field in an Impedance Unbroken Waveguide

As is well known [21, 22], the secondary (reflected) field in an unbroken waveguide can be determined from the wave equation for the Hertzian potential vector:

$$\nabla^2\Pi_z^r(x, y, z) + k^2\Pi_z^r(x, y, z) = 0 \tag{5.5}$$

Multiplying (5.5) by the factor $\exp\{-i\alpha x - i\beta y\}$ and using the Fourier transform of $\Pi_z^r(\alpha, \beta, z)$, we obtain the equation for the Fourier-transformant $\Pi_z^r(\alpha, \beta, z)$

$$\left[\frac{\partial^2}{\partial z^2} + (k^2 - \alpha^2 - \beta^2)\right]\Pi_z^r(\alpha, \beta, z) = 0 \tag{5.6}$$

the solution of which can be presented as:

$$\Pi_z^r(\alpha, \beta, z) = A(\alpha, \beta)\exp\{-iKz\} \tag{5.7}$$

where $K^2 = k^2 - \alpha^2 - \beta^2$, k is the wave number $k = \dfrac{2\pi}{\lambda}$. Using the inverse Fourier transform we can obtain the reflected field as

$$\Pi_z^r(x, y, z) = \frac{1}{(2\pi)^2}\int_{-\infty}^{+\infty}\int A(\alpha, \beta)e^{-iKz - i\alpha x - i\beta y}d\alpha\, d\beta \tag{5.8}$$

The first incident from the source field can be calculated using the direct Fourier transform of the free-space Green's function (5.4)

$$\Pi_z^i(\alpha, \beta, \gamma) = -\frac{4\pi i}{\omega}\mathbf{p}_z\frac{e^{i\gamma h}}{k^2 - \alpha^2 - \beta^2 - \gamma^2} \tag{5.9}$$

and the inverse Fourier transform with variable γ, after which we finally obtain the following expression:

$$\Pi_z^i(\alpha, \beta, z) = -\frac{4\pi i\mathbf{p}_z}{2\pi\omega}\int_{-\infty}^{+\infty}\frac{e^{-i\gamma(z-h)}}{K^2 - \gamma^2}d\gamma = \frac{\mathbf{D}}{2\pi}\int_C\frac{e^{-i\gamma(z-h)}}{K^2 - \gamma^2}d\gamma \tag{5.10}$$

Here, an integral along the semicircular contour C, around the pole branch points $\gamma_1 = +K$, $\gamma_2 = -K$ is introduced in Figure 5.3. Using Cauchy's theorem [23] for the branch points, we obtain the expression for the Hertzian source potential vector

$$\Pi_z^i(\alpha, \beta, z) = \begin{cases}\dfrac{\mathbf{D}}{2iK}e^{iK(z-h)}, & z > h\\ \dfrac{\mathbf{D}}{2iK}e^{-iK(z-h)}, & z < h\end{cases} \tag{5.11}$$

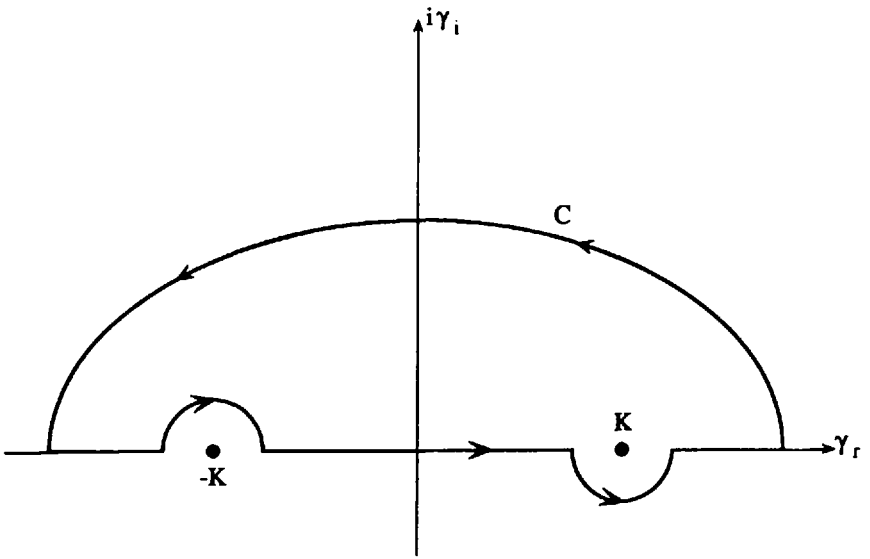

Figure 5.3 A scheme of integration paths for (5.10) in the complex K-plane.

where $\mathbf{D}$ is a constant vector, $\mathbf{D} = -\dfrac{4\pi i}{\omega}\mathbf{p}_z$. Now the field from the source (first field) can be presented as:

$$\Pi_z^i(x, y, z) = \frac{1}{(2\pi)^2}\int_{-\infty}^{+\infty}\int \Pi(\alpha, \beta)e^{\pm iK(z-h)-i\alpha x-i\beta y}d\alpha\, d\beta \qquad (5.12)$$

where sign "+" corresponds to $z > h$, sign "−" to $z < h$.

The total field in the unbroken waveguide can be rewritten in the following form:

$$\begin{aligned}\Pi_z(x, y, z) = &\frac{1}{2\pi^2}\int A(\alpha, \beta)e^{-iKz-i\alpha x-i\beta y}d\alpha\, d\beta \\ &+ \frac{1}{(2\pi)^2}\int \Pi(\alpha, \beta)e^{\pm iK(z-h)-i\alpha x-i\beta y}d\alpha\, d\beta\end{aligned} \qquad (5.13)$$

Here, as can be seen from (5.13), $\Pi(\alpha, \beta) = \dfrac{D}{2iK}$; $A(\alpha, \beta)$ is determined from boundary conditions, $D = |\mathbf{D}|$.

Let us now evaluate the boundary conditions in the impedance unbroken waveguide. It is well known that the electric and magnetic fields of an EM-wave relate to the Hertzian vector by formulas presented in Section 2.3:

$$\mathbf{E} = \nabla(\nabla \cdot \Pi_z) + k^2\Pi_z, \quad \mathbf{H} = -ik\nabla \times \Pi_z \tag{5.14}$$

from which we obtain:

$$\begin{aligned} E_x &= \frac{\partial^2 \Pi_z}{\partial x \partial z}, & H_x &= -ik\frac{\partial \Pi_z}{\partial y} \\ E_y &= \frac{\partial^2 \Pi_z}{\partial y \partial z}, & H_y &= ik\frac{\partial \Pi_z}{\partial x} \\ E_z &= \frac{\partial^2 \Pi_z}{\partial z^2} + k^2\Pi_z, & H_z &= 0 \end{aligned} \tag{5.15}$$

Using the boundary condition

$$E_y = Z_{EM}H_x, \quad E_x = -Z_{EM}H_y \tag{5.16}$$

we finally obtain at the boundaries $z = 0$ and $z = a$, respectively

$$\frac{\partial \Pi_z}{\partial z} = -ikZ_{EM}\Pi_z, \quad -\frac{\partial \Pi_z}{\partial z} = -ikZ_{EM}\Pi_z \tag{5.17}$$

Then, from (5.11) and (5.17) one can obtain:
for plane $z = 0$

$$\frac{\partial \Pi_z}{\partial z} + ikZ_{EM}\Pi_z = 0$$

or

$$(-ik + ikZ_{EM})A(\alpha, \beta) + (iK + ikZ_{EM})\Pi(\alpha, \beta) = 0$$

from which

$$A(\alpha, \beta) = \frac{1}{2iK}\frac{(K + kZ_{EM})}{(K - kZ_{EM})} = \frac{R_1}{2iK} \tag{5.18}$$

for plane $z = a$

$$-\frac{\partial \Pi_z}{\partial z} + ikZ_{EM}\Pi_z = 0$$

or

$$e^{iKa}[iK\Pi(\alpha, \beta) - ikZ_{EM}\Pi(\alpha, \beta)] + e^{-iKa}[-iKA(\alpha, \beta) - ikZ_{EM}A(\alpha, \beta)] = 0$$

from which

$$A(\alpha, \beta) = \frac{e^{2iKa}}{2iK}\frac{(K - kZ_{EM})}{(K + kZ_{EM})} = \frac{R_2 e^{2iKa}}{2iK} \tag{5.19}$$

Finally, the total field in the impedance unbroken waveguide can be presented as:
for $z = 0$

$$\Pi_z(x, y, z) = \frac{1}{(2\pi)^2}\iint R_1\Pi(\alpha, \beta)e^{-iKz - i\alpha x - i\beta y}d\alpha\, d\beta + \frac{1}{(2\pi)^2}\iint \Pi(\alpha, \beta)e^{-iK(z-h) - i\alpha x - i\beta y}d\alpha\, d\beta \tag{5.20}$$

for $z = a$

$$\Pi_z(x, y, z) = \frac{1}{(2\pi)^2}\iint R_2\Pi(\alpha, \beta)e^{iK(z+2a) - i\alpha x - i\beta y}d\alpha\, d\beta + \frac{1}{(2\pi)^2}\iint \Pi(\alpha, \beta)e^{iK(z-h) - i\alpha x - i\beta y}d\alpha\, d\beta \tag{5.21}$$

We shall use (5.8), (5.20), and (5.21) for the construction of the average field in the discrete multislit waveguide.

5.3 EM-Waves *n*-Times Reflected From the Screens in a Two-Dimensional Broken Waveguide

Here we consider a two-dimensional case without taking into account the effect of reflection from the road, which will be done in Section 5.5. We

assume that screens (walls) and slits (gaps between buildings) are distributed according to the Poisson law (see (5.3)). Reflection and diffraction from screens and their corners is taken into account by introducing the special *telegraph signal functions* $f_1(y)$ and $f_2(y)$ defined for the first and the second waveguide walls, respectively, as [16–19]

$$f_{1,2}(y) = \begin{cases} 1, \text{ on the screen} \\ 0, \text{ on the slit} \end{cases} \tag{5.22}$$

Next, we introduce the image sources as presented in Figure 5.2 and denote them for the reflections from surface $z = a$ by the symbol "+" and for the reflections from surface $z = 0$ the symbol "–." In the first stage we construct the reflected wave fields when the first reflection takes place from the waveguide wall $z = a$. From geometrical construction we define $r_1 = [(a - h)^2 + y_1^2]^{1/2}$; $y_1 = y_M(a - h)/(2a - h - z)$, from which we have a new calculated argument y_1 for the function f_1. Thus, the first wave field reflected from the plate $z = a$ at the point M on the image surface inside the waveguide and along the z-axis is:

$$\Pi_{z_1}^{+} \sim \frac{e^{ikr_1}}{r_1} f_1\left[\frac{(a - h)y_M}{2a - h - z}\right] \tag{5.23}$$

Using the same geometrical considerations for the second reflection from the wall, $z = 0$ (the corresponding image source is Π_2^+) in the derivation of $r_2 = [(2a - h)^2 + y_2^2]^{1/2}$, $y_2 = y_N(2a - h)/(2a - h + z)$, we obtain for the twice-reflected field at the point N inside the waveguide along the z-axis:

$$\Pi_{z_2}^{+} \sim \frac{e^{ikr_2}}{r_2} f_1\left[\frac{(a - h)y_N}{2a - h + z}\right] f_2\left[\frac{(2a - h)y_N}{2a - h + z}\right] \tag{5.24}$$

After the third reflection from the upper plate $z = a$ we obtain at point P for the function f_1 a new argument $y_3 = y_P(3a - h)/(4a - h - z)$, $r_3 = [(3a - h)^2 + y_3^2]^{1/2}$, (Figure 5.2), and the contribution from the third image source $\Pi_{z_3}^{+}$ is:

$$\Pi_{z_3}^{+} \sim \frac{e^{ikr_3}}{r_3} f_1\left[\frac{(a - h)y_P}{4a - h - z}\right] f_2\left[\frac{(2a - h)y_P}{4a - h - z}\right] f_1\left[\frac{(3a - h)y_P}{4a - h - z}\right] \tag{5.25}$$

Following the same procedure by the induction method, we obtain for the n-time reflected wave field, when the first reflection takes place from the plate $z = a$, the following expressions:
for even $n = 2m$, $m = 1, 2, 3 \ldots$

$$\Pi^{+}_{z_n} \sim \frac{e^{ikr_n}}{r_n} f_1\left[\frac{(a-h)y}{na-h+z}\right] f_2\left[\frac{(2a-h)y}{na-h+z}\right] \times \ldots \\ f_1\left[\frac{((n-1)a-h)y}{na-h+z}\right] f_2\left[\frac{(na-h)y}{na-h+z}\right] \tag{5.26a}$$

for odd $n = 2m + 1$, $m = 1, 2, 3, \ldots$

$$\Pi^{+}_{z_n} \sim \frac{e^{ikr_n}}{r_n} f_1\left[\frac{(a-h)y}{(n+1)a-h-z}\right] f_2\left[\frac{(2a-h)y}{(n+1)a-h-z}\right] \times \ldots \\ f_2\left[\frac{((n-1)a-h)y}{(n+1)a-h-z}\right] f_1\left[\frac{(na-h)y}{(n+1)a-h-z}\right] \tag{5.26b}$$

The same procedure can be used for the first reflection taking place from the second waveguide wall $z = 0$ (i.e., for the image sources Π^{-}_{n} (see Figure 5.2)). After similar geometric consideration we obtain the following expressions:
for even $n = 2m$, $m = 1, 2, 3, \ldots$

$$\Pi^{-}_{z_n} \sim \frac{e^{ikr'_n}}{r'_n} f_2\left[\frac{hy}{na+h-z}\right] f_1\left[\frac{(a+h)y}{na+h-z}\right] \times \ldots \\ f_2\left[\frac{((n-2)a+h)y}{na+h-z}\right] f_1\left[\frac{((n-1)a+h)y}{na+h-z}\right] \tag{5.27a}$$

for odd $n = 2m + 1$, $m = 1, 2, 3, \ldots$

$$\Pi^{-}_{z_n} \sim \frac{e^{ikr'_n}}{r'_n} f_2\left[\frac{hy}{(n-1)a+h+z}\right] f_1\left[\frac{(a+h)y}{(n-1)a+h+z}\right] \times \ldots \\ f_1\left[\frac{((n-2)a+h)y}{(n-1)a+h+z}\right] f_2\left[\frac{((n-1)a+h)y}{(n-1)a+h+z}\right] \tag{5.27b}$$

5.4 The Average Field in the Impedance Two-Dimensional Multislit Waveguide

As is shown in [16–19], the statistical moments of the reflected field inside the multislit waveguide relate to the statistical moments of *telegraph signal functions* $f_1(y)$ and $f_2(y)$ defined by (5.22) using the procedure

$$\langle f_i(y)\rangle = \chi = \frac{L}{L+l}, \quad i = 1, 2 \tag{5.28a}$$

$$\langle f_i(y_1) f_i(y_2)\rangle = \chi^2 K(y_1 - y_2) \tag{5.28b}$$

$$\langle f_i(y_1) f_i(y_2) f_i(y_3)\rangle = \chi^3 K(y_1 - y_2) K(y_2 - y_3) \tag{5.28c}$$

$$\langle f_i(y_1) f_i(y_2) \ldots f_i(y_2)\rangle = \chi^n \prod_{n=1}^{n-1} K(y_{n-1} - y_n) \tag{5.28d}$$

where $K(w)$ is the correlation function of the telegraph signal functions with any variable w (the detailed description of n-order moments of such functions are presented in [16–18])

$$K(w) = \chi^2 \left\{ 1 + \frac{l}{L} \exp\left[-\left(\frac{1}{L} + \frac{1}{l} \right) |w| \right] \right\} \tag{5.29}$$

Taking into account the fact that the slit and screen distributions in the street waveguide are statistically independent,

$$\langle f_1(y) f_2(y)\rangle = \langle f_1(y)\rangle \langle f_2(y)\rangle = \chi^2 \tag{5.30}$$

and using the relationships (5.28a) to (5.28c), one can derive for the n-times reflected fields the expression as a sum of two terms. The first one describes the average reflected field inside the waveguide when the first reflection was from the wall $z = a$:

$$\langle \Pi_{zn}^{+} \rangle = \frac{e^{ikr_n}}{r_n} \chi^n R^n \Pi(\alpha, \beta) e^{iK((n+1)a - z - h)} \times K^{n-2}\left(\frac{2ay}{(n+1)a - z - h} \right), \quad n = 2m + 1, \; m = 1, 2, \ldots \tag{5.31a}$$

$$\langle \Pi_{zn}^{+} \rangle = \frac{e^{ikr_n}}{r_n} \chi^n R^n \Pi(\alpha, \beta) e^{iK(na+z-h)} \times K^{n-2}\left(\frac{2ay}{na + z - h}\right), \; n = 2m, \; m = 1, 2, 3, \ldots \tag{5.31b}$$

The second term describes the average reflected field inside the waveguide when the first reflection was from the wall $z = 0$:

$$\langle \Pi_{zn}^{-} \rangle = \frac{e^{ikr_n'}}{r_n'} c^n R^n \Pi(\alpha, \beta) e^{iK((n-1)a+z+h)} \times K^{n-2}\left(\frac{2ay}{(n-1)a + z + h}\right), \; n = 2m + 1, \; m = 1, 2, \ldots \tag{5.32a}$$

$$\langle \Pi_{zn}^{-} \rangle = \frac{e^{ikr_n'}}{r_n'} c^n R^n \Pi(\alpha, \beta) e^{iK(na-z+h)} \times K^{n-2}\left(\frac{2ay}{na - z + h}\right), \; n = 2m, \; m = 1, 2, \ldots \tag{5.32b}$$

Here $R = \dfrac{K - kZ_{EM}}{K + kZ_{EM}}$ is the coefficient of reflections from the impedance walls. Next we estimate the values of $K^{n-2}(Z)$ in (5.31) to (5.32). For example:

$$K^{n-2}\left(\frac{2ay}{na + \alpha}\right) = \left\{1 + \frac{l}{L}\exp\left[-\frac{2ay}{na + \alpha}\left(\frac{1}{L} + \frac{1}{l}\right)\right]\right\}^{n-2} \tag{5.33}$$

For the moderate or small values of n, and for $y >> (L + l)$, we obtain

$$\frac{2ay}{na + \alpha}\left(\frac{1}{L} + \frac{1}{l}\right) >> 1, \; K^{n-2}\left(\frac{2y}{n}\right) \approx 1 \tag{5.34}$$

In the opposite case, when $2y/(\chi nl) << 1$ (large values of n), we obtain

$$\frac{2ay}{na + \alpha}\left(\frac{1}{L} + \frac{1}{l}\right) << 1, \; K^{n-2}\left(\frac{2y}{n}\right) \approx \frac{1}{\chi^{n-2}}\exp\left[-\frac{2y}{L}\right] << 1 \tag{5.35}$$

We finally note that in (5.31) to (5.32) with great accuracy $K^{n-2}(Z) = 1$.

Using this fact and after some straightforward calculations, we can present the spatial spectrum of an average n-time reflected field in the following form:

$$\Pi(\alpha, \beta, z) = \frac{D}{2iK}\left\{\left[\frac{\chi^2 R^2 e^{iK(2a-h)} + \chi R e^{iKh}}{1 - \chi^2 R^2 e^{i2Ka}}\right] e^{iKz} + \left[\frac{\chi^2 R^2 e^{iKh} + \chi R e^{-iKh}}{1 - \chi^2 R^2 e^{i2Ka}}\right] e^{iK(2a-z)}\right\} \tag{5.36}$$

Using the inverse Fourier transform for the second (reflected) field (5.36) and the direct field transformation:
for $z < h$

$$\Pi_z^i(\alpha, \beta, z) = \Pi(\alpha, \beta) e^{-iK(z-h)} \tag{5.37a}$$

for $z > h$

$$\Pi_z^i(\alpha, \beta, z) = \Pi(\alpha, \beta) e^{iK(z-h)} \tag{5.37b}$$

one can obtain the same integrals as in (4.21), which now describe the total field in the broken multislit waveguide:
for $z < h$

$$\Pi_z(x, y, z) = \frac{1}{(2\pi)^2} \int_{-\infty}^{+\infty}\int d\alpha\, d\beta \frac{D}{2iK} e^{-i\alpha x - i\beta y} \times \left\{\left[\frac{\chi R(\chi R e^{iK(2a-h)} + e^{iKh})}{1 - \chi^2 R^2 e^{i2Ka}}\right] e^{iKz} + \left[\frac{\chi R e^{iK(2a-h)} + e^{iKh}}{1 - \chi^2 R^2 e^{i2Ka}}\right] e^{-iKz}\right\} \tag{5.38a}$$

for $z > h$

$$\Pi_z(x, y, z) = \frac{1}{(2p)^2} \int_{-\infty}^{+\infty}\int d\alpha\, d\beta \frac{D}{2iK} e^{-i\alpha x - i\beta y} \times \left\{\left[\frac{\chi R(\chi R e^{iK(2a+h)} + e^{iK(2a-h)})}{1 - \chi^2 R^2 e^{i2Ka}}\right] e^{-iKz} + \left[\frac{\chi R e^{iKh} + e^{-iKh}}{1 - \chi^2 R^2 e^{i2Ka}}\right] e^{iKz}\right\} \tag{5.38b}$$

To evaluate these integrals, one can introduce the polar coordinate system: $\alpha = \rho\cos\varphi$; $\beta = \rho\sin\varphi$; $x = r\cos\psi$; and $y = r\sin\psi$, take into account the following form of the Bessel function $J_0(z)$ representation [23]:

$$J_0(\rho r) = \frac{1}{2\pi} \int_{0+\psi}^{2\pi+\psi} e^{-i\rho r \cos w} dw \tag{5.39}$$

Finally, we can rewrite the integrals (5.38a) to (5.38b) as follows:

$$\Pi_z(x, y, z) = \frac{D}{4\pi i} \int_0^{\infty} \frac{\rho F_1(\rho) J_0(\rho r)}{\sqrt{k^2 - \rho^2}} d\rho \tag{5.40a}$$

$$\Pi_z(x, y, z) = \frac{D}{4\pi i} \int_0^{\infty} \frac{\rho F_2(\rho) J_0(\rho r)}{\sqrt{k^2 - \rho^2}} d\rho \tag{5.40b}$$

Here, $F_1(\rho)$ and $F_2(\rho)$ are the functions in brackets in (5.38a) and (5.38b), respectively, where value K is replaced by $\sqrt{k^2 - \rho^2}$. Now, taking into account the relationship between the Bessel function, $J_0(z)$, and the first order, $H_0^{(1)}(z)$, and the second order, $H_0^{(2)}(z)$, Hankel functions, where $H_0^{(1)}(z) = -H_0^{(2)}(-z)$, that is, $J_0(z) = [H_0^{(1)}(z) + H_0^{(2)}(z)]/2$, we can rewrite the integrals in (5.40a) to (5.40b) in the simplified form:

$$\Pi_z(x, y, z) = \frac{D}{4\pi i} \int_0^{\infty} \frac{\rho F_{1,2}(\rho) H_0^{(1)}(\rho r)}{\sqrt{k^2 - \rho^2}} d\rho \tag{5.41}$$

The integrals (5.41) can be separated into two parts: the integral along the deformed contour C, on which the subintegrand function is analytic, and the integral along a branch cut contour γ near the poles, depicted in Figure 5.4. Here taking into account the requirement for the integrals (5.41) to be finite, the condition $\operatorname{Im} K > 0$ must be applied (i.e., the contour C must be closed in the upper-half plane as presented in Figure 5.4).

The discrete spectrum of total field. The integral along the closed contour C in the upper-half plane presents the discrete spectrum of the total field inside the multislit waveguide and can be calculated using Cauchy's theorem:

$$\oint_C = 2\pi i \sum_{n=0}^{\infty} \operatorname{Res}[H_0^{(1)}(\rho r) \rho F_{1,2}(\rho); \rho_n] \tag{5.42}$$

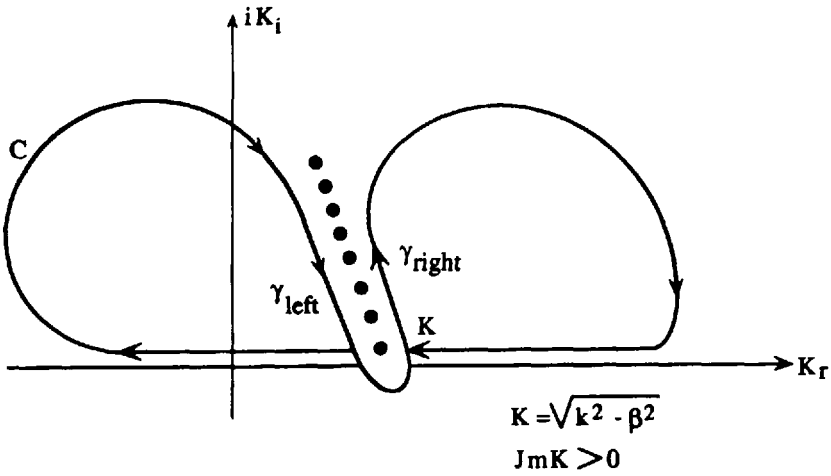

Figure 5.4 A scheme of integration paths for (5.41) in the complex K-plane.

The pole points are determined from the equation

$$1 - \chi^2 R^2 e^{i2Ka} = 0$$

from which the pole coordinates are determined:

$$\rho_n = (k^2 - K_n^2)^{1/2};\ K_n = \pm\frac{\pi n}{a} + i\frac{\ln|\chi|}{a} - \frac{\varphi_n}{a} = \mathrm{Re}K_n + \mathrm{Im}K_n, \quad (5.43)$$

$$n = 1, 2, 3, \ldots$$

Here, $R_n = \dfrac{K_n - kZ_{EM}}{K_n + kZ_{EM}}$ is the coefficient of reflection of normal modes in the impedance ($Z_{EM} \neq 0$) multislit waveguide, where φ_n is the phase, $|R_n|$ is the modulus:

$$|R_n| = \frac{\sqrt{[(\mathrm{Re}K_n)^2 + (\mathrm{Im}K_n)^2 - (kZ_{EM})^2]^2 + 4(\mathrm{Im}K_n)Z_{EM}^2}}{(\mathrm{Re}K_n + kZ_{EM})^2 + (\mathrm{Im}K_n)^2} \quad (5.44)$$

$$\varphi_n = \tan^{-1}\frac{2\mathrm{Im}K_n kZ_{EM}}{(\mathrm{Re}K_n)^2 + (\mathrm{Im}K_n)^2 - (kZ_{EM})^2}$$

Using formulas (5.42) to (5.44), one finally can obtain for the discrete spectrum for the case $z > h$

$$\Pi_z(x, y, z) = \frac{D}{2a} \frac{H_0^{(1)}(\rho_n r)}{\left[R_n - 2\dfrac{kZ_{EM}}{(K_n + kZ_{EM})^2}\right]} \times \left\{2R_n \cos[K_n(z-h)] + \frac{1}{\chi}[e^{-iK_n(z+h)} + e^{iK_n(z+h-2a)}]\right\} \tag{5.45a}$$

and for the case $z < h$

$$\Pi_z(x, y, z) = \frac{D}{2a} \frac{H_0^{(1)}(\rho_n r)}{\left[R_n - 2\dfrac{kZ_{EM}}{(K_n + kZ_{EM})^2}\right]} \times \left\{R_n e^{iK_n(z-h-a)} + e^{-iK_n(z+h+a)} + e^{iK_n(z+h-3a)} + \frac{1}{R_n} e^{-iK_n(z-h+3a)}\right\} \tag{5.45b}$$

Each index n in the poles (5.43) corresponds to a waveguide mode of an average reflected field. It is easy to show that for $r/a >> 1$, this discrete waveguide mode spectrum can be significantly simplified. Thus, for the case $z > h$ we obtain:

$$\Pi^d \approx \frac{C}{\sqrt{r}} \exp(i\rho_n^{(0)} r) \exp\left[-\frac{|\ln \chi R_n|}{\rho_n^{(0)} a}\left(\frac{\pi n - \varphi_n}{a}\right) r\right] \tag{5.46}$$

where $\rho_n^{(0)} = \sqrt{k^2 - \left(\dfrac{n\pi}{a}\right)^2}$, C = constant.

For the case of a perfectly conductive multislit waveguide model (i.e., in the case when $Z_{EM} = 0$ and $|R_n| = 1$, $\varphi_n = 0$), one can obtain from (5.45a) and (5.46) for $z > h$, respectively:

$$\Pi_z(x, y, z) = \frac{D}{2a} H_0^{(1)}(\sqrt{k^2 - K_n^2}\, r) \times \left\{2\cos[K_n(z-h)] \frac{1}{c}[e^{-iK_n(z+h)} + e^{iK_n(z+h-2a)}]\right\} \tag{5.47}$$

$$\Pi^d \approx \frac{C}{\sqrt{r}} \exp(i\rho_n^{(0)} r) \exp\left[-\frac{|\ln \chi|}{\rho_n^{(0)} a}\left(\frac{\pi n}{a}\right) r\right] \tag{5.48}$$

These formulas are the same as those obtained for the case of a perfectly conductive multislit waveguide and are presented for the case $z > h$ in [17].

In both waveguides the modes of the discrete spectrum attenuate exponentially inside the broken multislit waveguide according to (5.46) and (5.48) and their extinction lengths can be obtained from (5.46) using the assumption that it is a length on which the field decay level is ~exp(−1), or:

$$\exp\left[-\frac{|\ln \chi R_n|}{\rho_n^{(0)} a}\left(\frac{\pi n - \varphi_n}{a}\right)\zeta_n\right] = \exp(-1) \tag{5.49a}$$

from which we have

$$\zeta_n = \frac{\rho_n^{(0)} a}{\left(\frac{\pi n - \varphi_n}{a}\right)\ln|\chi R_n|} \tag{5.49b}$$

The extinction lengths depend on the number of reflections n, on the waveguide (street) width a, on the parameter of brokenness χ, and on the parameters of the wall's surface electric properties R_n. For the case of an unbroken perfectly conductive waveguide ($\chi \to 1$, $R_n \to 1$) it follows from (5.49) that $\zeta_n \to \infty$ and normal modes propagate as waves in an ideal waveguide without attenuation [21, 22]:

$$\Pi_n \sim \frac{2\pi P_z}{a\omega}\left[H_0^{(1)}(kr) + H_0^{(1)}\left(\sqrt{k^2 - \left(\frac{\pi n}{a}\right)^2}\, r\right)\cos\left(\frac{\pi n h}{a}\right)\cos\left(\frac{\pi n z}{a}\right)\right] \tag{5.50}$$

In the case of the impedance waveguide ($|R_n \neq 1|$), the character of reflected mode attenuation depends on the real values of the electrical impedance Z_{EM}. With increasing Z_{EM} ($Z_{EM} > 0$) the extinction length becomes smaller and the normal waves in the impedance multislit waveguide attenuate faster than in the case of the perfectly conductive multislit waveguide. Results of calculations of the extinction length ζ_n, as a function of the number of reflections, n, and the parameter of brokenness, χ, are presented in Figure 5.5. The same decrease of ζ_n is observed with an increase in the number of reflections n: the normal reflected modes in a multislit waveguide with numbers $n \geq 5$ attenuate very quickly (the corresponding extinction length ζ_n decreases). On the other hand, increasing the value of χ (decreasing the distances between buildings) leads to a decrease of the reflected wave attenuation factor (see Figure 5.5). In the limit of an unbroken waveguide ($\chi = 1$) the normal waves with numbers $n < 5$ (the main reflected modes) also propagate without appreciable (independent of parameter Z_{EM}) attenuation at large distances.

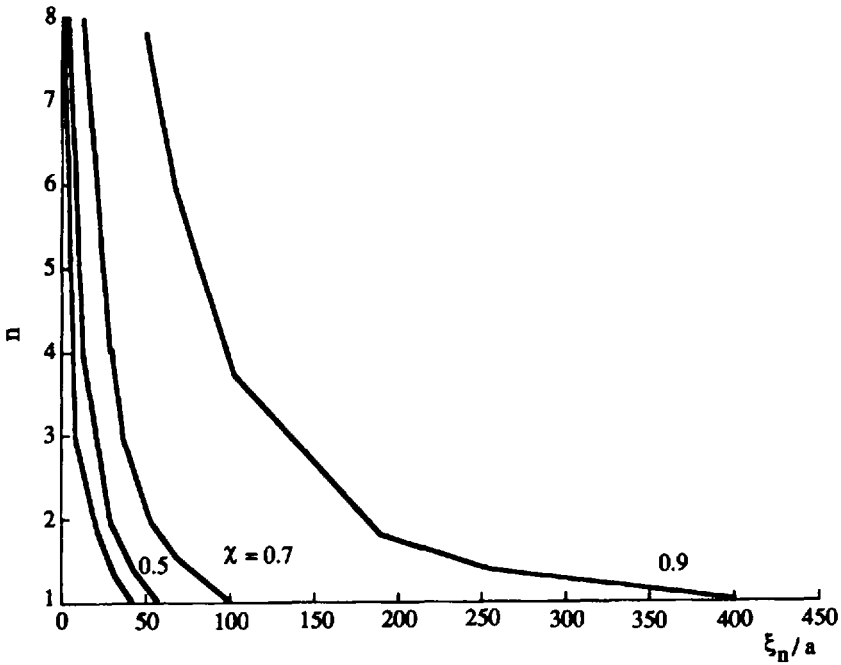

Figure 5.5 The extinction length ς_n, as a function of the number of reflections, n, and the parameter of brokenness, χ, in the case of the perfectly conductive waveguide.

The continuous spectrum of total field. A continuous spectrum has been evaluated from integration along the contour γ around the branch points (see Figure 5.4). We will examine this integral for the case $z > h$, adding it to the source field (5.37b), which is also found from the contour integral with branch-cut point $\rho = k$:

$$\Pi_z^i = \frac{1}{8\pi}\left(\int_{\gamma left} + \int_{\gamma right} \right) H_0^{(1)}(\rho r) \frac{iD}{\sqrt{k^2 - \rho^2}} e^{i\sqrt{k^2-\rho^2}(z-h)} \rho \, d\rho \quad (5.51)$$

Then, the continuous part of the total field can be presented as

$$\Pi_z^c = \frac{D}{8\pi i}\left(\int_k^{i\infty} + \int_{i\infty}^{k} \right) \frac{H_0^{(1)}(\rho r)}{\sqrt{k^2 - \rho^2}} [e^{i\sqrt{k^2-\rho^2}(z-h)} + P(z)] \rho \, d\rho \quad (5.52)$$

Here,

$$P(z) = \frac{\chi^2 R^2 e^{iK(2a-h)} + e^{iKh}}{1 - \chi^2 R^2 e^{i2Ka}} e^{iKz} + \frac{\chi^2 R^2 e^{iK(2a+h)} + e^{iK(2a-h)}}{1 - \chi^2 R^2 e^{i2Ka}} e^{-iKz} \tag{5.53}$$

Transforming the sum of two integrals in (5.52) to one integral, we obtain:

$$\Pi^e = \frac{D}{8\pi i} \int_k^{i\infty} \frac{H_0^{(1)}(\rho r)}{\sqrt{k^2 - \rho^2}} Q(z) \rho \, d\rho \tag{5.54}$$

where

$$\begin{aligned} Q(z) = {} & \frac{(\chi R e^{iKh} + e^{-iKh})(\chi R e^{iK(2a-z)} + e^{iKz})}{1 - \chi^2 R^2 e^{i2Ka}} \\ & + \frac{(\chi R e^{-iKh} + e^{iKh})(\chi R e^{-iK(2a-z)} + e^{-iKz})}{1 - \chi^2 R^2 e^{i2Ka}} \end{aligned} \tag{5.55}$$

This formula describes the continuous radiation (i.e., average continuous spectrum inside the multislit waveguide). We now transform the integration variables by including new arguments (see Figure 5.6): $\rho = k + is^2$; $d\rho = 2is\,ds$; $s = \exp\left\{-i3\frac{\pi}{4}\right\}(k - \rho)^{1/2}$. For these arguments we have a branch-cut point $s = \exp\left\{i\frac{\pi}{4}\right\}(2k)^{1/2}$ and poles $s^2 = ik \pm (-k^2 + [i \ln \chi |R_n|/a + (n\pi - \varphi_n/a)]^2)^{1/2}$, $\operatorname{Im}\left[\exp\left\{i3\frac{\pi}{4}\right\}(2k + is^2)^{1/2}\right] > 0$.

Using Cauchy's formula for the poles, we transform the integral (5.54) into the Fresnel integral [23]:

$$I_F(r) = \int_0^{\infty} \frac{\exp\left[-s^2 a\left(\frac{r}{a}\right)\right]\sqrt{a}}{s^2 a + \frac{(1 - \chi^2 R_n^2)^2}{4\chi^2 R_n^2 (\sqrt{2ka}\, e^{i\pi/4})^2}} ds \tag{5.56}$$

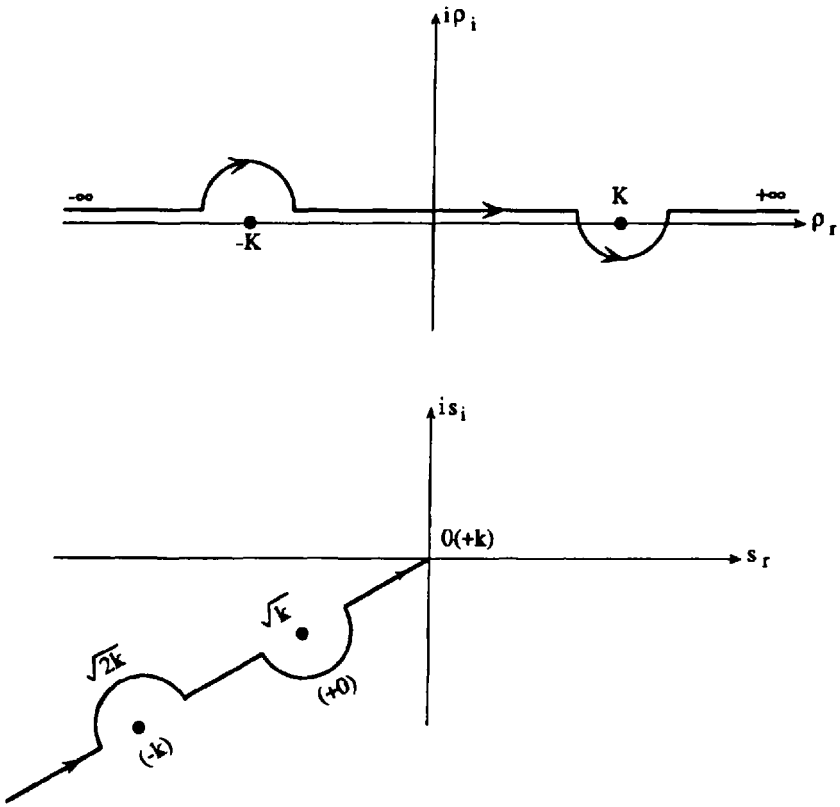

Figure 5.6 The transform of the integration variable $\rho = k + is^2$ by introducing a new argument $s = \exp\{-i3\pi/4\}(k - \rho)^{1/2}$.

From this integral for the case $r/a >> 1$ using the asymptotic approximation $H_0(\rho r) \sim (-2i/\pi\rho r)^{1/2}\exp\{i\rho r\}$, one can easily derive the continuous spectrum of the total field

$$\Pi^c \approx \sqrt{2}De^{i\frac{3\pi}{4}}\frac{1-\chi|R_n|}{1+\chi|R_n|}\frac{e^{ikr}}{4\pi r} \tag{5.57a}$$

For the case of a perfectly conductive multislit waveguide when $|R_n| = 1$, and $Z_{EM} = 0$, we can obtain from (5.57a) the same formula presented in [17]:

$$\Pi^c \approx \sqrt{2}De^{i\frac{3\pi}{4}}\frac{1-\chi}{1+\chi}\frac{e^{ikr}}{4\pi r} \tag{5.57b}$$

As can be seen from formulas (5.57a) to (5.57b) in the broken waveguide, the continuous part of the total field propagates as a spherical wave $\sim\frac{e^{ikr}}{r}$, and reduces to the unbroken waveguide case in the limit $\chi = 1$. But, if in the perfectly conductive unbroken waveguide for large distances $(r >> a)\,\Pi^c = 0$ (see (5.57b)), in the impedance unbroken waveguide the continuous part Π^c of total field does not vanish because for the case $\chi = 1$ and $|R_n| \neq 1$, the function Π^c, as can be seen from formula (5.57), differs from zero. This is a new principal result which is absent in the case of a perfectly conductive waveguide with continuous walls.

5.5 The Total Field-Intensity Attenuation Along the Street (Three-Dimensional Model)

Let us consider that the term $\Pi_n^{(+)}$ is the field reflected from the wall with coordinate $z = a$, and the term $\Pi_n^{(-)}$ is the field reflected from the wall with coordinate $z = 0$ (see Figure 5.2); then the average total field intensity inside the waveguide can be presented in the following form:

$$\langle J\rangle = \left\{\sum_{n=1}^{\infty}[\Pi_n^{(+)} + \Pi_n^{(-)}]\sum_{m=1}^{n}[\eta_1\Pi_n^{(+)*} + \eta_2\Pi_n^{(-)*}]\right\}(|R_n| + |D_{mn}|)^2 \tag{5.58}$$

where η_1 and η_2 are wave impedances; the sign (*) denotes the inverse complex field values. Using the differential distribution (5.3), the results of the procedure of averaging for the one- and two-order moments of telegraph functions $f_{1,2}(y)$ presented above, as well as the reflection from the road (Figure 5.1) with the coefficient R_g [18], we finally obtain for the total intensity inside the multislit waveguide:

$$\begin{aligned}<J> = {} & \sum_{n=-\infty}^{\infty}\Pi_z(na)\Pi_z^*(na)(|R_n|\chi)^{|n|}\eta_1\eta_2|R_g|[1 - (|R_n|\chi)^{|n|}] \\ & + \sum_{n=-\infty}^{\infty}\eta_1\eta_2\sum_{m=0}^{\infty}(|R_n| + |D_{mn}|)^2 \\ & \times 2\,\mathrm{Re}\{\Pi_z(na)\Pi_z^*(na)[(-1)^m(2m+1)](|R_n|\chi)^{(2m+1)|n|} \\ & \times |R_g|[1 - (|R_n|\chi)^{|n|}]\}\end{aligned} \tag{5.59}$$

Using the Fourier representation of the field

$$\Pi(y) = (D/2\pi i)\int d\beta \exp\{-i\beta y + ip|z|\}/2p$$

and introducing it in (5.59), we can calculate the average field intensity

$$\begin{aligned}\langle J\rangle = \mathrm{Re}\{(D/2\pi i)^2 \int_{-\infty}^{\infty}\int_{-\infty}^{\infty} \frac{d\beta' d\beta'' \exp[-i(\beta' - \beta'')y]4a^2}{\beta(2\alpha - \beta)} [\chi|R_n|e^{\alpha}/(1 - e^{\alpha})\\ + 2(\chi|R_n|)^3 e^{\alpha+\beta}/[1 - (\chi|R_n|)^3 e^{\alpha+\beta}]\\ + |R_g|(\chi|R_n|)^4/(1 + \chi|R_n|)^4\\ + |R_g|(1 - (\chi|R_n|)^2)/(1 - (\chi|R_n|)^2)]\}(|R_n| + |D_{mn}|)^2\end{aligned} \tag{5.60}$$

Here the polar coordinates $\beta' = \rho'\cos\phi'$, $\beta'' = \rho''\cos\phi''$, and new parameters $\alpha = i(p' - p'')a$ and $\beta = -2iap''$ were introduced, where $p' = (k^2 - \beta'^2)^{1/2}$, $p'' = (k^2 - \beta''^2)^{1/2}$; R_g is the coefficient of reflection from the road surface which is also considered for the impedance surface (in [17] it was assumed that the ground surface is perfectly conductive (i.e., $|R_g| = 1$)); all other parameters were introduced above. After integrating expression (5.60) and taking into account the intensity J_0 from a vertical electrical dipole in free space, we finally obtain the normalized average intensity for the numerical calculations

$$\begin{aligned}\langle \delta J\rangle = \langle J/J_0\rangle = \{(2\pi\chi|R_n|/ka)\sin(m_\nu a)[\cot(q_2^{(1)}/4)\mathrm{sh}(kp_2^{(1)})\\ - \cot(q_1^{(1)}/4)\mathrm{sh}(kp_1^{(1)})]\\ + [6\pi(\chi|R_n|)^3/ka]\sin(l_\mu a)[\cot(q_2^{(2)}/4)\mathrm{sh}(kp_2^{(2)})\\ - \cot(q_1^{(2)}/4)\mathrm{sh}(kp_1^{(2)})]\\ + \cos(\alpha_\nu y)R_g^2[(\chi|R_n|)^4/(1 + \chi|R_n|)^4]/y^2\\ + \cos(\beta_\mu y)R_g^2[(1 - (|\chi R_n|)^2/(1 + (\chi|R_n|)^2)]^2/y^2\}(|R_n| + |D_{mn}|)^2\end{aligned} \tag{5.61}$$

Here,

$$
\begin{aligned}
q_1^{(1)} &= -|\ln\chi|R_n|| + i2\pi\nu + ika, & q_1^{(2)} &= -|\ln\chi|R_n|| + i2\pi\mu + ika \\
q_2^{(1)} &= -|\ln\chi|R_n|| + i2\pi\nu - ika, & q_2^{(2)} &= -|\ln\chi|R_n|| + i2\pi\mu - ika \\
p_1^{(1)} &= -i|\ln\chi|R_n||/a + 2\pi\nu/a + k, & p_1^{(2)} &= i|\ln\chi|R_n||/a + 2\pi\mu/a + k \\
p_2^{(1)} &= -i|\ln\chi|R_n||/a + 2\pi\nu/a - k, & p_2^{(2)} &= i|\ln\chi|R_n||/a + 2\pi\mu/a - k \\
\alpha_\nu &= (3m_\nu^2 + 4k^2)^{1/2}, & \beta_\mu &= (3l_\mu^2 + 4k^2)^{1/2} \\
m_\nu &= i|\ln\chi|R_n||/a + 2\pi\nu/a, & l_\mu &= i|\ln\chi|R_n||/a + 2\pi\mu/a, \quad \nu, \\
& & & \mu = 1, 2, 3, \ldots
\end{aligned}
\tag{5.62}
$$

In formula (5.61) the first two terms describe the multiray reflection from the walls and diffraction from the walls' edges. They present normal modes generated in the multislit waveguide, which transform into normal waves in the unbroken waveguide (when $\chi = 1$) and propagate along the waveguide with exponential attenuation at large distances. The third term describes the reflection from the ground and then the reflection from the buildings' walls. The last term describes the direct wave and then reflections from the road surface and from the walls. In the case of the real impedance unbroken waveguide, when $\chi = 1$, but $0 < |R_n| < 1$, this term does not vanish (as was obtained in [17] for a perfectly conductive waveguide). Thus, in the case of an impedance waveguide, we must take into account all waves, direct from the source, reflected from the ground and then both reflected from the walls (as schematically presented in Figure 5.2). On the other hand, for $\chi << 1$ we tend to the case of free-space propagation above the perfectly conductive flat surface. In this case, the last term is much larger than other terms and describes the interference between the direct waves and those reflected from the road, which is described by the term $\sim\cos\beta_\mu y$. The field intensity attenuates as a spherical wave $\sim y^{-2}$. This case is close to the two-rays model presented, for example, in [4–6], where the plane wave propagates above the flat perfectly conductive surface. Moreover, because earlier in [16, 17] it was shown that both the two-dimensional and three-dimensional waveguide models give sufficiently accurate results of field intensity attenuation, it is very important for the prediction of experimental data to obtain the approximate expression of average field intensity inside the impedance multislit waveguide.

Taking into account that the average intensity can be approximately presented as $<I> \sim <\Pi_z\Pi_z^*>$, and after integrating formula (5.38) for field Π_z in the limits of $x = [0, h_b]$, $y = [0, \infty]$, and $z = [0, a]$ using the same procedure as in [17], we finally obtain the approximate expression for the average field intensity at a large range from the source ($r >> a$):

$$\langle I \rangle \approx C^2 R_g^2 (|R_n| + |D_{mn}|)^2 r^{-1} \exp\{-|\ln \chi| R_n|| [(\pi n - \varphi_n)/a] r/\rho_n^{(0)} a\} + D^2 R_g^2 [(1 - (|\chi R_n|)^2)/(1 + (\chi |R_n|)^2)]^2 r^{-2} \tag{5.63}$$

Here,

$$D = |\mathbf{D}| = 4i\pi |\mathbf{p}_z|/\omega;\ C \approx (D\sqrt{\lambda}/2\sqrt{h_T h_R})[h_T h_R/a^2 + h_b/a + 1]^{-1/2}$$

The expression of the reflection coefficient R_g is presented in Section 3.2 for different kinds of radiated field polarization. The approximate waveguide model (5.63) can be successfully used to describe the field-intensity attenuation along the street in LOS conditions (see Figure 5.7, curve 2). In fact, Figure 5.7 depicts the field intensity attenuation relative to the intensity in free space at the distance 100m from the source, using the approximate model according to (5.63) (curve 2), and the strict model according to (5.61) (curve 1) for $\chi = 0.5$, $|R_g| = 0.8$ and $|R_n| = 0.8$ for the case of a wide street ($a = 50$m, $h_b = 10$m, $h_T = 8$m, $h_R = 3$m). As seen from the illustration presented in Figure 5.7, both models (strict (5.61) and approximate (5.63)) predict two modes of field-intensity attenuation, from polynomial, r^{-2} to exponential, and the existence of a break point at the range $r_b \approx 160$m–180m (according to (5.65) presented below) for $f_0 = 900$–950 MHz. Because the approximate waveguide model gives closed results with the strict waveguide model (see Figure 5.7), one can use the simple formula (5.63) to obtain the path loss in LOS conditions along straight streets with great accuracy. Therefore let us now examine (5.63) for various actual experimental situations in the urban street scene.

Wide avenues. Let us assume that the street width is larger than the average building heights and both antenna heights, that is, $a > h_b$, h_T, h_R. In this case, at distances less than the break point in the approximate formula (5.63), the second term, which describes the direct wave and the waves reflected from the ground and which attenuates as a spherical wave $\sim r^{-2}$, is larger than the first term, which describes the attenuation of the normal reflecting modes along the multislit street waveguide. Beyond the break point, conversely, the first term in (5.63) is larger, and field intensity attenuates exponentially. This law of attenuation is close to that obtained experimentally in most measurements, where the attenuation mode of field intensity beyond the break point was $\sim r^{-q}$, $q = 5$–7. According to the two-ray model [4–6], one can obtain only two modes of field-intensity decay: $\sim r^{-2}$ before and $\sim r^{-4}$ beyond the break point. Moreover, no clear physical explanation of such a rapid polynomial (with $q = 5$–7) field-intensity attenuation in the farthest zones from the transmitter existed until now. This effect can be clearly understood using the waveguide street model and following from it the exponential attenuation of field intensity (which is close to mode $\sim r^{-q}$, $q = 5$–7) at distances beyond the break point. As was shown in [17], the waveguide model continuously tends

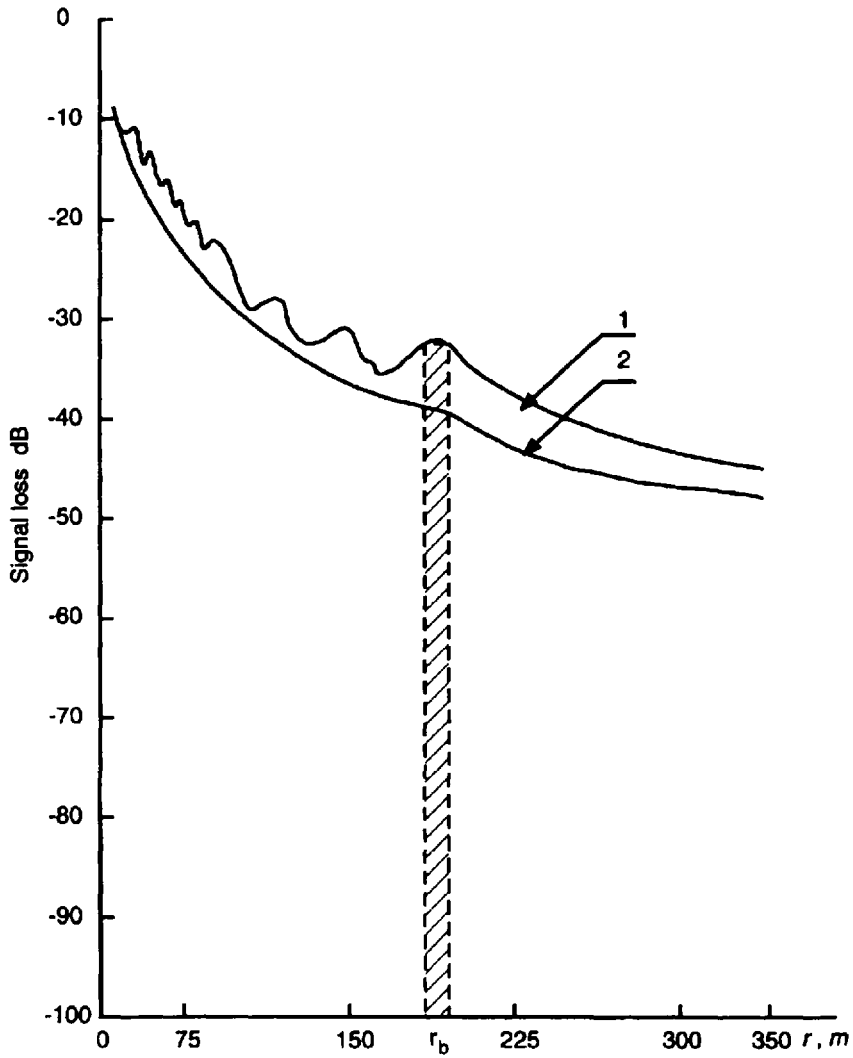

Figure 5.7 The normalized field-intensity attenuation (relative to the intensity in free space at the distance 100m from the source), using the approximate model (curve 2), and the strict model (curve 1), for $\chi = 0.5$, $|R_g| = 0.8$ and $|R_n| = 0.8$, for a wide street ($a = 50$m, $h_b = 10$m, $h_T = 8$m, $h_R = 3$m).

to the two-ray model in the case of wide streets. We can also show that the break-point range presented in [4–6], $r_b = 4h_T h_R/\lambda$, can be used to estimate the break-point range only for urban areas with wide streets (avenues). Moreover, the three-dimensional waveguide model allows us to obtain a stricter

expression for break-point range estimation, which continuously limits to the approximate formula, $r_b = 4h_T h_R/\lambda$, only for the case of $a > h_b$, h_T, h_R. In fact, let us define the break-point range as the range at which the first term in (5.63) is equal to the second one,

$$C^2 R_g^2 (|R_n| + |D_{mn}|)^2 r^{-1} \exp\{-|\ln\chi|R_n||[(\pi n - \varphi_n)/a]r/\rho_n^{(0)} a\} = D^2 R_g^2 [(1 - (|\chi R_n|)^2)/(1 + (\chi|R_n|)^2)]^2 r^{-2} \tag{5.64}$$

After the expansion of the exponent in the right-hand of (5.64) into the series $\exp\{-w\} \approx 1 - w + (1/2!)w^2 - \ldots \approx 1$ for $w << 1$ ($|\ln\chi|R_n| << 1$ and $[(\pi n - \varphi_n)/a]r/\rho_n^{(0)} a \leq 1$), and taking into account the fact that because $0 < \chi < 1$, $0 < |R_n| < 1$ and $0 < |D_{mn}| < 1$ all terms with their product are smaller than one, we finally obtain the approximate formula of break-point range for the waveguide street model

$$r_b = \frac{4h_T h_R}{\lambda} \frac{[(1 + \chi|R_n|)/(1 - \chi|R_n|)][1 + h_b/a + h_T h_R/a^2]}{(|R_n| + |D_{mn}|)^2} \tag{5.65}$$

which continuously (with constant $(|R_n| + |D_{mn}|)^2 \approx 1$ for $0 < |R_n| < 1$ and $0 < |D_{mn}| < 1$) tends to $r_b = 4h_T h_R/\lambda$ presented, for example, in [4–6] for the case when $a > h_b$ and $a^2 > h_T h_R$, (i.e., for the case of wide streets). So, in the case of a wide street, the approximate model (5.63) tends to the two-ray model [4–6], and formula (4.65) transforms into that with break-point range $r_b = 4h_T h_R/\lambda$, presented in [4–6]. We have a good transition from the waveguide model to the two-ray model in the particular case of wide avenues or canyons with building heights less than the street width.

Narrow streets. In the inverse case in an urban scene with narrow streets ($a < h_b$) the approximate waveguide model (5.63) can also be successfully used to describe the field-intensity attenuation along the street in LOS conditions (see Figure 5.7, curve 2). Additional estimations have showed that for the case of narrow streets the break point is farther from the transmitter than in the case of wide streets. For example, for the case of a narrow street with a = 10m, h_T = 8m, h_R = 3m, f_0 = 900–950 MHz, the break point has been observed at the range $r_b \approx$ 320m–330m for h_b = 10m and $r_b \approx$ 430m–440m for h_b = 20m according to (5.65).

Thus, as follows from formula (5.65) for $a << h_b$ and $a^2 < h_T h_R$, the range of the break point tends to infinity for the observed wavelength band, λ = 0.01m–0.3m with a decreasing street width or with an increasing building height. So, in the case of narrow streets the two-ray model cannot describe

the absence of break point and of two-mode field-intensity decay. In the case of narrow streets the multislit waveguide model predicts exponential attenuation of total field at the street level in microcellular propagation channels up to 2–3 km from the transmitter.

Contribution to path loss. In the impedance unbroken waveguide ($\chi = 1$) the existence of additional term (5.57) in the case of $Z_{EM} \neq 0$ ($|R_n| \neq 1$) leads to the additional losses of EM-waves propagated inside it. This is clearly seen from investigations of path loss. Thus taking into account the characteristics of a vertical electrical dipole field in free space and formulas (5.63), one can approximately obtain the path loss of radio wave intensity $\sim\langle \Pi \cdot \Pi^* \rangle$ in an impedance multislit waveguide

$$\begin{aligned} L \approx\ & 32.1 - 20 \log_{10}\left[\frac{(1 - \chi|R_n|)^2}{(1 + \chi|R_n|)^2}\right] \\ & + 17.8 \log_{10} r - 20 \log_{10}[|R_n| + |D_{mn}|] \\ & + 20 \log|R_g| - 8.6\left\{|\ln \chi|R_n||\left[\frac{\pi n - \varphi_n}{a}\right]\frac{r}{\rho_n^{(0)} a}\right\} \end{aligned} \tag{5.66a}$$

which for the case $Z_{EM} = 0$, $|R_n| = 1$, $|D_{mn}| = 1$, $\varphi_n = 0$, $|R_g| = 1$ is the same with path loss estimated for the case of perfectly conductive broken waveguide:

$$L \approx 32.1 - 20 \log_{10}\left[\frac{(1 - \chi)^2}{(1 + \chi)^2}\right] + 17.8 \log_{10} r - 8.6\left\{|\ln \chi|\left[\frac{\pi n}{a}\right]\frac{r}{\rho_n^{(0)} a}\right\} \tag{5.66b}$$

Formulas (5.66a) to (5.66b) are more general than the approximate formula obtained in [17] for the case of the two-dimensional waveguide model without taking into account the reflection from the road and actual dielectric properties of building walls.

5.6 Prediction of Loss Characteristics in LOS Conditions

Let us compare, first of all, the theoretically obtained results from formulas (5.61) to (5.63) according to the street multislit waveguide model with those obtained experimentally by the scientific group of Tadiran Telecommunications (Israel), in which the authors have taken a part as leaders both in the theoretical and experimental prediction of loss characteristics along straight streets in urban

and suburban areas. The first series of measurements were taken in the small town of Kefar-Yona, Israel, where the multigain wireless (MGW) local-loop system of Tadiran Telecommunications was under trial in conditions of direct visibility along the street (LOS conditions, see Figure 5.8). The tested environment is a typical small urban or suburban region of two- and three-story brick buildings with approximate uniform heights h = 8m–10m and with a right-angle crossing straight street plan (as schematically presented in Figure 5.8). The omnidirectional base-station antenna was located at a lower level than the buildings' roofs, at a distance of 4m–5m from the corner building surface, as depicted schematically in Figure 5.8.

The mobile omnidirectional radio-port antenna changed its position along the street in the middle of the road in LOS conditions (Figure 5.8). The tested MGW system was operated in the frequency band f = 902–928 MHz and utilized spread-spectrum (frequency hopping) digital radio communication. The base-station transmitter antenna was installed at the height $h_T \approx$ 7m; the moving radio-port antenna was also lower than rooftop level ($h_R \approx$ 2m–3m). The tested cell radius of such an area estimated from measurements was approximately 1–2 km. Field intensity measurements in decibels

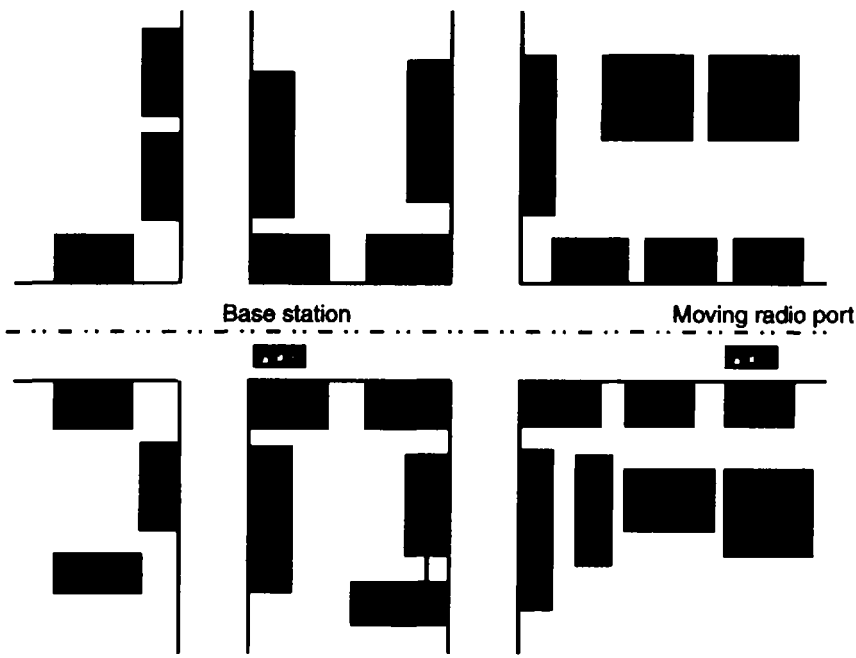

Figure 5.8 The simplified scheme of Kfar-Yona houses built on a retangular street grid and of the first experiments in LOS conditions along the street.

relative to intensity in free space at the range r = 100m (to compare with the three-dimensional waveguide model) and at the range r = 1 km (to compare with experiments carried out by Hughes [24]) were obtained to estimate the path loss and the field intensity attenuation in LOS conditions along the street.

In these estimations we take into account the actual dielectric properties of the brick walls of buildings and the real distribution of buildings along the street level. As mentioned above, the first experiments were carried out in LOS conditions where the transmitter and receiver antennas were placed at the street level with direct visibility below the roof tops, and the moving radio-port changed its distance from the stationary base station in the range 10m–300m (see Figure 5.7). In Figure 5.9, the normalized average field intensity decay in decibels (relative to the intensity in free space at the range of 100m) is presented versus the distance r from the transmitter along the street waveguide for the same conditions as presented in Figure 5.7 by curve 1 only for the strict model (5.61). The solid points correspond to experimental measurements at 920 MHz. As can be seen, the three-dimensional waveguide model (strict and approximate, because there is not sufficient difference between them, as follows from Figure 5.7) gives results which are close to experimental data and can be used for predicting the path-loss distribution and the range of the break point along the street in LOS conditions.

Now we will compare the results of theoretical prediction in LOS conditions estimated from the evaluated formulas (5.61) and (5.63) according to the street waveguide model with experimental data presented in [12] for conditions of direct visibility along the streets in the Manhattan grid-plan-street scene (New York, see [12]). Results of numerical calculations according to the strict waveguide model (5.61) (presented by a thin continuous curve in Figure 5.10) and the approximate model (5.63) (presented by a dotted curve in Figure 5.10) were compared with published experimental data [12] along Lexington Avenue in Manhattan (presented by a thick continuous curve in Figure 5.10). In our calculations we used the same conditions of measurements presented in [12] (i.e., the working frequency f_0 = 900 MHz (close to our experiment, see above)), h_T = 9.15m, h_R = 1.85m, $|R_g|$ = 0.75, $|R_n| = |D_{mn}|$ = 0.8 (ϵ = 15, σ = 7); the avenue width a = 30m; the average building height along the avenue h_b = 40m–50m. As can be seen from the illustration presented in Figure 5.10, both models, the strict (5.61) and the approximate (5.63), with a great accuracy (of 3–5 dB) predict the signal intensity decay in LOS conditions along the avenue at the distances up to the break point, located, as follows from (5.65), at the range $r_b \approx$ 500m from the transmitter. Beyond the break point a sharp signal decay is observed. This is why we can propose this range as an effective scale of a microcell in LOS conditions along the street level (see also Chapter 9).

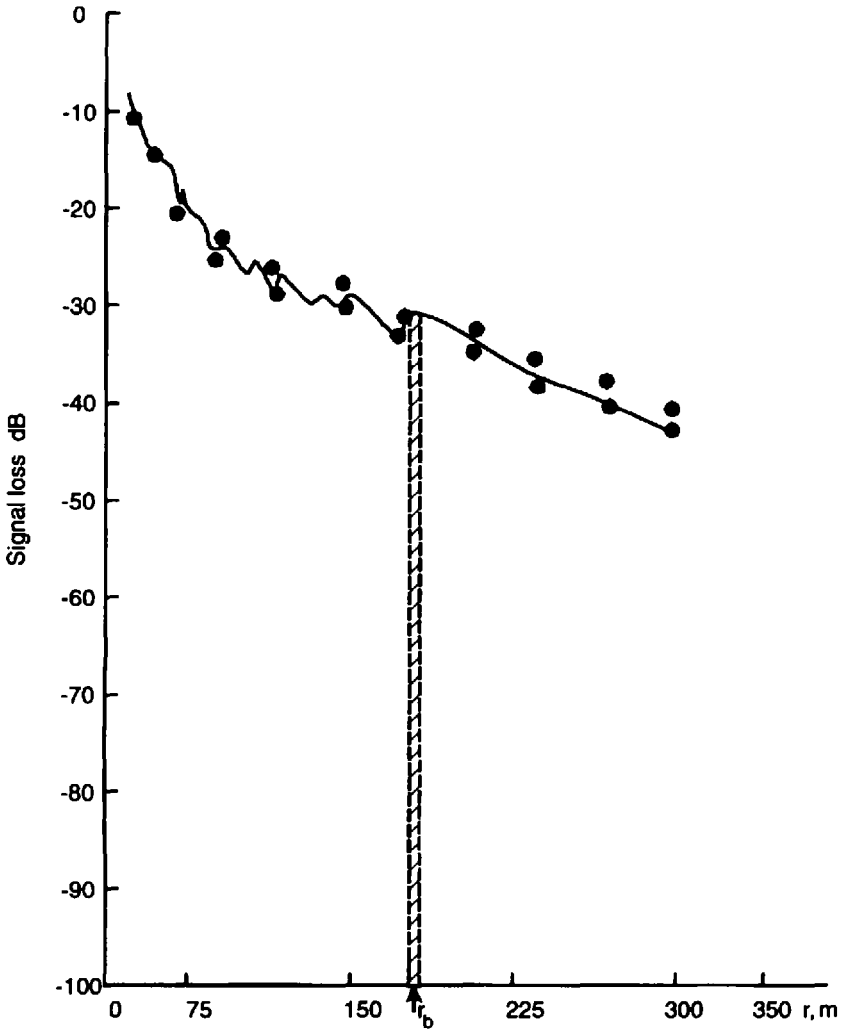

Figure 5.9 The field intensity (in decibels) versus the distance r from the transmitter (in meters). The solid curve represents the numerical calculations according the strict model (5.61) for the same conditions, as for Figure 5.7; the solid circles represent the experimental data of signal attenuation (its maximum and minimum values).

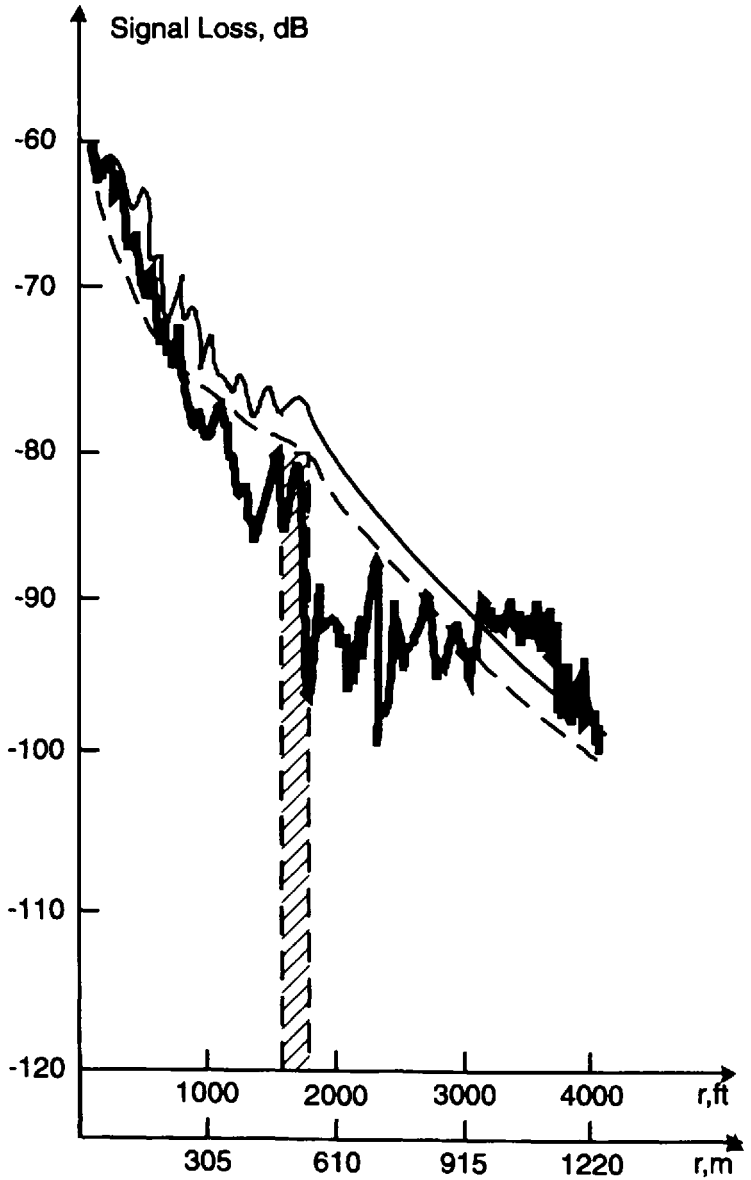

Figure 5.10 The field intensity (in decibels) versus the distance r from the transmitter (in meters). A thin continuous curve represents the strict model (5.61), a dotted curve the approximate model (5.63), a thick continuous curve is the experimental data [12]. Both calculated and measured data are presented for the same experimental conditions according to [12]: working frequency f_0 = 900 MHz, h_T = 9.15m, h_R = 1.85m, $|R_g|$ = 0.75, $|R_n|$ = 0.8 (ϵ = 15, σ = 7), a = 30m and h_b = 40m–50m.

The influence of real electrical properties of building walls can be seen in more detail from numerical calculations of the two-dimensional waveguide model according to [16, 17] presented as a family of curves in Figure 5.11 for parameters $|R_n| = 0.1$, 0.2, 0.4, 0.6 and 0.8, respectively, and $\chi = 0.8$, where I is the field intensity normalized to the wave intensity in free space at the distance $r = 1$ km from the transmitter, at a frequency $f_0 = 930$ MHz, versus the normalized distance r/a ($a = 20$m) along the street. In Figure 5.11 signs "+" and "o" correspond to experimental measurements carried out in [24] at a frequency of 936 MHz, using two mobile stations moving in two different areas of the city center. As seen from illustrations in Figure 4.11, the curves with $|R_n| > 0.5$ are closer to experimental data measured in a city area with multistory ferro-concrete buildings (depicted as "+" in Figure 5.11). The curves with $0.1 < |R_n| < 0.5$ are closer to the experimental data measured in an area with buildings of moderate height, usually constructed from bricks (depicted as "o" in Figure 5.11).

Now let us compare the results of numerical calculations obtained for the case of the two-dimensional and three-dimensional waveguide models with

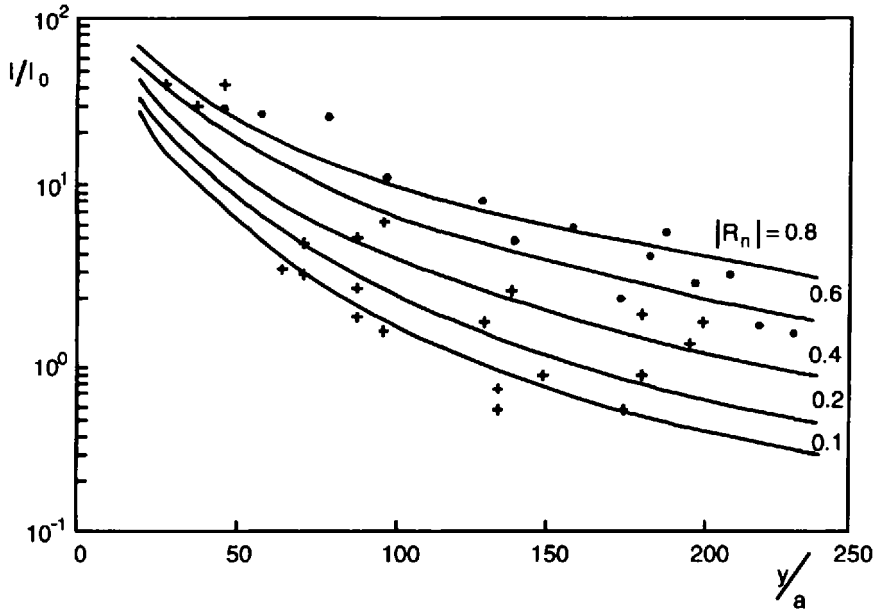

Figure 5.11 The normalized field intensity versus the normalized distance, y/a, from the base station for $\chi = 0.8$, $a = 20$m, and $|R_n| = 0.1$, 0.2, 0.4, 0.6, 0.8. Signs "+" represent measured data in a city region with multistoried ferro-concrete buildings; signs "o" represent measured data in a city region with moderate-storied brick buildings.

perfectly conductive walls ($|R_n| = 1$, $\varphi_n = 0$) with measurements carried out in the center of London in LOS conditions along straight streets [25]. Experimental data was collected using two mobile stations with antennas below the rooftops in the crossing-street center of the city [25]. This measured data is presented in Figures 5.12(a,b) as circles and crests. The circles correspond to measurements carried out in city areas with a higher density of buildings in the streets near the transmitter than the crests. Here, too, the results of the two-dimensional model are presented by the dashed curves. Those according to the three-dimensional model are presented by the continuous curves. In Figures 5.12(a,b) all curves are presented as linear functions in the logarithmic coordinate system for the both cases $\chi = 0.2$ and $\chi = 0.8$. The point where the field intensity attenuation law changes (break point) is approximately 250m–300m from the source. These results are also close to those obtained in [24], in which the position of the break point was about 250m–350m from the source. Moreover, from the results presented in Figure 5.12(a) for $\chi = 0.2$ and in Figure 5.12(b) for $\chi = 0.8$, it follows that with decreasing brokenness parameter χ the effect of transformation from the law $\sim y^{-2}$ to the exponential law becomes weaker. This fact is easily understood because with increasing parameter χ the guiding effects of waveguide are more essential and only normal waves propagate along the waveguide at large distances. At small distances the effect of interference between the direct source wave and that reflected from the ground, as in the case of wave propagation in free space above a plane surface, takes place. This result is also observed from the numerical calculations presented in Figures 5.12(a,b) at distances before the break point y_b = 250m–300m. So, using the above three-dimensional waveguide model, we obtain both the critical cases $\chi << 1$ and $\chi = 1$ and in the general case the experimentally observed break point at which the character of field intensity attenuation inside the waveguide is changed from a polynomial law with power $q = 2$ to an exponential one. We also must notice that the proposed model is correct only for distances up to 2–3 km, and only for cases $\chi > 0$, because from formula (5.63) for n-time reflected and diffracted fields from perfectly conductive buildings' walls and the road surface ($|R_n| = |D_{mn}| = |R_n| = 1$, $\varphi_n = 0$) at distances $y > y_b$

$$\ln I = \ln C - \ln r - \frac{2|\ln\chi|(\pi n/a^2)r}{[k^2 - (\pi n/a + i|\ln\chi|/a)^2]^{1/2}} \tag{5.67}$$

In the limit $\chi = 0$ formula (5.67) is not valid and a continuous transformation from the waveguide model to the free-space model does not exist. At the same time our model gives good agreement with propagation effects in the

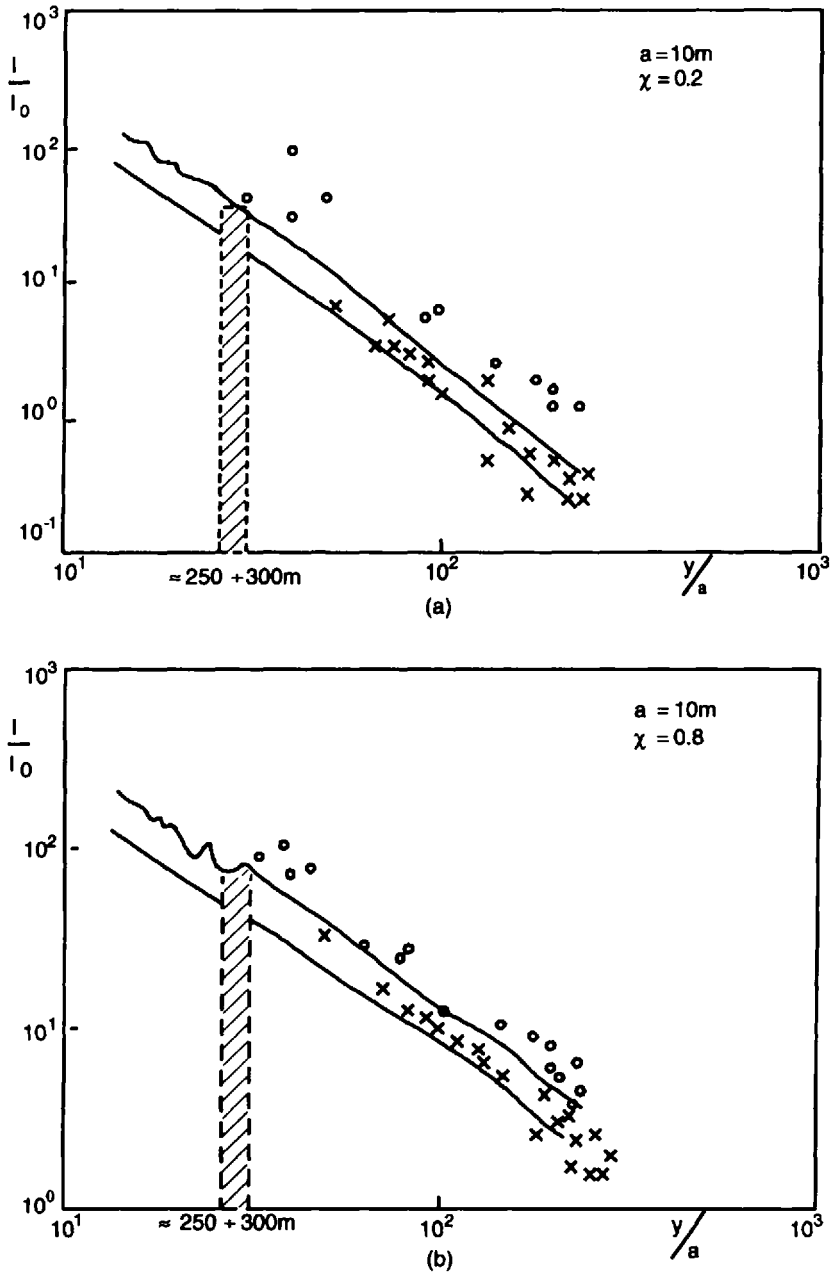

Figure 5.12 (a) The total field intensity attenuation along the street waveguide for $\chi = 0.2$ and $a = 10$m. The circles and crests represent the experimental data obtained in [25] for a city with high and low density of building, respectively. (b) The same as in Figure 5.12(a), but for $\chi = 0.8$.

ideal unbroken plate waveguide for the case $\chi = 1$, where $I \sim r^{-1}$, and the cylindrical normal waves propagate along the ideal unbroken waveguide [21, 22]. As seen from illustrations in Figures 5.12(a,b), the curves for the cases $\chi > 0.5$ (in particular $\chi = 0.8$) are closer to the experimental data obtained for a high building density (circles). The curves for the cases $\chi < 0.5$ (in particular $\chi = 0.2$) are closer to the experimental data measured in the regions with a lower building density (crests). At the same time, as seen from the comparison between the theoretical prediction models and results of measurements, the two-dimensional waveguide model obtained in [16, 17] does not explain the two different laws of field intensity attenuation before and after the break point observed experimentally [4–6, 24–28], because it does not take into account the reflection from the ground, and, hence, has no continuous limit (as has the three-dimensional model for the case $\chi << 1$) to the two-ray model, which is usually used for understanding much experimental data in LOS conditions in urban and suburban environments [4–6].

Both theoretically and experimentally obtained results give exponential attenuation of radio waves in the farthest zones from the source in LOS conditions along straight streets in regular straight street plan urban areas up to 2–3 km. Moreover, for experimentally observed ranges in the conditions of direct visibility, when both receiver and transmitter antennas are placed at the street below the rooftop level, we can use the nonregular multislit waveguide model and with great accuracy approximate formulas (5.63), (5.65) to (5.66) to estimate the propagation loss and break-point range at street level.

Summary

In this chapter we described the conditions of direct visibility between transmitter and receiver, or LOS conditions, along the straight streets in situations when both antennas, receiver and transmitter, are placed below the rooftop level above the flat terrain. The conclusions which follow from the above-presented multislit waveguide model can be described using a qualitative picture of wave propagation along the street multislit waveguide. Figures 5.13(a,b) are simple sketches that indicate the way in which the field strength of a vertical electric dipole (with pattern angle $\varphi = \pi$) may vary because of channeling street orientation. For the simplest classical case of an unbroken perfectly conductive waveguide [21, 22], the antenna pattern is not changed when the wave travels along the waveguide (see Figure 5.13(a)). In the case of a real street with randomly distributed walls (screens) and gaps (slits) the angle φ is smaller than π, because there exists losses of wave energy through the slits (see Figure 5.13(b)). In the case of a multislit street waveguide, the angle φ

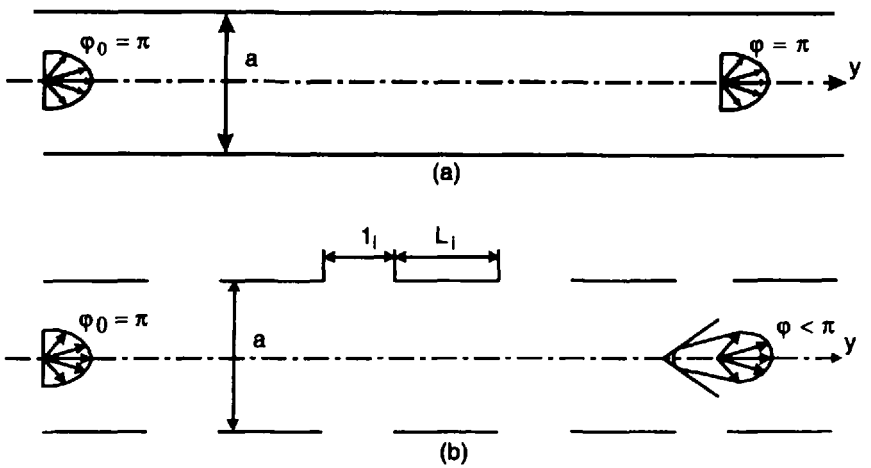

Figure 5.13 The simplified scheme of a continuous street waveguide (a); and of a broken street waveguide (b).

can be obtained from results presented in [16–19]. According to the two-dimensional waveguide model constructed in these works, the angle φ inside the multislit waveguide at the half level of field intensity can be presented for $y/a >> 1$ as:

$$\varphi = \tan^{-1}(a \cdot \log 2/y|\log\chi|R_n||) \tag{5.68}$$

Here, as above, y is the distance from the transmitter along the waveguide; a is the street width; $\chi = \langle L\rangle/(\langle L\rangle + \langle l\rangle)$ is the parameter of brokenness, $\langle L\rangle$ and $\langle l\rangle$ are the average values of screen length (L_i) and slit length (l_i), respectively; $i = 1, 2, 3, \ldots$ From (5.68) it follows that in the case of $y/a >> 1$ and $\chi \approx 0$ (propagation in free space) $\varphi \approx 0$. For the case $\chi \approx 1$ $\varphi = \pi$; that is, we limit ourselves in this case to an ideal unbroken waveguide depicted in Figure 5.13(a).

In the cases of radio communication along wide avenues or canyons with building heights less than the street width in line-of-sight conditions between receiver and transmitter, we obtained a good transition from the waveguide model to the two-ray model, when both of them predict two-law decay of field intensity before and beyond the break point. In the case of narrow streets the two-ray model is not valid and only the multislit waveguide model predicts an exponential attenuation of total field at street level in LOS conditions at ranges up to 2–3 km from the transmitter. That is why, in various situations along straight streets in LOS conditions the multislit waveguide model, more

generally than the two-ray model, predicts the propagation characteristics in an urban scene with different geometry of streets and for various street widths.

Moreover, because according to formula (5.65) the break-point range depends on the geometry of the street, the buildings' geometry, and their distribution along the street, the scale of a microcell in LOS conditions is also varied in different conditions along the street. Therefore, using the three-dimensional multislit impedance waveguide model, one can predict the signal loss and the effective scale of a microcell for various real situations in a straight street scene in conditions of direct visibility (see Chapter 9).

References

[1] Jacks, W. C., Jr., *Microwave Mobile Communications*, New York: John Wiley and Son, 1974, pp. 81–83.

[2] Parsons, L. D., *The Mobile Radio Propagation Channels*, New York: Pentech Press, 1992.

[3] Feuerstein, M. L., and T. S. Rappaport, *Wireless Personal Communication*, Norwood, MA: Artech House, 1992.

[4] Milstein, L. B., et al., "On the feasibility of a CDMA overlay for personal communications networks," *IEEE Select. Areas in Commun.*, Vol. 10, No. 4, 1992, pp. 665–668.

[5] Xia, H. H., et al., "Radio propagation characteristics for line-of-sight microcellular and personal communications," *IEEE Trans. Anten. and Propag.*, Vol. 41, No. 10, 1993, pp. 1439–1447.

[6] Bertoni, H. L., W. Honcharenko, L. R. Maciel, and H. H. Xia, "UHF propagation prediction for wireless personal communications," *Proc. IEEE*, Vol. 82, No. 9, 1994, pp. 1333–1359.

[7] Fumio, J., and J. Susumi, "Analysis of multipath propagation structure in urban mobile radio environments," *IEEE Trans. Anten. Propagat.*, Vol. 28, No. 4, 1980, pp. 531–538.

[8] Hata, M., "Empirical formula for propagation loss in land mobile radio services," *IEEE Trans. Veh. Technol.*, Vol. 29, No. 3, 1980, pp. 317–325.

[9] Ikegami, F., S. Yoshida, and M. Takahar, "Analysis of multipath propagation structure in urban mobile radio environments," *IEEE Trans. Anten. Propagat.*, Vol. 20, No. 4, 1980, pp. 531–537.

[10] Ikegami, F., T. Takeuch, and S. Yoshida, "Theoretical prediction of mean field strength for urban mobile radio," *IEEE Trans. Anten. Propagat.*, Vol. 39, No. 3, 1991, pp. 299–302.

[11] Lee, W. Y. C., *Mobile Communication Design Fundamentals*, New York: McGraw-Hill Publications, 1993.

[12] Rustako, A. J., Jr., et al., "Radio propagation at microwave frequencies for line-of-sight microcellular mobile and personal communications," *IEEE Trans. Veh. Technol.*, Vol. 40, No. 2, 1991, pp. 203–210.

[13] Levy, A. J., "Fine structure of the urban mobile propagation channel," *Proc. Commsphere 91*, Herzlia, Israel, Dec. 1991, pp. 5.1.1–5.1.6.

[14] Tan, S. Y., and H. S. Tan, "UTD propagation model in an urban street scene for microcellular communications," *IEEE Trans. Electromag. Compat.*, Vol. 35, No. 4, 1993, pp. 423–428.

[15] Tan, S. Y., and H. S. Tan, "A theory of propagation path loss characteristics in a city street-grid scene," *IEEE Trans. Electromagn. Compat.*, Vol. 37, No. 3, 1995, pp. 333–342.

[16] Blaunstein, N., and M. Levin, "VHF/UHF wave attenuation in a city with regularly spaced buildings," *Radio Sci.*, Vol. 31, No. 2, 1996, pp. 313–323.

[17] Blaunstein, N., and M. Levin, "Propagation loss prediction in the urban environment with rectangular grid-plan streets," *Radio Sci.*, Vol. 32, No. 2, 1997, pp. 453–467.

[18] Blaunstein, N., R. Giladi, and M. Levin, "LOS characteristics' prediction in urban and suburban environments," *IEEE Trans. on Vehic. Technol.*, Vol. 47, No. 1, 1998, pp. 11–21.

[19] Blaunstein, N., "Average field attenuation in the nonregular impedance street waveguide," *IEEE Trans. on Anten. Propagat.*, Vol. 46, No. 12, 1998, pp. 1782–1789.

[20] Keller, J. B., "Geometrical theory of diffraction," *J. Opt. Soc. America*, Vol. 52, No. 2, 1962, pp. 116–130.

[21] Felsen, L. B., and N. Marcuvitz, *Radiation and Scattering of Waves*, Englewood Cliffs, NJ: Prentice-Hall, 1973.

[22] Balanis, C. A, *Advanced Engineering Electromagnetics*. New York: Wiley, 1989.

[23] *Handbook of Mathematical Functions*, edited by Abramowitz, M., and I. A Stegun, New York: Dover Publications, Inc., 1972.

[24] Hughes, K. A., "Mobile propagation in London at 936 MHz," *Electron. Letters*, Vol. 18, No. 3, 1982, pp. 141–143.

[25] Stewart, K., and D. Schaeffer, "The microcellular propagation environment," *Proc. Symp. on Microcellular Technology*, Chicago, March 12–17, 1992.

[26] Samuel, R. Y., "Mobile radio communications at 920 MHz," *Proc. of 2nd Int. Conf. Anten. and Propag.*, Heslington, April 13–16, 1981, Pt. 2, pp. 143–147.

[27] Whitteker, J. H., "Measurements of path loss at 910 MHz for proposed microcell urban mobile systems," *IEEE Trans. Veh. Technal.*, Vol. 37, No. 3, 1988, pp. 376–381.

[28] Harley, P., "Short distance attenuation measurements at 900 MHz and 1.86 MHz using low antenna heights for microcells," *IEEE Sel. Areas Comm.*, Vol. 10, No. 1, 1989, pp. 7–16.

[29] Turin, G. L., et al., "A statistic model of urban multipath propagation," *IEEE Trans., Veh. Technol.*, Vol. 26, No. 4, 1977, pp. 358–362.

This page intentionally left blank

6

Propagation in NLOS Conditions in Built-Up Areas With Regularly Distributed Straight-Crossing Streets

We will now continue the subject of propagation characteristic prediction in an urban scene in obstructive conditions over the flat-ground surface, returning to the case of an array of buildings placed on a regular terrain. As is well known [1–18], personal, local, and mobile communication service systems are usually expected to employ base-station antennas and radio ports at street level heights *below* the rooftops (i.e., in shadow zones for one or both working antennas, receiver and transmitter). That is why, in this chapter, we consider radio propagation loss prediction in the urban environment with rectangular grid-plan streets.

In an urban scene with regularly distributed intersecting streets, it has been observed that the buildings lining the streets work as waveguides, affecting the propagation direction of the radio waves [1]. Tests described in [1, 2] carried out in New York City indicate that the subscribers at the street level, moving radially from the base station, or on the streets parallel to these, may receive a signal 10–20 dB higher than that received when moving on the perpendicular streets. This effect is more significant in the microcell area (up to 1–2 km away from the base station), becoming negligible at distances above 10 km, that is, in the macrocell area [2].

As pointed out in [3–13], it is very difficult to obtain a strict theoretical treatment of this channeling phenomenon. At the same time, the simple approach of representing the relative field strength by the density of arrows along the various streets indicates only the way in which field strength may

vary in an urban area because of street orientation, but not the real field strength distribution between streets and their intersections [4, 9]. Using this approach, the total path loss at the crossing-street level is a simple arithmetic summation of path loss at the radial street where the base station is located, and of path loss from the intersection to the side street, that is, $L_{total} = L_{radial} + L_{side}$ [6]. Experiments carried out in [11, 13] in the crossing-street area of Central London at 900 MHz and 1.7 GHz have shown a complicated two-dimensional shape of microcell coverage, similar to a Christmas tree with the base station near the foot of the tree (see Figures 6.1(a,b)). This complicated redistribution of field energy among the rectangular crossing streets cannot be understood using a simple geometric optic model, even taking into account diffraction from the building corners [7, 8].

In Section 6.1, when both antennas are below the rooftop level, we describe a two-dimensional crossing-waveguides model which is based on the preliminary results obtained from the two-dimensional multislit waveguide model presented in Chapter 5. This does not take into account reflection from the road to describe the radio wave propagation along the street in LOS conditions, or the results of detailed examinations of clutter conditions in an urban scene with a grid-streets plan, presented in [12]. The average intensity of signal decay in the intersections between streets and along the crossing streets is examined. The theoretical predictions were verified by path loss measurements obtained both by the communication group of Tadiran Telecommunication [12] and by other investigators (see [11, 13]). Section 6.2 describes the two-dimensional multidiffraction-deterministic model evaluated in [18–21] for the prediction of radio propagation loss characteristics in the urban environment with regularly distributed rows of buildings. In Section 6.3, comparisons between the two-dimensional waveguide model and the two-dimensional multidiffraction model—as well as with experimental data—are presented for predicting coverage effects. The construction of radio maps in urban areas with clutter conditions for both antennas placed above the flat-ground surface is also presented.

6.1 Two-Dimensional Crossing-Streets Waveguide Model

6.1.1 Modeling of Urban Areas With Rectangular Crossing Streets

Let us consider, as in Chapter 5, that the buildings on the street are replaced by randomly distributed nontransparent screens with scales L_n; the gaps between the buildings (slits) are defined as l_n, $n = 1, 2, 3 \ldots$ (see Figure 6.2, the radial waveguide I). The laws of their differential distribution are postulated

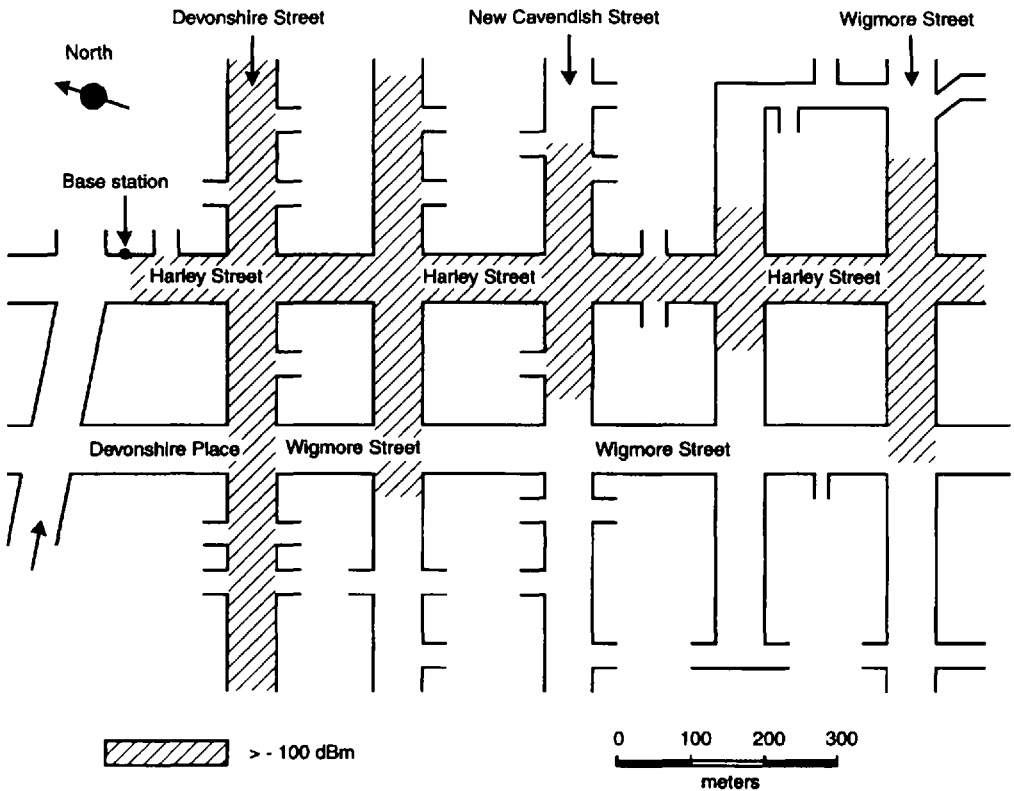

Figure 6.1 (a) The coverage effect in Central London obtained experimentally in [11]; (b) The coverage effect in Central London obtained experimentally in [13].

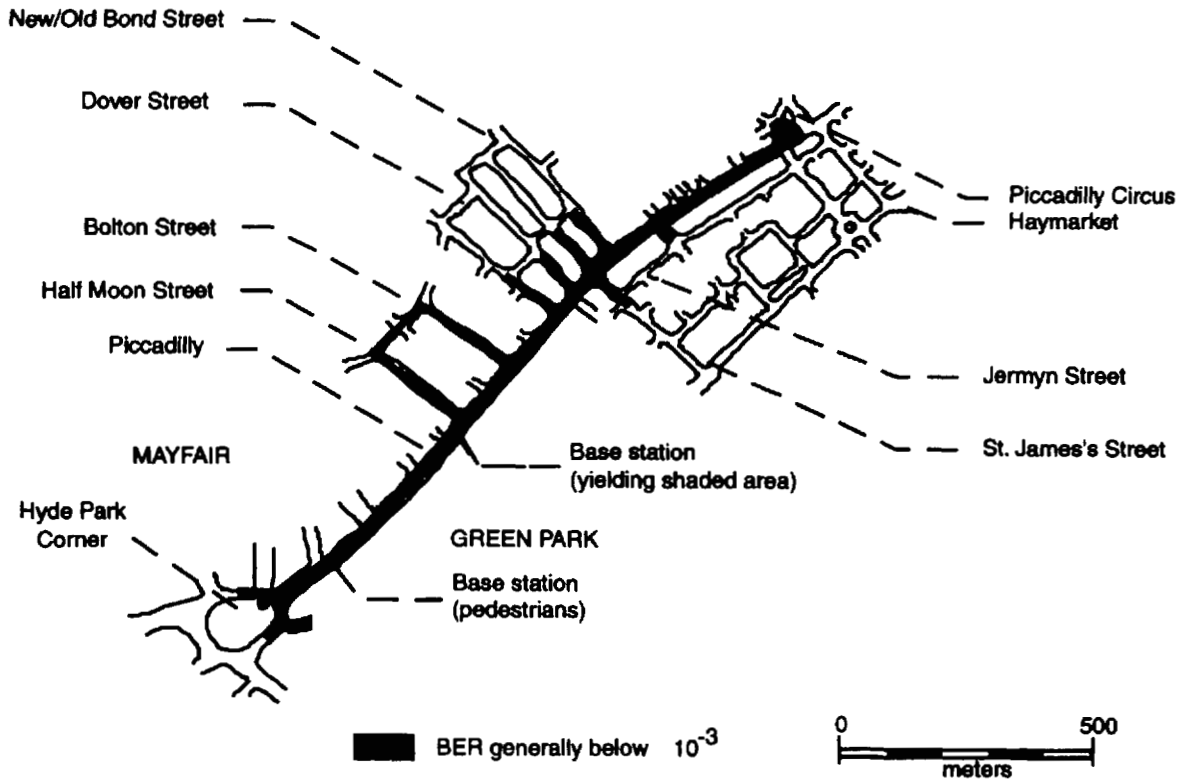

Figure 6.1 (b) (continued).

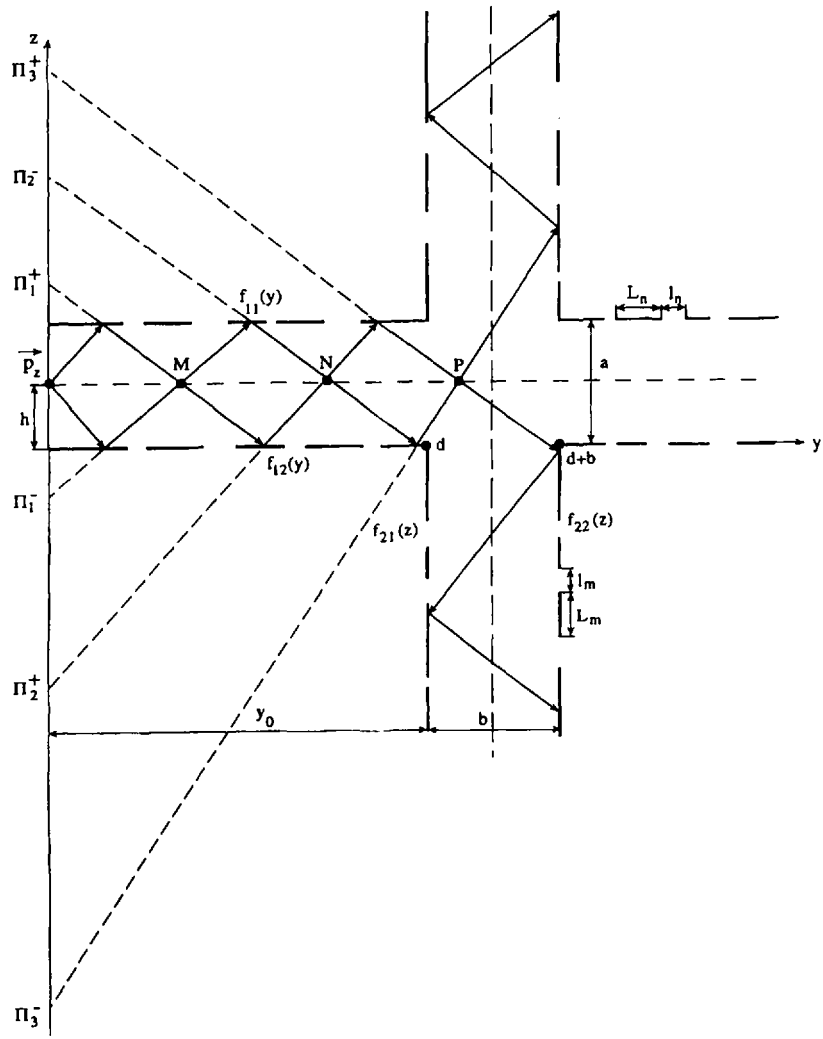

Figure 6.2 A two-dimensional model of the crossing-street waveguides; the coordinates of source are $y = 0$ and $z = h$; a and b are the radial and side street widths, respectively.

according to (5.1) (see Chapter 5) as independent and exponential with mean values $\langle L \rangle$ and $\langle l \rangle$ respectively.

Such a broken impedance radial waveguide with randomly distributed buildings along the street models a city street with receiver and transmitter at street level below the rooftops. One radial waveguide plane is placed at the waveguide side $z = 0$, and the second one at $z = a$ (a is the street width, see

Figure 6.2). We also assume that a vertical electric dipole, the active transmitter, is placed in the yz-plane with coordinates $z = h; y = 0$, where h is the transmitter location at the road. The same conditions are assumed for the crossing (side) waveguide (which is noted in Figure 6.2 by sign *II*) with screen and slit lengths L_m and l_m, respectively, $m = 1, 2, 3, \ldots$. One side waveguide plane is placed at the waveguide side $y = d$, and the second one at $y = d + b$ (b is the side street width, see Figure 6.2).

Taking into account that all dimensions are much greater than the radiation wavelength, λ, we use the approximation of the GTD for rays reflected from the walls and building corners. We also present the resulting field as a superposition of a direct wave field from the source, fields reflected from the walls, and fields diffracted from the building edges [12]. As mentioned in Chapter 5, for most measurements in the UHF/L-band, the conditions of GTD are true for distances $d < 2$–3 km [7, 8, 16, 18, 19, 22].

In order to calculate the total field from the source, as in Section 5.1, we substitute for each reflection from the walls an image source Π_n^+ (for the first reflection from the left-hand walls of the street waveguide) and Π_n^- (for the first reflection from the right-hand walls), where n is the number of the reflections (as schematically presented in Figure 6.2). According to the approach proposed in [12] and presented in Section 5.3, we also introduce the *telegraph signal functions*, $f_{11}(y)$ and $f_{12}(y)$ for the radial waveguide, and $f_{21}(z)$ and $f_{22}(z)$ for the side waveguide. These equal one when reflection from the walls (screens) takes place, and zero when rays pass through the spaces between the buildings, that is, fall into the slits of the waveguides. Thus segments with $f_{1i}(y) = 1$ and $f_{2i}(z) = 1$ represent screens, including their edges, but segments with $f_{1i}(y) = 0$ and $f_{2i}(z) = 0$ represent slits, $i = 1, 2$ (see Figure 6.2).

The real electric properties of building walls (screens) are defined by the surface electric impedance $Z_{EM} \sim \epsilon^{-1/2}$, $\epsilon = \epsilon_0 - i4\pi\sigma/\omega$ where:

ϵ is the dielectric permittivity of the wall surface,
ϵ_0 is the dielectric constant of vacuum,
σ is the electric conductivity of the wall surface,
ω is the angular frequency of the radiated wave,
$\omega = 2\pi f_0$,
f_0 is the frequency of the radiated wave.

6.1.2 Average Field Strength in the Crossing-Street Waveguide Model

Field strength inside the primary radial street. To calculate the average total field along the radial street multislit waveguide we, as in Chapter 5, take into account the exponential walls (screens) and slits distributions (6.3), the harmonic time-dependence of the electromagnetic field, and the definition of the horizontal

electric dipole field using the Hertzian potential vector $\Pi_z^i(x, y, z)$ according to formulas (5.3) to (5.4).

To now obtain the total field inside the primary broken multislit waveguide, we must use the procedure of field averaging by means of the properties of "telegraph signal" functions $f_{1i}(y)$ and $f_{2i}(z)$ introduced in Chapter 5. According to some straightforward calculations presented there, we can finally rewrite the formula (5.36) (Chapter 5) for the spectrum of the n-times reflected and diffracted field for the case of two-dimensional multislit waveguide model: for $z < h$:

$$\Pi_z(\beta, z) = \frac{\Pi(\beta)\exp(iKa)}{1 - \chi^2 R_{TE}^2 \exp(2iaK)} \{R_{TE}\exp(iKz) + \exp(-iKz)] \times [R_{TE}\exp(iK(a-h)) + \exp(-iK(a-h))]\}[|R_{TE}| + |D_{mn}|] \tag{6.1a}$$

for $z > h$:

$$\Pi_z(\beta, z) = \frac{\Pi(\beta)\exp(iKa)}{1 - \chi^2 R_{TE}^2 \exp(2iaK)} \{R_{TE}\exp(iKz) + \exp(-iKz)] \times [R_{TE}\exp(iK(a-h)) + \exp(-iK(a-h))]\}[|R_{TE}| + |D_{mn}|] \tag{6.1b}$$

Here, as in Chapter 5, we assume that the formulations of diffracted waves are similar with those obtained for reflected waves and in which the reflection coefficient R_{TE} of each reflected ray from the screen (wall) is simply replaced with a diffraction coefficient D_{mn} ($m = 1, 2, 3, \ldots$) for each diffracted ray from the wall's edge [14, 17, 23–25]. The coefficient of reflection for each reflected waveguide mode, R_{TE}, is presented in Chapter 5 by formula (5.44). As for the diffraction coefficient, D_m, its expressions are very complicated and are mostly presented in the literature (for example, referenced in [14, 17, 23–25]). All other parameters in formulas (6.1a) and (6.1b) are described in Chapter 5; $\chi = \langle L\rangle/(\langle L\rangle + \langle l\rangle)$ is the parameter of brokenness.

In (6.1a,b) we combined the reflected and diffracted waves with the direct wave (LOS component) from the source. To obtain the total average field along the radial street we will use for (6.1a,b) the inverse Fourier transform on coordinate y. Let us consider, for example, the case $z > h$, for which we obtain the total field inside the radial waveguide:

$$\Pi^I(y, z) = (D/\pi)\int_{-\infty}^{\infty} d\beta[\exp(-i\beta y)/K]\cos[K(a-z) - (i/2)\ln|R_{TE}\chi|] \times \frac{\cos[Kh - (i/2)\ln|R_{TE}\chi|]}{\sin[Ka - i\ln|R_{TE}\chi|]}[|R_{TE}| + |D_{mn}|] \tag{6.2}$$

As shown in Chapter 5 for a broken-impedance multislit waveguide, formula (6.2) contains two terms. The first term in (6.2) represents the continuous part of the total field spectrum, Π_c, which can be presented by formulas (5.57a) and (5.57b) in Chapter 5. The second term in (6.2) represents the discrete part of the total field spectrum, Π_n. It can be presented by formulas (5.46) to (5.48) in Chapter 5. As an example, in Figure 6.3, for parameters $\chi = 0.5$, $|R_{TE}| = 0.75$, the total average field intensity $J = \langle I \rangle / I_0 = \langle (\Pi_c + \Pi_n)(\Pi_c + \Pi_n)^* \rangle / I_0$ (continuous curve), relative to the intensity in free space I_0, the intensity of each normal mode of discrete spectrum J_n (dotted curves), and the continuous spectrum of total field intensity J_c (continuous curve), are presented versus the relative distance y/a along the main radial waveguide for $n = 1, \ldots, 20$. As can be seen, the continuous

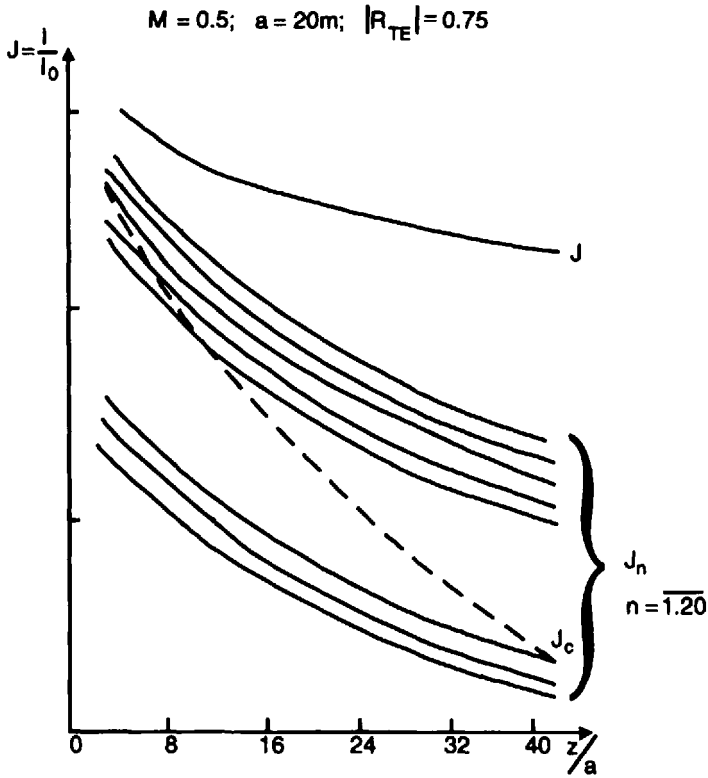

Figure 6.3 The total average intensity I loss relative to the intensity in free space I_0 inside the radial waveguide versus the relative distance y/a; J_n is the discrete spectrum, J_c is the continuous spectrum of total intensity J; $\chi = 0.5$, $a = 20$m, $|R_{TE}| = 0.75$.

part of the total intensity is attenuated more quickly (as a spherical wave) than that of discrete modes (which propagate as normal cylindrical waves) with increase of distance y along the street waveguide, and their superposition gives the total field intensity J along the radial waveguide, which is attenuated at long distances $y >> a$ as a cylindrical wave inside the main waveguide.

In the case of a perfectly conductive continuous radial waveguide ($\chi = 1$, $|R_{TE}| = 1$), the process of wave propagation inside it is continuously limited to the classical case, when normal modes propagate without attenuation [23, 25].

Average field strength in the side waveguide. Let us now assume that the second (side) waveguide crosses the radial waveguide at a distance $y = d$ from the source and has width b (see Figure 6.2). We will consider the excitation of electromagnetic waves from the radial waveguide inside the crossing waveguide. The process of wave propagation is described by the following wave equation:

$$\Delta\Pi^{II}(y, z) - k^2\Pi^{II}(y, z) = f(y, z) \tag{6.3}$$

or, using the Fourier transformation on coordinate z, by:

$$\frac{\partial^2\Pi_z^{II}(y, \gamma)_{(z=a)}}{\partial y^2} + (k^2 - \gamma^2)\Pi_z^{II}(y, \gamma)_{(z=a)} = f(y, a)\exp\{i\gamma a\} \tag{6.4}$$

where $f(y, a) = \dfrac{\partial\Pi_z^I(z = a)}{\partial y} + \Pi_z^I(z = a)$ is the radiated "source" created by the electromagnetic field inside the main radial waveguide I at the plane $z = a$.

Taking into account (6.2) describing the average field strength inside the radial waveguide I, we can obtain

$$\Pi_z^I(y, z = a) = \{iD/2\pi(\chi R_{TE})^{1/2}\}\int_{-\infty}^{\infty} d\beta[\exp\{-i\beta y\}/K] \times \frac{\cos[Kh - (i/2)\ln|\chi R_{TE}|]}{\sin[Ka - i\ln|\chi R_{TE}|]}[|R_{TE}| + |D_m|] \tag{6.5}$$

$$\frac{\partial \Pi_z^I(z=a)}{\partial y} = \{iD/2\pi(\chi R_{TE})^{1/2}\} \int_{-\infty}^{\infty} d\beta \exp\{-i\beta y\} \times \frac{\cos[Kh - (i/2)\ln|\chi R_{TE}|]}{\sin[Ka - i\ln|\chi R_{TE}|]} [|R_{TE}| + |D_m|] \tag{6.6}$$

Finally, (6.4) can be presented as follows:

$$\frac{\partial^2 \Pi_z^{II}(y, \gamma)}{\partial y^2} + \eta^2 \Pi_z^{II}(y, \gamma) = F(y, \gamma) \tag{6.7}$$

where $\eta^2 = k^2 - \gamma^2$ and

$$F(y, \gamma) = (iD/2\pi(R_{TE}\chi)) \int_{-\infty}^{\infty} d\beta \exp\{-\beta y\} \frac{\cos[Kh - (i/2)\ln|\chi R_{TE}|]}{\sin[Ka - i\ln|\chi R_{TE}|]} \times [|R_{TE}| + |D_m|](1 - \gamma/K) \tag{6.8}$$

Let us now construct Green's function for (6.7) which satisfies the equation

$$\frac{\partial^2 \Pi_z^{II}(y, \gamma)}{\partial y^2} \pm \eta^2 \Pi_z^{II}(y, \gamma) = \delta(y - y_0) \tag{6.9}$$

with the following boundary conditions:

$$\frac{\partial^2 \Pi_z^{II}(y, \gamma)}{\partial y^2} = \pm Z_2 \Pi_z^{II}(y, \gamma) \tag{6.10}$$

Here, signs "+" and "−" satisfy boundaries $y = d$ and $y = d + b$, respectively (see Figure 6.2). The coefficient Z_2 is the wave impedance inside the crossing waveguide, which characterizes the wave properties of the broken multislit waveguide. Its expression can be easily evaluated using the same procedure as for wave impedance Z_1 inside the radial waveguide (see [12]). Thus for $z = a$

$$Z_2 = -\eta \cot[(i/2)\ln|\chi R_{TE}|] \tag{6.11a}$$

for $z = 0$

$$Z_2 = -\eta\cot[\eta a - (i/2)\ln|\chi R_{TE}|] \tag{6.11b}$$

The solution of (6.9) can be found as follows:

$$\Pi^{II}(y, \gamma) = A\exp(i\eta y) + B\exp(-i\eta y) \tag{6.12}$$

Then

$$\frac{\partial\Pi^{II}(y, \gamma)}{\partial y} = i\eta[A\exp(i\eta y) + B\exp(-i\eta y)] \tag{6.13}$$

If the coordinate $y = y_0$ is the coordinate of some image line of observation inside the crossing waveguide II, as in Figure 6.2, Green's function can be constructed using the following expression [23, 25]
for $y < y_0$:

$$G(y, y_0) = (1/\mathbf{I})\Pi_1^{II}(y)\Pi_2^{II}(y_0) \tag{6.14a}$$

for $y > y_0$:

$$G(y, y_0) = (1/\mathbf{I})\Pi_1^{II}(y_0)\Pi_2^{II}(y) \tag{6.14b}$$

Here is the second-order determinant $\mathbf{I} = \Pi_1^{II}\dfrac{\partial\Pi_2^{II}}{\partial y} - \Pi_2^{II}\dfrac{\partial\Pi_1^{II}}{\partial y}$. The components and their derivatives can be obtained using expressions (6.11) to (6.13) for the ranges $d < y < y_0$ and $y < y_0 < d + b$, respectively, and from the boundary conditions (6.10). Thus for $y = d$, that is, $d < y < y_0 < d + b$, from (6.10) and (6.12) and taking into account (6.11), one can easily obtain the field component in the region $d < y < y_0$:

$$\Pi_1^{II} = -B_1\sin[\eta(y - d) - (i/2)\ln|\chi R_{TE}|] \tag{6.15a}$$

where $B_1 = B\exp(-i\eta d)\exp[-i(i/2)\ln|\chi R_{TE}|]$.

In the same way, for the range $y_0 < y = d + b$, that is, for $y = d + b$, the field component Π_2^{II} has the following form:

$$\Pi_2^{II} = A_1\sin[\eta(d + b - y) - (i/2)\ln|\chi R_{TE}|] \tag{6.15b}$$

where $A_1 = 2iA\exp\{i\eta(d + b)\}\exp\{i[-(i/2)\ln|\chi R_{TE}|]\}$.

Using (6.15a) to (6.15b) and their derivatives, we can obtain the second-order determinant as

$$\mathbf{I} = -A_1 B_1 \eta \sin[\eta b - i\ln|\chi R_{TE}|] \tag{6.16}$$

Finally, Green's function can be presented in the following form: for $d < y < y_0$

$$G_1 = \frac{\sin[\eta(y-d) - (i/2)\ln|\chi R_{TE}|]}{\eta \sin[\eta b - i\ln|\chi R_{TE}|]} \sin[(d + b - y_0) - (i/2)\ln|\chi R_{TE}|] \tag{6.17a}$$

for $y_0 < y < d + b$

$$G_1 = \frac{\sin[\eta(y_0-d) - (i/2)\ln|\chi R_{TE}|]}{\eta \sin[\eta b - i\ln|\chi R_{TE}|]} \sin[(d + b - y) - (i/2)\ln|\chi R_{TE}|] \tag{6.17b}$$

Using (6.17a) to (6.17b), we can now obtain the Fourier transform of the total average field inside the crossing waveguide as follows:

$$\Pi^{II}(y, \gamma) = \int_{d}^{d+b} d\gamma' G(y, \gamma') F(y', \gamma) \tag{6.18}$$

where y' and γ' are the current variables of integration. Using Cauchy's theorem for $F(y', \gamma)$ in integral (6.18) for the pole points $K_n = n\pi/a + (i/a)\ln|\chi R_{nTE}|$ we can derive $F(y', \gamma)$ as follows:

$$\begin{aligned} F(y', \gamma) = {} & D\exp\{i\gamma a\}/(\chi R_{TE})^{1/2} \sum_{n=0}^{\infty} R_{nTE}(K_n - \gamma) \\ & \times \cos[K_n b - (i/2)\ln|R_{nTE}\chi|]/(-1)^n a\beta_n Q_n \end{aligned} \tag{6.19}$$

Here $\beta_n^2 = k^2 - K_n^2$; $Q_n = \{R_{nTE} - 2ikZ_{EM}/[K_n^2 - (kZ_{TE})^2]\}$. Introducing (6.19) into integral (6.18) and using Cauchy's theorem once more for the pole points $hm = m\pi/b + (i/b)\ln|\chi R_{mTE}|$, and the inverse Fourier transform on the coordinate z, we finally obtain the expression for the total field spectrum inside the crossing waveguide for the case $d < y < y_0$:

$$\Pi_m^{II}(y, z) = -Di\frac{\exp\{i\gamma_m(z-a)\}}{(\chi R_{TE})^{1/2}} \sum_{n=0}^{\infty} R_{nTE}(K_n - \gamma_m) \frac{\exp\{i\beta_n d\}}{(-1)^n ab\beta_n \gamma_m Q_n}$$
$$\times \cos[K_n h - (i/2)\ln|\chi R_{nTE}|]\sin[\eta_m(y-d) - (i/2)\ln|\chi R_{nTE}|]$$
$$\times \left\{\frac{\exp[i(\eta_m + \beta_n)b] - 1}{i(\eta_m + \beta_n)} \exp[(1/2)\ln|\chi R_{nTE}|]\right.$$
$$\left. + \frac{\exp[-i(\eta_m + \beta_n)b] - 1}{i(\eta_m - \beta_n)} \exp[-(1/2)\ln|\chi R_{nTE}|]\right\} \tag{6.20}$$

Here:

$$\gamma_m = (k^2 - \eta_m^2)^{1/2} \approx \gamma_m^{(0)}\{1 + i\pi m \cdot \ln|\chi R_{mTE}|/b^2\gamma_m^{(0)}$$
$$+ (1/2)[(\pi m/b)^2 + (\ln|\chi R_{mTE}|/b)^2]\}$$
$$\beta_n = (k^2 - K_n^2)^{1/2} \approx \beta_n^{(0)}\{1 + i\pi n \cdot \ln|\chi R_{nTE}|/a^2\beta_n^{(0)} \tag{6.21}$$
$$+ (1/2)[(\pi n/a)^2 + (\ln|\chi R_{nTE}|/a)^2]\}$$

where $\gamma_m^{(0)} = (k^2 - (\pi m/b)^2)^{1/2}$ are the wave values of the principal normal modes which are propagated inside the crossing waveguide II; $\beta_n^{(0)} = (k^2 - (\pi n/a)^2)^{1/2}$ are the wave values of the principal normal modes which are propagated inside the radial waveguide I. From (6.20) one can obtain the expression for the average field spectrum inside the perfectly conductive waveguide, that is, for the case $Z_{EM} = 0$ and $R_{TE} = 1$.

The relative average total field intensity, J (relative to the intensity in free space I_0 at the distance $y = d$ from the source) can be approximately presented as a sum of each normal mode $\Pi_{n,m}$ in (6.20): $J_{n,m} \sim <\Pi_{n,m}\Pi_{n,m}^*>$, according to the approach proposed in [12]. Numerical calculations of J and of the principal modes $J_{n,m}$, $n = 1, 2, \ldots, 5$ for various $m = 5, \ldots, 20$, formed inside the main radial waveguide (continuous curves), and high-order modes $J_{n,m}$, $n = 5, \ldots, 10$, for various $m = 1, \ldots, 5$, formed inside the crossing waveguide (dotted curves), are presented in Figure 6.4.

The principal normal modes (with numbers $n < 5$) of the radial waveguide generate high-order modes into the crossing waveguide. At the same time, the high-order modes of the radial waveguide (with number $n > 5$) generate the principal modes inside the crossing waveguide (with number $m < 5$) which are attenuated more slowly (see dotted curves in Figure 6.4) than high-order modes (with $m > 5$), which were created by the principal modes of the main waveguide (with $n < 5$) (see continuous curves in Figure 6.4). This is why at

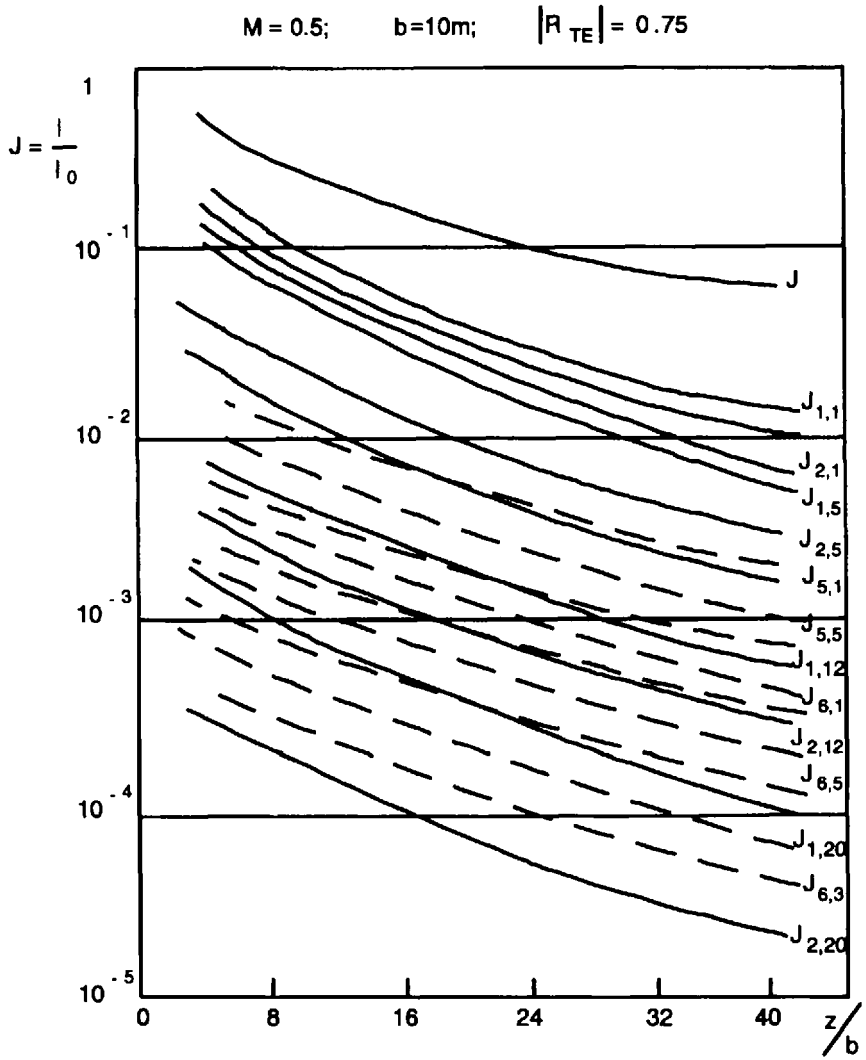

Figure 6.4 The total average intensity I loss relative to the intensity in free space I_0 into the crossing-side waveguide versus the relative distance z/b; J_{nm} is the discrete spectrum of total intensity J; $n, m = 1, 2, \ldots$; $\chi = 0.5$, $a = 20$m, $b = 10$m, $|R_{TE}| = 0.75$.

large distances from the source, the additional effect of modes with numbers $n > 5$ and $m < 5$ is more significant than those with numbers $n < 5$ and $m > 5$.

In Figures 6.5(a,b) both additional effects from the two kinds of mode are presented relative to the total field intensity versus the range z along the

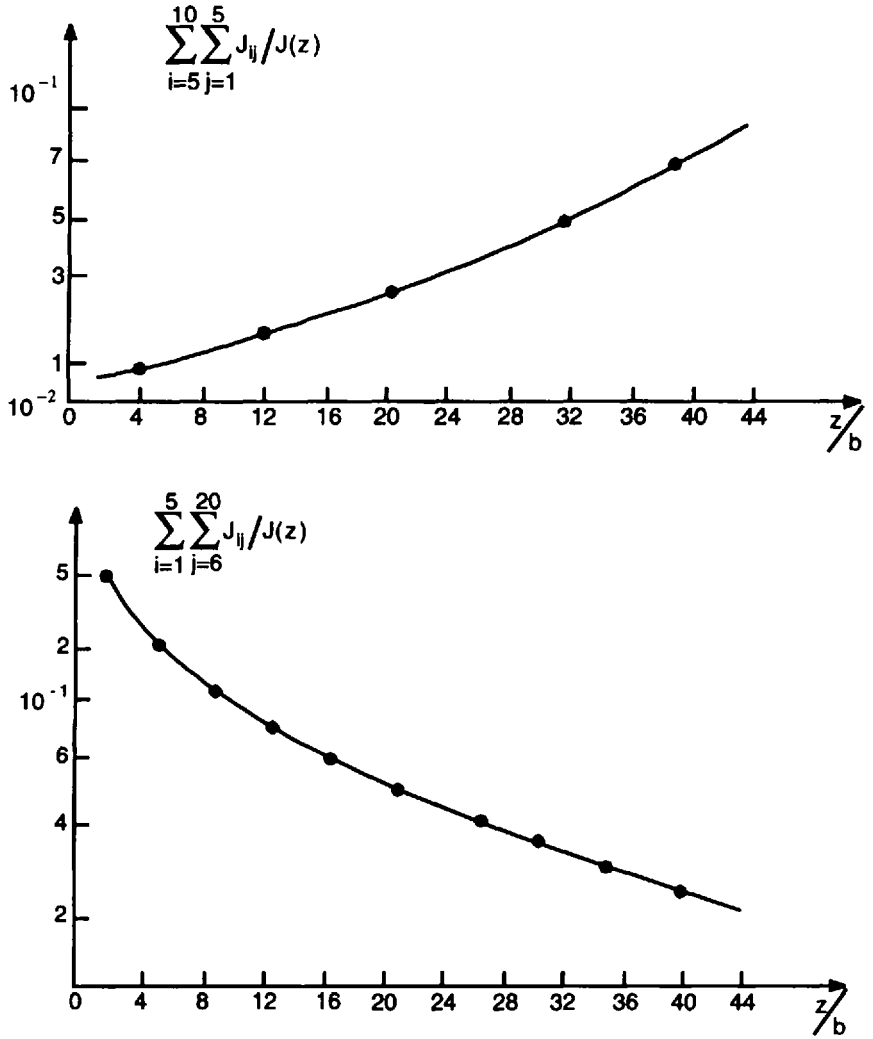

Figure 6.5 (a) The normalized principal modes ($j < 5$) of the total intensity spectrum $J(z)$ inside the crossing waveguide versus the normalized distance, z/b from the intersection for $\chi = 0.5$, $a = 20$m, $b = 10$m, $|R_{TE}| = 0.75$; (b) the same, as in (a), but for high-order modes ($j > 5$).

crossing waveguide at a distance $y > d$. As follows from Figure 6.5(a,b), the influence of the principal modes inside the crossing waveguide, created by the high-order waves from the radial waveguide, grows with increasing z, but the influence of high-order modes inside the crossing waveguide, created by the principal waves from the radial waveguide, falls. In the other words, there is not a simple bisection of the total field intensity at the intersection of

two crossing waveguides; a complicated redistribution of field energy between the normal modes is observed. More than half the total field energy penetrates from the radial to the crossing waveguide. The amount of field energy which penetrates depends on the width of both street waveguides and on the parameter of brokenness (i.e., on the gaps between buildings), and on the electric properties of building walls.

6.1.3 Comparison With Experimental Data

Let us now compare the theoretically obtained predictions with Tadiran's experimentally measured path loss along rectangular-crossing straight streets in the investigated urban area.

The measurements were taken in the same small town of Kefar-Yona (the conditions of experiments are described in detail in Chapter 5), where the MGW system of Tadiran Telecommunications was under trial in the conditions of rectangular grid-plan streets (see Figure 6.6). The omnidirectional base-station antenna was located at a lower level than the buildings' roofs, at a distance of 4m–5m from the corner building surface, as depicted schematically in Figure 6.6. The mobile omnidirectional radio-port antenna moved along the streets in the middle of the road (positions II, III, IV, . . . , as depicted schematically in Figure 6.6). The tested MGW system was operated in the frequency band f_0 = 902–928 MHz.

The tested environment is a typical small urban region of three- to five-story brick buildings with approximately uniform heights h = 8m–10m and with a right-angle crossing-straight street plan (as schematically presented in Figure 6.6). The base-station transmitter antenna was installed at the height h_T = 6m–7m (i.e., lower than rooftop level). The moving radio-port antenna was lower than rooftop level (h_R = 2m–3m) and changed its distance from the stationary base station in the range 10m–500m. The tested cell radius of such an area estimated from measurements was approximately 1 km. Field intensity measurements in dB relative to intensity in free space at the range r = 100m were obtained to estimate the field intensity attenuation along the crossing streets, taking into account actual dielectric properties of the brick walls of buildings (with ϵ_0 = 15–17, σ = 0.05–0.08 mho/m, $|R_{TE}|$ = 0.73–0.81) and the real distribution of buildings (χ = 0.5–0.6) along the street level for the radial and crossing-street widths a = 20m and b = 10m, respectively.

The measured relative intensity of received field in dB is presented as a set of points near each curve in Figure 6.7 for the different cases: measurements are at the main and first radial streets A_1 and A_2, respectively, and at the first, second, and third crossing streets B_i, i = 1, 2, 3, respectively (which are noted

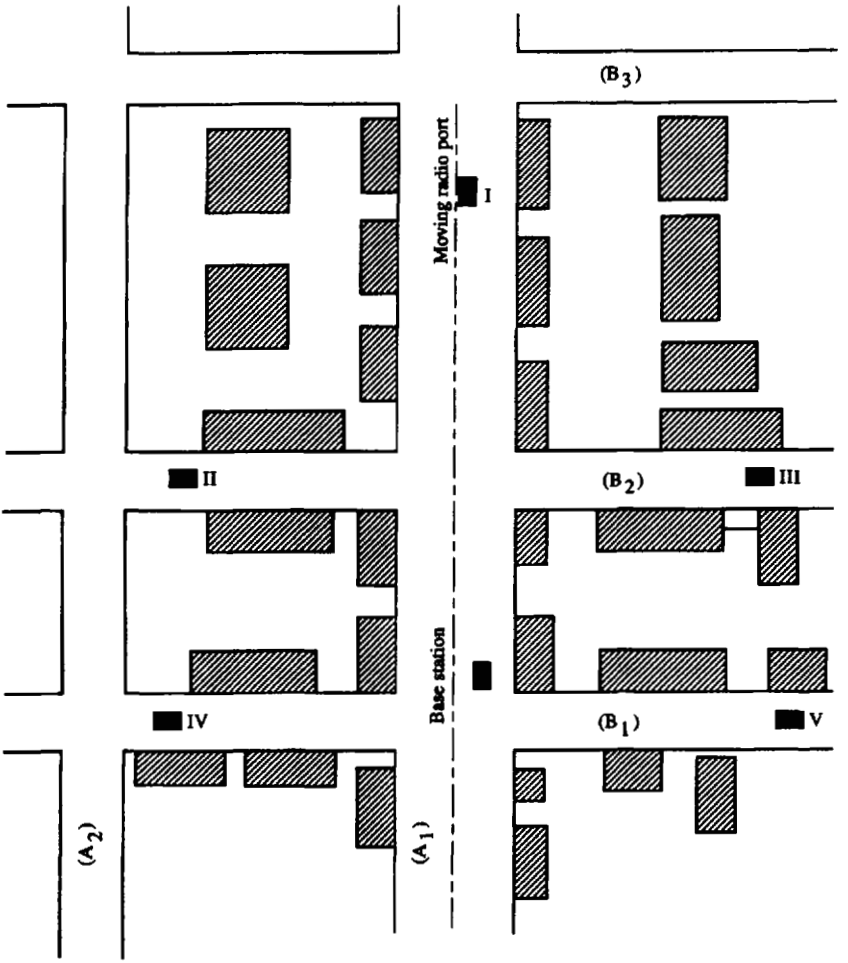

Figure 6.6 The simplified scheme of a Kefar-Yona area as a rectangular-crossing street grid. The main radial street, where the base station is located, is noted by A_1; other streets are noted by A_2 and B_i, $i = 1, 2, \ldots$; the positions of moving radio port are noted by Roman numerals I, II, III, ...

in Figure 6.6). The main continuous curve in Figure 6.7 represents numerical calculations of relative field intensity inside the main waveguide A according to formulas (5.46) and (5.57) (Chapter 5). The dotted curves represent the relative field intensity for crossing-street waveguides B_i using formula (6.20) and the side continuous curve represents the field intensity inside the first radial street A_2. Calculations were carried out for the following parameters: $a = 20\text{m}$, $a_1 = b_i = 10\text{m}$; $\chi = 0.5$; $|R_{TE}| = 0.75$. As seen from the comparison

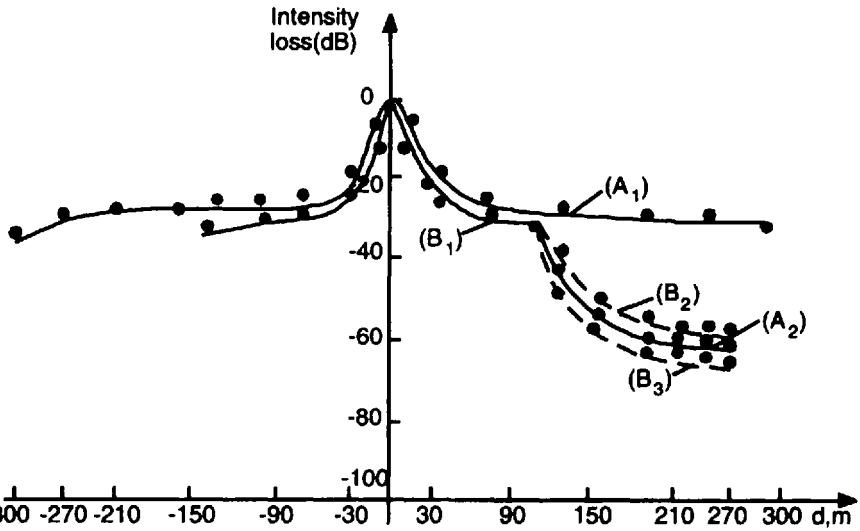

Figure 6.7 Field intensity loss along the crossing-street grid measured in dB in a Kefar-Yona area using the notation depicted in Figure 6.6.

between theoretical and experimental results, the waveguide model, which describes wave propagation along the radial waveguides using formulas (5.46) to (5.57), gives an intensity loss (with accuracy of 2–3 dB) close to that obtained experimentally in line-of-sight conditions, when both the base station and the moving radio port are in conditions of direct visibility. At the same time the two-dimensional waveguide model of rectangular crossing streets, proposed above, gives results comparable to experimentally obtained data with a lower accuracy of 3–5 dB. This also satisfies the real experimental conditions and accuracy of measurements (with error of 1–2 dB). From comparison between theoretical prediction and experimentally obtained data we notice that, with an accuracy of 3–5 dB, we can use two-dimensional waveguide models for microcell coverage and range predictions in urban and suburban areas with rectangular grid-plan streets for distances of up to 1–2 km from the base station.

6.2 Two-Dimensional Multidiffraction Model for Straight Rows of Buildings

In obstructive (clutter) conditions the receiver or transmitter antennas (or both) are placed in the shadow zones, when there are many nontransparent buildings surrounding them, and placed as straight rows on the flat-ground surface. In

this case the role of diffraction from the roofs and corners of buildings increases and the total field depends not only on the reflected, but also on the diffracted waves.

Let us consider, according to [18–21], that an elevated antenna (base station) radiates a field that propagates in an environment with regular distributed nontransparent buildings with various heights h_i and different separation distances d_i (i = 1, 2, 3 . . .) between them. The height of the base-station antenna, H, can be greater or smaller than the height of the first (near the antenna) building, h_1 (see Figures 6.8(a,b)).

In the case where the base antenna is higher than the first building ($H > h_1$, see Figure 6.8(a)), the radiating field propagates over the rooftops by a process of multiple diffraction past rows of buildings. As all buildings are nontransparent, the majority of the propagation paths cannot lie through the buildings (according to Bertoni et al. [18–21]; path 4 in Figure 6.8(a)). Moreover, when there is propagation between buildings the rays reflected from the ground after a second diffraction from the roofs (path 3 in Figure 6.8(a)) are quickly attenuated (according to the estimation obtained by Bertoni et al. [18–21]). As a result, the majority of the paths cannot be associated with propagation between the buildings. The propagation over the rooftops involves diffraction past a series of buildings with dimensions larger than wavelength λ, (i.e., h_i, $d_i >> \lambda$). At each building a portion of the field will be diffracted toward the ground. These fields can also be neglected [18–21] (rays in path 3 in Figure 6.8(a)). We therefore conclude, according to [18–21], that the primary propagation path lies over the tops of the buildings, as indicated by path 1 in Figure 6.8(a). The field reaching street level results from diffraction of the fields incident on the rooftops in the vicinity of the receiving antenna.

Contributions to path loss. Treating the base station as a transmitter and assuming that the receiver is at street level, we can obtain the path loss in dB as the sum of the free-space path loss (see Section 2.3)

$$L_0 = 10 \log\left(\frac{4\pi fr}{c}\right)^2 \tag{6.22}$$

and excess loss L_{ex}. The last can be presented as the sum of two parts [18–21]:

Part A: The diffraction of the fields at the rooftops before the receiver down to the street level is

$$L_{e1} = 10 \cdot \log\{(G_1(\theta_N)/\pi kr)[1/\theta_N - 1/(2\pi + \theta_N)]^2\} \tag{6.23}$$

where $G_1(\theta_N)$ is the gain of the receiving antenna pattern in the direction θ_N as represented in Figure 6.8(a), $k = 2\pi/\lambda$. Expression (6.23) was obtained in

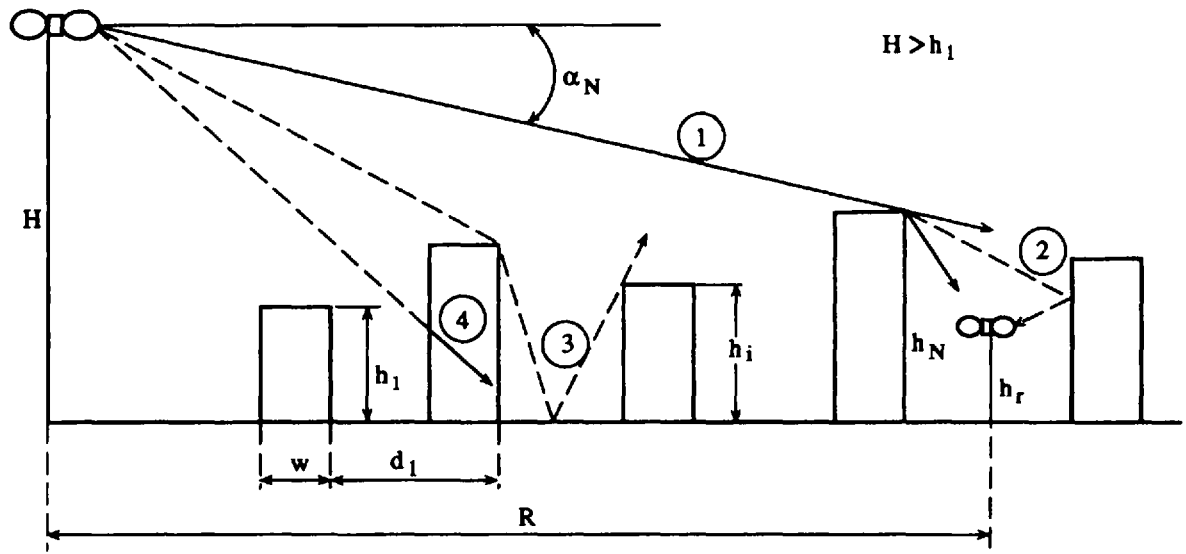

Figure 6.8 A scheme of a two-dimensional model of the urban region with regularly distributed rows of buildings in the case where the transmitter antenna is higher (a) and lower (b) than the first building in the vicinity of its position (i.e., $H > h_1$ and $H < h_1$).

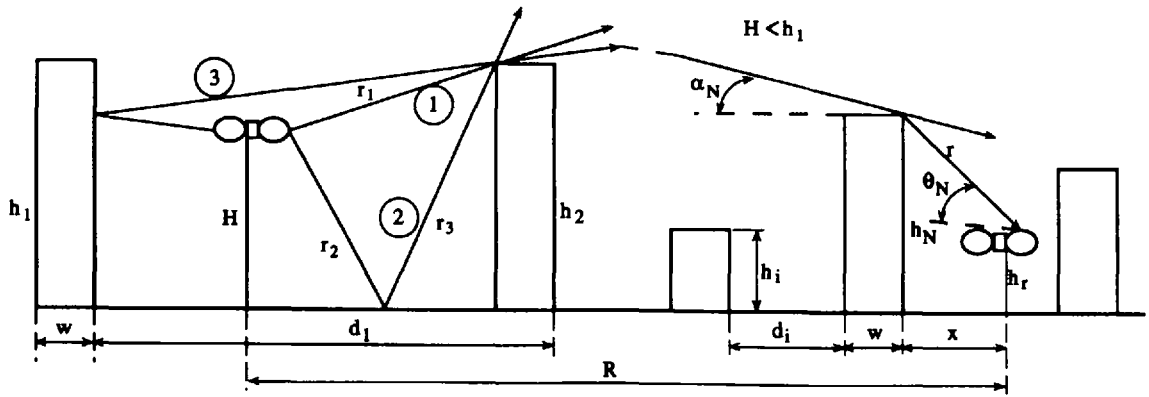

Figure 6.8 (continued).

[18–21] for the case $\alpha_N << \theta_N$. From the simple geometrical constructions according to Figure 6.8(a) one can obtain: $\theta_N = \tan^{-1}[(h_N - h_r)/x]$ and $r = [(h_N - h_r)^2 + x^2]^{1/2}$. Here x is the distance between the receiver and the last building, which is close to the receiver; h_r is the receiver antenna height.

Part B: The reduction of the field at the rooftop before the receiver as a result of propagation past the previous rows of buildings

$$L_{e2} = 10 \cdot \log\{G_2 W^2\} \tag{6.24}$$

where G_2 is the gain in the direction of the highest building edge visible from the base-station antenna. As the result, the total loss is: $L_{total} = -(L_0 + L_{e1} + L_{e2})$. In the case when the base antenna is *higher* than the first building ($H > h_1$, see Figure 6.8(a)), parameter W can be presented for small angle $\alpha_N = \tan^{-1}[(H - h_N)/R]$ and for $x << R$ according to [18–21] as (see Figure 6.8(a)):

$$W = \frac{(d_N - w)/(R - d_N + w)}{[2\pi k[(h_N - H)^2 + (d_N - w)^2]^{1/2}]^{1/2}} \times \left\{\frac{1}{\tan^{-1}[(h_N - H)/(d_N - w)]} + \frac{1}{2\pi + \tan^{-1}[(h_N - H)/(d_N - w)]}\right\} \tag{6.25}$$

In the case when the base antenna is *lower* than the first building ($H < h_1$, see Figure 6.8(b)), one can use the same formulas (6.22) to (6.24), but instead use (6.25) for parameter W to introduce for the same geometrical conditions (see Figure 6.8(b)) the following expression for W:

$$W = 2.35\{\tan^{-1}[H/(d_N - w)][(d_N - w)/\lambda]^{1/2}\}^{0.9} \tag{6.26}$$

Formulas (6.22) to (6.26) present the unified two-dimensional diffraction model constructed in [18-21] for prediction of radio propagation over and below regularly distributed rows of buildings for various situations regarding base-station antenna height (as is presented in Figures 6.8(a,b)).

Let us now present the formulas above in the form of an *equation of straight line*, as was done in Chapters 3 and 4. For this case we will simplify the problem so that the rows of buildings are regularly distributed at flat terrain with uniform building height h as a median value of rooftops, and with uniform gaps between buildings x as a median value of this parameter. In general, in a case using the formulas above, one can obtain the same equation of straight line.

In this assumption, we present the free-space path loss formula as

$$L_0 = 32.4 + 20 \log f_0 + 20 \log R \tag{6.27}$$

and excess due to the propagation over the rows of building excluding effects of terrain curvature (that is, for actual radio traces with ranges less than 10–20 km) according to (6.23)

$$L_{e1} = 68.9 - 9 \log x - 9 \log f_0 + 18 \log R - 18 \log(H - h_r) \tag{6.28}$$

and due to rooftop to street diffraction according to (6.24)

$$L_{e2} = -11.7 + 10 \log r + 10 \log f_0 + 20 \log \theta \tag{6.29}$$

where $\theta = \tan^{-1}[2(h - h_r)/x]$ is the angle presented in Figure 6.8, but for uniform distribution of buildings' height, that is, $\theta_N = \theta$, and $r = [(h - h_r)^2 + (x/2)^2]^{1/2}$.

If so, one can present the formulas above in the straight-line form:

$$L_{total} = -(L_0 + L_{e1} + L_{e2}) = L_q + 10\gamma \log R \tag{6.30}$$

where the intercept:

$$L_q = -89.6 - 21 \log f_0 + 9 \log x - 10 \log r + 18 \log(H - h_r) - 20 \log \theta \tag{6.31a}$$

the attenuation slope:

$$\gamma = 3.8 \tag{6.31}$$

So, as in Chapters 3 and 4, according to Bertoni, Walfisch, et al. [18–21] one can obtain using formulas (6.27) to (6.30) that the signal decay due to rooftop multidiffraction with the range between both antennas, transmitter and receiver, for the equal conditions in the urban scene of consideration (for $L_q = \text{const}$), is $\sim R^{-3.8}$, (i.e., the same as was obtained earlier for rural and residence areas by use of the empirical approaches (see Chapter 4)).

6.3 Prediction of Coverage Effects in an Urban Crossing-Street Scene

Let us now compare the theoretically obtained formulas for clutter conditions with Tadiran's experimentally measured received signal power spatial distribu-

tion (which in the literature is usually called *coverage effects*) in the urban area. For the LOS conditions in our first estimations of path loss we used formula (5.61) in Chapter 5. For clutter conditions for the moving radio port at the street level, including intersections between streets, we used both formula (6.20) obtained in [12], formulas (6.22) to (6.24), and (6.26) obtained in [18–21]. We took into account that the base station antenna is *lower* than the top of buildings surrounding it (see Figure 6.8(b)) in the real conditions of our experiments. This was done to compare the crossing-waveguides model (CW) for evaluation of field intensity attenuation inside the intersections between streets, using formula (6.20), with the two-dimensional multidiffraction model (two-dimensional MD), using formulas (6.22) to (6.24), and (6.26), to estimate loss characteristics in obstructive conditions for base-station and radio-port antennas between straight rows of buildings (see Figure 6.8(b)). The comparison between theoretical prediction according to the CW-model and the two-dimensional MD-model and measurements, schematically sketched in Figure 6.6, is presented in Figure 6.9, as a diagram of difference, Δ, in dB, between experimental data and theory for frequency f_0 = 930 MHz inside the radial street A_2 and three crossing streets B_i, i = 1, 2, 3, relative to the main road A_1 in which the base station is located (see Figure 6.6).

As can be seen, the CW model (the segments on the left side of each column) is closest to the experimental results, with an accuracy of 2–3 dB, compared with the two-dimensional MD model (the segments on the right side of each column), with an accuracy of 3–5 dB, only for the crossing streets which lie close to the main road. As for the radial streets and the crossing streets which lie far away relative to the main road, the two-dimensional MD model is more accurate: it is close to experimental data with an accuracy of 2–3 dB, but the CW model has an accuracy of 3–5 dB. This is why, for further comparison with the experimental data, we used the formula (5.63) or (5.61), because they are closer (see Chapter 5) to describing LOS conditions between both antennas, the formula (6.20) for loss prediction inside the closed junctions with the main radial street, and formulas (6.22) to (6.24), and (6.26) to describe clutter conditions along the streets farthest from the base station, which is *lower* than buildings' roofs.

From the net of measurements the *diamond-shape* of coverage curves (called *radio map*) of field intensity attenuation in the Kefar-Yona area was obtained. The curves obtained experimentally and those from theoretical predictions according to formulas (5.61) to (5.63), (6.20) and (6.22) to (6.24) and (6.26) have shown that the coverage curves are elongated along the main road, where the base station is located.

We also notice from comparison between experimentally and theoretically obtained values of signal-power loss that for urban areas with a sufficient

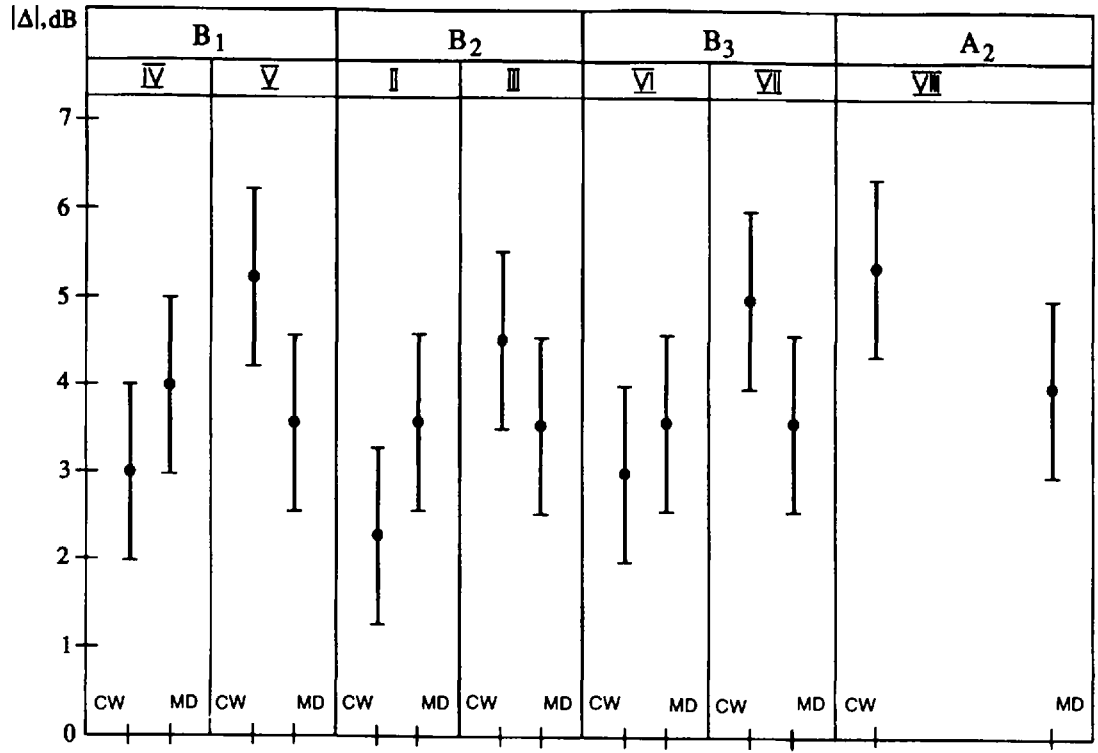

Figure 6.9 The comparison between theoretical prediction of path loss in dB according to the crossing-waveguide model described by formula (6.20) and the two-dimensional multidiffraction model [18–21] (described by formulas (6.22) to (6.24), and (6.26)) and the experimental data.

shadowing between receiver and transmitter when the transmitter antenna is lower than the rooftop level, we can use formulas (6.22) to (6.24), and (6.26) with great accuracy (of ~3–5 dB) at ranges from 500m to 2 km from the base station (micro-cellular propagation conditions, see Chapter 1).

Summary

In the propagation of radio waves in urban and suburban areas with regularly distributed rows of buildings placed in a regular layout, and with the transmitter and receiver antennas *below* the rooftops' level, the unified theoretical approach developed by Bertoni et al. [18–21] can be successfully used for estimations of field-intensity attenuation and coverage effects in obstructive (clutter) conditions taking into account the real distribution of their heights and the gaps between them.

At junctions between the straight streets the crossing-waveguides model [12] predicts (with the accuracy of 3–5 dB) the signal loss along the crossing streets near the intersections at ranges of 100m–200m from junctions for both antennas *below* the rooftops' level. By using the two-dimensional crossing-waveguides model one can obtain a good explanation of experimentally observed wave loss characteristics with the distance from the base station, the real redistribution of field energy at the intersections of crossing waveguides, and the cell coverage in such urban and suburban areas.

Using the two-dimensional crossing-waveguides model we, as in Chapter 5, present below a qualitative picture of wave propagation along the street multislit waveguide. Figure 6.10 is a simple sketch that indicates the way in which the field strength of a vertical electric dipole (with pattern angle $\varphi = \pi$) may vary because of channeling street orientation. The simplest cases of an unbroken waveguide and of a real street with randomly distributed buildings along it were discussed in Chapter 5 (see Figures 5.13(a,b)). Now we will consider two rectangular-crossed broken waveguides (as sketched in Figure 6.10). In this case the redistribution of field intensity from the source depends on the relation between the antenna pattern angle φ and angle φ_0 which defines the area of observation from the source as the intersection of waveguides (see in Figure 6.10). For $y_0 >> a$, we can estimate this angle as $\varphi_0 = a/y_0$. If $\varphi < \varphi_0$, the effect of the street *brokenness* is not significant and only a small part of the source energy penetrates the side waveguide (noted by II in Figure 6.10). That is, the intensity loss is small and at the same distance y from the source inside the radial waveguide (noted by I in Figure 6.10) with the intensity $J \approx J_0$. In the case when $\varphi \approx \varphi_0$, some energy of the source penetrates into the side waveguide II from the main radial waveguide

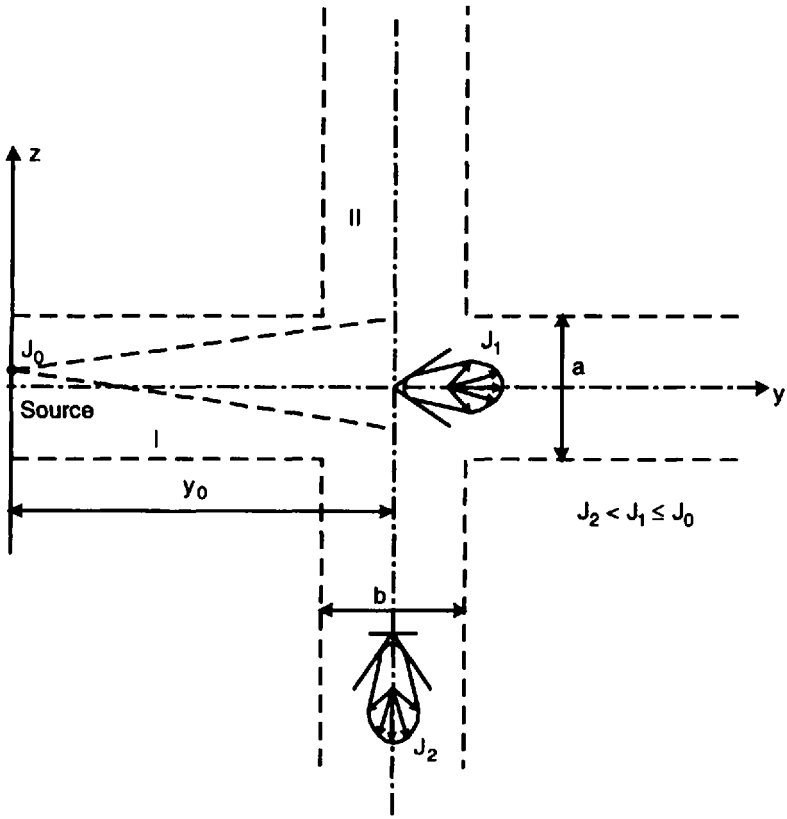

Figure 6.10 The simplified scheme of the rectangular crossing-street waveguides.

I. The amount of energy loss depends on the parameter of brokenness in the main radial waveguide and on the distance from the source (i.e., $J = J_0\varphi(\chi, y_0) < J_0$, where $\varphi(\chi, y_0)$ is presented by (5.68) (see Chapter 5)). For the case $\varphi > \varphi_0$, the waveguide modes, propagating along radial waveguide I, easily penetrate into the side waveguide II. The field intensity loss now depends on the gap distribution between buildings into both waveguides (i.e., $J = J_0\varphi(\chi_1, y_0)\varphi(\chi_2, z) << J_0$, where $\varphi(\chi_2, z)$) is presented by (5.68) in Chapter 5, but for the side waveguide. Moreover, as we have shown in Section 6.1.2, the low-order wave modes in the radial waveguide I generate high-order wave modes in the side waveguide II and, conversely, high-order wave modes in a radial waveguide generate low-order wave modes in a side waveguide. This is why the total field intensity of the main waveguide cannot be simply divided into two equal parts at the intersection of two crossing waveguides, as was done in [6, 9]. The redistribution of wave energy near each intersection inside

the rectangular grid-pattern of crossing streets depends on the processes inside each waveguide and on the parameters of brokenness, that is, on building distribution in each radial and perpendicular street waveguide inside the grid.

In the inverse case, when antennas are placed *at the rooftops level* or *higher*, only the multidiffraction model [18–21] can be used for predicting field intensity attenuation in clutter conditions, including intersections between the straight streets.

The above observations enable us to conclude that both approaches presented in Chapter 6 can be successfully used for the prediction of personal and mobile communication channels in obstructive urban and suburban environments which have a grid-plan of crossing-straight streets for microcells with effective sizes of not more than 2-3 km, using the real distribution of building heights and the gaps between them.

References

[1] Black, D. M., and D. O. Reudink, "Some characteristics of radio propagation at 800 MHz in the Philadelphia area," *IEEE Trans. Vehic. Techn.*, Vol. 21, No. 1, 1972, pp. 45–51.

[2] Reudink, D. O., "Comparison of radio transmission at X-band frequencies in suburban and urban areas," *IEEE Trans. Anten. Propagat.*, Vol. 20, No. 4, 1972, pp. 400–405.

[3] Harley, P., "Short distances attenuation measurements at 900 MHz and 1.8 GHz using low antenna heights for microcells," *IEEE J. Select. Areas Commun.*, Vol. 7, No. 1, 1989, pp. 5–11.

[4] Chan, G. K., "Propagation and coverage prediction for cellular radio systems," *IEEE Trans. Vehic. Techn.*, Vol. 40, No. 5, Nov. 1991, pp. 665–670.

[5] Erceg, V., M. Taylor, D. Li, and D. L. Schilling, "Urban/suburban out-of-sight propagation modeling," *IEEE Commun. Magazine*, No. 2, 1992, pp. 56–61.

[6] Stewart K, and D. Schaeffer, "The microcellular propagation environment," *Proc. of Symp. on Microcellular Technology*, IL, USA, March 1992, pp. 19–26.

[7] Tan, S. Y., and H. S. Tan, "UTD propagation model in an urban street scene for microcellular communications," *IEEE Trans. Electromag. Compat.*, Vol. 35, No. 5, 1993, pp. 423–428.

[8] Tan, S. Y., and H. S. Tan, "Propagation model for microcellular communications applied to path loss measurements in Ottawa City streets," *IEEE Trans. Vehic. Techn.*, Vol. 44, No. 3, 1995, pp. 313–317.

[9] Crosskopf, R., "Prediction of urban propagation loss," *IEEE Trans. Anten. Propagat.*, Vol. 42, No. 5, 1994, pp. 658–665.

[10] Dersch, U., and E. Zollinger, "Propagation mechanisms in microcell and indoor environments," *IEEE Trans. Veh. Technol.*, Vol. 43, No. 10, 1994, pp. 1058–1066.

[11] Chia, S. T. S., "Radiowave propagation and handover criteria for microcells," *British Telecom Tech. J.*, Vol. 8, No. 1, 1990, pp. 50–61.

[12] Blaunstein, N., and M. Levin, "Propagation loss prediction in the urban environment with rectangular grid-plan streets," *Radio Sci.*, Vol. 32, No. 2, 1997, pp. 453–467.

[13] Steele, R, "The cellular environment of lightweight hand-held portables," *IEEE Communication Magazine*, No. 1, 1989, pp. 20–29.

[14] Lampard, G., and T. Vu-Dinh, "The effect of terrain on radio propagation in urban microcells," *IEEE Trans. Vehic. Techn.*, Vol. 42, No. 3, 1993, pp. 314–317.

[15] Lawton, M. C., and J. P. McGreehan, "The application of deterministic ray launching algorithm for the prediction of radio channel characteristics in small-cell environments," *IEEE Trans. Vehic. Techn.*, Vol. 43, No. 10, 1994, pp. 955–969.

[16] Rustako, A. J., N. Amitay, G. J. Owens, and R. S. Roman, "Radio propagation at microwave frequencies for line-of-sight microcellular mobile and personal communications," *IEEE Trans. Veh. Technol.*, Vol. 40, No. 1, 1991, pp. 203–210.

[17] Vogler, L. E., "An attenuation function for multiple knife-edge diffraction," *Radio Sci.*, Vol. 17, No. 9, 1982, pp. 1541–1546.

[18] Walfisch, J., and H. L. Bertoni, "A theoretical model of UHF propagation in urban environments," *IEEE Trans. Anten. Propagat.*, Vol. 36, No. 12, 1988, pp. 1788–1796.

[19] Maciel, L. R., H. L. Bertoni, and H. H. Xia, "Unified approach to prediction of propagation over buildings for all ranges of base station antenna height," *IEEE Trans. Vehic. Techn.*, Vol. 42, No. 1, 1993, pp. 41–45.

[20] Xia, H. H., and H. L. Bertoni, "Diffraction of cylindrical and plane waves by an array of absorbing half-screens," *IEEE Trans. Anten. Propagat.*, Vol. 40, No. 2, 1992, pp. 170–177.

[21] Bertoni, H. L., et al., "UHF propagation prediction for wireless personal communications," *Proc. IEEE*, Vol. 82, No. 9, 1994, pp. 1333–1359.

[22] Green, E., "Radio link design for microcellular systems," *British Telecom Tech. J.*, Vol. 8, No. 1, 1990, pp. 85–96.

[23] Balanis, C. A., *Advanced Engineering Electromagnetics*, New York: Wiley, 1989.

[24] Kouyoumjian, R. G., and P. H. Pathak, " A uniform theory of diffraction for an edge in a perfectly conducting surface," in *Proc. IEEE*, Vol. 62, No. 10, 1974, pp. 1448–1461.

[25] Felsen, L. B., and N. Marcuvitz, *Radiation and Scattering of Waves*, Englewood Cliffs, NJ: Prentice-Hall, 1973.

This page intentionally left blank

7

Propagation Over Built-Up Irregular Terrain

In Chapter 4 we dealt with propagation models that describe how irregular terrain, which characterizes the rural environments containing obstructions such as hills and trees, affects VHF/L-band propagation. Some of these models adequately describe the situation in the urban scene, mostly in the suburban areas, where effects of foliage, usually negligible in city centers, can be quite important. At the same time, the effects of trees are similar to those of buildings, introducing additional path losses and producing spatial signal variations.

This chapter deals principally with propagation in built-up areas, when both terminals, transmitter and receiver, are located at the street level and one or both of the terminal antennas are lower than the buildings surrounding them. Earlier, in Chapters 5 and 6, we considered the same situation when both antennas were located in LOS and NLOS conditions at the street level, but assumed that streets and building rows were regularly distributed on the flat terrain. Now we will consider the situation where buildings are randomly distributed over irregular terrain, as a main case of city topography. We also present more actual and specific models that describe the propagation phenomena within the urban communication channel and predict the loss characteristics within it.

Before starting to describe these models it is important once more to point out that there is no general method or algorithm that is universally accepted as being the best prediction model. Each model can be useful for some specific cases in the urban scene and the accuracy of any particular technique or algorithm in some specific situation depends on the fit between

the parameters available for the area concerned and the parameters required by the model.

We shall begin with simple empirical and semi-empirical models, which are based on numerous experimental data and are concerned mostly with predicting average field strength or path loss in cellular urban and suburban environments for radio paths less than 5–10 km. Some of the models presented below can be successfully used for the description of propagation phenomena over rural and mixed environments for radio paths exceeding 10 km.

7.1 Empirical Models

7.1.1 Young's Propagation Prediction

Young did not develop a specific model or prediction technique; he carried out a series of measurements in New York City at frequencies from 150–3700 MHz [1]. Analysis of experimental data obtained by a moving vehicle in the city streets showed that the path loss was much greater than that predicted by the flat-terrain model (see Section 3.2). The tendency of path loss to increase with frequency was observed experimentally. In fact, as follows from some of his results shown in Figure 7.1, there is a good correlation

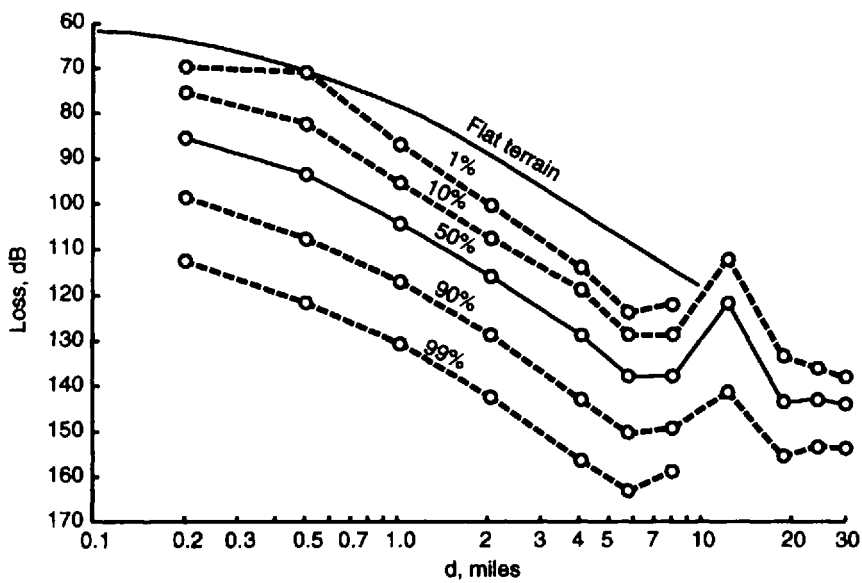

Figure 7.1 Measured path loss at 150 MHz in Manhattan and the Bronx.

between measurements and the flat-terrain model that gives an inverse fourth-power law of signal-strength decay. If so, the dependence of path loss versus range between transmitter and receiver, taking into account the obstructive conditions in built-up areas, can be presented in terms of the Egli empirical model (see Section 4.3) as

$$L_{50} = G_T G_R \left(\frac{h_T h_R}{r^2} \right)^2 \cdot \beta \tag{7.1}$$

We must note once more that here and in the following text we put notations h_T and h_R for description of transmitting and receiving antenna heights, respectively. But actually these notations are relative, because in wireless communication systems each vehicle can simultaneously operate as the transmitter and the receiver. In (7.1) β is the factor which is called a "clutter factor" and which represents losses due to buildings. It can be obtained from lines presented in Figure 7.1. In fact, for the 50% line and for 150 MHz, as follows from Figure 7.1, the parameter β is approximately 25 dB. The same path loss is plotted in this picture that was not exceeded at 1%, 10%, 50%, 90% and 99% of locations within the tested area. It was obtained from Young's measurements. However, Young did not state, and which follows from the depicted curves, that the variability of the signal strength can be described by a log-normal distribution.

7.1.2 Allsebrook's Model

In [2], a series of measurements in British cities at frequencies between 75–450 MHz were reported to produce a propagation prediction model. One of the cities had a hilly terrain and the other two had a smooth terrain. Figure 7.2 presents results of measurements at 167 MHz plotted as points. Here, too, the fourth-power range law of signal decay is shown. It provides a good fit to the experimental data. Where the terrain irregularity effects are negligible, the flat-city model can be used:

$$L_{50} = L_{FT} + L_B + \gamma \tag{7.2}$$

where as in Section 4.2, L_{FT} is the flat-terrain path loss, L_B is the diffraction losses due to buildings and γ is the additional UHF-correction factor intended for use if $f_0 > 200$ MHz. Comparison with (7.1) gives for this model $\beta = L_B + \gamma$.

For hilly and mountainous terrain the additional terrain losses must be taken into account by introducing the diffraction losses L_D, obtained using

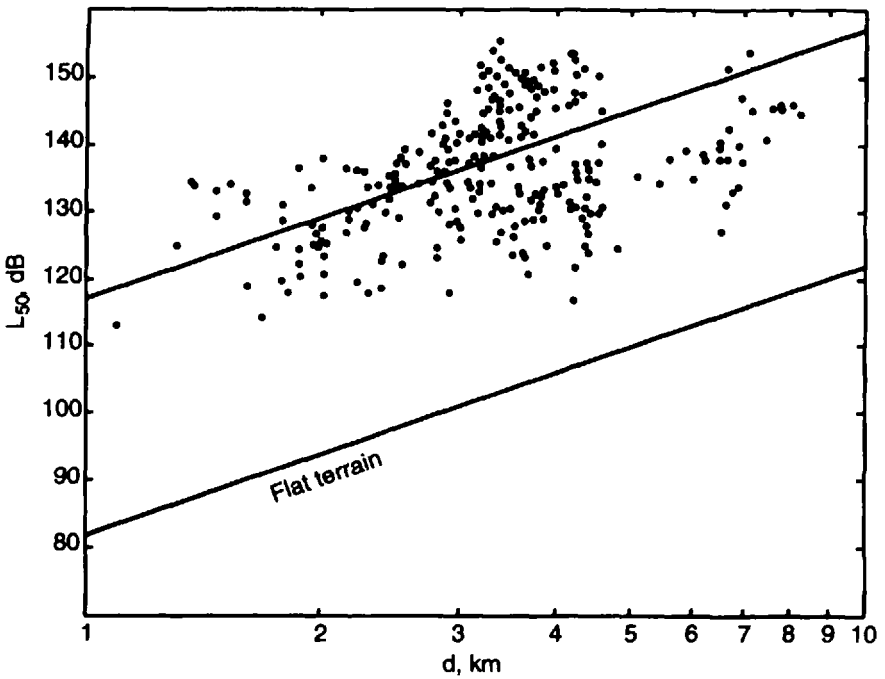

Figure 7.2 Average path loss between half-wave dipoles at 167.2 MHz.

the Japanese method (see Section 4.2), and combining them with other loss components from (7.2). Then the "hilly-city" model, which reduces to the "flat-city" model (7.2) if $L_D \to 0$, is

$$L_{50} = L_{FS} + [(L_{FT} - L_{FS})^2 + L_D^2]^{1/2} + L_B + \gamma \tag{7.3}$$

Here, as in Section 4.2, L_{FS} is free-space losses and L_D is the losses due to diffraction from natural obstructions such as hills, mountains, etc. The diffraction losses from buildings L_B were estimated in [2] using the geometry presented in Figure 7.3, where the receiver is assumed to be located exactly at the center of the street with effective width $a' = \dfrac{a}{2\sin\alpha}$, where a is the real width of the street. Figure 7.4 represents computations based on knife-edge diffraction (Section 4.2) in an average street, compared with measurements of *clutter factor*, β. As follows from the picture, there is good agreement between calculations and measurements only for lower frequencies, up to 200 MHz. As follows from (7.3), the correction factor γ must be accounted at frequencies greater than 200 MHz. Delisle et al. [3] have shown how to ignore this factor

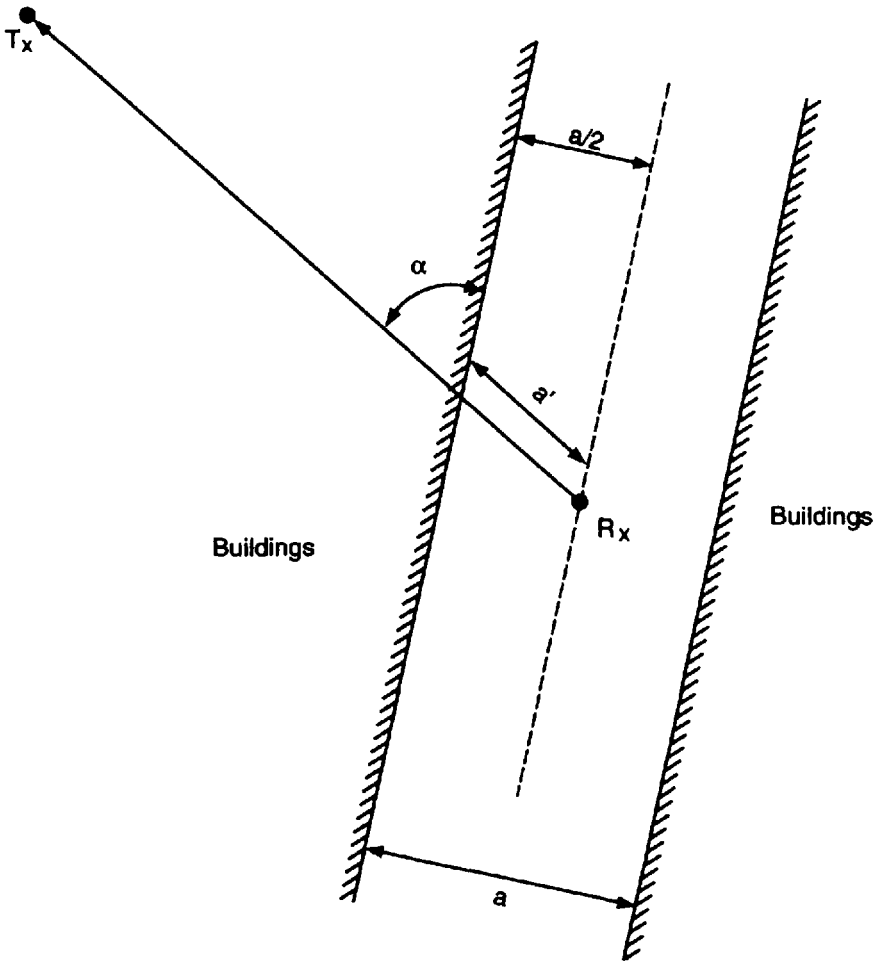

Figure 7.3 The street geometry for Allsebrook's model.

γ in (7.3) for UHF/L-band by introducing a new approximation for the parameter L_B that accounts for the effects of buildings:

$$L_B = 20 \log\left[\frac{(h_0 - h_R)}{548\sqrt{(a' \cdot 10^{-3}) \cdot f_0}}\right] + 16 \text{ dB} \tag{7.4}$$

where f_0 is the radiated frequency measured in MHz, h_R is the receiver antenna height, and h_0 is the average height of buildings in the immediate vicinity of the vehicle as a transmitter, and a' is the effective street width in km (see

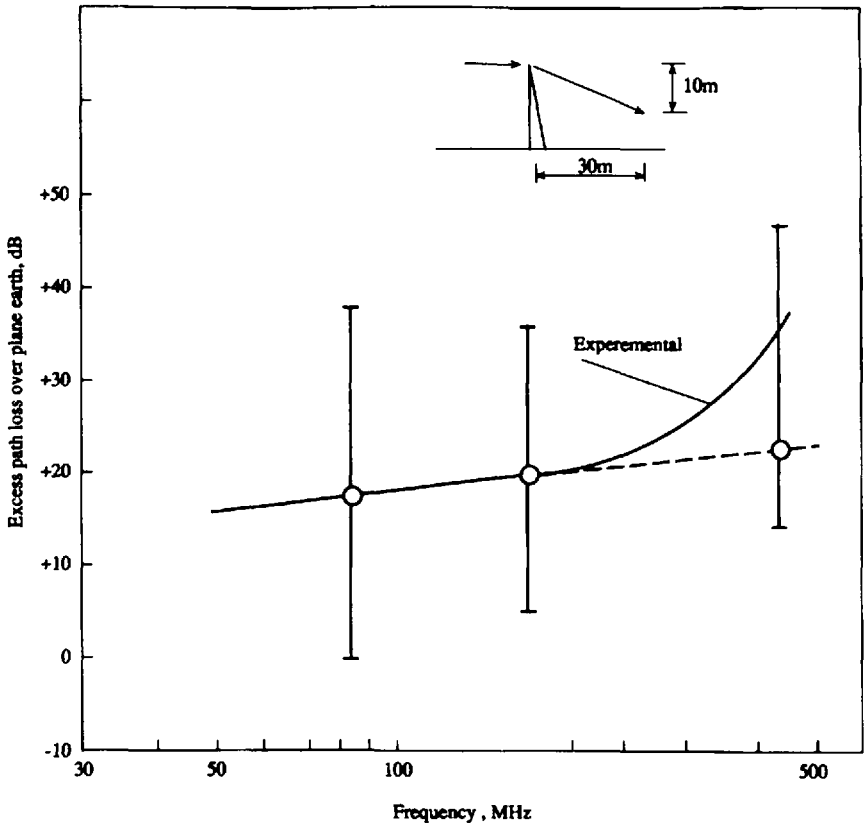

Figure 7.4 Comparison between Allsebrook's model and the experimental data for h_0 = 10m, h_R = 2m, W' = 30m.

Figure 7.4). As was shown in [3], the diffraction losses L_B are very sensitive to the value of h_0.

7.1.3 Okumura Technique

Based on numerous measurements carried out in and around Tokyo, Okumura [4] proposed an empirical method of predicting the average power within the communication channel "mobile-base station." The method is based on a series of curves describing the average attenuation $A_{Ru}(f, d)$ relative to free space for quasi-smooth terrain in an urban environment. We present the total losses according to [4]:

$$L_{50} = L_{FS} + A_{Ru}(f, d) + H_{Tu}(h_T, d) + H_{Ru}(h_R, d) \qquad (7.5)$$

Here, as above, L_{FS} is the losses in free space. The first correction factor in (7.5), $A_{Ru}(f, d)$, is expressed in Figure 7.5 as a function of frequency in the range 100 MHz to 1 GHz and distance from base station (denoted by T) in the range 1–100 km. The reference base station antenna height is h_T = 200m, and the reference moving vehicle antenna (denoted by R) height

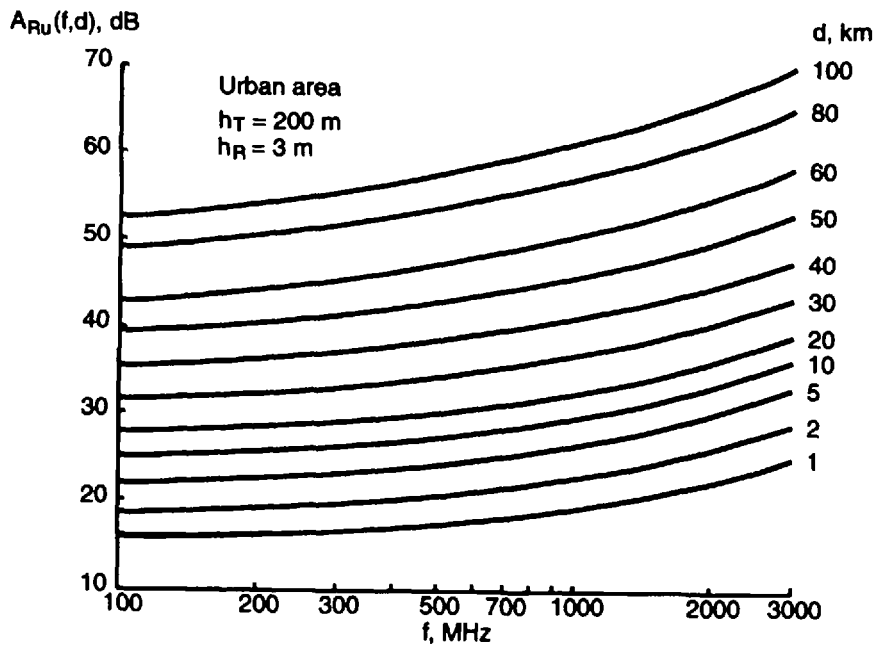

Figure 7.5 The basic average attenuation factor $A_{Ru}(f, d)$ versus the frequency and the range between antennas.

is h_R = 3m. The second correction factor in (7.5), $H_{Tu}(h_T, d)$, is the base station antenna gain factor presented in Figure 7.6 for the same reference heights of both antennas, h_T = 200m and h_R = 3m. The third correction factor in (7.5), $H_{Ru}(h_R, d)$, is the moving vehicle antenna height gain that is shown in Figure 7.7. Here once more, the reference antenna heights are h_T = 200m and h_R = 3m. All corrections in Figures 7.6 and 7.7 are changed in the positive and negative directions if the antenna heights differ more than h_T = 200m and h_R = 3m.

For more complicated urban environments consisting of rough terrain, such as: hills, mountains, vegetation, a general sloping terrain, mixed land-sea terrain, etc., the following adjustments were introduced by Okumura [4] on L_{50} from (7.5):

$$L'_{50} = L_{50} + L_{SO} + L_{TER} + L_{SP} + L_{LS} \tag{7.6}$$

Here, L_{SO} is the correction factor for suburban and open areas shown in Figure 7.8. As shown in Figure 7.9, L_{TER} is the rolling-hill terrain correction factor. As was mentioned in Section 4.2, the terrain undulation factor Δh, as a terrain irregularity parameter, is defined as the specific height taken over a

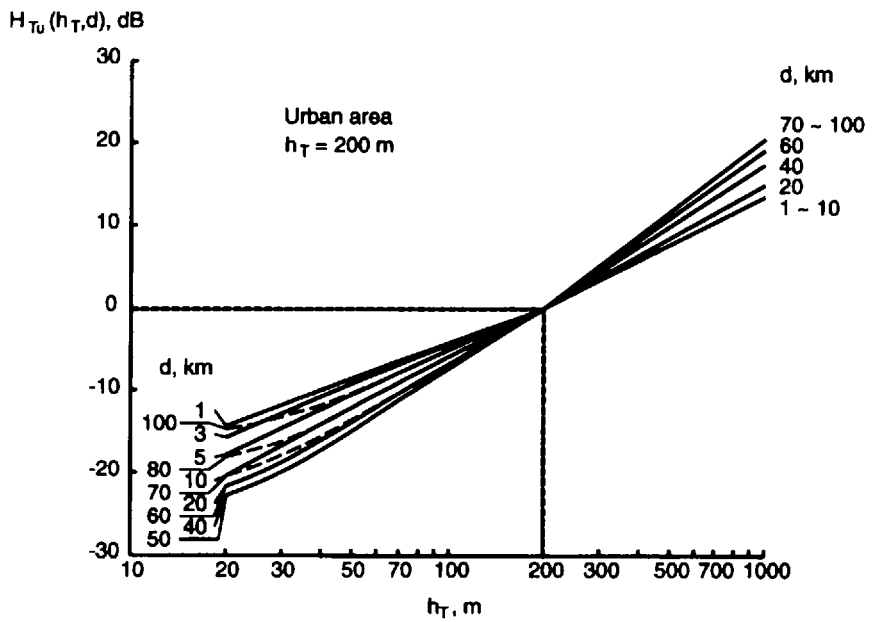

Figure 7.6 The height gain factor $H_{Tu}(h_T, d)$ versus the transmitter antenna height and the range between antennas.

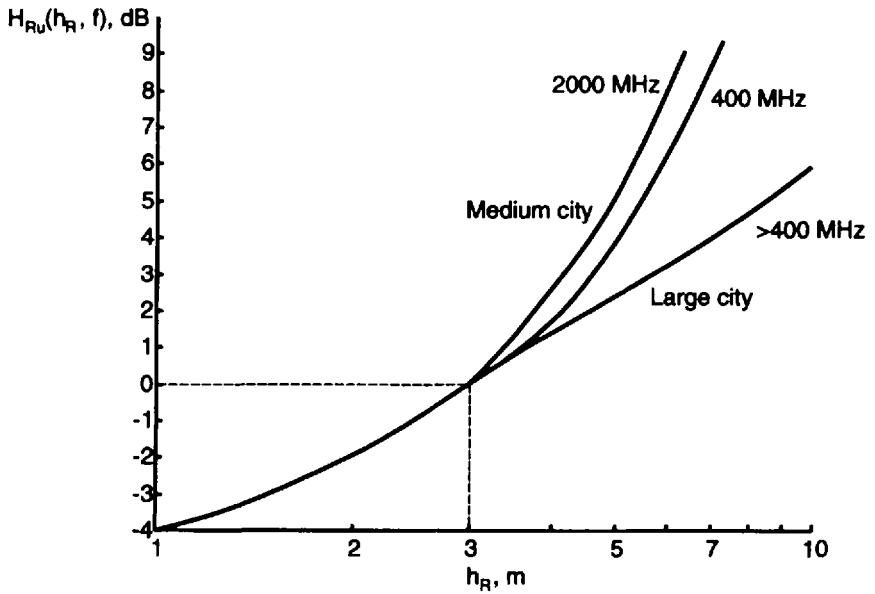

Figure 7.7 The height-gain factor $H_{Ru}(h_R, d)$ versus the receiver antenna height and the frequency and type of area urbanization.

distance of 10 km from the receiver in the direction towards the transmitter (see Figure 7.9). The correction factor for sloping terrain, L_{SP}, is shown in Figure 7.10. It follows from the presented illustration that the average slope parameter, angle θ, can be positive or negative and is measured for generally sloping terrain over 60 km, less than 10 km and about 30 km. The mixed land-sea correction factor, L_{LS}, is presented in Figure 7.11. It is determined by the percentage of total radio-path length covered with water.

The Okumura approach is probably the most widely quoted of the available models. It takes into account not only urban, suburban, and rural environments, but also describes the effects of different kinds of terrain. All phenomena and effects can be computed well in practice. However, it is rather cumbersome to implement this model with all correction factors in a computer because the data is available in graphical form. Thus, for computer implementation, data has to be entered in the computer memory in *point-to-point* form and interpolation routines have to be written for intermediate computations.

7.1.4 Hata Model

In an attempt to make the Okumura technique suitable for computer implementation and easy to apply, Hata [5, 6] developed an empirical model to describe

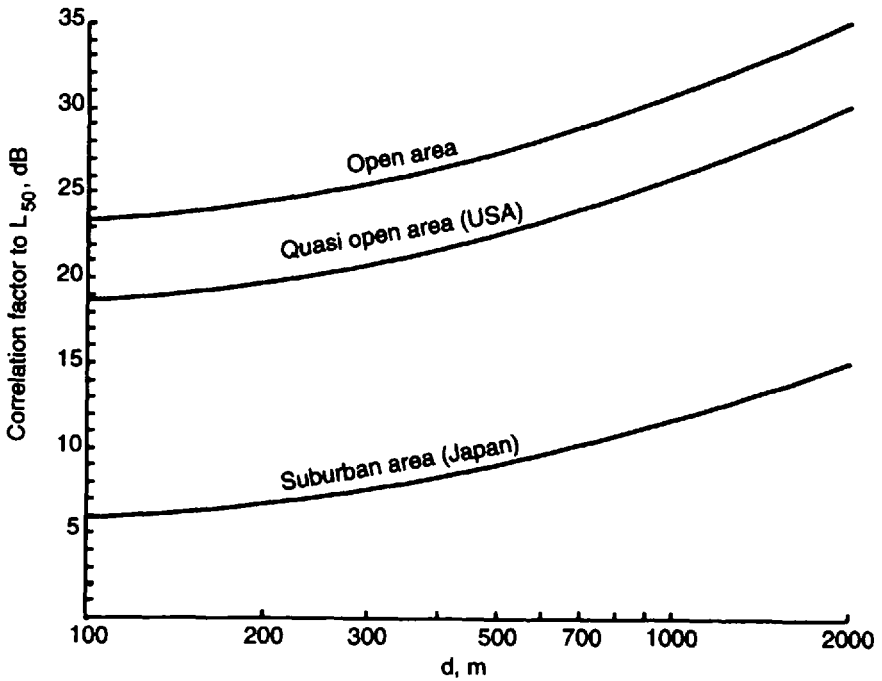

Figure 7.8 The correction factor for the Okumura method.

the graphical information given by Okumura. It is presented in Figures 7.5 to 7.11. His analytical expressions for average path loss, L_{50}, for urban, suburban, and rural areas are applicable only over quasi-smooth terrain and are limited by certain limitations of input parameters and are in dB

$$L_{50} = 69.55 + 26.16 \log f_0 - 13.82 \log h_T - a(h_R) + (44.9 - 6.55 \log h_T) \log d \tag{7.7}$$

where $150 \leq f_0 \leq 1500$ MHz, $30 \leq h_T \leq 200$m, $1 \leq h_R \leq 10$m, and $1 \leq d \leq 20$km. All parameters in (7.7) are the same as above in Section 7.1.3; the function $a(h_R)$ is the correlation factor for mobile antenna height that is computed as follows [5, 6]
for medium-size cities:

$$a(h_R) = (1.1 \log f_0 - 0.7)h_R - (1.56 f_0 - 0.8) \tag{7.8a}$$

for large cities:

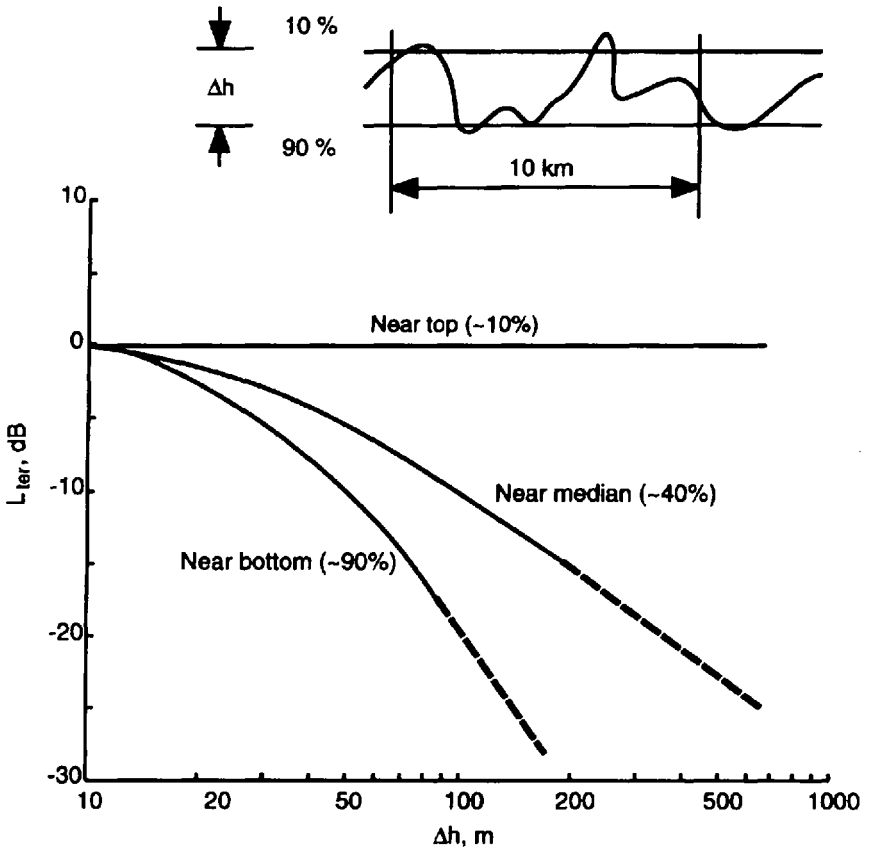

Figure 7.9 The rolling-hill terrain correction factor versus terrain undulation height.

$$\begin{aligned} a(h_R) &= 8.29 \cdot (\log 1.54\ h_R)^2 - 1.1, \quad f_0 \le 200 \text{ MHz} \\ &= 3.2 \cdot (\log 11.75\ h_R)^2 - 4.97, \quad f_0 \ge 400 \text{ MHz} \end{aligned} \tag{7.8b}$$

For suburban areas:

$$L_{50} = L_{50}(\text{urban}) - 2\left[\log\left(\frac{f_0}{28}\right)\right]^2 - 5.4 \text{ (dB)} \tag{7.9}$$

For open and rural areas:

$$L_{50} = L_{50}(\text{urban}) - 4.78[\log f_0]^2 - 18.33 \log f_0 - 40.94 \text{ (dB)} \tag{7.10}$$

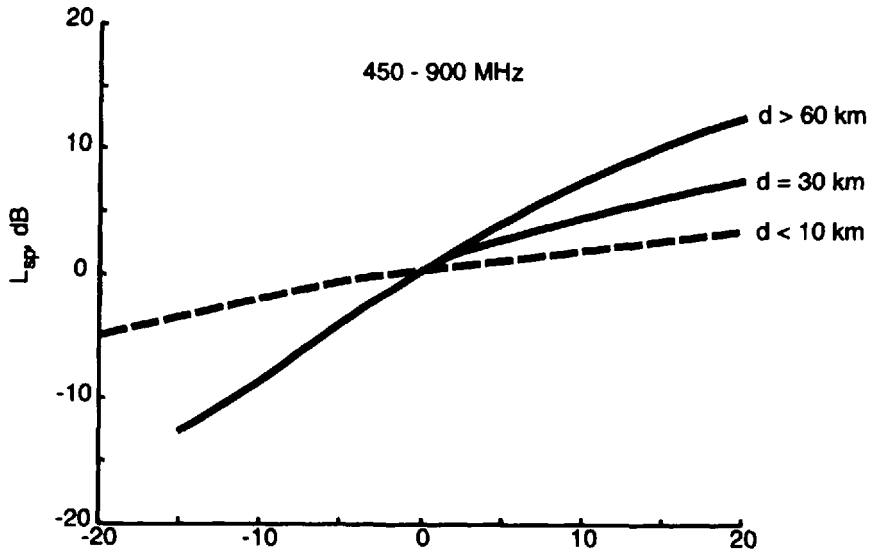

Figure 7.10 The slope-terrain correction factor obtained from measurements and from theoretical prediction.

As follows from the analytical relationships presented by Hata between parameters of consideration, the corrections have been made for both suburban and rural areas, where in (7.9) and (7.10), L_{50} (urban) denotes the path loss in an urban area according to (7.7) and (7.8). The last formulas also account for the difference in correction function for small, medium, and large cities. The difference between such cities can be found in Chapter 1, where these definitions were made in the context of general-terrain classification. The path loss difference for different built-up areas is presented in Figure 7.12, where the average path loss at 900 MHz for h_T = 200m and h_R = 3m has been plotted versus the distance between two terminals in kilometers. The difference in path loss is negligible for a small or large city, not exceeding 1–2 dB.

We must note that the Hata model does not include all specific corrections available in the original Okumura method. Nevertheless, a comparison between results given by Hata's formulations and data obtained from Okumura's original curves for urban areas and for reference antenna heights h_T = 200m and h_R = 3m reveals negligible differences that, as follows from Figure 7.13, rarely exceed 1–2 dB. Moreover, Hata's analytical expressions are, of course, very easily entered into a computer for computation.

7.1.5 Akeyama's Modifications

To use the Okumura method with Hata's expressions for prediction of communication channels in urban areas, one might ask if their approaches have been

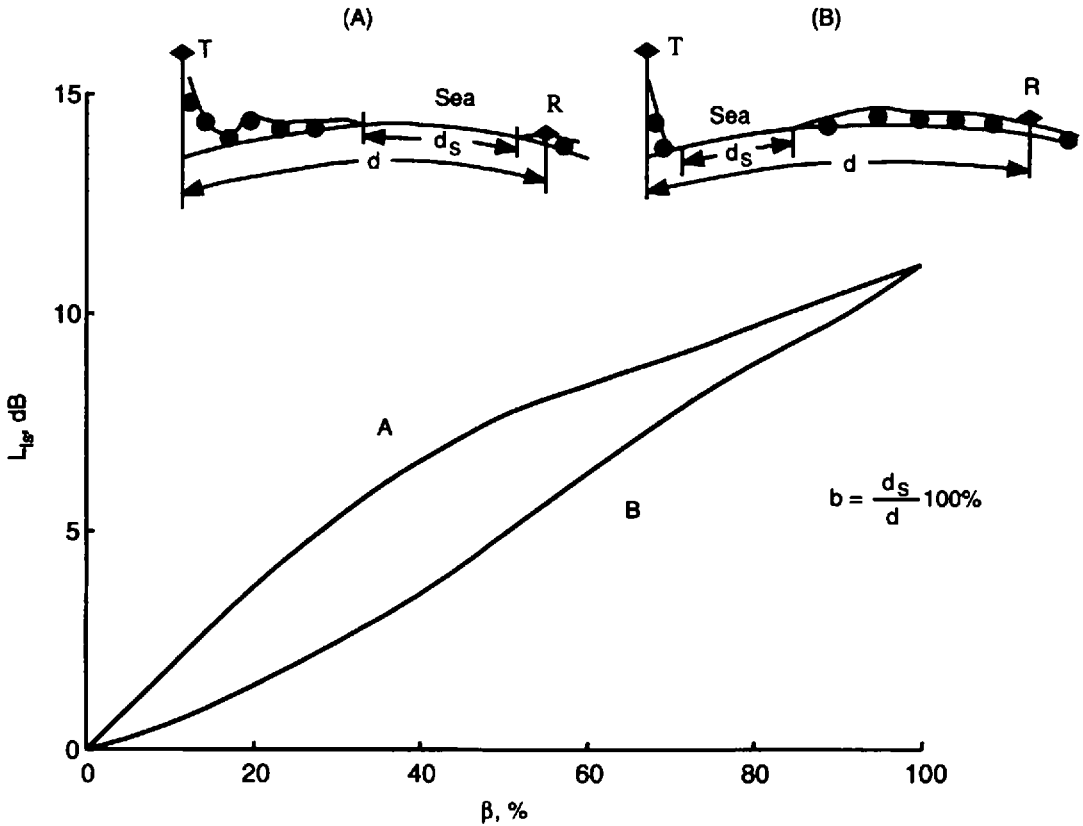

Figure 7.11 The land-sea correction factor versus distance ratio in percentage.

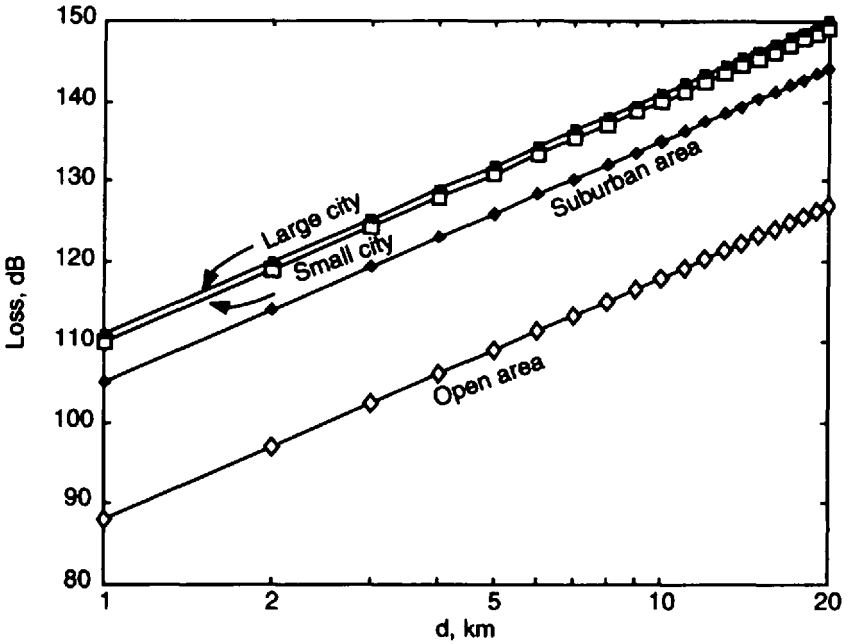

Figure 7.12 Average path loss versus distance from the transmitter.

adopted for different countries with various built-up profiles of terrain. In many countries, the urban situation is far different from that in Tokyo. Okumura's definition of urban, based only on the architecture and building type in Tokyo, may not be directly transferable to cities in North America or Europe. In fact, the typical United States suburban environment lies between Okumura's definition of suburban and open areas.

One other problem that must be taken into account is that the correction factor $a(h_R)$, which accounts for suburban, quasi-open, and open environments, is a function only of the buildings in the immediate vicinity of the vehicle. This factor is often more than 20 dB and cannot be objectively related to the real heights and density of buildings. There also exists a principal question of how Okumura's factors can be applied direct to cities which differ from Tokyo in their architectural style, construction, materials, and so on. Moreover, comparison of Hata expressions for a built-up area with the deterministic models described by Walfisch, Bertoni et al. in [7–9] (which is briefly presented in Section 6.2) and in [9] (which is denoted in Figure 7.14 as the "flat edge" model), shows that both in UHF/L-band propagation (955 and 1845 MHz) the deterministic approach gives a better fit with experimental data than the Hata model. The mean error from measurements for the deterministic approach

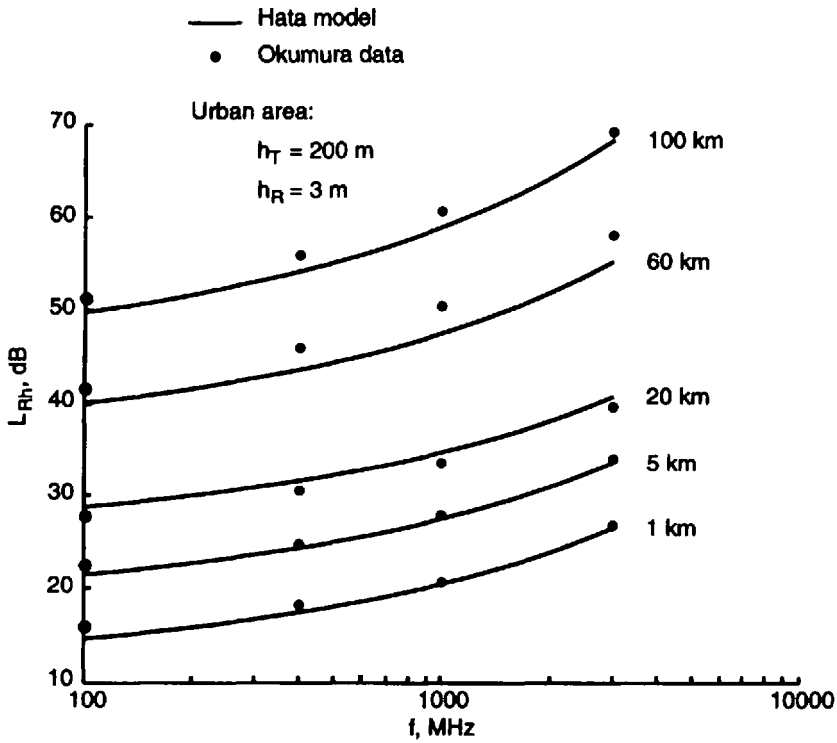

Figure 7.13 Comparison between the Okumura measurements (points) and the Hata prediction.

does not exceed 3–5 dB, whereas the Hata empirical approach based on Okumura's curves gives an error that exceeds 10–12 dB. To correct Okumura's curves, a new ground-cover factor that accounts for the degree of urbanization was introduced by Akeyama et al. [10]. To produce the best fit between experimental data depicted in Figure 7.15, a regression line was drawn according to an additional factor S, introduced by Akeyama as a deviation from Okumura's reference median curve at 450 MHz:

$$\begin{aligned} S &= 30 - 20 \log \alpha, && 5\% \le \alpha < 50\%, \\ &= 20 + 0.19 \log \alpha - 15.6 \cdot (\log \alpha)^2, && 1\% \le \alpha < 5\%, \\ &= 20, && \alpha < 1\% \end{aligned} \qquad (7.11)$$

Here, α is the percentage of the area covered by buildings in the built-up area.

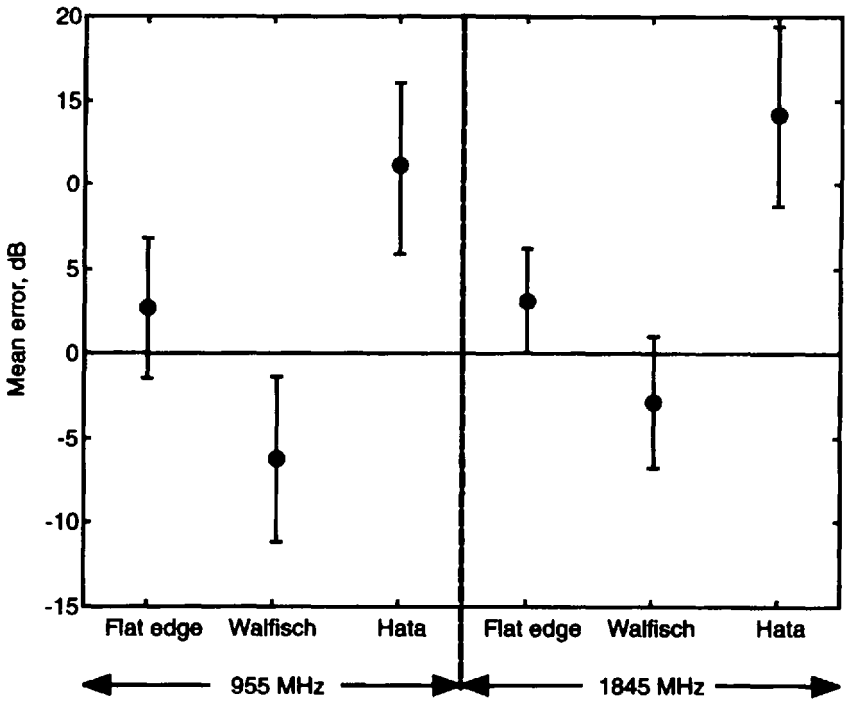

Figure 7.14 Comparison between the Hata empirical model, the deterministic two-dimensional diffraction model [7], the two-dimensional flat model [9], and experimental data.

7.2 Specific Models Based on Special Semi-Empirical Algorithms

Let us now discuss specific semi-empirical models that are based on the equation of a straight line presented in the same manner as for the plane-terrain model or the two-ray model, and on regression analysis to obtain the best fit between prediction empirical technique and experimental data.

7.2.1 Walfisch-Ikegami Model

This model gives a good path loss prediction for dense built-up areas such as medium and large cities [11]. It is based on important urban parameters such as building density, average building height, and street width. In this model antenna height is generally lower than the average buildings' height, so that the waves are guided along the street.

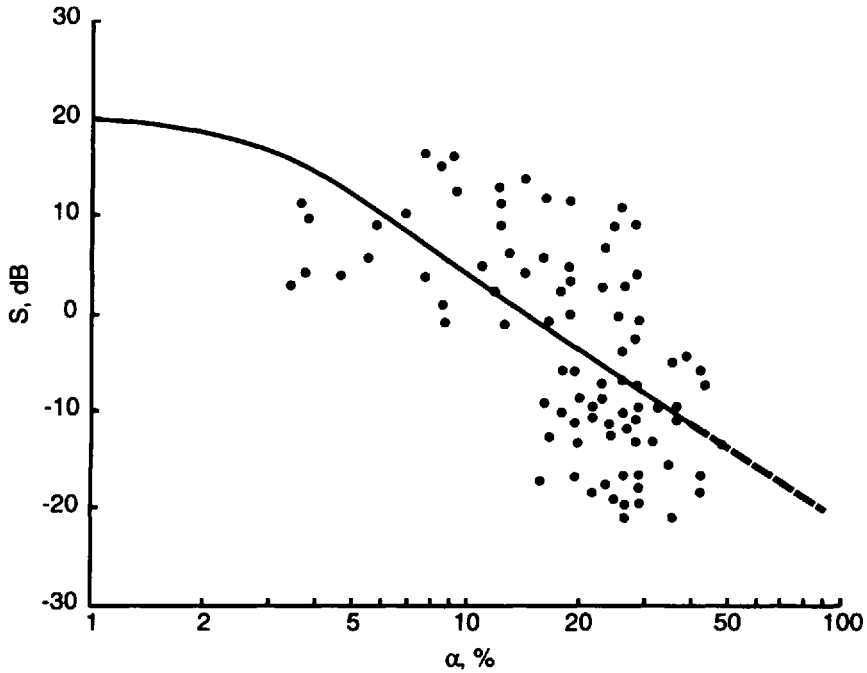

Figure 7.15 Deviation from reference average curve.

For LOS conditions, the path loss formula has the same form as the free-space formula changing only constants before a well-known parameter, the distance between terminals d:

$$L_{50}(LOS) = 42.6 + 20 \log f_0 + 26 \log d \tag{7.12}$$

which can be rewritten by means of the familiar equation of a straight line as

$$L_{50}(LOS) = L_0 + 10\gamma \log d \tag{7.13}$$

where L_0 is the intercept and γ is the attenuation slope (see Section 3.2) that can be defined as

$$\begin{aligned} L_0 &= 42.6 + 20 \log f_0 \\ \gamma &= 2.6 \end{aligned} \tag{7.14}$$

As follows from the free-space model in Section 2.3, $\gamma = 2$. Such a low attenuation slope $\gamma = 2.6$ (the distance dependence for receiving signal, $d^{-2.6}$,

obtained in [11] for the urban environment) was explained by the authors as a result of the low antenna heights at the street level below the rooftops. But this conclusion is in conflict with numerous experimental data obtained from the straight measurements and two-ray model, all of which gives the slope attenuation along the street beyond the break point as $\gamma = 4 - 7$ that limits the exponential attenuation obtained by use of the waveguide model (see Chapter 5 for discussions).

As for *NLOS conditions*, the semi-empirical path loss formula is [11]:

$$L_{50}(NLOS) = 32.4 + 20 \log f_0 + 20 \log d + L_{RD} + L_{MD} \quad (7.15)$$

where L_{RD} represents rooftop diffraction loss, and L_{MD} represents multiple diffraction loss due to surrounding buildings. The rooftop diffraction loss is characterized as

$$L_{RD} = -16.9 - 10 \log \Delta a + 10 \log f_0 + 20 \log \Delta h_R + L(0) \quad (7.16)$$

where

Δa is the distance between the vehicle and the building,
h_R is the mobile vehicle antenna height,
$L(0)$ is the loss due to elevation angle,
$\Delta h_R = h_{roof} - h_R$.

The multiple-diffraction component is characterized by the following equation:

$$L_{MD} = K_0 + K_a + K_d \cdot \log d + K_f \cdot \log f_0 - 9 \log a \quad (7.17a)$$

where

$$\begin{aligned} K_0 &= -18 \log(1 + \Delta h_T) \\ K_a &= 54 - 0.8\Delta h_T, \quad d \geq 0.5\text{km} \\ &= 54 - 1.3\Delta h_T, \quad d < 0.5\text{km} \\ K_d &= 18 - 15(\Delta h_T / h_{roof}) \\ K_f &= -4 + 0.7[(f_0/925) - 1], \quad \text{for suburban} \\ &= -4 + 0.7[(f_0/925) - 1], \quad \text{for urban} \end{aligned} \quad (7.17b)$$

Where a is the street width, h_T is the base-station antenna height, h_{roof} is the average height of small buildings ($h_{roof} < h_T$), $\Delta h_T = h_T - h_{roof}$. In the

Walfisch-Ikegama model it was initially assumed that the base-station antenna height is lower than a tall building but higher than the small buildings surrounding it.

Combining (7.15), (7.16) and (7.17), one obtains

$$L_{50}(NLOS) = L_0 + (20 + K_d) \cdot \log d = L_0 + 10\gamma \log d \quad (7.18a)$$

where

$$L_0 = 32.4 + (30 + K_f) \cdot \log f_0 + 20 \log \Delta h_R + L(0) - 16.9 - 10 \log a \quad (7.18b)$$

$$\gamma = (20 + K_d)/10 \quad (7.18c)$$

So, once again, the NLOS characteristics shown by (7.18a–c) exhibit a straight line with L_0 as the intercept and γ as the attenuation slope. The diffraction constant, K_d, depends on the surrounding buildings' heights, which vary from a few meters to tens of meters. Therefore, according to (7.17a), the typical attenuation slopes in these built-up areas deviate from $\gamma = 2$ for $\Delta h_T/h_{roof} = (h_T - h_{roof})/h_{roof} = 1.2$ to $\gamma = 3.8$ for $\Delta h_T/h_{roof} = 0$. Hence, with an increase of base-station antenna height with respect to the surrounding buildings' average height, the field attenuation's low limit is that in free space, when $\gamma = 2$. Then we can present path loss (because L_0 is constant for area for consideration) as:

$$L(\text{dB}) \propto 10\gamma \log d \quad (7.19a)$$

or in the linear case, as:

$$L(W) \propto d^{-\gamma}, \quad \gamma = 2 - 3.8 \quad (7.19b)$$

Because in a real situation in the urban scene, $\Delta h_T/h_{roof} < 1$, the slope attenuation parameter varies within the range $\gamma = 2.7 - 3.8$.

It is interesting now to compare both empirical models, the Hata model and the Walfisch-Ikegama model for a dense urban area. Let us rewrite formula (7.7) of the Hata model in the form of an equation for a straight line

$$L_{50}(LOS) = L_0 + 10\gamma \log d$$

and taking into account (7.7b), we have that the intercept L_0 and the path-loss slope γ are:

$$L_0 = 69.55 + 26.16 \log f_0 - 13.82 \log h_T - a(h_R)$$
$$\gamma = (44.9 - 6.55 \log h_T)/10 \tag{7.20}$$

For the typical base-station antenna height h_T = 6m–30m, the slope parameter is changed from 4 to 3.5. Hence, we can once more present the path loss and the signal power in dense urban area as

$$L(\text{dB}) \propto 10\gamma \log d \tag{7.21a}$$

or, in the linear case, as

$$L(W) \propto d^{-\gamma}, \quad \gamma = 3.5 - 4.0 \tag{7.21b}$$

We obtain from both empirical approaches approximately the same polynomial signal-power decay with $2.5 \leq \gamma \leq 4$ versus the distance from both terminals in the case of dense urban areas.

7.2.2 The Ibrahim-Parsons Method

Using numerous measurements carried out in London at three operating frequencies of 168, 445, and 900 MHz with a base-station antenna height of 46m above the ground, in [12], the equation of the straight line which gives a best fit with the experimental data was empirically obtained for each operating frequency. These equations were compared with the classical fourth-power signal decay according to the "plane-earth" model (see Section 3.2). The result of this comparison is presented in Table 7.1.

As follows from the results presented, the empirically obtained law of signal-power decay varies from $d^{-3.6}$ up to $d^{-4.3}$. To model the results obtained from the measurements, two approaches were proposed in [12]. The first is

Table 7.1
Comparison of the Plane-Earth Model and the Best Fit From [12]

Frequency	Average Path Loss (dB)	Prediction Error (dB)
168 MHz	Best fit: $1, 6 + 36.2 \cdot \log d$	5.3
	Fourth law: $-12.5 + 40 \cdot \log d$	5.5
455 MHz	Best fit: $-15.0 + 43.1 \cdot \log d$	6.18
	Fourth law: $-4.0 + 40 \cdot \log d$	5.5

based on multiple-regression analysis to derive an empirical expression for the path loss. The second one is based on the well-known plane-earth (or two-ray) model. We will not present here all the details of the authors' analysis. The reader can read the original reference [12] for more details.

Empirical approach. Using multiple-regression analysis, called empirical by the authors, the following empirical formula was obtained to describe the path loss:

$$L_{50} = -20\log(0.7h_T) - 8\log h_R + \frac{f_0}{40} + 26\log\frac{f_0}{40} - 86\log\left(\frac{f+100}{156}\right) \quad (7.22)$$
$$+ \left[40 + 14.15\log\left(\frac{f+100}{156}\right)\right]\log d + 0.265L - 0.37H + K$$

Here, factor $K = 0.087U - 5.5$ for highly urbanized areas, otherwise $K = 0$, and parameters L, K, and U must be obtained for the concrete situation in the urban scene from the corresponding topographic maps (the algorithm is presented in [12]). The base-station antenna height is $h_T = 46$m, the moving vehicle antenna height is $h_R \leq 3$m, and the distance between terminals varies in the range $0 < d \leq 10$km.

The semi-empirical model. This approach is based on the plane-earth model with an added excess clutter loss, β. For each operating frequency, 168, 455, and 900 MHz, this value was computed and, then, related to the urban environment factors, a best-fit equation for β was found. Finally, the following model was proposed (which is different from that obtained in Section 3.2):

$$L_{50} = 40\log d - 20\log(h_T h_R) + \beta \quad (7.23)$$

where

$$\beta = 20 + \frac{f_0}{40} + 0.18L - 0.34H + K \quad (7.24)$$

and $K = 0.094U - 5.9$.

Here again, K is applicable only for dense urbanized areas, otherwise $K = 0$. Comparisons with experimental data have allowed the authors to obtain the prediction error by the use of each proposed approach, which they summarize in Table 7.2.

As an illustration of β variations with an urban situation (with changes of parameters L, U, and H), let us present β for a flat terrain ($H = 0$) at frequency 900 MHz according to [12]:

Table 7.2
Prediction Error for Two Models (in dB):

Model	Frequency (MHz) 168	455	900
Empirical	2.1	3.2	4.19
Semi-empirical	2.0	3.3	5.8

$$\beta = 42.5 + 0.18L \tag{7.25}$$

Here, if parameter L lies in the range 0%–80%, then β lies between 42.5–57 dB. This result agrees well with those obtained independently through measurements, as seen in illustrations in Figure 7.16. Here, the best fit is obtained for $\beta = 49$ dB. The two approaches have been compared with independent measurements collected by Allsebrook [12] at 85, 167, and 441 MHz, and with the empirical model proposed by Atefi and Parsons [13] which in completed form was presented by Parsons [14]:

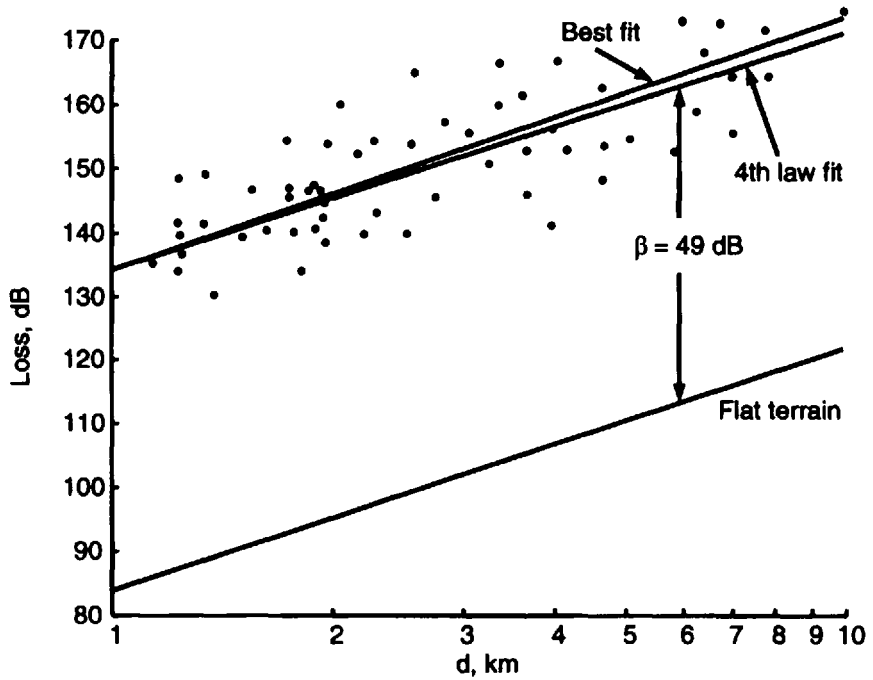

Figure 7.16 Comparison between measured and theoretically predicted path loss.

$$L_{50} = 82 + 26.16 \log f_0 + 30 \log d - 21.8 \log h_T - 0.15 \log h_R + L_d \text{ (dB)} \tag{7.26}$$

where L_d represents the diffraction loss that can be obtained by use of the Epstein-Peterson construction (see Section 4.2). The results of this comparison between the different approaches are summarized in Table 7.3.

The proposed empirical models are quite successful and give the same accuracy over a wide range of transmitted frequencies.

7.2.3 Lee's Model

This model was constructed to obtain UHF-band propagation characteristics over irregular terrain by use of two approaches: an area-to-area algorithm and a point-to-point algorithm [14, Chapter 3].

The area-to-area method. This approach is also based on the equation of straight line presentation of path loss by use of the following parameters: (a) average transmission loss at the range of 1 km, (b) slope of the path-loss curve according to plane-earth model (see Section 3.2), (c) adjustment factor. In this case, the average path loss in dB at distance d from the transmitter is given by the following expression:

$$L_{50} = L_0 + 10\gamma \log d + F_0 \tag{7.27}$$

Parameters L_0 and γ that were derived from experimental data are listed in Table 7.4.

It follows from Table 7.4 that with the exception of Tokyo, the value of γ for urban and suburban areas is always close to $\gamma = 4$ ($3.68 \leq \gamma \leq 4.31$), that is, the field intensity attenuates with distance as d^{-4}. The experimental results on which Table 7.4 is based were obtained using a transmission system with the following parameters.

Table 7.3
Comparison of Different Approaches

Frequency (MHz)	According to (7.26)	Allsebrook's Best Fit Straight Line	Ibrahim's Best Fit Straight Line
85.87	$97.4 + 38 \cdot \log d$	$98.0 + 38 \cdot \log d$	
167.2	$105.0 + 38 \cdot \log d$	$101.0 + 38 \cdot \log d$	$106.0 + 38 \cdot \log d$
441.0	$116.0 + 38 \cdot \log d$	$117.0 + 38 \cdot \log d$	$115.0 + 38 \cdot \log d$

Table 7.4
Path Loss Parameters for Different Areas:

Area of Interest	L_0	γ
Newark	−94.0	4.31
Tokyo	−114.0	3.05
Philadelphia:		
Urban	−100.0	3.68
Free space	−75.0	2.0
Open	−79.0	4.35

The reference base station antenna h_T = 30.5m,
the operating frequency is f_0 = 900 MHz,
the transmitter power is P = 10W,
the base-station antenna gain with respect to a $\lambda/2$ dipole is 6 dB (or in linear scale, (4),
the mobile antenna height is h_R = 3m.

The adjustment factor F_0 is introduced to compensate for the use of different values of these parameters and is expressed as

$$F_0 = F_1 F_2 F_3 F_4 \tag{7.28a}$$

The values of these various factors are given by

$$F_1 = \frac{[\text{Actual base station antenna height (m)}]^2}{(30.5\text{m})^2}$$

$$F_2 = \frac{[\text{Actual transmitter power } (W)]}{10\text{W}} \tag{7.28b}$$

$$F_3 = \frac{[\text{Actual gain of base station antenna}]}{4}$$

$$F_4 = \frac{[\text{Actual vehicle antenna height (m)}]^2}{(3\text{m})^2}$$

Lee also suggests that the propagation effects of changes in transmission frequency is $\sim(f/f_0)^n$, where according to Young [1] and Okumura [4] the parameter n is $2 \leq n \leq 3$.

Point-to-point method. In this more refined approach, Lee takes into account the terrain profile. In fact, according to [14], there are two possible

reflection points as shown in Figure 7.17. As seen, the effective one is the one closer to the mobile vehicle. From the geometry presented in Figure 7.17 one can easily obtain the effective height h_e that can be greater (case (a)) or less (case (b)) than the actual height above the local ground. Using the effective ground height, Lee corrected (7.27) to

$$L'_{50} = L_{50} + 20 \log(h_e/30) \tag{7.29}$$

where L_{50} is described by (7.27) and h_e is in meters.

As the mobile moves from point A to point I, the effective height of the base-station antenna, as follows from Figure 7.18(a), is also changed. The separate evaluation of (7.29) has to be made at each of these points and hence the term "point-to-point" has been used. Figure 7.18(b) shows the difference between the point-to-point prediction algorithm and predictions for flat-suburban terrain with $\gamma = 38.6$ dB/decade (or in linear scale $\gamma = 3.86$). For positions of the vehicle from point C to point G the value of h_e is greater that the actual height above local ground surface, so here the predicted loss (according to Lee) is smaller than follows from the plane-earth terrain model. Conversely, for positions of vehicle at H and I, the value of h_e is less than the actual height of terrain, and the predicted loss is higher. As was shown from additional estimations obtained by Lee, the second approach, point-to-point, better predicts the variations of the terrain surface. In fact, the standard deviation to predict the average path loss of the first algorithm (area-to-area) is 8 dB, but in the point-to-point model it falls to less than 3 dB.

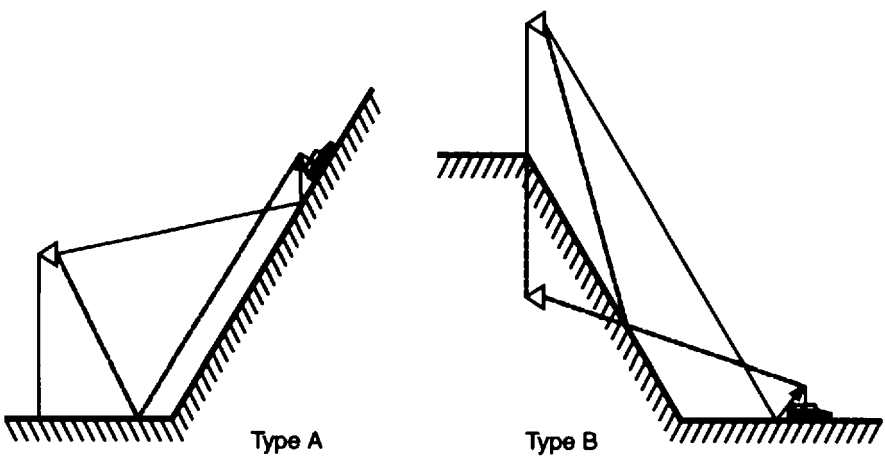

Figure 7.17 Geometry of reflection from the hill surface for two variants of base station and vehicular antennas location.

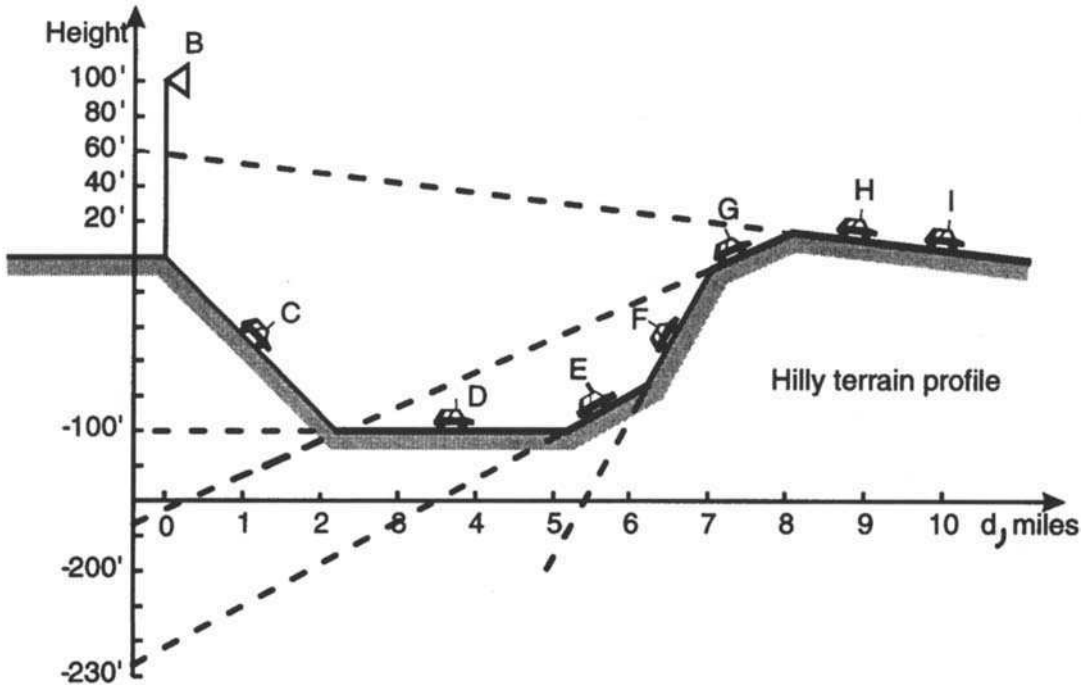

Figure 7.18 (a) Hilly terrain contour and various positions of moving vehicle relative to base-station antenna. (b) Point-to-point prediction compared with path loss slope.

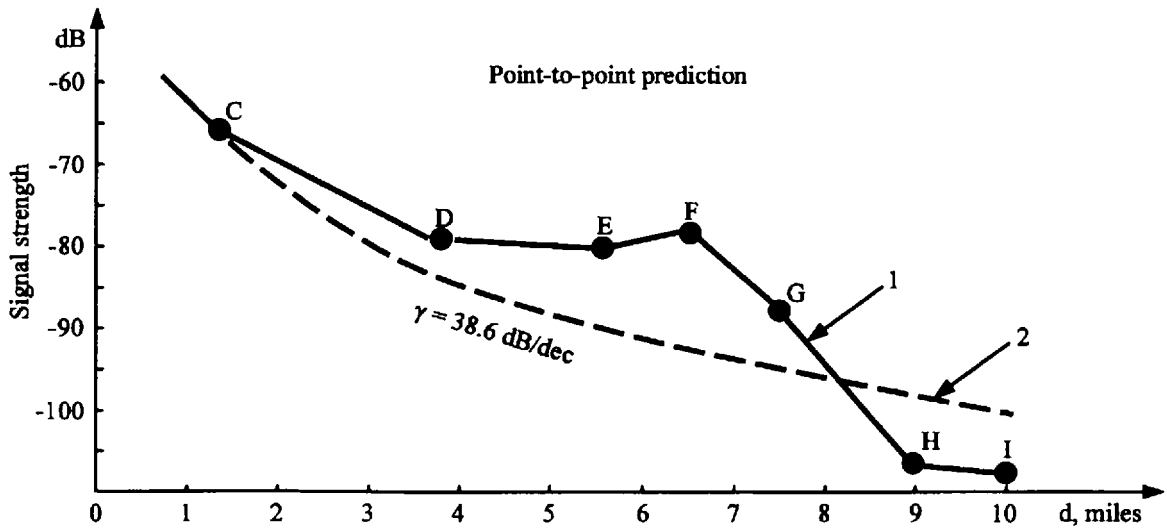

Figure 7.18 (continued).

7.3 Deterministic Models

We will now discuss deterministic approaches that more effectively predict loss characteristics in built-up areas sprawling over irregular terrain.

7.3.1 Parabolic Equation Method

This method was used by Janaswamy and Andersen [15, 16] to predict the path loss in two-dimensional urban areas with buildings spread over rough terrain, as shown in Figure 7.19. Here, the position of the transmitter (T_x) and the receiver (R_x), as well as the terrain and building profile, are presented assuming that the vertical walls of the buildings are absorbing nontransparant screens and the roofs are flat and reflective. The ground parameters, ϵ_{rg} and σ_g, are different with respect to those for the walls and rooftops, ϵ_b and σ_b. Let us briefly discuss the subject of the computational technique proposed in [15, 16].

The model description. This proposed technique is based on the standard parabolic equation, which assumes a time dependence $\sim e^{-i\omega t}$ according to [15, 16] and can be presented as:

$$\frac{\partial U(x, z)}{\partial x} = \frac{i}{2k_0} \frac{\partial^2 U(x, z)}{\partial z^2} \tag{7.30}$$

where

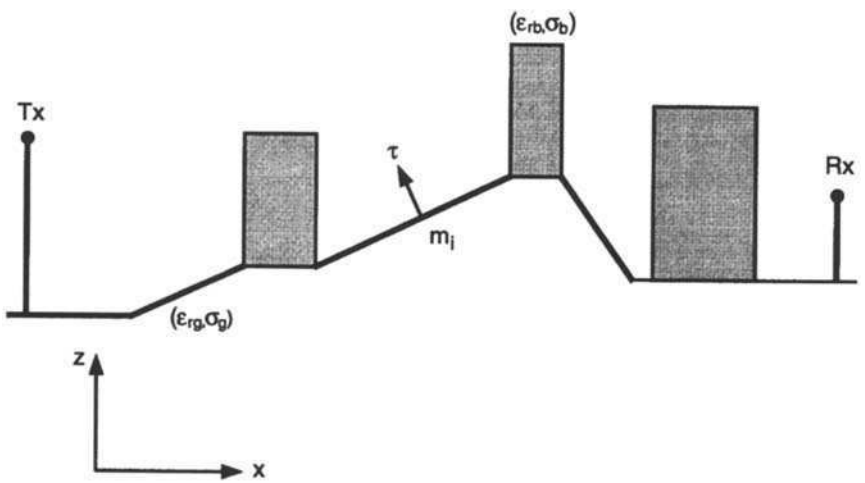

Figure 7.19 Geometry of propagation over irregular built-up terrain.

$$U(x, z) = \sqrt{r \cdot \sin\theta} \cdot \exp\{-ik_0 x\} \cdot E_\varphi(r, \theta), \text{ horizontal polarization} \quad (7.31)$$

$$= \sqrt{\frac{r \cdot \sin\theta}{\epsilon_0}} \cdot \exp\{-ik_0 x\} \cdot H_\varphi(r, \theta), \text{ vertical polarization}$$

is the reduced field variable in a spherical coordinate system $\{r, \theta, \varphi\}$ with an origin at the center of the earth. For the flat-terrain approximation the relations between Cartesian coordinates $\{x, z\}$ and spherical coordinates in a two-dimensional plane are [15, 16]: $x = R_e \cdot \theta$, and $z = r - R_e$, where R_e is the radius of the earth introduced in Chapter 3. The transmitter is located along $\theta = 0°$ as shown in Figure 7.19. In (7.31) the quantities E_φ and H_φ are the φ-components of the electric and magnetic fields, respectively; $k_0 = \omega \cdot \sqrt{\epsilon_0 \mu_0}$ is the free-space wavenumber which is introduced in Chapter 2.

The boundary conditions on the ground can be presented for the smoothly varying terrain profile, for which the radius of curvature is much greater with respect to wavelength, in the terms of the U variable for either polarization in the form [16]:

$$\frac{\partial U}{\partial r} + ik_0 Z_S U = 0, \text{ at the terrain profile} \quad (7.32)$$

where Z_S is the normalized surface impedance which depends on the ground parameters and the angle of incidence of the wave with respect to the normal **r** on the ground (see Figure 7.19). Equation (7.30) with boundary conditions (7.32) was solved numerically by use of a split-step Fourier algorithm and presenting the computational coordinates in the following form [15, 16]:

$$\zeta = x, \quad \eta = z - f(x) \quad (7.33)$$

where $f(x)$ is the terrain-profile function.

In the split-step algorithm, the field at the new range, $x + \Delta x$, was obtained in terms of the field at the old range, x, as [15, 16]:

$$U(x + \Delta x, \eta) = \frac{e^{im\left(\eta + \frac{m}{2}\Delta x\right)}}{2\pi} \int_{-\infty}^{\infty} e^{-\frac{ip^2 \Delta x}{2}} e^{ip\eta} dp \quad (7.34)$$

$$\times \int_0^{\infty} [e^{-ip\tau} + \Gamma(p) e^{ip\tau}] e^{-im\tau} U(x, \tau) d\tau$$

where m is the slope of the terrain between the two ranges. In (7.34) all spatial variables are normalized with the wavenumber k_0. The quantity $\Gamma(p)$ may be interpreted as a complex reflection coefficient for a plane-wave incident on sloping terrain and equals:

$$\Gamma(p) = \frac{p - \Gamma_t}{p + \Gamma_t} \tag{7.35}$$

Here, $\Gamma_t = \Gamma_0 \cos\nu + m(1 + \cos\nu)/2$ and Γ_0 is equal to $\sqrt{\epsilon_{rc}}$ for horizontal polarization and $1/\sqrt{\epsilon_{rc}}$ for vertical polarization, where the complex dielectric constant ϵ_{rc} is presented in Chapter 3.

The function within the square brackets in (7.34) is the eigenfunction of the operator appearing on the right-hand side of the standard parabolic equation (7.30). If the field variable goes to zero on the terrain (the *first order* boundary conditions, see Chapter 2), we set $\Gamma(p) = -1$ and the eigenfunctions reduce to sine functions. If the normal derivative of the field vanishes on the terrain (the *second order* boundary conditions, see Chapter 2), we set $\Gamma(p) = +1$ and the eigenfunctions reduce to cosine functions. In the inverse transform integral in (7.34) the exponential function $e^{-\frac{ip^2\Delta x}{2}}$ is the free-space propagator for the standard equation (7.30). A wide-angle parabolic equation may be obtained by replacing the right-hand side in (7.30) with the pseudo differential operator:

$$ik_0\left(\sqrt{1 + \frac{1}{k_0^2}\frac{\partial^2 U}{\partial z^2}} - 1\right) \tag{7.36}$$

As was shown in [15, 16], although the eigenfunctions of the wide-angle parabolic equation remain the same as those of the narrow-angle parabolic equation over flat terrain, a similar statement cannot be made over a sloping terrain. It has not been possible to find the eigenmodes for the wide-angle parabolic equation over a sloping terrain. In the split-step algorithm (7.34), it is possible to replace the narrow-angle free-space propagator $e^{-\frac{ip^2\Delta x}{2}}$ with the wide-angle free-space propagator $e^{i\Delta x(\sqrt{1-p^2}-1)}$. This replacement is rigorous for the case of flat terrain, but at the same time, it is at best an approximation over sloping terrain. This new propagator for the wide-angle parabolic equation was used in [15, 16] to obtain the path loss over sloping terrain.

Numerical results. In all results of computation the actual field was normalized to the field which would exist under free-space conditions. The first

example shown in Figure 7.20 describes the situation in the urban scene when a series of nontransparent screens (knife edges) are placed on a curved hill. The shape of the hill is parabolic with a peak height of 5m and width of 203m. Other parameters about screens and frequency of operating are shown in Figure 7.20. Results are given for the normalized field at the top of the screens and are compared with the sloped-diffraction results described in [17].

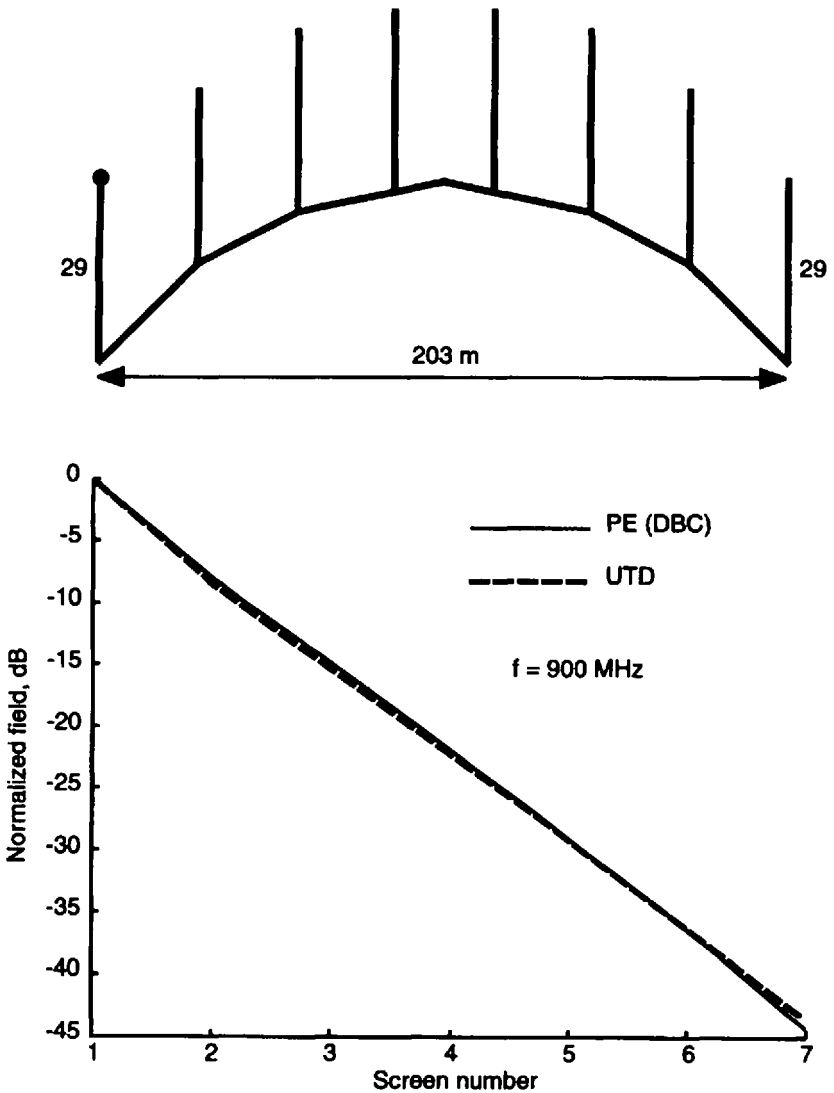

Figure 7.20 The normalized path loss over screens placed on a parabolic hill.

They are presented briefly in Section 4.2 for a similar screen profile, but, without the ground.

As follows from Figure 7.20, good agreement between two theoretical approaches with a maximum deviation of around 0.2 dB near the peak of the hill is observed. Figure 7.21 shows another comparison obtained in [15, 16] of a wide-angle approxiation according to (7.34) to (7.36) with a sloped-

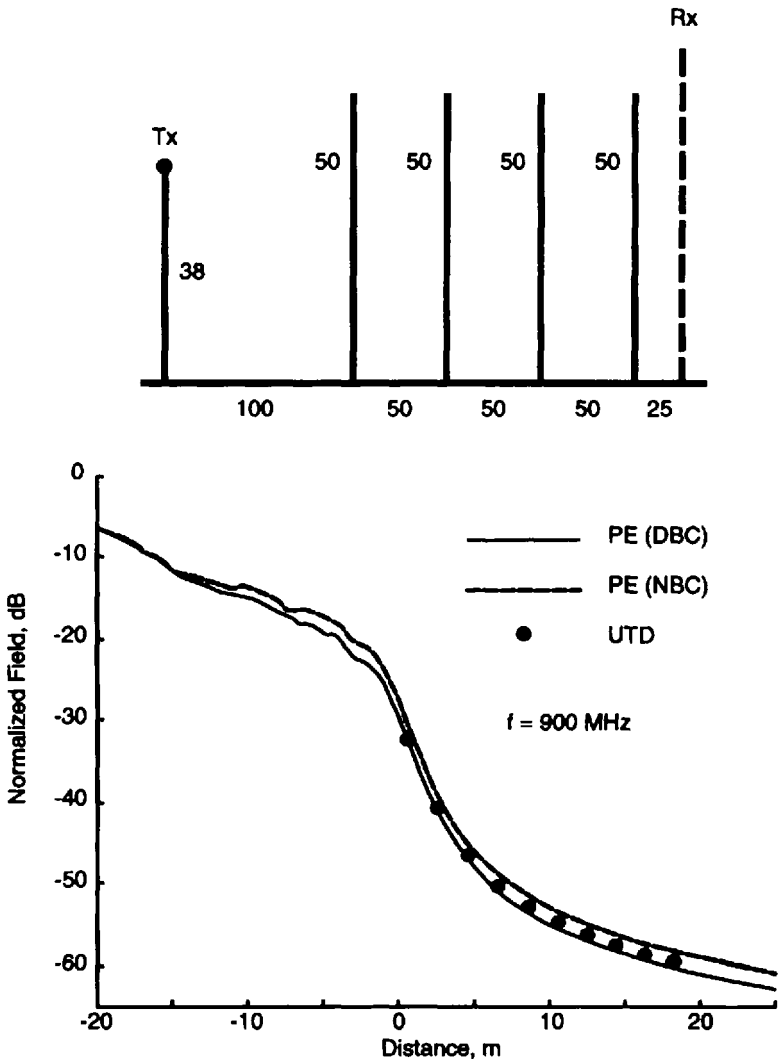

Figure 7.21 The normalized path loss over multiple knife edges by use of the wide-angle numerical technique.

diffraction approximation obtained by Andersen [17] (see also Section 4.2) for propagation over multiple screens placed on flat terrain. A good agreement for both approaches is also seen. It is interesting to note that all the presented curves obtained for various boundary conditions (BC) are rather insensitive to the exact nature of subsoil media. The terrain medium situations considered in Figure 7.21 correspond to zero field on the terrain (first, called Dirichlet, boundary conditions (DBC)), zero normal derivative (second, called Neumann, boundary conditions (NBC)), or a mixture of the two (for $\epsilon_{rg} = 10$, $\sigma_g = 20$mS/m). To compare both techniques used in [15, 16], the narrow-angle and the wide-angle approximation, the normalized field calculated for both of them satisfying the DBC on the terrain is shown in Figure 7.22. As shown, there is good agreement between the two techniques except for the deep shadow zone from the screens.

The wide-angle parabolic equation approximation was also compared with results obtained with WISE which is a ray-tracing tool developed at Bell Laboratories [18]. As follows from Figure 7.23, a transmitter of height 30m is located at zero range where the terrain has zero elevation. In a test profile two screens of heights 40m and 50m are located on a terrain with variable topography, the numbers indicated in the picture for the terrain are its height in meters; the maximum slope angle of the terrain is about 7.5 degrees, the receiver height is 1.5m above the local terrain. The ground medium is assumed to be perfectly reflecting, having a reflection coefficient of -1. In comparison the authors have excluded regions close to the screens where propagation angles are in excess of 45 degrees. Figure 7.23 shows good agreement between the analytical and the ray-tracing models for propagation angles within 45 degrees.

The authors have also compared their approach with the four-ray approximation [10] (see also Section 4.1) for one screen placed on flat terrain and with the UTD approach [19] for the case of a single rectangular building, and have obtained good agreement between the different approaches. Also, for the more realistic case presented in Figure 7.24, when instead of thin screens there are rectangular buildings placed on flat terrain, the authors [15, 16] obtained good agreement with the model that takes into account reflections from rooftops [20, 21].

Here, in Figure 7.24, comparison between results obtained in [15, 16] for two different boundary conditions on the terrain and rooftops is presented together with results of computations for one knife edge. We see that there is a significant difference (of about 45 dB) between two different boundary conditions in the deep shadow zone. The field attenuation depends on the dielectric properties of rooftops, and can vary within a wide range depending on the construction materials of the buildings. As for the one knife-edge model, its results lie between the two other limit cases.

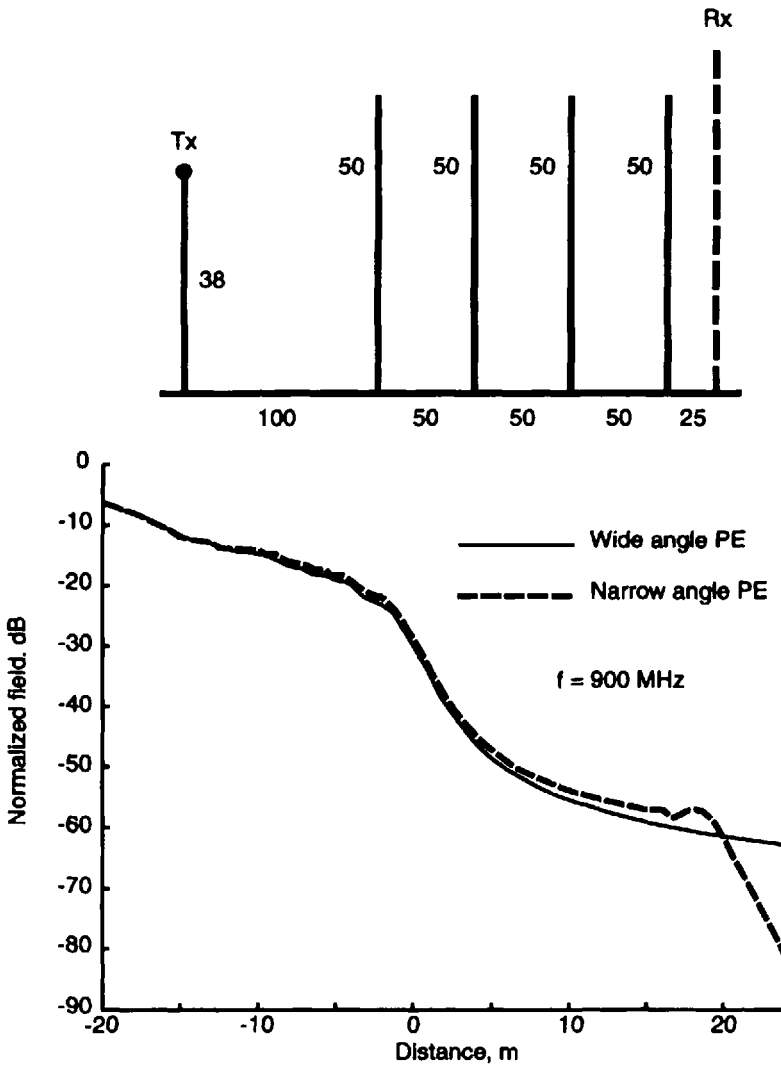

Figure 7.22 Comparison between narrow-angle and wide-angle techniques for propagation over multiple knife edges.

The model presented here may be used in a real scenario in the urban scene by generating two-dimensional results in several vertical planes about the transmitter. The results of wide-angle approximation are accurate within about ± 45 degrees and are rigorous for flat terrain but approximate for irregular terrain. Also, the results are good when the contribution by the lateral propagating waves can be ignored. Furthermore, this technique allows us to

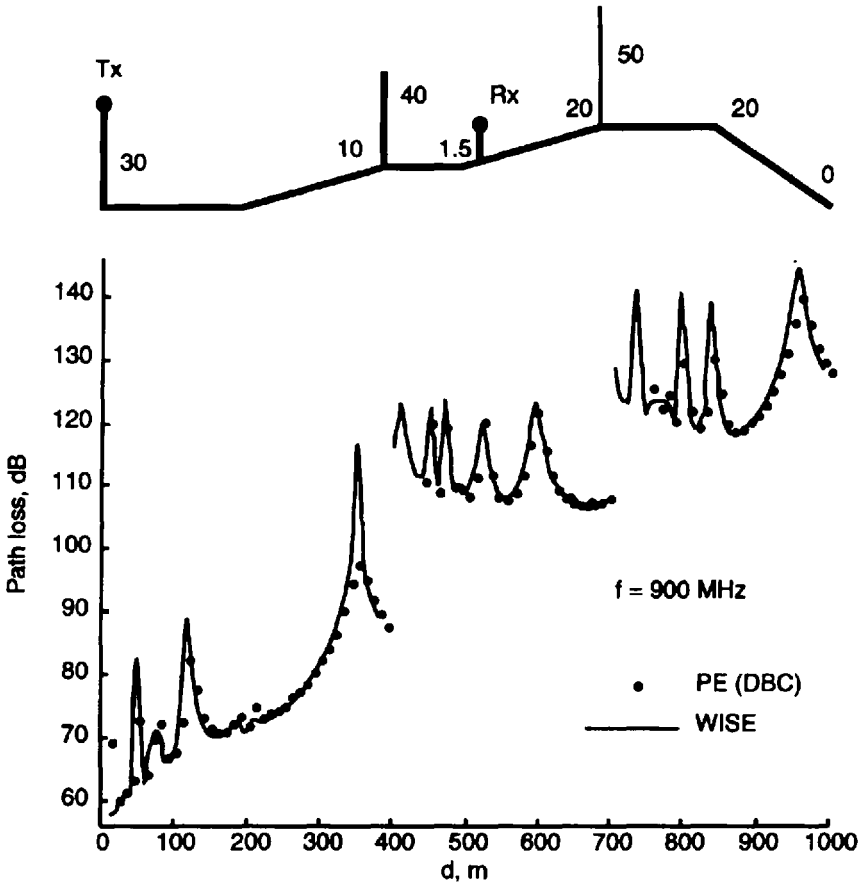

Figure 7.23 The path loss versus distance from transmitter by use of the parabolic equation (PE) technique and the ray-tracing tool (WISE).

obtain the total field in the situation when a receiver lies between two buildings along the propagation path, namely, taking into account the first-order back reflection by the building at the far end and summing it with forward-propagating waves (the reader can find more details in [15, 16]).

7.3.2 Multiple Knife-Edges Diffraction Method

This method can be considered as an extension of a two-dimensional model of multiple forward diffraction over rows of buildings placed on flat terrain [7–9, 22–25] in the case of rough (hilly) terrain [26] by use of a numerical technique based on a Kirchhoff-Huygens integrals presentation of the diffracted

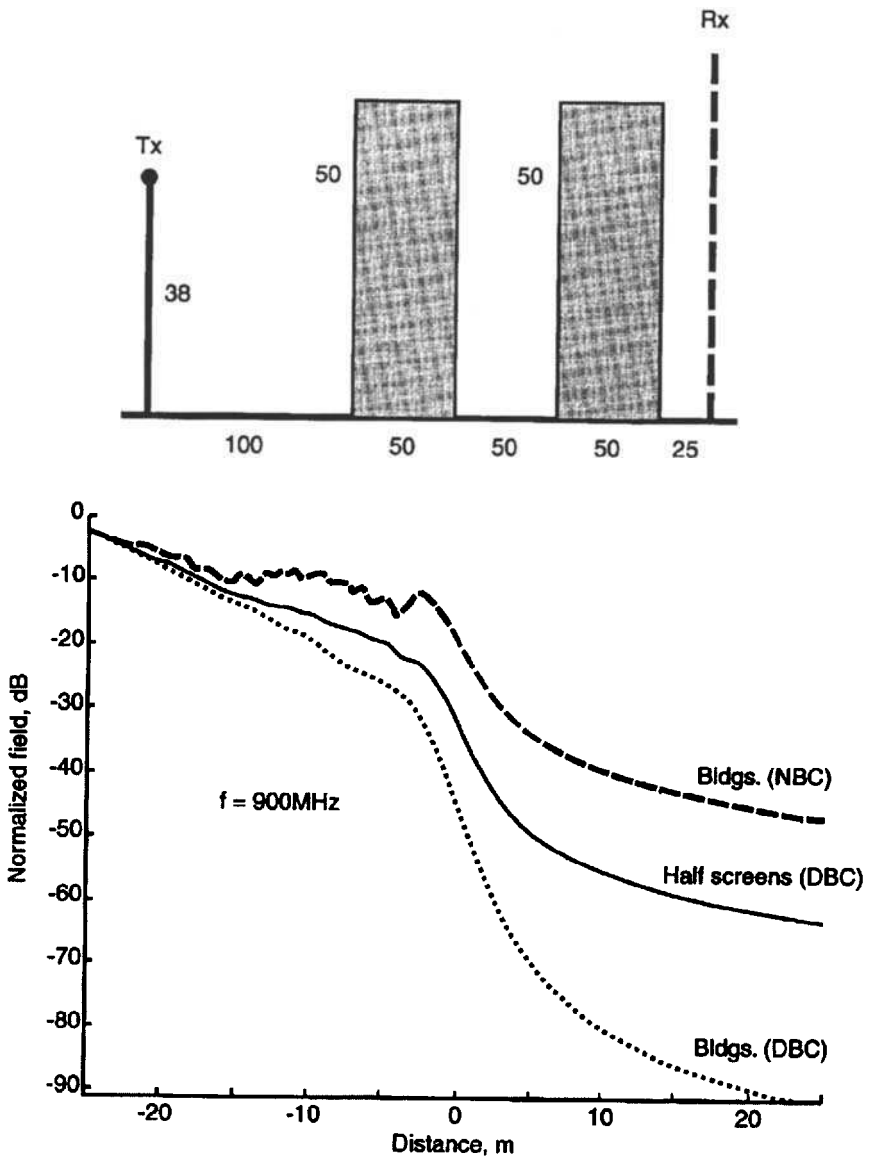

Figure 7.24 The normalized path loss over rectangular buildings.

field (see all definitions in Section 4.1) for description of forward diffraction past many absorbing half screens (knife edges).

Effects of the terrain profile. Figure 7.25 illustrates in cross-section rows of houses that are equally spaced along parallel streets, with the streets running perpendicular to the slope of the hills. It also describes the situation in an

urban scene with the transmitting antenna at the same level as the maximum height of terrain plus the building height. For area 1 in Figure 7.25, the path loss can be estimated by use of the Walfisch-Bertoni model [7] (presented also in Section 6.2), accounting for the terrain slope. Instead of the angle α, it introduces in incidence on the rooftops the angle α_1 to the local tangent plane, as indicated in Figure 7.25. In this case the path-loss ratio between isotropic antennas, in watts at the receiver to watts at the transmitter, is given by

$$P_{T/R} = \left(\frac{\lambda}{2\pi R}\right)^2 P_D[Q(\alpha_1)]^2 \tag{7.37}$$

The factor P_D is the diffraction loss from the last rooftop before the moving vehicle is down the street (see Formula (6.61) as a first excess term), and $Q(\alpha_1)$ is the multiple-screen diffraction loss (see Formula (6.62) as a second excess term) which can be presented as a polynomial function [7–9, 22–24]:

$$Q(\alpha_1) = 3.502 \cdot \alpha_1\sqrt{\frac{w}{\lambda}} - 3.327\left(\alpha_1\sqrt{\frac{w}{\lambda}}\right)^2 + 0.962\left(\alpha_1\sqrt{\frac{w}{\lambda}}\right)^3 \tag{7.38}$$

Here, w is separation between rows of buildings. By introducing the dimensionless parameter $g_p = \alpha_1\sqrt{\frac{w}{\lambda}}$, one can show that the working range of g_p is $0.01 < g_p < 1.00$, because for $g_p > 1.0$, the previous rows of buildings have almost no effect on wave propagation and $Q(\alpha_1) \approx 1$. In region three in Figure 7.25, one must account for the blocking effect of the terrain between the receiver (vehicle) and the transmitter (base station) and must multiply the loss (7.37) by an appropriate loss factor P_D to account for the intervening hill losses. Figure 7.26 shows one possibility, to replace the real hill by an absorbing knife edge or dielectric wedge [27, 28] (see also Section 4.1). In the case of an absence of buildings on top of the hill, the blockage effect can be modeled

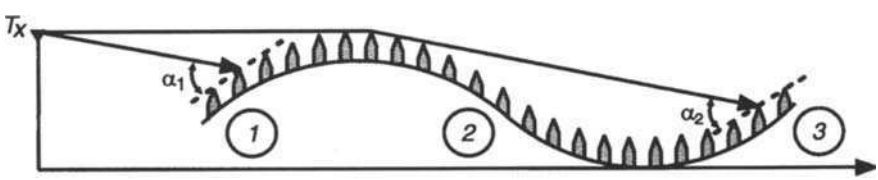

Figure 7.25 The schematic presentation of rows of buildings on rolling terrain.

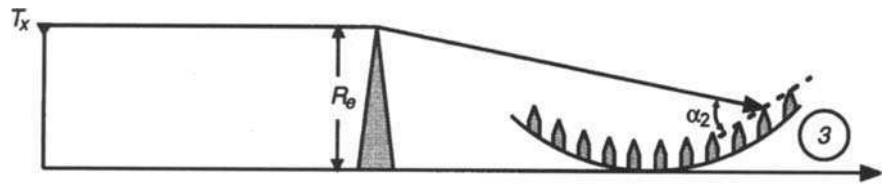

Figure 7.26 The schematic presentation of diffraction by an isolated hill.

by a circular diffracting cylinder, as shown in Figure 7.27, whose radius best fits the hill's curvature. In this case, according to [26, 29, 30], P_D is the diffraction loss for a cylinder, which is typically a function of the cylinder radius R_h and the angle θ between two tangent lines to the cylinder, one from the transmitter and the other from the rooftop before the vehicle (see Figure 7.27). The value of P_D when buildings are present on the hill does not appear to have been previously considered. Similarly, the field reduction in region two of Figure 7.25 has not been previously considered and is even more complex than the other regions due to the curvature of the ground surface.

The calculations were carried out for an isolated cylindrical hill with the geometry presented in Figure 7.28 and with the transmitter as a line source by using two techniques: (a) the Kirchhoff-Huygens approximation, as was

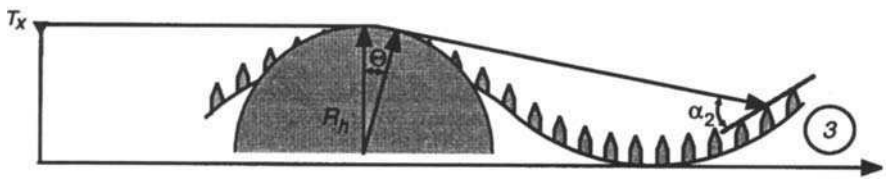

Figure 7.27 The schematic presentation of diffraction by an isolated hill as a cylinder.

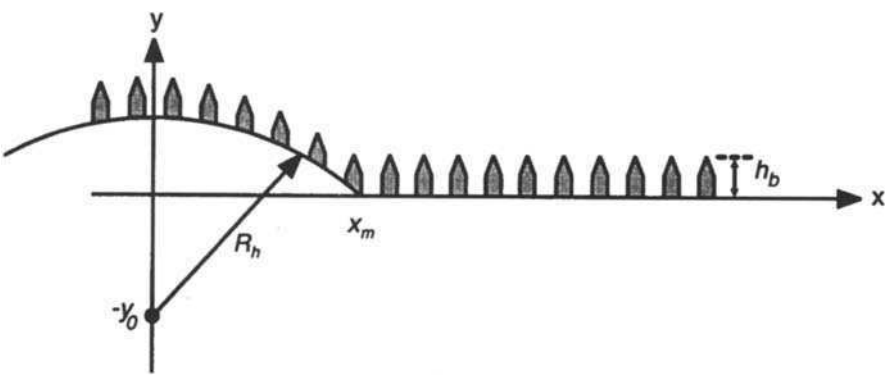

Figure 7.28 The schematic presentation of buildings on an isolated cylindrical hill.

done in [22] by use of formula (7.37) numerical integration, and (b) the creeping ray representation by a circular cylinder (ray-optics technique [31, 32]).

In [26] the general formulas were obtained for a line source by accounting for the spreading of rays in the directions perpendicular to the plane of incidence for different locations of the vehicle. At points on the shadow side of a hill, such as location two in Figure 7.25, the path-loss ratio between receiving and transmitting power was obtained in the following form:

$$P_{P_{TIR}} = \left(\frac{\lambda}{2\pi}\right)^2 \frac{\exp\{-2\psi\theta\}}{RL_1} D_H^2 P_D \tag{7.39}$$

where R is the range between the base station (transmitter) and the vehicle (receiver), L_1 is the distance from the transmitter to the hill along the ray that is just tangent to the hill (Figure 7.25). The diffraction loss down to the vehicle from the preceding building is given by P_D according to [7, 8, 22] (see Section 6.2). The excitation coefficient D_H is determined from the multiple numerical integration and can be analytically found from the fit to the numerical result. Its variations with the screen separation d, hill radius R_h, and wavelength λ, can be approximated according to computations in [26]

$$\ln D_H = 3.75 + [-0.648 + 0.072 \ln(d/\lambda)] \cdot \ln(R_h/\lambda) - 0.259 \ln(d/\lambda) \tag{7.40}$$

The values of D_H obtained from this expression are indicated by the continuous curves in Figure 7.29 for the case of d = 50m. The various points for frequencies 900 MHz and 1.8 GHz present the numerical integration using the ray-optics technique. The approximate expression for the exponent loss factor in (7.39) was also obtained by fitting the numerical results based on the ray-optics technique, as a function of hill radius R_h, frequency, and screen spacing d, such as

$$\psi = 2.02 \cdot \left(\frac{\pi R_h}{\lambda}\right)^{1/3} - 1.4 \cdot \sqrt{\frac{d}{\lambda}} \tag{7.41}$$

which reduces to the theoretical diffraction result over a smooth hill for *TE* (vertical) polarization [32] when $\sqrt{d/\lambda} = 0$. The variations of attenuation coefficient predicted by (7.41) are indicated by the continuous curves in Figure 7.30 for 900 MHz and for d = 50m and 100m. From Figure 7.30, this approximation gives a good fit to the value ψ obtained from the numerical

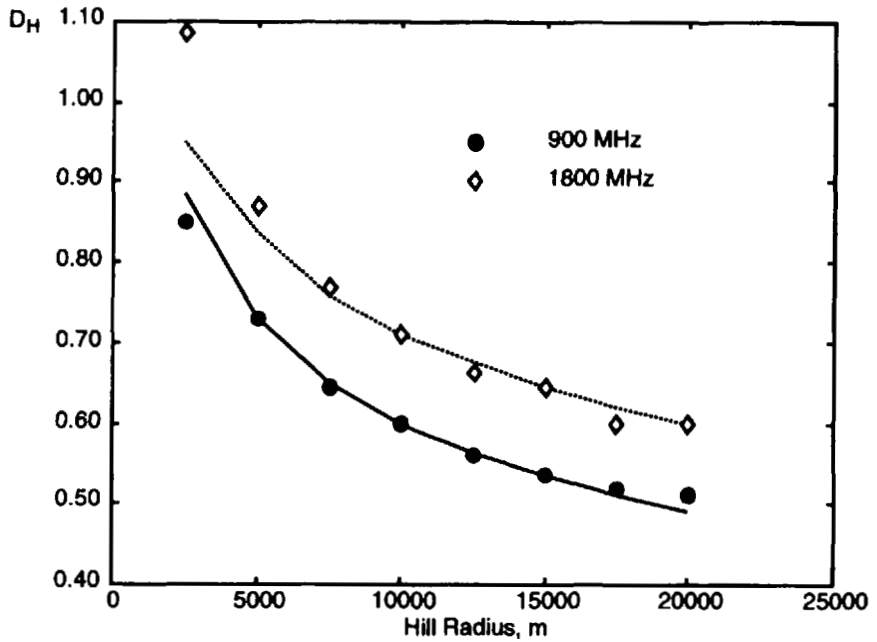

Figure 7.29 The coefficient D_H versus hill radius at 900 and 1800 MHz.

results by use of the ray-optics technique according to [32]. For other vehicle locations, such as three in Figure 7.25, that are shadowed by a previous hill, the path-loss ratio is

$$P_{P_{TIR}} = \left(\frac{\lambda}{2\pi}\right)^2 \frac{\exp\{-2\psi\theta\}}{RL_1L_2} D_1^2 Q^2(\alpha) P_D \tag{7.42}$$

where R and L_1 are the previously defined geometric parameters of the radio path, L_2 is the distance from the launch point on the hill to the building just before the vehicle, $Q(\alpha)$ is the multiple diffraction loss due to the rows of buildings before the vehicle defined by (7.38), and finally, D_1 is the ray-optics coefficient used in the creeping ray formulation according to [31, 32] and is described by the following function of hill radius R_h, frequency, and screen spacing d [26]:

$$\ln D_1 = 2.22 + [0.19 + 0.031 \ln(d/\lambda)] \cdot \ln(R_h/\lambda) - 0.79 \ln(d/\lambda) \tag{7.43}$$

The approximate fit given by (7.42) is plotted in Figure 7.31 as the continuous curves for 900 and 1800 MHz and for d = 50m passing through

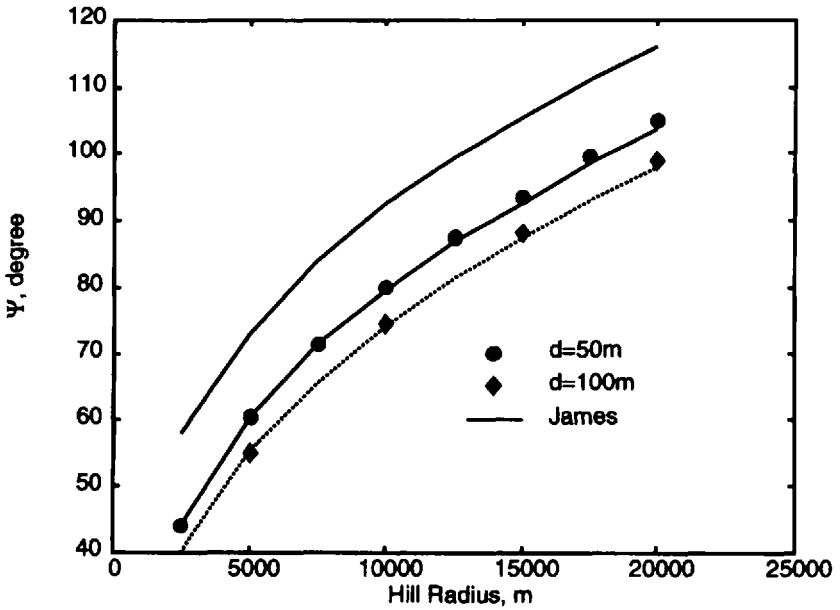

Figure 7.30 The exponent loss factor ψ versus hill radius at 900 MHz for d = 50, 100m and the theory for a smooth cylinder from [32].

the numerically computed points obtained by the ray-optics technique. Once more, we obtain good agreement between the ray-optics approach and approximate prediction by means of numerical integration.

Summary

From models presented in this chapter we reach the same conclusion that we repeat through each chapter devoted to descriptions of different types of propagation: There is no general approach or model which completely describes the process of wave propagation in various situations over the terrain. Each model can only deal with some specific propagation situations in an over-terrain communication channel.

Of the empirical models presented above, the Okumura method with Hata formulations is more general, because it describes quite well the situation in urban and suburban areas with buildings placed on smooth terrain. But this technique cannot be used for describing propagation effects over irregular terrain, and, as was shown by Akeyama et al. [6, 10] and Delisle et al. [3], neither for description of wave propagation over rural terrain. All modifications

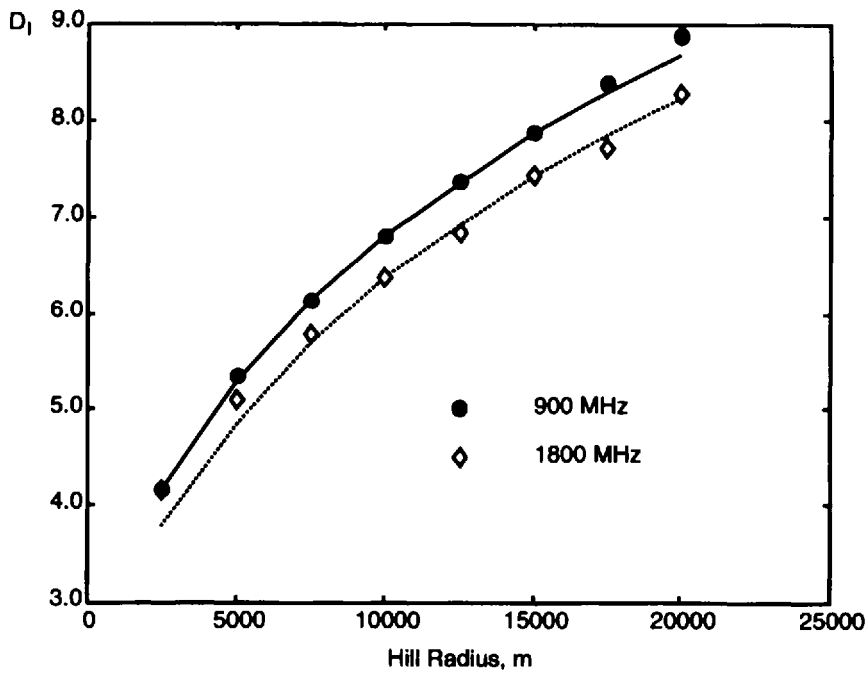

Figure 7.31 The coefficient D_1 versus hill radius for d = 50m.

to take into account for the terrain profile and specific building structure, such as introduced by Lee's effective antenna height (Section 7.2.3), the degree of urbanization introduced by Akeyama (Section 7.1.5) and Ibrahim and Parsons (Section 7.2.2), or the hilly terrain factor introduced by Allsebrook (Section 7.1.2), cannot in general predict loss propagation characteristics in actual built-up areas with different architecture and type of building construction, buildings distribution on the ground surface, and specific variations of terrain profile.

The deterministic models described in Section 7.3 which are based on the numerical solution of a parabolic equation [16] and on ray optics for diffraction over obstacles [26], are also limited to predicting real situations in the urban scene because they do not describe the multireflection and multiscattering phenomena observed experimentally in actual built-up areas, where multiray effects form an interference picture of the received signal, the effect that is mostly observed for mobile communication channels when both antennas are below the rooftops. This is because both models presented above in Section 7.3 are two-dimensional models. They describe propagation over buildings placed on hilly terrain in the vertical plane of wave propagation and do not take into account the side effects that take place in the horizontal plane after

multiscattering and multireflection from side obstructions such as buildings, trees, hills, and so on.

This is why, in Chapter 8, we will continue to consider the situation in the urban scene where buildings are randomly distributed and placed on rough terrain. We will also present a model which describes new phenomena that follow from "side reflections and scattering" from buildings (also a two-dimensional model, but in the horizontal plane). Then we will introduce a three-dimensional model, taking into account both the diffraction effects over the buildings and the side effects due to multiscattering and multireflection from the buildings which surround both antennas, transmitter and receiver.

References

[1] Young, W. R., "Comparison of mobile radio transmission at 150, 450, 900 and 3700 MC," *Bell Syst. Tech. J.*, Vol 31, 1952, No. 6, pp. 1068–1085.

[2] Allsebrook, K., and J. D. Parsons, "Mobile radio propagation in British cities at frequencies in the VHF and UHF bands," *IEEE Proc.*, Vol. 124, No. 1, 1977, pp. 95–102.

[3] Delisle, G. Y., J. P. Lefevre, M. Lecours, and J. Y. Chourinard, "Propagation loss prediction: a comparative stady with application to the mobile radio channel," *IEEE Trans. Vehicular Technol.*, Vol. 34, No. 1, 1985, pp. 85–96.

[4] Okumura, Y., et al., "Field strength and its variability in the VHF and UHF land mobile radio service," *Review Elec. Commun. Lab.*, Vol. 16, 1968, pp. 825–843.

[5] Hata, M., "Empirical formula for propagation loss in land mobile radio services," *IEEE Trans. Vehicular Technology*, Vol. 29, No. 3, 1980, pp. 317–325.

[6] Mehrotra, A., *Cellular Radio Performance Engineering*, Norwood, MA: Artech House, 1995.

[7] Walfisch, J., and H. L. Bertoni, "A theoretical model of UHF propagation in urban environments," *IEEE Trans. Anten. Propagat.*, Vol. 38, No. 12, 1988, pp. 1788–1796.

[8] Xia, H. H., and H. L. Bertoni, "Diffraction of cylindrical and plane waves by an array of absorbing half screens," *IEEE Trans. Anten. Propagat.*, Vol. 40, No. 2, 1992, pp. 170–177.

[9] Saunders, S. R., and F. R. Bonar, "Prediction of mobile radio wave propagation over buildings of irregular heights and spacing," *IEEE Trans. Anten. Propagat.*, Vol. 42, pp. 137–144, 1994.

[10] Akeyama, A., T. Nagatsu, and Y. Ebine, "Mobile radio propagation characteristics and radio zone design method in local cities," *Review Elec. Commun. Lab.*, Vol. 30, 1982, pp. 308–317.

[11] Saleh Faruque, *Cellular Mobile Systems Engineering*, Norwood, MA: Artech House, 1994.

[12] Ibrahim, M. F., and J. D. Parsons, "Signal strength prediction in built-up areas. Part 1: median signal strength," *IEE Proc.*, Vol. 130, Part F, 1983, pp. 377–384.

[13] Atefi, A., and J. D. Parsons, "Urban radio propagation in mobile radio frequency bands," *Comms 86 IEE Conference Publication*, Birmingham, No. 262, 1986, pp. 13–18.

[14] Parsons D., *The Mobile Radio Propagation Channel*, London: Pentech Publishers, 1992.

[15] Janaswamy, R., "A curvilinear coordinate based split-step parabolic equation method for propagation predictions over terrain," *IEEE Trans. Anten. Propagat.*, Vol. 46, No. 7, 1998, pp. 1089–1097.

[16] Janaswamy, R., and J. B. Andersen, "Path loss predictions in urban areas sprawling over irregular terrain," *Proc. of PIMRC'98*, Boston, USA, 1998, pp. 874–878.

[17] Andersen, J. B., "UTD multiple-edge transition zone diffraction," *IEEE Trans. Anten. Propagat.*, Vol. 45, No. 7, 1997, pp. 1093–1097.

[18] Valenzuela, R. A., "Ray tracing approach to predicting wireless transmission," *Proc. IEEE 43rd Vehicular Technology Conference*, 1993.

[19] Witteker, J. H., "Diffraction over a flat-topped terrain obstacle," *IEE Proc.*, Vol. 137, No. 1, 1990, pp. 113–116.

[20] Barrios, A. E., "A terrain parabolic equation model for propagation in the troposphere," *IEEE Trans. Anten. Propagat.*, Vol. 42, No. 1, 1994, pp. 90–98.

[21] Rizk, K., et al., " Lateral, full-3D and vertical plane propagation in microcells and small cells," *COST 259*, Technical Document No. 98, 1998, pp. 47.

[22] Maciel, L. R., H. L. Bertoni, and H. H. Xia, "Unified approach to prediction of propagation over buildings for all ranges of base station antenna height," *IEEE Trans. Vehicular Technol.*, Vol. 42, No. 1, 1993, pp. 41–45.

[23] Bertoni, H. L., et al., "UHF propagation prediction for wireless personal communications," *Proc. IEEE*, Vol. 82, No. 6, 1994, pp. 1333–1359.

[24] Maciel, L. R., H. L. Bertoni, and H. H. Xia, "Propagation over buildings for paths oblique to the street grid," *Proc. Int. Symp. Personal Indoor Mobile Radio Commun.*, Boston, MA, 1992, pp. 75–79.

[25] Vogler, L. E., "An attenuation function for multiple knife-edge diffraction," *Radio Sci.*, Vol. 19, No. 7, 1982, pp. 1541–1546.

[26] Piazzi, L., and H. L. Bertoni, "Effect of terrain on path loss in urban environments for wireless applications," *IEEE Trans. Anten. Propagat.*, Vol. 46, No. 6, 1998, pp. 1138–1147.

[27] Bullington, K., "Radio propagation for vehicular communications," *IEEE Trans. Vehicular Technol.*, Vol. 26, No. 2, 1977, pp. 295–308.

[28] Lampard, G., and T. Vu-Dinh, "The effect of terrain on radio propagation in urban microcells," *IEEE Trans. Vehicular Technol.*, Vol. 42, No. 2, 1993, pp. 314–317.

[29] Eliades, D. E., "Alternative derivation of the cascaded cylinder diffraction model," *Proc. Inst. Elect. Eng.*, Vol. 140, 1993, pp. 279–284.

[30] Berg, J. E., and H. Holmquist, "An FFT multiple half-screen diffraction model," *Proc. Veh. Techol. Conf.*, Stockholm, Sweden, 1994, pp. 195–199.

[31] Keller, J. B., "Diffraction by a convex cylinder," *IEEE Trans. Anten. Propagat.*, Vol. 24, No. 2, 1956, pp. 312–321.

[32] James, G. L., *Geometrical Theory of Diffraction for Electromagnetic Waves*. Stevenage, UK: Peter Peregrinus Ltd., 1976.

8

Propagation in an Urban Environment With Nonregularly Distributed Buildings Placed on Rough Terrain

8.1 Introduction

As discussed in Chapters 1 and 7, modern cities, from the point of view of radio wave propagation, are complicated areas and the analytical description of this process cannot be presented without some simplifications for the practical radio-link situation [1–9]. For UHF/L-band radio waves, most of the larger city buildings, in practice, are opaque and their dimensions are larger than the wavelength, λ. In such a situation, a wide spectrum of shadow zones is observed inside the street level and very sharp boundaries between light and shadow zones are created [10–13]. Moreover, in the cases in which buildings are randomly distributed on a rough-ground surface, all specific properties of city topography form the particular conditions of wave propagation at the street level [14–26].

In such situations we have only some simplifications, namely the two-dimensional deterministic models, as shown in Chapter 7. Or, we might introduce the statistical description of the real building pattern inside the city [27–32] and determine the field strength on its base, as was done by [1–3]. To obtain the statistical description of the city based on its topography map, we need detailed information about the spatial distribution of city buildings and natural obstacles, the sizes and ranges of reflective and diffractive surface sections of the ground relief, and the spatial distribution of the scattering features of each building placed in areas surrounding the receiver and transmitter antennas.

In [1, 2] an array of randomly distributed buildings and obstacles placed on the rough-ground surface was considered. The heights of the ground relief were described in the coordinate system (x, y, z) placed at the plane $z = 0$ of ground surface by the generalized function $Z(x, y)$ according to Shwartz [33]. This function describes the nonregular rough-ground surface relief $z = Z(x, y)$ (see Figure 8.1).

But as was mentioned above, both approaches, the deterministic based on the over-the-roofs diffraction model and the parabolic-equation model (presented in Chapter 7), and the statistics based on two-dimensional *side effects* due to multireflection and multiscattering from buildings' walls [1], are two-dimensional models. To describe a more general case in the urban scene, which corresponds both to communication between two mobile vehicles and to communication between a base station located above the rooftops and the mobile vehicle, we need to combine these two approaches and construct a

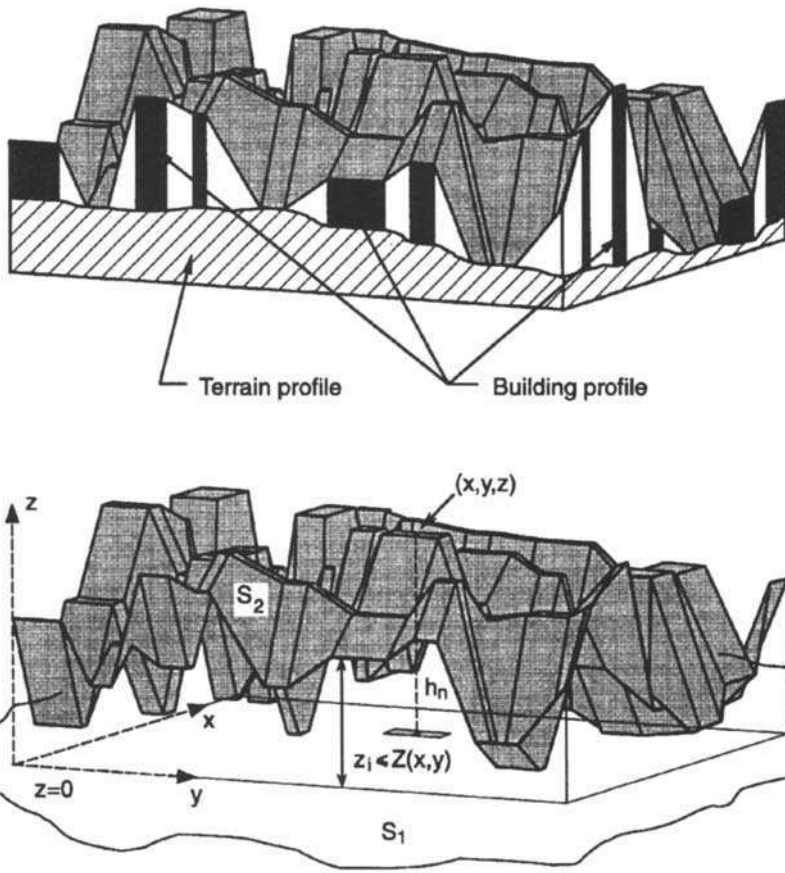

Figure 8.1 The nonregular rough-ground surface relief [$z = Z(x, y)$].

three-dimensional model that takes into account both the *vertical* diffraction effect and the "side" single- and multi-scattering effect [1, 2].

In Section 8.2, following the approach presented in [1, 2], we introduce a parametric model that combines both deterministic and statistical approaches. Here, the average intensity of the total wave field in the layer of city building with randomly distributed obstacles above the rough terrain is presented by using the single- and multi-scattering effects. The propagation channel for UHF/X-band waves in the city is modeled by the array of randomly distributed buildings placed on rough terrain. The law of buildings distribution is assumed to be Poissonian [1]. Then, in Section 8.3, we describe the statistical characteristics of the terrain and the loss characteristics by taking into account the diffraction from the rooftops (three-dimensional model) [1, 2]. In Section 8.4, we present a comparison between the theoretical predictions based on this statistical parametric three-dimensional model and the results of numerous experiments carried out in various urban areas with nonregularly distributed buildings for different positions of transmitter and receiver antennas [3]. The possibility of using this parametric model for predicting loss characteristics in cluttered (NLOS) urban conditions is examined.

8.2 Statistical Model for the Description of Loss Characteristics in the City Layer with Randomly Distributed Buildings

Below we model the city by the array of randomly distributed buildings placed on rough terrain.

8.2.1 Statistical Description of City Relief

Spatial distribution of city buildings. Following [1, 2], let us consider the characteristic function $\xi(\mathbf{r}) = \xi(x, y, z)$ as a relief of some boundary surface between two semispaces: $\xi(\mathbf{r}) = 0$ for $z > Z(x, y)$ and $\xi(\mathbf{r}) = 1$ for $z < Z(x, y)$ (see Figure 8.1). For the case $z > 0$, one can present such a function according to [1, 2] as

$$\xi(x, y, z) = \sum_{n=1}^{N} \xi_n(x, y)\xi_a^b(z) \tag{8.1}$$

where N is the number of buildings randomly distributed at the surface plane $z = 0$; function $\xi_n(x, y) = 1$ if the projection of point (x, y, z) at the plane $z = 0$ hits inside or at the boundary of building contour and $\xi_n(x, y) = 0$ in the opposite case; $b = h_n$ is the height of building with number n; $\xi_a^b(z)$ is

the characteristic function which is equal to 1 inside the range $a < z < b$ (parameter a can be equal zero) and is equal to 0 outside this interval.

After some straightforward calculations, according to [1, 2], one can present the average value of $\xi(\mathbf{r})$ for the ensemble of its possible realizations in the following form:

$$\langle \xi(\mathbf{r}) \rangle = XP_h(z),\ X = \left\langle \sum_{n=1}^{N} \xi_n(x, y) \right\rangle \tag{8.2}$$

$$P_h(z) = \int_z^{\infty} w(h_n) dh_n = \langle \xi_a^b \rangle \tag{8.3}$$

Here, $w(h_n)$ is the density of building height distribution and determines the probability of the event that $z < h_n$. The multiplier X in (8.2) determines the probability of the event when the projection of the point $\mathbf{r}$ on the plane $z = 0$ hits inside any building.

The statistical functions constructed above allow us to calculate the probability of the direct visibility between two observed points, $\mathbf{r}_1$ and $\mathbf{r}_2$, within the layer of city buildings. For the statistical quasi-homogeneous building area, this probability can be presented as [1]:

$$P_{12} = \exp\left\{-\gamma_0 |q_\perp| q_z^{-1} \int_{z_1}^{z_2} [P_h(z)][1 - XP_h(z)]^{-1} dz\right\} \tag{8.4}$$

$$= \exp\{-\gamma_0 \gamma_{12} r_{12}\},\ z_2 > z_1$$

This formula was obtained for the case of $z_2 > z_1$ and the arbitrary space orientation of the unit vector $\mathbf{q}$, $|\mathbf{q}| = 1$; $l = |\mathbf{r}_2 - \mathbf{r}_1|$, $\mathbf{r}_2 - \mathbf{r}_1 = \mathbf{q}l$; $r_\perp$ and $q_\perp$ are the projection of corresponding vectors on the plane $z = 0$; $q_z^2 = 1 - q_\perp^2$; γ_0 is the density of buildings in the plane of $\mathbf{q}_\perp = (q_x, q_y)$.

From (8.4) one can obtain the average distance of direct visibility ρ_{12} from point $\mathbf{r}_1$ to point $\mathbf{r}_2$, which equals

$$\rho_{12} = (\gamma_0 \gamma_{12})^{-1} \tag{8.5}$$

where

$$\gamma_{12} = (z_2 - z_1)^{-1} \int_{z_1}^{z_2} [P_h(z)][1 - XP_h(z)]^{-1} dz, \; z_2 > z_1 \tag{8.6}$$

These formulas allow us to obtain the probability of direct visibility between arbitrary observers inside the layer of city buildings. If $\overline{L}$ is the average length of screens (buildings) surrounding the points $A(\mathbf{r}_1)$ and $B(\mathbf{r}_2)$ (see Figure 8.2), then the probability of intersections of the line AB with the building screens is equal to

$$P_{12} = \exp\{-2\overline{L} r_{12}/\pi\} \tag{8.7}$$

from here we can easily define the parameter γ_0 as

$$\gamma_0 = 2\overline{L}\nu/\pi \tag{8.8}$$

Here ν is the density of buildings in the investigated area of 1 km^2. The parameter γ_0 determines the average horizontal distance of the line-of-sight $\overline{\rho}$ and $\overline{\rho} = \gamma_0^{-1}$.

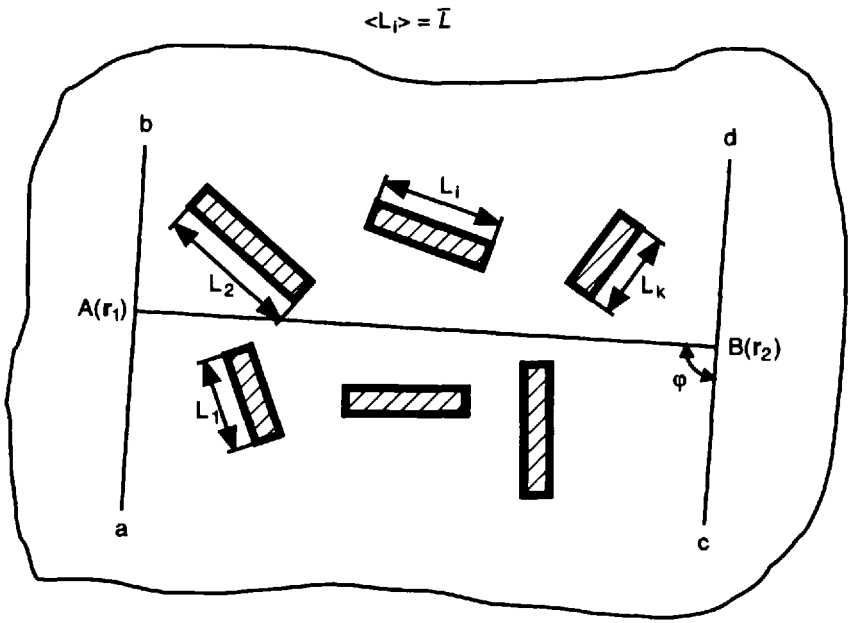

Figure 8.2 The buildings' distribution between points $A(\mathbf{r}_1)$ and $B(\mathbf{r}_2)$.

The dimensions of reflected surface sections. Let us consider the case when the direct visibility exists between two points $\mathbf{r}_1$ and $\mathbf{r}_2$. The point $\mathbf{r}_2$ belongs to the vertical screen (see Figure 8.3(a)). If a horizontal segment with length l could be seen from the point $\mathbf{r}_1$, a vertical segment with width l can be seen from this point as well (see Figure 8.3(a)). Let us now determine the probability that from the point $A(\mathbf{r}_1)$ the horizontal segment which includes the point $B(\mathbf{r}_2)$ inside it can be observed. The vertical screen forms an angle Ψ with the line AB (see Figure 8.3(b)). After some straightforward calculations we can obtain the probability of direct visibility of the segment cd with the length l from point A at range r_{12}:

$$P_{cd} = \exp(-\gamma_0 \gamma_{12} r_{12} - \nu \epsilon_{12} r_{12} |\sin \Psi| j \tag{8.9}$$

$$\epsilon_{12} = (z_2 - z_1)^{-1} \int_{z_1}^{z_2} P_h(z)(z - z_1)(z_2 - z_1)^{-1} dz,\ z > z_1,\ z_2,\ X = 1 \tag{8.10}$$

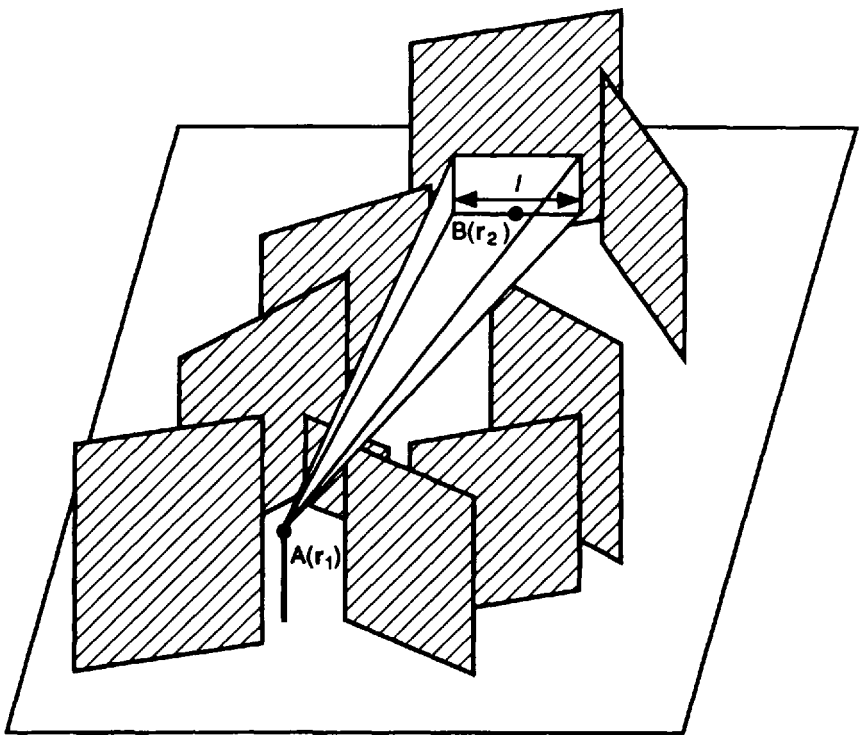

Figure 8.3 (a) Observation from point $\mathbf{r}_2$, the vertical screen with the horizontal segment of length l and the vertical segment of width l. (b) Geometry of single screen observation from point $\mathbf{r}_2$.

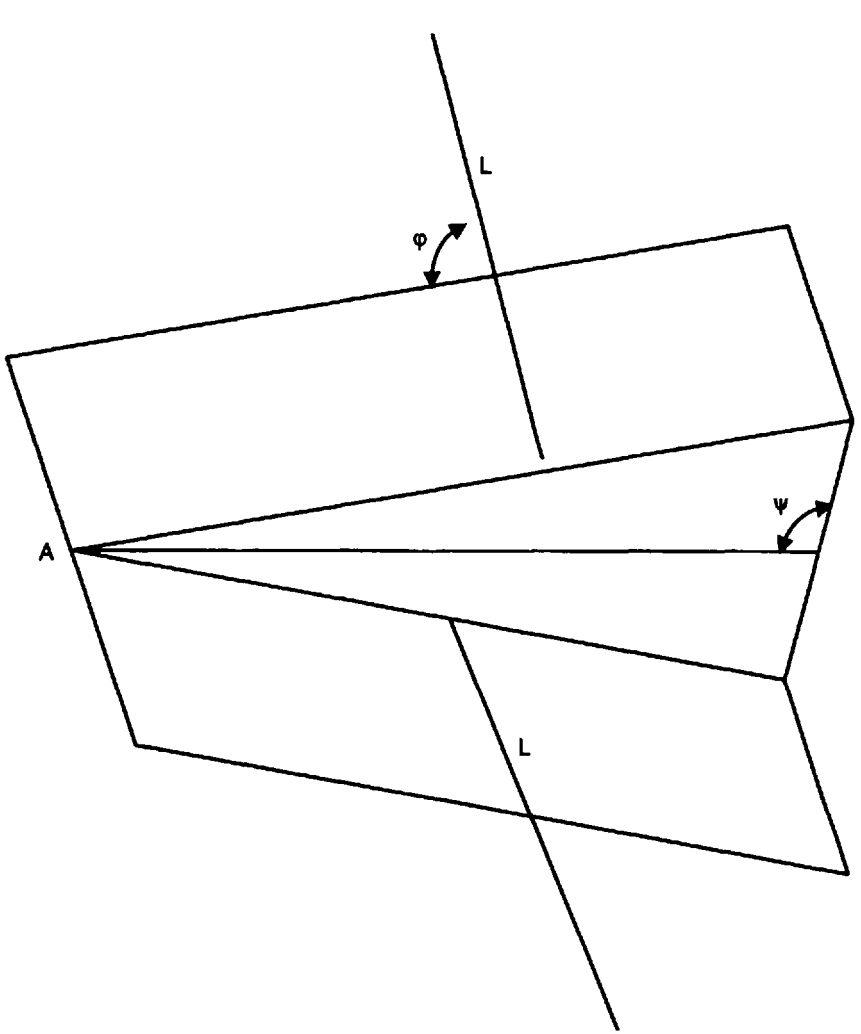

Figure 8.3 (continued).

where $\bar{l} = [\nu r_{12}\epsilon_{12}|\sin \Psi|]^{-1}$ is an average value of the segment cd; ν is the density of buildings on the surface $z = 0$; γ_{12} is the parameter determined in (8.6). From formula (8.9) it follows that the probability density of visibility of the segment l from point A is

$$w(l) = \nu r_{12}\epsilon_{12}|\sin \Psi|\exp\{-\nu\epsilon_{12}r_{12}l|\sin \Psi|\} \tag{8.11}$$

We have to note that the results obtained above are correct and, for the case of X, not equal to one. However, for this more general case, instead of

the formula (8.10) we have to introduce into (8.9) the following expression for the parameter ϵ_{12}:

$$\epsilon_{12} = (z_2 - z_1)^{-1} \int_{z_1}^{z_2} (z - z_1)(z_2 - z_1)^{-1} P_h(z)[1 - XP_h(z)]^{-1}\, dz \tag{8.12}$$

The spatial distribution of scattering points. As was shown in [1, 2], the role of the one-time scattering is important when one of the antennas (mostly, the base-station antenna) is above the roofs' level, but another is below the building roofs. This case is presented in Figure 8.4, where the reflected point C is inside the building contour with the height h. The building orientation is determined by the angle Ψ_s to the vector $(\mathbf{r}_s - \mathbf{r}_1)$. The receiver (or transmitter) is placed at the point $B(\mathbf{r}_2)$, the transmitter (or receiver) is placed at the point $A(\mathbf{r}_1)$. The density of the scattering points distribution can be presented as follows:

$$\mu(\mathbf{r}_s) = \gamma_0 \nu \sin^2(\alpha/2)[r_{1s}\epsilon_{1s} + r_{s2}\epsilon_{s2}]P_{1s}H_sP_{s2} \tag{8.13}$$

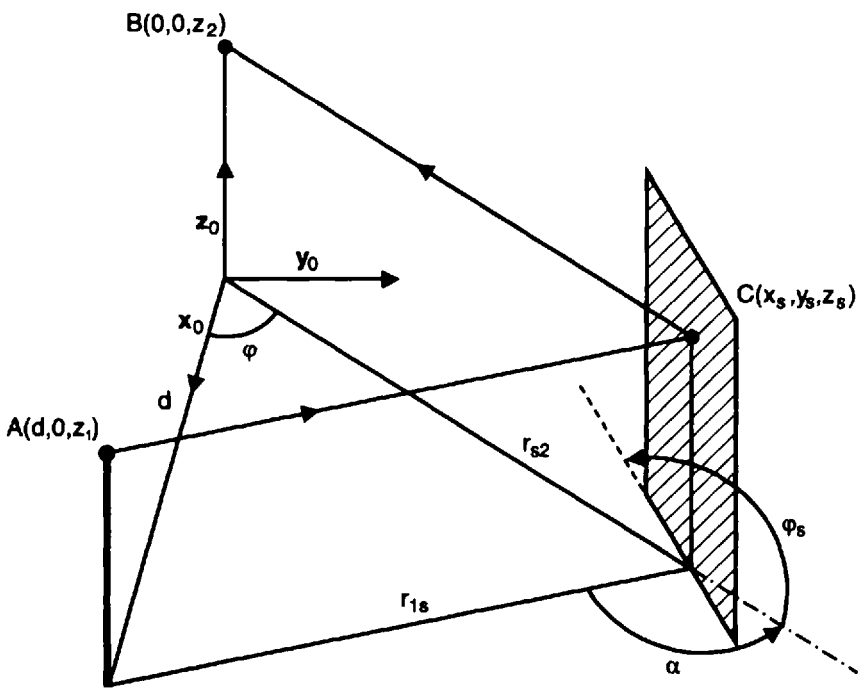

Figure 8.4 Three-dimensional geometry of single scattering from the screen.

Here, ϵ_{1s} and ϵ_{s2} are described by (8.12) and P_{1s} and P_{s2} are described by (8.9). The function H_s describes the height profile of the urban-building layer. If we can divide all buildings on the surface into N groups with the height h_i and with frequency p_i, $i = 1, 2, \ldots, N$, the function H_s can be presented as:

$$H_s = \sum_{i=1}^{N} \frac{p_i H(h_i - z_s)}{h_i} \tag{8.14}$$

where $H(w)$ is the Heaviside function [1]. If we now introduce the polar coordinate system (r, φ) with point B as a base point on the plane $z = 0$ (Figure 8.4), then for discrete distributed sources the density of scattered point distribution can be presented as follows:

a) for $z_1, z_2 < h$

$$\mu(r, \varphi) = 0.5\nu\gamma_0 \, r\sin^2(\alpha/2)(r + \bar{r})\exp\{-\gamma_0(r + \bar{r})\} \tag{8.15a}$$

b) for $z_1 < h, z_2 > h$

$$\begin{aligned}\mu(r, \varphi) = {} & (\nu\gamma_0 r/2h)\, \sin^2(\alpha/2)\exp\{-\gamma_0(r + \bar{r})\} \\ & \int_0^h [(r + \bar{r}) - r((z_2 - h)/(z_2 - z))^2] \\ & \cdot \exp\{\gamma_0 r(z_2 - h)/(z_2 - z)\}dz\end{aligned} \tag{8.15b}$$

or for $\gamma_0 r >> 1$

$$\begin{aligned}\mu(r, \varphi) = {} & 0.5\nu\sin^2(\alpha/2)\{\gamma_0 hr(r + \bar{r})\exp[-\gamma_0(\bar{r} + hr/z_2)]/z_2\} \\ & + 0.5\nu\sin^2(\alpha/2)\{(z_2 - h)\bar{r}\exp[-\gamma_0\bar{r}]/h\} \\ = {} & \mu_1(r, \varphi) + \mu_2(r, \varphi)\end{aligned} \tag{8.15c}$$

where $\bar{r} = (d^2 + r^2 - 2rd\cos\varphi)^{1/2}$; h is the average buildings' height. From comparison between (8.15a) and (8.15c), the *first summand* in (8.15c), $\mu_1(r, \varphi)$, is the same as that described by (8.15a) for the case $z_2 = h$. Both of them describe *rare scatterers* which are distributed over a large area of city far from the receiver. Additional significant changes in the scatterers distribution for the case $z_2 > h$ gives the *second summand*, $\mu_2(r, \varphi)$. For $z_2 = h$, its value is zero, but even a small increase of z_2 above h (i.e., when $z_2 > h$) gives an

essential influence on the total scatterers' distribution according to (8.15c). It describes the "illumination" of a small area near the upper boundary of a building layer in the $\overline{\rho}$-region of a moving transmitter, which can be determined by the buildings' density ($\sim \nu$) around the receiver.

The distribution of reflected points. From numerous points of single scattering in built-up areas, the more interesting ones are those of specular reflections, which are described by the geometrical optics laws. Thus we can present the density of points of specular reflections within the building layer as [1]:

$$\mu(\tau, \varphi) = \frac{\nu\gamma_0 d^3}{4} \frac{(\tau^2 - 1)}{(\tau - \cos\varphi)} P_h(z_c) \exp\{-\gamma_0 \gamma_{12} \tau d\} \tag{8.16}$$

where $P_h(z_c)$ is described by formula (8.3) (see Section 8.1) with variable

$$z_c = z_2 - \frac{(\tau^2 - 1)}{2(\tau - \cos\varphi)} \frac{(z_2 - z_1)}{\tau} \tag{8.17}$$

Here, we changed the variable r at the relative time τ ($\tau = (r + \tilde{r})/d$) of one-scattered waves propagating from the transmitter to the receiver through the built-up using the function presentation (8.15c). We also assume that the height of point B (receiver) is higher than that of point A (transmitter) (i.e., $z_2 > z_1$), and is higher than the average buildings' height h (i.e., $z_2 > h$). The contribution of each level in the building layer described by (8.16) is different from zero only for those values of τ and φ, for which, for fixed heights z_1 and z_2, the coordinate z_c lies inside the building layer (i.e., $0 < z_c < h$). To obtain the average number of points in the specular reflection, we integrate initially (8.16) over τ and, then, over φ. In other words, we analyze the reflection points' distribution $\mu(\tau, \varphi)$ in the arrival-angle domain and in the arrival-time domain considering that the building layer is uniform. This also assumes that within this layer the building heights' distribution is uniform (i.e., $h_i = h$ = constant), and introducing the nondimensional parameter $\varsigma = \dfrac{(z_2 - h)}{(z_2 - z_1)}$. Let us now examine qualitatively how the specular reflection points' distribution is changed at the plane (x, y) (at the real terrain surface). For this purpose let us construct the region G at which approximately 90% of specular reflected points are located. The boundaries of such a region will consist of arcs of ellipses with $\tau = \tau_{0.9}$, for which $\tau_{0.9}$ is determined from the relation

$$\int_1^{\tau_{0.9}} d\tau \int_0^{2\pi} d\varphi \mu(\tau, \varphi) = 0.9 \int_1^{\infty} d\tau \int_0^{2\pi} d\varphi \mu(\tau, \varphi) \tag{8.18}$$

and from the arcs of circles, the equations are:

$$\tau^2 - 1 = 2\varsigma\tau(\tau - \cos\varphi) \tag{8.19}$$

Equation (8.19) can be presented by using nondimensional coordinates $\xi = x/d$ and $\eta = y/d$ in the following form:

$$\left(\xi - \frac{\varsigma^2}{2\varsigma - 1}\right)^2 + \eta^2 = \left[\frac{\varsigma(1 - \varsigma)}{2\varsigma - 1}\right], \quad z_2 \geq h > z_1 \tag{8.20}$$

From the illustrations in Figure 8.5, one can see how the region G and its boundaries are changed with changes of height factor ς from 0 to 1. In Figure 8.5, the region G and its boundaries (arcs of ellipses) are presented by the dotted curves, and the arcs of circles are presented by the continuous curves. These curves were constructed for the ranges between terminals $d \approx$ 500m–600m, which is close to the conditions of the experiments carried out by Tadiran Telecommunications (see below).

Estimations show that the region G is limited by a single ellipse with two focuses in the points A and B for $z_2 = h$, (i.e., $\varsigma \approx 0$), that is, for the receiving antenna (at the point B) located near the rooftops level of neighborhood buildings. The density of specular points distribution has a maximum height located near these points (Figure 8.5).

Moreover, the specular points' distribution does not equal zero at the segment (AB), because there are some intersections of the segment (AB) with one of the arbitrary buildings (screens) which crosses the path AB (see Figure 8.2, Section 8.1). With increase of the height of point B above the rooftops (when $z_2 > h$) the region G, where these specular reflections are observed, is concentrated mostly around the transmitting point A. In other words, there is no specular reflection in the neighborhood of the receiving point B. Thus for $\varsigma = 0.2$ (h = 20m, z_2 = 25m), the region which is "prohibited" for specular reflections has the shape of a circle, the center and the boundary of which are determined by (8.19). Moreover, this region with increase of height factor $\varsigma(z_2 > h)$ spreads (for $\varsigma = 0.4$, h = 20m, z_2 = 33m) and occupies all of the left half-plane (for $\varsigma = 0.5$, h = 20m, z_2 = 40m). With further increasing of height factor $\varsigma(\varsigma \to 1)$, the specular reflections can be obtained only in the neighborhood of point A. Hence, with an increase in height of observing point

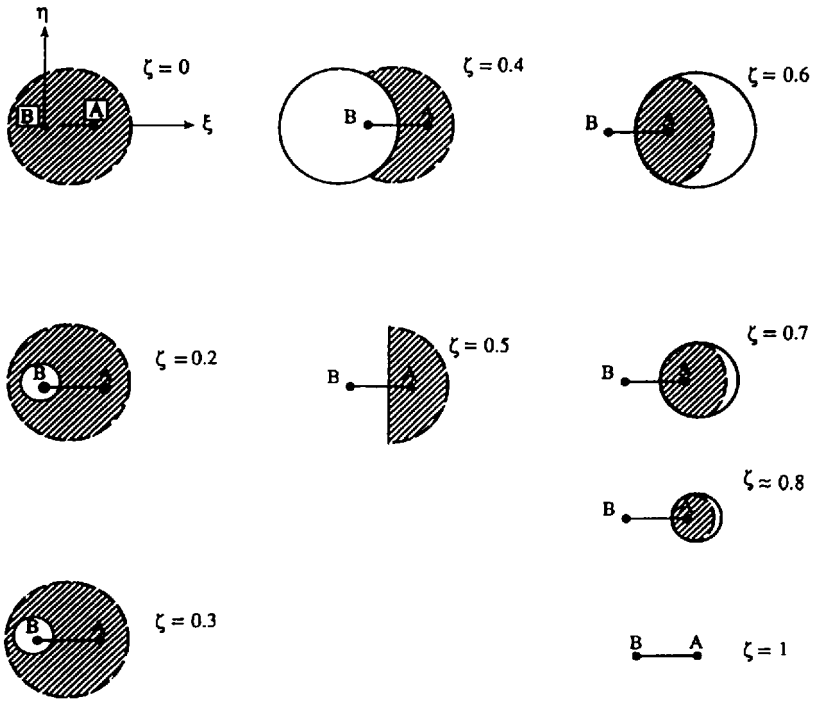

Figure 8.5 The region G and its boundaries change with changes in height factor ς from 0 to 1. Here the region G and its boundaries (arcs of ellipses) are presented by the dotted curves, and the arcs of circles are presented by the continuous curves.

B relative to the average height of buildings surrounding it (with an increase ς from 0 to 1) the built-up area, where the specular reflected points are observed, limits the neighborhood of point A (see cases $\varsigma = 0.6$, $z_2 = 50$m and $\varsigma = 0.8$, $z_2 = 100$m).

Multiscattering effects. The same analysis as above can be carried out for the multiscattering phenomenon from the buildings (screens). Using the above-mentioned Poison distribution, we can finally calculate the probability of the event of at least one ray being received after n-time scattering from the randomly distributed screens:

$$P_n = 1 - \exp\{-\langle N_n(r)\rangle\} \tag{8.21}$$

Here, the average amount of n-time scattered rays from the screens can be obtained from the probability of the scattered points' distribution $\mu_n(\mathbf{r}_0|\mathbf{r}_1, \mathbf{r}_2, \ldots \mathbf{r}_n)$:

$$\langle N_n(\mathbf{r}, \mathbf{r}_0)\rangle = \int \ldots \int \mu_1(\mathbf{r}_0|\mathbf{r}_1, \mathbf{r}_2, \ldots, \mathbf{r}_n) \ldots$$
$$\mu_n(\mathbf{r}_0|\mathbf{r}_1, \mathbf{r}_2, \ldots \mathbf{r}_n) d\mathbf{r}_n d\mathbf{r}_{n-1} \ldots d\mathbf{r}_1$$

where

$$\mu_i(\mathbf{r}_0|\mathbf{r}_1, \mathbf{r}_2, \ldots, \mathbf{r}_n) = \exp\left\{-\gamma_0 \sum_{i=0}^{n} |\mathbf{r}_{i+1} - \mathbf{r}_i|\right\} \prod_{i=0}^{n} 0.5\gamma_0 \nu\{|\mathbf{r}_{i+1} - \mathbf{r}_i| + |\mathbf{r}_i - \mathbf{r}_{i-1}| \sin^2(\alpha_i/2)\} \tag{8.22}$$

The angle α_i is an angle between vectors $(\mathbf{r}_{i+1} - \mathbf{r}_i)$ and $(\mathbf{r}_i - \mathbf{r}_{i-1})$ for all $i = 1, 2, \ldots, n$; $(\mathbf{r}_0, \mathbf{r}_1, \mathbf{r}_2, \ldots, \mathbf{r}_n)$ are the radius-vectors of points $A, C_1, C_2, \ldots, C_n, B$, respectively (see Figure 8.6). The examples of average values of one-, two- and three-times-scattered rays from the randomly distributed buildings can be presented by using the Macdonald functions $K_n(w)$ of the order $n = 1; 2; 3$, respectively:

$$\langle N_1(r)\rangle = 0.25\pi\nu r^2 K_2(\gamma_0 r) \tag{8.23a}$$

$$\langle N_2(r)\rangle = 9(\pi\nu r^2)^2\{K_4(\gamma_0 r)/8!! + (0.5\pi\gamma_0 r)^{-1/2} K_{7/2}(\gamma_0 r)/7!!\} \tag{8.23b}$$

$$\langle N_3(r)\rangle = 8(\pi\nu r^2)^3\{K_5(\gamma_0 r)/10!! + (0.5\pi\gamma_0 r)^{-1/2} K_{11/2}(\gamma_0 r)/11!!\} \tag{8.23c}$$

The probability that a single scattered wave (curve 1), a double scattered wave (curve 2), and a three-times scattered wave, calculated according to (8.21) to (8.23), can be observed at the range of 1–2 km from the source is presented in Figure 8.7. In microcellular conditions ($r <$ 1–2 km), the probability of observing at the receiver single-to-three-times scattered waves is equal to the unity. At the same time, at short ranges from the transmitter only one-time scattered waves can be observed. At the far zone the effect of the multiscattering becomes stronger compared to the single-scattering effect.

8.2.2 Field Intensity Attenuation in the Building Layer With Randomly Distributed Buildings

The problem of single scattering. Let us consider the city building layer described by the random surface S, which was introduced earlier as a superposition of a flat-perfect reflecting surface S_1 and of a random built-up relief S_2 (see Figure 8.1). Taking into account the approach presented in [1, 28–32], we can present

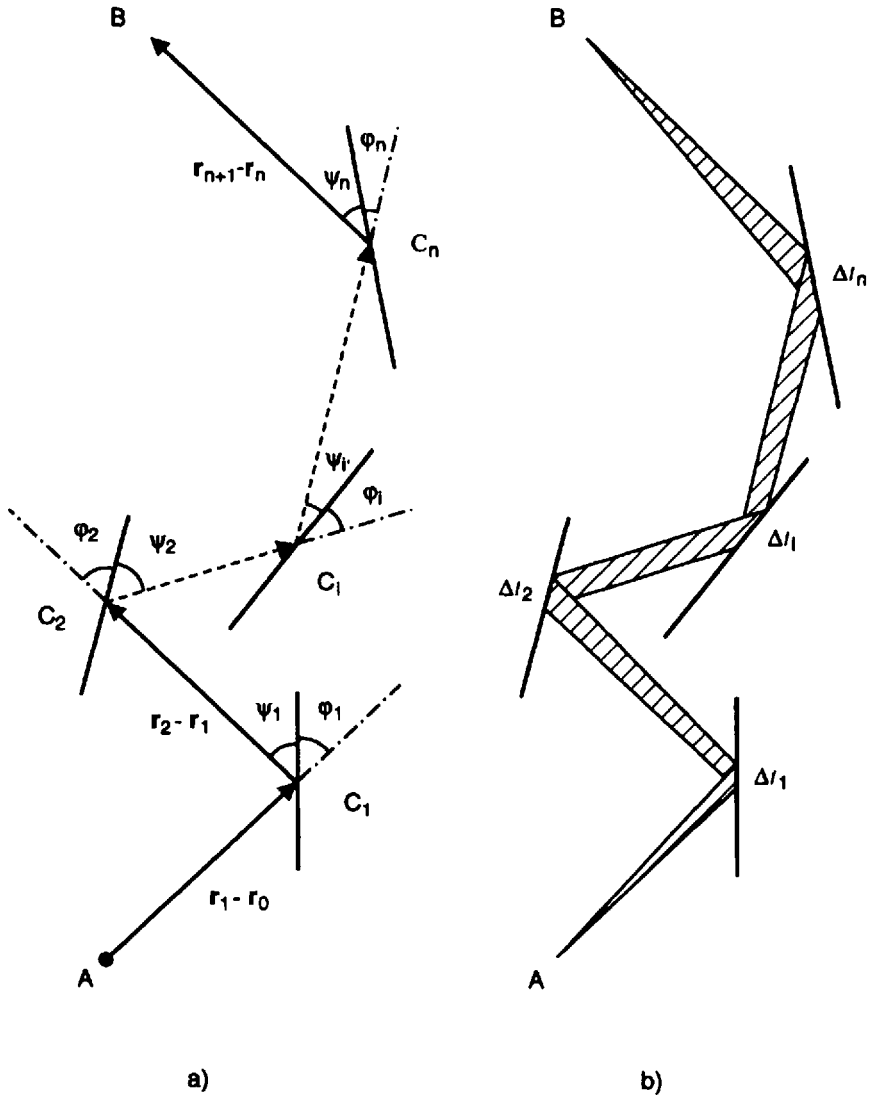

Figure 8.6 Geometry of multiscattering from n randomly distributed screens.

the field over the rough terrain using Green's theorem in its integral form (see Chapter 2):

$$U(\mathbf{r}_2) = U_i(\mathbf{r}_2) + \int_S \left\{ U(\mathbf{r}_s) \frac{\partial G(\mathbf{r}_2, \mathbf{r}_s)}{\partial \mathbf{n}_s} - G(\mathbf{r}_2, \mathbf{r}_s) \frac{\partial U(\mathbf{r}_s)}{\partial \mathbf{n}_s} \right\} dS \tag{8.24}$$

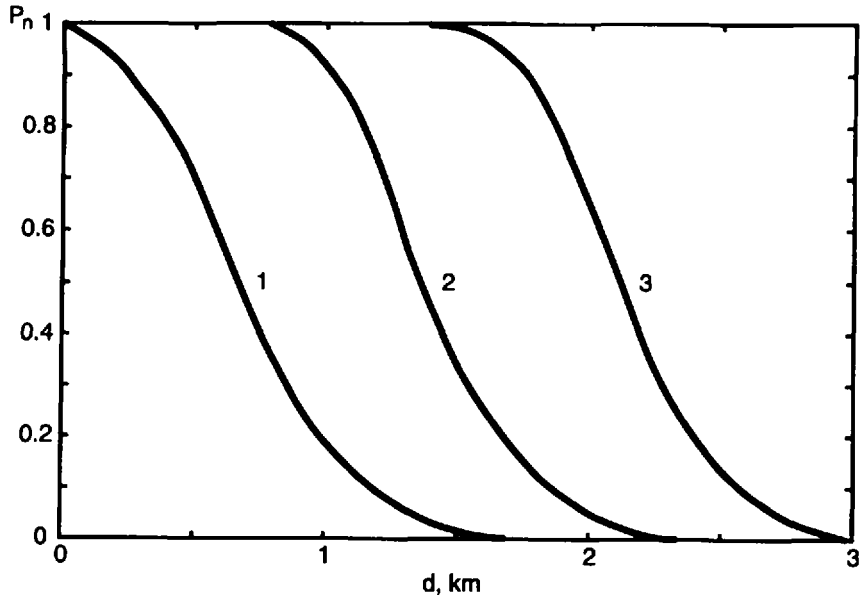

Figure 8.7 Probability to observe single-, double-, and three-times-scattered waves in the microcell (d < 2–3 km) environment.

where $U_i(\mathbf{r}_2)$ is the incident wave field, $G(\mathbf{r}_2, \mathbf{r}_s)$ is Green's function of the semispace (Section 2.2)

$$G(\mathbf{r}_2, \mathbf{r}_1) = \frac{1}{4\pi}\left\{\frac{\exp[ik|\mathbf{r}_2 - \mathbf{r}_1|]}{|\mathbf{r}_2 - \mathbf{r}_1|} \pm \frac{\exp[ik|\mathbf{r}_2 - \mathbf{r}_1'|]}{|\mathbf{r}_2 - \mathbf{r}_1'|}\right\} \tag{8.25}$$

and $\mathbf{n}_s$ is the vector normal to the terrain surface S at the scattering point $\mathbf{r}_s$. Here $\mathbf{r}_1'$ is the point symmetrical to $\mathbf{r}_1$ relative to the earth's surface S_1; $k = 2\pi/\lambda$, λ is the wavelength. We consider in integral (8.24) the random surface S (relief of the terrain with obstructions) as the superposition of ideal flat-ground surface S_1 ($z = 0$) and the rough surface S_2 that is created by the tops of the obstructions. We construct Green's function in such a form (8.25) to satisfy a general electrodynamic approach. That is, to describe both vertical (sign "+" in (8.25)) and horizontal (sign "−" in (8.25)) polarization with the corresponding boundary conditions. In fact, by introducing Green's function (8.25) with sign "+" in integral (8.24) we satisfy the Dirihlet boundary conditions at the flat (nondisturbed) earth's surface S_1 ($z = 0$), that is, $G_{z=0} = 2$ and $\dfrac{\partial u}{\partial \mathbf{n}_s} = 0$. At the same time, using sign "−" we satisfy the Neumann boundary

conditions at the plane $z = 0$, that is, $G_{z=0} = 0$ and $u = 0$. We must notice here that the authors in [1] used only Green's function with sign "–" and, hence, despite the fact that they have declared the possibility of using their approach in a general electrodynamic case, their analysis presented is correct only for the scalar case or for the electrodynamic case of wave propagation with horizontal polarization.

Hence, if the source is described by formula (8.25), assuming the surface S_1 as perfectly reflecting, we can exclude the integration over nondisturbed surface S_1 using the approach presented in [32, 33] (e.g., using the integration only over disturbed surface S_2, and immediately reduce the scattered field presentation (8.24) in the following form):

$$U(\mathbf{r}_2) = G(\mathbf{r}_2, \mathbf{r}_1) + 2\int_S \{U_r(\mathbf{r}_s) \cdot (\mathbf{n}_s \cdot \nabla_s) G(\mathbf{r}_2, \mathbf{r}_s)\} \tag{8.26}$$

where $\nabla_s = \left(\frac{\partial}{\partial x_s}, \frac{\partial}{\partial y_s}, \frac{\partial}{\partial z_s}\right)$

Using the Kirchhoff approximation [28–33], let us determine the scattered field $U_r(\mathbf{r}_s)$ from the building layer as a superposition of an incident wave $U_i(\mathbf{r}_s)$, the reflection coefficient $\Gamma(\varphi_s, \mathbf{r}_s)$, and the shadow function $Z(\mathbf{r}_2, \mathbf{r}_1)$, which equal 1, if the scattered point $\mathbf{r}_s$ inside the city layer can be observed from both points $\mathbf{r}_1$ and $\mathbf{r}_2$ of the transmitter and receiver locations (see Figure 8.8), and equals zero in all other cases. Taking into account what is mentioned above, the last formula (8.26) can be rewritten in the case of single scattering as

$$\begin{aligned} U(\mathbf{r}_2) &= Z(\mathbf{r}_2, \mathbf{r}_1) G(\mathbf{r}_2, \mathbf{r}_1) \\ &+ 2\int_{S_2} \{Z(\mathbf{r}_2, \mathbf{r}_s, \mathbf{r}_1)\Gamma(\varphi_s, \mathbf{r}_s) G(\mathbf{r}_s, \mathbf{r}_1) \cdot (\mathbf{n}_s \cdot \nabla_s) G(\mathbf{r}_2, \mathbf{r}_s)\} dS \end{aligned} \tag{8.27}$$

where $\sin\varphi_s = \mathbf{n}_s \cdot \frac{\mathbf{r}_s - \mathbf{r}_1}{|\mathbf{r}_s - \mathbf{r}_1|}$ (see Figure 8.8).

Assuming now that $\lambda << \overline{\rho}$, h_i, z_1, $z_2 << |\mathbf{r}_2 - \mathbf{r}_1|$, where $\overline{\rho}$ is determined by (8.8), z_1, z_2 are the height of source and receiver, respectively, and h_i is the height of a local obstacle placed on flat terrain, we can present the term $(\mathbf{n}_s \cdot \nabla_s) G(\mathbf{r}_2\ \mathbf{r}_s)$ in integral (8.27) approximately as $ik\sin\psi_s G(\mathbf{r}_2, \mathbf{r}_s)$ (this follows from the geometry presented in Figures 8.5 and 8.8). Using this approximation we finally obtain from (8.27)

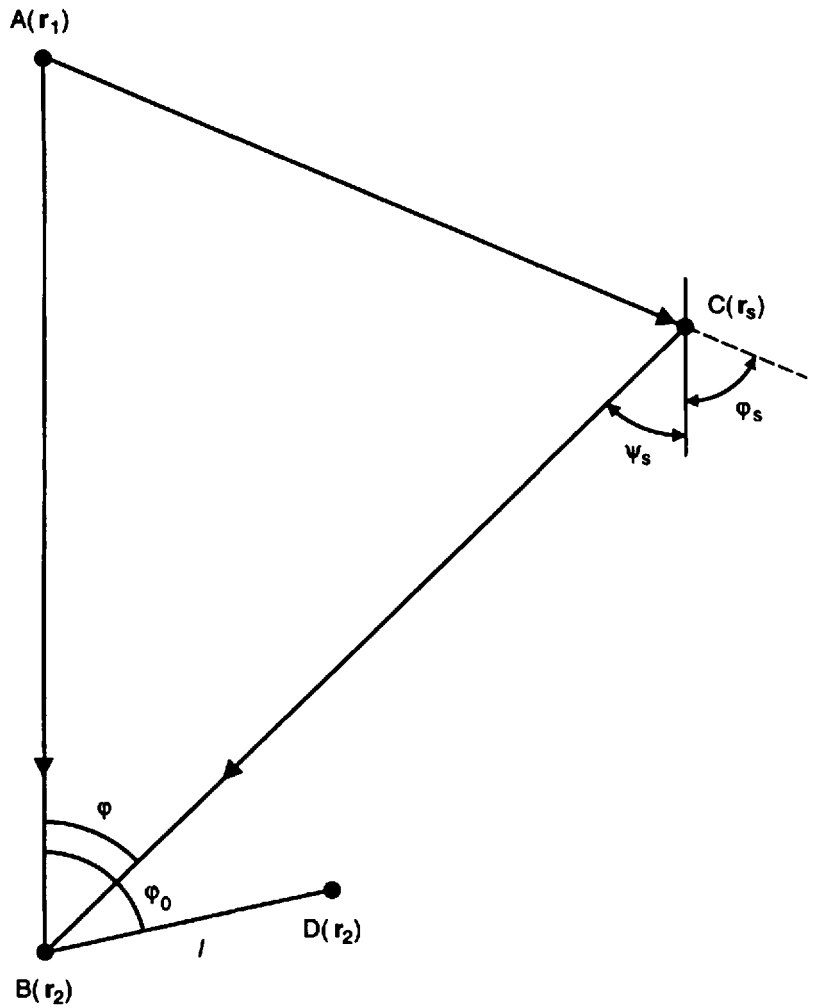

Figure 8.8 Two-dimensional geometry of single scattering from the screen.

$$U(\mathbf{r}_2) = Z(\mathbf{r}_2, \mathbf{r}_1)G(\mathbf{r}_2, \mathbf{r}_1) + 2ik\int_{S_2}\{Z(\mathbf{r}_2, \mathbf{r}_s, \mathbf{r}_1)\Gamma(\varphi_s, \mathbf{r}_s)\cdot \sin\Psi_s \cdot G(\mathbf{r}_s, \mathbf{r}_1)\cdot G(\mathbf{r}_2, \mathbf{r}_s)\}dS \tag{8.28}$$

According to [1], we assume in (8.28) that the coefficient of reflection from the building surface, $\Gamma(\varphi_s, \mathbf{r}_s)$, is a random but independently distributed function at the building surface, that is, $\langle\Gamma(\varphi_s, \mathbf{r}_s)\rangle = 0$. If so, one can obtain,

after averaging (8.28) over the phase interval $[0, 2\pi]$ with equal probability of the phase distribution for the coefficient of reflection and over the position of all buildings, the following expression for average field strength:

$$\langle U(\mathbf{r}_2)\rangle = \langle Z(\mathbf{r}_2, \mathbf{r}_1)\rangle \cdot G(\mathbf{r}_2, \mathbf{r}_1) = P_{12} \cdot G(\mathbf{r}_2, \mathbf{r}_1) \tag{8.29}$$

As seen from (8.29), the average field at the receiving point can be determined by the probability of signal reception P_{12} according to (8.4).

The knowlege of average field strength allows us to present the correlation function of wave field $K(\mathbf{r}_2, \mathbf{r}_2') = \langle U(\mathbf{r}_2) \cdot U^*(\mathbf{r}_2')\rangle$ in the following form:

$$\begin{aligned} K(\mathbf{r}_2, \mathbf{r}_2') = 4k^2 \Bigg\langle \int_{S_2} dS_2 \int_{S_2} dS_2' \cdot Z(\mathbf{r}_2, \mathbf{r}_s, \mathbf{r}_1) \\ \cdot Z(\mathbf{r}_2', \mathbf{r}_s', \mathbf{r}_1) \cdot \Gamma(\varphi_s, \mathbf{r}_s) \cdot \Gamma(\varphi_s', \mathbf{r}_s') \\ \times \sin\Psi_s \cdot \sin\Psi_s' \cdot G(\mathbf{r}_s, \mathbf{r}_1) \cdot G(\mathbf{r}_2, \mathbf{r}_s) \cdot G^*(\mathbf{r}_2', \mathbf{r}_s') \cdot G^*(\mathbf{r}_s', \mathbf{r}_1) \Bigg\rangle \end{aligned} \tag{8.30}$$

As stated above for mean field strength, we must use the procedure of averaging over the buildings' number, their reflection properties, and their spatial distribution to derive the correlation function presented by (8.30). We will do this procedure step-by-step, first by averaging (8.30) over the phase interval $[0, 2\pi]$ with equal probability of the phase distribution for the coefficient of reflection (the result we denote as $K_\Gamma(\mathbf{r}_2, \mathbf{r}_2')$). The result is

$$\begin{aligned} K_\Gamma(\mathbf{r}_2, \mathbf{r}_2') = 4k^2 \int_{S_2} dS_2 \int_{S_2} dS_2' \cdot Z(\mathbf{r}_2, \mathbf{r}_s, \mathbf{r}_1) \cdot Z(\mathbf{r}_2', \mathbf{r}_s', \mathbf{r}_1) \cdot \sin^2\Psi_s \\ \times \langle \Gamma(\varphi_s, \mathbf{r}_s) \cdot \Gamma(\varphi_s', \mathbf{r}_s')\rangle \cdot G(\mathbf{r}_s, \mathbf{r}_1) \cdot G(\mathbf{r}_2, \mathbf{r}_s) \\ \cdot G^*(\mathbf{r}_2', \mathbf{r}_s') \cdot G^*(\mathbf{r}_s', \mathbf{r}_1) \end{aligned} \tag{8.31}$$

Here, both points $\mathbf{r}_2$ and $\mathbf{r}_2'$ are located at the same building screen. If we now introduce at each building screen a local coordinate system $\{\xi, \eta\}$ with the origin at the point $\mathbf{r}_s'$ and with the axis 0ξ oriented vertically and the axis 0η oriented horizontally with respect to the ground surface, we can determine in this coordinate system the following correlation function for the reflection coefficient:

$$\langle \Gamma(\varphi_s, \mathbf{r}_s) \cdot \Gamma(\varphi_s', \mathbf{r}_s')\rangle = \Gamma(\varphi_s) \cdot \exp\left\{-\frac{|\xi|}{l_v} - \frac{|\eta|}{l_h}\right\} \tag{8.32}$$

and obtain from (8.31) after integration over ξ and η that

$$K_\Gamma(\mathbf{r}_2, \mathbf{r}_2') = 4k^2 \int_{S_2} dS_2 Z(\mathbf{r}_2, \mathbf{r}_s, \mathbf{r}_1) \cdot Z(\mathbf{r}_2', \mathbf{r}_s', \mathbf{r}_1)$$
$$\cdot \sin^2 \Psi_s \Gamma(\varphi_s) |G(\mathbf{r}_2, \mathbf{r}_s)|^2 \, |G(\mathbf{r}_s, \mathbf{r}_1)|^2 \tag{8.33}$$
$$\times \exp\{ikl \cos(\varphi - \varphi_0)\} \frac{4kl_h}{1 + (kl_h)^2(\cos\psi_s - \cos\varphi_s)^2}$$
$$\cdot \frac{4kl_v}{1 + (kl_v)^2(\cos\theta_2 - \cos\theta_1)^2}$$

where

$$l = |\mathbf{r}_2 - \mathbf{r}_2'|,$$
$$\cos\varphi = \left(\frac{\mathbf{r}_2 - \mathbf{r}_1}{|\mathbf{r}_2 - \mathbf{r}_1|} \cdot \frac{\mathbf{r}_2 - \mathbf{r}_s}{|\mathbf{r}_2 - \mathbf{r}_s|}\right),$$
$$\cos\psi = \left(\frac{\mathbf{r}_2 - \mathbf{r}_1}{|\mathbf{r}_2 - \mathbf{r}_1|} \cdot \frac{\mathbf{r}_2 - \mathbf{r}_2'}{|\mathbf{r}_2 - \mathbf{r}_2'|}\right),$$
$$\sin\theta_1 = (z_s - z_1)/|\mathbf{r}_s - \mathbf{r}_1|,$$
$$\sin\theta_2 = (z_2 - z_s)/|\mathbf{r}_2 - \mathbf{r}_s|$$

(see Figure 8.8). Here the typical correlation scales, l_h and l_v, describe the correlation distances in horizontal and vertical directions for each invidual screen, as an obstruction (i.e., a typical distance between balconies, windows, a typical height of a floor in a building, and so on).

After averaging over the buildings' spatial distribution and their numbers for $kl_h >> 1$, $kl_v >> 1$, we obtain the following expression for the correlation function of total field in built-up areas:

$$K(\mathbf{r}_2, \mathbf{r}_2') = 16\pi \int_V d\mathbf{r} \cdot P(\mathbf{r}_1, \mathbf{r}) \cdot \langle \sigma(\mathbf{r}_2, \mathbf{r}, \mathbf{r}_1) \rangle \cdot P_h(z) \cdot P_{BD} \tag{8.34}$$
$$\times |G(\mathbf{r}_2, \mathbf{r}_s)|^2 \, |G(\mathbf{r}_s, \mathbf{r}_1)|^2 \cdot \exp\{ikl \cos(\varphi - \varphi_0)\}$$

where $P(\mathbf{r}_1, \mathbf{r})$ is the probability of direct visibility between two points $\mathbf{r}_1$ and $\mathbf{r}$ according to (8.4). The relief function $P_h(z)$ is defined by (8.3); P_{BD} according to (8.9) determines the probability of the event that the wave, after scattering

from point $\mathbf{r}$ and after arriving at point $\mathbf{r}_2$ under the angle φ, will illuminate the horizontal segment l oriented to $(\mathbf{r}_2 - \mathbf{r}_1)$ under the angle φ_0 (see Figure 8.8); $\langle \sigma(\mathbf{r}_2, \mathbf{r}, \mathbf{r}_1) \rangle$ is the differential cross-section of scattering from buildings:

$$\langle \sigma(\mathbf{r}_2, \mathbf{r}, \mathbf{r}_1) \rangle = \frac{\gamma_0 \Gamma(\alpha/2)}{4\pi} \cdot \sin^2 \frac{\alpha}{2} \frac{4kl_v}{1 + (kl_v)^2(\cos\theta_2 - \cos\theta_1)^2} \tag{8.35}$$

where α is the angle between vectors $(\mathbf{r}_s - \mathbf{r}_1)$ and $(\mathbf{r}_2 - \mathbf{r}_s)$ (see Figure 8.8).

The integration in (8.34) is over the volume V of the urban building layer, where $d\mathbf{r}$ is the element of volume V in three-dimensional space.

We must note that formula (8.34) fully determines the correlation function in the short-wave (VHF/X-band) single-scattering approximation. From this formula, according to the relation between the correlation function and the average intensity of the total field, one can determine the latter function as:

$$\begin{aligned} \langle I(\mathbf{r}_2) \rangle &\equiv K(\mathbf{r}_2, \mathbf{r}_2) \\ &= 16\pi \int_V d\mathbf{r} \cdot P(\mathbf{r}, \mathbf{r}_2) \cdot \langle \sigma(\mathbf{r}_2, \mathbf{r}, \mathbf{r}_1) \rangle \cdot P_h(z) \cdot P_{BD} \\ &\quad \times |G(\mathbf{r}_2, \mathbf{r})|^2 \, |G(\mathbf{r}, \mathbf{r}_1)|^2 \cdot \exp\{ikl\cos(\varphi - \varphi_0)\} \end{aligned} \tag{8.36}$$

The average intensity of scattered field at the observed point $\mathbf{r}_2$ can be obtained from (8.36) according the approach presented in [1], taking into account (8.4) and (8.25):

$$\langle I(\mathbf{r}_2) \rangle = \frac{\Gamma \lambda l_v}{8\pi[\lambda^2 + (2\pi l_v \gamma_0 (h - z_1))^2] d^3} (z_2 - h) \tag{8.37}$$

where there is the absolute value of the average reflection coefficient introduced earlier in (8.32) and (8.35).

As is well known [1, 2, 28–33], the total wave field intensity from the transmitter is a superposition of a scattered (incoherent) spectrum $\langle I_{inc} \rangle$ described by (8.37) and a coherent spectrum $\langle I_{co} \rangle$ of total field energy which can be presented as [1]:

$$\langle I_{co} \rangle = \exp\left[-\gamma_0 \frac{d(h - z_1)}{z_2 - z_1} \right] \frac{[\sin(kz_1 z_2)/d]^2}{4\pi^2 d^2} \tag{8.38}$$

For the case $z_2 = h$, the single-scattered wave intensity $\langle I_{inc} \rangle = 0$, (i.e., is equal to zero), the physically incorrect result, which follows from [1]. To correct formula (8.37) we must consider the process of diffraction from buildings according to [2], which will be done in the next section. Nevertheless, (8.37) correctly describes the frequency dependence of the propagation process inside the layer of city buildings: $\sim f^{-n}$ with $n < 0$ for frequencies in the VHF-band and lower part of UHF-band ($f << 1$ GHz), and $\sim f^{-n}$ with $n > 0$ for UHF-band and higher ($f > 0.5$ GHz). This complicated frequency dependence is seen from (8.37) for the opposite cases of $\lambda^2 >> [2\pi l_v \gamma_0 (h - z_1)]^2$ (in this case we have $\sim f^1$) and $[\lambda^2 << 2\pi l_v \gamma_0 (h - z_1)]^2$ (here we have $\sim f^{-1}$), respectively. As was shown from additional estimations, the frequency dependence below 100 MHz is $\sim f^0$.

The multi-scattering problem. In the case when both antennas are below the rooftop level ($0 < z_1, z_2 < h$), the effect of multiscattering from the buildings becomes stronger than the effect of single-scattering. The evaluation of statistical field characteristics is a very complicated problem, because in this case many randomly distributed nontransparent screens (buildings) are placed between receiver and transmitter and form the complicated multi-ray field at the observation point. However, in certain cases the problem is analogous to the one described above. According to the approach presented in [1], let us calculate the average intensity of the scalar field from the point source. As above, the two-dimensional nontransparent screens with average length $\overline{L}$ and average height h are randomly distributed along the earth's surface. Their spatial distributions are independent on the plane $z = 0$ and their average density is ν.

For the case $0 < z_1, z_2 < h$, the probability of direct visibility between two points $\mathbf{r}_1(x_1, y_1, z_1)$ and $\mathbf{r}_2(x_2, y_2, z_2)$ is determined by the expression:

$$P(\mathbf{r}_1, \mathbf{r}_2) = \exp\{-\gamma_0 |\rho_1 - \rho_2|\}, \quad \rho_i = (x_i, y_i), \; i = 1, 2 \qquad (8.39)$$

where as above, $\gamma_0 = 2\nu\overline{L}/\pi$, $\gamma_0^{-1} = \overline{\rho}$ is an average horizontal range of the direct visibility within the layer $0 < z < h$. We assume as well that the reflection coefficient Γ is distributed randomly (but independently) on the building surface. Thus, $\langle \Gamma \rangle = 0$. The inhomogeneity of the screen surface is described by the scales of correlation of the coefficient Γ in the horizontal, l_h, and the vertical, l_v, directions. We also assume that $l_h, l_v << h, \overline{\rho}, \overline{L}$. As above, we present the source field $\bar{G}(\mathbf{r}_1, \mathbf{r}_2')$ at the point $\mathbf{r}_1$ above the surface $z = 0$ through the conventional Green's function of free space:

$$\tilde{G}(\mathbf{r}_1, \mathbf{r}_2) = G(\mathbf{r}_1 - \mathbf{r}_2) \pm G(\mathbf{r}_1 - \mathbf{r}_2') \tag{8.40}$$

$$G(\mathbf{r}) = \frac{\exp(ik|\mathbf{r}|)}{4\pi|\mathbf{r}|}$$

where $\mathbf{r}'$ is the point symmetrical to the point $\mathbf{r}$ relative to the plane $z = 0$. Obviously, $\tilde{G}(\mathbf{r}_1, \mathbf{r}_2)$ is Green's function of the semispace. Using Green's theorem and the expansion of Green's function into the set (see Section 2.1) and assuming that kl_h, $kl_v >> 1$ and $kz_1 >> 1$, but $z_1 < h$, we obtain the coherent part $\langle I_{co} \rangle$ of average intensity of the total field:

$$\langle I_{co}(\mathbf{r}_2) \rangle = P(\mathbf{r}_2, \mathbf{r}_1) |G(\mathbf{r}_2, \mathbf{r}_1)| \tag{8.41}$$

For the incoherent part $\langle I_{inc} \rangle$ of the total field intensity, we can use the Laplace method [1] to obtain a simple formula for the case $\gamma_0 \rho >> 1$ and $a = \gamma_0 \Gamma/8$ as well:

$$\langle I_{inc}(\rho) \rangle = 2a^{1/2} \exp[-\gamma_0 \rho] \{2/\gamma_0 \rho + a\pi^{1/2}/\gamma_0 (2\gamma_0 \rho)^{1/2} + (a/\gamma_0)^3\}/(4\pi)^2 \rho \tag{8.42}$$

As seen from (8.42), the first term in brackets is the average intensity of the single-scattered wave:

$$\langle I_{inc1}(\rho) \rangle = a^{1/2} \exp[-\gamma_0 \rho]/(2\pi)^2 \gamma_0 \rho^2$$

Other terms do not essentially change the value of the total intensity at the distances $\rho_0 < 8\gamma_0/\pi a^2$. This is correct for the real condition of closed communication channels between moving responders in a city area with randomly distributed buildings. We can also present the coherent part in a more accurate form than in (8.38):

$$\langle I_{co}(\rho) \rangle = \exp[-\gamma_0 \rho] \frac{[2 \sin(kz_1 z_2)/\rho]^2}{16\pi^2 \rho^2} \tag{8.43}$$

so that the total field intensity is:

$$\langle I(\rho) \rangle = \langle I_{co}(\rho) \rangle + \langle I_{inc}(\rho) \rangle \tag{8.44a}$$

or the path loss in dB is given by (see definition of path loss in Chapter 1):

$$L_{total} = -10 \log(\langle I(\rho) \rangle) \tag{8.44b}$$

Additional investigations have shown that we have to take into account the effect of diffraction from the building rooftops. This is important for the upper part of UHF- and L-frequency-band and for urban channels longer than 1 km, an effect that will be analyzed in the next section.

8.3 Effects of Diffraction From the Building Layer

Let us now examine the influence of diffraction phenomena on the field intensity attenuation. Here we consider the field diffraction phenomenon due to buildings' rooftops. As follows from formula (8.37), for the case of a receiving antenna located at the rooftop level ($z_2 = h$), the physically incorrect result that the average intensity of the received signal is equal to zero can be obtained. Evidently, to exclude this result, one must take into account the effect of diffraction of the scattered field above the building layer. To account for this effect we use the Huygens-Kirchhoff approximation. For the derivation of the diffraction field we introduce the surface S_B of virtual sources that is normal to the building layer S and the surface of infinite semisphere S_R that contains the source of radiation inside it, as shown in Figure 8.9a. The effect of all virtual sources placed at the semisphere S_R is negligible, because it is limited to zero when the radius of this semisphere is limited to infinity. Then the field $U(\mathbf{r}_2)$ at the receiver can be rewritten as

$$U(\mathbf{r}_2) = 2ik \int_{S_B} \{U(\mathbf{r}_{S_B}) \cdot G(\mathbf{r}_2, \mathbf{r}_{S_B}) \cdot \cos\psi_{S_B}\} dS_B \tag{8.45}$$

where $U(\mathbf{r}_{S_B})$ is the field at the surface S_B obtained by use of approximation (8.27) for single scattering; $\cos\psi_{S_B} = (\mathbf{n}_{S_B} \cdot (\mathbf{r}_2 - \mathbf{r}_{S_B})/|\mathbf{r}_2 - \mathbf{r}_{S_B}|)$, $\mathbf{n}_{S_B}$ is the unit vector normal to surface S_B (Figure 8.9a). If so, the average intensity of received field $\langle I(\mathbf{r}_2) \rangle = \langle U(\mathbf{r}_2) \cdot U^*(\mathbf{r}_2) \rangle$ can be presented according (8.27) as:

$$\langle I(\mathbf{r}_2) \rangle = 4k^2 \int_{S_B} dS_B \int_{S_B} dS_B' \cdot K(\mathbf{r}_{S_B}, \mathbf{r}'_{S_B}) \cdot G(\mathbf{r}_2, \mathbf{r}'_{S_B}) \cdot G(\mathbf{r}_2, \mathbf{r}_{S_B}) \cos\psi_{S_B} \cos\psi'_{S_B} \tag{8.46}$$

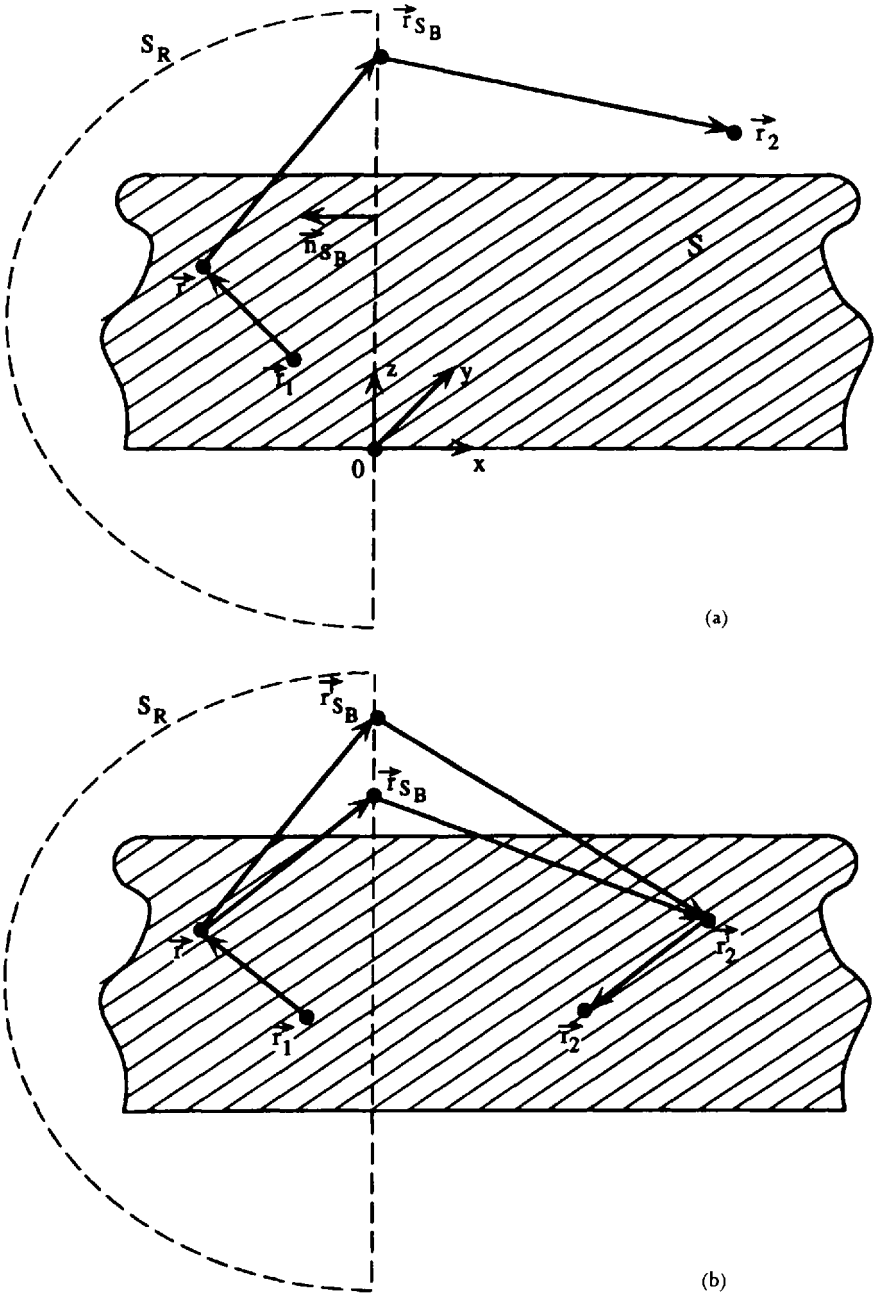

Figure 8.9 (a) Geometry of single scattering and single diffraction over the built-up layer. (b) Geometry of double scattering and double diffraction over the built-up layer.

where $K(\mathbf{r}_{S_B}, \mathbf{r}'_{S_B})$ is the correlation function of total field at points $\mathbf{r}_{S_B}$ and $\mathbf{r}'_{S_B}$ located at the surface S_B in conditions when the source is located at the point $\mathbf{r}_1$:

$$K(\mathbf{r}_{S_B}, \mathbf{r}'_2) = 4k^2 \Big\langle \int_{S_B} dS_B \int_{S_B} dS'_B \cdot Z(\mathbf{r}_2, \mathbf{r}_{S_B}, \mathbf{r}_1) \cdot Z(\mathbf{r}'_2, \mathbf{r}'_{S_B}, \mathbf{r}_1) \cdot \Gamma(\varphi_{S_B}, \mathbf{r}_{S_B}) \times \Gamma^*(\varphi'_{S_B}, \mathbf{r}'_{S_B}) \cdot \sin\psi_{S_B} \cdot \sin\psi'_{S_B} \cdot G(\mathbf{r}_2, \mathbf{r}_{S_B}) \cdot G(\mathbf{r}_{S_B}, \mathbf{r}_1) \cdot G^*(\mathbf{r}'_2, \mathbf{r}'_{S_B}) \cdot G^*(\mathbf{r}'_{S_B}, \mathbf{r}_1) \Big\rangle \tag{8.47}$$

Here the reflection coefficient $\Gamma(\varphi_S, \mathbf{r}_S)$ and the shadow function $Z(\mathbf{r}_2, \mathbf{r}_1)$, as well as other parameters are introduced in Section 8.2. By averaging (8.47) over the nontransparent screens spatial distribution, over their number and over the reflection properties of screens [1], after straightforward derivations we finally obtain the following formula for the single-scattered field taking into account the diffraction from the building layer:

$$\langle I(\mathbf{r}_2) \rangle = \frac{\Gamma \lambda l_v}{8\pi[\lambda^2 + (2\pi l_v \gamma_0(h - z_1))^2] d^3} [(\lambda d/4\pi^3) + (z_2 - h)^2]^{1/2} \tag{8.48}$$

For the case where the base-station antenna, as a receiver, is higher than the average building height, that is $(\lambda d/4\pi^3) << (z_2 - h)^2$ (8.48) is limited to the incoherent spectrum (8.37) obtained above without taking into account processes of diffraction. Moreover, with increase of z_2, the process of diffraction becomes more important and for $z_2 = h$ the single-scattered wave intensity $\langle I_{inc} \rangle \sim (\lambda d/4\pi^3)^{1/2}$ (i.e., is not equal to zero, as follows from results obtained in [1]). In both cases the distance dependence is only the same $\sim d^{-3}$ when $(\lambda d/4\pi^3) << (z_2 - h)^2$. In the inverse case, when $(\lambda d/4\pi^3) >> (z_2 - h)^2$ this dependence is $\sim d^{-2.5}$. In this case as well, the frequency dependence is changed from $\sim f^1$ and $\sim f^{-1}$, when there is no diffraction, to $\sim f^{0.5}$ and $\sim f^{-0.5}$, when diffraction is predominant. The coherent spectrum $\langle I_{co} \rangle$ of the total field energy can be presented by (8.38).

The same result can be obtained for double scattering with double diffraction, as presented in Figure 8.9b. Here the wave propagates from source point $\mathbf{r}_1$. After scattering at any point $\mathbf{r}$ inside the building layer and diffraction on the tops of obstacles surrounding the transmitter and receiver (double diffraction that we account for by introducing two virtual sources $\mathbf{r}_{S_B}$ and $\mathbf{r}'_{S_B}$ at surface

S_B, as follows from Figure 8.9b) it finally scatters from any point $\mathbf{r}'$ and comes to the receiver placed at point $\mathbf{r}_2$. Using the same presentation of average intensity of total field, as (8.46):

$$\langle I(\mathbf{r}_2)\rangle = 4k^2 \int_{S_B} dS_B \int_{S_B} dS_B' \cdot K(\mathbf{r}_{S_B}, \mathbf{r}'_{S_B}|\mathbf{r}, \mathbf{r}_1) \cdot K(\mathbf{r}_{S_B}, \mathbf{r}'_{S_B}|\mathbf{r}', \mathbf{r}_1') \cos\psi_{S_B} \cos\psi'_{S_B} \tag{8.49}$$

where $K(\mathbf{r}_{S_B}, \mathbf{r}'_{S_B}|\mathbf{r}, \mathbf{r}_1)$ and $K(\mathbf{r}_{S_B}, \mathbf{r}'_{S_B}|\mathbf{r}', \mathbf{r}_1)$ are the correlation functions of the total field at the surface of virtual sources of diffraction which is determined by (8.47). After averaging of (8.49) over the nontransparent screens spatial distribution, over their number, and over the reflection properties of screens, we obtain the following formula for the double-scattered field taking into account double diffraction from the building layer:

$$\langle I_{inc}(\mathbf{r}_2)\rangle = \frac{\Gamma^2 \lambda^3 l_v^2}{24\pi^2[\lambda^2 + (2\pi l_v \gamma_0(h - z_1))^2][\lambda^2 + (2\pi l_v \gamma_0(h - z_2))^2]d^3} \tag{8.50}$$

In this more general case, the average intensity attenuates proportionate to $\sim d^{-3}$ with the increase of distance between subscribers, which is closer to measurements than that obtained proportionate to $\sim d^{-2}$ from (8.42) without considering diffraction. Moreover, (8.50) correctly describes the frequency dependence of the propagation process inside the layer of city buildings: $\sim f^{-n}$ with $n < 0$ for frequencies in the VHF-band and lower part of the UHF-band ($f << 1$ GHz), and $\sim f^{-n}$ with $n > 0$ for the UHF-band and higher ($f > 0.5$ GHz). This complicated frequency dependence can be clearly seen from (8.50) for the opposite cases of $\lambda^2 >> [2\pi l_v \gamma_0(h - z_1)]^2$ and $\lambda^2 << [2\pi l_v \gamma_0(h - z_1)]^2$, respectively.

8.4 Influence of the City Building Profile

Let us now consider the influence of the city building profile on the average field intensity for the case of single-scattered waves. Taking into account that the real areas of the urban environment are distributed inhomogeneously, we must present the probability of direct visibility between two points, $\mathbf{r}_1$ and $\mathbf{r}_2$, according to (8.4) as

$$P(\mathbf{r}_1, \mathbf{r}_2) = \exp\left\{-\gamma_0 r_{12}(z_2 - z_1)^{-1} \int_{z_1}^{z_2} P_h(z)dz\right\} \tag{8.51}$$

where $r_{12} = [(x_2 - x_1)^2 + (y_2 - y_1)^2]^{1/2}$. Function $P_h(z)$ was introduced earlier in Section 8.2.1 as the probability that point z is located below the building roof's level. According to (8.3), this function is related to density of building heights' distribution $w(h)$. The average height of buildings in the investigated urban area also related to the function $w(h)$ as

$$h = \int_0^h h' w(h')dh' \tag{8.52}$$

Taking into account (8.3) and assuming the height profile of buildings inside the city layer in the following form:

$$P_h(z) = H(h_1 - z) + H(z - h_1)H(h_2 - z)\left[\frac{(h_2 - z)}{(h_2 - h_1)}\right]^n, \tag{8.53}$$

$$n > 0,\ 0 < z < h_2$$

we can obtain for the case of $\gamma_0 r >> 1$ the following expression for the incoherent part of the total field intensity:

$$\langle I(\mathbf{r}_2)\rangle = \frac{\gamma_0 \Gamma l_v \lambda z_2}{8\pi[\lambda^2 + (2\pi l_v \gamma_0 Q(z_1, z_2))^2]d^3}\,[-2\pi/f''(x_m)]^{1/2}\exp\{f(x_m)\} \tag{8.54}$$

Here

$$Q(z_1, z_2) = \int_{z_1}^{z_2 - x_m} P_h(z)dz \tag{8.55}$$

function $f(x)$ equals:

$$f(x) = \gamma_0 d(1 - x)^{-1} \int_0^h P_h(z_2 x')dx' + \ln P_h(z_2 x) \tag{8.56}$$

but x_m is determined from $df(x)/dx = 0$. The function $H(x)$ is the Heaviside "step function," equal to 1, if $x > 0$, and equal to 0, if $x < 0$.

The coherent part of total field intensity can also be obtained more generally taking into account the function's $P_h(z)$ distribution:

$$\langle I_{co} \rangle = \exp\left\{-\gamma_0 d(z_2 - z_1)^{-1} \int_{z_1}^{z_2} P_h(z)dz\right\} \frac{\sin^2(kz_1 z_2/d)}{4\pi^2 d^2} \tag{8.57}$$

As can be seen from (8.54) to (8.57), the character of field intensity attenuation depends on the function's $P_h(z)$ distribution, which we presented in a more general form than in [1]. Thus, for $n >> 1$ $P_h(z)$ describes the case, when above the city layer with height h_1, buildings with $h_i > h_1$ very rarely exist. For $n << 1$ we obtain the case, when all buildings inside the city layer have heights close to h_2. For $n > 0$, all buildings have the same level equal to h_2, for $n < \infty$ all buildings have the same level with h_1. Hence, the height distribution (8.53) describes a wide spectrum of city building models: from one-level up to various levels with heights h_i of buildings distributed with equal probability from h_1 up to h_2 (the minimum and maximum heights of a city layer), when $n = 1$. For the case $z_2 > h_2$ and $(z_2 - h)/d << 1$ for $n > 0.2$ (quasi-homogeneous distribution of building heights), one can obtain from (8.53) and (8.54) the intensity of single-scattered waves:

$$\langle I(\mathbf{r}_2) \rangle = \frac{\Gamma \lambda l_v}{8\pi[\lambda^2 + (2\pi l_v \gamma_0 f(z_1))^2]d^3} (z_2 - h) \tag{8.58a}$$

without diffraction phenomena, and

$$\langle I(\mathbf{r}_2) \rangle = \frac{\Gamma \lambda l_v}{8\pi[\lambda^2 + (2\pi l_v \gamma_0 f(z_1))^2]d^3} [(\lambda d/4\pi^3) + (z_2 - h)^2]^{1/2} \tag{8.58b}$$

taking into account diffraction from buildings' corners and roofs. One can obtain the same result according to (8.50) for double-scattered and double-diffracted waves:

$$\langle I_{inc}(\mathbf{r}_2) \rangle = \frac{\Gamma^2 \lambda^3 l_v^2}{24\pi^2[\lambda^2 + (2\pi l_v \gamma_0 f(z_1))^2][\lambda^2 + (2\pi l_v \gamma_0 f(z_2))^2]d^3} \tag{8.59}$$

Here,

$$f(z_1) = H(h_1 - z_1)(h - z_1) + H(z_1 - h_1)H(h_2 - z_1)\frac{(h - z_1)^{n+1}}{(n + 1)(h_2 - h_1)^n} \tag{8.60a}$$

and

$$f(z_2) = H(h_2 - z_2)(h - z_2) + H(z_2 - h_1)H(h_2 - z_2)\frac{(h - z_2)^{n+1}}{(n + 1)(h_2 - h_1)^n} \tag{8.60b}$$

where the average building's height h is determined by the following expression

$$h = h_2 - n(h_2 - h_1)/(n + 1) \tag{8.61}$$

Comparison between formulas (8.58), (8.37), and (8.48) allow us to conclude that the existence of a building distribution profile (8.56) does not change the dependence of field attenuation with distance d and with changes of height z_2, but it gives an additional effect for the frequency dependence of field intensity. Moreover, the profile (8.56) limits to (8.60) for the case of quasi-homogeneous distribution of buildings' heights. What also follows from (8.60) is that this building heights' distribution is more general and realistic then that obtained in [1]. Hence we can with great accuracy approximate the city layer with an inhomogeneous building heights' distribution (8.56) by the quasi-homogeneous one according to (8.60) with some average height h from (8.61).

8.5 Numerical Simulation of Scattering and Diffraction Phenomena

To examine the influence of different propagation phenomena, such as multireflection, multiscattering, and multidiffraction, as well as of the parameters of city building and the situation regarding both antennas on field intensity attenuation, we separately calculated and investigated the coherent and incoherent parts of the total field for two variants of scattered field obtained above: single and double scattering with diffraction. We also examined the case of inhomogeneous distribution of the building layer, taking into account its profile described by formulas (8.60a) and (8.60b) for different parameters of the polynomial function $f(z)$.

In the first case of single-scattering with diffraction, we numerically examined the terms $-10\log\langle I_{inc}\rangle$ and $-10\log\langle I_{co}\rangle$, according to formulas (8.58b) and (8.57), respectively, and the total loss by formula $-10\log\langle I_{total}\rangle = -10\log[\langle I_{inc}\rangle + \langle I_{co}\rangle]$. We present this case at the top side of all figures. For the case of double-scattering with diffraction we derived formulas (8.59) and (8.57) by using the same form: $-10\log\langle I_{inc}\rangle$, $-10\log\langle I_{co}\rangle$, respectively, and the total field as $-10\log\langle I_{total}\rangle$. In our simulations we changed the parameter n of the polynomial height profile $h_i(z)$ to be close to the tall buildings' height h_2 ($n = 0.1$, $n << 1$), for the case where $h_i(z)$ is uniformly distributed between h_1 and h_2 ($n = 1$) with the mean value $h = (h_1 + h_2)/2$, and for $h_i(z)$ close to low buildings' height h_1 ($n = 5$, $n >> 1$).

Results of numerical calculations for all the above-mentioned variants are presented in Figures 8.10 to 8.12 for various situations in the city scene:

(a) $z_2 = 50$m, $z_1 = 2$m, $h_2 = 25$m, $h_1 = 5$m (Figure 8.10);

(b) $z_2 = 10$m, $z_1 = 2$m, $h_2 = 25$m, $h_1 = 5$m (Figure 8.11);

(c) $z_2 = 4$m, $z_1 = 2$m, $h_2 = 25$m, $h_1 = 5$m (Figure 8.12). In these cases we obtain from (8.61): $h \approx 23$m, for $n = 0.1$; $h = 15$m, for $n = 1$; $h \approx 8$m, for $n = 5$.

In the case (a), when $z_1 < h_1 < h << z_2$, results of numerical simulations according to the model of single-scattering (MSS) (top-side of Figure 8.10) and the model of double-scattering (MDS) (bottom-side of Figure 8.10), take into account the diffraction from buildings surrounding both antennas. The coherent part (dotted curves) of the total field exponentially attenuates with sharp oscillations up to ~500m–700m from the source. Beyond this range the smooth decay of $\langle I_{co}\rangle$ is observed. As for the incoherent part $\langle I_{inc}\rangle$ of the total field (dashed curves), the stronger attenuation according to the polynomial law $\sim d^{-3}$ is observed at the whole range from the transmitter up to 3–5 km (for "microcell" ranges). At the same time, as follows from the top-side graph, the coherent component of the total field exceeds the incoherent one at ranges up to 3–4 km (denoted by points at the curve's intersection), that is, the effects of scattering from buildings is important only for far zones from the transmitter. In areas near the transmitter (less than 1 km) only direct waves and waves reflected from the building layer, which form the coherent component of total wave field, reach the point of observation.

With decrease of the height of the transmitter ($z_2 = 10$m, case (b)), when $z_1 < h_1 < z_2$, $z_2 < h$ ($n = 0.1$, 1) and $z_2 > h$ ($n = 5$), as follows from illustrations in Figure 8.11, both models, MSS and MDS, predict the same effects that were presented earlier in Figure 8.10. In fact, at the ranges 3–4 km from the transmitter, the direct component (coherent part) of the total field exceeds the scattered component (incoherent part).

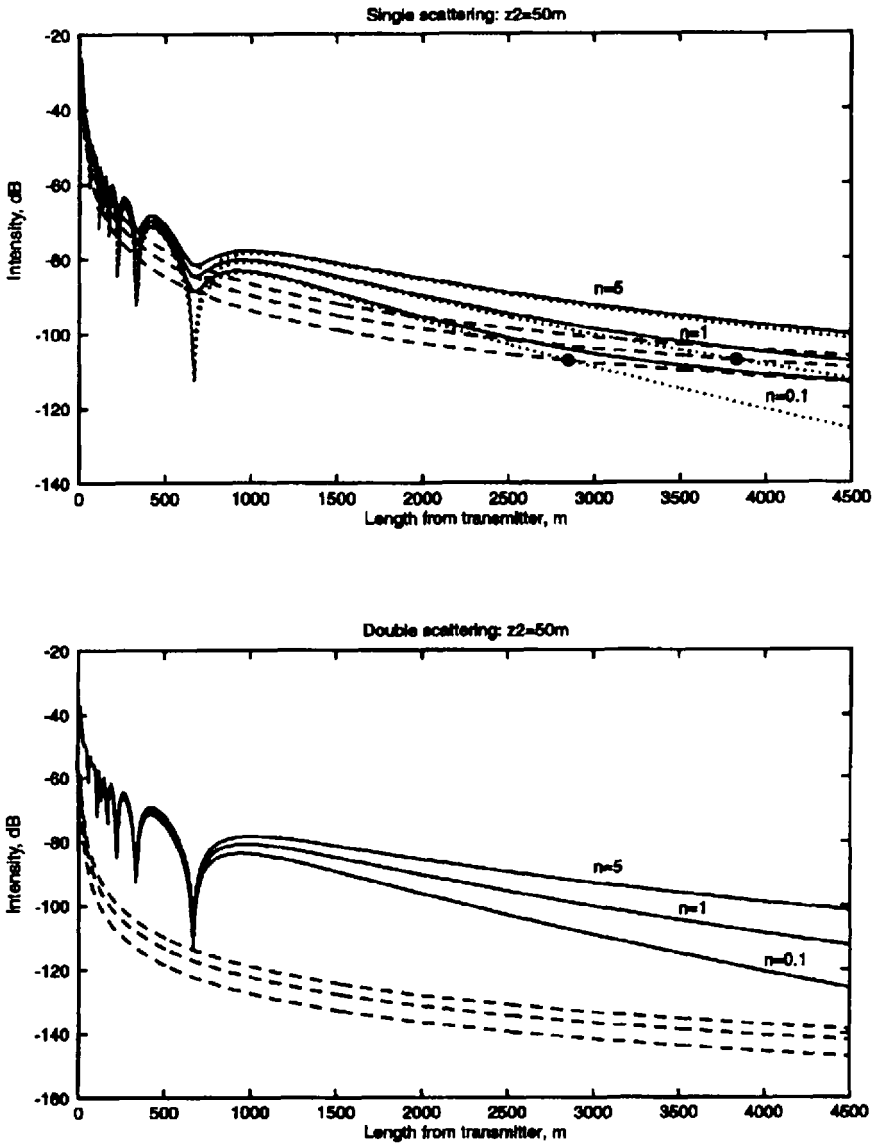

Figure 8.10 Incoherent and coherent parts of total field intensity versus distance from the transmitter for single (top side) and double scattering (bottom side) with diffraction for $z_1 = 2m$, $z_2 = 50m$, $h_1 = 5m$, $h_2 = 25m$, $n = 0.1, 1, 5$.

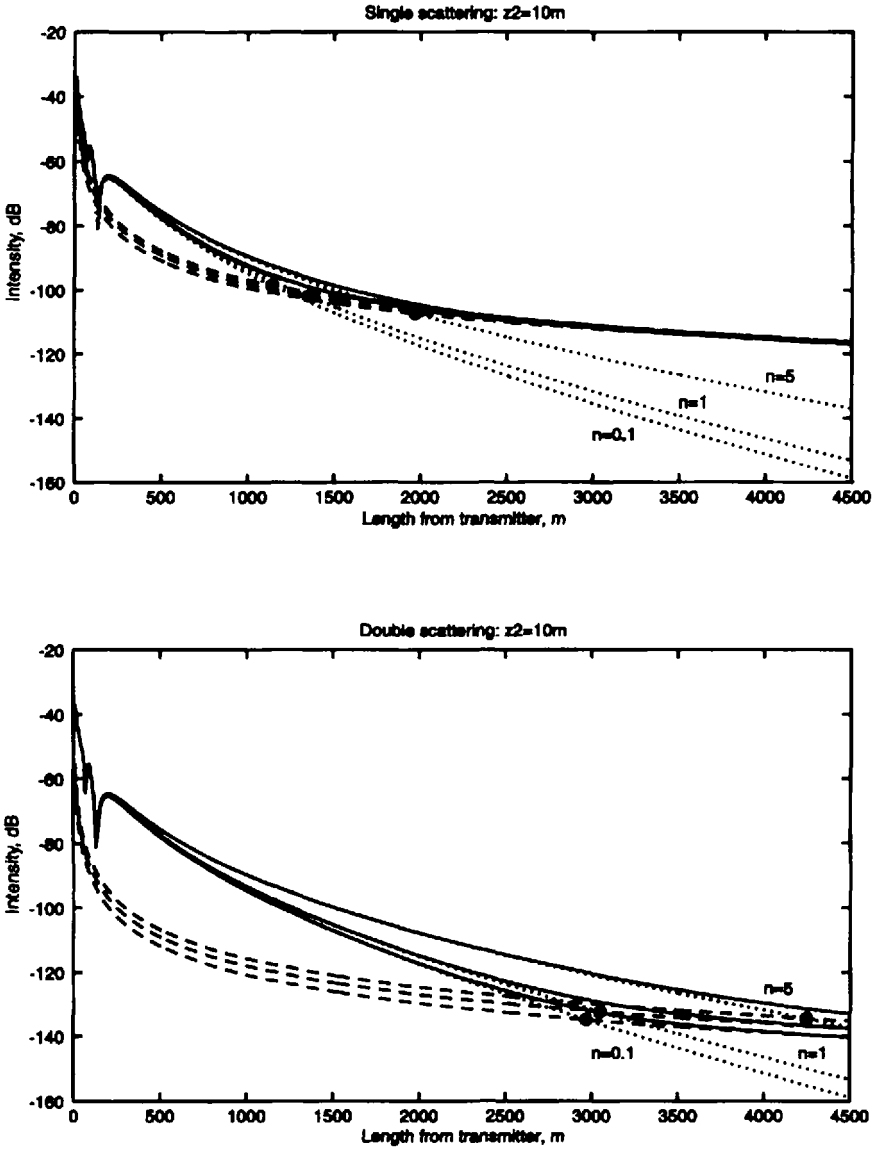

Figure 8.11 Incoherent and coherent parts of total field intensity versus distance from the transmitter for single (top side) and double scattering (bottom side) with diffraction for $z_2 = 10m$.

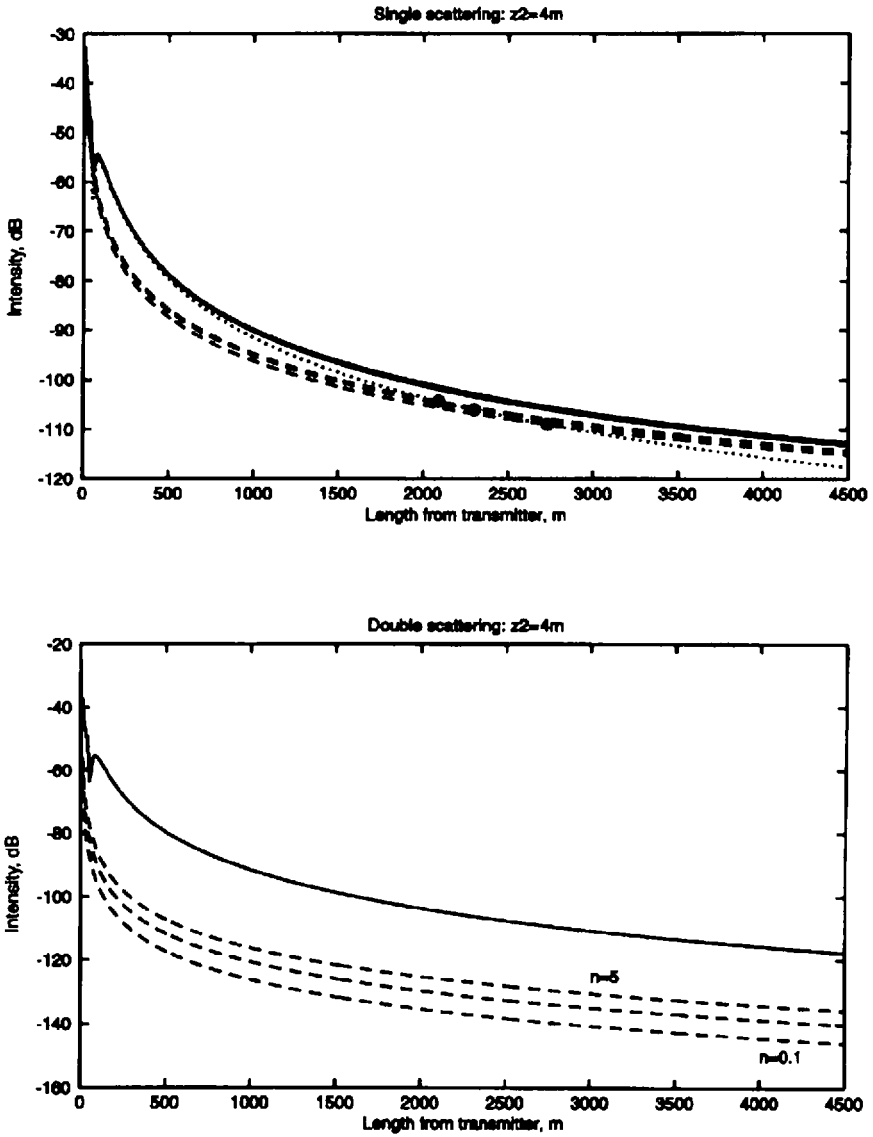

Figure 8.12 Incoherent and coherent parts of total field intensity versus distance from the transmitter for single (top side) and double scattering (bottom side) with diffraction for $z_2 = 4m$.

In the case when both antennas are below the building's height profile (i.e., $z_1 < h_1 < z_2 < h < h_2$, case (c) mentioned above), which is presented in Figure 8.12, two models, MSS and MDS, predict the existence of break points at the ranges of 1–2 km (for MSS) and at the ranges 3–4.5 km (for MDS), the effect that depends on buildings' height distribution (on the parameter n in (8.60)). Moreover, using MDS we obtain the increase of the scattered component (incoherent part) and, finally, of the total field beyond the break point $r_b \sim$ 3–5 km from the transmitter.

8.6 Prediction of Path Loss in Various Urban Environments

We compare the results of theoretical prediction of the total field intensity attenuation according to the proposed parametric model with results of the experiment carried out in Israel and Jamaica [3]. Using the proprietary wireless local loop system, measurements of the radio signal strength indication (RSSI) were produced in the various urban and rural environments. We present below some experimentally obtained results and their comparison with the above theoretical model.

In the measurement system the stand-alone radio port unit (RPU) played the role of the transmitter. The fixed access unit (FAU) was used as the receiver which during the experiment was moved from point to point. The RPU and the FAU communicate using frequency hopping in one of the specified frequency bands. According to the FAU specification, its measurement accuracy is equal to 2 dB. The measurements have been produced in three cities: Kingston (Jamaica), Holon and Jerusalem (Israel). The terrain in Kingston as well as in Holon is relatively flat while the terrain of Jerusalem is hilly. The urban condition in Kingston is rural. The notion of the small and medium urban area is more relevant to the Holon and Jerusalem propagation conditions, respectively. Two or three samples were taken at each point and the average values based on these measurements were found. To determine RSSI values from the above expressions of average intensity of the field, we have to multiply these expressions by the effective antenna aperture that is equal to $\lambda^2/4\pi$ [34].

Let us consider the two cases with the quasi-flat terrain, Holon and Kingston. In both cases the frequency band is 1.9 GHz. In the former case the building density is ν = 258 km^{-2}, the average building length $\overline{L}$ = 30m and the average building height h = 13m. The RPU installation height was z_2 = 30m and the FAU height z_1 = 6m. In the latter case (Kingston), the urban conditions can be described by the following parameters: ν = 213 km^{-2}, $\overline{L}$ = 32m and h = 10m. The installation heights of the receiving and transmitting antennas were also different from the previous case:

z_2 = 26m and z_1 = 11.2m. Additionally, in this and all the following cases, we assumed two things. First, the vertical correlation scale is significantly larger than the wavelength and is equal to l_v = 1.85m. Secondly, almost all the buildings are made of concrete (this is a rough assessment) with parameters found in [14]. Based on these results we shall take the relative permittivity of concrete $\epsilon \approx 6.49$ and its conductivity $\sigma \approx 1.37$ mho/m. The comparison between measurement and simulated results of the total field intensity $-10\log I(\mathbf{r}) = -10\log[I_{inc}(\mathbf{r}) + I_{co}(\mathbf{r})]$ according to the MSS with diffraction (8.58b) and (8.57), and to the MDS with diffraction (8.59) and (8.57), presented in Figures 8.13(a,b), respectively, for the Holon case (for quasi-uniform distribution of buildings' height with n = 1). Here, the samples of measurement are indicated by circles. The theoretical function of RSSI and the straight line that is close to it in the mean square metric are shown by the solid and dashed lines, respectively. The indicated number pair is the standard deviation value (*StDiv*) and the following distance (in the l_2-space metric) between two point sets:

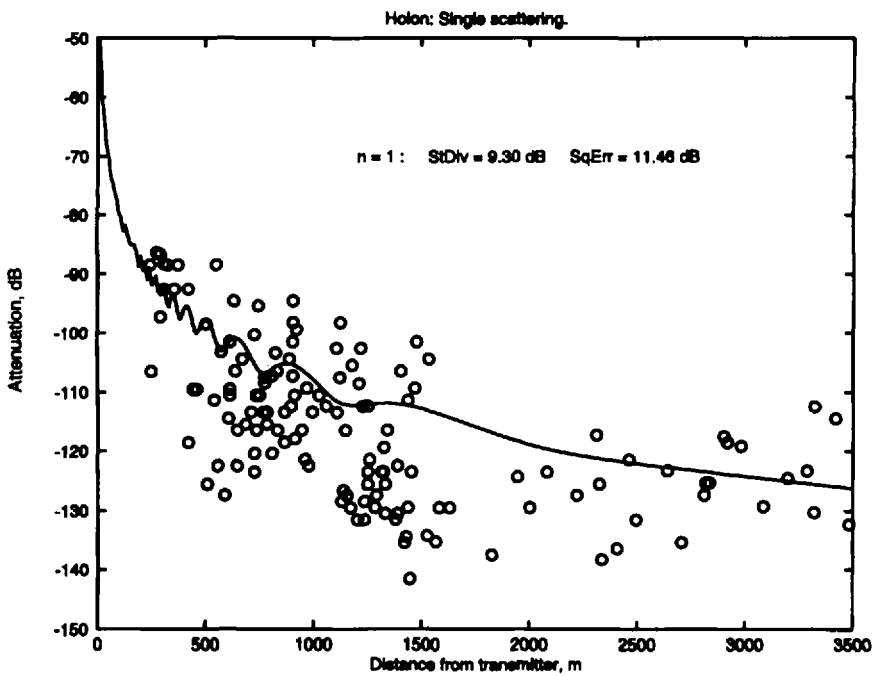

Figure 8.13 (a) Comparison between the measured (circles) and calculated (continuous curve) average total field intensity according to single-scattering model obtained for conditions of the Holon area. (b) The same, as in Figure 8.13(a), but by use of double-scattering model.

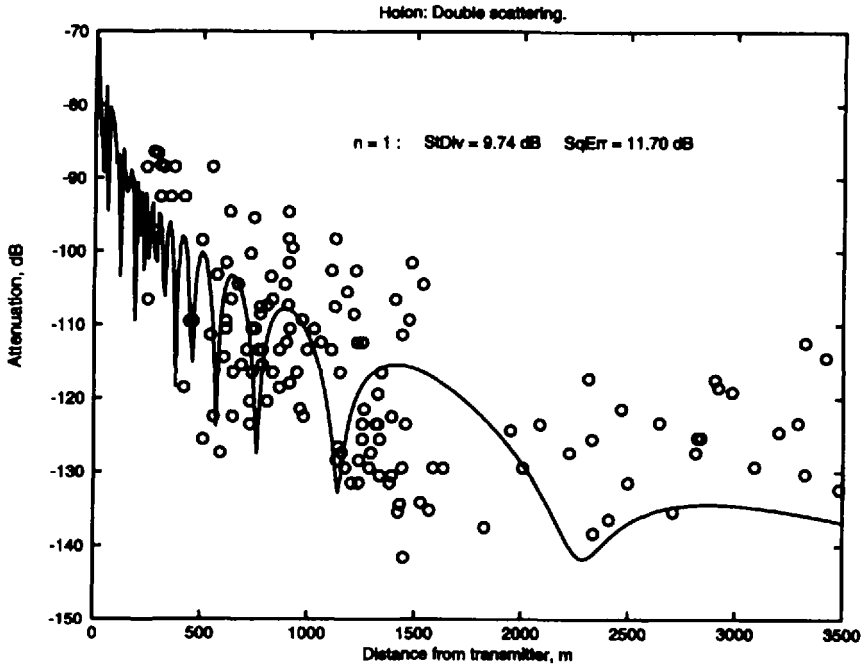

Figure 8.13 (b) (continued).

$$SqErr = \sqrt{\frac{1}{N}\sum_{i=1}^{N}(R_i - r_i)^2} \tag{8.62}$$

Here, N is the set dimension, R_i and r_i are respectively the measured and theoretically obtained RSSI value. The indicated deviations have been computed as deviations between the measured RSSI values and the corresponding points on the above-mentioned straight line.

In Figures 8.14(a–d) we present results of the comparison between the measurement results obtained in Kingston and the theoretical prediction results obtained according to the parametric model with the same uniform (with $n = 1$) distribution of buildings' height. After selection, the measurement results have been divided into two groups relating to the availability of the LOS for the chosen FAU location. The results for LOS conditions have been shown with theoretical results in Figures 8.14(a,b) according to the single- and double-scattering parametric models taking diffraction into account, respectively. The NLOS results are presented in Figures 8.14(c,d). In Figure 8.14(c) these results are compared with the predicted ones according to the MSS and in Figure 8.14(d), they are compared with the prediction of the MDS.

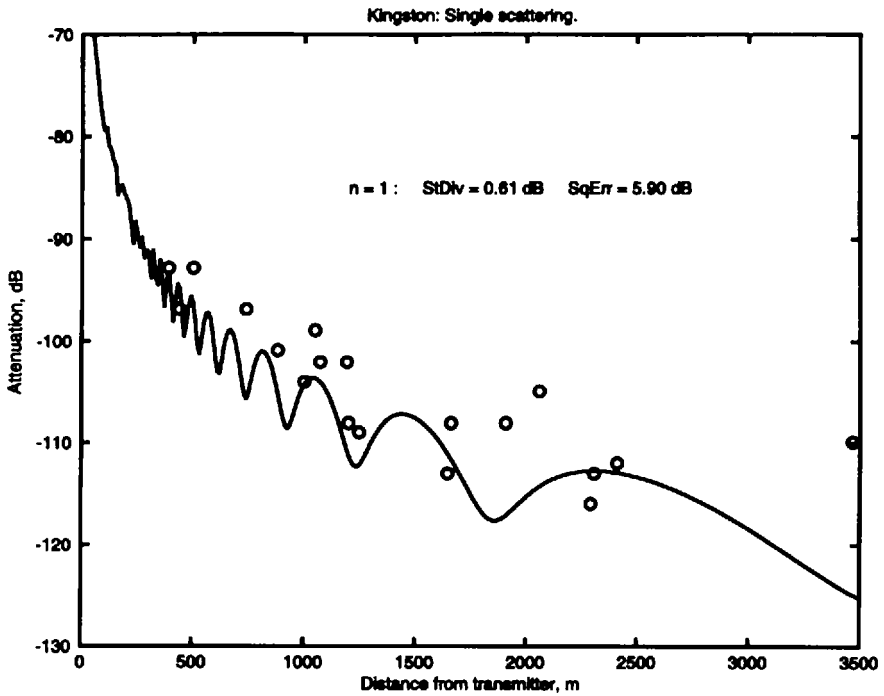

Figure 8.14 (a) The same, as in Figure 8.13(a), but obtained for the LOS conditions in the Kingston area by use of single-scattering model. (b) The same, as in Figure 8.14(a), but obtained for the LOS conditions by use of double-scattering model. (c) The same, as in Figure 8.14(a), but obtained for the NLOS conditions in the Kingston area. (d) The same, as in Figure 8.14(b), but obtained for the NLOS conditions.

The results presented in Figures 8.13 and 8.14 show that in small urban and rural environments the proposed parametric model gives a good explanation of the signal intensity decay both in LOS conditions, by use of the single-scattering model with diffraction, and in NLOS conditions by use of the double-scattering model with diffraction.

A greater challenge than in the previous cases was to apply the above assumption of quasi-smooth built-up terrain with $n = 1$ to the Jerusalem conditions. The major problem is the nonflat terrain profile of Jerusalem and the existence of substantial height differences between relatively close points in the area. In this situation, in the urban scene the accuracy of the theoretical prediction is reduced. Additionally, the complex terrain can affect the distance of direct visibility and this influence, that is the diffraction phenomena, has to be taken into consideration. To overcome these difficulties, we took into

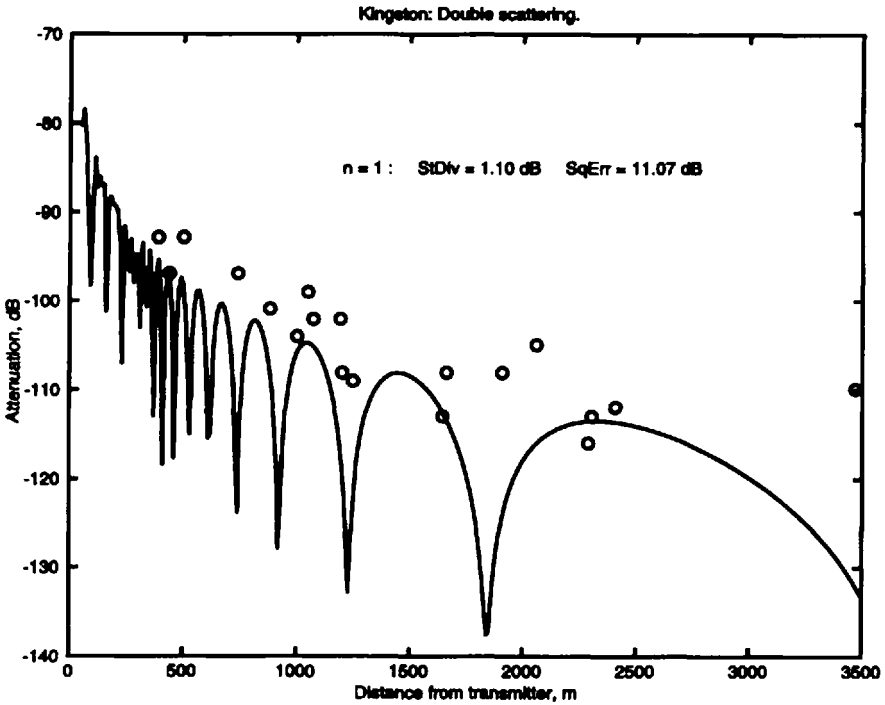

Figure 8.14 (b) (continued).

account the ground height for determining the actual FAU height as a function of its location. We added the ground heights to the building heights as well and then determined the average building height. Moreover, we obtained from the topographic map that we can approximate the built-up layer profile by the polynomial functions (8.60) with the parameter n that lies from 4 to 6. From the topographic map of Jerusalem, we obtained the following parameters of the built-up terrain: the building density is $\nu = 1039\ \text{km}^{-2}$, the average building length is $\overline{L} = 18\text{m}$, and the average building height (not including the local ground height) is $h = 8.3\text{m}$. All the local ground heights were determined by using the GPS system. The measurements were made at 930 MHz bandwidth using the transmitting antenna with a height $z_2 = 42\text{m}$. The results are presented in Figures 8.15(a,b). In Figure 8.15(a) the measurement results are compared with the single-scattering model with diffraction according to formulas (8.58b) and (8.57). In Figure 8.15(b) we show the prediction according to the double-scattering model, taking into account diffraction from the buildings' roofs according to formulas (8.59) and (8.57). Results of calculations presented both for $n = 1$ (uniform terrain) and $n = 5$ (nonuniform terrain).

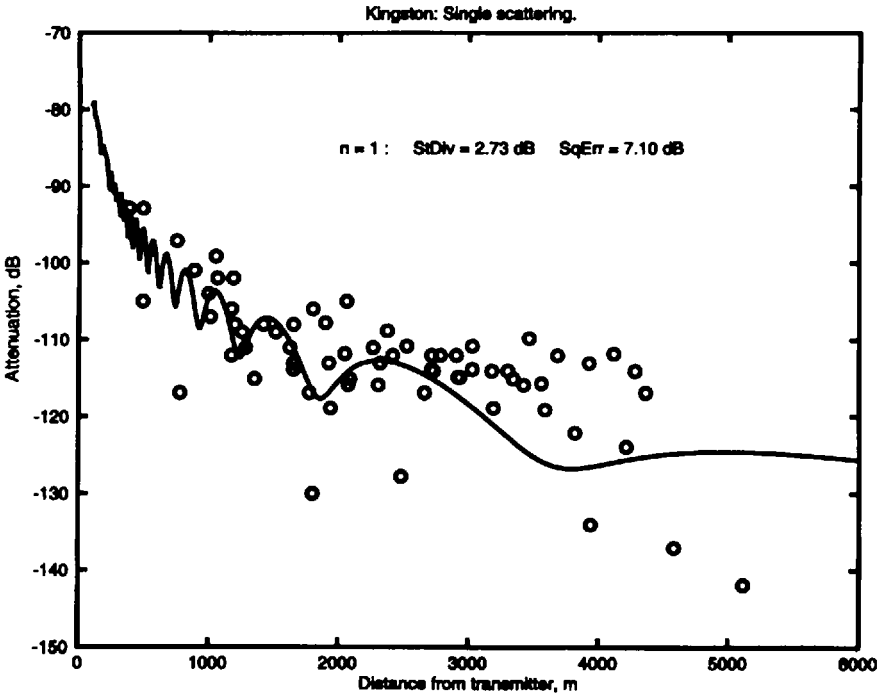

Figure 8.14 (c) (continued).

As follows from presented illustrations, the poor convergence between the theoretical prediction and experimental data in the last case that was obtained in Holon and Kingston, can be improved at least on 3–7 dB by taking into account the real built-up layer relief. In any case the proposed parametric model still gives more accurate predictions than the Hata small-medium model [15]. The comparison between experimental results obtained in Jerusalem and the calculations according to the Hata small-medium model is presented in Figure 8.16. In this case, the value of the standard deviation is about twice as large as that obtained by using the parametric model. Additionally, we have to note that one of the substantial advantages of the presented method is its relative simplicity and that it does not need to be calibrated.

Summary

In this chapter we presented the three-dimensional model of wave scattering and diffraction from randomly distributed buildings and other kind of obstacles placed in rough terrain. Using such a model we can accurately predict the loss

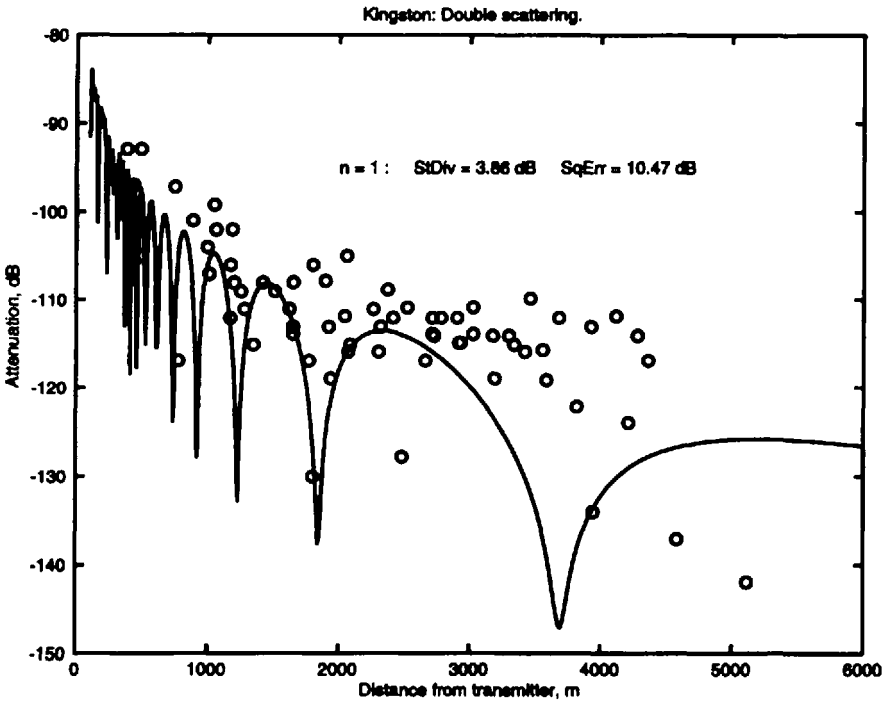

Figure 8.14 (d) (continued).

of characteristics in built-up areas for various kinds of terrain profile and for different positions of transmitting and receiving antennas with respect to rooftops. Using this multiparametric model and its input parameters, such as the buildings' spatial distribution, their density over the terrain, as well as each building's characteristic dimensions and reflection properties, one can describe the coverage effects and construct a "radio map" of the built-up area under consideration.

Furthermore, as shown in Chapter 9, this probabilistic approach allows us to obtain the characteristic scale of cellular maps of built-up areas for various situations of receiver and transmitter (stationary or moving, higher or lower with respect to building heights) in the urban scene.

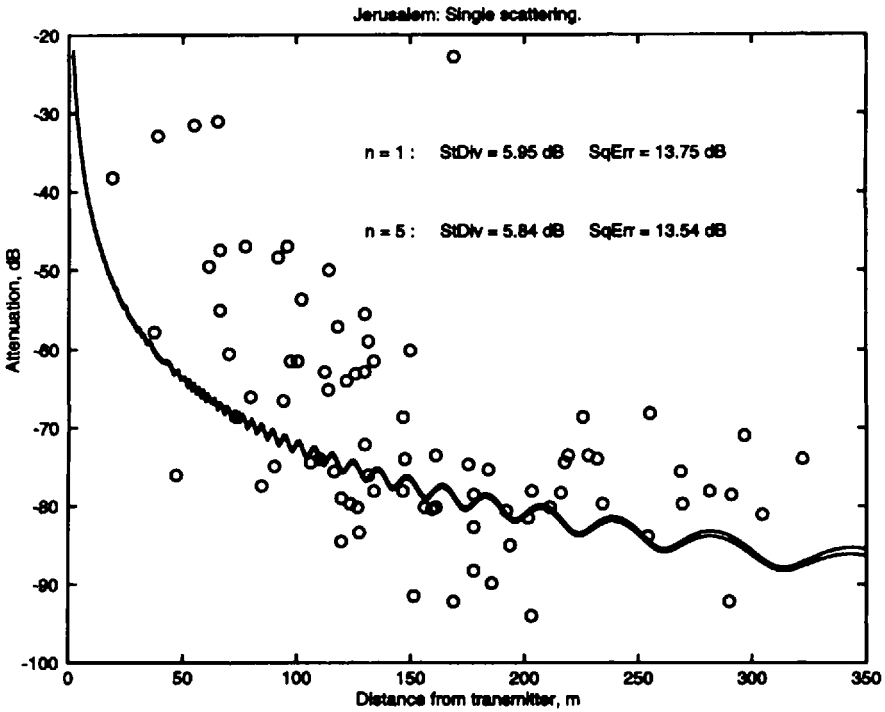

Figure 8.15 (a) The same, as in Figure 8.14(c), but obtained for the Jerusalem area by use of single-scattering model. (b) The same, as in Figure 8.14(d), but obtained for the Jerusalem area by use of double-scattering model.

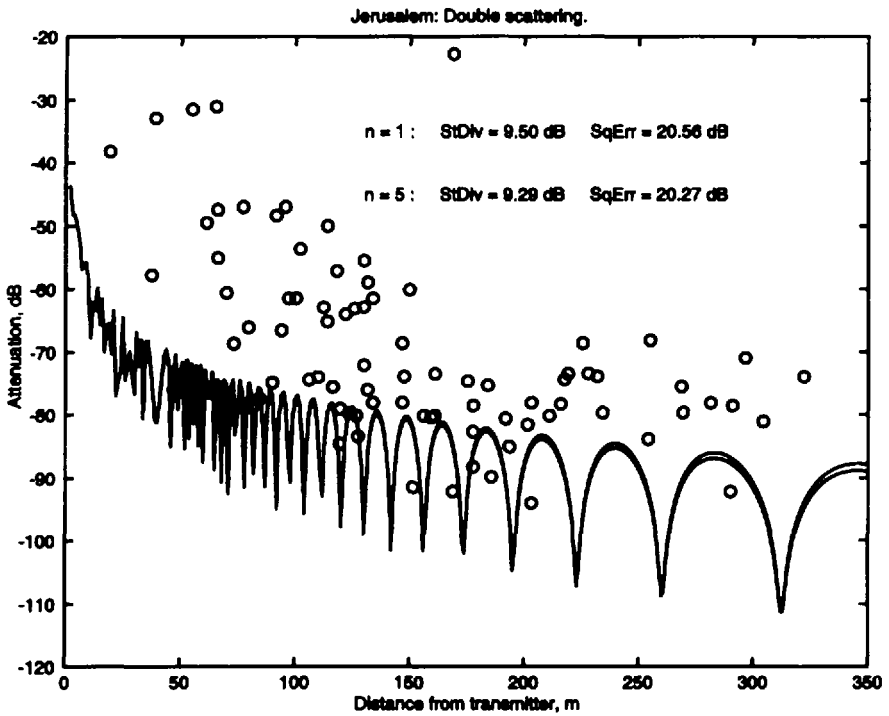

Figure 8.15 (b) (continued).

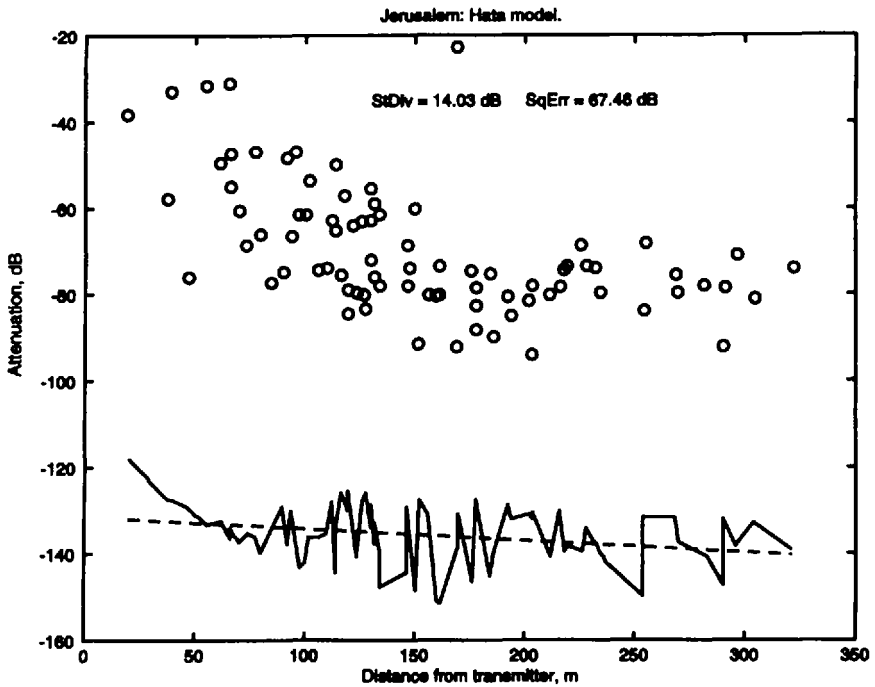

Figure 8.16 The same, as in Figure 8.15(a) but obtained by use of Hata model.

References

[1] Ponomarev, G. A., A. N. Kulikov, and E. D. Telpukhovsky, *Propagation of Ultra-Short Waves in Urban Environments*, Tomsk, USSR: Rasko, 1991.

[2] Blaunstein, N., and M. Levin, "Parametric model of UHF/L-wave propagation in city with randomly distributed buildings," *Proc. of IEEE Antennas and Propagation Society Int. Symp.*, Atlanta, Georgia, June 21–26, 1998, Vol. 3, pp. 1684–1687.

[3] Blaunstein, N., et al., "Prediction of loss characteristics in urban environments with non-regularly distributed buildings placed at the rough terrain," *Proc. of International URSI/IEEE Conference*, Athens, Greece, May 14–18, 1998, pp. 121–124.

[4] Ikegami, F., et al., "Propagation factors controlling mean field strenth on urban streets," *IEEE Trans. Anten. Propagat.*, Vol. 32, No. 8, 1984, pp. 822–831.

[5] Ikegami, F., and S. Yoshida, "Analysis of multipath propagation structure in urban mobile radio environments," *IEEE Trans. Anten. Propagat.*, Vol. 28, No. 4, 1980, pp. 531–537.

[6] Delisle, G. Y., et al., "Propagation loss prediction: a comparative study with application to the mobile radio channel," *IEEE Trans. Vehicular Technol.*, Vol. 34, No. 1, 1985, pp. 85–96.

[7] Ibrahim, M. F., and J. D. Parsons, "Signal strength prediction in built-up areas. Part 1: median signal strength," *IEE Proc.*, Vol. 130, Part F, 1983, pp. 377–384.

[8] Hughes, K. A., "Mobile propagation in London at 936 MHz," *Electron. Letters*, Vol. 18, No. 3, 1982, pp. 141–143.

[9] Atefi, A., and J. D. Parsons, "Urban radio propagation in mobile radio frequency bands," *Comms 86 IEE Conference Publication*, Birmingham, AL, No. 262, 1986, pp. 13–18.

[10] Rana, D., A. R. Webster, and M. Sylvain, "Surface reflection at low-angle propagation," *IEEE Trans. Anten. Propagat.*, Vol. 43, No. 7, 1995, pp. 639–652.

[11] Allsebrook, K., and J. D. Parsons, "Mobile radio propagation in British cities at frequencies in the VHF and UHF bands," *IEEE Proc.*, Vol. 124, No. 1, 1977, pp. 95–102.

[12] Suzuki, H. A., "Statistical model for urban radio propagation," *IEEE Trans. Communic.*, Vol. 25, No. 7, 1977, pp. 673–680.

[13] Reudink, D. O., "Properties of mobile radio propagation above 400 MHz," *IEEE Trans. Vehicular Technol.*, Vol. 23, No. 1, 1974, pp. 143–160.

[14] Sato, K., T. Manabe, J. Polivka, T. Ihara, Y. Kasashima, and K. Yamaki, "Measurement of the complex refractive index of concrete at 57.5 GHz," *IEEE Trans. Anten. Propagat.*, Vol. 44, No. 1, 1996, pp. 35–39.

[15] Parsons, J. D., *The Mobile Radio Propagation Channel*, New York: Halsted Press, 1992.

[16] Lin, S. H., "Statistical behaviour of a fading signal," *Bell Syst. Tech. J.*, Vol. 50, No. 10, 1971, pp. 3211–3270.

[17] Gans, M. J., "A power-spectral theory of propagation in the mobile-radio environment," *IEEE Trans. Vehicular Technol*, Vol. 21, No. 1, 1972, pp. 27–38.

[18] Kozono, Sh., and K. Watanabe, "Influence of environmental buildings on UHF land mobile radio propagation," *IEEE Trans. Communic.*, Vol. 25, No. 10, 1977, pp. 1133–1143.

[19] Cox, D. C., "Multipath delay spread and path loss correlation for 910-MHz urban mobile radio propagation," *IEEE Trans. Vehicular Technol.*, Vol. 26, No. 4, 1977, pp. 340–344.

[20] Black, D. M., and D. O. Reudink, "Some characteristics of mobile radio propagation at 836 MHz in the Philadelphia area," *IEEE Trans. Vehicular Technol*, Vol. 21, No. 2, 1972, pp. 45–51.

[21] Reudink, D. O., "Comparison of radio transmission at X-band frequencies in suburban and urban areas," *IEEE Trans. Anten. Propagat.*, Vol. 20, No. 4, 1972, pp. 470–473.

[22] Turin, G. L., et al., "A statistical model of urban multipath propagation," *IEEE Trans. Vehicular Technol.*, Vol. 21, No. 1, 1972, pp. 1–9.

[23] Krishen, K., "Scattering of electromagnetic waves from a layer with rough front and plane back (small perturbation method by Rice)," *IEEE Trans. Anten. Propagat.*, Vol. 19, No. 3, 1970, pp. 573–576.

[24] Cox, D. C., and R. P. Leck, "Distributions of multipath delay spread and average excees delay for 910-MHz urban mobile radio paths," *IEEE Trans. Anten. Propagat.*, Vol. 23, No. 2, 1975, pp. 206–213.

[25] Cox, D. C., "910 MHz urban mobile radio propagation: multipath characteristics in New York City," *IEEE Trans. Communic.*, Vol. 21, No. 10, 1973, pp. 1188–1194.

[26] Zander, J., "A stochastic model of the urban UHF radio channel," *IEEE Trans. Vehicular Technol.*, Vol. 30, No. 1, 1981, pp. 145–155.

[27] Bass, F. G., and I. M. Fuks, *Wave Scattering from Statistically Rough Surfaces*, Oxford: Pergamon Press, 1979.

[28] Ishimaru, A., *Electromagnetic Wave Propagation, Radiation, and Scattering*, Englewood Cliffs, NJ: Prentice-Hall, 1991.

[29] Charnotskii, M. I., and V. I. Tatarskii, "Tilt-invariant theory of rough-surface scattering: I," *Waves in Random Media*, Vol. 5, No. 4, 1995, pp. 361–380.

[30] Tatarskii, V. I., and M. I. Charnotskii, "On the universal behaviour of scattering from a rough surface from small grazing angles," *IEEE Trans. Anten. Propagat.*, Vol. 46, No.1, 1995, pp. 67–72.

[31] Al'pert, Ya. L., V. L. Ginsburg, and E. L. Feinberg, *Radiowave Propagation*, Moscow: State Printing House for Technical-Theoretical Literature, 1953.

[32] Voronovich, A. G., *Wave Scattering from Rough Surfaces*. Berlin, Germany: Springer-Verlag, 1994.

[33] Shwartz, L., *Mathematical Methods for the Physical Sciences*, New York, 1963.

[34] Balanis, C. A., *Antenna Theory: Analysis and Design*, New York: John Wiley & Sons, 1982.

This page intentionally left blank

IV

Propagation Aspects of Cell Planning

This page intentionally left blank

9

Cellular Systems Concept

Usually, in the literature for designing wireless systems, the *cellular concept* of wireless communication in built-up areas is introduced [1–9], which allows the designers of such systems to assume decreased natural background noises within the propagation channels, and to exclude deep interference phenomena from affecting the signal at the input of receiver.

These phenomena are mostly manifested for moving subscribers, that is, for mobile communication systems, so the cellular concept is presented here mostly for the purposes of mobile communications. Let us ask a question: What is the cellular principle and how may we construct each cell in a completed cellular system?

The simplest *radio cell* one can construct uses a base station (radio port) at the center of a cell and predicts the coverage area from this station's antenna. This coverage area is defined by the range where a stable signal from this station can be received. Figure 9.1 illustrates the distribution of such cells. As seen, there exist regions of overlap with neighboring radio cells, where stable reception from neighboring base stations can be obtained. From this scheme it also follows that different frequencies should be used in these cells which surround the tested central cell. On the other hand, the same frequencies can be used for the cells farthest from the central one. This is the *cells repeating* or *reuse of operating frequencies* principle. At the same time, the reuse of the same radio channels and frequencies within the neighboring cells is limited by preplanned *cochannel interference.* Moreover, in the process of cellular systems design in various built-up areas, it is important to predict the influence of propagation phenomena within the corresponding communication channels on variations of the main parameters of the cellular system, and on the construction and splitting of cellular maps. All these questions will be discussed below.

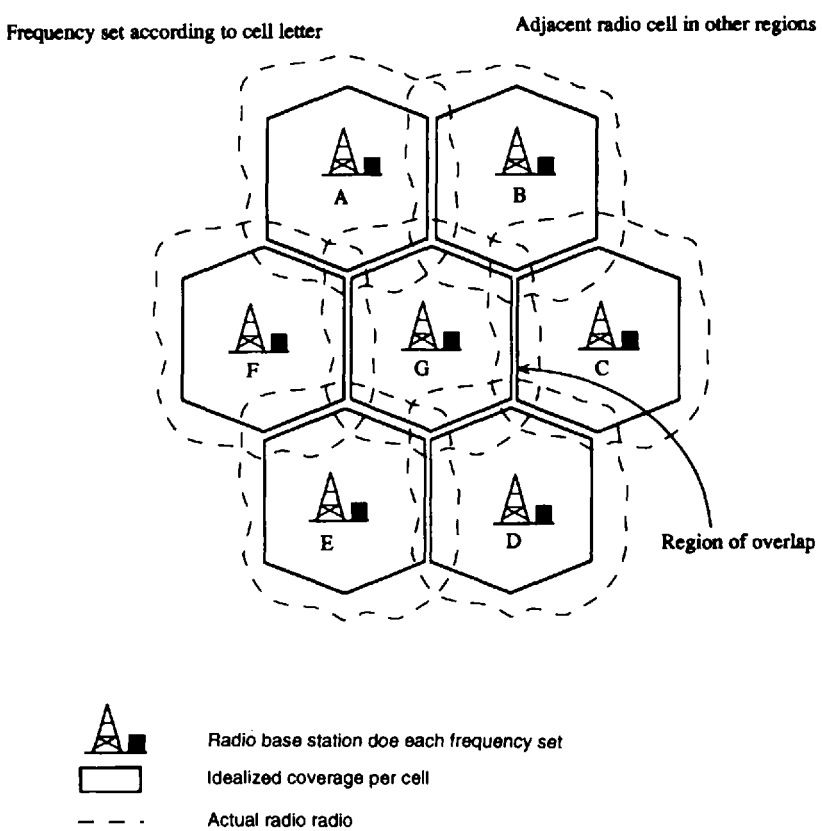

Figure 9.1 The concept of cell distribution and cellular map pattern.

9.1 Main Characteristics of a Cell

Now we will describe the main characteristics of a *cell.* The real distance from the center of a cell, where the base station is located (*based cell*), to the center of the *repeat cell* (which is denoted in Figure 9.6 (see below) by the same letter) is called the *reuse distance, D.* The cell size is determined by its *radius, R.* Relationships between these main parameters will be presented later.

Now let us consider the radio coverage of a single cell, which is presented in Figure 9.2 according to [5]. Here, the base station antenna radiates a power P_T; the antenna gain is G_T. Together they can give a sufficient transmitted power, for example, in excess of 10W. A sensitive low-noise receiver, a portable transmitter, and an elementary antenna (for example, a telephone antenna), are assembled within the car, as in Figure 9.2. Because the signal decay is stronger when increasing the range between the base station and a car, it is

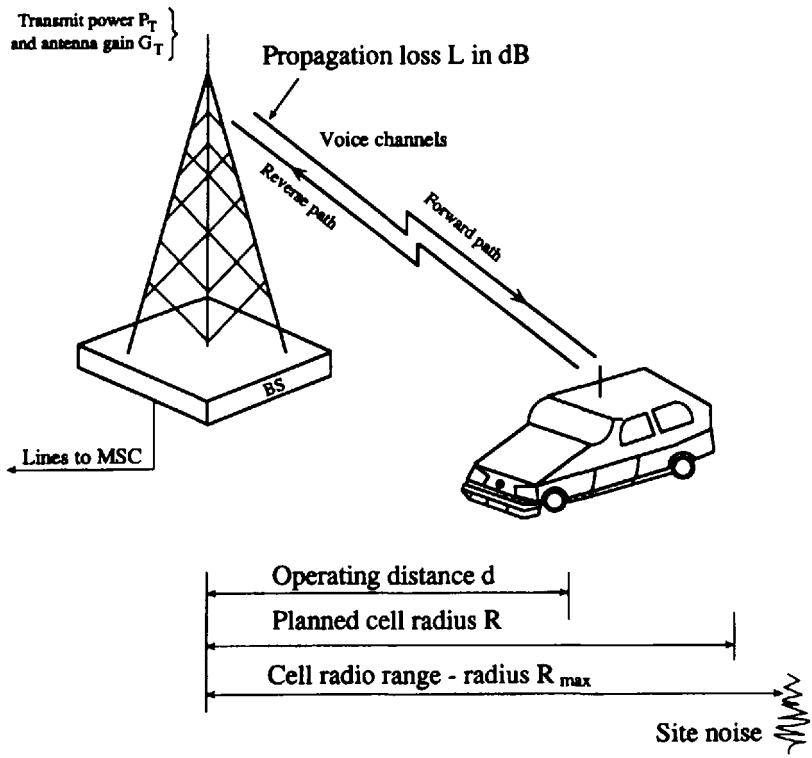

Figure 9.2 The fundamental radio cell and associated parameters.

important to obtain the law of signal decay versus this range. Using this law of signal attenuation, one can evaluate the range of stable reception of signals from both sources. Hence, to characterize the single cell, one can use the following characteristics (as presented in Figure 9.2):

- operating range, d;
- maximal radio range, that is, the cell size limited by noise, by propagation factor of wave field decay within the cell, by transmitter power, and so on, R_{max};
- planned size of the cell, R, which is less than R_{max} and depends on the conditions of cell design, its radio coverage by the base station antenna, etc.

For a flat terrain, R can be defined as the radius of a circle surrounding the base station on the topographical map of a selected area. The area that is

covered by the base-station antenna is approximately $\sim \pi R^2$ (in km^2). For example, if the radius is $R = 2$ km, the single cell coverage area is $S = 6.28$ km^2, which provides a service to about 200 subscribers of a wireless personal communication channel [5]. For $R = 20$ km, then $S = 628$ km^2 and the number of subscribers grows to 20,000. But to service 120,000 subscribers, the cell should be designed with a radius of $R = 25$ km, and an area $S = 1{,}960$ km^2 [5].

As follows from the above estimations, to use only a single cell for stable wireless communication in urban conditions with their complicated multipath propagation phenomena (caused by the multireflections, multidiffraction, multiscattering, etc.), is in practice quite unrealistic.

9.2 Cells' Design Strategy

The concept of cellular wireless communication has been introduced with numerous cells of a small radius, which provide a sufficient signal-to-noise ratio and a low level of interference with received signals within the communication channel. As an example, a characteristic cell-layout plan for London, UK, is presented in Figure 9.3 according to [5], at an early stage of its implementation. As follows from this figure, the early strategy of cell communications design is based on the following principles:

- With an increase of the number of subscribers, the dimensions of the cells become smaller (usually this was done for centers of cities, where the number of cars is larger and building density is higher).
- Cells are arranged in *clusters*. Only clusters with a hexagonal shape are possible. The designed cluster sizes of 4, 7, and 12 cells are shown in Figure 9.3.
- Cells are split. The installation of additional base stations within each cell depends on the degree of cell density in each cluster and on the coverage effect of each base-station antenna.

The same strategy of cell design has been proposed for use in the European Terrestrial Cellular Telephone System [5], where each base-station antenna, with an effective power of 100 mW, covers a cell with radius $R = 1$ mile (~ 1.6 km). At the same time, to cover the area of one cell with radius $R = 10$ miles (~ 16 km), the transmitting antenna requires a power of 100 W (i.e., 1000 times higher).

Thus, the antenna power problem has been successfully solved by using a cell-splitting strategy. However, the question regarding the regions of overlap of coverage between neighboring cells is not solved yet (as seen from Figure

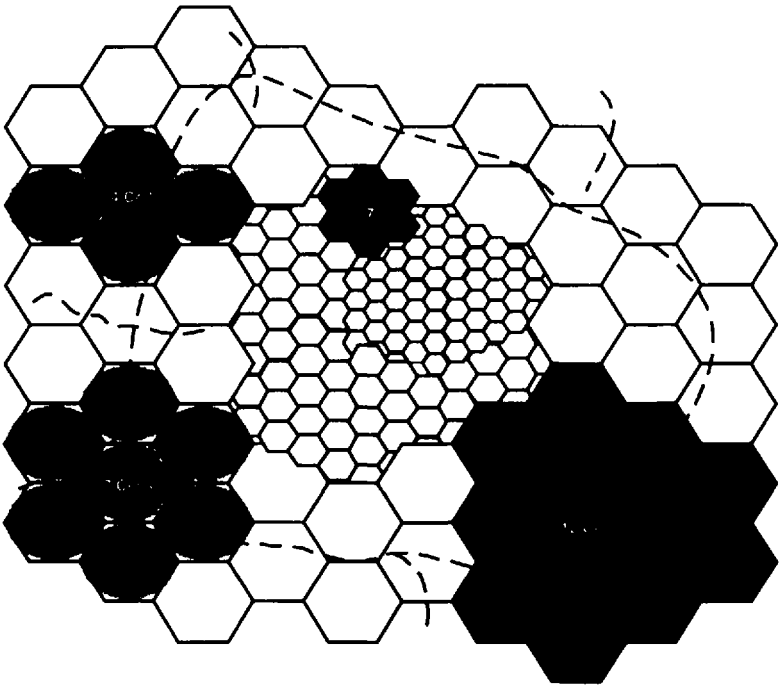

Figure 9.3 A typical city cellular map, where cluster sizes of 4, 7, and 12 are also indicated.

9.1). The circle-shaped cell was therefore replaced by a regular hexagon-shaped cell. As seen in Figure 9.4, where both circle-shaped and regular hexagon-shaped cells are presented, the hexagon-shaped cell is more geometrically attractive than the circle-shaped cell.

Moreover, in the hexagon-shaped multiple cells structure (plan), the hexagonal cells are closely covered by each other. Thus, each hexagonal cell can be packed into clusters "side-to-side" with neighboring cells. The size of such hexagonal cell can be defined by using its radius R and a 120-degree angle (see Figure 9.4).

The cluster size is designated by the letter N and is determined by the equation [2–5]:

$$N = i^2 + ij + j^2 \tag{9.1}$$

where $i, j = 0, 1, 2, \ldots,$ etc.

As follows from (9.1), only the cluster sizes 3, 4, 7, 9, 12, etc., are possible. However, each cluster can be divided into three clusters, each consisting

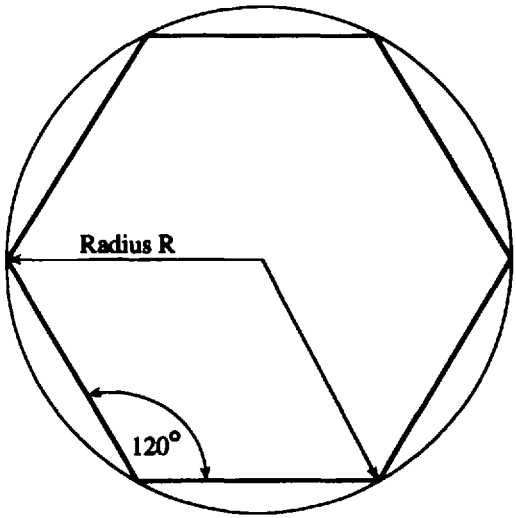

Figure 9.4 Circle-shaped and regular hexagon-shaped cells presentation.

of three cells. It is called a 3/9-cell cluster (see Figure 9.5). Other variants of sectored clusters are presented in Figure 9.5. Each sector has one base-station antenna (or radio port).

One can ask the reasonable question: Why is it necessary to divide clusters into subclusters? It is necessary to use the same repeating frequencies in different cells. Therefore, earlier concepts of *reuse distance, D,* and *reuse frequencies* were introduced. How can one use these concepts? If we focus on the popular 7-cell cluster arrangement, which is depicted in Figure 9.6, we first notice that the allocation of frequencies into seven sets is required. In Figure 9.6, the mean reuse distance is explained, in which the cells (say, denoted by $G \leftrightarrow G$) use the *same frequency set.* This is a simple way to use the repeat frequency set in the other clusters.

Between D and the cell radius R (see Figure 9.7) there exists a relationship which is called the *reuse ratio.* This parameter for a hexagonal cell is a function of cluster size, that is [2–5]

$$\frac{D}{R} = \sqrt{3N} \tag{9.2}$$

Thus for a 7-cell cluster of 2-mile-radius cells, the repeat cell centers which operate with the same frequency set would be separated by:

$$D = R\sqrt{3N} = 2\sqrt{21} \approx 9.2 \text{ miles} \tag{9.3}$$

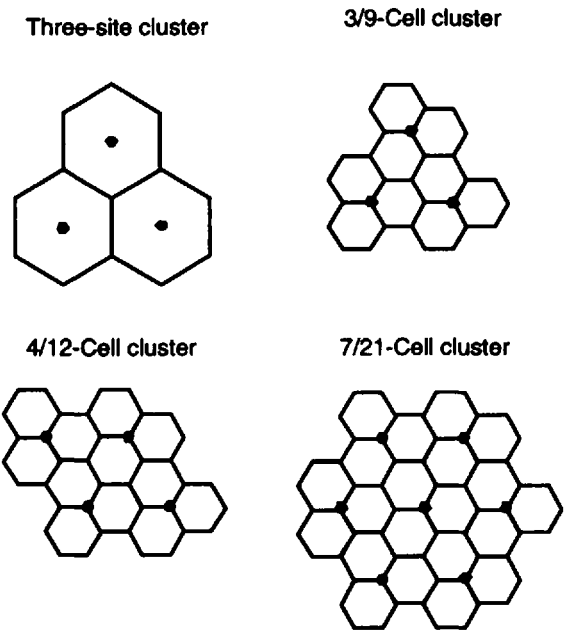

Figure 9.5 Different variants of sectored clusters.

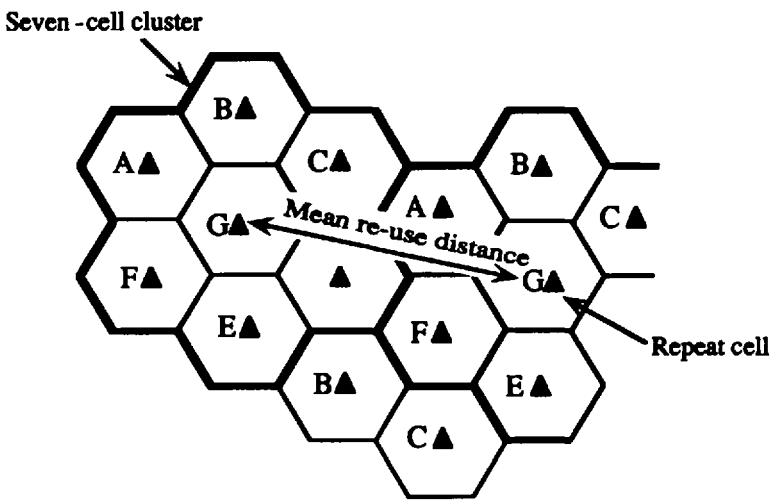

Figure 9.6 The popular seven-cell cluster arrangement: *D* is the reuse distance, *R* is the radius of cell.

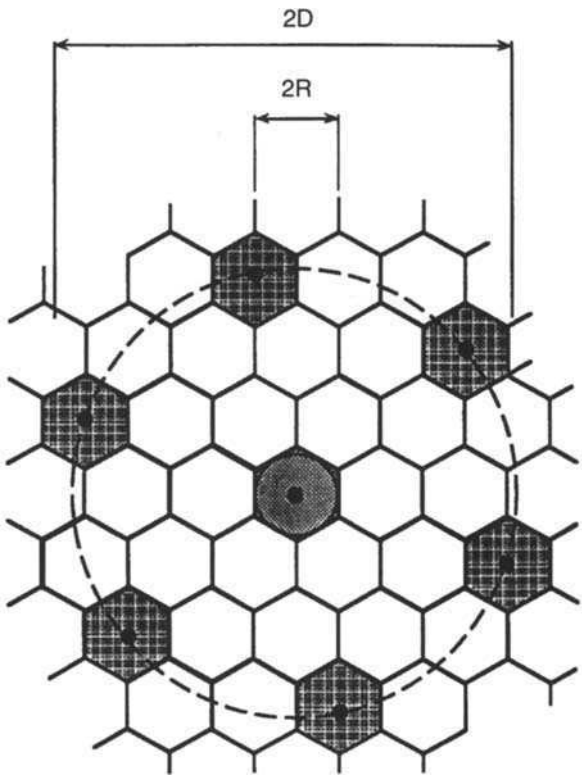

Figure 9.7 Directional frequency reuse plan.

Within other cells in a cluster, interference inside the communication channel can be expected at the same frequencies. Hence, for a seven-cell cluster there could be up to six immediate interferers, as it is shown in Figure 9.7.

Now we will discuss the question of how to predict the optimal cell size and the cluster splitting using the law of signal decay, described by many independent models constructed to predict the propagation phenomena within various wireless communication channels. Let us start with the description of special parameters characterizing the concrete situation in cellular environments.

While passing from cell to cell, the subscriber in the moving vehicle can be interrupted while talking to any other subscriber (stationary or moving). Because this is caused by a large signal attenuation due to obstructions surrounding them, the *hand-off* parameter is usually introduced. Hand-off is a process that allows a cellular mobile vehicle to move from cell to cell without service interruptions (Figure 9.8). Once the hand-off is complete, a ping-pong effect is unlikely, since the difference in the receiving signal level (RSL) between the old and the new cell increases rapidly. This will also reduce hand-off requests, thus enhancing the capacity.

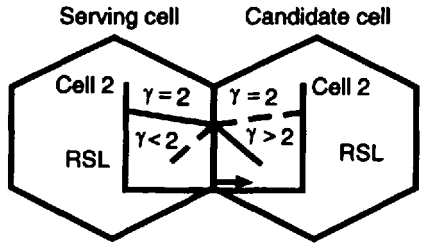

Figure 9.8 LOS hand-off scenario.

Now we will consider another major problem of moving subscriber servicing using the cellular concept which is connected with cochannel interference caused by frequent reuse of channels within the cellular communication system. To illustrate the concept of cochannel interference, let us consider a pair of cells with radius R, separated by a reuse distance D, as shown in Figure 9.9. Since the cochannel site is located far from the transmitter ($D >> R$), which is located within the initial cell, its signal at the servicing site will suffer multipath attenuation. We consider here the situation in the urban scene where both antennas are lower than the surrounding buildings' rooftops.

To predict the degree of cochannel interference in such a situation with moving subscribers within the cellular system, a new parameter, *carrier-to-interference ratio, C/I*, is introduced in the literature [5–9]. This parameter in turn depends on frequency planning and antenna engineering. As pointed out in [9], a cochannel interferer has the same nominal frequency as the desired frequency. It arises from multiple use of the same frequency. Thus, referring to the part of cellular map depicted in Figure 9.10, we find that cochannel sites are located in the second cluster. For omnidirectional antennas located inside each site, the theoretical cochannel interference in dB is given by [9]:

$$\frac{C}{I} = 10 \log\left[\frac{1}{j}\left(\frac{D}{R}\right)^{\gamma}\right] \tag{9.4}$$

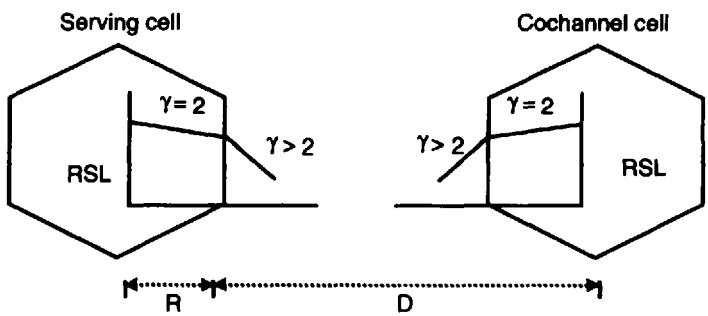

Figure 9.9 LOS cochannel interference.

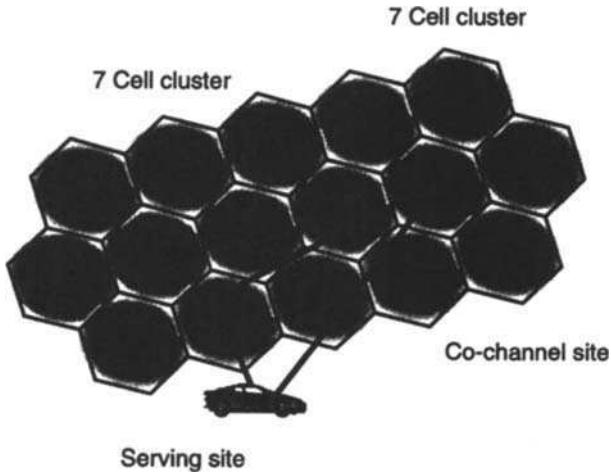

Figure 9.10 Cochannel interference evaluation scheme.

where j is the number of cochannel interferers ($j = 1, 2, \ldots, 6$), and γ is the path-loss slope constant, which determines the signal decay in various propagation environments. For a typical seven-cell cluster ($N = 7$) with one cell as basic (with the transmitter inside it) and with six other interferers ($j = 6$) as the cochannel sites, this parameter depends on conditions of wave propagation within the urban communication channel. To understand this fact, let us present, according to [5], a simple propagation model for the regular urban environment with $\gamma = 4$ (see Chapters 5 and 6). In this case one can rewrite (9.4) as:

$$\frac{C}{I} = 10 \log\left[\frac{1}{6}\left(\frac{D}{R}\right)^4\right] \tag{9.5}$$

Then, according to (9.2), $D/R = \sqrt{3N} = 4.58$, and $C/I = 18.6$ dB. In the general case, by introducing (9.2) in (9.5) we have that

$$\frac{C}{I} = 10 \log\left[\frac{1}{6}(3 \cdot N)^2\right] = 10 \log(1.5 \cdot N^2) \tag{9.6}$$

The carrier-to-interference ratio is also a function of cluster size N and is increased with the increase of cell numbers in each cluster; or with the decrease of cell radius R. Let us now introduce the important cellular parameters and present them in Table 9.1.

Table 9.1
Cellular Parameters

Cluster Size (N)	(a) (D/R)	(b) ($279/N$)	(c) ($C_i = C/I$), dB	(d) ($\tilde{N}$)
3	3.0	93	11	2583
4	3.5	69	14	1840
7	4.6	39	18	937
9	5.2	31	21	707
12	6.0	23	23	483
21	7.9	14	28	245

In column (a) the reuse ratio D/R is presented; number of channels per cell is presented in column (b). The data presented in column (c) is obtained by use of the standard presentation of formula (9.6), that is, $C_i = C/I = 1.5 \cdot N^2$. To obtain the number of subscribers in the urban area considered, described by column (d) in Table 9.1, we need additional information about the urban area and additional formulations, such as:

- the urban area of operation and servicing - A, km^2;
- the number of citizens in the operating urban area - P (per thousands);
- the mean radius of the cell - R, km;
- the number of channels in one cell - n_c.

Thus, in Figure 9.11, the dependence of n_c versus cells' number N for various C/I-ratios is shown. If, for example, 30 subscribers use the same channel in the considered cell, then the number of subscribers in this cell equals

$$\tilde{n} = 30 \cdot n_c \approx 10 \cdot \pi \cdot n_c \tag{9.7}$$

For regularly distributed cells over the built-up terrain, the number of cells in the urban area concerned equals

$$K = \frac{A}{\pi R^2} \tag{9.8}$$

Then the total number of subscribers in the urban area considered equals:

$$\tilde{N} = \tilde{n} \cdot K = \frac{10 \cdot n_c \cdot A}{R^2} \tag{9.9}$$

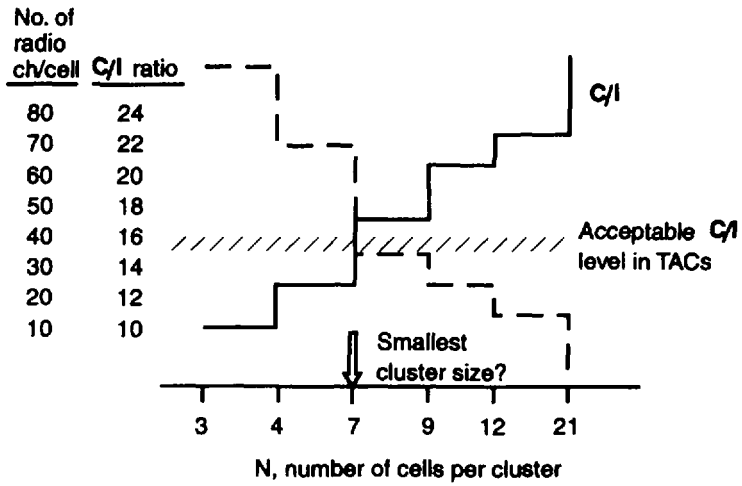

Figure 9.11 Number of channels per cell n_c versus cells number N for various C/I-ratios.

The parameter $\tilde{N}$ calculated by use of this formula is presented in column (d) in Table 9.1. From (9.9) we can estimate as a percentage the number of subscribers from the population located in the urban area. Thus,

$$\tilde{N}(\%) = \frac{10 \cdot n_c \cdot A}{R^2 \cdot P \cdot 1000} \cdot 100\% = \frac{A \cdot n_c}{P \cdot R^2}(\%) \qquad (9.10)$$

Example: Number of city citizens is 600,000 located within an area with a radius of R_a = 8 km. The cell size is R = 2 km, the number of channels in each cell is n_c = 40. We need to determine the number of subscribers (in percentage) for effective servicing by a wireless communication system.

Solution:

First step: We calculate a city area: $A = \rho R_a^2 \approx 200$ km^2.

Second step: We calculate the number of citizens per thousands:

$$P = \frac{600{,}000}{1{,}000} = 600.$$

Third step: We calculate using (9.10), that: $\tilde{N}(\%) = \frac{200 \cdot 40}{600 \cdot 4} \approx 3.3\%$.

The result of this example shows that for cities with a high-density population (A/P is small), it is very hard to plan the wireless service by use of a simple propagation model. If we try to increase (up to the maximum) the number of channels by splitting the operating radio-frequency band, the cell size (radius R) remains critically limited by the conditions of radio wave propagation in the urban area. Moreover, as follows from (9.4) to (9.6), the

law of signal decay (determined by parameter j) affects cochannel interference parameter C/I. This question is discussed in detail later. Now we will note that Formula (9.10) can be rewritten by introducing into it new parameters as the frequency band of the total cellular service system, ΔF, and the frequency band of each channel, Δf_c. In this case the number of radio channels in each cell equals

$$n_c = \frac{\Delta F}{\Delta f_c \cdot N} \tag{9.11}$$

Then the number of subscribers which can effectively communicate by using the existing cellular servicing system equals, as a percentage,

$$\tilde{N}(\%) = \frac{A \cdot \Delta F}{\Delta f_c \cdot P \cdot N \cdot R^2} \tag{9.12}$$

Formulas (9.10) and (9.12) show that to increase the efficiency of the cellular communication system in various urban environments, an effective frequency splitting strategy over the channels within each cell is required. Moreover, by decreasing the cell size and the cluster size (or number N) one can also increase the efficiency of the cellular system. The latter depends on the strategy of cellular map construction and splitting. We show how to do this below.

The experience of cellular systems designers shows that it is very dificult to decrease the number N of cells in each cluster (see Figure 9.11). Apparently, as follows from this picture, number $N = 7$ is the smallest size of cluster constructed, because for $N < 7$ the acceptable C/I level of 16 dB cannot be reached. Initially the parameter N was selected as $N = 12$ by the TACS cellular system constructed in England. However, while analyzing the C/I-ratio and its optimization, the optimal number $N = 7$ was found. In fact, as follows from Figure 9.11, for 300-working radio channels with 21 channels required to control the total cellular system, we obtain for $N = 7$ and $N = 12$, respectively, $n_c = 39$ and $n_c = 23$ communication channels in each cell. This result follows from Table 9.1 and Figure 9.11, where value 23 from first column in the table lies between 20 and 30 (the level corresponding to $N = 12$) and value 39 from this column lies between 30 and 40 (the level corresponding to $N = 7$).

9.3 The Method of Cellular Map Construction

As mentioned above, the strategy of topographical maps splitting at cells, the cellular maps' construction, and the cellular characteristics optimization (namely, improving the clearance between subscribers within the cell, increasing cochannel interference parameter C/I, etc.) is based on knowlege of propagation phenomena inside the cellular communication channels. More strictly, it is based on the law of signal-power decay for the concrete situation in the urban scene.

First we will discuss the question of clearance between arbitrary subscribers within the cell and introduce the recipe for predicting the cell radius (size) for the concrete propagation situation.

The recipe of topographical map splitting at cells. As follows from all the previous chapters, a better clearance between two arbitrary subscribers in clutter conditions may be reached in LOS conditions (or direct visibility between them). In this case, as follows from the two-ray model (see Chapter 3) and the waveguide-street model (Chapter 5), that cell size, R, cannot be larger than the break-point range, r_B. If so, the law of signal-power decay within each cell with radius $R \leq r_B$ is $\sim R^{-2}$. Beyond the break point the law of signal decay, described by path-loss slope parameter γ, depends on the concrete situation in the urban scene, and $\sim R^{-4}$ for propagation in open built-up areas (see Chapters 3, 4) or $\sim R^{-5-7}$ (i.e., close to exponential decay), observed in LOS conditions along straight streets (see Chapter 5). This situation regarding signal-decay law is shown in Figure 9.12 (top graph).

The wave-propagation phenomena in urban environments with both antennas in NLOS (clutter) conditions were described in Chapters 6 to 8. As follows from models described there, in rural and residental areas with a separated building distribution the path-loss slope parameter γ describing the received signal decay is changed from $\gamma = 2.4$ to $\gamma = 4.8$ (see empirical and deterministic models decribed there). In other words, in such areas field attenuation is faster than that in LOS conditions over flat terrain and in free space. At the same time, as follows from numerical calculations of the multiparametric model described in Chapter 8, for various situations when both antennas are placed in a built-up area with a high density of irregularly distributed buildings, the law of signal power decay is changed with distance d between antennas from $\sim d^{-\gamma}$ ($\gamma = 2$) before the break point r_B (where the coherent part of total field is predominant) to $\sim d^{-\gamma}$ ($\gamma = 3$) beyond the break point r_B (where the incoherent part of total field is predominant). That is why it is logical now to ask the question of how to obtain the cell size R_{cell}, which can be defined by the break point r_B in different propagation situations in built-up areas.

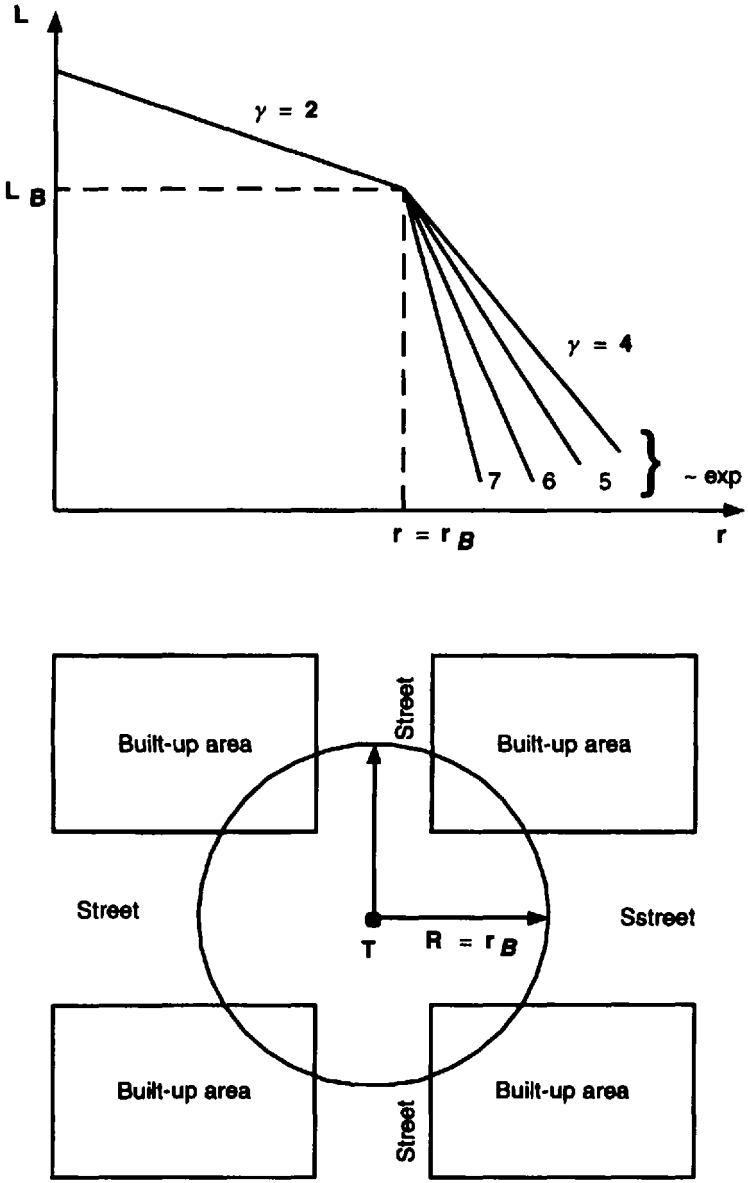

Figure 9.12 A cell in an urban area with grid-plan streets.

A city with regularly planned streets. Let us consider the situation in urban areas with a rectangular grid plan of straight-crossing streets. In this case, as follows from the multislit street waveguide model described in Chapter 5, the cell size can be described by formula (5.65), which we repeat once more as

$$R_{cell} \equiv r_B = \frac{4h_T h_R}{\lambda} \frac{(1+\chi)}{(1-\chi)} \frac{[1 + h_b/a + h_T h_R/a^2]}{[|R_n| + |D_{mn}|]^2} \tag{9.13}$$

where all parameters in (9.13) are described in Chapter 5. As follows from (9.13), using information about street geometry (street width a), height of buildings h_b, and mean gaps between buildings lining the street (i.e., the parameter of brokenness χ), about both antennas' height, h_T and h_R, as well as the building walls' material (which determines the absolute values of reflection coefficient R_n and diffraction coefficient D_{mn}), one can obtain the cell radius along the street in LOS conditions. An example of cell coverage which corresponds to one special case of perfectly conductive walls ($|R_n|$ and $|D_{mn}| \to 1$) and $a > h_T$, h_R, $a \leq h_b$, is shown in Figure 9.12 (bottom graph).

The city with nonregularly planned streets. In the case of built-up areas with nonregularly distributed buildings placed on rough terrain, consisting of hills, trees, and other obstructions located in residental zones, the cell size can be obtained by using the probabilistic approach presented in Chapter 8 according to the multiparametric model.

As follows from this approach, the average distance of the direct visibility $\overline{\rho}$ between two arbitrary points, the source and the observer, is described by formula (8.5) which we will rewrite here in the following form:

$$\overline{\rho} = (\gamma_0 \gamma_{12})^{-1} \text{ (km)} \tag{9.14}$$

where

$$\gamma_{12} = (z_2 - z_1)^{-1} \int_{z_1}^{z_2} [P_b(z)][1 - XP_b(z)]^{-1} dz, \; z_2 > z_1 \tag{9.15}$$

$$\gamma_0 = 2\overline{L}\nu/\pi \tag{9.16}$$

Formula (9.14) is general and describes the situation when the buildings' height is nonuniformly distributed above the terrain profile $z = Z(x, y)$ (see Section 8.1). For uniform distribution of buildings' height, this formula can be simplified as:

$$\overline{\rho} = (\gamma_0)^{-1} = \frac{\pi}{2\overline{L}\nu} \text{ (km)} \tag{9.17}$$

If one now obtains the information about servicing area, that is, the terrain profile, the average buildings' height h and length $\overline{L}$, as well as the density of buildings per square kilometer, it is easy to estimate the cell radius within the tested area by use of formulas (9.14) or (9.17).

Hence, by use of two new models, as the combinations of deterministic and statistical approaches, presented in this book in Chapters 5 and 8, respectively, the reader can easily obtain the optimal cell radius for different built-up areas with various situations of the terminals, transmitter and receiver. A new concept of cellular map constructions based on these two models (and recommended for the reader) is more general than that based on two-ray model and described in [5, 9] both for LOS and NLOS conditions, without any detailization of the terrain profile.

The frequency planning concept. The same detailed frequency planning strategy for cellular systems design, based on the models described in Chapters 5 and 8, can be done to optimize the *cochannel interference parameter* C/I (see Section 9.2).

According to the propagation situation in the urban scene, the servicing and cochannel sites can lie both inside and outside the break-point range r_B. If both of them are within this range, as follows from Figure 9.10, the cochannel interference parameter can be described instead of (9.4) by the C/I-ratio prediction equation (in dB) as

$$\frac{C}{I} = 10 \log\left[\frac{1}{6}\left(\frac{D}{R}\right)^2\right] \tag{9.18}$$

For cell sites located beyond the break-point range, this equation can be modified, taking into account the multipath phenomenon and obstructions which change the signal-decay law from D^{-2} to $D^{-\gamma}$, $\gamma = 2 + \Delta\gamma$, $\Delta\gamma \geq 1$. Hence, we finally have instead of (9.18):

$$\frac{C}{I} = 10 \log\left[\frac{1}{6}\left(\frac{D^{(2+\Delta\gamma)}}{R^2}\right)\right] \tag{9.19}$$

According to the concepts of cellular map construction presented above, the signal strength decay is weaker within each cell (with path-loss slope parameter $\gamma = 2$) and corresponds to that in free space. At the same time, due to obstructions, the signal strength decay is stronger in regions outside the

servicing cell and within the cochannel site (with path-loss slope parameter $\gamma = 2 + \Delta\gamma$, $\Delta\gamma \geq 1$).

We can now rewrite (9.19) versus number of cells in cluster N, and of radius of the individual cell, R, by use of (9.2):

$$\frac{C}{I} = 10 \log\left[\frac{N}{2}(3N)^{\Delta\gamma/2} R^{\Delta\gamma}\right] \tag{9.20}$$

Let us examine this equation for two typical cases described above.

The city with regularly planned streets. In this case for a typical straight, wide avenue, for which according to multislit street waveguide model $\Delta\gamma = 2$ ($\gamma = 4$) (see Chapter 5) and

$$\frac{C}{I} = 10 \log\left[\frac{3}{2}(N)^2 R^2\right] \tag{9.21}$$

For the case of narrow streets (a more realistic case in an urban scene) one can put in (9.20) $\Delta\gamma = 3 - 7$ ($\gamma = 5 - 9$), which is close to the exponential signal decay that follows from the street waveguide model.

The city with nonregularly planned streets. For the case of propagation over irregular built-up terrain, as follows from the probabilistic approach, presented in Chapter 8, $\Delta\gamma = 1$ and the C/I-ratio prediction equation is:

$$\frac{C}{I} = 10 \log\left[\frac{N}{2}(3N)^{1/2} R\right] \tag{9.22}$$

As follows from (9.20) to (9.22), the C/I-ratio strongly depends on conditions of wave propagation within the urban communication channels (on path-loss slope parameter $\gamma = 2 + \Delta\gamma$, $\Delta\gamma \geq 1$) and on the cellular-map splitting strategy (on parameters N and R). In fact, as follows from formulas presented above, the C/I performance is enhanced if the cell radius R is within the break-point range and the reuse distance D is beyond this range. At the same time, stated differently for a given C/I-ratio, a channel can be reused more often, enhancing the cellular system capacity. This pure engineering subject, as well as the same engineering questions of cellular system performance, lie outside the purpose and main goal of this book. All these questions the reader can find described in detail in [5–9].

Summary

To summarize the principal results described in this chapter, as well as those lying in most chapters of this book, we present a general technique for predicting radio coverage and constructing the respective radio map and cellular map for the concrete built-up area considered. We present this prediction concept in the form of a prediction algorithm (Figure 9.13).

Algorithm

Initial Data. The initial data, which are the input parameters of cellular map construction, are as follows:

1. Terrain elevation data, that is, the digital terrain map consisting of ground heights as grid points $h_q(x, y)$.
2. Clutter map, that is, the ground cover by artificial and natural obstructions as a distribution of grid points $h_0(x, y)$; the average length of the obstructions, $\overline{L}$; the average height of obstructions in the tested area, $\overline{h}$, and the obstructions density per km^2, ν.
3. Contour map of obstructions, that is, the list of contour height for each obstruction.
4. Effective antenna height, that is, the antenna height plus a ground or obstruction height, if antenna is assembled on the concrete obstruction, z_1 and z_2 for transmitter and receiver, respectively.
5. Antenna pattern or directivity and its effective radiated power (ERP); frequency of operating, f.
6. Traffic distribution pattern (mostly for mobile wireless communication).

First step of the algorithm. To introduce the built-up terrain elevation data for three-dimensional radio-path profile construction. As the result, there is a digital map (cover) with actual heights of obstructions present in the computer memory.

Second step of the algorithm. Using all parameters of built-up terrain and of both antennas, transmitter and receiver (according to above initial data), the three-dimensional digital map is analyzed to theoretically predict the clearance conditions between antennas and the localization of the obstructions, as reflectors, surrounding both antennas.

Case One: In this case, where the tested area is built as a street grid, (e.g., blocks), the additional parameters presented in Chapters 5 and 6 are needed:

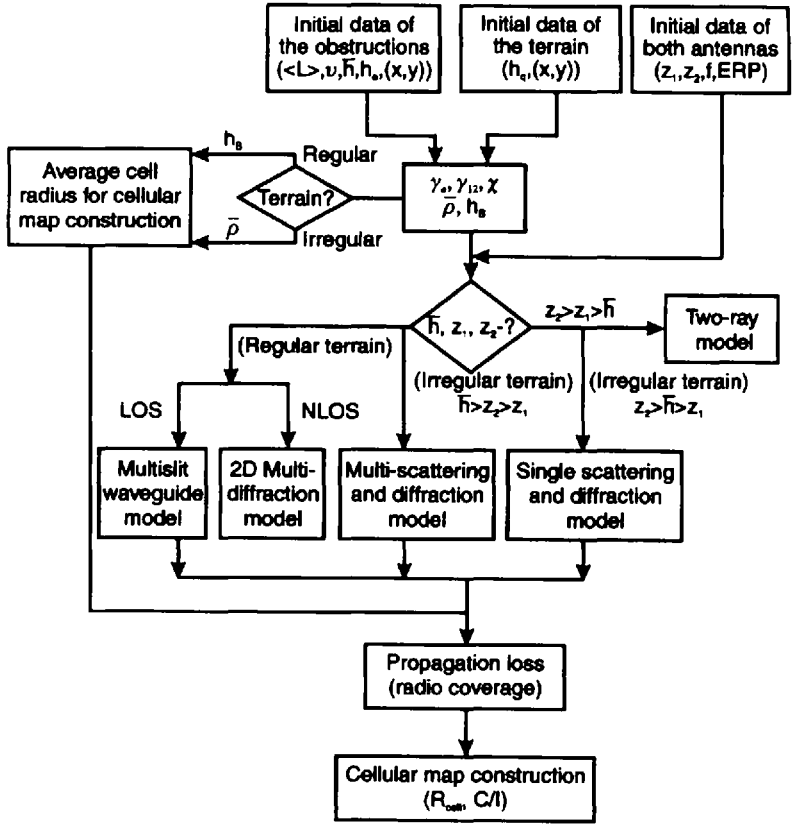

Figure 9.13 The block-scheme of the algorithm of cellular map construction.

For *LOS conditions* along the street: the average street width a; the average length of buildings (screens) and gaps between them (slits), $\langle L \rangle = L$ and $\langle l \rangle = l$, respectively; the average height of buildings, h, lining the street; the type of building material dominant in the tested area (brick, wood, concrete, etc.). All these parameters allow us to obtain the parameter of "breakness" $\chi = L/(L + l)$, which indicates the density of buildings lining the street in the block, the characteristic impedance of the building materials $Z_{EM} = (\epsilon_r - j2\sigma/f)^{-1/2}$, the normal wave propagation constant $K_n = (\pi n + j|\ln \chi|)/a$, and finally, the modules $|R_n|$ and phase φ_n of reflection coefficient R_n of normal modes that propagate along the street waveguide according to formula (5.44). All these parameters allow us to obtain the break range according to (9.13), as a distance of clearance between two subscribers, that is, the cell radius.

For *NLOS conditions*: all additional parameters about the height of neighboring buildings with respect to both antennas and the distances between them, as shown in Figures 6.8(a,b) for two types of transmitter antenna location.

Case Two: In the case of rough terrain with *randomly distributed* buildings in NLOS conditions between both antennas, the follow parameters must be taken into account: the density of buildings in the investigated area of 1 km^2, ν; the average buildings' length, $\overline{L}$; the typical correlation scales of the obstructions, l_v and l_h (see Sections 8.1 and 8.2); the type of building material dominant in the tested area.

Finally, all these parameters allow us to obtain the density of building contours in the horizontal plane $z = 0$ (the ground level), $\gamma_0 = 2\overline{L}\nu/\pi$, and then the clearance conditions between antennas, receiver and transmitter, (e.g., the average horizontal distance of the line-of-sight $\overline{\rho}$) as a cell radius $\overline{\rho} = \gamma_0^{-1}$.

Third step of the algorithm. The various factors obtained earlier are then used for the computer program based on the three-dimensional multislit waveguide model in LOS conditions, and the Bertoni et al. model in NLOS conditions for urban areas with regularly distributed rectangular crossing streets (according to Section 5.5 and Section 6.2) which we denoted here as the first case. For the case of the irregular built-up terrain (which we denoted as the second case), the three-dimensional multiparametric model according to Section 8.2.2 must be used.

In the first case, the following formula is used to describe the field intensity decay along the straight streets in LOS conditions (see Section 5.5):

$$\langle I \rangle \approx C^2 R_g^2 (|R_n| + |D_{mn}|)^2 r^{-1} \exp\{-|\ln \chi| R_n || [(\pi n - \varphi_n)/a] r/\rho_n^{(0)} a\} + D^2 R_g^2 [(1 - (|\chi R_n|)^2)/(1 + (\chi |R_n|)^2)]^2 r^{-2} \tag{9.23}$$

and formulas (6.22) to (6.26) are used to describe the situation in urban scene with rectangular crossing-streets plan in NLOS conditions. All parameters in (9.23) are described in Section 5.5.

In the second case of irregular built-up terrain with *uniform* building heights distribution, the single-scattering with diffraction formula

$$\langle I_{inc}(\mathbf{r}_2)\rangle = \frac{\Gamma\lambda l_v}{8\pi[\lambda^2 + (2\pi l_v \gamma_0 (h - z_1))^2]d^3}\,[(\lambda d/4\pi^3) + (z_2 - h)^2]^{1/2} \tag{9.24}$$

for the incoherent part of total field is taken into account, if one of the antennas is higher than building rooftops, and the multiscattering with diffraction formula

$$\langle I_{inc}(\mathbf{r}_2)\rangle = \frac{\Gamma^2\lambda^3 l_v^2}{24\pi^2[\lambda^2 + (2\pi l_v \gamma_0 (h - z_1))^2][\lambda^2 + (2\pi l_v \gamma_0 (h - z_2))^2]d^3} \tag{9.25}$$

for the incoherent part of total field is taken into account, if both antennas are lower than the rooftops.

In the case of irregular built-up terrain with *nonuniform* building heights distribution, the corresponding formulas, instead of those described by (9.24) and (9.25), for single-scattering with diffraction

$$\langle I_{inc}(\mathbf{r}_2)\rangle = \frac{\Gamma\lambda l_v}{8\pi[\lambda^2 + (2\pi l_v \gamma_0 f(z_1))^2]d^3}\,[(\lambda d/4\pi^3) + (z_2 - h)^2]^{1/2} \tag{9.26}$$

and for double-scattering with diffraction

$$\langle I_{inc}(\mathbf{r}_2)\rangle = \frac{\Gamma^2\lambda^3 l_v^2}{24\pi^2[\lambda^2 + (2\pi l_v \gamma_0 f(z_1))^2][\lambda^2 + (2\pi l_v \gamma_0 f(z_2))^2]d^3} \tag{9.27}$$

must be taken into account.

Here the functions $f(z_1)$ and $f(z_2)$ describe the built-up terrain profile

$$f(z_1) = H(h_1 - z_1)(h - z_1) + H(z_1 - h_1)H(h_2 - z_1)\,\frac{(h - z_1)^{n+1}}{(n + 1)(h_2 - h_1)^n} \tag{9.28a}$$

and

$$f(z_2) = H(h_2 - z_2)(h - z_2) + H(z_2 - h_1)H(h_2 - z_2)\frac{(h - z_2)^{n+1}}{(n + 1)(h_2 - h_1)^n} \tag{9.28b}$$

where the average buildings' height h is determined by the following expression

$$h = h_2 - n(h_2 - h_1)/(n + 1) \tag{9.29}$$

As a result, the signal power distribution over the terrain is obtained. All presented formulas are derivated for the case of isotropic antenna pattern. To take into account the directivity of transmitting and receiving antennas, one must take into account formulas (9.23) to (9.27), the EPR of both antennas. These data must be constructed on the computer display as a two-dimensional regular or color radio map, a contour map, which describes a ground cover by radio signal for a tested built-up area and for given positions of both antennas.

Fourth step of the algorithm. At this last step, the reader can split the coverage map on a set of cells to obtain the *cellular map* of the tested urban area. Because the shape and size of each cell depends on the propagation phenomena, we recommend the reader use the technique described above in Section 9.3 by using formulas (9.13) and (9.14) to (9.17) for a corresponding concrete situation in an urban scene.

And, finally, the technique of cellular map construction described above is sufficiently accurate and more general than that presented in [5–9]. It is also simple to use and recommended as a basic technique for cellular system planning.

References

[1] Jakes, W. C., Jr., *Microwave Mobile Communications*, New York: John Wiley and Sons, 1974.

[2] Lee, W. C., *Mobile Communication Engineering*, New York: Nill Book Co., 1985.

[3] Rappaport, T. S., *Wireless Communications*, New York: Prentice-Hall PTR, 1996.

[4] Feuerstein, M. L., and T. S. Rappaport, *Wireless Personal Communication*, Norwood, MA: Artech House, 1992.

[5] Mehrotra, A., *Cellular Radio Performance Engineering*, Norwood, MA: Artech House, 1994.

[6] Lee, W. Y. C., *Mobile Cellular Telecommunications Systems*, New York: McGraw-Hill Publications, 1989.

[7] Linnartz, J. P., *Narrowband Land-Mobile Radio Networks*, Norwood, MA: Artech House, 1993.

[8] Parsons, L. D., *The Mobile Radio Propagation Channels*, New York-Toronto: Pentech Press, 1992.

[9] Faruque, S., *Cellular Mobile Systems Engineering*, Norwood, MA: Artech House, 1995.

Acronyms

2DMD	two-dimensional multidiffraction
C/I	carrier-to-interference level
CW	crossing-waveguide model
EBU	European Broadcasting Union
ELF	extremely low frequency
EM	electromagnetic
FAU	fixed access unit
GTD	geometrical theory of diffraction
HF	high frequency
LF	low frequency
LOS	line-of-sight
MDS	model of double scattering
MGW	multigain wireless
MSS	model of single scattering
NLOS	no line-of-sight
RPU	radio port unit
RSL	receiving signal level
RSSI	radio signal strength indication
(S/N)	signal-to-noise ratio
UHF	ultra high frequency
VHF	very high frequency
VLF	very low frequency

This page intentionally left blank

About the Author

Dr. Nathan Blaunstein received his B.S. and M.S. degrees in radio physics and electronics from Tomsk University, Tomsk (Soviet Union), in 1972 and 1975, respectively. He received his Ph.D. and D.S. degrees in radio physics from the Institute of Terrestrial Magnetism, Ionosphere, and Radiowave Propagation (IZMIR) at the Academy of Sciences, Moscow, in 1985 and 1991, respectively. He is currently a scientific adviser at ECI-Innowave Telecom, a company in Israel, where he actively participates in wireless local-loop system performance and services.

The text is based upon the author's work as a researcher in cellular communication. Dr. Blaunstein has more than 25 years of experience as a theoretician in problems of radio-wave propagation through various media, examining propagation phenomena in urban, atmospheric, and ionospheric channels for the purposes of cellular mobile, personal, and satellite communication, as well as for radar applications. In the past several years he has been investigating special problems of UHF/L-band propagation in various environments for the purpose of increasing the efficiency of the multigain wireless (MGW) local-loop systems produced by Innowave-ECI Telecom (formerly Tadiran Telecom) of Israel. He is also an Associate Professor, teaching courses on radio-wave propagation in urban cellular channels for undergraduate and postgraduate students of electrical and communication engineering at Ben Gurion University in Beer-Sheva, and Tel-Aviv University.

Prior to coming to Israel, Dr. Blaunstein was a senior scientist, then an Associate Professor and a Professor at Beltsy University, Moldova. His research interests include problems of radio wave propagation, diffraction and scattering in various media for purposes of radio location, mobile satellite and terrestrial communications, and cellular and mobile systems performance and products.

This page intentionally left blank

Index